Sheet Metal Forming Simulation Using Explicit Finite Element Methods

Nielsen, Karl Brian

Publication date:
1997

Document Version
Publisher's PDF, also known as Version of record

Sheet Metal Forming Simulation using Explicit Finite Element Methods

by

Karl Brian Nielsen

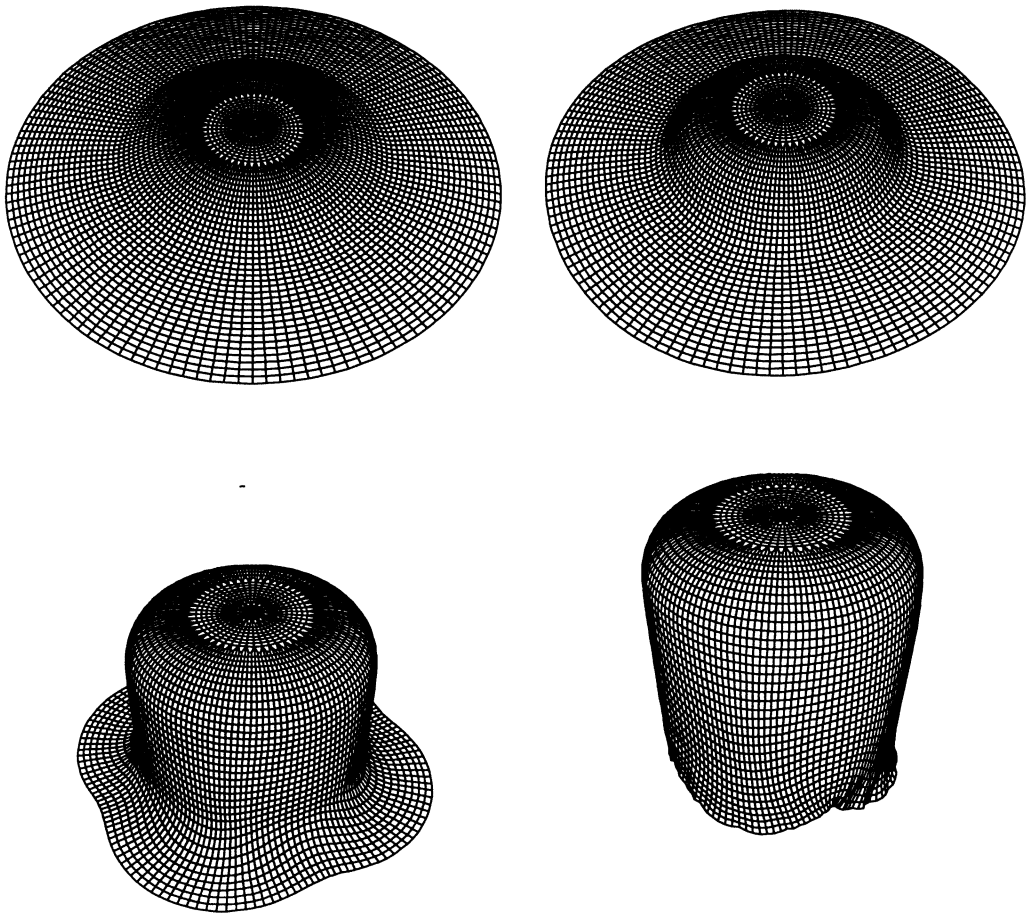

Third Edition
Marts 2000
The Sheet Metal Forming Group
Department of Production
Aalborg University
Denmark
ISBN 87-89767-69-6

Preface

The present Third Edition of Sheet Metal Forming Simulation using Explicit Finite Element Methods has been made available due to an apparent request for literature to cover the coupling between the area of continuum mechanics with the area of advanced product and process development with emphasis on sheet metal forming.

This Third Edition is essentially identical with the first version published in 1997 apart from minor corrections.

It is my sincere hope that readers can benefit from my presentation and I will be very pleased to receive any comments that may improve eventual forth coming editions.

Aalborg, Marts 2000

Karl Brian Nielsen

Preface to the first edition

This thesis present the main results of a five years research period, the research has been conducted in the field of sheet metal forming at the Department of Production, Aalborg University, Denmark. The present thesis is one of the requirements to be fulfilled to acquire a Ph.D. degree.

The work reported in this thesis has been aimed at obtaining state of the art concerning finite element methods used in analysis of sheet metal forming processes and has been carried out during the period November 1991 to January 1997. One of the purposes with the project has been to introduce and integrate the FE-technique in the Sheet Metal Forming Group at Aalborg University.

The basic idea and goal behind the writing of the thesis have been to give a firm foundation which may be used by engineers currently skilled within the area of sheet metal forming to become acquainted with finite element analysis as a practical tool, and the reversal: For people currently active in finite element methods/mechanical engineering in a more broad sense wishing to get an impression of most of the practical (and theoretical) problems typically arising in connection with sheet metal forming.

Acknowledgements

The financial support from the Faculty of Engineering and Science during the period as well as financial support from Nordisk Industrifond is greatly acknowledged.

First of all I would like to thank my supervisor Professor Joachim Danckert for his constant encouragement, vivid engagement, inspiring and supporting guidance, immense competence within the field of sheet metal forming and his successful efforts to provide good research conditions and facilities for our research group.

Also a thank to Dr. John O. Hallquist, Livermore Software Technology Corporation and Dr. Larsgunnar Nilsson, Engineering Research AB for providing the possibility of using LS-Dyna3d and associated products in my research.

Another special thank goes to Niclas Brännberg for his valuable help on many matters especially concerning computers and software, becoming my friend and colleague during my two stays at Linköping University. Another thank to Professor Larsgunnar Nilsson for letting me into his group at Linköping University, inspiring me to work on the Current Stiffness Parameter and not least for arranging social events as well.

Furthermore I would like to thank my colleagues and friends Jens Mortensen, Jens Folkmar Andersen, Keld Albrektsen, Torben Gade Faurholt, Morten Rikard Jensen and Shi-Hong Zhang for our joint work on numerous matters during the period.

Also a thank to Poul Højbjerg for always being willing to assist in the laboratory and to Lis Bach, Hanne Skjellerup and Pia Marshall for carefully correcting my written english.

Almost last but not least I would like to thank all the people at the Department of Production, Aalborg University and at the Division of Solid Mechanics, Linköping University whom I came to know over the years.

Finally, I would like to give my sincere thank to my wife Hanne and daughters Nicla and Nicole who, luckily, escaped the experience of having to put up with me during the writing of this thesis.

Aalborg, September 1997

Karl Brian Nielsen

The front page figure shows a deep drawn cylindrical cup at four stages in the process. The blank is made from mild steel and material behaviour is modelled with Barlat's 2D yield criterion.

Contents

Abstract

The objective of this project has been to illustrate and evaluate the use of the explicit finite element method in connection with simulation of sheet metal forming processes. A review of the most common failures in sheet forming is given and it is concluded that a majority of process faults are related to structural and material instability.

The thesis gives a short overview of FE-approches typically used in the simulation of sheet forming; from this overview it is concluded that the most suitable approach is the one based on explicit finite element. A discussion of the explicit method used in connection with simulation of quasi-static problems is given. The theory of plasticity is presented along with a discussion of the numerical integration procedures. Based on a review of yield criteria, Barlat's 2D criterion and Hill's 48 criterion are found suitable for modelling the anisotropic behaviour of metal sheets and are chosen for implementation.

Structural instability is discussed and the use of three proposed methods is illustrated and discussed. The three metods are based on: The Current Stiffness Parameter, Hill's uniqueness criterion and the Rayleigh coefficient. The methods lead to additional information concerning the stability of the problem without increasing the computational effort significantly, however, it is evaluated that in order to become direct usuable the methods need refinement. It is shown that anisotropy influences wrinkling behaviour strongly, an aspect which has previously often been overlooked. Analyses included in the thesis may indicate that the stability criteria utilized previously are too simplified and they only detects the resulting wrinkle appearance. Examples show that the instability appears at an earlier stage in the process than at the time where the resulting wrinkling mode appear. Wrinkling behaviour is shown to be strongly influenced when scaling the loading rate too much. For stable processes the process velocity can on the contrary often be scaled with factors of thousands without effecting the predicted geometry significantly.

A review of fracture criteria is given including a short discussion on damage mechanics leading to the conclusion that the most promising approach to improve the reliability in the prediction of fracture is to include damage theories in the constitutive modelling. In connection with the evaluation of forming limits a programme based on the Marciniak-Kuczynski theory is developed which, in contrast to previous approaches, includes 1) elasticity, 2) the possibility to use different material models for the homogeneous and the imperfection zone, 3) arbitrary orientation of the material coordinate system and 4) arbitrary strain paths.

Some of the most common test methods are reviewed, primarily with consideration for

the determination of forming limit diagrams, leading to the conclusion that the Marciniak Double Blank Method seems to be superior to the other methods. Another result is that the Erichsen Index is shown to be a formability measure which between two sheets can indicate effects opposite to the effects indicated by the forming limit diagrams. It is also shown that many processes are very sensitive to variation in boundary conditions, an aspect which is found to be of outmost importance to take into account when modelling sheet metal forming processes.

The implemented material model is shown to give very accurate results for many examples, however, it is indicated that the predictions are best for forming problems dominated by stretching. Regarding strain, geometry and wrinkling formation accurate information can be obtained, however, it is concluded that the primary advantage is obtained from the qualitative results - and it is postulated that companies where the efficiency of sheet metal forming processes is vital must apply the advantages from FE-analysis in order to remain competitive.

By examples it is illustrated how explicit FE-analysis may be used in order to evaluate process severity, final part geometry as well as trouble shooting. It is also shown that the FE-method can be efficiently combined with a numerical optimization scheme.

Danish Abstract

Formålet med dette projekt er at illustrere og vurdere brugen af den explicitte finite element metode i forbindelse med simulering af metal plade formgivningsproces. Afhandlingen opsummerer de mest almindelige fejltyper inden for pladeformgivning og det konkluderes, at størstedelen af proces fejltyperne er relateret til strukturel- og materialeinstabilitet.

Afhandlingen sammenfatter, de for simulering af plade formgivning, typisk anvendte FE-metoder; baseret herpå konkluderes det, at den bedst egnede metode er explicit finite element metoden. I afhandlingen behandles den explicitte metode anvendt til simulering af quasi-statiske problemer. Plasticitetsteorien præsenteres, og i den forbindelse diskuteres numeriske integrationsmetoder. En række flydekriterier opstilles og på baggrund heraf vælges det at implementere Barlats 2D flydekriterie og Hill 48 flydekriterie, da disse findes bedst egnede til modellering af den anisotrope materialeopførsel, som typisk opstår for metal plade.

Strukturel instabilitet behandles og anvendelsen af tre foreslåede metoder til prediktering af instabilitit illustreres og behandles. De tre metoder er baseret på: The Current Stiffness Parameter, Rayleigh koefficienten og Hill's uniqueness kriterie. Metoderne giver yderligere information vedr. strukturel instabilitet uden at øge beregningstiden væsentligt, det vurderes dog, at metoderne skal forfines for at blive direkte anvendelige i forbindelse med FE-simulering. Det vises, at material anisotropi i væsentlig grad påvirker dannelsen af folder; et aspekt, som oftest har været negligeret. De i afhandlingen inkluderede analyser indikerer, at de tidligere anvendte stabilitetskriterier er for simplificerede. Disse metoder finder kun fremkomsten af folder. Eksempler viser at instabilitet optræder i processen tidligere end formationen af den type folder, som ses på den færdige komponent. Foldedannelse vises ligeledes at være afhængig af den anvendte skalering af proceshastigheder. Modsat dette vises det, at stabile processer ofte kan modelleres med proceshastigheder, som er skaleret tusindfold uden at den predikterede geometri påvirkes i væsentlig grad.

Der foretages en summering af brudkriterier, som inkluderer en kort diskussion af damage mechanics, hvilket fører til konklusionen, at den mest lovende mulighed for forbedring af brudestimatet er at inkludere damage mechanics i den konstitutive modellering. I forbindelse med vurderingen af formbarhedsgrænser er der udviklet et program baseret på Marciniak-Kuczynski teorien. Dette program åbner i forhold til tidligere anvendelser af teorien mulighed for at inkludere 1) elasticitet, 2) forskellige materialemodeller i henholdsvis den homogene zone og imperfektions zonen, 3) arbitrær orientering af material koordinatsystemet og 4) vilkårlige tøjningsveje.

Et udvalg af de mest anvendte test metoder sammenfattes, primært med henblik på bestemmelse af formbarhedsgrænse kurver. Sammenfatningen leder til konklusionen, at Marciniak Double Blank Method er de andre metoder overlegen. Et andet resultat i denne forbindelse er, at det påvises, at Erichsen Indekset er et formbarhedsmål, der kan indikere effekter fra en plade til en anden, som er modsat de effekter, som indikeres af pladernes formbarhedsgrænse kurver. Det vises ligeledes, at mange processer er sensitive overfor variationer i randbetingelser; et aspekt, som det har stor betyding at inkludere, når pladeformgivningsprocesser modelleres.

Den implementerede materialemodel viser sig at give nøjagtige resultater i mange eksempler, men det indikeres ligeledes, at de predikterede deformationer er bedst for problemer, som domineres af strækformning. Hvad angår tøjninger, geometri og dannelse af folder kan der opnås gode kvantitative resultater, men det konkluderes, at den primære fordel er de kvalitative resultater - og det postuleres at for virksomheder, hvor effektiviteten af pladeformgivningsprocesser er vigtig, er det nødvendigt at udnytte fordelene ved FE-analyse for at forblive konkurrencedygtige.

Gennem eksempler er det vist, hvorledes explicit FE-analyse kan anvendes til vurdering af processikkerhed og slutgeometrier for den formede komponent samt til trouble shooting. Det vises ligeledes, at FE-metoden kan kombineres effektivt med numeriske optimeringsalgoritmer.

Chapter 1

Introduction and Background

Sheet metal forming processes are among the most common processes used in industry, and a high total volume is produced by using this type of process. The high volume mainly arises from the automotive industry, but also packages are consuming large amounts of sheet metal, for example beer cans, medicine packages, food containers. Although sheet metal forming has been subject to tremendous experimental and analytical work throughout the years, there are still many mechanisms, especially related to evolution laws, instability problems, surface defects, constitutive behaviour (incl. friction) which are not described and understood in detail.

Analyses and simulations of metal forming processes using finite element (FE) methods were first seen in the middle of the 1970's. These first attempts to simulate sheet metal forming processes were based on rather simple approaches (e.g. Kobayashi et al. [128, 132] and Wang and Budiansky [217]), nevertheless, they can be regarded as pioneers within the field. In the beginning of the 1980's a very strong development in the solution methods for non-linear problems was noticed mainly initiated by the rapid increase in computer performance/computer cost. This rapid development has together with a big industrial and academic interest during the last 10 years resulted in very encouraging results, and major industries, mainly the automotive industry, are today using the FE-method routinely for simulating sheet metal forming processes before choosing the final design of parts and before production of the tools for the process. Metal forming processes are, due to the strong non-linearity and complexity, among the most difficult processes to simulate which can explain the academic interest in the problem. The area is also interdisciplinary involving fields as:

- Mechanics.
- Material behaviour.
- Numerical methods.
- Computer science.
- Mathematics.
- Manufacturing.

There are several reasons for the industries using sheet metal forming as an important process to engage in research within the area of FE-simulation of sheet metal forming. Typical goals are to improve the ability to:

- Evaluate manufacturability, number of stamping steps, etc.
- Estimate target geometry, spring back, bulging.
- Determine areas of necking or areas with high risk of fracture.
- Determine press size.
- Find where to put draw beads, choose lubrication, design tool geometry.
- Evaluate tool wear.
- Gain more insight in the processes.
- Decrease costs and shorten time for development of new tools/processes.
- Improve quality of the products, e.g. optimize shape, reduce residual stresses, etc.

The main reason is of course to remain competitive and today this means to be able to develop new products and models as fast as or faster than the competitors. Especially the automotive industry experiences a high demand for fast prototype development. In other industries it may be the cost per unit which is critical, e.g. in the package industry. Sheet metal forming is very complex and to be able to perform realistic simulations many areas must be mastered including:

- Non-linear and plastic material behaviour.
- Large displacement and large rotations.
- Large strains.
- Inhomogeneous deformation(localization, Lüder's band).
- Material fracture.
- Spring back.
- Wrinkling.
- Buckling.
- Surface defects.
- Fretting.
- Tribology and wear.
- Variations in material properties.
- Knowledge about new steel and aluminum types.

In many of the fields mentioned above the mechanics are not sufficiently understood and the development of better methods, constitutive theories, etc, must still be considered very important and challenging for engineers who work within the field.

In several cases the areas are studied co-operatively by industry, academia and government laboratories. This kind of constellation is especially seen in Europe and Asia, and of course the industrial and the government interest leads to favourable conditions for researchers who work in the area.

Tremendous improvements have been seen within the fundamental areas but also a pronounced switch from implicit to explicit FE-codes can be noticed during the last 5-10 years. Some of the first to take advantage of the explicit method were Honecker and Mattiasson in 1989, [98]. At the second Numisheet conference, 1993 [139] around 40 per cent of the benchmark contributions utilized the explicit method. At Numisheet'96, [131] an even more clear use of explicit FE-codes can be seen: More than 60 per cent of the reported

numerical benchmarks were based on a dynamic explicit time integration.

Previously several approaches utilizing the implicit finite element techniques have been made in order to obtain a general and reliable FE-formulation. Here it was very often realized that the main problem is lack of convergence in the solutions, a problem which is not encountered by using the explicit finite element technique.

Another reason for the rapid switch from implicit to explicit codes is that the explicit finite element codes already existed and were well developed and documented in the middle of the 1980's; this was mainly due to big resources being spent by defence and automotive industry. Typical kinds of analyses made with explicit codes have been simulation of explosive events, penetrations and crashworthiness.

In the sheet metal forming area the first hurdle has been to convince academia that a dynamic approach to a problem traditionally treated by quasi-static methods was possible. There is an ongoing discussion about whether the explicit methods are suitable for this kind of processes because wave propagation is utilized to determine material behaviour for processes which are typically regarded as quasi-static.

A schematic presentation of a future simulation system is given in figure 1.1. The figure presents the most important parts of the development of a new product where it has been chosen to use deep drawing as the process. The considerations regarding choice of process must be made in advance. In principle the figure represents what can be considered as the ultimate goal for a project of the present type, but it must be realized that only specific areas can be treated. A discussion about the chosen emphasized areas is given in section 1.3.5. Here it is chosen to review numerous typical deep drawing defects which are likely to occur. In my opinion an analysis tool should primarily be judged on the basis of a comparison between its capability to predict commonly experienced structural behaviour and the deformation mechanisms most likely to appear in a practical operation.

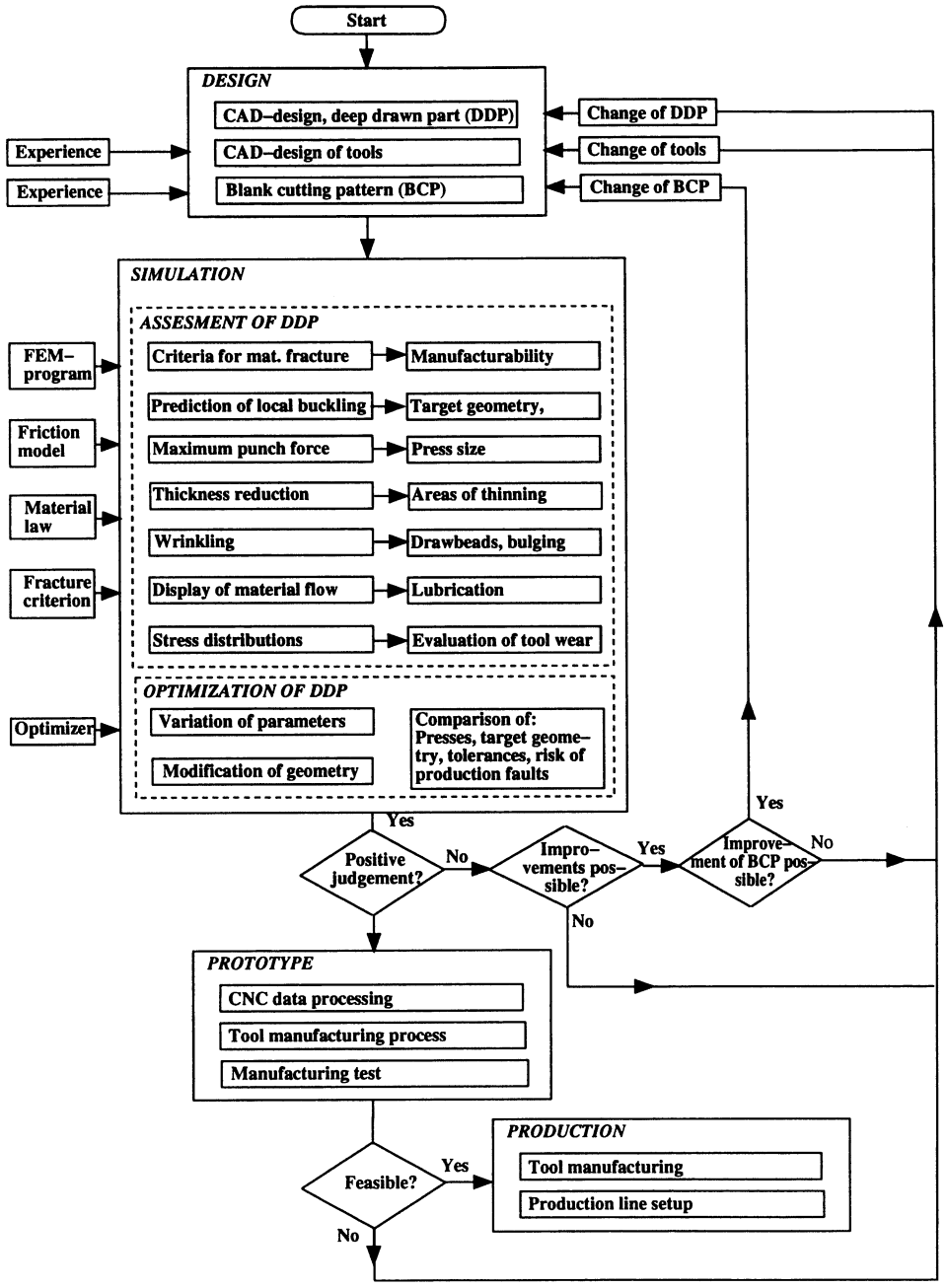

Figure 1.1: *A possible system for evaluation and optimization of a deep drawing process.*

1.1 Typical deep drawing defects

In the deep drawing process many defects can occur, and many of the final defects are caused by an instability during the process, the instability can be due to geometrical and material instabilities. In the following a number of defects and a short description of the types are given. The possibilities for modelling the defects with FEM are evaluated.

1.1.1 Flange wrinkling

A typical flange wrinkling for a deep drawn cylindrical cup is shown in figure 1.2. This

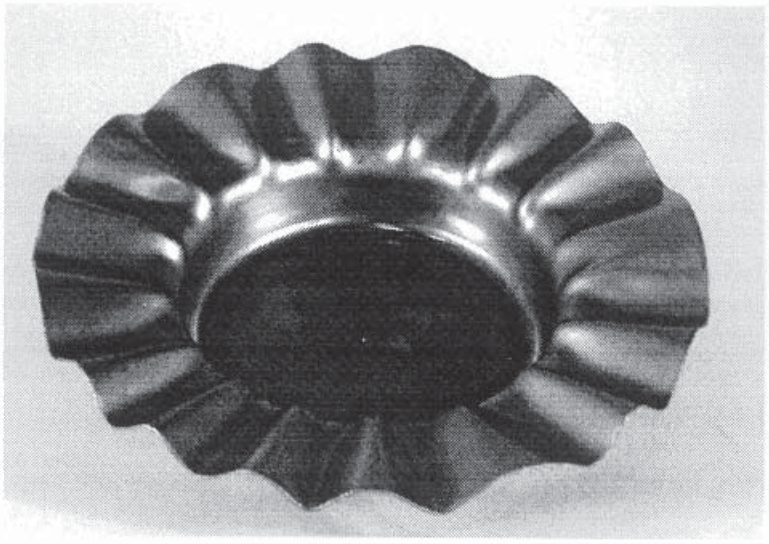

Figure 1.2: *Example of formation of wrinkles in the flange of a stainless steel cup. This formation type is normally called first order wrinkles.*

failure mode is clearly due to an instability caused by the circumferential stress. It is evaluated that this kind of instability can be modelled fairly accurately. Later in the thesis some examples are given where the predicted configuration of failed parts is compared to experiments. Often this type of instability can be eliminated by an increase in the blank holder force, but it can in some cases be a limitation to the process. For instance, when increasing the blank holder force in order to prevent wrinkles this increase can lead to fracture. Marciniak and Duncan [141] state that a blank holder pressure between 1 and 2 per cent of the yield strength of the blank is sufficient to avoid formation of wrinkles.

Many authors have dealt with the prediction of wrinkles using FEM, e.g. Kawka and Makinouchi [115] and Huo and Nakamachi [104] have obtained good results with codes of the explicit type. Other authors report difficulties in predicting wrinkles using implicit approaches, e.g. Nagtegaal and Taylor, [156] and Honecker and Mattiason, [97]. In section 6.12 an example is discussed in more detail with regard to prediction of the wrinkling behaviour and it is shown to be of importance to include anisotropic behaviour as well as to perform a careful evaluation of results obtained using explicit FE.

1.1.2 Wall wrinkling

Although the wrinkling between the blank holder and the die is normally avoided, it can for more complicated parts be difficult to avoid wrinkles, due to shear or compressive loading of local areas which are unsupported by tool parts. An example is shown in figure 1.3, where the circumferencial stresses have caused wrinkles in regions which are unsupported by tool surfaces. This type of instability can be difficult to avoid without changing the

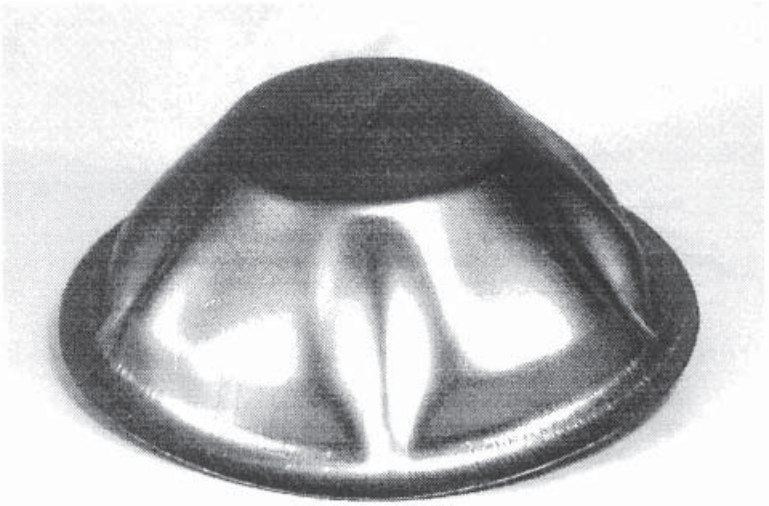

Figure 1.3: *Example of wrinkle formations in the zone between the die and the punch. Normally denoted second order wrinkles.*

tool geometry. This failure type, where only a minor part of the cup is affected, often gives rise to a following defect, burnishing, as the load redistributes in a non-uniform way already before the wrinkles become visible. For larger parts this defect can be rather local depending on the geometry, and it can often be seen in regions which are subject to severe shear straining. This kind of failure is in principle of the same nature as flange wrinkling and can be modelled just as well with FEM.

1.1.3 Evolution of puckers

In some cases puckers are formed. As they primarily are formed during unloading due to release of elastic stresses after punch removal, they are difficult to handle in practice. An often employed technique is to increase the drawing resistance at the end of the process and hereby introduce higher membrane stresses, whereby the effects of the bending stresses are eliminated or reduced. This will normally reduce the problems with puckers that are formed due to a inhomogeneous stress distribution in the sheet. For bigger parts, e.g. panels for automobiles, this failure type can be very small in dimensions (height of puckers), but can nevertheless, due to cosmetic reasons, cause the part to be scrapped. This type of failure can be an instability problem (snap-through like behaviour which often leads to fixability problems), but very often the final shape is formed in a stable manner (elastic unloading). Both effects are possible to analyse with FEM. However, for more flexible parts this may be problematic when using explicit finite element methods. As the parts become more and more flexible problems arise when performing spring back analysis using artificial damping.

One example where almost all explicit analyses failed to predict the final shape was the front fender benchmark from Numisheet'93. Another aspect of importance within the area of spring back is whether elastic parameters, Young's modulus and Poisson's ratio, can be assumed to be unaffected by plastic deformation.

1.1.4 Step rings

Step rings are caused by the initial contact between tool and blank and the marks are in some cases directly visible. In figure 1.4 step rings that typically occur in reversal deep drawing are illustrated. When thickness profiles are measured these zones become even

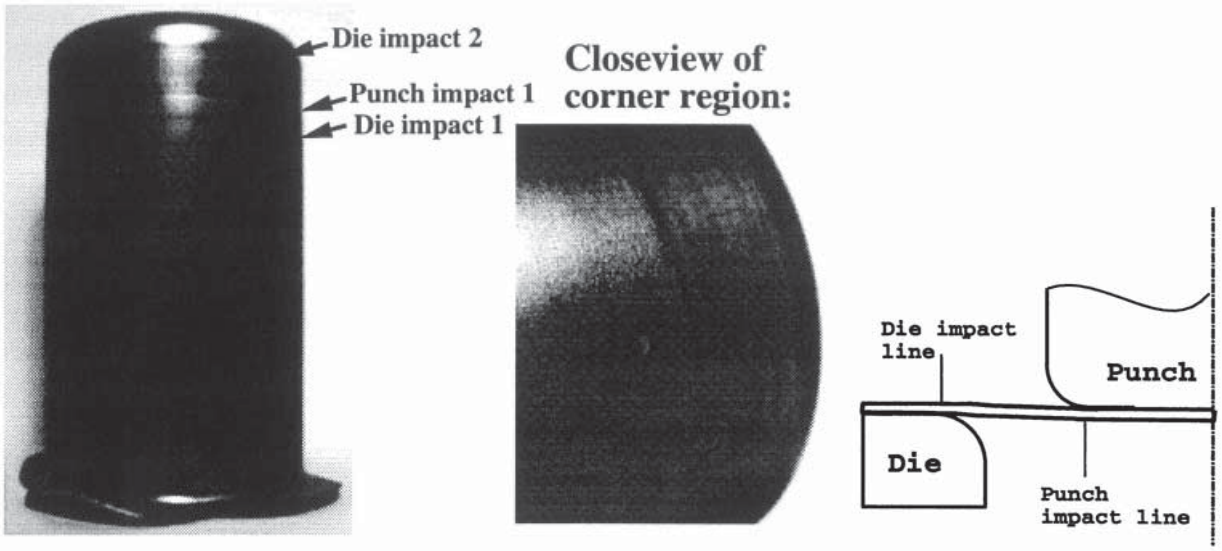

Figure 1.4: *Cylindrical cup formed by reversal drawing. In this case the step rings are directly visible. Sketch over position of step rings.*

more clear. Especially for rotational symmetric specimens the effect is characteristic, and it is in general rather difficult to avoid. As shown in section 9.1 (Deep drawing of cylindrical cups) these defects can be clearly detected using FE-analysis.

1.1.5 Orange peel

The orange peel effect is caused by rotation of big grains that lead to an orange like surface appearance. The effect is mainly observed in aluminum, where the big grains are due to abnormal grain growth during heat treatment. This failure type is evaluated not to be realistic to simulate, but it may be possible to develop constitutive models that are capable of describing these effects or to make post-processing facilities, which can be used for calculation of the risk of orange peel based on the straining history and the heat treatment.

1.1.6 Draw marks and galling

Draw marks are often seen in sheet metal forming; They can be due to wear or pick up, but also defects that are present in the blank, can cause this type of defects. Presently

draw marks cannot be predicted using FEM, as the sheet is assumed homogeneous and as the effects of wear are seldom included in the process modelling.
Draw marks must be characterized as a surface defect with only limited effect on the process. They normally occur due to initial defects of surfaces, either on the tools or the blank. In general it must be evaluated that these events cannot be taken into account in a general sheet forming analysis. An example on draw marks due to galling is shown in figure 1.5 in the second stage of a reversal drawing. The galling takes place due to a poor die surface used in the second stage of a reversal drawing. It can also be noticed that 6

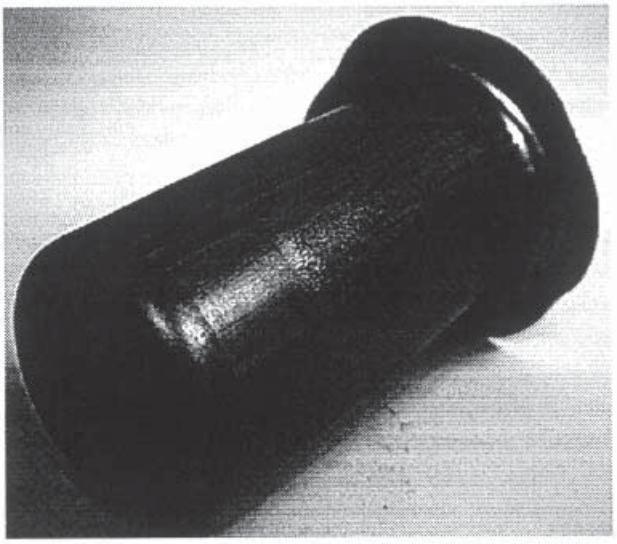

Figure 1.5: *Reverse drawn cup showing scratches. Another interesting aspect for this particular cup is the number of ears. In this case 6 ears are formed which is rather uncommon. The particular steel had Lankford coefficients on 0.84, 1.11 and 1.09 in 0°, 45° and 90° to the rolling direction, respectively.*

ears are formed in contrast to the normal 4 ears. This effect can be seen for various sheets in the reversal drawing process. Also, figure 1.5 shows very clearly the border between the material which has been in contact with the die and the material which initially is placed over the punch-die gab.

1.1.7 Fractured rim

Deep drawn parts can fracture at the rim, for example as a consequence of flange wrinkling. If wrinkles develop in the flange the punch load can increase significantly as the wrinkles are squeezed in the tool gab. The reason why the part fracture at the rim can be due to reduced formability (the wrinkles lead to significant additional plastic straining), and/or due to an inhomogeneous distribution of the tensile load arising from the squeezing.

This failure is caused by an instability (diffuse instability succeeded by local instability) and at least the diffuse instability can be modelled reasonably accurate in a FE analysis. The very local effects of squeezing cannot be expected to be solved accurately using shell elements which are based on the assumption of zero transversal stress. However, if the increased drawing resistance is due to wrinkles the part must normally be scrapped due to the wrinkles even if no fracture occurs at the rim.

1.1.8 Fractured bottom

The weakest area in a cylindrical cup is normally the zone around the punch nose region, where the material is primarily stretched. Material placed higher on the cup wall has experienced bending as well as unbending that lead to a higher strain hardening without reaching the same degree of thinning. At the same time this higher placed material has been drawn into a smaller radius leading to a thickening effect in the upper part of the cup wall. If the localization process leading to the fracture shown in figure 1.6 is to be modelled

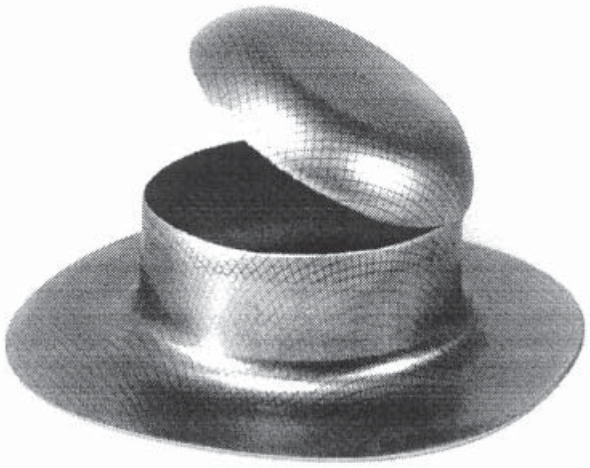

Figure 1.6: *Partly drawn cup made from mild steel. This example gives a very good picture of the fracture placed directly at the beginning of the straight part of the punch. A typical draw fracture occurs very close to the actual line of tool to blank contact.*

with some accuracy the most commonly used technique today is to use adaptive remeshing. The purpose of such an approach is normally to follow the development of the fracture, which seen from a productional point of view is less interesting. Here one is satisfied with the evaluation: fracture - no fracture. Many authors have dealt with prediction of this kind of necking failure in connection with FE-simulations, e.g. Cao et al. [41] by using a FLD approach to evaluate process severity, and Hora et al. [99] who discuss the possibilities to predict failure in a direct way by using FE-simulation of the real deformation state and the indirect way by performing a comparison between stress or strains with critical values. Another approach to better model necking behaviour has been employed, see e.g. de Borst et al. [57] and Yu et al. [225]. They use non-local theories of plasticity to better model the localization effect. Using this approach raise the need of an additional material parameter: An internal length scale.

Regarding the prediction of fracture with FE it is evaluated that for materials which fracture shortly after diffuse instability it is possible (with a reasonable accuracy) to predict fracture. The behaviour after localization can on the other hand not be expected to be accurate - it will strongly depend on the utilized mesh. My experience is that predicted fracture for deep drawing operation with mild steel and stainless steel is quite accurate, but one cannot generalize these observations as the fracture can be strongly affected by the deformation history.

1.1.9 Corner fracture

For a more complex part, especially when sharp corners are to be produced, corner fracture can become a problem. To overcome this problem, it will often be necessary to compromise between wanted and obtainable shape. Again, the failure is due to instability. Figure 1.7 shows a rectangular box which failed in the region just after the curvature of the die. This failure type is, however, not the only type experienced for rectangular boxes. In figure 1.8 is shown another type of failure; punch corner fracture.

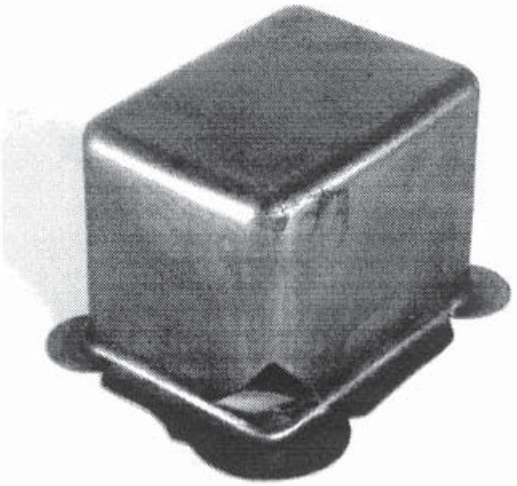

Figure 1.7: *One of the typical failures for parts with relatively sharp corners. The material is mild steel.*

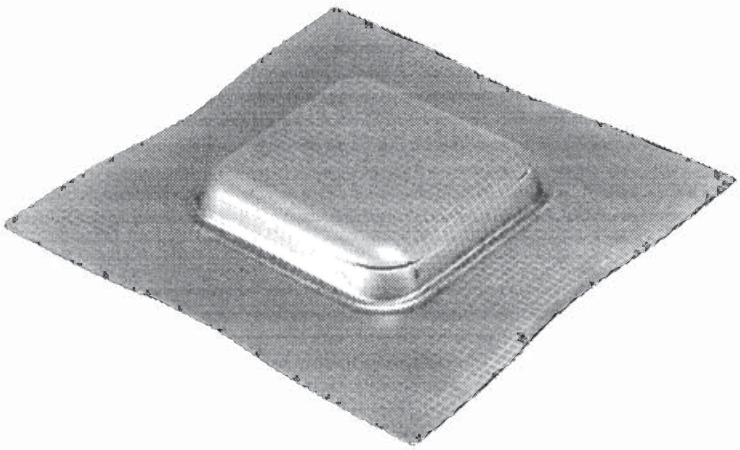

Figure 1.8: *Deep drawn aluminum box that shows a typical corner failure in the region around the punch shoulder radius.*

1.1.10 Directional earing

Earing is often unwanted, and this problem is especially inevitable when materials with in-plane anisotropy are used. Figure 1.9 shows a typical formation of ears for a mild steel with a pronounced in-plane anisotropy. Seen from a modelling point of view, it is a question

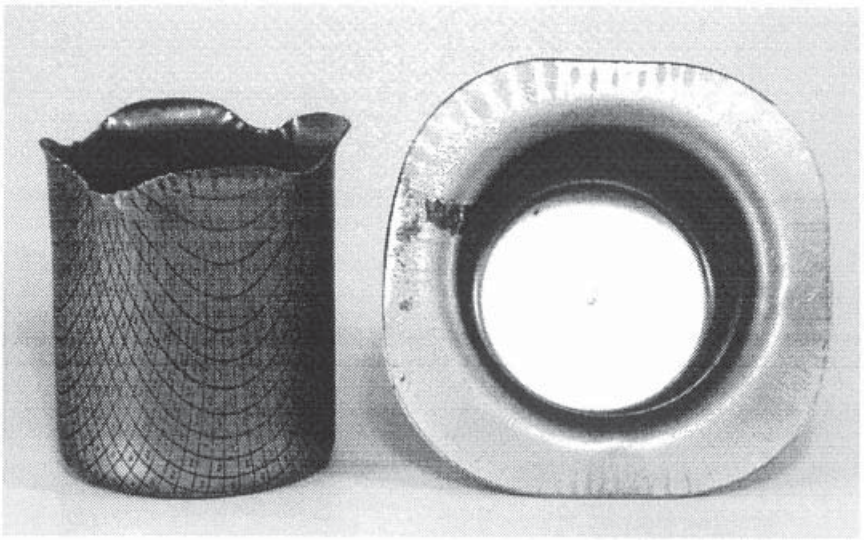

Figure 1.9: *Deep drawn cylindrical cups which show a high degree of earing due to in-plane anisotropy. Both cups are made from mild steel.*

of modelling the anisotropic behaviour correctly in order to predict the earing. As listed in section 5.7 there are many models which are at least to some degree capable of modelling anisotropic behaviour. Assuming the constitutive behaviour is well described no problems are involved in predicting the earing tendencies with FEM. Another defect which can be caused by in-plane anisotropy is an easier onset of wrinkling due to an inhomogeneous thickness distribution. When differences in thickness arise then the blank holder pressure redistributes and may result in zones of thinner materials starting to fold.

1.1.11 Miss-strike

Misplacement of the blank leads to miss-strikes and normally failure, see figure 1.10. The best way to avoid this kind of defect is to design the tools in a way that excludes the possibility for position faults. The effects of miss-strikes can be illustrated clearly using FE-analysis. On the basis of FE-analyses it is possible to determine how accurately the blank has to be positioned to produce a sound product. However, I have found no publications that deal with this type of process safety evaluation in connection with FE-simulations.

1.1.12 Earing

For parts with a large flange and/or a high draw-in ratio earing (tool earing) can become a problem leading to failure. For large flange problems, say a double symmetric part, a small misalignment in tools (or a nonsymmetric blank holder distribution due to other reasons) may cause so high difference in the conditions for the draw-in of the flange that

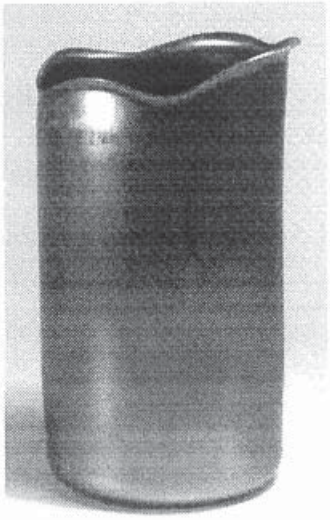

Figure 1.10: *Example of an earing which is caused by either misplacement of the blank or misalignment of the tool parts.*

one ear (or side) of the part so to speak gets stuck leading to an asymmetric drawin. But as for the directional earings and miss-strikes it is a question of modelling the parameters that influence the earing. One example is deep drawing of square boxes which is rather sensitive to the distribution of blank holder pressure: Most analyses reported on this process are based on the assumption that blank hold and die are completely aligned, but in practice it often turns out that the alignment of tools is difficult (and very time consuming). The effect of a poor alignment of tools may result in a part as illustrated in figure 1.10.

Most deep drawing tools are trimmed in order to produce parts with a satisfactory quality. An example is the deep drawing of bathtubs: Here the starting point is normally that die and blank holder are plane. When running the process certain regions of the flange will thicken and increase the resistance. If this effect is allowed to develop, a sort of earing can be the result. In order to reduce the effect of a too high local blank holder pressure the die is ground in specific regions. This trimming is normally performed by craftsmen with a lot of practical experience. Here it shall perhaps be mentioned that serious concern has been raised by industry due to an increasing lack of people with these skills, these people with practical experience in tool trimming are hard to find and are typically at the age of 50 or more.

An obvious use of FE is to improve the prediction of the resulting geometries for a given tool geometry, but one should not expect that the practical skills can be completely spared. On the other hand one can benefit from the FE-method due to two reasons: Firstly, by reducing the trimming cost and secondly, by obtaining a better documentation of the production tools. I have in several cases experienced that the documentation of tool geometry and process condition differs significantly from the actual tool geometry and the actual process conditions after trimming. For instance this problem may occur if a blank holder gap has been changed or a draw die radius has been ground to overcome production problems without the necessary feed back to the construction engineers. This is one aspect which may be important for the success of industrial use of simulation tools: Simulation of

processes can indeed lead to better documentation, but on the other hand simulations may also demand better documentation (for example when using FE-simulations for trouble shooting it is necessary that the geometry is documented correctly).

1.1.13 Burnishing

Burnishing between the blank and the tool is caused by a too small punch to die clearance or by sliding under high normal pressure. The risk can to some degree be evaluated by evaluating predicted surface load or the final thickness of the part. Here some FE-related problems may occur when using shell elements in the analysis as normal stresses are not included in the constitutive treatment and this may give raise to erroneous results. It is possible to model the transversal stress effects when these effects are of major interest, for instance in ironing and stretching operations, but a direct evaluation of burnishing is considered unrealistic.

1.1.14 Stress relief cracking

In some cases residual stresses can cause cracking of the cups after forming. Especially when forming stainless steel this type of problems can be seen and often special means must be used in order to reduce the residual stresses. Figure 1.11 shows a cup that is drawn from stainless steel which cracks after the forming operation. There is a wide range

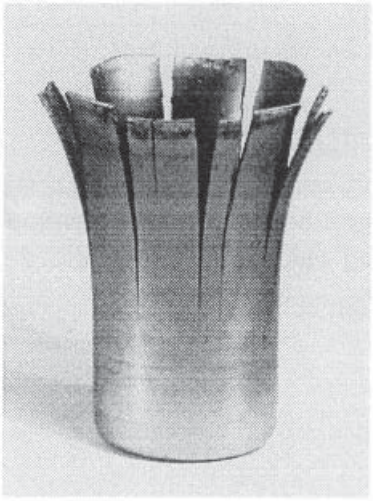

Figure 1.11: *Example of cup made from stainless steel where the formation of cracks is due to severe residual stresses. The cup is formed in a two stage deep drawing process.*

of possibilities of reducing the level of residual stresses in a deep drawn component. As the residual stresses primarily are due to the unbending one way to reduce the level is to alter the tool geometry, e.g. by using a tractrix shaped die instead of dies with the conventional round die profile as shown by Danckert [52] or by ironing as shown by Mortensen [150]. Both authors use FE-simulations to reach their conclusions so at least on a qualitative level residual stresses can be predicted with FE-technique. As the FE-technique (here considered) is based on macroscopic modelling of constitutive behaviour and it is evaluated that stress relief cracking is initiated on a microscopic level, the current level of theoretical

approaches hardly makes it possible to predict or, what is even more unlikely, to model the stress relief cracking.

1.1.15 Summary of failure types

To summarize on the failure types there are mainly two types of failures which are important in sheet metal forming: Necking and wrinkling. The wrinkling can to a reasonable degree be analysed by finite element methods where in contrast the necking seems to be more troublesome.

Some process problems arise due to material anisotropy and frictional problems. Here it must be remembered that simulation results can by no means become better than what is provided by the constitutive models. Even when using advanced models for contact and material behaviour the models put restrictions on the possible response. On the other hand, even simple models can often give an understanding of a process problem - this understanding can then be used to solve the process problem more efficiently.

The remaining defects are primarily surface defects, these defects will demand special approaches in order to predict them from simulations with FEM. No further attempts will be made to treat this kind of failures in this work. However, if a process is leading to galling it may be possible to avoid the galling by changing tool geometry in a way that leads to lower interface pressure - this improvement can be made very efficient using the FE-method.

1.2 Product development

If we regard a simplified presentation of a product development, we can present the development method with and without the use of numerical simulation:

TRADITIONAL APPROACH:

- 1: Design of part and tools.
- 2: Experimental test/Production test.
- 3: Evaluation of parameters for improvement of process.
- 4: Eventual return to 1.

APPROACH UTILIZING NUMERICAL SIMULATION:

- 1: Design of part and tools.
- 2: Simulation of process.
- 3: Evaluation of parameters for improvement of process.
- 4: Eventual return to 1.
- 5: Experimental test/Production test.
- 6: Evaluation of parameters for improvement of process.
- 7: Eventual return to 1.

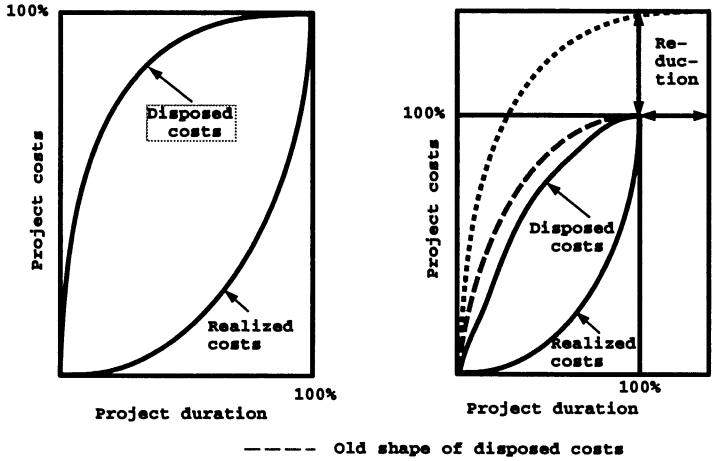

Figure 1.12: *Illustration of expected changes in the total costs when using simulation of processes.*

By using simulation in the design phase it is possible to make try-outs of various designs before testing in the workshop. Hereby, it is possible at the same time to decrease the lead time and the number of experimental tests which lead to a decrease in total development costs. This effect can be illustrated in the well known presentation of realized and disposed costs, see e.g. Mikkelsen and Riss [148]. Figure 1.12 illustrates two main reasons for performing simulations already in the design phase: 1) To decrease both development costs and the lead time, but also 2) to makes it possible to choose the final design with a better background and to delay the disposal of costs. The use of simulation tools make it possible to operate with more alternative designs for a longer period in the development phase.

Another important aspect for series production is the importance of that the process is efficient and that break downs are avoided. Nevertheless, starting a series often leads to problems owing to: wear, lubrication conditions, change in process parameters, etc. Here it can also be of great interest to be able to perform simulations in order to identify essential parameters and hereby to obtain a better background for changing and controlling parameters. Simulating the effect of tool modification or change in process parameters before the actual production is an obvious way to decrease costs.

Simulation can also be effectively used to clarify production problems and hereby make a more systematic correction possible.

1.3 Numerical solution of sheet metal forming problems

In the area of simulating sheet metal forming four essentially different methods are seen today [183]. The methods are listed below.

- Inverse methods.
- Plane strain.
- 3D Flow shell.
- 3D Elasto-plastic shell.
  - Quasi-static approach.
  - Quasi-dynamic approach.

Some more specific software tools are of course used for different applications. Examples on these methods are finite difference methods used to model deep drawing of cylindrical cups which can be found in Andersen [6], Zhang [226, 227]. Another type of software tools is expert systems as presented by for example Tisza [207] or the programme Rota developed by Schwager, (The Technical University Chemnitz-Zwickau).

The main limitation of the specific softwares is the lack of generality in their formulation, e.g. with regard to arbitrary geometries, etc. These special purpose software tools will not be discussed further in this report.

In the following some of the characteristics of the methods are given and the methods will be discussed briefly.

1.3.1 Inverse method

This method has in principle some of the wanted characteristics of an effective numerical tool to assist in the design of deep drawn parts. Based on the final geometry and an initial blank geometry it is tested whether the process is feasible. The method is based on assumption of proportional loading (quasi-static), Hencky plasticity, Coulomb friction and a simple load distribution. The method is capable of treating anisotropy and large deformations and the calculations are quick. A disadvantage of this method is that bending effects are not included directly, and hereby there is no possibility of treating wrinkling and spring back. In my opinion the method has some serious drawbacks: It is based on membrane formulations and the Hencky plasticity theory and I find the Hencky plasticity theory insufficient in many practical applications. It may be possible to extend the method to overcome some of the mentioned drawbacks and in that case the method will become interesting as an effective design tool.

This method has been developed and used by e.g. Chung and Richmond [45], Sklad [192] and El-Mouatassim et al. [69]. Batoz et al. extend the method to include bending effects [18, 19].

1.3.2 Plane strain method

Many sheet metal forming operations include areas for which it is possible to select strips which can be analysed by assuming plane strain deformation. One method, which is used here, is known as the "plane strain" method (or quick analysis of sheet forming using sectional FEM). Among authors Wagoner et al. [215] have used the method for sheet forming problems.

By this method one considers a plane strip of sheet. Punch form and blank holder force must be specified. By using an updated Lagrangian formulation and the penalty approach to treat contact a consistent formulation can be made. The method is normally solved using implicit time integrations and membrane elements. The advantage of the method is that it is quick. On the other hand the method suffers from assumption of plane strain and that no bending and wrinkling effects are included. It is, however, possible to extend the method to include spring back evaluations. This approach is very quick, but due to the many simplifications it is inapplicable as a general purpose tool.

1.3.3 3D Flow shell

The work on the 3D flow shell method was initiated by Onate and his group in Barcelona. The method is somewhat different compared to the other methods which are discussed in this chapter. The main idea of this approach is to take advantage of the similarities between elasticity and viscoplasticity. The method is described in detail by Sosnowski and Onate [194], Onate and Saracibar [167] where also further references can be found.

The simulations are based on a viscoplastic formulation where elastic strains are neglected. This theory is analog to the small strain shell theory, and in principle one can use a traditional FE-code to perform the analysis (provided that contact can be treated); table 1.1 gives the relation between the elastic and the viscoplastic formulation. The only nonlinearity taken into account is related to material behaviour. The advantage of the method

Elastic shell	Viscous shell
Displacements	Velocities
Strains	Strain rates
G,ν	$G = \frac{\sigma_y}{3\dot{\epsilon}}, \nu = \frac{1}{2}$

Table 1.1: *Relations between elastic shell theory and viscous shells.*

is that it is very quick and it is still possible to treat arbitrary geometries. One problem, however, is that elastic effects are neglected and that the method cannot directly treat wrinkling and spring back.

1.3.4 3D Elasto-plastic shell

Today most methods used for analyses of sheet metal forming problems are based on 3D shell elements combined with an elasto-plastic formulation of the constitutive behaviour.

This approach has been used by many authors and in order to get an overview of the methods that are used within the area of sheet metal forming I refer to the proceedings from the conferences: Numisheet'93 [97] for many aspects on sheet metal forming, Numiform'92 [139] for the more overall simulation of plastic forming operations and the Complas'92 and 95 Proceedings [176],[52] for detailed discussions on plasticity and algorithmic issues.

The advantage of using 3D elasto-plastic shell elements in a FE-simulation is the fact that the solution includes membrane-bending effects, history dependency and handles the contact-friction problem correctly. Wrinkling simulation can be included, and at least as regards the explicit codes treated without difficulties. Spring back can easily be included in implicit codes and it can also to some degree be treated with explicit FE. The process can be simulated as quasi-static or dynamic (or quasi-dynamic with increased loading rate) and in general more accurate and detailed results can be obtained compared to the three previous methods.

The use of 3D elasto-plastic shell elements makes is possible to perform very accurate analyses even for complicated geometries. I find that the method is the most reliable method, and it has been chosen in this work. The other methods have been left out. However, many of the topics which are discussed in the following can be utilized in other methods. The primary limitation of the method today is due to uncomplete understanding and description of the constitutive behaviour (both for plasticity as well as contact).

1.3.5 Conclusion

Based on the above discussion, the sources from the text and the additional sources, that are listed in the references, it can be concluded that much effort is today put on the following activities (see for example Wagoner [216] 1992):

- Examples of industrial applications.
- Linkage between analysis tools and CAD/CAM systems.
- Transfer of technology to the engineers who are responsible for sheet forming design and production.

The last item should be given more attention as it is necessary for the research community to be able to convince engineers, who are involved in the practical establishment of production, that simulations indeed can improve performance both in connection with part design and tool design, as well as in connection with quality aspects for existing products, otherwise it will take several years to obtain a widespread utilization. Though the methods seem mature for industrial use and are used today by major automotive industries fundamental problems still exist such as:

- Simulation of wrinkle configurations.
- Whether explicit or implicit integration methods should be used.
- Measurement and modelling of fundamental material laws.
- Boundary conditions, friction laws, etc.

Based on the discussion I have chosen to focus mainly on the following aspects in this thesis:

- Analyses of a number of relatively simple processes, where the results can be used for verification as well as demonstration purposes.
- Material modelling of metal sheets to take the most pronounced effects into account as well as some discussions on formability.
- Analyses of instability problems, especially wrinkling effects.
- To work out by means of examples and theoretical discussions some guidelines for how to obtain stable and accurate solutions of sheet metal forming problems by using explicit FE-techniques.

The attention will, in general, be focused on the FEM-programme, the material behaviour and the fracture criterion (see perhaps figure 1.1) together with an attempt to document my experience with practical sheet metal forming simulation, especially with regard to obtaining reliable and efficient analyses. Two other major topics, friction and optimization, will only be included through examples, e.g. illustration of the influence from friction conditions or use of optimization techniques to improve product quality.

In the following there will on several occasions be given a short introduction to/background for the subject/example which is being discussed/analysed. Generally, I have only used a limited number of sources - due to lack of time, it has not been possible to make an extensive literature study of all the subjects discussed in the report.

1.4 Contents of thesis

First is given a very brief restatement of the continuum mechanical formulations followed by the finite element discretization and formulation in chapter 2. In the latter part a discussion of implicit versus explicit methods is also given.

Chapters 3 and 4 have been devoted to a discussion on solution strategies by using explicit FE-codes, and chapter 4 also includes an evaluation of several shell elements which are available in LS-Dyna3d (illustrated by example).

Chapter 5 introduces the theory of plasticity, and a list of yield functions proposed for modelling sheet metals is given and to some degree discussed. Some existing criteria are selected for implementation. Also a list of the most common hardening laws and a scheme for implementing strain rate effects are presented. Expressions for the plastic multiplyer are established for strain and work hardening materials, respectively. A discussion on different numerical approaches to implement constitutive models is given and a scheme for a general algorithm is established and utilized for the implementations of some specific yield criteria.

Chapter 6 introduces some approaches to indicate/predict instabilities with explicit FE. The approaches are then verified on a number of rather simple, elastic problems with

geometric instability. Subsequent sections document a number of examples of processes involving failure due to instability and the examples are used as a further evaluation of the approaches.

Chapter 7 and 8 are sort of multi purpose chapters discussing matters on sheet metal testing, formability and some computational aspects. The chapters were initially based on modelling the Marciniak test, but they have been extended to include some other test methods for characterizing sheet metals and fracture. The areas as forming limit diagrams and forming limit stress concept are also included as the importance of the areas became more and more obvious during my work.

Chapter 9 is the last chapter apart from the conclusion, and it gives a number of examples of which some are verified with experiments. Some of the examples are used to illustrate topics which are discussed earlier in the report, and others can be seen as concrete industrial problems which are analysed in order to propose solutions or just to obtain a better understanding of the problem.

Finally, conclusions which are drawn from topics discussed in the thesis are given together with proposals for future work.

Chapter 2

Continuum Mechanical Formulation and FE-discretization

To describe the general finite element (FE) theory it is necessary to state the basic continuum mechanical relations. Based on these a discretization is performed and a set of equations which can be solved by a computer are established. Schemes for performing the time integration are discussed in section 3.3.

This and the following section include a number of theories. To avoid too much confusion, areas like plasticity, dynamic relaxation, etc have been left out. It is therefore possible to treat the continuum mechanical relations and to follow the solution schemes in a slightly simpler way.

Continuum mechanics consist of four major parts: definition of stresses, motions and deformations, conservation laws and constitutive equations. The following sections give a short review of the most important aspects and definitions for the above mentioned parts, except for constitutive equations. Constitutive equations will be discussed in chapter 5, which is devoted to plasticity. The presentation of continuum mechanics is by no means a complete discussion, it should rather be regarded as a compressed presentation of some important aspects with emphasis on subjects with direct relevance to the FE-technique which is discussed in the last part of the chapter. For a more extensive discussion I refer to the general text books of: Malvern [140], Spencer [196], Gurtin [82] who cover most of the continuum mechanical theories. Malvern's book is a very good textbook which also includes many aspects of constitutive modelling and at the same time it is easy to comprehend.

2.1 True stress

Figure 2.1 illustrates a continuous body which occupies the region V with the surface S. Let P be a point on the surface S and $\mathbf{n}$ the outward normal vector (normalized) in P, and let a force $\delta\mathbf{p}$ act on a surface element with the area δS around P, we then have the relation:

$$\delta\mathbf{p} = \mathbf{t}\delta S \tag{2.1}$$

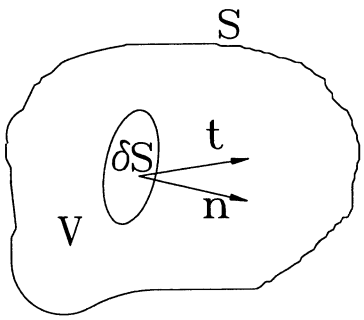

Figure 2.1: *Illustration of the surface traction* $\mathbf{t}$ *which acts on a surface element with the area* δS *and the normal vector* $\mathbf{n}$.

where $\mathbf{t}$ is introduced as the mean surface traction and it is apparently a function of the position P as well as of the direction $\mathbf{n}$. Letting $\delta S \rightarrow 0$ we obtain the surface traction:

$$\mathbf{t} = \lim_{\delta S \rightarrow 0} \frac{\delta \mathbf{p}}{\delta S} \tag{2.2}$$

At the point P there is a traction $\mathbf{t}$ which is associated with each direction through P. Depending on the orientation of the surface element the traction may vary. Given a Cartesian coordinate system with base vectors $\mathbf{e}_i$ we can write the three traction vectors $\mathbf{t}_i$ which correspond to each of the base vectors as:

$$\begin{aligned} \mathbf{t}_1 &= \sigma_{11}\mathbf{e}_1 + \sigma_{12}\mathbf{e}_2 + \sigma_{13}\mathbf{e}_3 \\ \mathbf{t}_2 &= \sigma_{21}\mathbf{e}_1 + \sigma_{22}\mathbf{e}_2 + \sigma_{23}\mathbf{e}_3 \\ \mathbf{t}_3 &= \sigma_{31}\mathbf{e}_1 + \sigma_{32}\mathbf{e}_2 + \sigma_{33}\mathbf{e}_3 \end{aligned} \tag{2.3}$$

where $\mathbf{t}_1$ is the force per unit area exerted on a surface normal to the x_1-axis and similar for traction $\mathbf{t}_2$ and $\mathbf{t}_3$. Alternatively, these relations can be expressed as:

$$\mathbf{t}_i = \sigma_{ij}\mathbf{e}_j \qquad i,j = 1,2,3 \tag{2.4}$$

Multiplying the three vector equations given in 2.4 first with $\mathbf{e}_1$ and then with $\mathbf{e}_2$ and $\mathbf{e}_3$, we can when it is noticed that $\mathbf{e}_i\mathbf{e}_j = \delta_{ij}$ obtain:

$$\sigma_{ij} = \mathbf{t}_i\mathbf{e}_j \tag{2.5}$$

which defines the stress tensor denoted the Cauchy or true stress tensor in the following. In this thesis all stresses and stress increments reported will be treated as true stress.

2.2 Motion and deformation

For a system which is undergoing a relatively large deformation it can be necessary to take non-linear straining effects into account. We regard a particle in a continuous body with the current position vector $\mathbf{x}$. If the body is deformed each particle of the body is displaced from its initial position to the current position by the displacement vector $\mathbf{u}$:

$$\mathbf{x}(t) = \mathbf{x}(0) + \mathbf{u}(t) = \mathbf{X} + \mathbf{u}(t) \tag{2.6}$$

$\mathbf{X}$ describes the undeformed configuration of the body. In the equation we identify each point by its material coordinates at the time 0, $\mathbf{x}_0 = \mathbf{x}(0) = \mathbf{X}$, which leads to:

$$\mathbf{x}(\mathbf{x}_0, t) = \mathbf{x}_0 + \mathbf{u}(\mathbf{x}_0, t) \tag{2.7}$$

This approach is called a Lagrangian description and we restrict ourselves to this description throughout the report. A strain measure is necessary to characterize the deformation of the body.

2.2.1 The Green strain tensor

In the following the Green strain is derived. If we regard a vector $d\mathbf{x}_0$ in the reference configuration, see figure 2.2, we can express its length ds_0 as:

$$ds_0^2 = d\mathbf{x}_0^T d\mathbf{x}_0 \tag{2.8}$$

We can now express the Green strain ϵ_G for the direction $\frac{d\mathbf{X}}{ds_0}$:

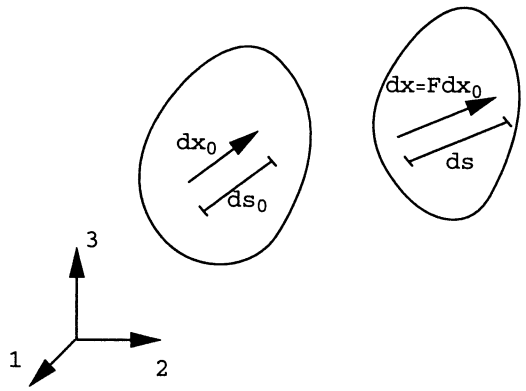

Figure 2.2: *The initial length ds^0 and the current length ds of the infinitesimal vector $d\mathbf{x}^0$ before and after deformation.*

$$\epsilon_G = \frac{ds^2 - ds_0^2}{2ds_0^2} = \frac{d\mathbf{x}^T d\mathbf{x} - d\mathbf{x}_0^T d\mathbf{x}_0}{2d\mathbf{x}_0^T d\mathbf{x}_0} \tag{2.9}$$

Expressing the vector $d\mathbf{x}$ on component form we have:

$$dx_i = \frac{\partial x_i}{\partial X_j} dx_j = \left(\delta_{ij} + \frac{\partial u_i}{\partial X_j}\right) dx_j \tag{2.10}$$

To simplify the equations both the deformation gradient tensor $\mathbf{F}$ and the displacement gradient tensor $\mathbf{D}$ are introduced:

$$F_{ij} = \frac{\partial x_i}{\partial X_j} = \frac{\partial (X_i + u_i)}{\partial X_j} \tag{2.11}$$

$$D_{ij} = \frac{\partial u_i}{\partial X_j} \tag{2.12}$$

The relation:

$$\mathbf{F} = \mathbf{I} + \mathbf{D} \tag{2.13}$$

gives the deformation gradient as the sum of the identity tensor and the displacement gradient tensor. After deformation the vector can now be written as:

$$d\mathbf{x} = \mathbf{F}d\mathbf{x}_0 = (\mathbf{I} + \mathbf{D})d\mathbf{x}_0 \tag{2.14}$$

Substitution into 2.9 leads to:

$$\epsilon_G = \frac{(\mathbf{F}d\mathbf{x}_0)^T\mathbf{F}d\mathbf{x}_0 - d\mathbf{x}_0^T d\mathbf{x}_0}{2ds_0^2} = \frac{d\mathbf{x}_0^T}{ds_0}\frac{1}{2}(\mathbf{F}^T\mathbf{F} - \mathbf{I})\frac{d\mathbf{x}_0}{ds_0} \tag{2.15}$$

The first and last factor define the initial direction and the matrix in the middle is defined as the Green strain tensor:

$$\mathbf{E} = \frac{1}{2}(\mathbf{F}^T\mathbf{F} - \mathbf{I}) = \frac{1}{2}\left((\mathbf{I} + \mathbf{D})^T(\mathbf{I} + \mathbf{D}) - \mathbf{I}\right) = \frac{1}{2}(\mathbf{D} + \mathbf{D}^T) + \frac{1}{2}\mathbf{D}^T\mathbf{D} \tag{2.16}$$

or rewritten on component form:

$$E_{ij} = \frac{1}{2}\left(\frac{\partial u_i}{\partial x_j} + \frac{\partial u_j}{\partial x_i}\right) + \frac{1}{2}\frac{\partial u_k}{\partial x_i}\frac{\partial u_k}{\partial x_j} \tag{2.17}$$

2.2.2 Typically used strain measures

For geometric non-linear systems many measures of deformation are available; the most commonly used strain measures in connection with a Lagrangian description are:

- The velocity strain tensor:

$$\dot{\epsilon}_{ij} = \frac{1}{2}\left(\frac{\partial \dot{u}_i}{\partial x_j} + \frac{\partial \dot{u}_j}{\partial x_i}\right) \tag{2.18}$$

  which is also denoted as the stretching or rate of deformation. Later on we will make use of the spin tensor as well:

$$\omega_{ij} = \frac{1}{2}\left(\frac{\partial \dot{u}_i}{\partial x_j} - \frac{\partial \dot{u}_j}{\partial x_i}\right) \tag{2.19}$$

  which expresses the rate of rotation of a material element.

- The Green strain tensor as discussed above:

$$E_{ij} = \frac{1}{2}\left(\frac{\partial u_i}{\partial x_j} + \frac{\partial u_j}{\partial x_i}\right) + \frac{1}{2}\frac{\partial u_k}{\partial x_i}\frac{\partial u_k}{\partial x_j} \tag{2.20}$$

- The Almansi strain tensor:

$$E_{ij}^A = \frac{1}{2}\left(\frac{\partial u_i}{\partial x_j} + \frac{\partial u_j}{\partial x_i} - \frac{\partial u_k}{\partial x_i}\frac{\partial u_k}{\partial x_j}\right) \tag{2.21}$$

  which is also denoted as the Eulerian strain tensor.

  For comparison we have the definition of engineering strain:

- The engineering strain:

$$e_{ij} = \frac{1}{2}\left(\frac{\partial u_i}{\partial x_j} + \frac{\partial u_j}{\partial x_i}\right) \tag{2.22}$$

Finally, we have the logarithmic strain, which is typically used in connection with sheet metal forming problems:

- The logarithmic strain for uniaxial stretching:

$$\epsilon_L = \int_{l_0}^{l_1} \frac{dl}{l} = ln\left(\frac{l_1}{l_0}\right) \tag{2.23}$$

and if we generalize to 3 dimensions:

$$d\epsilon_{ij}^L = \dot{\epsilon}_{ij}dt = \frac{1}{2}\left[\frac{\partial(\dot{u}_i dt)}{\partial x_j} + \frac{\partial(\dot{u}_j dt)}{\partial x_i}\right] \tag{2.24}$$

where t is used as the time measure. But a generalization to a total deformation measure is not possible for arbitrary deformations. In case the principal axes do not rotate during the deformation it is possible to perform the integration to obtain the total logarithmic strain measure. As regards the increments, the use of logarithmic strains and the rate of deformation are essentially equivalent ($d\epsilon_{ij}^L = \dot{\epsilon}_{ij}dt$).

2.2.3 Rigid body rotation and engineering strain

A general requirement in continuum mechanics as well as in finite element theories is that rigid body motion must not introduce straining of the material. The following shows that this requirement cannot be fulfilled if the engineering strain definition is used.

We regard a rigid body which is exposed to a rotation. This can be expressed through the displacements field, and if we only consider a two dimensional example we have:

$$u_i = (R_{ij} - \delta_{ij})x_j = \left(\begin{bmatrix} cos(\theta) & -sin(\theta) \\ sin(\theta) & cos(\theta) \end{bmatrix} - \delta_{ij}\right) x_j \tag{2.25}$$

where R_{ij} is the orthogonal transformation matrix which consists of the direction cosines. The corresponding engineering strains e_{ij} are calculated as:

$$e_{ij} = \frac{1}{2}(R_{ij} + R_{ji} - 2\delta_{ij}) = \begin{bmatrix} cos(\theta) - 1 & 0 \\ 0 & cos(\theta) - 1 \end{bmatrix} \tag{2.26}$$

We have clearly a spurious strain that has arised from the rigid body rotation. By using a Taylor expansion it can be recognized that the error is of the order θ^2, for which reason the measure can be used without notable errors in small strain and small rotation analyses.

It is therefore necessary to use more advanced measures of deformation when analysing structures that are undergoing significant rotations. This is typically a problem when performing analysis of shell/plate structures where rotation can be significant even though

the stresses and strains are small. It is, however, still possible to base such an analysis on engineering strains, but there must be taken special precaution to include the rotational effects. In this thesis this topic is not discussed further, but this type of problems are discussed by e.g. Crisfield [47].

Bathe [17] gives a good discussion on both strain and stress measures as well as on the problems which are associated with their use.

It is also necessary to be aware that the time derivative of the Cauchy stress tensor is not frame invariant. When using the Cauchy stress tensor in the evaluation of constitutive relations it is not possible to include the time derivatives $\frac{d\sigma}{dt}$ in the modelling of material response. In this case it can be more suitable to use the 2nd Piola-Kirchoff stress tensor, whose time derivatives are frame invariant (and hereby indirectly choose the Green strain measure). The 2nd P.-K. tensor, however, has the disadvantage that the stress components do not have any direct physical interpretation, which necessitates calculations of for example the Cauchy stress tensor in the postprocessing. Different stress measures arise when using different strain measures. Bathe [17], Malvern [140] and Crisfield [47] give a more detailed discussion on the measures and some of the problems involved when they are used. In Belytschko [23] is given a discussion of various strain measures and their use in connection with FE-discretization.

Figure 2.3 illustrates the difference between the strain measures which are discussed above when a material element undergoes a uniaxial deformation. From figure 2.3 it can be

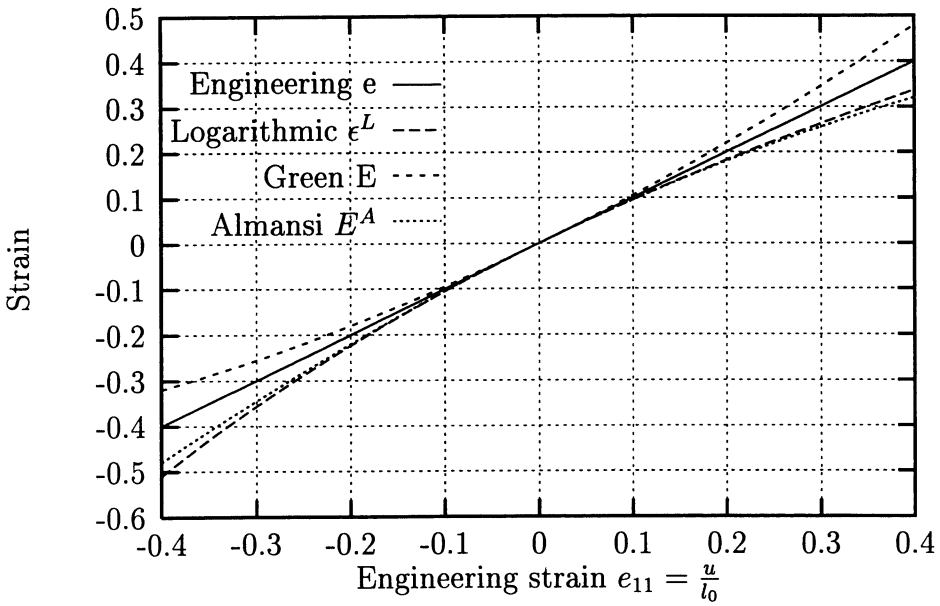

Figure 2.3: *The strain measures: Engineering, Green, Almansi and accumulated velocity strain (calculated as logarithmic). The deformation prescribed is* $\frac{u}{l_0}$ *or in other words the engineering strain.*

seen that the difference between the strain measures is very small as long as the strain is small (less than 5 per cent), but as deformation increases the second order terms become significant.

2.2.4 Use of logarithmic strains in connection with sheet metal experiments

In connection with experimental measurements the logarithmic strain can be used as an effective measure by using the following procedure which is proposed by Sowerby et al. [195], who assume pure homogeneous deformation. Three nodes (P_1, P_2, P_3) on the sheet surface have the initial coordinates X_i, Y_i. After deformation the coordinates are (x_i, y_i). The three nodes specify a triangle and if we translate the initial triangle and the triangle after deformation so that P_1 is placed at origo for both situations, we can by assuming in-plane deformation write the relation between the current and initial state as 2.14:

$$\left\{ \begin{array}{c} x_i \\ y_i \end{array} \right\} = \mathbf{F} \left\{ \begin{array}{c} X_i \\ Y_i \end{array} \right\} \qquad i = 1,3 \tag{2.27}$$

which leads to the following expression for the deformation gradient $\mathbf{F}$:

$$\mathbf{F} = \frac{2}{X_2Y_3 - X_3Y_2} \left[\begin{array}{cc} x_2Y_3 - x_3Y_3 & -x_2X_3 + x_3X_2 \\ y_2Y_3 - y_3Y_2 & -y_2X_3 + y_3X_2 \end{array} \right] \tag{2.28}$$

The Cauchy-Green deformation tensor $\mathbf{C} = \mathbf{F}^T\mathbf{F}$ can be calculated and the two eigen-values of $\mathbf{C}$ are derived as:

$$\lambda_i^2 = \frac{F_{11}^2 + F_{21}^2 + F_{12}^2 + F_{22}^2}{2} \pm \sqrt{\left(\frac{F_{11}^2 + F_{21}^2 - F_{12}^2 - F_{22}^2}{2} \right)^2 + (F_{11}F_{12} + F_{21}F_{22})^2} \tag{2.29}$$

and the principal logarithmic strains (in the plane of the sheet) are calculated as $\epsilon_{ii}^L = ln(\lambda_i)$. The third principal logarithmic strain component follows then from the assumption of volume constancy.

This principle of calculating the final strains is used in the computer based strain analysis system ASAME system from Camsys, Inc. [15].

2.3 The principle of virtual work

A very important principle in continuum mechanics is the principle of virtual work. It has many applications, and one of the most important applications today is the derivation of FE-equations. We regard a body with the volume V and the surface S in which the stress field satisfies the equilibrium equation:

$$\frac{\partial \sigma_{ij}}{\partial x_i} + \rho b_j = \rho \frac{Dv_j}{Dt} \tag{2.30}$$

where ρ is the density and $\mathbf{b}$ the body forces per unit mass and we have a velocity field $\mathbf{v}$ leading to the strain rate tensor:

$$\dot{\epsilon}_{ij} = \frac{1}{2} \left(\frac{\partial v_i}{\partial x_j} + \frac{\partial v_j}{\partial x_i} \right) \tag{2.31}$$

Forming and integrating the product $\sigma_{ij}\dot{\epsilon}_{ij}$ over the entire region gives:

$$\begin{aligned}
\int_V \sigma_{ij}\dot{\epsilon}_{ij}dV &= \tfrac{1}{2}\int_V \sigma_{ij}\left(\tfrac{\partial v_i}{\partial x_j}+\tfrac{\partial v_j}{\partial x_i}\right)dV \\
&= \int_V \sigma_{ij}\tfrac{\partial v_i}{\partial x_j}dV && \text{(symmetry)} \\
&= \int_V \left\{\tfrac{\partial}{\partial x_i}(\sigma_{ij}v_j) - v_j\tfrac{\partial \sigma_{ij}}{\partial x_i}\right\}dV && \text{(reduction)} \\
&= \int_V \left\{\tfrac{\partial}{\partial x_i}(\sigma_{ij}v_j) + \rho v_j b_j - \rho v_j \tfrac{Dv_j}{Dt}\right\}dV && \text{(equilibrium)}
\end{aligned} \tag{2.32}$$

Using the divergence theorem leads to:

$$\int_V \sigma_{ij}\dot{\epsilon}_{ij}dV = \int_S \sigma_{ij}v_j n_i dS + \int_V \rho v_j b_j dV - \int_V \rho v_j \frac{Dv_j}{Dt}dV \tag{2.33}$$

where n_i is the direction cosines of the outward normal. 2.33 is the mathematical expression of the principle of virtual work for a continuum and states that the rate of work of the stress field σ_{ij} in the velocity field is equal to the sum of the rates of work of the surface and body forces associated with σ_{ij} in the same field minus the work of the inertial forces.

Establishing the variation of the virtual work now leads to:

$$\delta\Pi = \int_V \rho\dot{v}_i\delta v_i dV + \int_V \sigma_{ij}\delta v_{i,j}dV - \int_V \rho b_i \delta v_i dV - \int_S t_i \delta v_i dS = 0 \tag{2.34}$$

It should here be mentioned that the term **v** appearing in the accelerations is not varied in the virtual velocity field, see e.g. Malvern [140]. When using different strain measures it becomes necessary to use a correct measure of stress in order to obtain correct expressions for the virtual work. By using the expression for the virtual work it is possible to obtain the relations between the defined strain measure and its conjugate stress and the rate of work, see e.g. Crisfield [47].

2.4 Conservation of mass

One of the most important conservation laws is the law of mass conservation. It can rather easily be derived. Consider a body which occupies the volume V_0 in the undeformed configuration; no matter how severely the body is deformed we can calculate the current mass by integrating the density over the current volume V_t:

$$m = \int_{V_t} \rho(\mathbf{x}(\mathbf{x}_0, t))dV \tag{2.35}$$

Stating conservation leads to:

$$\int_{V_0} \rho(\mathbf{x}_0)dV_0 = \int_{V_t} \rho(\mathbf{x}(\mathbf{x}_0, t))dV \tag{2.36}$$

When using the knowledge of the relation between deformed and undeformed configuration we can express the mass in the current configuration 2.35:

$$m = \int_{V_0} \rho(\mathbf{x}(\mathbf{x}_0, 0))det\left(\mathbf{F}(\mathbf{x}, t)\right)dV_0 \tag{2.37}$$

and hereby the relation between deformation and density:

$$\rho(\mathbf{x}, t)det\left(\mathbf{F}(\mathbf{x}, t)\right) = \rho_0(\mathbf{x}_0) \tag{2.38}$$

2.5 Conservation of energy

The kinetic energy of a body is defined as:

$$K = \frac{1}{2}\int_V \rho v_i v_i dV \tag{2.39}$$

Introducing an internal energy density e the internal energy can be calculated as:

$$E = \int_V \rho e dV \tag{2.40}$$

The statement of conservation of energy can be formulated as: The material derivative of $K + E$ is equal to the sum of the rate at which mechanical work is done by the body and the surface forces acting on the body and the rate at which other energy enters the body. Introducing q_i as the heat-flux vector we can write the mathematical formulation for the law stated above (omitting interior heat source effects):

$$\frac{D}{Dt}\int_V \rho(\frac{1}{2}v_i v_i + e)dV = \int_V \rho b_i v_i dV + \int_S (\sigma_{ij}v_j - q_j)n_j dS \tag{2.41}$$

Transforming the surface integral into a volume integral and taking advantage of conservation of mass:

$$\rho\frac{D}{Dt}(\frac{1}{2}v_i v_i + e) = \rho b_i v_i + \frac{\partial}{\partial x_j}(\sigma_{ij}v_j - q_j)n_j \tag{2.42}$$

Rearranging and using $\frac{Dv_i}{Dt} = \dot{v}_i$ gives:

$$-v_i\left(\frac{\partial \sigma_{ij}}{\partial x_j} + \rho b_i - \rho\dot{v}_i\right) + \rho\frac{De}{Dt} - \sigma_{ij}\frac{\partial v_i}{\partial x_j} + \frac{\partial q_j}{\partial x_j} = 0 \tag{2.43}$$

and as the term in the bracket must equal zero due to equilibrium it leads to:

$$\rho\frac{De}{Dt} = \sigma_{ij}\frac{\partial v_i}{\partial x_j} - \frac{\partial q_j}{\partial x_j} \tag{2.44}$$

2.6 Finite element discretization

In this section the governing equations for a FE-discretized system are derived, first for a system undergoing small deformations and second for a system exposed to large deformations. Shell elements available in LS-Dyna3d are discussed and results obtained for a typical deep drawing operation are compared. For a more rigorous discussion about the elements see Hallquist et al. [84, 83] as well as the sources cited in these two publications.

2.6.1 FE-discretization for a system with small deformations

It has been chosen to work out the equation for a system which is undergoing small deformations first. Hereby the equations are somewhat simplified, and it is easier to obtain a more fundamental understanding. We start out from the equation of equilibrium 2.30:

$$\frac{\partial \sigma_{ij}}{\partial x_j} + \rho b_i = \rho\ddot{u}_i \tag{2.45}$$

As only small deformations are considered we utilize the engineering strain:

$$e_{ij} = \frac{1}{2}\left(\frac{\partial u_i}{\partial x_j} + \frac{\partial u_j}{\partial x_i}\right) \tag{2.46}$$

The constitutive law relates the strain rates and stress rates:

$$\dot{\sigma}_{ij} = C_{ijkl}\dot{e}_{ij} \tag{2.47}$$

where C_{ijkl} is the constitutive matrix. For a linear material law we can relate total stress and strain:

$$\sigma_{ij} = C_{ijkl}e_{ij} \tag{2.48}$$

Taking the expression for the conservation of energy, formula 2.44 it can be written as:

$$\rho\frac{De}{Dt} = \sigma_{ij}\frac{\partial \dot{u}_i}{\partial x_j} - \frac{\partial q_k}{\partial x_k} \tag{2.49}$$

In the expression an eventual heat source is not included. If the heat flux is also omitted we obtain:

$$\rho\frac{De}{Dt} = \sigma_{ij}\frac{\partial \dot{u}_i}{\partial x_j} \tag{2.50}$$

which becomes the definition of internal energy. Mortensen and Nielsen [152] give an example of the use of generated heat in constitutive modelling, but in the present thesis it will be omitted.

To obtain a discrete system of equations, which can be solved by using a computer, we have to introduce a spatial finite element discretization.

To perform the discretization the solid volume V is divided into elements. The displacement field is approximated by using the element's shape functions N_I which are functions of space alone and the nodal displacement u_{iI} which incorporates the time dependency. The continuous displacement field for an element is then approximated as:

$$u_i(\mathbf{x}, t) \approx \Sigma_{I=1}^{n_{nodes}} u_{iI}N_I(\mathbf{x}) \tag{2.51}$$

The derivatives of the displacements are now found as:

$$\frac{\partial u_i}{\partial x_j} = B_{jI}u_{iI} \qquad with \qquad B_{jI} = \frac{\partial N_I}{\partial x_j} \tag{2.52}$$

Hereby we can write the discrete form of the strain-displacement equation:

$$e_{ij} = \frac{1}{2}(B_{iI}u_{jI} + B_{jI}u_{iI}) \tag{2.53}$$

The element volume considered has the boundary S that consists of S_u with displacement constraints u_i^* and S_σ with the traction τ_1^*:

$$\begin{aligned} u_i &= u_i^* \qquad on\ S_u \\ \sigma_{ij}n_j &= \tau_i^* \qquad on\ S_\sigma \end{aligned} \tag{2.54}$$

If we let the test function $\mathbf{v} = \mathbf{0}$ on S_u we can write the variational form of 2.45, see also 2.33:

$$\dot{E}_{int}(\mathbf{u}, \mathbf{v}) + F_{d'Alembert}(\mathbf{u}, \mathbf{v}) = \dot{E}_{ext}(\mathbf{u}, \mathbf{v}) \tag{2.55}$$

for all variations of $\mathbf{v}$ that vanish on S_u. This expression is identical to the principle of virtual work. $\dot{E}_{int}$ is the increment of internal work associated with $\mathbf{v}$:

$$\dot{E}_{int}(\mathbf{u}, \mathbf{v}) = \int_V v_{i,j}\sigma_{ij}(\mathbf{u})dV = \frac{1}{2}\int_V \left(\frac{\partial v_i}{\partial x_j} + \frac{\partial v_j}{\partial x_i}\right)\sigma_{ij}dV = \int_V \dot{e}_{ij}\sigma_{ij}dV \tag{2.56}$$

where $\dot{e}_{ij}$ is the variation in strain due to $\mathbf{v}$. $F_{d'Alembert}(\mathbf{u}, \mathbf{v})$ is the d'Alembert inertial force:

$$F_{d'Alembert}(\mathbf{u}, \mathbf{v}) = \int_V \rho v_i \ddot{u}_i dV \tag{2.57}$$

$\dot{E}_{ext}(\mathbf{u}, \mathbf{v})$ is the increment of external work:

$$\dot{E}_{ext}(\mathbf{u}, \mathbf{v}) = \int_V v_i b_i dV + \int_{S_\sigma} v_i \tau_i^* dS \tag{2.58}$$

If we for the test functions $\mathbf{v}$ use the same shape functions as for $\mathbf{u}$ and introduce:

$$M^e_{ijIJ} = \int_{V_e} \rho N_I N_J \delta_{ij} dV \quad f_{iI}^{(e)int} = \int_{V_e} B_{jI}\sigma_{ij}dV \quad f_{iI}^{(e)ext} = \int_{V_e} N_I b_i dV + \int_{S_\sigma} N_I \tau_i^* dS \tag{2.59}$$

performing an expansion from element level to the total FE-system we obtain:

$$\mathbf{v}^T(\mathbf{f}_{int} + \mathbf{M}\ddot{\mathbf{u}} - \mathbf{f}_{ext}) = 0 \tag{2.60}$$

As this equation must hold for arbitrary test functions it can be reduced to:

$$\mathbf{M}\ddot{\mathbf{u}} + \mathbf{f}_{int} = \mathbf{f}_{ext} \tag{2.61}$$

Hereby we have obtained a system of ordinary differential equations. In case of a linear system the internal force vector can be written as

$$\mathbf{f}_{int} = \mathbf{K}\mathbf{u} \tag{2.62}$$

where $\mathbf{K}$ is the stiffness matrix defined by

$$\mathbf{K} = \sum_{e=1}^{N_{ele}} \int_{V_e} \mathbf{B}^T \mathbf{E}^E \mathbf{B} dV \tag{2.63}$$

and $\mathbf{E}^E$ is the elastic constitutive matrix and $\mathbf{B}$ is the displacement-strain relation matrix. Formula 2.61 is then rewritten as:

$$\mathbf{M}\ddot{\mathbf{u}} + \mathbf{K}\mathbf{u} = \mathbf{f}_{ext} \tag{2.64}$$

2.6.2 Large deformation, Cauchy stress and Lagrangian formulation

As discussed earlier the Cauchy stress has the advantage that it is directly interpretable. At the same time we can utilize a Lagrangian formulation which has the advantage that the expressions obtained are very similar to the scheme used for small deformations.

Starting out similar to the previous approach we have 2.45:

$$\frac{\partial \sigma_{ij}}{\partial x_j} + \rho b_i = \rho \ddot{u}_i \tag{2.65}$$

The velocity strain is used as measure of deformation:

$$\dot{\epsilon}_{ij} = \frac{1}{2}\left(\frac{\partial \dot{u}_i}{\partial x_j} + \frac{\partial \dot{u}_j}{\partial x_i}\right) \tag{2.66}$$

As mentioned earlier the time derivative of the Cauchy stress tensor is not frame-invariant. In LS-Dyna3d the Jaumann stress rate is for some elements used to update stresses.

To update stresses incrementally in time we have:

$$\sigma_{ij}(t+dt) = \sigma_{ij}(t) + \dot{\sigma}_{ij}dt \tag{2.67}$$

where the material time derivative of the stress is found as:

$$\dot{\sigma}_{ij} = \sigma_{ij}^{\nabla} + \omega_{ik}\sigma_{kj} + \omega_{ki}\sigma_{jk} \tag{2.68}$$

wheree ω_{ij} is the spin tensor and:

$$\sigma_{ij}^{\nabla} = C_{ijkl}\dot{\epsilon}_{ij} \tag{2.69}$$

is the Jaumann co-rotational stress rate. Here incremental linearity is assumed. It is not always recognized that the demand of incremental linearity is a limitation on the constitutive behaviour. In connection with explicit FE it is of minor importance as many steps are used in the solution, but for large strain increments it may be crucial. Boundary conditions are specified again and here extended to take contact into account (see [83]):

$$\begin{aligned} u_i &= u_i^* && on\ S_u \\ \sigma_{ij}n_j &= \tau_i^* && on\ S_\sigma \\ (\sigma_{ij}^+ - \sigma_{ij}^-)n_i &= 0 && on\ S_i \end{aligned} \tag{2.70}$$

where S_i is an interior boundary. If contact takes place, points on the boundaries obey $x_i^+ = x_i^-$. The expression for the weak form of the momentum equations are equal to the expression for the small strain system:

$$\dot{E}_{int}(\mathbf{u},\mathbf{v}) + F_{d'Alembert}(\mathbf{u},\mathbf{v}) = \dot{E}_{ext}(\mathbf{u},\mathbf{v}) \tag{2.71}$$

which can be rewritten when taking the contact condition into account:

$$\int_V v_{i,j}\sigma_{ij}(\mathbf{u})dV - \int_V \rho v_i \ddot{u}_i dV = \int_V \rho v_i b_i dV + \int_{S_\sigma} v_i \tau_i^* dS + \int_{S_i} v_i(\sigma_{ij}^+ - \sigma_{ij}^-)n_j dS \tag{2.72}$$

The first term may be rewritten by using $\dot{\epsilon}_{ij}$:

$$\int_V v_{i,j}\sigma_{ij}(\mathbf{u})dV = \int_V \dot{\epsilon}_{ij}\sigma_{ij}dV \tag{2.73}$$

and we can proceed as for the small strain system to obtain:

$$\mathbf{M}\ddot{\mathbf{u}} + \mathbf{f}_{int} = \mathbf{f}_{ext} \tag{2.74}$$

The internal forces on an element basis may still be expressed:

$$\mathbf{f}_{iI}^{(e)int} = \int_{V_e} \mathbf{B}_{jI}\sigma_{ij}dV \tag{2.75}$$

2.6.3 Diagonal forms of the mass matrix

In connection with explicit time integration (treated in section 3.3.1) it is important that the mass matrix is reduced to a diagonal form. Some of the possibilities to obtain this are presented. The consistent mass matrix is obtained through the shape functions:

$$M_{ij}^e = \int_{V_e} \rho N_i N_j dV \tag{2.76}$$

This procedure leads to a matrix with sparsity characteristics corresponding to the stiffness matrix $\mathbf{K}$. To overcome this problem a number of different lumping procedures have been proposed. The simplest is to assign an equal fraction of the mass to the nodes:

$$M_{ij}^e = \frac{\delta_{ij}}{N_{nodes}} \int_{V_e} \rho dV \tag{2.77}$$

where N_{nodes} is the number of nodes per element. Zienkiewicz [229] recommends another method, where the diagonal components (M_{ii}) are computed by summing up the corresponding row of the matrix:

$$M_{ii}^e = \Sigma_{j=1}^{N_{nodes}} M_{ij}^e \tag{2.78}$$

This method can be shown to conserve mass. Another approach is to utilize integration schemes where the quadrature points are placed in the nodes. Only shape functions corresponding to the particular node (integration point) contribute to the integral. This procedure leads to a diagonalised mass matrix:

$$M_{ii}^e = \int_{V_e} \rho N_i N_i dV \tag{2.79}$$

According to Belytschko [23] this procedure does not guarantee conservation of mass, but the procedure may lead to more accurate calculations for irregular shaped elements. However, all the methods above are usable and the difference between the lumping schemes will according to Zienkiewicz [229] only result in minor discrepancies. In the present context it is evaluated that the specific scheme is of minor importance as we are not interested in the transient response. In LS-Dyna3d [83] the second mentioned lumping method given in formula 2.78 is implemented.

2.6.4 Mass matrices and shell elements

When shell elements are used some problems arise due to a rather low inertial resistance against rotation. This will lead to small allowable time steps in the integration procedure. In LS-Dyna3d a method proposed by Hughes, Liu and Levit to overcome these problems is used for all shell elements.

The translational masses are computed according to 2.78 whereas the rotational generalized masses are taken as a scaling of the corresponding translational resistance:

$$M_i^{rot} = \alpha M_i^{tra} \tag{2.80}$$

where α is given as:

$$\alpha = max\left(\left(\frac{z_i^+ + z_i^-}{2}\right)^2 + \frac{1}{12}(z_i^+ - z_i^-)^2, \frac{V_e}{8h_e}\right) \tag{2.81}$$

here V_e and h_e is the volume and the thickness of the element respectively, and z describes the coordinate of the outer surfaces in relation to the reference plane.

2.6.5 Hourglass modes and methods to control them

In this section the hourglassing phenomena are discussed briefly, as it is an important aspect for explicit FE-methods due to the integration rules which are employed for evaluating internal forces (one point quadrature). For a more extensive discussion sources as Hallquist [83], Benson [28], Zienkiewicz [229], Belytschko [23, 25, 24, 72], Cook [46] are recommended. An hourglass mode (also called a zero-energy mode) of an element arises due to an element displacement $\mathbf{u}_e$ which is not a rigid body motion, but nevertheless it does not produce straining energy. That is; some deformation modes can be present without being recorded in the strain energy ($\int \sigma_{ij}\dot{\epsilon}_{ij}dV = 0$). Such deformations are clearly non-physical and should be avoided.

A very clear and simple explanation can be given [28]: Consider a plane four node element which has eight degrees of freedom. To have a proper element we demand that the three rigid body modes are not resisted by stresses. This means we have still five independent modes of deformation which must be resisted, but in two dimensions we have only three stresses to resist them. Two of the modes (the hourglass modes) are therefore not resisted by the element.

In order to overcome the problem, or at least reduce it, it is necessary with two steps: 1) to define the zero mode shapes and 2) to define a resisting force. Several methods exist; some are based on an addition of viscous terms and others on addition of stiffness against the particular zero-energy modes. In LS-Dyna3d there are several options for applying hourglass resistance. My experience is that for most sheet metal forming applications it seems to be most reliable to use the method proposed by Flanagan and Belytschko (stiffness based hourglass resistance [83]).

2.7 Finite elements

Most sheet metal forming processes can be treated as plane stress problems, wherefore shell elements may be the obvious choice. However, in certain applications very high normal stresses can be seen, e.g. in an ironing process. The ironing process is indeed a sheet forming operation, but the stress state in the deformation region can best be characterized as one of bulk forming. In such processes it is evident that shell elements cannot be used. The following gives a short presentation of some of the elements available in LS-Dyna3d.

2.7.1 Solid elements

The volume V is subdivided into N_e finite elements, each of the volume V_e. The displacement field within each element e is approximated by the time dependent nodal displacements by using the shape functions $N_j(\xi, \eta, \zeta)$, see figure 2.4. Thus,

$$u_i(\mathbf{x}, t) = \sum_{j=1}^{k} u_i^j(t) N_j(\xi, \eta, \zeta) \tag{2.82}$$

where k is the number of nodal points that define the element, and u_i^j is the nodal displacements of the jth node in the ith direction. The shape functions $N_j(\xi, \eta, \zeta)$ are defined

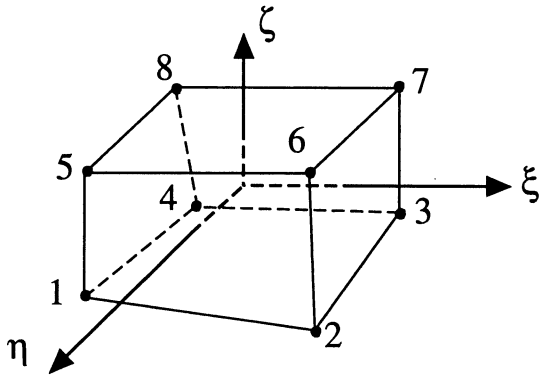

Figure 2.4: *Isoparametric 8-node solid hexahedron (brick element).*

for the 8-node hexahedron as

$$N_j = \frac{1}{8}(1 + \xi\xi_j)(1 + \eta\eta_j)(1 + \zeta\zeta_j) \tag{2.83}$$

where ξ_j, η_j and ζ_j take on their nodal values of ± 1.

2.7.2 Shell elements

One of the major choices when developing a proper finite element model is the choice of element formulation. The purpose of this section is to provide some information about the different shell elements that are available in LS-Dyna3d. In LS-Dyna3d a total of 9 shell element formulations can be used (seven four node and two three node elements); in this section only the four noded elements are considered.

In connection with simulation of sheet metal forming it is by intuition clear that shell elements will be the most effective. Primarily because most sheet forming operations are dominated by in-plane stresses but also due to the choice of the explicit time integration scheme (discussed later in section 3.3.1) which makes it unrealistic to use solid elements for most sheet forming problems. In case solid elements are used to discretize the sheet it is necessary with 5 to 7 elements through the thickness to model the bending/unbending effects whereby the typical length for an element becomes very small.

The 9 shell elements available in LS-Dyna3d are more or less based on two different formulations: The Belytschko-Lin-Tsay (BLT) element and the Hughes-Liu (HL) element. The characteristics of the BLT-element are:

- Co-rotational stress update instead of the Jaumann stress rotation.
- The coordinate system embedded in the element can give raise to discrepancy between the rotation of the local element coordinate system and the material rotation
- Mindlin plate theory is utilized.
- "Through thinning" is available for this element.

Due to the theoretical limitation of the BLT-element, it may in some cases be necessary to use the Hughes-Liu element (HL) instead. The main characteristics of the HL-element are:

- It is incrementally objective and rigid body rotations do not generate strains allowing for the treatment of finite strains.
- It is compatible with brick elements as it is based on a degenerated brick element.
- Finite transverse shear strains are included.
- A through thickness thinning option is available.

2.7.3 Comparison of shell elements used in a metal forming simulation

To compare the behaviour of various elements it has been chosen to simulate the deep drawing of a cylindrical cup, which is to be further investigated in section 9.1. For the present analyses 5 integration points through the thickness are used. The discretization used is shown in figure 2.5. A similar analysis has been made by Galbraith and Hallquist [75], where they use a square box deep drawing process as test case. In their analyses 7 integration points through the thickness are used. The results obtained with the present analyses as well as the results given in [75] will be presented for comparison.

The elements considered are:

- 1 Selective reduced Hughes-Liu shell (SRHL).
- 2 Selective reduced co-rotational Hughes-Liu shell (SRCOHL).
- 3 Hughes-Liu shell (HL).
- 4 Englemann-Whirley shell (EW).

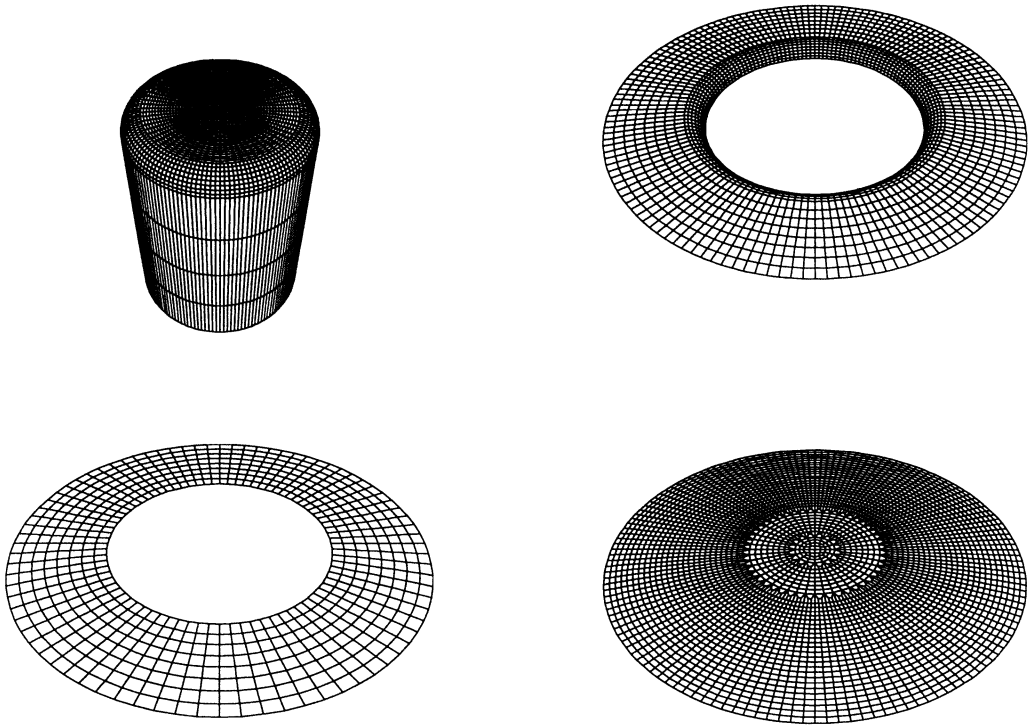

Figure 2.5: *The discretized models of punch, die, blank holder and blank used for comparison of shell elements.*

- 5 Co-rotational Hughes-Liu shell (COHL).
- 6 Belytschko-Lin-Tsay shell (BLT).
- 7 Belytschko-Wong-Chiang shell (BWC).

Figure 2.6 gives the predicted punch forces for the 7 elements listed above. From the figure it can be noticed that the response is relatively scattered wherefore the analyses must be judged to be performed with a too high loading rate and/or a too coarse discretization, however, for the present purpose this is of less importance. The curves for the individual elements are very similar and all the dynamic effects seem to be the same for the elements. So with regard to the overall behaviour (predicted punch force) no significant difference can be seen. This conclusion is also reached by Galbraith and Hallquist for the shell elements investigated. In their analyses two membrane elements are also included and the predicted punch force for the membrane elements is $\approx$ 10 per cent lower than the corresponding forces predicted using shell elements. Figure 2.7 shows the predicted thickness variation along the cup height for the investigated elements. Here one element seems to differ from the others. The Englemann-Whirley shell (4) does predict thinner regions for the thinnest part of the cup and it also over-estimates the thickness of the cup compared to the other elements. The remaining elements do more or less lead to the same thickness distribution. Figure 2.8 gives the CPU-costs for analysis of the deep drawing process with various shell elements. If we consider the CPU-costs shown in figure 2.8 for the different elements some

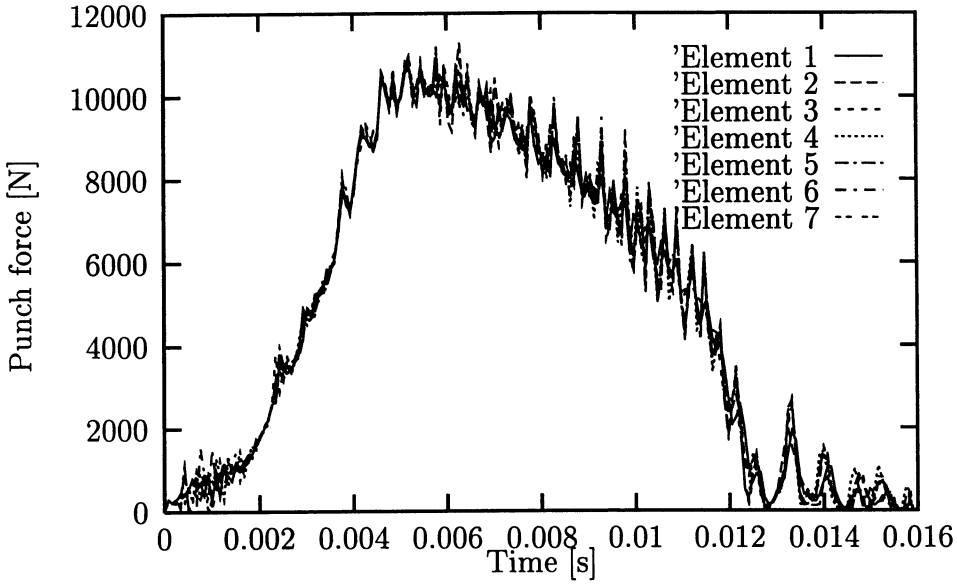

Figure 2.6: *Predicted punch force for the 7 elements investigated.*

characteristics can be noticed. The number of time steps are the same for all analysis and it seems that the time needed for treating contact is the same for all elements. If we subtract the time needed for contact handling from the total CPU-cost the curve with label Element is obtained. Here it can be seen that a significant decrease occurs when going from elements 1 and 2 to elements 3 to 7.

Elements 1 and 2 used a 2x2x5 integration rule (2x2x7 for Galbraith and Hallquist's analyses) leading to a significant raise in computations. Elements 3 to 7 use a one 1x5 integration rule. Element 1 uses the Jaumann stress rotation whereas element 2 is based on a co-rotational formulation which reduces CPU-cost (from 21.00 to 13.59 hours for the square box, and from 5300 to 4100 seconds for the cylindrical cup).

Element 3 is the Hughes-Liu element with a 1x5 integration leading to a significant reduction of total CPU-cost, but still essentially more expensive that the formulations based on the BLT-element.

Element 4 is similar to the BLT-element apart from the inclusion of a constitutive based hourglass control founded on assumed strain fields. This element seems to be competitive with the BLT-element seen from a computational point of view, however, in the present analyses this element (4) is the only element which leads to a significant variation in the predicted thickness when compared to the other 6 elements.

Element 7 is also based on the BLT-formulation, the difference to the BLT-element is that warpage terms are included. The overall behaviour is very similar to the BLT-element and the costs are only slightly higher. Use of membrane elements do lead to a decrease in the CPU-cost, but Galbraith and Hallquist conclude that the membrane elements are too inaccurate compared to the shell elements. The analyses of the cylindrical cups led to folding at a so early stage in the process that it was judged to be of no relevance to include them in the present comparison.

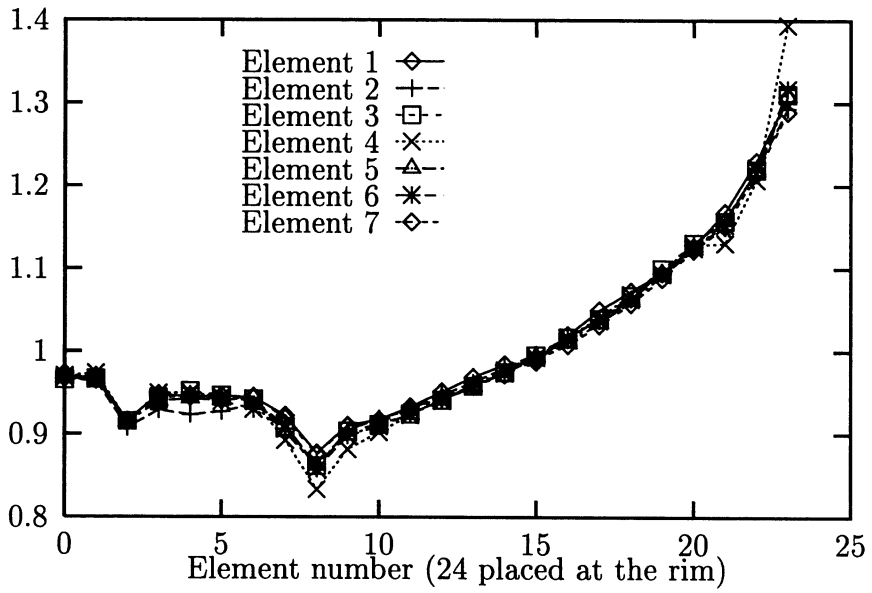

Figure 2.7: *Predicted thickness variation for the 7 elements investigated plotted as function of element number (counted along the x-axis). The two peaks appearing on the curves correspond to punch and die impact lines.*

Galbraith and Hallquist do not include the co-rotational HL-element with one point integration (element 5). For the present analyses this element seems to lead to the same thickness variation as the HL-element with the Jaumann rotation (element 3), but the total CPU-cost is only slightly higher than for the BLT-element(6).

2.7.4 Summary of shell elements

Seen from a theoretical point of view the HL-element seems superior compared to the BLT element, but as shown in section 2.7.3 the results obtained in practical simulations are almost identical for the two element types. And as the computational effort when using

Element number	Total CPU-time [hours]	Total CPU-time [seconds]	Relative CPU-use	Relative CPU-use
1 SRHL	21.00	5300	6.50	2.58
2 SRCOHL	13.59	4100	4.18	2.00
3 HL	4.92	2400	1.52	1.17
4 EW	3.39	2100	1.05	1.02
6 BLT	3.23	2059	1.00	1.00

Table 2.1: *CPU-consumption for various element formulation. The second column gives the total CPU-use for deep drawing of a square box (from Galbraith and Hallquist [75]). The third column gives the total CPU-use for deep drawing of a cylindrical cup. Column four and five is the relative variation corresponding to column 2 and 3, respectively.*

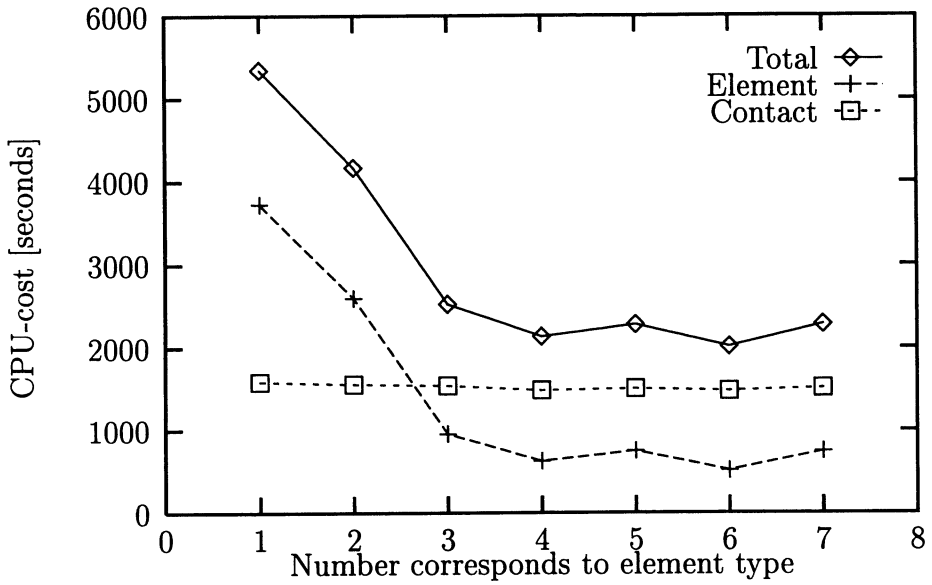

Figure 2.8: *CPU-costs using different element types. The figure shows the total CPU usage and also the contributions from contact and element algorithms.*

the HL-element is significantly higher than for the BLT-element (4066 mathematical operations for the HL-element versus 725 for the BLT-element [83]), my proposal is to use the BLT-element in most cases. In should be noticed that the example investigated is not strongly influenced by warping wherefore other elements may be superior for problems where warping tends to be a problem.

Based on the results and on the consumption of CPU-time, it is concluded that the Belytschko-Lin-Tsai element is the most efficient and at the same time it is sufficiently accurate.

Chapter 3

Numerical Solution of FE-systems

In this chapter different solution schemes are discussed, and the explicit time integration is presented in a more detailed manner.

We can for a general discretized system write the equations that describe the problem to time $t = \tau$ as:

$$\mathbf{M}\ddot{\mathbf{u}} + \mathbf{C}\dot{\mathbf{u}} + \mathbf{f}_{int} = \mathbf{f}_{ext} \tag{3.1}$$

where the solution is considered to be known. $\mathbf{C}\dot{\mathbf{u}}$ is the viscous forces which must be included in case the system is artificially damped. Similarly, we can for the unknown configuration write the equations at time $t = \tau + \Delta t$ as:

$$\mathbf{M}\ddot{\bar{\mathbf{u}}} + \mathbf{C}\dot{\bar{\mathbf{u}}} + \bar{\mathbf{f}}_{int} = \bar{\mathbf{f}}_{ext} \tag{3.2}$$

The general problem is now to determine the configuration $\bar{\mathbf{u}}$ at this state (and also the corresponding velocities and accelerations).

Depending on the problem different solution approaches are suitable. If the problem can be treated as linear elastic and the loading is static equation 3.2 reduces to:

$$\bar{\mathbf{f}}_{int} = \bar{\mathbf{f}}_{ext} \quad \rightarrow \quad \mathbf{K}\bar{\mathbf{u}} = \bar{\mathbf{f}}_{ext} \tag{3.3}$$

This class of problems are solved with just one loading step. Another problem class is the quase-static problems. These problems are characterized by a so slow loading rate, that the inertial effects have no influence on the results. This approach has previously been the traditional way to treat sheet forming, e.g. when performing analytical evaluation of geometric simple problems. In this kind of analysis we have, however, a path dependency wherefore loading typically must be described as a function of a loading parameter λ. Due to the nonlinearities it is necessary to divide the loading into load increments and to solve the equation of equlibrium for each loading level:

$$\bar{\mathbf{f}}_{int}(\mathbf{u}_n) = \bar{\mathbf{f}}_{ext}(\lambda_n) \tag{3.4}$$

where index n indicate a given load level. This problem class where we have a path dependency can, however, be solved very effectively if the quasi-static problem is treated as a quasi-dynamic problem. The problem still is more or less physically independent of time,

but nevertheless time (or pseudo time) is used as the loading parameter. The major difference compared to the quasi-static solution is in the analysis; instead of a loading parameter λ time t is used to perform the advance in the process of simulation through integration of the dynamic equilibrium equations (instead of fulfilment of the static equilibrium equations).

The last group is the dynamic problems. This class of problems will always include a time dependency and often the problems will show a path dependency.

Sheet metal forming processes can be characterized as either quasi-static or dynamic, but as mentioned above it may be found reasonable to treat a quasi-static process as a quasi-dynamic problem - in fact that is what is done when using explicit time integration.

There are two generally different types of methods for solving the ordinary differential equations which are derived for the problem: explicit time integration or implicit time integration methods. The implicit methods lead to a system of non-linear equations which have to be solved. The implicit integration scheme can be made unconditionally stable, and the time step is only chosen on the basis of the desired accuracy. Unfortunately, one very often experiences problems with convergence for highly non-linear problems when using implicit solution schemes. Sheet metal forming is characterized by many non-linearities due to structural and material non-linearity, but also arising and vanishing contact between the bodies makes the problem highly non-linear. However, by using explicit time integration these non-linearities are treated without problems and this combined with the ability to handle the process instabilities often experienced in sheet forming are the major reasons for the fast development of explicit codes suitable for metal forming simulations.

Although many FE-solution schemes for sheet forming problems have been proposed, they can roughly be categorized into three groups:

- Static - implicit
- Static - explicit
- Dynamic - explicit

These are the main solution methods which are used today for simulation of metal forming. Of course one can take a dynamic implicit solution scheme into consideration, but in practice this procedure will only have relevance when strain rate effects are of major importance and when inertial effects come to play an important role for the process. However, this type of processes normally lasts few milliseconds and for problems of this nature the explicit time integration is also very suitable. For processes like rolling and extrusion which in some cases can be analysed with assumption of a steady-state material flow it may be suitable to use a dynamic implicit approach.

3.1 Static solution of non-linear FE-systems

As listed above we have in practice two different static approaches to the solution of a non-linear static problem. These approaches are briefly described in the following subsections.

3.1.1 Static implicit solution

When using this method we have at the time $t = \tau$ obtained a solution that fulfills:

$$\mathbf{f}_{int}(\tau) = \mathbf{f}_{ext}(\tau) \tag{3.5}$$

Starting from the point of equilibrium the problem is now to solve the following equation with regard to $\Delta\mathbf{u}$ at time $t = \tau + \Delta t$:

$$\Phi(\Delta\mathbf{u}) = \bar{\mathbf{f}}_{ext}(\tau + \Delta t) - \bar{\mathbf{f}}_{int}(\mathbf{u}(\tau + \Delta t)) = \mathbf{0} \tag{3.6}$$

Introducing a tangent stiffness matrix, which is evaluated at the current approximate solution $\Delta\mathbf{u}^*$:

$$\mathbf{K}_t = -\left.\frac{\partial\Phi}{\partial\Delta u}\right|_{\Delta\mathbf{u}^*} \tag{3.7}$$

From 3.6 we can evaluate the residual $\Phi(\Delta\mathbf{u}^*)$ and using the tangent stiffness we can estimate the relation between the residual and iterative displacements:

$$\Phi(\Delta\mathbf{u}^*) = \mathbf{K}_t\delta\mathbf{u} \tag{3.8}$$

From equation 3.8 the iterative displacements $\delta\mathbf{u}$ is found and the displacements can be updated:

$$\Delta\mathbf{u}^* = \Delta\mathbf{u}^* + \delta\mathbf{u} \tag{3.9}$$

The solution $\Delta\mathbf{u}$ is obtained by iteration as:

$$\Phi \to O \tag{3.10}$$

To perform the iterations one of the Newton-Raphson schemes can be used; two of these schemes are presented along with the incremental explicit method in section 3.2.1.

3.2 Static explicit solution

Another approach is the static explicit method. This method is also called the explicit incremental method, which refers to the fact that the solution is obtained at the time $\tau + \Delta t$ from quantities known at time τ. Here the updated configuration is obtained by solving only linear equations and no iterations are used to improve the solution (reduce the residual).

$$\bar{\mathbf{f}}_{int}(\tau + \Delta t) - \mathbf{f}_{int}(\tau) = \bar{\mathbf{f}}_{ext}(\tau + \Delta t) - \mathbf{f}_{ext}(\tau) \tag{3.11}$$

Expressed in the displacements this can be written as:

$$\mathbf{K}_t\Delta\mathbf{u} = \Delta\mathbf{f}_{ext} \tag{3.12}$$

Evaluating $\mathbf{K}_t$ at the end of the previous step we can solve equation 3.12 for the increment in displacements, and the configuration is updated to:

$$\mathbf{u}(\tau + \Delta t) = \mathbf{u}(\tau) + \Delta\mathbf{u} \tag{3.13}$$

This method can lead to serious errors. For instance, the use of this approach when updating constitutive relations will nearly always lead to lack of accuracy due to drifting. A simple way to improve the method slightly is to take the out of balance forces at the end of the increment and include them in the next load increment.

3.2.1 Summary of static methods

Table 3.1 shows the necessary steps for the explicit incremental, the Newton-Raphson(NR) and the modified Newton-Raphson method. The principles of the three methods are il-

Explicit incremental	Newton-Raphson	Modified Newton-Raphson
load steps n=1,2,...	load steps n=1,2,...	load steps n=1,2,....
$\mathbf{f}_{ext}^{n} = \mathbf{f}_{ext}^{n-1} + \Delta\mathbf{f}_{ext}$	$\mathbf{f}_{ext}^{n} = \mathbf{f}_{ext}^{n-1} + \Delta\mathbf{f}_{ext}$	$\mathbf{f}_{ext}^{n} = \mathbf{f}_{ext}^{n-1} + \Delta\mathbf{f}_{ext}$
	$\mathbf{u}_n^0 = \mathbf{u}_{n-1}$	$\mathbf{u}_n^0 = \mathbf{u}_{n-1}$
$\mathbf{K}_{n-1} = -\frac{\partial\Phi}{\partial\Delta u}\|_{\mathbf{u}_{n-1}}$	iterations i=1,2,....	$\mathbf{K}_{n-1} = -\frac{\partial\Phi}{\partial\Delta u}\|_{\mathbf{u}_{n-1}}$
$\Phi_n = \mathbf{f}_{ext}^{n} - \mathbf{f}_{int}(\mathbf{u}_{n-1})$	$\mathbf{K}_n^{i-1} = -\frac{\partial\Phi}{\partial\Delta u}\|_{\mathbf{u}_n^{i-1}}$	iterations i=1,2,...
$\delta\mathbf{u}_n = [\mathbf{K}_{n-1}]^{-1}\Phi_n$	$\Phi_n^i = \mathbf{f}_{ext}^{n} - \mathbf{f}_{int}(\mathbf{u}_n^{i-1})$	$\Phi_n^i = \mathbf{f}_{ext}^{n} - \mathbf{f}_{int}(\mathbf{u}_n^{i-1})$
$\mathbf{u}_n = \mathbf{u}_{n-1} + \delta\mathbf{u}_n$	$\delta\mathbf{u}_n^i = [\mathbf{K}_n^{i-1}]^{-1}\Phi_n^i$	$\delta\mathbf{u}_n^i = [\mathbf{K}_{n-1}]^{-1}\Phi_n^i$
	$\mathbf{u}_n^i = \mathbf{u}_n^{i-1} + \delta\mathbf{u}_n^i$	$\mathbf{u}_n^i = \mathbf{u}_n^{i-1} + \delta\mathbf{u}_n^i$
	stop iteration when:	stop iteration when:
	$\|\|\Phi_n^i\|\| < c\|\|\mathbf{f}_{ext}\|\|$	$\|\|\Phi_n^i\|\| < c\|\|\mathbf{f}_{ext}\|\|$
end of load step	end of load step	end of load step

Table 3.1: *Schematic presentation of the explicit incremental, the Newton-Raphson, and the modified Newton-Raphson methods.*

lustrated in figure 3.1. It is characteristic of the NR method that problems occur when a

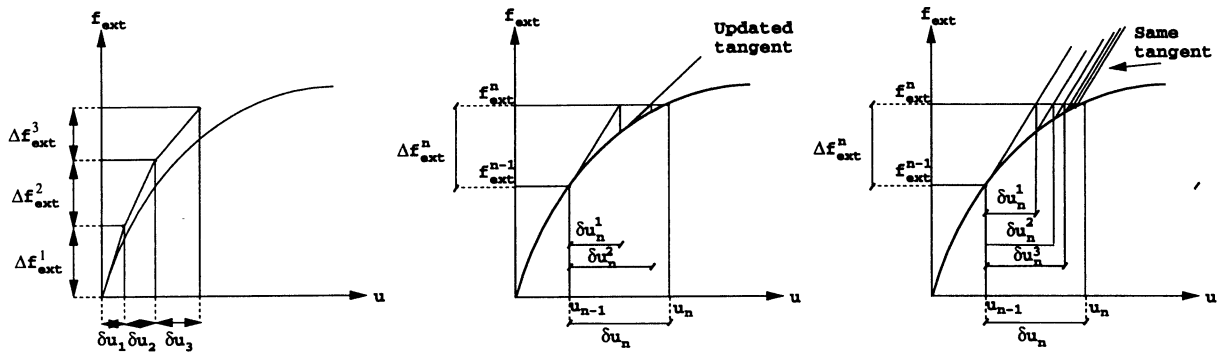

Figure 3.1: *Illustration of the explicit incremental, Newton-Raphson and modified Newton-Raphson method.*

load maximum is reached, and that the modified NR fails to converge in case of a hardening system. The NR scheme converges rapidly (second order convergence) whereas the modified NR has a slower convergence measured in iteration steps. But the modified NR will often be more effective, seen from a computational point of view, as decomposition of the stiffness matrix is avoided in the iterations.

More advanced solution schemes can be formed, for instance the BFGS and DFP update, as well as arc length methods and line search procedures. These methods and principles have been investigated and developed by researchers as for instance Bergan and Crisfield. In Bjaerum [33], Zienkiewicz and Taylor [229] and Crisfield [47] a detailed discussion on

solution methods can be found together with a comprehensive list of references. The methods have the disadvantage that they do not guarantee a solution, and it is often necessary to shift between iteration procedures to obtain a complete solution. It can be necessary to go from a load controlled solution to displacement control; this will be the case with many problems with instability, load maximum, etc.

3.3 Dynamic solution of non-linear FE-equations

The implicit method of time integration can be expressed as:

$$\mathbf{u}_{n+1} = f(\dot{\mathbf{u}}_{n+1}, \ddot{\mathbf{u}}_{n+1}, \mathbf{u}_n, \dot{\mathbf{u}}_n, ...) \tag{3.14}$$

and the explicit time integration as:

$$\mathbf{u}_{n+1} = f(\mathbf{u}_n, \dot{\mathbf{u}}_n, \ddot{\mathbf{u}}_n, \mathbf{u}_{n-1}, \dot{\mathbf{u}}_{n-1}, ...) \tag{3.15}$$

The implicit method requires knowledge of the time derivatives at step n+1 which are unknown, whereas the explicit method is based on known quantities at step n. This gives an important distinction between the methods. If the problem is non-linear the implicit methods necessitate an iterative procedure in order to determine the update of the displacements. With the explicit method the updates are determined directly from known quantities in the previous time steps and no iterations are needed.

The methods are often seen categorized as either single-step or multi-step methods. When information from state n is used to determine state $n+1$, the method is a single step method, and if state $n-1$ and state n are included in the integration scheme it is a so-called two-step method. The following section gives a derivation of the central difference method. Due to its simplicity it has become one of the most popular methods used in explicit FE-context as well as in many other numerical applications, e.g. vibration analysis.

3.3.1 Dynamic explicit solution

When an explicit time integration of the equations of motion of the FE-system is carried out, the equilibrium equation is established at a known state n at the time t^n where from the unknown state $\mathbf{u}_{n+1}$ at the time t^{n+1} is determined. This procedure corresponds in principle to the incremental explicit method apart from taking the dynamic terms into account too. In principle one can expect the same kind of problems with drifting. However, the explicit method is only conditionally stable - to ensure stability the Courant criterion must be fulfilled (section 3.3.2), and hereby many time steps must be used improving the solution (but never eliminating drifting effects). Drifting will give an out of balance force, which is included in the following step (steps), and which corresponds to the method for improvement of the static explicit method mentioned in section 3.2.

We write the equation of motion for the FE-system at the time t^n as:

$$\mathbf{M}\ddot{\mathbf{u}}^n + \mathbf{C}\dot{\mathbf{u}}^n + \mathbf{f}_{int}^n = \mathbf{f}_{ext}^n \tag{3.16}$$

If the damping matrix $\mathbf{C}$ is diagonal, the system may be transformed into an uncoupled system of equations. In the following we assume that the damping matrix $\mathbf{C}$ is proportional to the diagonal of the mass matrix $\mathbf{M}$, i.e.

$$\mathbf{C} = c\mathbf{M} \tag{3.17}$$

First we make a truncated Taylor expansion to approximate the velocity and acceleration:

$$\dot{\mathbf{u}}^{n-\frac{1}{2}} = \frac{-\mathbf{u}^{n-1} + \mathbf{u}^n}{\Delta t^{n-\frac{1}{2}}} \qquad \ddot{\mathbf{u}}^n = \frac{-\dot{\mathbf{u}}^{n-\frac{1}{2}} + \dot{\mathbf{u}}^{n+\frac{1}{2}}}{\Delta t^n} \tag{3.18}$$

where for highly non-linear problems it may be necessary with an approximation of time steps as well.

$$\Delta t^{n-\frac{1}{2}} = \frac{\Delta t^{n-1} + \Delta t^n}{2} \tag{3.19}$$

Normally, it will not be necessary to utilize different time steps in an analysis. The expression for the velocity at the time t^n is obtained by averaging the velocities at the time $t^{n-\frac{1}{2}}$ and the time $t^{n+\frac{1}{2}}$

$$\dot{\mathbf{u}}^n = \frac{1}{2}(\dot{\mathbf{u}}^{n-\frac{1}{2}} + \dot{\mathbf{u}}^{n+\frac{1}{2}}) \tag{3.20}$$

In some cases where non-diagonal damping is utilized, one can use a scheme where external damping forces are evaluated a half time step delayed compared to the presented scheme. It is hereby still possible to decouple the equations as done in formula 3.24. By substituting the equations in (3.18) and (3.20) into equation (3.16), we find the following system of equations:

$$\mathbf{M}\left[\frac{(-\dot{\mathbf{u}}^{n-\frac{1}{2}} + \dot{\mathbf{u}}^{n+\frac{1}{2}})}{\Delta t^n} + \frac{c}{2}(\dot{\mathbf{u}}^{n-\frac{1}{2}} + \dot{\mathbf{u}}^{n+\frac{1}{2}})\right] + \mathbf{f}_{int}^n = \mathbf{f}_{ext}^n \tag{3.21}$$

Solving equation 3.21 for the velocity $\dot{\mathbf{u}}^{n+\frac{1}{2}}$ we find:

$$\dot{\mathbf{u}}^{n+\frac{1}{2}} = \frac{(\frac{1}{\Delta t^n} - \frac{c}{2})}{(\frac{1}{\Delta t^n} + \frac{c}{2})}\dot{\mathbf{u}}^{n-\frac{1}{2}} + \frac{\mathbf{M}^{-1}(\mathbf{f}_{ext}^n - \mathbf{f}_{int}^n)}{(\frac{1}{\Delta t^n} + \frac{c}{2})} \tag{3.22}$$

The displacement at the time t^{n+1} is then by using 3.18 found to be:

$$\mathbf{u}^{n+1} = \mathbf{u}^n + \Delta t^{n+\frac{1}{2}}\dot{\mathbf{u}}^{n+\frac{1}{2}} \tag{3.23}$$

If a diagonal mass matrix is used, we can write equations 3.22 and 3.23 in their component forms:

$$\dot{u}_i^{n+\frac{1}{2}} = \frac{(2 - c\Delta t^n)}{(2 + c\Delta t^n)}\dot{u}_i^{n-\frac{1}{2}} + \frac{2\Delta t^n}{2 + c\Delta t^n}(f_{ext,i}^n - f_{int,i}^n)\frac{1}{M_{ii}} \tag{3.24}$$

$$u_i^{n+1} = u_i^n + \Delta t^{n+\frac{1}{2}}\dot{u}_i^{n+\frac{1}{2}} \tag{3.25}$$

That means we directly evaluate the new state without solving a system of equations. To obtain a diagonalized mass matrix the methods presented in section 2.6.3 can be used.

In order to start the time integration, step by step, initial conditions must be specified at the time t^0:

$$\mathbf{u} = \mathbf{u}^0 \qquad \dot{\mathbf{u}} = \dot{\mathbf{u}}^0 \tag{3.26}$$

and further we must estimate the velocities at $-\frac{\Delta t}{2}$, which can be done as:

$$\dot{\mathbf{u}}^{-\frac{1}{2}} = \dot{\mathbf{u}}^0 - \frac{\Delta t}{2}\ddot{\mathbf{u}}^0 \tag{3.27}$$

where $\ddot{\mathbf{u}}^0$ is obtained from the dynamic equilibrium at the time 0, that is equation 3.16.

3.3.2 The stability criterion

The explicit time integration scheme is only conditionally stable. In case the damping matrix is non-diagonal the stable time step for the central difference method is given by, (see e.g. Belytschko [23])

$$\Delta t^n \leq \min \frac{2}{\omega_l}\left(\sqrt{1+\xi_l^2} - \xi_l\right) = \Delta t_{stab} \tag{3.28}$$

where ω_l is the lth natural frequency of the FE-system and ξ_l is the fraction of the critical damping used in this mode. The minimum of equation (3.28) is usually given by the maximum frequency of the system:

$$\Delta t_{stab} = \frac{2}{\omega_{max}}\left(\sqrt{1+\xi_{max}^2} - \xi_{max}\right) \tag{3.29}$$

where ξ_{max} is the fraction of critical damping of the maximum frequency present in the system. From equation (3.29) we see that the stable time step will increase if the system is undamped. We also note, that if the maximum frequency is critically damped the stable time step reduces to about 60 per cent of the stable time step of the undamped system. This will seldom be the case as the lowest eigen-frequency is normally dominating the response, and one will normally obtain the most effective damping by using a critical damping of the lowest eigen-mode. For almost any FE-mesh there will be a big difference between the lowest and the highest eigen-frequency.

According to Cook [46] diagonalized damping does not affect the stable time step when using equation 3.21 (with diagonalized damping) and the limitation on the time step (the Courant condition) becomes

$$\Delta t \leq \frac{2}{\omega_{max}} \tag{3.30}$$

This is, however, only valid in case of linear systems, and in practice a fraction of the limiting time step is utilized in the analysis. LS-Dyna3d defaults the value to 90 per cent of the critical time step, and in the analyses, which is performed in connection with this work,

no problems regarding stability have been encounted. In other areas, which are analysed with explicit FE, e.g. penetration problems, a much smaller time step must be used.

Hoff and Taylor [95] present a new higher order explicit one step scheme with which it is possible to achieve an accuracy which is better than the second order accuracy obtained by the central difference method. In the article this is done with a generalized algorithm, including the central difference method. In regard to computational efficiency it seems impossible to improve the efficiency, but it may be possible to achieve some improvements in accuracy. Hoff and Taylor show that it is possible to double the stable time step size, but the cost is a doubling of the function evaluations. This may be important in analyses where the transient response is of major interest, but in the present work it is evaluated to be of minor importance.

3.3.3 Explicit methods

Explicit finite element methods have been extensively used for problems involving high velocity and short duration of loading. In these problems the high frequency response demands a high time resolution and the solution does not suffer from the demand that the time step must be less than the critical time step ($\Delta t \leq \Delta t_{stab}$). Due to the small stable time step, the solution of quasi-dynamic problems like sheet metal forming can take a considerable amount of time.

Nevertheless, some aspects make the explicit formulation superior in comparison with an implicit formulation, especially for problems where the stiffness variations are dominated by contact condition, see e.g. Nagtegaal and Taylor [156]. Some of the advantages of the explicit formulation are listed below:

- Few computations are required per time step.
- The algorithm is simple in logic and structure, so complex non-linearities are easily handled.
- It requires little data storage compared to direct elimination methods (Newton-Raphson).
- It is ideal for testing new ideas because it requires less coding.
- It is reliable in accuracy and completion of computation.

The explicit method has only one (or indirectly two) obvious disadvantage: It is only conditionally stable which leads to a very small time step, and a very high number of time steps is hereby needed (which can lead to accuracy problems due to round-off errors).

Seen in relation to sheet metal forming, which is normally a rather slow process, one can at first glance evaluate the explicit method as non-suitable when we bear in mind the traditional analysis performed with explicit methods. This indicates that special means must be taken into account in order to perform efficient analysis within the area of sheet metal forming. This is of course a disadvantage but seen in relation to the simulation of forming processes the major advantages are that the explicit method without problems handles complex contact phenomena (due to the small time increment) as well as instability phenomena as for instance buckling and formation of wrinkles.

3.3.4 Summary of explicit methods

In general it can be concluded that explicit finite element methods are directly suitable for short time events, i.e. events where the transient response is of interest. This kind of problems are typically analysed over a time interval in the range of milliseconds. Then we have a sort of paradox as sheet metal forming is a relatively slow process, typically in the range of 0.1-10 sec. The problem can be expressed as the relation between the process time and the Courant criterion:

$$t_{process} >> \Delta t_{Courant} = \frac{L_{typical}}{c_{sound}} = \frac{L_{typical}}{\sqrt{\frac{E}{\rho(1-\nu^2)}}} \tag{3.31}$$

stated here for shell elements. c_{sound} is the speed of sound in the material and $L_{typical}$ is a typical length for the element. The physical interpretation of the Courant criterion is that Δt must be small enough that information does not propagate across more than one element per time step. Waves are propagating with the speed of sound and the time for propagation is then dependent on a typical length for the element. Several ways to choose the typical length do exist, e.g. to choose the shortest element side or, for a four node plane element, to take the diameter of the smallest circles touching 3 element sides. This latter criterion also explains the importance of a regular mesh, if the mesh becomes to distorted the typical length becomes small leading to a small stable time step. A too small stable time step decreases the computational efficiency.

At first glance there seems to be two ways to improve the computational efficiency: To decrease the process time or increase the stable time step by scaling of density ρ (not forgetting the effect of modelling with a suitable mesh). This problem and various methods to improve solution schemes are discussed and illustrated in more detail in chapter 4.

When comparing explicit and implicit methods a dramatic increase in demand for storage as well as computer power can be seen when using implicit methods (see table 3.2): Table

	Storage requirements		CPU requirements	
Element type	2D elem.	3D elem.	2D elem.	3D elem.
Implicit	n^5	n^7	n^5	n^7
Explicit	n^2	n^3	n^3	n^4

Table 3.2: *Comparison between implicit and explicit methods, from Brännberg [36]. n is the number of elements.*

3.2 shows that the requirements depend on the size of the problem and the formulation utilized, e.g. the storage requirements for a 3 dimensional analysis grows with the element number to the power of 7 for the implicit FE formulation, whereas the explicit formulation only grows with the number of elements to the power of 3. Especially when the problems become geometrically complex and hereby demand a huge number of elements the explicit method seems superior. In the last few years a number of iterative solvers for use with implicit methods have been developed. The development seems to improve the solution capability of the implicit methods considerably, however, these methods demand a well

conditioned stiffness matrix in order to be effective.

Previously explicit FE has been used to obtain solutions to linear static problems, when the number of degrees of freedom became so high that computer storage of the stiffness matrix tended to be the primary problem. Even very large problems can be treated incore when the explicit FE-method is used.

Chapter 4

Solution of Metal Forming Problems using Explicit Methods

When using explicit FEM to simulate metal forming processes modifications must be made in order to keep the computation time within reasonable limits. Some simulation strategies are discussed below and illustrated with examples.

The first way to decrease the computation time is to increase the loading rate. It has been shown by various authors that substantial scaling of the loading rate can be performed without introducing too high disturbances in the solution, see for instance Brännberg and Nielsen [37, 161, 162], Keck et al. [116], Di Pasquale et al. [61], Wagoner et al. [214], Lindgren and Edberg [137], Galbraith et al. [74, 75], Haug et al. [86], Honecker and Mattiason [98, 145], Aita et al. [3], Schwiezerhof et al. [186].

However, a too severe scaling of the loading rate can introduce inertial effects in the solution which are not seen in the real process; in some of those cases artificial damping may be utilized to improve the simulation.

When using different materials with large variations in the modulus of elasticity and/or density, one can in some cases obtain improvements in computational efficiency by using subcycling. This can also be the case for meshes where regions are characterized by elements of similar size.

We can typically split a forming process up into two parts: a) The forming process and b) The spring back when removing tool parts. The first part of the forming process is characterized by an initial elastic loading followed by a more severe plastic deformation, whereas the spring back is dominated by elastic deformation; in most cases a pure elastic deformation. In the following we will restrict ourselves to the explicit time integration method and we will look at the solution of quasi-static problems in a broad sense.

4.1 A system with one-degree of freedom

In the following a simple system consisting of a mass, a spring and a damper as illustrated in figure 4.1 is considered. The purpose of the section is to illustrate some aspects of a

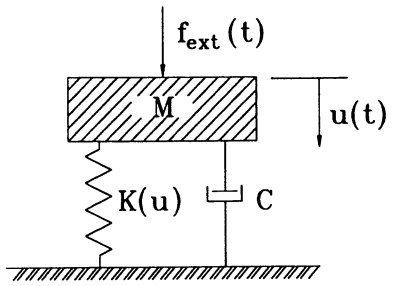

Figure 4.1: *Illustration of a one-dimensional system.*

dynamic system. Especially aspects on how to obtain a solution close to quasi-static is emphasized. Although the considerations are strongly simplified compared to a sheet metal forming process many of the computational aspects are similar. The characteristics of the simple system can be found for the much more complicated problem; to simulate sheet metal forming processes with explicit FE.

To simulate quasi-static processes with an explicit time integration the first demand to the analyst is, that a sound understanding of which problems the dynamic approach may cause is present. For that purpose it seems justified with some discussion of a one-degree of freedom system. If the system shown in figure 4.1 is exposed to a unit step load we find the response [204]:

$$u(t) = \frac{f_{ext}}{K}\left[1 - e^{-\xi\omega_n t}\left\{cos\left(\sqrt{1-\xi^2}\omega_n t\right) + \frac{\xi}{\sqrt{1-\xi^2}} sin\left(\sqrt{1-\xi^2}\omega_n t\right)\right\}\right] \tag{4.1}$$

where ω_n is the undamped eigen-frequency ($\sqrt{K/M}$) and ξ gives the fraction of critical damping as:

$$\xi = \frac{c}{c_{cr}}, \qquad c_{cr} = 2m\omega_n \tag{4.2}$$

If we only regard a critical damped system ($\xi = 1$) we obtain:

$$u(t) = \frac{f_{ext}}{K}\left[1 - (1 + \omega_n t)e^{-\omega_n t})\right] \tag{4.3}$$

as

$$\frac{sin\left(\sqrt{1-\xi^2}\omega_n t\right)}{\sqrt{1-\xi^2}\omega_n t} \rightarrow 1 \quad for \quad \xi \rightarrow 1 \tag{4.4}$$

The time which is needed to get within a tolerance of 0.1 per cent of the static solution can be found from:

$$0.999\frac{f_{ext}}{K} = \frac{f_{ext}}{K}\left[1 - (1 + \omega_n t)e^{-\omega_n t})\right] \rightarrow 0.001 = (1 + \omega_n t)e^{-\omega_n t} \tag{4.5}$$

which leads to:

$$t = \frac{9.23}{\omega_n} \tag{4.6}$$

If the explicit time integration is used for the analysis a number of time steps are necessary in order to fulfil the stability criterion, which for a damped system is [46]:

$$\Delta t \leq \frac{2}{\omega_n}\left(\sqrt{\xi^2+1}-\xi\right) \tag{4.7}$$

and which for the critical damped system leads to:

$$\Delta t \leq \frac{0.828}{\omega_n} \tag{4.8}$$

Combining equation 4.8 with 4.6 leads to the minimum number of time steps:

$$N_{steps} \geq \frac{t}{\Delta t} = \frac{9.23}{0.828} = 11.14 \tag{4.9}$$

To obtain a solution within 0.1 per cent of the static solution we must therefore use a total of 12 time steps.

If we consider the system the only parameter needed to obtain the static response is the stiffness. To find the static deflection by using explicit time integration, we are in principle free to choose values for damping as well as mass. However, we cannot obtain the static solution within fewer time steps than the 12 steps necessary when using critical damping as illustrated in the example. A similar analysis is reported by Brännberg [36].

4.1.1 Explicit integration of a one-degree of freedom system

To discuss the problems related to simulation of quasi-static processes it can be useful to look at the simple problem with one-degree of freedom. To obtain responses more easily to a number of problems a small Fortran programme was made. The programme uses the explicit solution scheme as given in the following scheme:

- 1: Input: mass M, fraction of critical damping ξ, spring and load characteristica $K(u)$ and $f_{ext}(t)$.
- 2: Initialize: Calculate eigen-frequency ω_n, critical time step and set damping to $C = 2\sqrt{MK}\xi$. Set initial conditions: $u = u_0 = 0$, $\dot{u} = \dot{u}_0 = 0$, $\dot{u}_{-\frac{1}{2}} = 0$
- 3: Calculate f^n_{int} corresponding to u_n and f^n_{ext}.
- 4: Update displacement: $u_{n+1} = \frac{\Delta t^2}{M}\left(f^n_{ext} - f^n_{int} + \frac{M}{\Delta t^2}(u_n + \Delta t\dot{u}_{n-\frac{1}{2}}) - C\dot{u}_{n-\frac{1}{2}}\right)$
- 5: Update velocity: $\dot{u}_{n+\frac{1}{2}} = (u_{n+1} - u_n)/2$
- 6: Output and set $n = n+1$, $t = t + \Delta t$. Go to step 3.

A more detailed discussion of explicit solution schemes can be found in Cook [46], Belytschko [27, 26], Zienkiewicz and Taylor [229]. Figure 4.2 shows the response for a linear, one-degree of freedom system for various degrees of damping ranging from 0.2 to 1.4 times the critical damping. When overcritical damping is applied the response is delayed and as

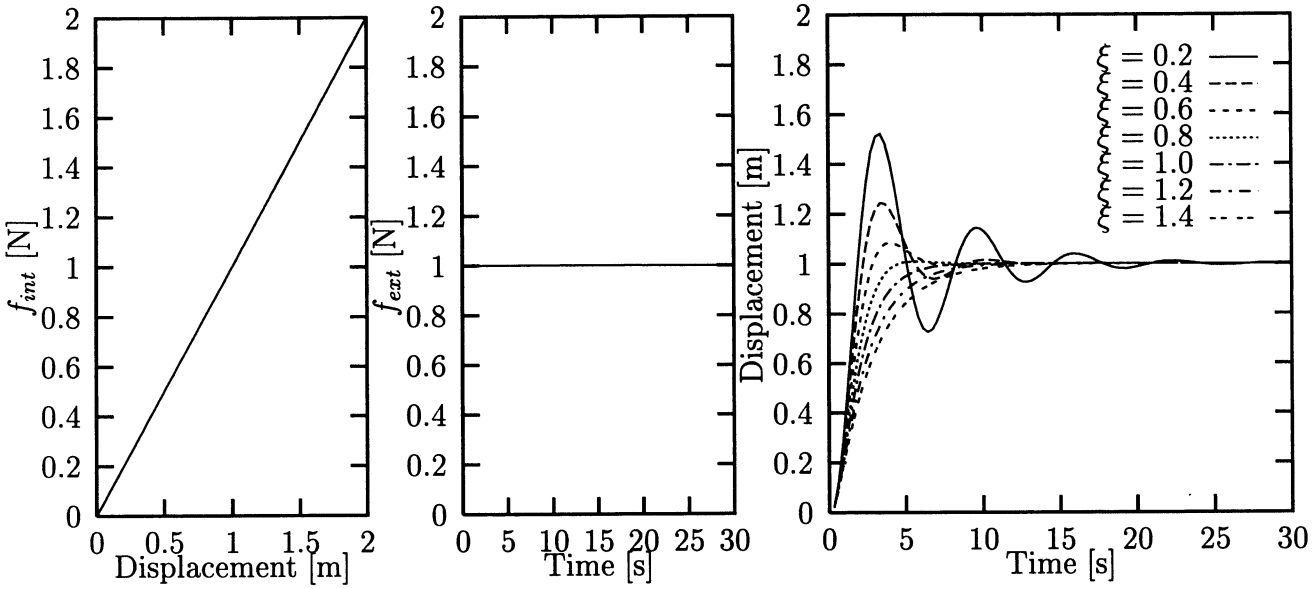

Figure 4.2: *Left: Spring characteristic. Middle: Applied external force. Right: Response for various fractions of critical damping ξ ranging from 0.2 to 1.4.*

regards undercritical damping there will be an overshoot in the solution.

For a step load the static solution for a linear elastic, one-degree of freedom system can be obtained within 12 time steps (within 0.1 per cent of the exact solution). This corresponds to the solution of a linear set of equations by using a dynamic relaxation approach, which solves the system $\mathbf{f} = \mathbf{Ku}$ as the static response of the equivalent dynamic system $\mathbf{M\ddot{u}} + \mathbf{C\dot{u}} + \mathbf{Ku} = \mathbf{f}$.

A one-degree of freedom system without damping

If instead the main problem is considered to be the determination of a quasi-static solution (i.e. to achieve a good estimation of the response during loading by use of explicit methods), we start considering the three spring characteristica and the two load cases shown in figure 4.3 (left and middle): Figure 4.3 (right) gives the predicted response for the three types of springs loaded with the linearly increasing force and the figure shows that there will be a change in eigen-frequency during loading for the non-linear springs. To distinct the curves: The linear spring response is overlaid with a vibration with constant frequency, the softening gives higher and higher periods and for the hardening spring the period decreases. Furthermore, it can be noticed that because the problem is force driven the response for the softening spring becomes uncontrolled as the maximum load carrying capacity of 1.125 N is exceeded, which leads to a dynamic growth, but still the solution is stable. This is one of the characteristics of the explicit method compared to the static implicit method: The same problem will lead to problems if it is solved with an implicit method as a static solution does not exist. If instead the problem is displacement controlled, it is possible to follow the solution with an implicit solution scheme. For a more general problem it can be necessary to change the implicit integration scheme when reaching a maximum load (see for instance Crisfield [47], Krenk [126], Zienkiewicz and Taylor [229]). Figure 4.4 shows the response to the second load case where the external

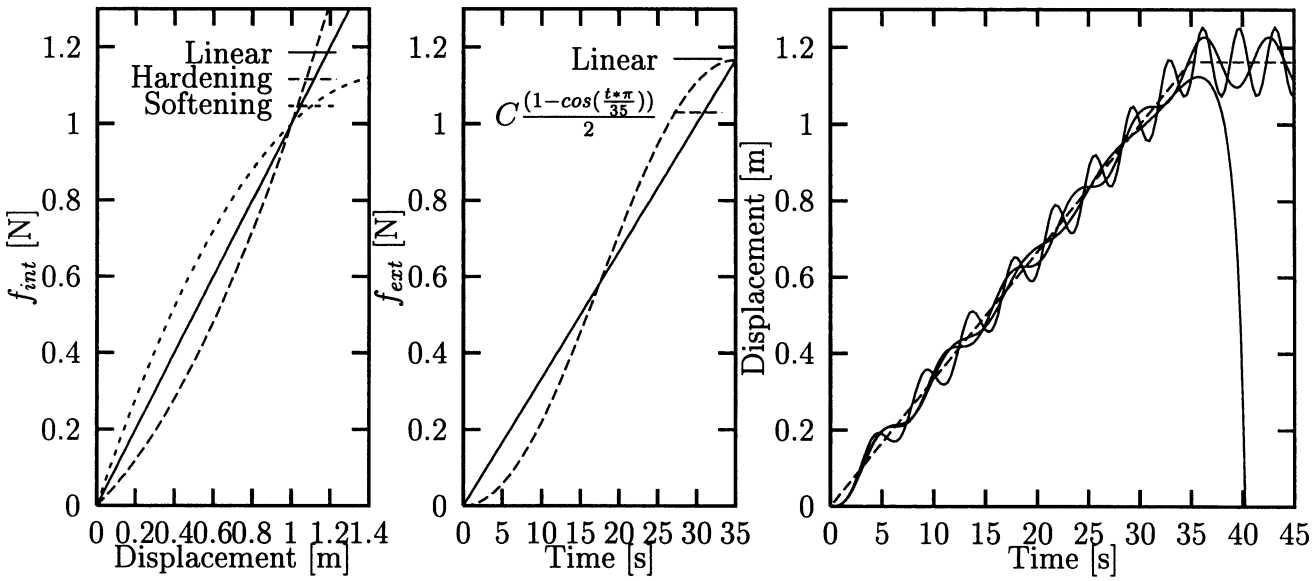

Figure 4.3: *Left: Illustration of three spring characteristics. Middle: Quasi-static load profiles (linear and cosine shaped). Right: The obtained response for an undamped system by using the linear load and the three spring characteristics, respectively. The dotted line is the quasi-static displacement response, which remains constant for* $t > 35$ *sec.*

force is prescribed to follow a cosine profile. There is a marked difference between figure 4.3 and figure 4.4: The overlaid vibration amplitude in the curves becomes much smaller than the corresponding results to a load applied linearly. This corresponds to the definition of a quasi-static process stated by Cook et al. [46]: "If the frequency of excitation applied to a structure is less than roughly one third of the structure's lowest eigen-frequency of vibration, the effects of inertia can be neglected and the problem is quasi-static".

For the example analysed in figure 4.4 the excitation frequency is approximately $\frac{1}{8}$ to $\frac{1}{6}$ of the lowest eigen-frequency and we can draw a reverse conclusion: If we can apply the load with an excitation frequency lower than $\frac{1}{3}$ of the lowest eigen-frequency we can expect accurate solutions to a quasi-static problem when using the explicit integration method.

This leads to the proposal to estimate, if possible, the lowest eigen-frequency and specify loading profile as a Fourier expansion, where only terms with frequencies lower than $\frac{1}{3}$ of the lowest structural vibration frequency are included.

However, this approach will in some cases be difficult to employ as we will for a system with a very low lowest eigen-frequency need a very long simulation time. Another problem is that most sheet forming processes behave in a very non-linear way leading to a lowest eigen-frequency which changes during the process.

A one-degree of freedom system with damping

When a quasi-dynamic approach is used to integrate the equations of equilibrium there is a risk of overshoots in the solution. These can be reduced by the choice of loading functions, but in the general case we cannot expect to avoid this kind of problems. For problems

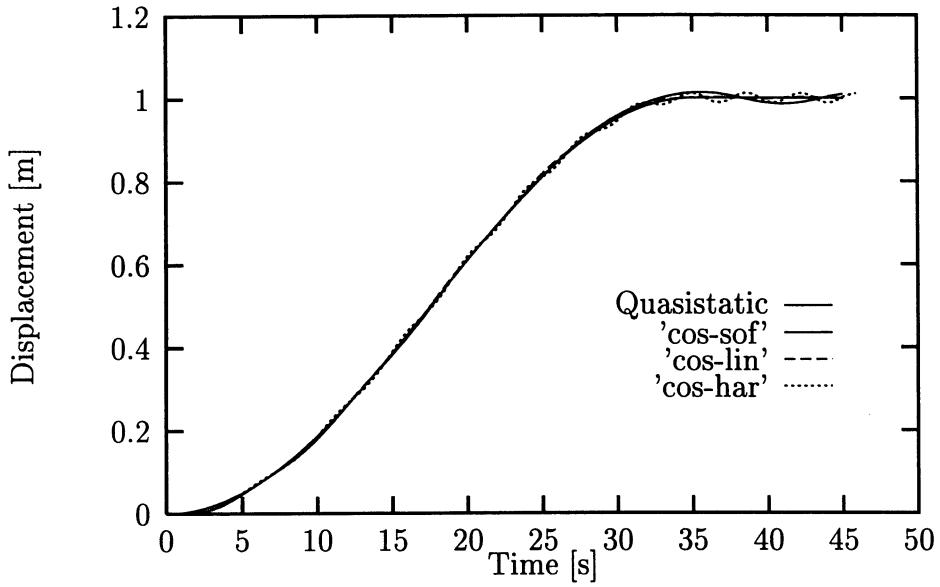

Figure 4.4: *The obtained response for the spring characteristics in the previous figure and a cosine shaped load profile* $(0.5(1 - cos(\frac{\pi t}{30}))$ *for* $t < 30$ *and constant otherwise.*

involving plastic deformations an overshoot cannot even if it is small be allowed due to path dependency. This is of importance for both the treatment of the constitutive equations and for the structural response. For instance an overshoot for the one-dimensional problem will lead to an unphysical plastic straining which is not seen in the quasi-static process and should obviously be avoided - or at least be reduced to an acceptable level.

Another aspect which is important for a sheet metal forming operation is that there normally is a heavy damping due to plastic dissipation of energy. To illustrate the effect of damping, the one-degree of freedom system is loaded with an external force ramped to reach a constant level whereupon vibrations are damped out. Figure 4.5 shows the out of balance force $(f_{int} - f_{ext})$ for various degrees of damping between 0.2 and 4.0 times the critical damping. By using the loading: $f(t) = Ct$ we can as shown in figure 4.5 obtain the discrepancy between the quasi-static solution and the one obtained with the explicit integration method for various degrees of damping. As regards the quasi-static solution the out of balance force will be zero, but depending on the amount of damping a delay will exist for the dynamic solution. As long as the spring is linear it is sufficient to damp the system overcritically to avoid overshooting. As long as the load is increasing we can avoid vibrational effects by applying a damping of 0.8 time the critical. However, when the force reaches the constant level at 35 msec this damping is not sufficient to avoid a small overshoot as the out of balance force reaches positive values. On the other hand, it is clear that the use of damping leads to a delay of the response compared to the quasi-static response.

4.1.2 Summary

To ensure that unphysical plastic straining due to overshoots in the solution does not take place, it can be necessary to specify an artificial damping. It can also be concluded that

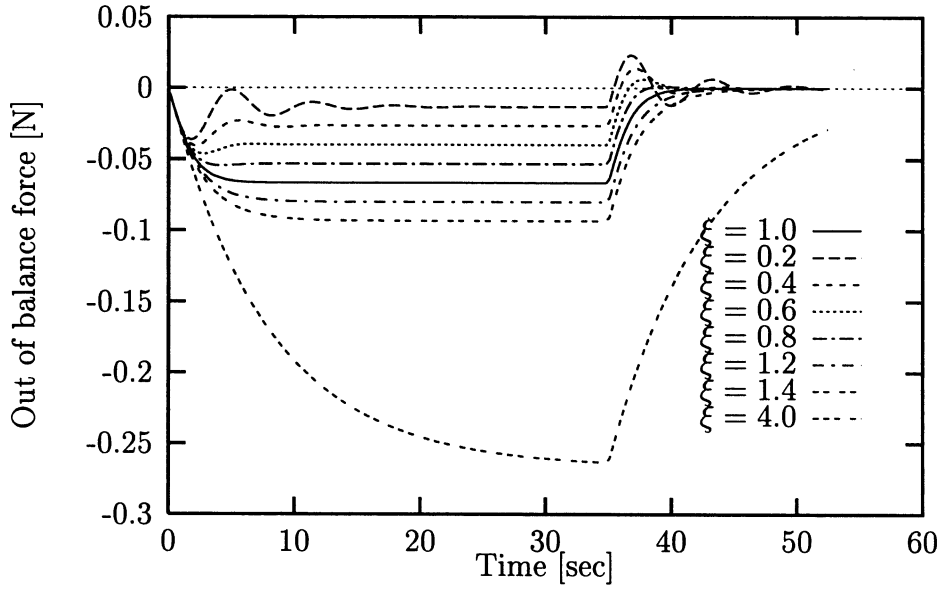

Figure 4.5: *Response illustrated by the difference between applied and internal force for the linear elastic one-dimensional system when applying the load as a ramp function ($f = Ct$ for $t < t_0, f = Ct_0$ for $t > t_0, C = \frac{1}{t_0}$, $t_0 = 35$ sec) for various degrees of damping ($\xi = 0.2 - 4.0$).*

when using this approach it is necessary to extend the analysis time beyond the specified time to reach maximum load and damp out the velocity after having reached the maximum load. The effect of this is illustrated in figure 4.5 where the delay between a damped system and the quasi-static solution is clearly demonstrated.

With the one-dimensional models in mind it can be concluded that artificial damping can be used to obtain solutions corresponding to the load response of an static system. Also for a load driven problem involving non-linearities, e.g. plasticity, an accurate solution can be expected, but in this case problems can be expected with regard to the determination of the lowest eigen-frequency.

For the situation where the problem is to find the response to a static load the most effective way is to apply the load and damp the system critically. Also, in the case where the spring is non-linear the most effective way to obtain the solution is to choose the damping according to the current value of the spring stiffness (as well as the time step size); this choice is easy to make in cases where information concerning the lowest eigen-frequency is directly available, but in more complex problems it can be difficult to obtain a good estimation of the eigen-frequency.

If instead the time history is of importance it becomes clear that a significant improvement can be obtained by specifying the load following a cosine shape. Hereby it is avoided to introduce a too high inertial resistance in the first part of the analysis. By specifying artificial damping it is clear that overlaid vibrations can be reduced - but it is also evident that this approach will lead to a delay in the response. This type of delay should to some degree be expected in a more general analysis of sheet forming due to dissipation of energy.

4.2 Systems with more degrees of freedom

If we continue our discussion on solution of linear static elastic problems and now look at systems with more degrees of freedom we can write the governing dynamic equations:

$$\mathbf{M}\ddot{\mathbf{u}} + \mathbf{C}\dot{\mathbf{u}} + \mathbf{K}\mathbf{u} = \mathbf{f}(t) \tag{4.10}$$

The viscous damping forces are chosen to be proportional to the mass ($\mathbf{C} = c\mathbf{M}$). By using this definition of damping the equations can be uncoupled (other types of damping can also be uncoupled in the explicit time integration). First a modal matrix $\mathbf{P}$ is introduced:

$$\mathbf{P} = [\{\mathbf{e}_1\}, \{\mathbf{e}_2\}, ...\{\mathbf{e}_n\}] \tag{4.11}$$

The matrix $\mathbf{P}$ consists of the n eigenvectors. If each column in the matrix is divided by the square root of the generalized mass M_i the weighted modal matrix $\tilde{\mathbf{P}}$ is obtained. If $\mathbf{u} = \tilde{\mathbf{P}}\mathbf{y}$ is substituted into the governing equation and the equation is multiplied by $\tilde{\mathbf{P}}^T$ we obtain:

$$\tilde{\mathbf{P}}^T\mathbf{M}\tilde{\mathbf{P}}\ddot{\mathbf{y}} + \tilde{\mathbf{P}}^T\mathbf{C}\tilde{\mathbf{P}}\dot{\mathbf{y}} + \tilde{\mathbf{P}}^T\mathbf{K}\tilde{\mathbf{P}}\mathbf{y} = \tilde{\mathbf{P}}^T\mathbf{f}(t) \tag{4.12}$$

This is a set of uncoupled equations which can be written on the alternative form:

$$\ddot{y}_i + 2\xi_i\omega_i\dot{y}_i + \omega_i^2 y_i = \tilde{f}_i(t) \tag{4.13}$$

The masses and damping terms can be chosen arbitrarily, and it is then with the explicit method possible to obtain a solution of the static problem with a certain accuracy compared to the correct solution in the same way as discussed in section 4.1.

4.2.1 A three degree of freedom system

Below the simple three degree of freedom system shown in figure 4.6 is investigated and some conclusions are drawn. To illustrate the procedure a numerical example is given.

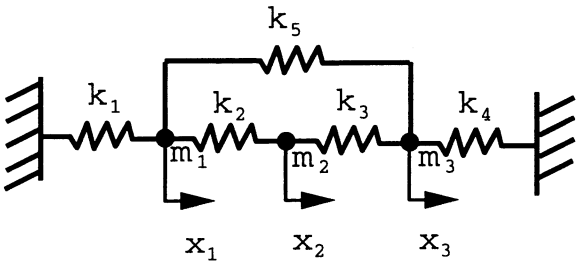

Figure 4.6: *A simple three-degree of freedom system consisting of 5 springs and 3 masses.*

With spring coefficients $k_1 = 100$, $k_2 = 200$, $k_3 = 300$, $k_4 = 400$ and $k_5 = 500$ and nodal masses $m_1 = 10$, $m_2 = 20$ and $m_3 = 30$ the matrices $\mathbf{M}$ and $\mathbf{K}$ become:

$$\mathbf{M} = \begin{bmatrix} 10 & 0 & 0 \\ 0 & 20 & 0 \\ 0 & 0 & 30 \end{bmatrix} \qquad \mathbf{K} = \begin{bmatrix} 800 & -200 & -500 \\ -200 & 500 & -300 \\ -500 & -300 & 1200 \end{bmatrix} \tag{4.14}$$

Determination of the eigen-values and eigen-frequencies yields:

$$\lambda_i = \left\{ \begin{array}{c} 95.8230 \\ 7.2618 \\ 41.9151 \end{array} \right\} \qquad \omega_i = \left\{ \begin{array}{c} 9.7889 \\ 2.6948 \\ 6.4742 \end{array} \right\} \tag{4.15}$$

Corresponding to the eigen-values we have $\mathbf{P}$ consisting of the eigenvectors:

$$\mathbf{P} = \left[\begin{array}{ccc} -0.9590 & 0.0777 & 0.2724 \\ -0.5241 & -0.7026 & -0.4814 \\ -0.3715 & 0.7192 & -0.5747 \end{array} \right] \tag{4.16}$$

$$\mathbf{M}_{generalized} = \mathbf{P}^T\mathbf{M}\mathbf{P} = \left[\begin{array}{ccc} 11.5445 & 0 & 0 \\ 0 & 19.5708 & 0 \\ 0 & 0 & 21.9222 \end{array} \right] \tag{4.17}$$

$$\mathbf{K}_{generalized} = \mathbf{P}^T\mathbf{K}\mathbf{P} = \left[\begin{array}{ccc} 1106.2 & 0 & 0 \\ 0 & 142.1 & 0 \\ 0 & 0 & 918.9 \end{array} \right] \tag{4.18}$$

Making the coordinate transformation $\mathbf{u} = \mathbf{P}\mathbf{y}$ in equation 4.10 and premultiplying with $\mathbf{P}^T$ results in:

$$\mathbf{P}^T\mathbf{M}\ddot{\mathbf{y}} + c\mathbf{P}^T\mathbf{M}\dot{\mathbf{y}} + \mathbf{P}^T\mathbf{K}\mathbf{P}\mathbf{y} = \mathbf{P}^T\mathbf{f} \tag{4.19}$$

which can be written on the form:

$$\ddot{y}_i + 2\xi_i\omega_i\dot{y}_i + \omega_i^2 y_i = \tilde{g}_i(t) \tag{4.20}$$

The solution is in general controlled by the lowest eigen-frequency ω_1, but the stability of the time integration will be controlled by the highest frequency ω_3. In this example the solution can be obtained by using different time steps (as the equations have been decoupled) for the three equations in (4.20), but normally one prefers to use the same time step for the overall solution. To get within a tolerance of 0.1 per cent of the static solution we can use the procedure given previously, where the total analysis time is obtained from:

$$e = (1 + \omega_n t)e^{-\omega_n t}) \tag{4.21}$$

leading to

$$t = \frac{9.23}{\omega_1} \tag{4.22}$$

The stable time step is controlled by the maximum eigen-frequency:

$$\Delta t \leq \frac{2}{\omega_{max}} \left(\sqrt{\xi_{max}^2 + 1} - \xi_{max} \right) \tag{4.23}$$

which when the lowest eigen-frequency is critically damped leads to:

$$\Delta t \leq \frac{0.962}{\omega_3} \tag{4.24}$$

which again leads to the required number of time steps:

$$N_{steps} \geq \frac{t}{\Delta t} = \frac{9.23}{0.962}\frac{\omega_3}{\omega_1} = 34.85 \tag{4.25}$$

In contrast to the one-dimensional system there is a mutual influence between the nodal displacements which necessitates the use of more than 12 time steps to reach the solution (within 0.1 per cent of the static solution).

The modal decomposition method must be judged unrealistic in the general case. An approach using modal decoupling will for a non-linear system demand decompositions during the relaxation which for a system with many degrees of freedom leads to an unacceptable increase in CPU-time.

If we regard the three degrees of freedom system we can conclude that in order to obtain efficient solution schemes for more general problems, the major problem is to reduce the ratio:

$$\frac{\omega_{max}}{\omega_{min}} \tag{4.26}$$

In the above example masses are chosen arbitrary and as the mass matrix can be chosen freely, as long as we are only interested in the static solution, we may consider alternative ways to select nodal masses.

Papadrakis mentions two methods to select the elements in the diagonal mass matrix:

$$m_{ii} = \sum_{j}^{N} |K_{ij}| \qquad or \qquad m_{ii} = K_{ii} \tag{4.27}$$

The two methods of selecting the diagonal element of the mass matrix will in general have an improving effect on the computational efficiency compared to the use of the diagonal mass matrix that arises from lumping; although the methods affect both ω_{max} and ω_{min} the ratio of $\frac{\omega_{max}}{\omega_{min}}$ will decrease (see Underwood [210]).

As shown in the following small example these simple ways of choosing the element masses can lead to an improvement in the computational efficiency.

Let us take the simple three degrees of freedom system discussed previously (4.14). This system has the analytical eigen-frequencies:

$$\omega_i = \{9.7889, 2.6948, 6.4742\} \qquad i = 1,3 \qquad and \qquad \frac{\omega_{max}}{\omega_{min}} = 3.6325 \tag{4.28}$$

Choosing the diagonal mass elements as $m_{ii} = k_{ii}$ leads to the eigen-frequencies:

$$\omega_i = \{0.4303, 1.2314, 1.1382\} \qquad i = 1,3 \qquad and \qquad \frac{\omega_{max}}{\omega_{min}} = 2.8617 \tag{4.29}$$

and choosing $m_{ii} = \sum_{j=1}^{N} |k_{ij}|$ gives:

$$\omega_i = \{0.3181, 0.9312, 0.8155\} \qquad i = 1,3 \qquad and \qquad \frac{\omega_{max}}{\omega_{min}} = 2.9274 \tag{4.30}$$

For this example a reasonable improvement in the computation efficiency can be obtained. For more general problems there will typically be a larger difference between the lowest and highest eigen-frequencies which means that the potential improvement of the explicit time integration can be significant if the masses can be selected reasonably. Unfortunately, the above used methods will demand knowledge of the stiffness terms. These terms will normally not be available when using the explicit time integration which makes it difficult to utilize the methods more generally.

The optimum way to perform the time integration would be to choose the elements m_{ij} so that a ratio $\frac{\omega_{max}}{\omega_{min}} = 1$ is reached. Starting out from 4.10 with $m_{ij} = k_{ij}$ and premultiplying with M^{-1} we obtain:

$$\mathbf{M}^{-1}\mathbf{M}\ddot{\mathbf{u}} + \mathbf{M}^{-1}c\mathbf{M}\dot{\mathbf{u}} + \mathbf{M}^{-1}\mathbf{K}\mathbf{u} = \ddot{\mathbf{u}} + c\dot{\mathbf{u}} + \mathbf{u} = \mathbf{M}^{-1}\mathbf{f}(t) \tag{4.31}$$

whereby a system of n-uncoupled equations with $\omega_i = 1$ is obtained. These equations can be solved (within 0.1 per cent of the static solution) with just 12 integration steps. This seems to be very effective, but in order to perform this decoupling with $\mathbf{M}^{-1}$ one could just as well solve the static problem directly: $\mathbf{u} = \mathbf{K}^{-1}\mathbf{f} = \mathbf{M}^{-1}\mathbf{f}$ as the necessary operations are involved in the decoupling.

4.3 Dynamic relaxation

In LS-Dyna3d some options for performing approximate analysis of quasi-static problems are implemented. The simplest method is to perform a simulation where a damping close to the critical is chosen.

System damping

One possibility to limit vibrations in the response is to apply a viscous damping to the FE-system. By using this approach a damping proportional to the nodal mass and velocity is applied to the system:

$$\mathbf{f}_{damp} = c\mathbf{M}\dot{\mathbf{u}} \tag{4.32}$$

Using this direct approach c must be estimated in advance. To critically damp out the lowest eigen-frequency, which is normally the dominating mode, a damping coefficient of:

$$c = 2\omega_{min} \tag{4.33}$$

must be applied. This will be the most efficient damping which can be performed, but for meshes where high rates of mass scaling have been utilized, this may introduce non-physical bending effects due to the increased mass and velocity and hence, for plastic deformation this may influence the final results. Another problem is to obtain a good estimate of the lowest eigen-frequency (as discussed previously), which for most of the forming operations changes drastically during the process.

Another approach is proposed by Papadrakis [171]. This approach is presented here in

a way very similar to the LS-Dyna3d theoretical manual [83], where a list of further references are given. The list can be consulted for a more detailed study. In contrast to the theoretical manual hourglass resistance is omitted here.

The governing equation including a damping resistance becomes:

$$\mathbf{M}\ddot{\mathbf{u}}^n + \mathbf{C}\dot{\mathbf{u}}^n + \mathbf{f}_{int}^n = \mathbf{f}_{ext}^n \tag{4.34}$$

where the damping matrix [C] is assumed to be proportional to the mass matrix, [C]=c[M]. By approximating velocity and acceleration and assuming an averaged value for $\dot{u}^n$ one gets:

$$\dot{\mathbf{u}}^{n+\frac{1}{2}} = \frac{(\mathbf{u}^{n+1} - \mathbf{u}^n)}{\Delta t} \qquad \ddot{\mathbf{u}}^n = \frac{\left(\dot{\mathbf{u}}^{n+\frac{1}{2}} - \dot{\mathbf{u}}^{n-\frac{1}{2}}\right)}{\Delta t} \qquad \dot{\mathbf{u}}^n = \frac{1}{2}\left(\dot{\mathbf{u}}^{n+\frac{1}{2}} + \dot{\mathbf{u}}^{n-\frac{1}{2}}\right) \tag{4.35}$$

Hereby the expressions for velocity and updated displacements are obtained:

$$\dot{\mathbf{u}}^{n+\frac{1}{2}} = \left(\frac{1}{\Delta t}\mathbf{M} + \frac{1}{2}\mathbf{C}\right)^{-1}\left[\left(\frac{1}{\Delta t}\mathbf{M} - \frac{1}{2}\mathbf{C}\right)\dot{\mathbf{u}}^{n-\frac{1}{2}} + \mathbf{f}_{ext}^n - \mathbf{f}_{int}^n\right] \tag{4.36}$$

$$\mathbf{u}^{n+1} = \mathbf{u}^n + \Delta t\dot{\mathbf{u}}^{n+\frac{1}{2}} \tag{4.37}$$

$\mathbf{M}$ is assumed to be diagonal and we obtain the velocity as:

$$\dot{u}_i^{n+\frac{1}{2}} = \frac{2 - c\Delta t}{2 + c\Delta t}\dot{u}_i^{n-\frac{1}{2}} + \frac{2\Delta t}{2 + c\Delta t}\frac{f_{ext_i}^n - f_{int_i}^n}{m_{ii}} \tag{4.38}$$

For a quasi-static solution procedure the initial conditions are:

$$\dot{\mathbf{u}}^0 = \mathbf{0} \quad \textit{and} \quad \mathbf{u}^0 = \mathbf{0} \tag{4.39}$$

As the average value for velocity is zero we have the condition: $\dot{\mathbf{u}}^{-\frac{1}{2}} = \dot{\mathbf{u}}^{\frac{1}{2}}$ and hereby the velocity at step $n = \frac{1}{2}$:

$$\dot{\mathbf{u}}^{\frac{1}{2}} = -\frac{\Delta t}{2}\mathbf{M}^{-1}\{\mathbf{f}_{int}^0 - \mathbf{f}_{ext}^0\} \tag{4.40}$$

To select the optimal c it is chosen to damp out the lowest eigen-frequency critically, which leads to: $\mathbf{C} = \mathbf{C}_{cr} = c_{cr}M = 2\omega_{min}m_{ii}$ with m_{ii} as nodal mass. Hereby, the dynamic relaxation is nothing but a critically damped dynamic system, and many of the considerations, which are made in section 4.1.1, are also valid for this more complex situation. In the theoretical manual [83] it is also concluded that an eigen-frequency analysis is too costly and instead the estimation of the eigen-value is based on the following measure according to Papadrakis [171]:

$$\lambda_D = \frac{\| u^{n+1} - u^n \|}{\| u^n - u^{n-1} \|} \tag{4.41}$$

When this value has converged to an almost constant value, the minimum eigen-value of the structure can be estimated as:

$$\omega_{min}^2 = -\frac{\lambda_D^2 - \lambda_D\beta + \alpha}{\lambda_D\gamma} \tag{4.42}$$

where

$$\alpha = \frac{2 - c\Delta t}{2 + c\Delta t} \qquad \beta = \alpha + 1 \qquad \gamma = \frac{2\Delta t^2}{2 + c\Delta t} \tag{4.43}$$

An upper bound for the maximum eigen-frequency is already known from the analysis and is based on element properties:

$$\omega_{max} \leq \frac{2}{\Delta t} \tag{4.44}$$

Based on ω_{max}, ω_{min} and the optimal convergence rate the damping coefficient can be updated as:

$$c = \frac{4}{\Delta t} \frac{\omega_{min}\omega_{max}}{(\omega_{min}^2 + \omega_{max}^2)} \tag{4.45}$$

If $\omega_{max} \gg \omega_{min}$ we can use:

$$c = \frac{4}{\Delta t} \frac{\omega_{min}}{\omega_{max}} = \frac{4}{\frac{2}{\omega_{max}}} \frac{\omega_{min}}{\omega_{max}} = 2\omega_{min} \tag{4.46}$$

That is, if the ratio between maximum and minimum frequencies is high, it corresponds directly to critically damping of the system. The method is adaptive and at the same time rather cost effective seen with regard to the extra computations needed.

Another principle which is implemented in LS-Dyna3d follows the simple scheme:

$$\{\dot{u}\}^{n+\frac{1}{2}} = \eta\{\dot{u}\}^{n-\frac{1}{2}} + \{\ddot{u}\}^n \Delta t \tag{4.47}$$

where η is a damping factor (typical 0.995) and as convergence criterion the global kinetic energy is chosen:

$$E_{kin} < tol * E_{kin}^{max} \tag{4.48}$$

Zhang et al. [226, 227] use a similar approach to damp out the vibrating system in order to obtain the solution of a quasi-static problem (sheet metal forming by bending). Their solution to the problem is obtained by applying the load stepwise followed by a period with artificial damping. The damping coefficient is determined from:

$$c = 2\left(\frac{\mathbf{u}_n^T \mathbf{f}_{int}}{\mathbf{u}_n^T \mathbf{M} \mathbf{u}_n}\right) \tag{4.49}$$

To determine the initial displacement vector for each loading step Zhang et al. perform an analysis without damping leading to two extrema for the displacement vector, say $\mathbf{u}_i^*$ and $\mathbf{u}_i^{**}$. Afterwards the initial displacement vector is set to $\mathbf{u}_i = \frac{1}{2}(\mathbf{u}_i^* + \mathbf{u}_i^{**})$. This principle is similar to the estimation in equation 4.41 (Papadrakis' estimation of the lowest eigen-frequency). Zhang argues that this method (the modified adaptive dynamic relaxation) is more effective than traditional dynamic relaxation. Underwood [210] and Key et al. [121] use a very similar approach apart from the estimation of initial displacements.

The general idea of these methods is to perform an estimation of the lowest eigen-frequency. Stillman (course notes on "Advanced FE-processing and 3-Dimensional Structures with LS-Ingrid, Linköping, 1992") pointed out that in his opinion the adaptive methods are not fully reliable and he proposes to perform some exterior estimation of the lowest eigen-frequency, either by analytic means or just by running a pre-analysis without damping, followed by a specification of a damping coefficient. In many cases I have found this approach to be just as fast and in general much more reliable.

Further discussion on these topics can be found in Underwood [210], Key [121], Papadrakis [171], Park [174], Wathen [218], [209] and Brew et al. [39].

The above relations are especially related to spring back analyses, however, in some cases they may be found suitable for use in the first part of the forming operation. The problem for both methods is that the efficiency of the relaxation is highly dependent on the estimated eigen-frequencies and the ratio between maximum and minimum frequencies, an aspect also reported by Papadrakis [171] and Underwood [210].

4.4 Subcycling

Many FE-analyses demand a very high element resolution in some areas. If the area of high resolution is limited when compared to the remaining part of the model the overall computational efficiency will suffer significantly due to the Courant criterion. In some of these cases an approach called subcycling may be used to improve the overall efficiency. In LS-Dyna3d it is possible to use subcycling to improve computational efficiency.

The typical way to perform subcycling is first to assign a node, i, the minimum stable time step $\Delta t_{i,min}$. This time step is found as the minimum time step for elements connected to the node. Following each element, j, is assigned the minimum time step for the j'th element's node (found from the first sorting). Then the elements are grouped in blocks depending on the size of the time step. Each block consists of elements with a given range of stable time steps, typically some even multiple of the smallest element time step size ($2^{n-1}\Delta t_{stab} < \Delta t_{i,min} \leq 2^{n-1}\Delta t_{stab}$).

The efficiency of subcycling is strongly dependent on how often the elements must be resorted due to changes in element time step and also the boundaries between blocks play a role, especially if efficient parallellisation is to be made. For more discussion on the issue reference is made to Belytschko [23].

4.5 Interface damping

In the previous section methods and strategies to improve computational efficiency when using relaxation have been discussed. The following principle "interface damping" is meant as a method to eliminate some of the dynamic effects which may occur due to the speed-up of solutions and the discretized surfaces.

Use of discretized interfaces will always lead to introduction of dynamic scatter in the calculation of interface forces. To limit this effect Hallquist et al. [83] propose an interface damping value as a percentage of the critical damping d_c , with

$$d_c = m\omega_c = m\sqrt{\frac{k(m_{slave} + m_{master})}{(m_{slave}m_{master})}} \tag{4.50}$$

k is the interface stiffness, m is the minimum value of the master surface mass and the slave surface mass.

Chapter 9 gives an example where this method is used to reduce contact noise and it is concluded that the interface damping is very efficient for a typical deep drawing in 1 mm steel. However, I have experienced that the deep drawing of a can made from a 0.22 mm thick sheet led to contact instabilities causing uncontrolled growth of the mesh; the solution to this problem was to omit the interface damping.

4.6 Increased loading rate

This section gives some methods which can be used in a more general analysis to speed-up the solution phase and some examples of how the methods may influence the simulation of sheet metal forming problems are given. As discussed earlier faster loading rates are employed to limit the number of time steps. Here it is normally necessary to avoid too high velocities when the first point of contact between materials is reached. In sheet forming this problem typically arises when the blank holder and the punch reach the blank. In the present work it has in most cases been found suitable to utilize sine shaped velocity profiles for the punch movement, that is specifying a zero velocity at the beginning and end of the punch stroke and hereby avoid the severe stroke effects and reduce the level of kinetic energy at the end of the punch stroke.

In the middle of the stroke very high velocities are specified leading to a relatively high kinetic energy, but there is normally a very efficient damping present due to plasticity whereby disturbances are reduced.

To limit impact effects between the tools and the blank a very small initial gap is specified, typically an initial gap of 0.0001 mm has been used for 1 mm sheet thickness. A small gab is necessary in order to avoid initial penetration.

4.7 Mass scaling

Using mass scaling to accelerate the solution means that the ratio between the maximum and minimum eigen-frequency of the system is controlled by changing the density of elements. For this purpose two proposals are typically used for selecting a proper mass matrix.

Underwood [210] and Key et al. [121] suggest that the densities ρ_i are selected on an

element by element basis to get the same specified transit time in all elements. This concept is called "mesh homogenization" or "mass scaling" and it can be expressed as:

$$\Delta t_i \leq \frac{L_i}{c_i} \quad c_i = \sqrt{\frac{E}{\rho_i}} \quad \rho_i \geq \left(\frac{T}{L_i}\right)^2 E \tag{4.51}$$

where the index "i" refers to the i'th element and ρ_i is the material density for the element, L_i is the characteristic element length (usually the shortest element side or the shortest diagonal of the element), c_i is the sound speed of the material, E is the Young's modulus and $T = \Delta t_i$ is the desired constant time step. This approach will in general increase the total mass of the system and may influence on the structural response (leading to a change in the lowest eigen-frequency) and hereby reduce the effectiveness.

Another very similar scheme can be utilized where densities are decreased if the element time step is greater than the wanted time step. The determination of density in this approach is:

$$\rho_i = \left(\frac{T}{L_i}\right)^2 E \tag{4.52}$$

The use of the above approaches can be very efficient for some meshes, but in some cases it can even increase the ratio $\frac{\omega_{max}}{\omega_{min}}$. In the following is given a simple example of the analysis of a cantilever beam in which the effects of mass scaling are clearly demonstrated.

4.7.1 Mass scaling utilized for a cantilever beam

In this section the effects of mass scaling are illustrated with a simple example: We want the static solution for a cantilever beam exposed to a load at the free end. Figure 4.7 shows the loading case (left) and right the three FE-meshes used in the analyses. The models are

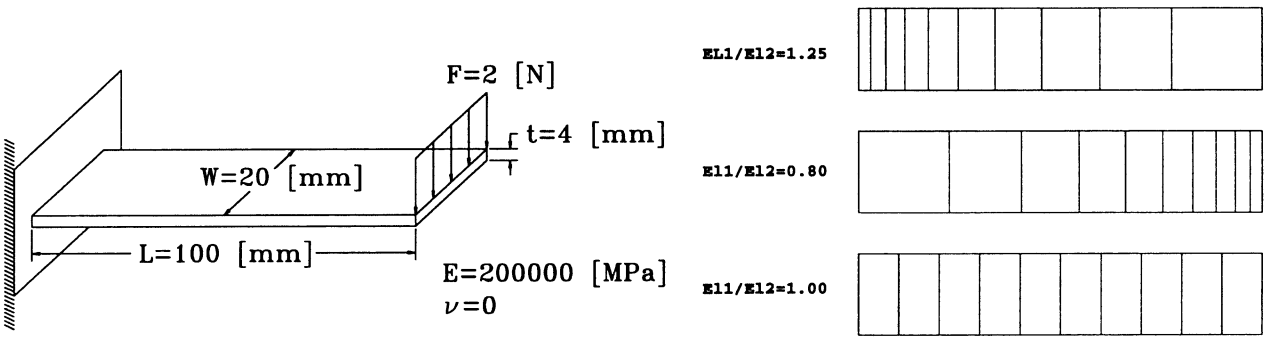

Figure 4.7: *Illustration of the cantilever beam problem (left) and the three principles of discretization investigated. The beam is discretized with 10 BLT elements.*

all analysed by using the same time step ($\Delta t = 1.8\mu$sec). The strategy for the analysis is first to determine the eigen-frequency of the system by performing an undamped analysis and then to restart the analysis with a specified system damping corresponding to critical damping.

The eigen-frequencies (in rad/s) are determined to: $\omega_{1.00} = 2049$, $\omega_{0.80} = 785$, $\omega_{1.25} = 2005$

using the approach where element densities are scaled if the critical time step is lower than the prescribed (equation 4.51) and to $\omega_{1.00} = 2049, \omega_{0.80} = 820, \omega_{1.25} = 2807$ for the method where all elements have the same transit time (equation 4.52).

The immediate conclusion is that when using mass scaling, the approach with equal time step in all elements will give the lowest eigen-frequency higher or equal to the eigen-frequency that is obtained with the first mentioned method (equation 4.51). This is obvious as a decrease in the total mass must result in a higher value of the lowest eigen-frequency.

Figure 4.8 shows the responses obtained for the meshes and methods discussed above. The figure shows that the mesh has a strong effect on the convergence rate. For the

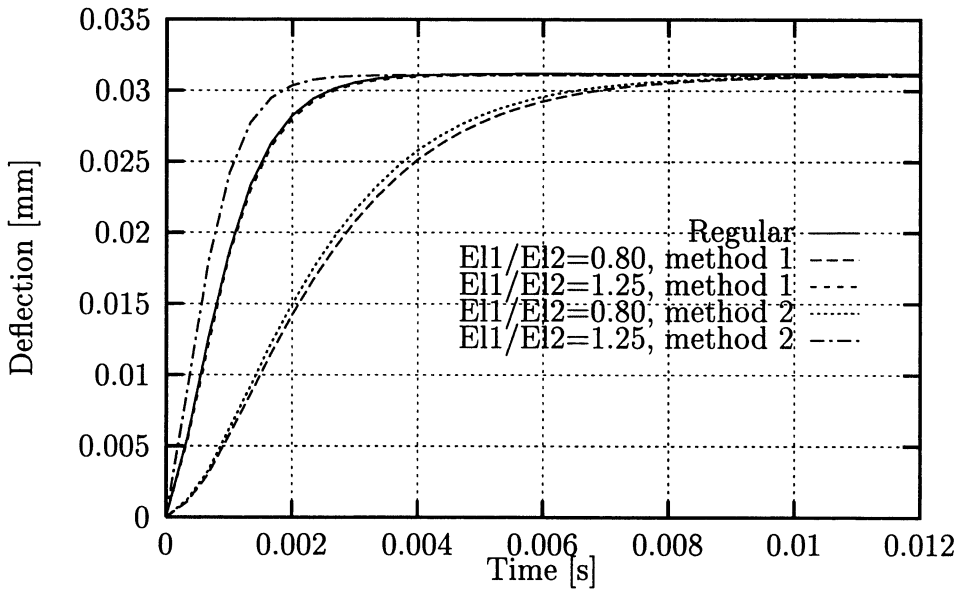

Figure 4.8: *Obtained response with the 2 mass scaling approaches for various meshes.*

mesh indicated with El1/El2=0.8 the number of time steps needed to get within a certain accuracy are increased with approximately a factor of 2.6 as the mass at the free end is increased. For the El1/El2=1.25 mesh an improvement can be seen when using the method with a fixed time step as the eigen-frequency is raised to 1.37 times the frequency for the regular beam and at the same time the upper bound is fixed at the same level due to the prescribed time step. For method number one the efficiency is slightly decreased: The influence from the mass distribution is essentially the same as for the regular mesh as the most outer element is larger than for the regular mesh.

My experience is that the scaling of masses (or the selection of masses) can be very efficient (see later sections), but rules of how and when to use high scalings are hard to establish as the possible improvement in computational efficiency is strongly coupled to the nature of the problem and the utilized discretization; this is clearly illustrated with the cantilever beam example.

4.8 Modelling aspects

As mentioned above the methods for improving computational efficiency are highly dependent on the generated model. Aspects as mesh density, initial configuration or subsequent distortion of elements, etc are determining how much can be gained using the methods discussed above. Having a fixed discretization means that we can only to a certain degree obtain improvements in efficiency without influencing the results unacceptably. In some cases it is possible to improve solutions by applying damping. However, applying artificial damping in the loading phase can lead to a wrong response as a significant increase in deformation resistance may appear due to the damping.

4.9 Analytical representation of interfaces

In most metal sheet forming processes the tool deformation is of minor importance as the rigidity of tools is several factors higher than the part being formed. Therefore, it is normally chosen to represent tool parts by rigid bodies in order to increase efficiency in the calculations. With the last versions of LS-Dyna3D(v.936) it has become possible to use an analytical representation of interfaces, VDA-surfaces, in LS-Dyna3d. This approach is expected to improve results as faceted surfaces for the tool parts can be avoided and at the same time, as the contact search is much faster, also the computational efficiency can be improved.

4.10 Conclusion regarding the solution of metal forming problems

At the end of this part of the thesis a few conclusions can be drawn:

- Loadings should be applied in a way which reduces inertial resistance as much as possible. Typically the most steady response is obtained by using a loading profile which is cosine shaped (for prescribed displacements) and sine shaped when specifying velocities of e.g. the punch. Using such profiles can reduce impact effects which may lead to a significant overshoot.
- Damping terms can be utilized to avoid overshooting, but as the physics of the problem are affected, one should be very cautious.
- The "design" of the model is of vital importance to the results like in all FE-analyses, but due to the explicit formulation it is also of importance to the computational efficiency.

Very often mass scaling is chosen to increase the stable time step, but depending on the mesh this will to some degree reduce the lowest eigen-frequency as discussed in section 4.7.1. If the simulation of a deep drawing consists of a drawing phase followed by a damping phase (spring back), one should not uncritically scale the mass. In the loading phase the response may look very stable (an easy method, which is often employed, is to judge the influence of mass scaling by evaluating the predicted punch force) but in a subsequent spring back

analysis the lowest eigen-frequency may be lowered so much that what is gained (with regard to computational efficiency) during the loading phase may be lost in the relaxation phase.

4.10.1 Possible methods for adaptive control and judgement of analysis

Performing simulations by using scaling of the loading rates as well as mass distribution can lead to analysis results which are completely wrong compared to the physical process. This can lead to wrong conclusions when postprocessing data: Effects may be due to inertial effects and not due to process limitations. Some examples on this problem type are given in sections 6.11 and 9.2.

If we consider a process problem which is of a quasi-static nature two simple ways of controlling the quality could be to check relations between energies or to check interface forces. The methods may be used to give an impression of whether the analysis can be expected to be close to reality or not and the methods may hereby be used to develop adaptive methods (strategies) of how to obtain reliable analyses.

4.10.2 Energy measure

Most deep drawing processes can be characterized as being dominated by plastic deformation. An effective measure of how severe the model is influenced by dynamic effects can be to monitor the ratio between internal energy and plastic dissipated energy, or the ratio between total work performed on the system and the plastic energy. A major problem is to estimate a critical ratio in advance.

In some cases a natural load maximum exists as regards the process, e.g. when deep drawing a cylindrical cup a maximum punch force is reached around 1/3 of the total punch stroke. When a load maximum is passed a relatively large part of the blank will unload elastically and this can lead to large variations in the energies.

In connection with relaxation a method is mentioned by Papadrakis [171]: If the kinetic energy of the system is monitored an effective way to damp out oscillations can be to set the nodal velocity to zero for the displacement vector at the time when an apparent maximum is reached.

4.10.3 Interface force control

The main idea is to control the loading rate by checking interface forces. The difference between supporting and driving forces can be used as a measure of the current inertial forces. By introducing an allowable difference this measure may be used as guide for when to increase or decrease the loading rate.

4.11 Analysis of hydraulic bulging of square diaphragms

Bulging of square diaphragms is performed by clamping a rectangular sheet between a die and a blank hold. The side of the blank away from the die is then exposed to a controlled fluid pressure. During the process related values of pressure and pole height are recorded to characterize the process. The process is very suitable for experiments as it is easy to conduct and the consumption of sheet material is limited. Another benefit of the process is that a relation between biaxial yield stress and plastic straining can be established.

To illustrate some of the considerations made previously, a number of analyses of a force driven process have been made. One of these processes is hydraulic bulging of a rectangular diaphragm and it can be considered force driven at least up to load maximum. After it has reached maximum pressure, the diaphragm expands in an uncontrolled manner if the pressure is increased further. This is an aspect which will not normally be seen in the laboratory as the physical process after reaching process instability becomes a flow controlled process. This example is used in connection with evaluation of implemented material models, see section 7.6.2. As shown in figure 4.9 the model consists of two dis-

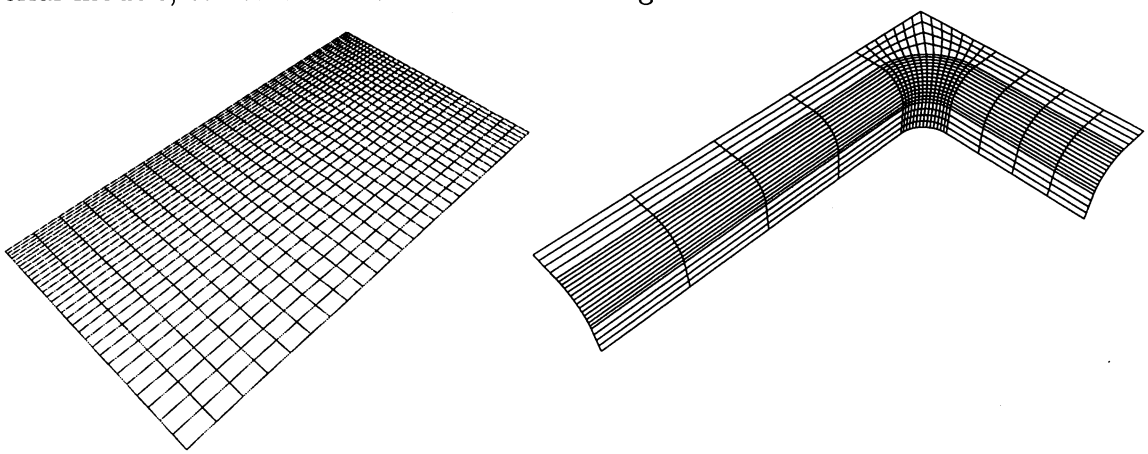

Figure 4.9: *FE-discretization used for the modelling of bulging rectangular diaphragms with the blank (left) and the die (right). Only a quarter of the problem is analysed due to symmetry.*

cretized parts; the blank and the die. It was first attempted only to model the process by specifying the boundary conditions of the sheet and omitting the die, but in order to obtain results comparable with the reported experiments [67, 66, 68] (see section 7.6.2) it was found that the contact between the die shoulders and the sheet is of major importance. However, it was also found that the specified friction between the blank has no significant influence on the process due to the relatively limited sliding between die and blank. The modelling aspects and parameters kept constant in the simulations are as follows:

- The material behaviour is modelled as elastic-plastic with a von Mises' yield criterion, and the hardening is modelled as isotropic Hollomon-Swift hardening ($\sigma_Y = K{\epsilon^p_{eff}}^n, K = 593[MPa], n = 0.275$, Young's modulus E=206000 [MPa] and Poisson's ratio $\nu = 0.3$. No strain rate effects have been taken into account.
- The number of elements are in total 1533 and a quarter of the sheet consists of 961 elements and 1024 nodes.

- Symmetry conditions are imposed on two sides of the blank, the other two sides (outer sides) are free to move in the direction perpendicular to the blank and constrained in the two other translational degrees of freedom in the plane of the blank. This is done to get an interface force, which for a quasi-static analysis will sum up to the applied force ($F_{applied} = pA$ where A is the area of the sheet).
- Contact (and sliding) is modelled by Coulomb friction with a friction coefficient of 0.1.
- The loading is specified with various rates and also load/time profile is varied. The particular loading situation will be mentioned in connection with the presentation of the results. Artificial damping is used to damp out vibration and to limit overshoot effects. In all the analyses a minimum time step of 0.9 μsec is used, which leads to a scaling of the initial mass on 17.3. The same mesh and mass scaling is used in all analyses.

First a load situation where the applied pressure is specified as a unit ramp ($p = Ct$ for $t < 0.1T$, $p = 0.1CT$ for $t > 0.1T$) is studied, and four analyses are performed with a total analysis times T equal to 15, 20, 25 and 50 ms, respectively. In the four analyses a damping factor c equal to 1600 $[s^{-1}]$ is used, which corresponds approximately to 71 per cent of the critical damping for the initial flat blank clamped at the edges.

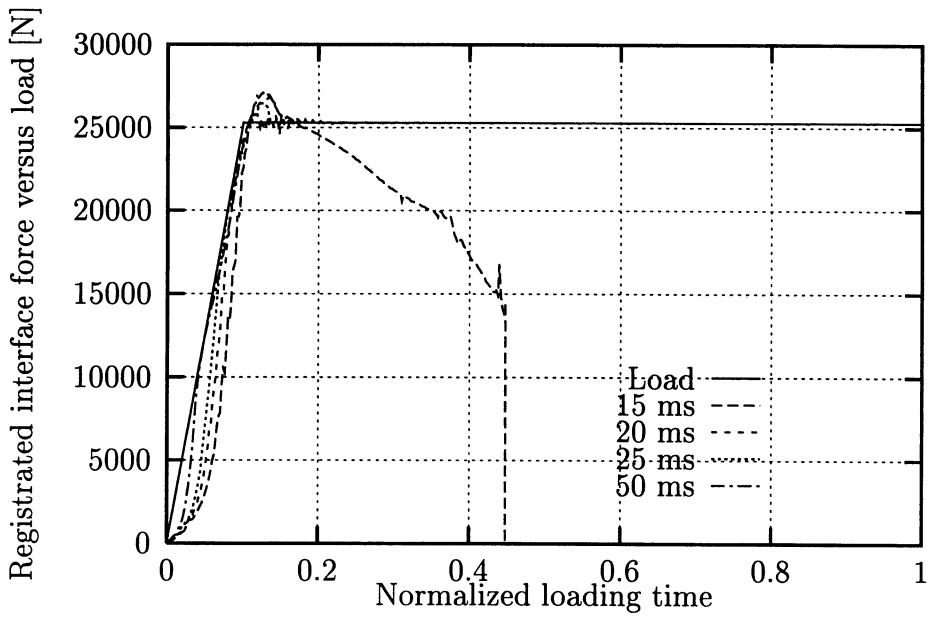

Figure 4.10: *Interface forces obtained for loading times of 15, 20, 25 and 50 msec, respectively, versus the prescribed load. The load is specified as a unit ramp raising from zero at time 0 to 1 at 0.1 (normalized loading time).*

The eigen-value for the plate (1120 $\frac{rad}{s}$ at the initial stage) is determined by using the same model which is loaded with a step load without reaching the beginning of plastic deformation and by applying a damping term equal to zero. This approach is chosen as mass scaling is used in the analysis which makes it difficult to obtain the analytical value; it is clear that the specific damping is relatively close to the critical only in the beginning of the process. After some deformation plastic deformation takes place leading to a drop in the tangential stiffness - at the same time there will be a significant stiffening of the

blank due to geometric changes.

Figure 4.10 gives the predicted interface force under four loading conditions. The load is applied as a ramp function reaching maximum load at 10 per cent of the total analysis time which are 15, 20, 25 and 50 msec for the analyses, respectively. The full line in the figure gives the prescribed load. In figure 4.10 the major difference between the force-time curves is that the example analysed with T=15 msec leads to fracture although the peak value is close to the peak value obtained with T=20 msec. The 15 msec curve indicates clearly a global loss of resistance after having reached maximum load. The other curves are very similar to each other, the shorter the analysis time the higher the overshoot. It can also be noticed by means of this example that the necessary relaxation time is of the same order as the loading time: During the period $0.1 < t < 0.2$ (normalized time) the vibrations are almost damped out.

In section 4.1.1 it is indicated that a loading with a harmonic function seems to lead to a good correlation between the internal force and the load. Figure 4.11 shows the results where the pressure is applied as:

$$p = \begin{cases} \frac{p_{max}}{2}(1 - cos(\frac{\pi}{10T}t)) & for \quad t \leq 0.1T \\ p_{max} & for \quad t > 0.1T \end{cases} \tag{4.53}$$

Three analyses were performed here with analysis times of 15, 25 and 50 msec, respectively, and in figure 4.11 the resulting interface forces are given. The results are very similar to

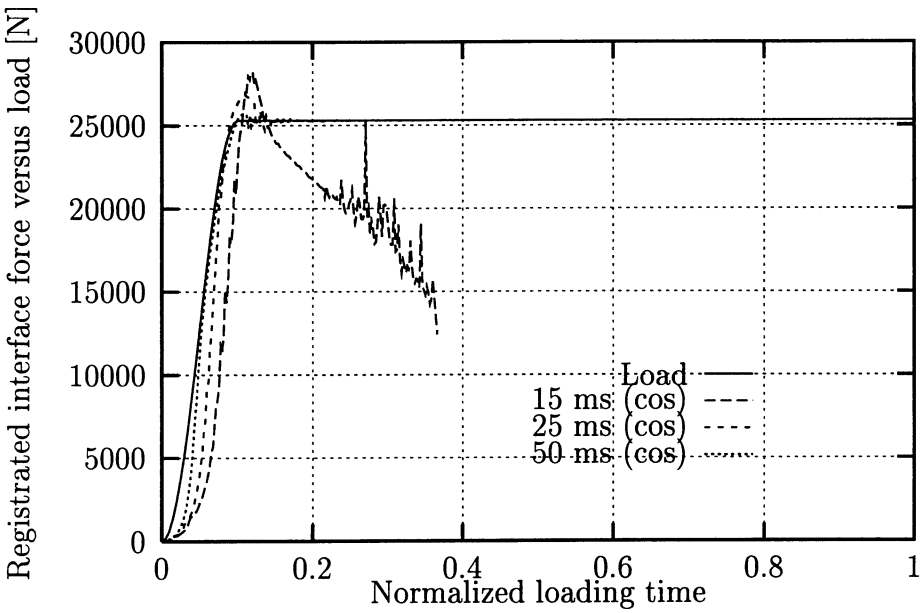

Figure 4.11: *Interface forces obtained for loads following a cosine profile and with loading times of 15, 25 and 50 msec, respectively.*

the results which were obtained with the load specified as a unit ramp (figure 4.10). This indicates that the loading rate is a bit too high if reference is made to the results from the one-dimensional case shown in figure 4.4. The overshoot is also of the same magnitude. One may judge that the overshoot is rather limited, but in order to obtain better results the following two approaches can be used: 1) Increase the amount of damping or 2) increase

the time of loading. The first approach has the disadvantage that it delays the response, which for the load driven case makes it difficult to obtain the relation between load (here pressure) and deflection.

If we scale the damping first with factors of 2 and 4, respectively, we obtain the results shown in figure 4.12, where the load was specified as a unit ramp. Figure 4.12 shows that

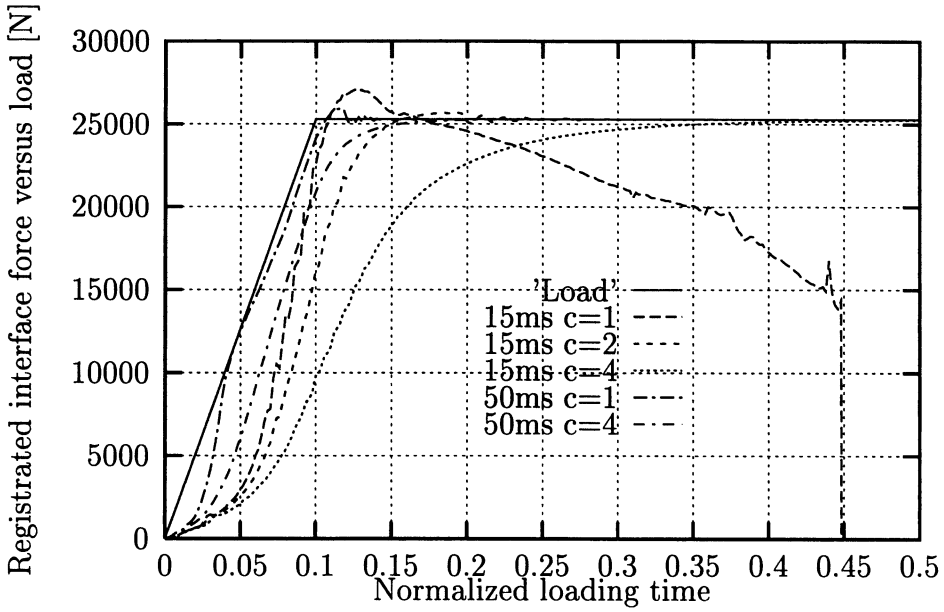

Figure 4.12: *Interface forces obtained for two loading times (15 and 50 msec) and various damping coefficients (1600 (c=1), 3200 (c=2) and 6400 (c=4) [sec^{-1}]) versus the prescribed load (fully drawn line).*

increased damping delays the response, but on the other hand overshooting is avoided. Depending on which information is wanted from an analysis, damping can be used to avoid overshooting, especially if the final state is the most interesting. Otherwise, if the loading path is of primary interest the second approach mentioned above is the most suitable. The curve obtained for an analysis time of 50 msec (loading 5 msec) is apart from the very beginning close to the applied load. The lowest damped 15 msec curve indicates fracture (same analysis as reported above), but when increasing the damping the fracture is avoided, but especially for the heavily damped 15 msec curve a large delay can be seen. The medium damped case (15 msec) seems to give a constant delay, but the shape is in good correlation to the load, and it must be remembered that the CPU time needed is only 30 per cent of the time needed for a 50 msec analysis.

Figure 4.13 shows the results for various loading rates (cosine profiles). The total analysis time is in all cases 15 msec, but the time which is used to obtain maximum load is set to 1.5, 7.5 and 11.25 msec, respectively. We now see a clear improvement of the predicted response compared to the previous figures. Only one thing needs to be taken care of: We have a small delay for both loading times on 7.5 and 11.25 msec due to the applied damping. The conclusion so far is that it is possible to perform analysis for load controlled problems even with a very high load raise without destroying the quasi-static nature of the problem.

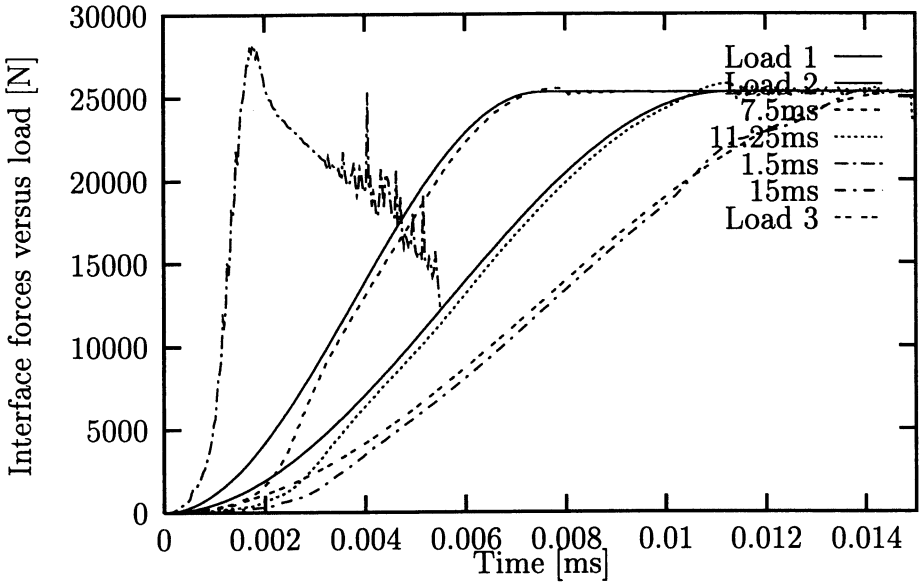

Figure 4.13: *Interface forces for various loading rates and cosine shaped load profiles.*

From the previously discussed figures we can draw the conclusion that the only way to obtain a better agreement between load raise and response is to lower the loading rate.

Chapter 5

Constitutive Modelling - Plasticity

So far specific evaluation of constitutive equations has been avoided in order not to introduce too many (unnecessary) aspects to the discussions in the previous part of the thesis.

The area of plasticity is very important and as the solutions depend strongly on how well material behaviour is modelled, a chapter is devoted to this subject. The purpose of this chapter is to recapture some characteristics of sheet metals, give an overview of the historical development in the theory of plasticity and state the theory of plasticity used in later sections.

In case of non-linear events and especially when dealing with plasticity and/or viscoplasticity special care must be taken when evaluating element stiffness for an implicit solution scheme. Although the element stiffness is not determined when using the explicit time integration scheme, it is of major importance that the computations (stress updates) are effective seen from a computational point of view; therefore it has been chosen to include a brief discussion on numerical integration of the constitutive equations.

5.1 Historical overview

The history of plasticity started with the flow criterion proposed by Tresca in 1872 and the work of Barre de Saint Venant in connection with torsion of shafts. In 1860 Bauschinger described the Bauschinger effect which is noticed in many metals. In 1900 Mohr introduced a failure criterion based on Mohr's circle. Prandtl introduced the membrane analogy in 1903, and the Prandtl-Reuss relation was published in 1924 (Prandtl) and in 1939 (Reuss). The von Mises' flow criterion was proposed by Huber (1904) and by von Mises (1913). von Mises derived his expression from a mathematical approach and this led to an expression sufficiently simple to be employed for analytical approaches (simple when compared to Tresca's criterion). Later it has been shown that the criterion is an expression for maximum distortion energy; Tresca's criterion can be considered as a maximum shear theory. von Mises' criterion is widely used in many applications, both for relating a 3 dimensional stress situation to a scalar measure in elastic problems and for prediction of plastic flow.

In 1923 and 1924 Hencky introduced the slip-line theory which later became known as

Hencky's laws. Hencky's theory of plasticity is often called the total deformation theory as, in contrast to the incremental laws, it relates stress and total strains. This theory is still used for some special purpose codes (and for calculations by hand), for instance Sklad [192] uses this approach.

In 1933 Odqvist introduced a hardening parameter; Odqvist's parameter. The plastic potential was proposed by Melan in 1938 and the same year he also came up with the shake down theory.

Bridgman made major contributions in the years 1940-1952, for instance the Bridgman factor which makes it possible to estimate the stress-strain behaviour after diffuse instability. Within sheet metal forming a similar correction factor still remains to be found. As localization does occur rather early in a tensile test (typically at 20 to 40 per cent straining) only a limited range is well described. A forming operation (deep drawing) often involves effective plastic strains as high as 100 per cent and it is evident that a very drastic extrapolation is made in most cases, and with this in mind, it is surprising how good predictions can be made by using the finite element method.

Ilyushin solved in 1943 problems involving plasticity by the method of successive elastic solutions and in 1948 Ilyushin came up with his stability postulate.

In 1948 Zener introduced rheological models and the same year Hill stated the maximum dissipation principle. The following year (1949) Hodge and Prager stated the minimum principle. Prager also gave the continuity requirement from which the classical theory of plasticity employed today can be expressed (used in section 5.3). Greenberg gave a new minimum principle in 1949 and Drucker's inequality appeared in 1951. In 1951 Symonds performed limit analysis and studied collapse mechanics. In 1960 Koiter gave a kinematic approach to the shake down theory. In 1963 Ziegler used a thermodynamic approach to plasticity and made a non-linear generalization of Onsager's relations.

In 1969 Lee introduced the multiplicative decomposition of finite deformation gradient, and in 1975 Halphen and Nguyen Quoc Son published the work on the concept of a generalized standard material. Their approach is based on a thermodynamic approach and is very often used in more recent publications that threat plasticity and viscoplasticity. Using this very general approach and making the numerical implementation according to this makes it possible to utilize the same numerical framework for many types of material behaviour. This approach has been used by for example Peric [176] and Simo and Taylor [190], [191].

Strang, Suquet and Temam introduced functions of bounded variations in elasto-plasticity in 1979 and 1980.

The development of damage can be described within a combined formulation of plasticity and damage. This is discussed very briefly in section 8.12 which deals with the forming limits and damage. Landmarks in this area are the work of Woehler (1858-1870) discussing cyclic loading and introducing Woehler curves. Norton (1929) discussed creep and proposed what has later become known as Norton's law, Kachanov (1958) with the

observation and description of damage and Rabotnov (1963) introducing the damage parameter. In recent years researchers Tvergaard, Needleman, Gurson and Lemaitre have made many contributions in the area of modelling and numerical treatment of damage.

To obtain the theory of plasticity a number of different approaches can be used. In the present it has been chosen to base the approach on Drucker's postulate [65]. This approach has some advantages as the considerations may be explained by uniaxial problems for the sake of clarity and then later on expanded to general stress states. The following section is mainly based on Ottosen [170].

5.2 Hardening plasticity

Let us first consider uniaxial tension and include hardening as well as softening plasticity as shown in figure 5.1. Considering the following situation: We have a stress state cor-

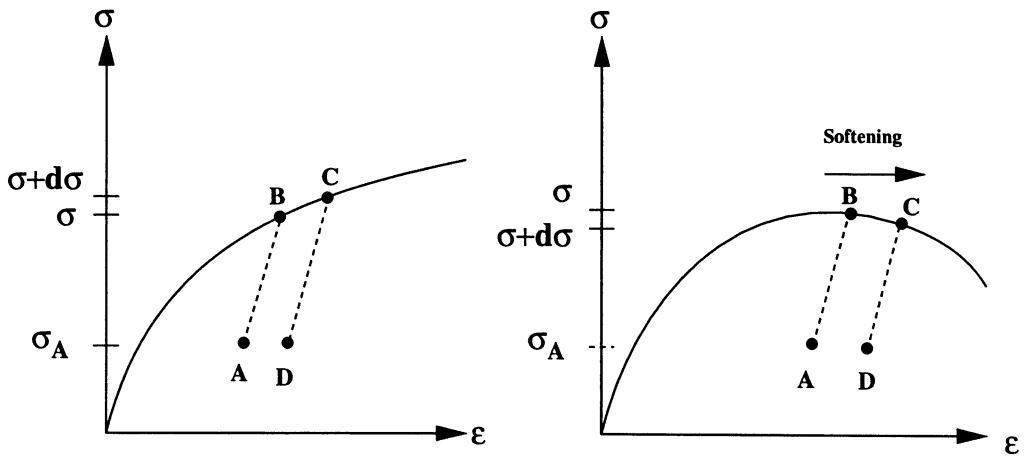

Figure 5.1: *Uniaxial tensile tests showing hardening and softening plasticity (left and right, respectively).*

responding to point A in figure 5.1; then the specimen is loaded up to point B (onset of yielding). In the case of hardening a further increase in stress $d\sigma$ brings the stress state to point C. In the case of softening plasticity we must specify an increment in strain instead as we otherwise unload elastically and do not reach point C at all. After reaching point C we unload the previously applied loads and return to the stress state in D, equal to the stress state in A.

We now consider the work made during the stress cycle: A to B to C to D, which is expressed as:

$$W_{ext} = \int_{ABCD} (\sigma - \sigma^A) d\epsilon \tag{5.1}$$

Assuming that the strain increment can be divided into a plastic and an elastic increment we have:

$$d\epsilon = d\epsilon^e + d\epsilon^p \tag{5.2}$$

This assumption is very commonly used and widely accepted.

As the loading from A to B and the unloading from C to D are purely elastic, we can rewrite the above expression for the work to:

$$W_{ext} = \int_{ABCD} (\sigma - \sigma^A) d\epsilon^e + \int_{BC} (\sigma - \sigma^A) d\epsilon^p \tag{5.3}$$

Assuming we have isotropic elasticity (an assumption which will be used throughout the report) we can express the elastic strain increment:

$$d\epsilon^e = \frac{d\sigma}{E} \tag{5.4}$$

where Young's modulus E is assumed to be constant. Reexpressing the work:

$$W_{ext} = \frac{1}{E} \int_{ABCD} \sigma d\sigma - \frac{\sigma^A}{E} \int_{ABCD} d\sigma + \int_{BC} \sigma d\epsilon^p - \sigma^A \int_{BC} d\epsilon^p \tag{5.5}$$

The path A-B-C-D corresponds to a complete stress cycle and the contribution from the first two parts (elastic) equals zero.

If we denote the positive plastic strain increment from B to C (or A to D) $d\epsilon_p$ we can by applying the trapezoidal rule obtain:

$$W_{ext} = (\sigma - \sigma^A) d\epsilon^p + \frac{1}{2} d\sigma d\epsilon^p \tag{5.6}$$

This expression is valid for all choices of σ^A. If we choose $\sigma = \sigma^A$ equation 5.6 shows that $W_{ext} > 0$ in case of hardening and $W_{ext} < 0$ in case of softening plasticity.

The postulate of Drucker defines hardening plasticity by considering the external work made by applying additional stresses slowly to an already stressed material and hereby create plastic strains and then slowly remove the added set of stresses. As for the uniaxial case it is postulated that the work made in such a cycle is non-negative. The principle is illustrated in figure 5.2. The postulate of Drucker now expresses that the external work must be non-negative:

$$\int_{ABCDA} (\sigma_{ij} - \sigma_{ij}^A) d\epsilon_{ij} \geq 0 \tag{5.7}$$

Only the path between B and C involves plasticity, the remaining section of the cycle is elastic, and as the initial stress state at A, σ_{ij}^A, is constant we can rewrite the postulate:

$$\int_{ABCDA} \sigma_{ij} d\epsilon_{ij}^e - \int_{ABCDA} \sigma_{ij}^A d\epsilon_{ij}^e + \int_{BC} (\sigma_{ij} - \sigma_{ij}^A) d\epsilon_{ij}^p \geq 0 \tag{5.8}$$

The first integral expresses the change in elastic strain energy over a complete cycle and it must thus be equal to zero. As we end up in point A with the same stress state we must also have the same elastic strains after having completed the cycle and the second term above must hereby also be equal to zero.

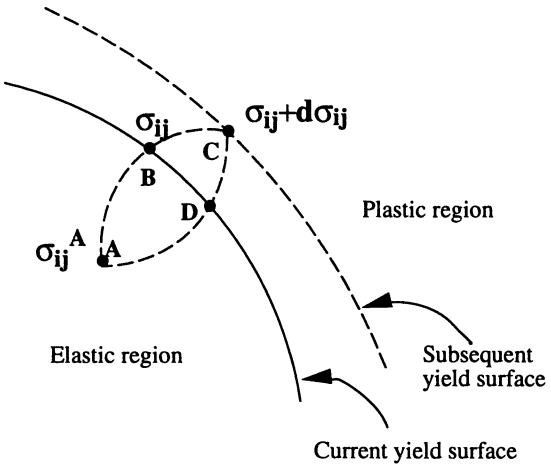

Figure 5.2: *Schematic presentation of a stress cycle producing additional plastic strains.*

$d\epsilon_{ij}^p$ is the total plastic strain increment between B and C, and by using $d\sigma_{ij}$ to express the corresponding stress increment we have by using the trapezoidal rule:

$$(\sigma_{ij} - \sigma_{ij}^A)d\epsilon_{ij}^p + \frac{1}{2}d\sigma_{ij}d\epsilon_{ij}^p \geq 0 \tag{5.9}$$

This inequality is fundamental in the formulation of the plasticity theory, which is demonstrated below.

Considering the case where σ_{ij}^A is sufficiently different from σ_{ij} the second term in equation 5.9 becomes of second order and we have:

$$(\sigma_{ij} - \sigma_{ij}^A)d\epsilon_{ij}^p \geq 0 \tag{5.10}$$

If we consider the stress space and also plot the plastic strains using the same axis, equation 5.10 states that the scalar product between the vectors $\sigma_{ij} - \sigma_{ij}^A$ and $d\epsilon_{ij}^p$ is always non-negative or in other words the angle between $\sigma_{ij} - \sigma_{ij}^A$ and $d\epsilon_{ij}^p$ is never obtuse. This situation is illustrated in figure 5.3.

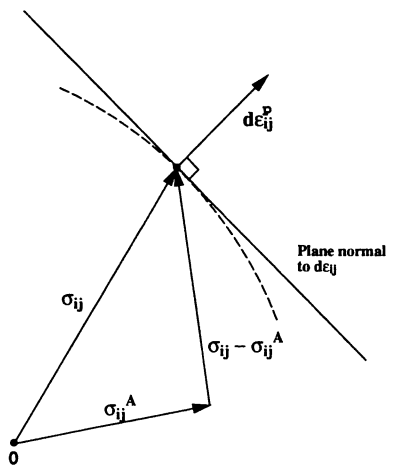

Figure 5.3: *Illustration of the convexity requirement.*

The stress state σ_{ij} is located on the yield surface (due to the plasticity) and the initial stress state (arbitrary) σ_{ij}^A is placed inside or on the yield surface. This means that all points on or inside the yield surface must be located in the space opposite the plastic strain direction and limited by the plane normal to $d\epsilon_{ij}^p$. As we can choose arbitrary points on the yield surface, the above corresponds to the demand that the yield surface must be convex (in the stress space).

If we consider 5.9 and the case where $\sigma_{ij}^A = \sigma_{ij}$ the following is obtained:

$$d\sigma_{ij} d\epsilon_{ij}^p \geq 0 \tag{5.11}$$

If the yield surface is smooth then both 5.10 and 5.11 state that $d\epsilon_{ij}^p$ must be normal to the yield surface:

$$d\epsilon_{ij}^p = d\lambda \frac{\partial f}{\partial \sigma_{ij}} \tag{5.12}$$

Using Drucker's postulate we reach the associated flow rule derived by Levy and von Mises first and later by Prandtl and Reuss. f denotes the yield surface and the function can for a more general case be expressed as:

$$f(\sigma_{ij}, \alpha_{ij}, \kappa_\beta) = 0 \tag{5.13}$$

The tensor α_{ij} is a symmetric second order tensor that describes the current centre of the yield surface, and κ_β is used for describing some internal parameters, typically the hardening behaviour.

Drucker's postulate defines hardening plasticity, and the two most important points are; 1) the yield surface must be convex and 2) the plastic strain increments must be normal to the yield surface. At the same time Drucker's postulate gives a definition of stability which corresponds to the intuitive concepts of stable material behaviour.

Using this approach leads to a limited, however, very broad class of materials. For materials which show a clear softening effect, e.g. concrete and soil, Drucker's postulate is violated, and also materials with coupling between plastic deformation and elastic parameters do not fulfil the postulate.

All the materials which are considered in the remaining part of the report will be treated under the above restrictions.

5.2.1 Ideal plasticity

Drucker's postulate is a definition of hardening plasticity, but it can easily be extended to ideal plasticity. For ideal plasticity we have the yield surface in the form

$$f(\sigma_{ij}) = 0 \tag{5.14}$$

Again two cases can be considered:

Firstly, where $\sigma_{ij}^A \neq \sigma_{ij}$ we obtain:

$$(\sigma_{ij} - \sigma_{ij}^A) d\epsilon_{ij}^p \geq 0 \tag{5.15}$$

It is the same relation as obtained for hardening plasticity, or in other words; to be able to move from one stress state on the yield surface to another it is necessary to perform some external work. The relation states both convexity as well as the normality condition.

Secondly, in the case where $\sigma_{ij}^A = \sigma_{ij}$ we have for the uniaxial case $d\sigma = 0$. Generalizing this we obtain:

$$d\sigma_{ij} d\epsilon_{ij}^p = 0 \tag{5.16}$$

This expression is quite obvious: For ideal plasticity a stress point must move on the fixed yield surface and at the same time we have that the strain increments must be normal to the yield surface, leading to the demand that the scalar product between these two quantities must equal zero.

5.3 General plasticity

First it is assumed that we have an expression for the yield surface defined in such a way that inside the yield surface only linear elastic deformation occurs. The yield criterion is expressed as:

$$f(\sigma_{ij}, \alpha_{ij}, \kappa_\beta) = 0 \tag{5.17}$$

To ensure a continuous material response we must require that no plastic strains will develop for stress changes tangential to the yield surface.

There are two ways to move from one point to another on the yield surface: Through elastic straining to move inside the surface or to move on the surface. Thus, we cannot allow plastic strain development for such a situation. It can be depicted as shown in figure 5.4. If the stress changes are tangential to the yield surface and produce plastic strains we

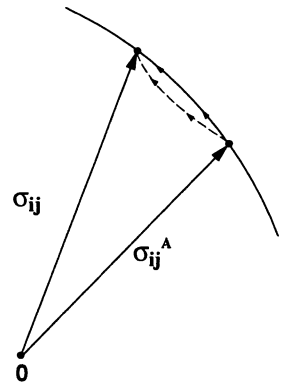

Figure 5.4: *Illustration of two stress paths between stress σ_{ij}^A to σ_{ij}. The first path is lying directly on the yield surface and the other lying close, but with a small distance, to the surface.*

have two possibilities of moving from one point on the yield surface to another: Choosing either a path leading to plastic strain or another path infinitesimal close to the first, however, this path can be a purely elastic change of stress. This will clearly lead to a

discontinuous response, which should not be allowed by intuition. To overcome this discontinuous behaviour Prager [178] gave his continuity requirement leading to the situation of neutral loading. It can be noticed that this is in contradiction to what is written above about ideal plasticity.

When discussing elastic-plastic material behaviour three situations must be handled: loading, neutral loading and unloading.

- Loading: f=0 and $\frac{\partial f}{\partial \sigma_{ij}} d\sigma_{ij} > 0$
- Neutral loading: f=0 and $\frac{\partial f}{\partial \sigma_{ij}} d\sigma_{ij} = 0$
- Unloading: $f < 0$ (implies elastic behaviour)

The situation where $f > 0$ is seen from the point of plasticity non-physical. When discussing viscoplasticity the situation is somewhat different as there are stress points outside the yield surface due to strain rates. It has been chosen to exclude viscoplasticity and concentrate on rate independent plasticity in this thesis. However, rate effect can very easily be taken into account within the same framework by using multiplicative yield functions where the current yield surface extension becomes a function of plastic straining and strain rate. Some possibilities discussing this approach are given in section 5.5.5. Some strain rate options are included in the material model I have implemented.

Returning to the plasticity theory we start out assuming an incrementally linear relation between plastic strain and stress increments on the form:

$$d\epsilon^p_{ij} = C_{ijkl} d\sigma_{kl} \tag{5.18}$$

where C_{ijkl} is a compliance tensor depending on the same parameters as the yield function in 5.17, but it is assumed that the tensor does not depend on either $d\sigma_{kl}$ or $d\epsilon^p_{ij}$ as such a dependency will destroy the linearity of expression 5.18.

For a given plastic loading we decompose $d\sigma_{ij}$ into components tangential and normal to the yield surface, see figure 5.5. Rewriting 5.18 leads to:

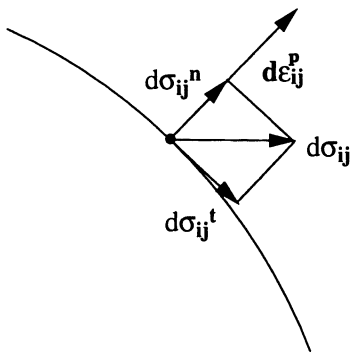

Figure 5.5: *Decomposition of $d\sigma_{ij}$ into $d\sigma^t_{ij}$ and $d\sigma^n_{ij}$.*

$$d\epsilon^p_{ij} = C_{ijkl} d\sigma^n_{kl} + C_{ijkl} d\sigma^t_{kl} = C_{ijkl} d\sigma^n_{kl} \tag{5.19}$$

as the component $d\sigma_{ij}^t$ corresponds to neutral loading and therefore does not generate any plastic strains. To obtain a unit vector normal to the yield surface we normalize the gradient:

$$n_{ij} = \frac{\frac{\partial f}{\partial \sigma_{ij}}}{\sqrt{\frac{\partial f}{\partial \sigma_{kl}} \frac{\partial f}{\partial \sigma_{kl}}}} \tag{5.20}$$

The length of $d\sigma_{ij}^n$ is given by the product $n_{ij} d\sigma_{ij}$

We can then obtain the component of $d\sigma_{ij}^n$ as:

$$d\sigma_{ij}^n = n_{ij} n_{kl} d\sigma_{kl} = \frac{\frac{\partial f}{\partial \sigma_{kl}}}{\frac{\partial f}{\partial \sigma_{mn}} \frac{\partial f}{\partial \sigma_{mn}}} d\sigma_{kl} \frac{\partial f}{\partial \sigma_{ij}} \tag{5.21}$$

Using the expression 5.21 in 5.19 leads to:

$$d\epsilon_{ij}^p = C_{ijkl} d\sigma_{kl}^n = C_{ijkl} \frac{\frac{\partial f}{\partial \sigma_{kl}}}{\frac{\partial f}{\partial \sigma_{mn}} \frac{\partial f}{\partial \sigma_{mn}}} \frac{\partial f}{\partial \sigma_{pq}} d\sigma_{pq} = B_{ij} \frac{\partial f}{\partial \sigma_{kl}} d\sigma_{kl} \tag{5.22}$$

and based on the assumption of incrementally linearity we can state that B_{ij} is also independent of the stress increment. B_{ij} depends only on the same parameters as used in the yield criterion. To obtain an expression for B_{ij} we define a scalar function:

$$g(\sigma_{ij}, \alpha_{ij}, \kappa_\beta) = 0 \tag{5.23}$$

and we set:

$$B_{ij} = \frac{1}{H} \frac{\partial g}{\partial \sigma_{ij}} \tag{5.24}$$

This is a very general formulation, however, it is a limitation compared to 5.22. By using the scalar function g we can express the plastic strain increment as:

$$d\epsilon_{ij}^p = \frac{1}{H} \frac{\partial g}{\partial \sigma_{ij}} \frac{\partial f}{\partial \sigma_{kl}} d\sigma_{kl} \tag{5.25}$$

Two important assumptions are made to achieve 5.25: The continuity requirement that tangential loading does not lead to plastic straining and that the incremental relation between $d\epsilon_{ij}^p$ and $d\sigma_{ij}$ can be considered linear. At the same time it may be noticed that the expression is also valid in the case of softening plasticity but the loading/unloading conditions listed above do not apply to this situation. H is the generalized plastic modulus and g is termed the plastic potential.

When f is different from g we have so-called non-associated plasticity. If g is equal to f we have associated plasticity. Most sources state that in the case of metal plasticity a sufficiently accurate description can be obtained by using associated plasticity.

If we accept Drucker's postulate and assume associated plasticity we have from 5.25:

$$d\epsilon_{ij}^p = d\lambda \frac{\partial f}{\partial \sigma_{ij}} \tag{5.26}$$

with the plastic multiplyer:

$$d\lambda = \frac{1}{H}\frac{\partial f}{\partial \sigma_{kl}} d\sigma_{kl} \tag{5.27}$$

Rewriting Drucker's postulate:

$$d\sigma_{ij} d\epsilon^p_{ij} = d\lambda \frac{\partial f}{\partial \sigma_{ij}} d\sigma_{ij} = \frac{1}{H}\left(\frac{\partial f}{\partial \sigma_{kl}} d\sigma_{ij}\right)^2 \geq 0 \tag{5.28}$$

As we have $\frac{\partial f}{\partial \sigma_{ij}} d\sigma_{ij} \geq 0$ for plastic loading as well as for neutral loading we can conclude that in the case of hardening plasticity $d\lambda$ and H are positive quantities.

5.3.1 Inversion of the constitutive relations

By using both the decoupling of strain increments into elastic and plastic parts and Hooke's relation for elasticity we can, for a given increment in stresses, obtain the strain increments directly. In an explicit finite element context we need normally to do the inverse: To estimate the stress increments knowing the strain increments. In implicit formulations the same problem arises; here we are, however, searching for the unknown increments in displacements from which the strains can be derived directly. In both cases we do need the possibility to predict the stress increments from the corresponding strain increments.

To start out we take Hooke's law in an incremental form:

$$d\sigma_{ij} = D_{ijkl}\left(d\epsilon_{kl} - d\epsilon^p_{kl}\right) \tag{5.29}$$

D_{ijkl} is the elastic stiffness matrix, which may be written on the form:

$$D_{ijkl} = \frac{E}{2(1+\nu)}\left(\delta_{ki}\delta_{lj} + \delta_{li}\delta_{kj}\right) + \frac{\nu E}{(1+\nu)(1-2\nu)}\delta_{ij}\delta_{kl} \tag{5.30}$$

Rewriting 5.29 we find:

$$D_{ijkl} d\epsilon_{kl} = d\sigma_{ij} + D_{ijkl} d\epsilon^p_{kl} = d\sigma_{ij} + D_{ijkl}\frac{1}{H}\frac{\partial g}{\partial \sigma_{kl}}\frac{\partial f}{\partial \sigma_{mn}} d\sigma_{mn} \tag{5.31}$$

Multiplying by $\frac{\partial f}{\partial \sigma_{ij}}$:

$$\frac{\partial f}{\partial \sigma_{ij}} D_{ijkl} d\epsilon_{kl} = \frac{\partial f}{\partial \sigma_{ij}} d\sigma_{ij} + \frac{\partial f}{\partial \sigma_{ij}} D_{ijkl}\frac{1}{H}\frac{\partial g}{\partial \sigma_{kl}}\frac{\partial f}{\partial \sigma_{mn}} d\sigma_{mn} \tag{5.32}$$

Reordering:

$$\frac{\partial f}{\partial \sigma_{ij}} D_{ijkl} d\epsilon_{kl} = \frac{\partial f}{\partial \sigma_{mn}} d\sigma_{mn}\left(1 + D_{ijkl}\frac{1}{H}\frac{\partial g}{\partial \sigma_{kl}}\frac{\partial f}{\partial \sigma_{mn}}\right) \tag{5.33}$$

$$\frac{\partial f}{\partial \sigma_{mn}} d\sigma_{mn} = \frac{\frac{\partial f}{\partial \sigma_{ij}} D_{ijkl} d\epsilon_{kl}}{1 + D_{ijkl}\frac{1}{H}\frac{\partial g}{\partial \sigma_{kl}}\frac{\partial f}{\partial \sigma_{ij}}} \tag{5.34}$$

Using expression 5.34 and 5.25 we obtain the plastic strain increments expressed as a function of the total strain increments:

$$d\epsilon_{ij}^{p} = \frac{\partial g}{\partial \sigma_{ij}} \frac{\frac{\partial f}{\partial \sigma_{mn}} D_{mnst} d\epsilon_{st}}{H + D_{pqkl} \frac{\partial g}{\partial \sigma_{pq}} \frac{\partial f}{\partial \sigma_{kl}}} \tag{5.35}$$

Using the expression for the plastic strain increments in 5.29 we have the relation:

$$d\sigma_{ij} = D_{ijkl}^{ep} d\epsilon_{kl} \tag{5.36}$$

where the tangential elasto-plastic stiffness tensor is given:

$$D_{ijkl}^{ep} = D_{ijkl} - \frac{D_{ijst} \frac{\partial g}{\partial \sigma_{st}} \frac{\partial f}{\partial \sigma_{mn}} D_{mnkl}}{H + D_{pqst} \frac{\partial f}{\partial \sigma_{pq}} \frac{\partial g}{\partial \sigma_{st}}} \tag{5.37}$$

Below only associated plasticity will be considered, that is g is equal to f.

To obtain a good description of material behaviour we need a good hardening description (to achieve H) and also a yield function capable of showing the characteristic material behaviour during deformation.

5.4 Hardening behaviour

After yielding most materials are capable of resisting even further increase in load. This effect is due to hardening of the material. Many models can be used to model this effect and in the following section some of the most common models for metal forming calculations are given. One of the most essential choices is whether to model the material as isotropic hardening or kinematic hardening. In some cases, where the material deformation can be regarded as monotonic, it is not necessary to be that concerned about the hardening rule. But in many cases reversed deformation is present (this could be bending and subsequent unbending) and here it can be of major importance to include the correct type of hardening.

In order to take Bauschinger effects into account it is necessary to use a kinematic model where the centre of the yield surface is translated with the plastic straining.

Two different models are often employed: strain or work hardening. Below the expressions for the plastic multiplier derived from the tangency conditions are given.

5.4.1 Isotropic hardening

As regards isotropic hardening it is assumed that the shape of the yield surfaces remain the same, but it is extended as function of the effective plastic strain (isotropic strain hardening) or the plastic work (isotropic work hardening).

Isotropic strain hardening

In the case where a hardening effect is present the condition for yielding can be written:

$$f = \sigma_e - \sigma_Y(\epsilon_{ps}) \tag{5.38}$$

σ_e is the equivalent stress and σ_Y is now a function that defines the relation between current yield stress and equivalent plastic strain:

$$\epsilon_{ps} = \Sigma \delta \epsilon_{ps} = \int d\epsilon_{ps} \tag{5.39}$$

The increments in plastic strain for a von Mises material are found as:

$$d\epsilon_{ps} = \sqrt{\frac{2}{3} d\epsilon_{ij}^p d\epsilon_{ij}^p} \tag{5.40}$$

for the three dimensional case. In case of plane stress plasticity the relation can be rewritten as:

$$d\epsilon_{ps} = \frac{2}{\sqrt{3}} \sqrt{d\epsilon_{11}^{p\,2} + d\epsilon_{22}^{p\,2} + d\epsilon_{11}^p d\epsilon_{22}^p + d\epsilon_{12}^{p\,2}} \tag{5.41}$$

If we regard uniaxial tension and assume that there is no change in volume due to plastic deformation we have: $\sigma_{11} \neq 0$, $d\epsilon_{22}^p = d\epsilon_{33}^p = -\frac{1}{2} d\epsilon_{11}^p$. Defining the generalized plastic modulus as:

$$H = \frac{\partial \sigma_Y}{\partial \epsilon_{ps}} \tag{5.42}$$

H can then be determined by using the uniaxial stress/plastic strain relationship:

$$H = \frac{\partial \sigma_{11}}{\partial \epsilon_{11}^p} \tag{5.43}$$

Using H the tangency condition can be written as:

$$df = \frac{\partial f}{\partial \sigma_{ij}}^T d\sigma_{ij} + \frac{\partial f}{\partial \sigma_Y} \frac{\partial \sigma_Y}{\partial \epsilon_{ps}} d\epsilon_{ps} = \frac{\partial f}{\partial \sigma_{ij}}^T d\sigma_{ij} - H d\epsilon_{ps} = 0 \tag{5.44}$$

Using the Prandtl-Reuss flow rule we now have (equation 5.26):

$$d\epsilon_{ij}^p = d\lambda \frac{\partial f}{\partial \sigma_{ij}} \tag{5.45}$$

in the expression for the plastic strain increment (equation 5.39):

$$d\epsilon_{ps} = B(\sigma_{ij}) d\lambda \tag{5.46}$$

For von Mises' yield criterion $B(\sigma_{ij})$ equals 1, but for other criteria $B(\sigma_{ij})$ may differ due to the use of equation 5.43 to determine H. The tangency equation 5.44 can then be rewritten as:

$$df = \frac{\partial f}{\partial \sigma_{ij}}^T d\sigma_{ij} - HBd\lambda = \frac{\partial f}{\partial \sigma_{ij}}^T d\sigma_{ij} - Ad\lambda = 0 \tag{5.47}$$

which defines A.

Finally solving for the plastic multiplyer $d\lambda$:

$$d\lambda = \frac{\frac{\partial f}{\partial \sigma_{ij}} C_{ijkl} d\epsilon_{kl}}{\frac{\partial f}{\partial \sigma_{ij}} C_{ijkl} \frac{\partial f}{\partial \sigma_{kl}} + A} \tag{5.48}$$

which corresponds to 5.27

Isotropic work hardening

It is often chosen to describe the hardening as function of plastic work W_p. The yield condition is now written as:

$$f = \sigma_e - \sigma_Y(W_p) \tag{5.49}$$

W_p is given by:

$$W_p = \int \sigma_Y d\epsilon_{ps} = \int \sigma_{ij} d\epsilon_{ij}^p = \int \sigma_{ij} \frac{\partial f}{\partial \sigma_{ij}} d\lambda \tag{5.50}$$

The increment in plastic work is:

$$dW_p = \sigma_Y d\epsilon_{ps} = \sigma_{ij} d\epsilon_{ij}^p = d\lambda \sigma_{ij} \frac{\partial f}{\partial \sigma_{ij}} \tag{5.51}$$

When introducing A:

$$A = \frac{H \sigma_{ij} \frac{\partial f}{\partial \sigma_{ij}}}{\sigma_Y} \tag{5.52}$$

we can write the tangency condition as:

$$df = \frac{\partial f}{\partial \sigma_{ij}} d\sigma_{ij} + \frac{\partial f}{\partial \sigma_Y} \frac{\partial \sigma_Y}{\partial W_p} dW_p = \frac{\partial f}{\partial \sigma_{ij}} d\sigma_{ij} - d\lambda \frac{\partial \sigma_Y}{\partial W_p} \frac{\partial f}{\partial \sigma_{ij}} = \tag{5.53}$$

$$\frac{\partial f}{\partial \sigma_{ij}} d\sigma_{ij} + d\lambda \frac{\partial \sigma_y}{\partial \epsilon_{ps}} \frac{\partial \epsilon_{ps}}{\partial W_p} \frac{\partial f}{\partial \sigma_{ij}} \sigma_{ij} = \frac{\partial f}{\partial \sigma_{ij}} d\sigma_{ij} - d\lambda \frac{H}{\sigma_Y} \frac{\partial f}{\partial \sigma_{ij}} \sigma_{ij} = \frac{\partial f}{\partial \sigma_{ij}}^T d\sigma - A d\lambda = 0$$

When von Mises' yield criterion is used strain and work hardening coincide. One benefit from the presentation above is that strain hardening as well as work hardening can be treated within the same numerical framework.

5.4.2 Kinematic hardening

For kinematic hardening the size and shape of the yield surface remain constant, but the origo of the yield surface (at α_{ij}) is translated with the plastic strain and it is often assumed that the change in backstress α_{ij} is proportional to the plastic strain increments:

$$d\alpha_{ij} = c d\epsilon_{ij}^p \tag{5.54}$$

Of course these simple models of a very complex behaviour cannot be expected to be very accurate. In general the main problem is that not only the hardening influences the material behaviour, but the yield function shape will normally also change with increasing plastic deformation. Very few proposals have been made to take the variation of anisotropic parameters as function of strain and/or strain path into account. However, a growing interest in the area can be seen and quite recently Suh et al. [201] discussed the influence of plastic straining on the exponent of various yield criteria.

5.5 Description of hardening

In the following is given a list of some hardening laws. The laws have been utilized in connection with sheet metal forming. Most of these criteria are established from uniaxial tests, but the criteria are used for more complicated stress states to relate the equivalent stress obtained from the yield function to the effective plastic strain.

Many materials are affected by the rate with which they are loaded. In the area of plasticity this effect is normally taken into account by applying a relatively simple model for the strain rate dependency. A few examples of these models are included in section 5.5.5. A couple of the models are implemented in the material routine developed. Typically the loading rate is scaled when using an explicit time integration scheme. This will clearly give some difficulties if one wants to include strain rate effects for the physical process. In order to be able to better take the strain rate effects into account simple rules are given to rescale the strain rate.

5.5.1 Linear hardening

The simplest hardening model is linear hardening. After reaching the initial yield stress σ_{Y0} the yield stress grows linearly as function of the effective plastic strain ϵ^p_{eff}.

$$\sigma_Y = \sigma_{Y0} + H\epsilon^p_{eff} \tag{5.55}$$

5.5.2 Hollomon's hardening model

One of the most popular models used for sheet metals is the one proposed by Hollomon in 1945. The model uses a power law to relate yield stress to the effective plastic strain:

$$\sigma_Y = K{\epsilon^p_{eff}}^n \tag{5.56}$$

Here, only two parameters K and n are needed to describe the hardening.

5.5.3 Voce's hardening model

A similar expression was given by Voce in 1948:

$$\sigma_Y = K(1 - Ae^{B\epsilon^p_{eff}}) \tag{5.57}$$

where three coefficients, A,B and K are needed.

5.5.4 Swift's model

Swift proposed in 1952 an extension of Hollomon's expression:

$$\sigma_Y = K(\epsilon_0 + \epsilon^p_{eff})^n \tag{5.58}$$

The law proposed by Swift (or Krupkowsky) is maybe more suitable than the criterion by Hollomon, at least there is an additional parameter, ϵ_0, which may improve the overall

correlation with tensile curves. ϵ_0 has also been used for describing initial yielding which is a capacity which the the Hollomon hardening rule lacks. In some cases the expression is utilized for estimating the initial yield stress (in numerical routines), this is done by calculating ϵ_0 as:

$$\epsilon_0 = \left(\frac{E}{K}\right)^{\frac{1}{n-1}} \tag{5.59}$$

where E is the elasticity modulus. LS-Dyna3d uses this method in some of the material models, [83]. Although this method under-estimates the yield stress, especially when n is large, it is very convenient only to specify two coefficients, K and n; values which are often reported by material suppliers.

This way of determining ϵ_o will for most plastic forming operations be without importance as the plastic deformation reaches a level well above the initial yielding. When estimating a too low initial yield strength one advantage is that the effects of stress peaks due to wave propagation are reduced, or in other words absorbed as plastic works.

However, it is in some examples very important to model the stress-strain relations accurately as the tangent stiffness drops significantly when reaching the yield limit.

5.5.5 Strain rate effects

Many metals are sensitive to the strain rate, normally the apparent yield strength increases with increasing strain rate. This effect can be included in the constitutive model by using an elastic-viscoplastic representation. A classical method is to use a different work hardening function introducing a multiplicative flow function, $F(\epsilon^p_{eff}, \dot{\epsilon}^p_{eff})$. If we denote the quasi-static hardening function $k = k(\epsilon^p_{eff})$, we can express this type as:

$$k^*(\epsilon^p_{eff}, \dot{\epsilon}^p_{eff}) = k(\epsilon^p_{eff})F(\epsilon^p_{eff}, \dot{\epsilon}^p_{eff}) \tag{5.60}$$

where k^* is used in the expression for the yield criterion instead of k. The method corresponds to an isotropic expansion/contraction of the yield surface with an increase/decrease in the strain rate. Some proposed models are:

The Norton model

$$\sigma_Y = K\epsilon^{p^n}_{eff}\dot{\epsilon}^{p^m}_{eff} \tag{5.61}$$

The Wagoner-Swift model

$$\sigma_Y = K(\epsilon_0 + \epsilon^p_{eff})^n \left(\frac{\dot{\epsilon}^p_{eff}}{\dot{\epsilon}_{ref}}\right)^m \tag{5.62}$$

where $\dot{\epsilon}_{ref}$ is some reference strain rate (can also be considered an additional material parameter).

The Sokoloski-Malvern model

$$F = 1 + mln(1 + D\dot{\epsilon}^p_{eff}) \tag{5.63}$$

The Cowper-Symonds model

$$F = 1 + \left(\frac{\dot{\epsilon}^p_{eff}}{D}\right)^{\frac{1}{m}} \tag{5.64}$$

The Johnson-Cook model

$$F = 1 + mln\left(\frac{\dot{\epsilon}^p_{eff}}{D}\right) \tag{5.65}$$

The three last expressions are based on two material parameters m and D which must be determined from experiments.

The Jones model

$$F = 1 + \left(1 + \frac{(\epsilon_u - \epsilon_y)\dot{\epsilon}^p_{eff}}{D_y(\epsilon_u - \epsilon^p_{eff}) + D_y(\epsilon^p_{eff} - \epsilon_y)}\right)^{\frac{1}{m}} \tag{5.66}$$

This expression is a bit more flexible than the previously mentioned methods, but more material parameters must be determined (ϵ_u, ϵ_y, D_y).

Extension of the Swift (Krupkowsky) model

An extension of for instance the Swift model can be made to take strain rate effects into account:

$$\sigma_Y(\epsilon^p_{eff}) = K_{ref}X^a\left[\epsilon^p_{eff} + \epsilon_{0ref}\right]^{n_{ref}X^c} \tag{5.67}$$

where $X = \frac{\dot{\epsilon}_{eff}}{\dot{\epsilon}_{ref}}$. The coefficients a,b and c are regarded as material constants. The values with the subscript ref are the values that are determined for a reference situation. This expression is reported to give a good representation for strain rates in the range from 10^{-3} to 1 s^{-1} and various sheet materials, [175].

5.6 Integration procedures for elasto-plasticity

As we have the constitutive relation given on a rate form, we have to perform a numerical integration. Most solution techniques are based on a predictor/corrector scheme which assumes a linear strain path within the increment. This means that although equilibrium requirements are fulfilled after the increment there can be errors in the integration of the

flow rules. As these errors are strongly related to the adopted procedure it is very important to be aware of this, both when developing programme routines and when using standard software. There will often be a risk of accumulating numerical errors or, if explicit integration schemes are utilized, a risk of drifting.

In this project it has been chosen entirely to use the explicit finite element technique. This means that we get the updated geometric configuration without needing the iterations to reduce the out of balance forces in the same way as for an implicit solution scheme. As it is not necessary to calculate structural and element stiffness at all with explicit codes, implementation of material models is much easier than for an implicit code. This makes the explicit formulation very suitable for testing material models. In combination with the guarantee of a solution, explicit codes are especially suited for research that focuses more on material and process behaviour than on the behaviour of computational algorithms.

We have in section 5.3 established the standard elasto-plastic modular matrix, which is in theory sufficient for solution of the problem: Updating the stress state from knowledge of the strain increment, as long as we use infinitesimal increments. In practice this is impossible, wherefore the choice of integration scheme is of major importance. The purpose of this section is not to give a complete mathematical discussion on the solution techniques in detail, but instead to discuss some advantages/disadvantages of different solution techniques. The books of Simo and Hughes [189] and Crisfield [47], the articles by De Borst [145], [56], Runesson and Samulesson [182], Ortiz and Popov [168], and the many articles written by Simo discuss these matters in details. Another important aspect beside the theoretical development is the use of reliable integration procedures. Some of the most used procedures are mentioned and a strategy for the implementation is discussed. According to Crisfield [47] the most frequently used procedures are:

- Forward Euler scheme.
- Sub increment technique.
- Backward Euler scheme.
- Midpoint (or generalized) Euler scheme.

In the literature one can find several variations of the above methods but also many more specific approaches to solve non-linear problems.

5.6.1 The location of the intersection between elastic stress and the yield surface

Many algorithms for stress updating need the location of the intersection point between the elastic stress vector (predictor) and the yield surface. Knowing an elastic increment in stresses, $\Delta\sigma_{ij}^{*}$, the condition can be written as:

$$f(\sigma_{ij0} + \alpha\Delta\sigma_{ij}^{*}) = 0 \tag{5.68}$$

when it is assumed that $f_X = f(\sigma_{ij0}) < 0$ (it is within the yield surface).
If the total stress increment leads to a point outside the yield surface, as shown in figure 5.6,

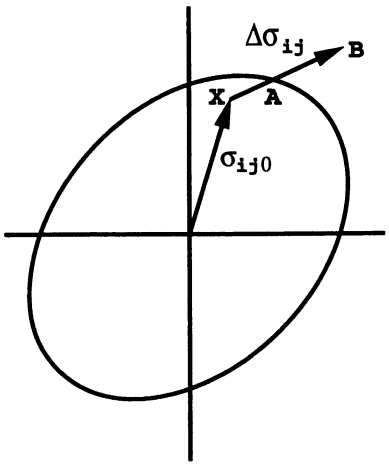

Figure 5.6: *Illustration of the forward Euler procedure: Location of the intersection point A.*

the following strategy can be used for determination of α: First the value of f corresponding to $\alpha = 1$ (f_B) is used to obtain an initial value for α:

$$\alpha_0 = \frac{-f_X}{f_B - f_X} \tag{5.69}$$

α_0 is then used to determine f_C and consequently a first order Taylor expansion is performed to estimate the change $\delta\alpha$ leading to $f_D = 0$:

$$f_D = f_C(\sigma_{ij0} + \alpha_0 \Delta\sigma_{ij}) + \frac{\partial f}{\partial \sigma_{ij}} \frac{\partial \sigma_{ij}}{\partial \alpha} \delta\alpha = f_C + \frac{\partial f}{\partial \sigma_{ij}} \Delta\sigma^*_{ij} \delta\alpha = 0 \tag{5.70}$$

leading to:

$$\delta\alpha = \frac{-f_C}{\frac{\partial f}{\partial \sigma_{ij}} \Delta\sigma^*_{ij}} \tag{5.71}$$

After determination of $\alpha = \alpha_0 + \delta\alpha$ the rest of the increment $(1-\alpha)\Delta\sigma^*_{ij}$ can be treated as elasto-plastic. If the intersection is not determined with a sufficient accuracy the scheme can be repeated by using $f_C = f_D$ and $\alpha_0 = \alpha_0 + \delta\alpha$.

5.6.2 Forward Euler return, prediction method 1

When moving from the rate form with infinitesimal increments to final increments it is inevitable to introduce errors. If we regard equation 5.44 without hardening effects and replace $d\sigma_{ij}$ with final increments $\Delta\sigma_{ij}$ we have:

$$\Delta f = \frac{\partial f}{\partial \sigma_{ij}} \Delta\sigma_{ij} \tag{5.72}$$

If we evaluate $\frac{\partial f}{\partial \sigma_{ij}}$ at the beginning of the increment (at the intersection) and utilize 5.48 to calculate $\Delta\lambda$:

$$\Delta\lambda = \frac{\frac{\partial f_A}{\partial \sigma_{ij}} D_{ijkl} \Delta\epsilon_{kl}}{\frac{\partial f_A}{\partial \sigma_{ij}} D_{ijkl} \frac{\partial f_A}{\partial \sigma_{kl}}} \tag{5.73}$$

Here we scale the stress back with the direction calculated at A. We here see that it is inevitable to make an error and the increment will always lead to a stress state outside the yield surface. The problem is illustrated in figure 5.7. The stresses are then updated as:

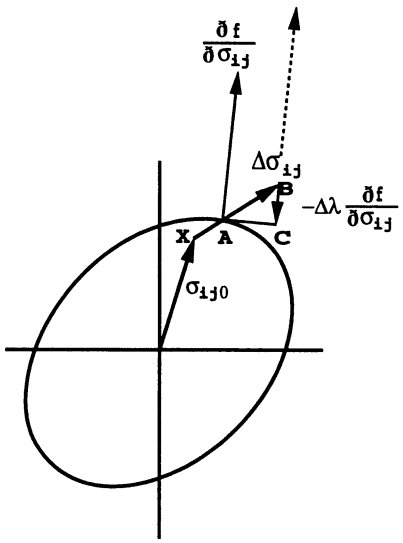

Figure 5.7: *Illustration of the forward Euler procedure: Location of the intersection point A and the subsequent back scaling of trial stress B to point C.*

$$\sigma_{ijC} = \sigma_{ijB} - \Delta\lambda D_{ijkl}\frac{\partial f_A}{\partial \sigma_{kl}} \tag{5.74}$$

An improvement can be to use a second order expansion of the tangency condition which of course will lead to a better approximation.

5.6.3 "Backward Euler return", prediction method 2

Another first estimation of the updated stress can be made by using a method normally called a backward Euler return. Here we make a Taylor expansion around point B, see

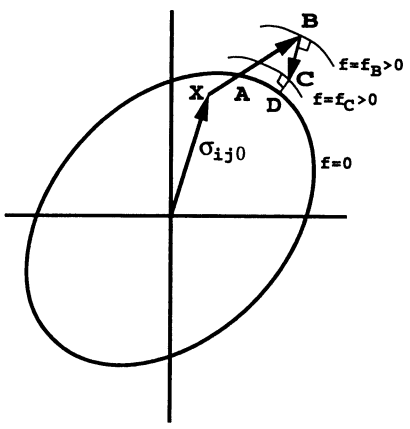

Figure 5.8: *Illustration of the backward Euler procedure.*

figure 5.8, from which the plastic multiplier is determined:

$$f_C = f_B + \frac{\partial f_B}{\partial \sigma_{ij}} \Delta\sigma_{ij} - \Delta\lambda A \tag{5.75}$$

using equation 5.29 for the determination of $\Delta\sigma_{ij}$ with $\Delta\epsilon_{ij} = 0$ because the total strain increment is used for the elastic trial going from X to B. A is determined from equation 5.47. Solution of equation 5.75 for $f_C = 0$ leads to:

$$\Delta\lambda = \frac{f_B}{\frac{\partial f_B}{\partial \sigma_{ij}} D_{ijkl} \frac{\partial f_B}{\partial \sigma_{kl}} + A} \tag{5.76}$$

A and $\frac{\partial f}{\partial \sigma_{kl}}$ are here calculated at B and one avoids hereby to calculate the intersection with the initial yield surface. The stresses at C are now calculated as:

$$\sigma_{ijC} = \sigma_{ijB} - \Delta\lambda D_{ijkl} \frac{\partial f_B}{\partial \sigma_{kl}} \tag{5.77}$$

5.6.4 Operator splitting

As discussed above the two methods of predicting the stress at point C will lead to stresses outside the yield surface. To improve the condition $f = 0$ one can simply scale the stresses with a factor until the yield function obtains the value 0, but this will normally include elastic components and should be avoided in the general case. The method is used for the radial return method where it turns out to be a very effective method (for the von Mises' criterion represented in the deviatoric space). A method similar to the radial return (a fully implicit Euler backward algorithm) can be obtained for Hill's 48 criterion as described by De Borst [56].

A method which is widely used is the operator splitting method proposed by Ortiz and Simo [169]. Again the total strains are kept fixed (as in prediction method 2) and further relaxation is applied at point C. We update the stresses as:

$$\sigma_{ijD} = \sigma_{ijC} - \delta\lambda_C D_{ijkl} \frac{\partial f_C}{\partial \sigma_{kl}} \tag{5.78}$$

with the multiplier calculated at C:

$$\delta\lambda_C = \frac{f_C}{\frac{\partial f_C}{\partial \sigma_{ij}} D_{ijkl} \frac{\partial f_C}{\partial \sigma_{kl}}} \tag{5.79}$$

If the resulting value of the yield function is not sufficiently close to 0 further relaxation can be applied leading to the stress update sequence:

$$\Delta\sigma_{ij} = D_{ijkl}\Delta\epsilon_{kl} - \Delta\lambda_B D_{ijkl} \frac{\partial f_B}{\partial \sigma_{kl}} - \delta\lambda_C D_{ijkl} \frac{\partial f_C}{\partial \sigma_{kl}} - \delta\lambda_D D_{ijkl} \frac{\partial f_D}{\partial \sigma_{kl}} - \ldots\ldots \tag{5.80}$$

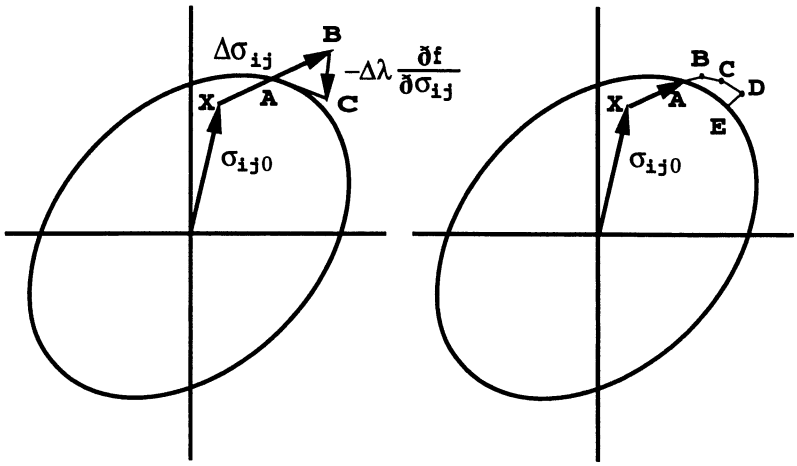

Figure 5.9: *Illustration of the backward Euler procedure and the effect of sub-incrementation.*

5.6.5 Sub-incrementation

A way to improve the forward Euler integration technique is to perform a sub-incrementation. The method is illustrated in figure 5.9. Although this method improves the forward Euler method there will still be a tendency to drifting, i.e. the value of f in point E will be larger than zero. One benefit of the method is that it is rather simple seen from a computational point of view. As we have many small time steps in normal sheet metal forming simulations using explicit time integration and therefore relatively small strain increments the method may be found appropriate for the stress update.

5.6.6 Generalized integration algorithm

The methods discussed above can be included in a scheme proposed by Ortiz and Popov [168]; the generalized trapezoidal or mid-point algorithm. The stress at C is calculated as:

$$\sigma_{ijC} = \sigma_{ijA} + D_{ijkl}(\Delta\epsilon_{ij} - \Delta\epsilon^p_{ij}) = \sigma_{ijB} - D_{ijkl}\Delta\epsilon^p_{ij} \tag{5.81}$$

with the plastic strains calculated from:

$$\Delta\epsilon^p_{ij} = \Delta\lambda\left[(1-\eta)\frac{\partial f_A}{\partial\sigma_{ij}} + \eta\frac{\partial f_C}{\partial\sigma_{ij}}\right] \tag{5.82}$$

or from:

$$\Delta\epsilon^p_{ij} = \Delta\lambda\left[\frac{\partial f_A}{\partial\sigma_{ij}}((1-\eta)\sigma_{ijA} + \eta\sigma_{ijC})\right] \tag{5.83}$$

with the value of f at point C estimated as:

$$f_C = \sigma_{refC}(\sigma_{ijC}) - \sigma_{YC}(\epsilon_{psC}) = \sigma_{refC}(\sigma_{ijC}) - \sigma_{YC}(\epsilon_{psB} + \Delta\epsilon_{ps}(\Delta\epsilon^p_{ij})) \tag{5.84}$$

If $\eta = 0$ equations 5.82 and 5.83 coincide and the explicit forward Euler scheme is obtained.

With $\eta = 1$ we get a backward Euler procedure, which in contrast to the method described in section 5.6.7, involves the normality ($\frac{\partial f}{\partial \sigma_{ij}}$) evaluated at point C. If the normality cannot be determined from values known at A and B it may be necessary with an iterative procedure to fulfil the tangency condition in equation 5.84. Figure 5.10 shows the procedure for the general return and the backward Euler return from inside the yield surface.

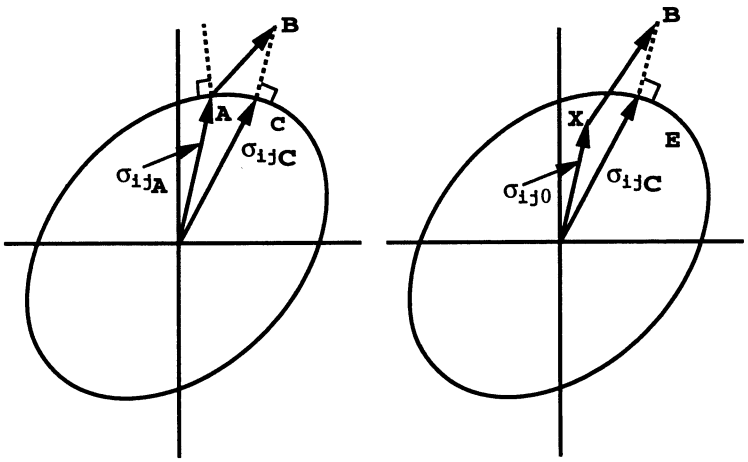

Figure 5.10: *Left: Illustration of the general return using knowledge of the intersection point. Right: A backward Euler return based on a stress state placed inside the yield surface.*

5.6.7 A Backward Euler scheme

If we choose $\eta = 1$ in equation 5.82 or 5.83 we have a backward Euler return. The stress at C is calculated by using the normality condition at C:

$$\sigma_{ijC} = \sigma_{ijB} - \Delta\lambda D_{ijkl}\frac{\partial f_C}{\partial \sigma_{kl}} \tag{5.85}$$

This expression will generally not give the exact solution and if the error is expressed as:

$$r_{ij0} = \sigma_{ijC} - (\sigma_{ijB} - \Delta\lambda D_{ijkl}\frac{\partial f_C}{\partial \sigma_{kl}}) \tag{5.86}$$

a new residual can be calculated from a first order Taylor expansion:

$$r_{ijN} = r_{ij0} + \delta\sigma_{ijC} + \delta\lambda D_{ijkl}\frac{\partial f_C}{\partial \sigma_{kl}} + \Delta\lambda D_{ijkl}\frac{\partial a_{klC}}{\partial \sigma_{ko}}\delta\sigma_{ol} \tag{5.87}$$

with $a_{ij} = \frac{\partial f}{\partial \sigma_{ij}}$. Setting this residual to 0 gives the increment in stresses as:

$$\delta\sigma_{ij} = -\left(\delta_{Cij} + \Delta\lambda D_{ijkl}\frac{\partial a_{kl}}{\partial \sigma_{mn}}\right)^{-1}(r_{mn0} + \delta\lambda D_{mnop}\frac{\partial f}{\partial \sigma_{op}}) = \tag{5.88}$$

$$-Q^{-1}_{ijkl}r_{kl0} - \delta\lambda Q^{-1}_{ijmn}D_{mnkl}\frac{\partial f_C}{\partial \sigma_{ko}} \tag{5.89}$$

where δ_{Cij} is the Kronecker delta, not to be confused with δ which in the above is used for a variation. From equation 5.84 we can make an expansion of the yield function leading to:

$$f_{CN} = f_{C0} + \frac{\partial f_C}{\partial \sigma_{ij}}\dot{\sigma}_{ij} + \frac{\partial f_C}{\partial \epsilon_{ps}}\delta\epsilon_{ps} = f_{C0} + \frac{\partial f_C}{\partial \sigma_{ij}}\delta\sigma_{ij} + A_C\delta\lambda = 0 \tag{5.90}$$

which solved for $\delta\lambda$ leads to:

$$\delta\lambda = \frac{f_{C0} - \frac{\partial f_C}{\partial \sigma_{ij}}Q^{-1}_{ijkl}r_{kl0}}{\frac{\partial f_C}{\partial \sigma_{ij}}Q^{-1}_{ijkl}D_{klmn}\frac{\partial f_C}{\partial \sigma_{mn}} + A_C} \tag{5.91}$$

Now the iterative stress change can be found from 5.89. If the von Mises' yield criterion is utilized in the backward Euler return we obtain what is known as the radial return proposed by Wilkins [220].

5.6.8 Consistent tangent modular matrix

The standard backward Euler return is based on the expression:

$$\sigma_{ijC} = \sigma_{ijB} - \Delta\lambda D_{ijkl}\frac{\partial f_C}{\partial \sigma_{kl}} \tag{5.92}$$

Change in stresses can be expressed by:

$$\delta\sigma_{ij} = D_{ijkl}\delta\epsilon_{kl} - \delta\lambda D_{ijkl}\frac{\partial f_C}{\sigma_{ij}} - \Delta\lambda D_{ijkl}\frac{\partial f_C}{\sigma_{lm}}\delta\sigma_{mk} \tag{5.93}$$

leading to:

$$\begin{aligned}\delta\sigma_{ij} = \left(\delta_{ijkl} + \Delta\lambda D_{ijop}\frac{\partial f_C}{\partial \sigma_{op}}\right)^{-1} D_{klmn}(\delta\epsilon_{mn} - \delta\lambda\frac{\partial f_C}{\sigma_{mn}}) = \\ Q^{-1}_{ijmn}(\delta\epsilon_{mn} - \delta\lambda\frac{\partial f_C}{\sigma_{mn}}) = R_{ijmn}(\delta\epsilon_{mn} - \delta\lambda\frac{\partial f_C}{\sigma_{mn}})\end{aligned} \tag{5.94}$$

Application of the tangency condition $\delta f = 0$ gives:

$$\frac{\partial f}{\partial \sigma_{ij}}\delta\sigma_{ij} = \frac{\partial f}{\partial \sigma_{ij}}R_{ijkl}\delta\epsilon_{kl} - \delta\lambda\frac{\partial f}{\partial \sigma_{ij}}R_{ijkl}\frac{\partial f}{\partial \sigma_{kl}} - A\delta\lambda = 0 \tag{5.95}$$

The two latter equations lead to the consistent modular matrix C_{CT}:

$$\delta\sigma_{ij} = C_{CTijkl}\delta\epsilon_{kl} = \left(R_{ijkl} - \frac{R_{ijop}\frac{\partial f_C}{\partial \sigma_{op}}\frac{\partial f_C}{\partial \sigma_{mn}}R_{klmn}}{\frac{\partial f_C}{\partial \sigma_{ij}}R_{ijkl}\frac{\partial f_C}{\partial \sigma_{kl}} + A}\right)\delta\epsilon_{kl} \tag{5.96}$$

5.6.9 Summary of integration of constitutive equations

The backward Euler scheme in section 5.6.7 has a very good convergence rate, however, as it can be seen from the solution methods discussed in section 3.2.1 it often turns out that a somewhat poorer method (with regard to convergence) can be more efficient seen

from a computational point of view. Krenk [126] mentions that this is a problem for the Newton-Raphson method, compared with the modified Newton-Raphson method. This is also the case for the integration of constitutive equations. The use of consistent methods (section 5.6.7 and 5.6.8), leads to second order convergence, but demands calculation of second order derivatives and also inversion of the Q matrix. This involves a number of additional mathematical operations compared to the simpler backward Euler method described in section 5.6.3. The additional operations are sufficient to destroy the gaining from an improved convergence.

Due to the above mentioned differences in computational performance it is chosen to use the backward Euler method from section 5.6.3 followed by additional relaxation as described in section 5.6.4 for the implementation of material models as described in section 5.10. A secondary benefit from this choice is that debugging of the routine is much simpler due to the reduced number of mathematical calculations (primarily because the second order derivatives do not need to be calculated).

5.7 Yield functions

As stated in section 5.3.1 it is necessary with an accurate and detailed description of both yielding and hardening. Based on a limited literature study a list of yield functions is given. Functions which are suitable for modelling the mechanics of metal sheet are discussed, but the list must not be regarded as complete. The order of the yield functions is made according to time of publication. One of the most recently proposed functions, (Barlat [133], [14], [136]) is discussed in more detail together with Hill's 48 criterion. The basis for the study has in general been literature dedicated to aspects within the area of metal forming, no special research has been performed to give a total overview. The review should rather be considered as a state of the art review of what has been commonly used for simulation of (sheet) metal forming.

The main reason for the discussion is to give an overview and at the same time to discuss advantages and disadvantages. The disadvantages should be seen from a practical as well as a numerical point of view. Several very advanced yield functions have been proposed, e.g. the ICT theory [146]. Though some are reported to give very good results in particular cases, they are not commonly used and as judged by Besdo [31] advanced models based on polycrystallographic theories are not yet ready for implementation. This is mainly due to problems with many material parameters. Therefore it is mainly yield functions described by few, easily obtainable parameters which are in focus. This choice is also evaluated to be the most reasonable seen from an industrial point of view. Very often only the most common yield functions are available in commercial FE-codes. Implementation of advanced criteria is time consuming, expensive tests must be performed to obtain sufficient material parameters and computational efficiency is often decreasing with raising complexity of the plastic evolution laws, etc.

As most sheet forming operations are dominated by in-plane stresses, as long as we disregard examples like ironing, etc, where considerable stresses are imposed normally to the sheet, it has been chosen primarily to give the yield functions on their 2-D form. If a triaxial loading exists it is possible to take this state $(\sigma_{xx}, \sigma_{yy}, \sigma_{zz})$ into account as the plane stress equivalent $(\sigma_{xx} - \sigma_{zz}, \sigma_{yy} - \sigma_{zz})$, when it is assumed that a hydrostatic pressure or tension can be superimposed without effect. However, it can be shown that considerable contact stresses do occur in conventional deep drawing, see for instance Damborg and Jensen [49] and Mortensen [151], who report contact pressures as high as 600-800 N/mm^2 for deep drawing of cups in stainless steel.

5.7.1 Tresca

The first proposed yield criterion, the Tresca yield criterion, is still considered a very good choice in many areas. The criterion is based on the assumption that shear stress is the major reason for fracture (or plastic deformation) and normally it is written as a function of the principal stresses:

$$\Phi = max\{|\sigma_I - \sigma_{II}|, |\sigma_{II} - \sigma_{III}|, |\sigma_{III} - \sigma_I|\} \tag{5.97}$$

Although simple, the criterion necessitates that problems with discontinuous derivatives must be handled.

5.7.2 von Mises

One of the most popular criteria is the one proposed by von Mises in 1913, here written for plane stress:

$$\Phi = \sigma_{11}^2 + \sigma_{22}^2 - \sigma_{11}\sigma_{22} + 3\sigma_{12}^2 \tag{5.98}$$

One reason for the popularity is that one can very often employ this criterion and expect reasonable results just by having a description of the hardening behaviour. Another reason is that the possibility of using a radial return scheme in the integration of constitutive equations turns out to be very efficient seen from a computational point of view.

5.7.3 Hill's 48 criterion

In 1948 Hill proposed his anisotropic criterion which has been widely used for modelling both transversal anisotropy (in-plane isotropic) and in-plane anisotropy. The general form is:

$$\begin{aligned}\Phi = F(\sigma_{22} - \sigma_{33})^2 + G(\sigma_{33} - \sigma_{11})^2 + H(\sigma_{11} - \sigma_{22})^2 + \\ 2L\sigma_{23}^2 + 2M\sigma_{31}^2 + 2N\sigma_{12}^2 - 1 = 0\end{aligned} \tag{5.99}$$

This criterion can for plane stress be reduced to:

$$\Phi = \sigma_{11}^2 + \sigma_{22}^2 - \frac{2R}{R+1}\sigma_{11}\sigma_{22} + 2\frac{2R+1}{R+1}\sigma_{12}^2 - \sigma_b^2 = 0 \tag{5.100}$$

when in-plane isotropy is assumed. Including in-plane anisotropy the plane stress version can be written as:

$$\Phi = F\sigma_{22}^2 + G\sigma_{11}^2 + H(\sigma_{11} - \sigma_{22})^2 + 2N\sigma_{12}^2 - 1 = 0 \tag{5.101}$$

These criteria are very useful mainly because they are easy to implement, the need of material coefficients are limited (3 Lankford coefficients and the hardening curve for specifying the coefficients for the in-plane anisotropic criterion). And still the complexity of the expressions is so limited that analysis by analytical methods is possible for many geometries. This has led to many numerical studies, both of the expressions alone and also in connection with specific forming operations. Very often one sees the above criterion written in the form:

$$g\sigma_I^2 + f\sigma_{II}^2 + h(\sigma_I - \sigma_{II})^2 = \sigma_b^2 \tag{5.102}$$

The coefficients g, f and h in the form given by 5.102 must of course be in a range that fulfils convexity requirements.

5.7.4 Gotoh's yield criterion

In 1977 Gotoh proposed a fourth order yield criterion with multiple coefficients.

$$\begin{aligned}\sigma_b^4 = C_1\sigma_{11}^4 + C_2\sigma_{11}^3\sigma_{22} + C_3\sigma_{11}^2\sigma_{22}^2 + C_4\sigma_{11}\sigma_{22}^3 + C_5\sigma_{22}^4 + \\ \sigma_{12}\left(C_6\sigma_{11}^2 + C_7\sigma_{11}\sigma_{22} + C_8\sigma_{22}^2\right) + C_9\sigma_{12}^4\end{aligned} \tag{5.103}$$

According to Hill [93] the criterion is unsuited to represent important orthotropic response, primarily the anomalous behaviour (the effect when the variation of yield stress is the same as for the R-values). Nevertheless, Barlat [12] finds this criterion capable of predicting two essential aspects of plastic deformation: 1) To take planar anisotropy into account and include effects of shear stresses and 2) encompass the anomalous behaviour.

5.7.5 Bassani's criterion for planar isotropy

Also in 1977 Bassani proposed a criterion for planar isotropy:

$$|\sigma_I + \sigma_{II}|^{m_1} + \frac{m_1}{m_2}(1+2R)\sigma_b^{m_1-m_2}|\sigma_1 - \sigma_{II}|^{m_2} = \sigma_b^{m_1}\left(1 + \frac{m_1}{m_2}(1+2R)\right) \tag{5.104}$$

5.7.6 Hosford's proposal 79

A quite different criterion was proposed by Hosford in 1979 in the form:

$$g|\sigma_I|^m + f|\sigma_{II}|^m + h|\sigma_I - \sigma_{II}|^m = \sigma_b^m \tag{5.105}$$

Hosford proposes to use m=6 for body centred and 8 for face centred crystal structure, but Hill argues for arbitrary values m greater than 1. This criterion has the advantage of being rather simple, but it is not capable of showing "anomalous behaviour" which is often seen in a sheet with planar anisotropy. The criterion is very similar to the old Hill criterion (for plane stress) but it opens up the possibility to choose the exponent more freely.

5.7.7 Hill's 79 criterion

To overcome the problem that most previously given yield criteria are not able to describe the anomalous behaviour, Hill proposed a criterion in 1979:

$$g|\sigma_I|^m + f|\sigma_{II}|^m + h|\sigma_I - \sigma_{II}|^m + a|2\sigma_I - \sigma_{II}|^m + b|\sigma_I - 2\sigma_{II}|^m + c|\sigma_I + \sigma_{II}|^m = \sigma_b^m \tag{5.106}$$

The demands to this criterion in order to model anomaluos behaviour are that the values: m=2, a+b+c=0 or f+g+h=0 are avoided. The major limitation of this yield criterion is that the principal stress axis and anisotropic axis must coincide and any state involving shear stresses cannot be accounted for.

Hill's 79 criterion was proposed independently of Hosford, the Hosford criterion is included in Hill's criterion.

5.7.8 Budianski's plane stress criterion

In 1984 Budianski proposed a criterion for a general state of planar anisotropy, which can be expressed parametrically as:

$$\frac{\sigma_1 - \sigma_2}{2\sigma_s} = f_p(\alpha)sin(\alpha) \tag{5.107}$$

$$\frac{\sigma_1 + \sigma_2}{2\sigma_b} = f_p(\alpha)cos(\alpha) \tag{5.108}$$

where f_p is a function so that $f_p(0) = f_p(\frac{\pi}{2}) = f_p(-\frac{\pi}{2}) = 1$ and σ_s and σ_b are the current yield stresses in pure shear and balanced biaxial tension respectively.

5.7.9 Barlat and Lian's plane stress criterion

One major demand to a yield criterion is that it is convex in stress space. Barlat and Lian used this as a base when they formed their plane yield stress function: Two convex functions can be summarized without destroying convexity. Another operation which must be valid is that a linear transformation of stress must conserve convexity. Using these two assumption Barlat and Lian [14] reached a criterion for modelling in-plane anisotropy:

$$\Phi = a|K_1 - K_2|^M + a|K_1 + K_2|^M + c|2K_2|^M = 2\sigma_b^M \tag{5.109}$$

where the coefficients K_1 and K_2 are obtained as:

$$K_1 = \frac{\sigma_{11} + h\sigma_{22}}{2} \tag{5.110}$$

$$K_2 = \sqrt{\left(\frac{\sigma_{11} - h\sigma_{22}}{2}\right)^2 + p^2\sigma_{12}^2} \tag{5.111}$$

This yield criterion has different advantages compared to many other criteria. By choosing a high value of M one obtains a yield criterion almost identical to Tresca's but without sharp corners. Such a sharp corner will normally cause problems in the theoretical as well as in the numerical treatment of the yield surface in connection with the derivatives.

Also von Mises' yield criterion can be obtained by choosing the isotropic version and m equal to 2. By varying the exponent M between 2 and infinity we have the possibility to model materials which yield between the von Mises and the Tresca criterion. In many older text books on continuum mechanics an example is given where points of initial yielding for steel, copper and aluminum is positioned between these two criteria. In addition, by varying the parameters (a, h and p) in-plane anisotropic behaviour can be modelled. Due to the many advantages which can be obtained from this criterion I have implemented this criterion in LS-Dyna3d and the criterion is tested in various applications presented in later sections.

5.7.10 Hill's 90 criterion

In 1990 Hill proposed an extension to his 48-criterion:

$$|\frac{1}{2}(\sigma_I + \sigma_{II})|^m + h|\sigma_I - \sigma_{II}|^m + (\sigma_I^2 + \sigma_{II}^2)^{\frac{m-2}{2}}(\sigma_I - \sigma_{II})(k\sigma_I - l\sigma_{II}) = \sigma_b^m \tag{5.112}$$

In the case where we have in-plane isotropy the criterion is reduced to the simple expression:

$$|\frac{1}{2}(\sigma_I + \sigma_{II})|^m + h|\sigma_I - \sigma_{II}|^m = \sigma_b^m \tag{5.113}$$

5.7.11 Montheillet's proposal

In 1991 Montheillet proposed a criterion rather similar to the one shown above (reduced to in-plane isotropy), but he used two additional parameters to take in-plane anisotropy into account:

$$|a\sigma_I + b\sigma_{II}|^m + h|\sigma_I - \sigma_{II}|^m = \sigma_b^m \tag{5.114}$$

5.7.12 Barlat's six-component criterion

Barlat et al. [13] proposed in 1991 a yield criterion for the 3-D stress state including anisotropic behaviour. Based on linear transformations of stresses and on building the yield criterion from invariants of the resulting tensor S_{ij} he proposes the criterion:

$$\Phi = |S_I - S_{II}|^m + |S_{II} - S_{III}|^m + |S_{III} - S_I|^m = 2\sigma_Y^m \tag{5.115}$$

where S_I, S_{II} and S_{III} are the principal values of the tensor with coefficients:

$$S_{11} = \frac{c(\sigma_{11} - \sigma_{22}) - b(\sigma_{33} - \sigma_{11})}{3} \tag{5.116}$$

$$S_{22} = \frac{a(\sigma_{22} - \sigma_{33}) - c(\sigma_{11} - \sigma_{22})}{3} \tag{5.117}$$

$$S_{33} = \frac{b(\sigma_{33} - \sigma_{11}) - a(\sigma_{22} - \sigma_{33})}{3} \tag{5.118}$$

$$S_{23} = f\sigma_{23} \qquad S_{31} = g\sigma_{31} \qquad S_{12} = h\sigma_{12} \tag{5.119}$$

This criterion can be regarded as an extension of the criterion proposed by Hershey in 1954 and Hosford in 1972 having shear components. This criterion can, however, not be reduced to the plane stress criterion proposed by Barlat et al. in [14], [136] although the main ideas in the construction are almost the same: The convexity of the resulting yield surface is secured as long as only linear translations and scalings of the stresses are performed.

5.7.13 Hill's 93 criterion

Based on a review of some of the most important yield criteria Hill [93] proposed in 1993 a criterion, which seems very promising. Parameters in the criterion can be determined from Lankford coefficients and yield stresses in 0° and 90° and the biaxial yield stress σ_b. The parameters in most other criteria are determined from either Lankford coefficients or yield stresses and the variation of the other is then given. Hill's latest proposal can be written as:

$$\frac{\sigma_I^2}{\sigma_0^2} - \frac{c\sigma_I\sigma_{II}}{\sigma_0\sigma_{90}} + \frac{\sigma_{II}^2}{\sigma_{90}^2} + \left\{(p+q) - \frac{p|\sigma_I| + q|\sigma_{II}|)}{\sigma_b}\right\}\frac{\sigma_I\sigma_{II}}{\sigma_0\sigma_{90}} = 1 \tag{5.120}$$

This criterion does clearly have some advantages, but unfortunately it is limited to the situation where principal stress directions coincide with principal material axis.

5.7.14 Summary of yield functions

From the above discussion I conclude that especially the criteria proposed by Barlat seem attractive. The criteria are seen from a computational point of view relatively simple, however, still capable of showing a high degree of flexibility. In order to improve the capability of modelling sheet metal forming by using LS-Dyna3d it was chosen to implement the 2-D criterion. At the time when this work was carried out the 3-D criterion was already implemented. This criterion, however, suffers from the need of 7 material parameters and although the model can be used for thin shells no option for reduction of the number of parameters seems available (in LS-Dyna3d) although three parameters can be eliminated directly by assuming plane stress and incompressibility.

Through the years Hill's 48 criterion has attracted a significant interest from researchers working in the area of sheet metal forming. To obtain a reference model to be used in connection with evaluation of Barlat's 2-D criterion and at the same time being more advanced than von Mises' criterion, I have chosen to include Hill's 48 criterion in the implementation of yield criteria in LS-Dyna3d.

For a more detailed discussion on Hill's 48 criterion and Barlat's 2-D criterion along with a discussion on the determination of parameters, please see sections 5.8 and 5.9.

5.8 Hill's 48 criterion

Although Hill's criterion is rather old it is still used for many applications. The reason for incorporating this criterion in the report is that it will be used for comparison with other criteria. The discussion will be very limited and only the most important aspects seen with regard to numerical implementation and prediction of FLDs will be included.

Both Hill's 48 criterion and von Mises' criterion have been implemented to verify the adopted numerical scheme and to test the scheme that is used in connection with the implementation of Barlat's 2-D criterion. By implementing von Mises' and Hill's criteria it is easy to verify the behaviour of the implemented Barlat's 2D criterion when Barlat's criterion is reduced to von Mises' and Hill's criteria by a proper choice of parameters.

Only the plane stress version of Hill's criterion will be discussed, as it is the most relevant form in connection with sheet metal forming, which traditionally is treated on the assumption of plane stress. This assumption is important with respect to the explicit FE-simulation due to the maximum allowable time step in the time integration as discussed in section 3.3.

5.8.1 In-plane anisotropy modelled by Hill's 48 criterion

For the three dimensional case the yield criterion can be expressed as:

$$\begin{aligned}\Phi = F(\sigma_{22}-\sigma_{33})^2 + G(\sigma_{33}-\sigma_{11})^2 + H(\sigma_{11}-\sigma_{22})^2 \\ +2L\sigma_{23}^2 + 2M\sigma_{31}^2 + 2N\sigma_{12}^2 - 1 = 0\end{aligned} \tag{5.121}$$

In the case where in-plane anisotropy is included, the plane stress version can be written as:

$$\begin{aligned}\Phi = F\sigma_{22}^2 + G\sigma_{11}^2 + H(\sigma_{11}-\sigma_{22})^2 + 2N\sigma_{12}^2 - 1 = \\ (G+H)\sigma_{11}^2 - 2H\sigma_{11}\sigma_{22} + (H+F)\sigma_{22}^2 + 2N\sigma_{12}^2 - 1 = 0\end{aligned} \tag{5.122}$$

Starting from this expression we can calculate the plastic strain increment vector as:

$$\begin{Bmatrix}\dot{\epsilon}_{11}\\ \dot{\epsilon}_{22}\\ \dot{\epsilon}_{12}\end{Bmatrix} = 2\dot{\lambda}\begin{Bmatrix}(G+H)\sigma_{11} - H\sigma_{22}\\ (F+H)\sigma_{22} - H\sigma_{11}\\ N\sigma_{12}\end{Bmatrix} \tag{5.123}$$

Lankford coefficients can now be calculated assuming that an uniaxial stress is applied in the directions 0°, 45° and 90°, respectively. Application of an uniaxial stress in 0° leads to:

$$\begin{Bmatrix}\dot{\epsilon}_{11}\\ \dot{\epsilon}_{22}\\ \dot{\epsilon}_{12}\end{Bmatrix} = 2\dot{\lambda}\begin{Bmatrix}(G+H)\sigma_{11}\\ -H\sigma_{11}\\ 0\end{Bmatrix} \tag{5.124}$$

and the Lankford coefficient can, assuming incompressibility, be calculated as:

$$R_0 = \frac{\dot{\epsilon}_{perp}}{\dot{\epsilon}_{33}} = -\frac{\dot{\epsilon}_{perp}}{\dot{\epsilon}_{para}+\dot{\epsilon}_{perp}} = \frac{H}{G} \tag{5.125}$$

where the strain increments $\dot{\epsilon}_{perp}$ and $\dot{\epsilon}_{para}$ indicate in-plane strain increments transverse to and parallel to the loading direction. Similarly, we find for a tension applied at 90°:

$$R_{90} = \frac{H}{F} \tag{5.126}$$

For a tensile test specimen cut in an angle ϕ to the rolling direction we have the relation between the applied stress σ and the stresses (σ_{11}, σ_{22}, σ_{12}):

$$\left\{ \begin{array}{c} \sigma_{11} \\ \sigma_{22} \\ \sigma_{12} \end{array} \right\} = \left\{ \begin{array}{c} cos^2(\phi)\sigma \\ sin^2(\phi)\sigma \\ sin(\phi)cos(\phi)\sigma \end{array} \right\} \tag{5.127}$$

and similar relations in between the strain increments:

$$\left\{ \begin{array}{c} \dot{\epsilon}_{para} \\ \dot{\epsilon}_{perp} \end{array} \right\} = \left\{ \begin{array}{l} cos^2(\phi)\dot{\epsilon}_{11} + sin^2(\phi)\dot{\epsilon}_{22} + 2sin(\phi)cos(\phi)\dot{\epsilon}_{12} \\ sin^2(\phi)\dot{\epsilon}_{11} + cos^2(\phi)\dot{\epsilon}_{22} - 2sin(\phi)cos(\phi)\dot{\epsilon}_{12} \end{array} \right\}$$

The Lankford coefficient for any direction, ϕ, is expressed as:

$$R_\phi = -\frac{\dot{\epsilon}_{perp}}{\dot{\epsilon}_{para} + \dot{\epsilon}_{perp}} \tag{5.128}$$

which with $\phi = 45°$ leads to:

$$R_{45} = -\frac{\frac{1}{2}\dot{\epsilon}_{11} + \frac{1}{2}\dot{\epsilon}_{22} - \dot{\epsilon}_{12}}{\dot{\epsilon}_{11} + \dot{\epsilon}_{22}} \tag{5.129}$$

Substituting the strain increments with the derivative of the yield criterion lead to the expression for an arbitrary angle ϕ to the rolling direction:

$$R_\phi = \frac{H + (2N - F - G - 4H)sin^2(\phi)cos^2(\phi)}{Fsin^2(\phi) + Gcos^2(\phi)} \tag{5.130}$$

Using this approach makes it possible to calculate the coefficients in the plane stress version when Lankford coefficients are known in three directions. Normally one would use the coefficient for 45° leading to:

$$R_{45} = \frac{N}{G + F} - \frac{1}{2} \tag{5.131}$$

Rewriting the yield criterion to the form, which is used in the implementation: $\Phi = \sigma_E - \sigma_Y = 0$, the following expression is obtained:

$$\Phi = \sqrt{\sigma_{11}^2 - A\sigma_{11}\sigma_{22} + B\sigma_{22}^2 + C\sigma_{12}^2} - \sigma_Y = 0 \tag{5.132}$$

where:

$$A = \frac{2R_{00}}{1 + R_{00}} \quad B = \frac{R_{00}(1 + R_{90})}{R_{90}(1 + R_{00})} \quad C = \frac{2(R_{45} + 0.5)(R_{90} + R_{00})}{R_{90}(1 + R_{00})} \tag{5.133}$$

5.9 Barlat's 2-D criterion

The following section includes a more detailed discussion on topics related to Barlat's superquadratic yield criterion, equation 5.109.

To model sheet metal forming requires an accurate description of anisotropic material behaviour and hence, it is found interesting to further investigate the yield function proposed by Barlat, [14],[136]. This yield function is capable of showing in-plane anisotropic behaviour and it includes the Tresca criterion, the von Mises' criterion as well as Hill's 48 criterion (reduced to plane stress) as special cases. These three yield criteria have been used extensively for analysing the plastic behaviour of sheet metals. This capability to include some of the most utilized criteria could justify the work used for implementation of the criterion.

The criterion has a further advantage compared to the three above mentioned criteria because the exponent at least in principle can be chosen freely. The exponent has a very strong influence on the shape of the yield function, which again has been shown to influence the analytical predicted forming limit diagrams strongly , [12, 14, 136] (using the Marciniak and Kuczynski approach, [142]). And hence, it is desirable to use the same constitutive model both in the process analysis and in the prediction of failure strains.

The last reason for an investigation of the criterion is that it is rather simple seen from a mathematical point of view and only a limited number of parameters need to be specified. These parameters can be determined from standard material tests. This easy way to obtain material parameters may lead to a rapid progress for this criterion compared to many others, which are just as good/better to describe the plastic behaviour. A discussion on determination of material data from normally known test data is given in section 7.1.2.

5.9.1 Determination of parameters in Barlat's 2-D criterion

In general one can choose between two different approaches to determine the parameters in Barlat's yield criterion. As proposed by Barlat et al. [133], [14], [136] the yield stresses in the rolling and transverse to the rolling directions together with the shear stresses that cause yielding can be used. This approach has the disadvantage that it is necessary to determine the shear yield stresses experimentally, which is not a simple task. Instead it is more appropriate to determine the parameters from Lankford coefficients. These values are easily obtained from uniaxial tests and the procedure to predict parameters in the yield criterion is hereby straight forward. The method is similar to the method shown in the section concerning Hill's in-plane anisotropic criterion.

Parameters determined from Lankford coefficients

A tension σ is applied uniaxially in a direction inclined ϕ to the rolling direction. In the original coordinate frame (x_1 the rolling direction, etc) this leads to the stress components:

$$\sigma_{11} = cos^2(\phi)\sigma \qquad \sigma_{22} = sin^2(\phi)\sigma \qquad \sigma_{12} = sin(\phi)cos(\phi)\sigma \tag{5.134}$$

The in-plane strain components (plastic increments) parallel and perpendicular to the load direction can be found as:

$$\begin{aligned} \dot{\epsilon}_{para} &= cos^2(\phi)\dot{\epsilon}_{11} + sin^2(\phi)\dot{\epsilon}_{22} + 2sin(\phi)cos(\phi)\dot{\epsilon}_{12} \\ \dot{\epsilon}_{perp} &= sin^2(\phi)\dot{\epsilon}_{11} + cos^2(\phi)\dot{\epsilon}_{22} - 2sin(\phi)cos(\phi)\dot{\epsilon}_{12} \end{aligned} \tag{5.135}$$

These strain increments can be determined from the normality condition:

$$\dot{\epsilon}_{11} = \lambda\frac{\partial\phi}{\partial\sigma_{11}}, \qquad \dot{\epsilon}_{22} = \lambda\frac{\partial\phi}{\partial\sigma_{22}}, \qquad \dot{\epsilon}_{12} = \lambda\frac{\partial\phi}{\partial\sigma_{12}}, \tag{5.136}$$

Where the partial derivatives are:

$$\begin{aligned} \frac{\partial\Phi}{\partial\sigma_{11}} = M\Big\{ & a(K_1+K_2)|K_1+K_2|^{M-2}\left(\frac{1}{2} - \frac{\sigma_{11}-h\sigma_{22}}{4K_2}\right) + \\ & a(K_1-K_2)|K_1-K_2|^{M-2}\left(\frac{1}{2} + \frac{\sigma_{11}-h\sigma_{22}}{4K_2}\right) + \\ & 2^M(2-a)(K_2)^{M-1}\frac{\sigma_{11}-h\sigma_{22}}{4K_2}\Big\} \end{aligned} \tag{5.137}$$

$$\begin{aligned} \frac{\partial\Phi}{\partial\sigma_{22}} = M\Big\{ & a(K_1-K_2)|K_1-K_2|^{M-2}\left(\frac{h}{2} + h\frac{\sigma_{11}-h\sigma_{22}}{4K_2}\right) + \\ & a(K_1+K_2)|K_1+K_2|^{M-2}\left(\frac{h}{2} - h\frac{\sigma_{11}-h\sigma_{22}}{4K_2}\right) - \\ & 2^M(2-a)(K_2)^{M-1}\frac{\sigma_{11}-h\sigma_{22}}{4K_2}\Big\} \end{aligned} \tag{5.138}$$

$$\begin{aligned} \frac{\partial\Phi}{\partial\sigma_{12}} = M\Big\{ & a(K_1+K_2)|K_1+K_2|^{M-2} - a(K_1-K_2)|K_1-K_2|^{M-2} + \\ & 2^M(2-a)K_2^{M-1}\Big\}\frac{\sigma_{12}}{2K_2} \end{aligned} \tag{5.139}$$

The parameter c in Barlat's 2D criterion is obtained from $c = 2 - a$, see equation 5.149. The Lankford coefficient at ϕ is determined from:

$$R_\phi = -\frac{\dot{\epsilon}_{perp}}{\dot{\epsilon}_{para}+\dot{\epsilon}_{perp}} = -\frac{1}{\frac{\dot{\epsilon}_{para}}{\dot{\epsilon}_{perp}}+1} = -\frac{1}{\frac{cos^2(\phi)\dot{\epsilon}_{11}+sin^2(\phi)\dot{\epsilon}_{22}+2sin(\phi)cos(\phi)\dot{\epsilon}_{12}}{sin^2(\phi)\dot{\epsilon}_{11}+cos^2(\phi)\dot{\epsilon}_{22}-2sin(\phi)cos(\phi)\dot{\epsilon}_{12}}+1} \tag{5.140}$$

For 0° and 90° the R-values can be expressed as:

$$R_{00} = -\frac{1}{\frac{\frac{\partial\Phi}{\partial\sigma_{11}}}{\frac{\partial\Phi}{\partial\sigma_{22}}}+1}, \qquad (\sigma_{11}\neq 0,\ \sigma_{22}=\sigma_{12}=0) \tag{5.141}$$

$$R_{90} = -\frac{1}{\frac{\frac{\partial\Phi}{\partial\sigma_{22}}}{\frac{\partial\Phi}{\partial\sigma_{11}}}+1}, \qquad (\sigma_{22}\neq 0,\ \sigma_{11}=\sigma_{12}=0) \tag{5.142}$$

From the expressions for R_{00} and R_{90} we can obtain the values of a and h in an explicit form:

$$a = 2 - 2\sqrt{\frac{R_{00}}{1+R_{00}}\frac{R_{90}}{1+R_{90}}} \tag{5.143}$$

$$h = \sqrt{\frac{R_{00}}{1+R_{00}}\frac{1+R_{90}}{R_{90}}} \tag{5.144}$$

If R_{45} is calculated we can obtain:

$$R_{45} = \frac{\frac{\partial\Phi}{\partial\sigma_{12}}}{\left(\frac{\partial\Phi}{\partial\sigma_{11}} + \frac{\partial\Phi}{\partial\sigma_{22}}\right)} - \frac{1}{2}, \qquad (\sigma_{11} = \sigma_{22} = \sigma_{12} \neq 0) \tag{5.145}$$

which is a nonlinear equation which must be solved with regard to p (see equation 5.111). The equation is to be solved using an iterative method, the only variable being p. The relation between p and R_{45} is assumed to be monotonic when equation 5.145 is solved.

Parameters determined from yield stresses

The following section repeats the approach (see Barlat et al. [133], [14] and [136]) to determine the parameters a,c,h,p for a given exponent M when the yield stresses σ_{90} (yield stress for uniaxial tension in the transverse direction), τ_{S1} (shear yield stress such that $\sigma_{yy} = \sigma_{xx} = 0$, $\sigma_{xy} = \tau_{S1}$) and τ_{S2} (shear yield stress such that $\sigma_{yy} = -\sigma_{xx} = \tau_{S2}$) are known. The yield stresses lead to:

$$a = 2 - c = \frac{2\left(\frac{\sigma_{00}}{\tau_{S2}}\right)^M - 2\left(1+\frac{\sigma_{00}}{\sigma_{90}}\right)^M}{1+\left(\frac{\sigma_{00}}{\sigma_{90}}\right)^M - \left(1+\frac{\sigma_{00}}{\sigma_{90}}\right)^M} \tag{5.146}$$

$$h = \frac{\sigma_{00}}{\sigma_{90}} \qquad p = \frac{\sigma_{00}}{\tau_{S1}}\left(\frac{2}{2a+2^M c}\right)^{\frac{1}{M}} \tag{5.147}$$

Parameters determined from biaxial yield stress

The previous approach using shear yield stresses has the disadvantage that it is necessary to determine the shear yield stresses which is difficult experimentally, and therefore Barlat suggests to use the Bishop-Hill model to predict these values.

In many applications it is more important to predict biaxial yielding (stretching) conditions better than to be able to predict R-values (tension). In order to improve the performance of the criterion it can thus be better to determine the parameters from biaxial yield stresses.

In the following I propose an alternative approach where the relation between biaxial stress and yielding can be used for the determination of parameters.

The demands for the yield criterion are now that uniaxial loading at 0° and 90° shall

lead to the correct values of the yield stresses. Additionally, it is demanded that a biaxial yield stress state is modelled correctly when the principal stresses are applied so that σ_I is inclined in an angle 0° and 45° to the rolling direction. When the principal stresses are not aligned with the material principal directions we obtain a stress state where a shear stress term is included. A way to obtain the biaxial stress states could be to use bulging of elliptic diaphragms.

Using the situation $\sigma_{xx} = \sigma_{00}$ in the yield criterion (equation 5.109) leads to:

$$\sigma_{00}^M = \frac{a}{2}|\sigma_{xx}|^M + \frac{c}{2}|\sigma_{xx}|^M = \left(\frac{a}{2} + \frac{c}{2}\right)|\sigma_{xx}|^M \tag{5.148}$$

which leads to the relation:

$$a = 2 - c \tag{5.149}$$

The situation $\sigma_{yy} = \sigma_{90}$ gives the expression:

$$\sigma_{00}^M = \left(\frac{a}{2} + \frac{c}{2}\right) h^M \sigma_{yy}^M \tag{5.150}$$

which leads to:

$$h = \frac{\sigma_{00}}{\sigma_{90}} \tag{5.151}$$

Additionally, there should be a biaxial stress state causing yielding applied at for example 45° to the rolling direction ($\sigma_{xx}^{45} = \alpha\sigma_{yy}^{45}$) leading to the stress situation:

$$\sigma_{xx} = \sigma_{xx}^{45} cos^2(45) + \sigma_{yy}^{45} cos^2(135) = \frac{1}{2}\sigma_{xx}^{45} + \frac{1}{2}\sigma_{yy}^{45} = \frac{1}{2}\sigma_{yy}^{45}(1+\alpha) \tag{5.152}$$

$$\sigma_{yy} = \sigma_{xx}^{45} sin^2(45) + \sigma_{yy}^{45} sin^2(135) = \frac{1}{2}\sigma_{xx}^{45} + \frac{1}{2}\sigma_{yy}^{45} = \frac{1}{2}\sigma_{yy}^{45}(1+\alpha) \tag{5.153}$$

$$\sigma_{xy} = \sigma_{xx}^{45} sin(45)cos(45) + \sigma_{yy}^{45} sin(135)cos(135) = \frac{1}{2}\sigma_{xx}^{45} - \frac{1}{2}\sigma_{yy}^{4}5 = \frac{1}{2}\sigma_{yy}^{45}(\alpha - 1) \tag{5.154}$$

Calculating the equivalent stress leads to:

$$\begin{aligned}
{\sigma_{eq}}^M = \left(\sigma_{yy}^{45}\right)^M \Bigg\{ & \frac{a}{2}\left|\frac{(1+\alpha)(1+h)}{4} + \sqrt{\left(\frac{(1+\alpha)(1-h)}{4}\right)^2 + p^2(\frac{1}{2}(\alpha-1))^2}\right|^M \\
& + \frac{a}{2}\left|\frac{(1+\alpha)(1+h)}{4} - \sqrt{\left(\frac{(1+\alpha)(1-h)}{4}\right)^2 + p^2(\frac{1}{2}(\alpha-1))^2}\right|^M \\
& + \frac{2-a}{2}\left|2\sqrt{\left(\frac{(1+\alpha)(1-h)}{4}\right)^2 + p^2(\frac{1}{2}(\alpha-1))^2}\right|^M \Bigg\}
\end{aligned} \tag{5.155}$$

Demanding a biaxial stress state applied in 0° $\sigma_{xx} = \alpha\sigma_{yy}$ leads to the stress situation:

$$\sigma_{xx} = \alpha\sigma_{xx} \quad \sigma_{yy} = \sigma_{yy} \quad \sigma_{xy} = 0 \tag{5.156}$$

In case h is less than 1 the equivalent stress becomes:

$$\sigma_{eq}{}^{M} = (\sigma_{yy})^{M} \left\{ \frac{a}{2} \left| \frac{(1+\alpha)}{2} \right|^{M} + \frac{a}{2} \left| \frac{(1+\alpha)(h)}{2} \right|^{M} + \frac{2-a}{2} \left| \frac{(1+\alpha)(1-h)}{2} \right|^{M} \right\} \tag{5.157}$$

from which a can be determined as:

$$a = \frac{2\frac{\sigma_{eq}{}^{M}}{\sigma_{yy}^{M}} - \frac{(1+\alpha)(1-h)}{2}}{|\frac{(1+\alpha)}{2}|^{M} + |\frac{(1+\alpha)(h)}{2}|^{M} + |\frac{(1+\alpha)(1-h)}{2}|^{M}} \tag{5.158}$$

Summary of determination of parameters

To determine the parameters in Barlat's 2D yield criterion several possibilities are available. It is evident that the principle used has influence on the obtained yield surface, and hereby can influence the overall simulation results.

The easiest way to determine the parameters is to use the Lankford coefficients, but this may not be the optimum way for problems dominated by deformation which is far from tension.

In the remaining part of the thesis I have used Lankford coefficients to determine the parameters a, c, h and p.

5.9.2 Influence from the exponent on the shape of the yield surface

Some authors argue that the exponent of M should be set to 6 or 8 for bcc- and fcc-materials, respectively, whereas others propose to use M as an additional material parameter (which can even be assumed to vary as function of the straining). Figure 5.11 shows how variation of M-values influences the shape of the yield function. The figure is plotted in the case where σ_{12} equals zero and the parameters a, c, h and p are determined from R-values for a mild steel. The yield criterion can lead to a shape quite different from Hill's 48 criterion (however, identical for M=2). For a M value of 6, which is one of the values often recommended (based on crystallografic theories), a strong decrease of the stresses which can be resisted for biaxial loading can be seen compared to the situation for M=2. It can also be seen from the figure that the value of M has a marked influence on the predicted yield stress at balanced stretching whereas the yield stress transverse to the rolling direction (the y-axis) is unaffected by the M value (the only parameter coupling the yield stress at 0° and 90° is h). For problems dominated by stretching it thus seems to be of major importance to use the correct value of M. If the criterion is compared to Hill's 48 criterion there is a pronounced difference: The curve with M equal to two is identical to what would be obtained from Hill's criterion, but as can be seen a significant change can be made just with another choice of M. The effect on a forming operation when varying the value of M is demonstrated with an example in section 7.4.

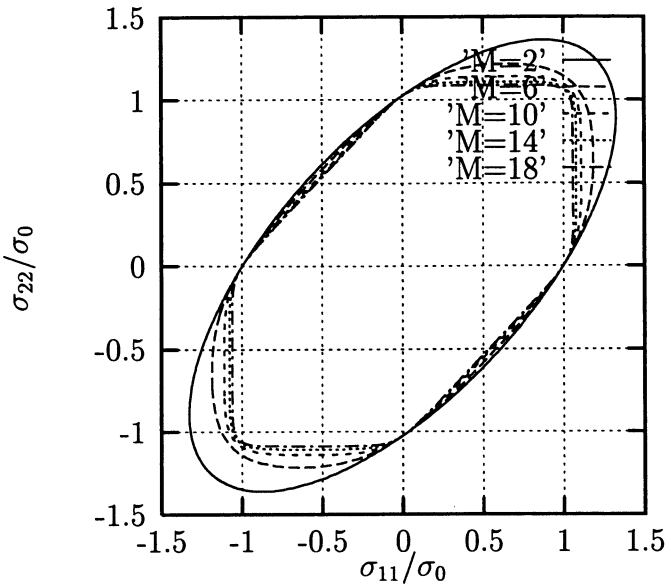

Figure 5.11: *Yield surface generated with various values of the exponent M in Barlat's 2D criterion ($\sigma_{12} = 0$). The values used for generating the curves are: $R_{00} = 1.781$, $R_{45} = 1.303$, $R_{90} = 2.072$ corresponding to a typical mild steel.*

Predicted R-value and yield strength

When the parameters a, c, h and p are determined we can calculate the values of R-values and yield stresses for various angles to the direction of rolling. Below are given two examples where parameters are determined from R_{00}, R_{45} and R_{90}.

The variation of the R-values can in some cases be very large; Barlat et al. [14], [136] use values of $R_{00} = 0.7$, $R_{45} = 5.0$, $R_{90} = 1.0$ for a brass sheet. So large variation and values can also be obtained for titanium.

The first example is made in order to verify the programmes used for calculating R-value and yield stress variation. The variations are shown in figure 5.12 and 5.13. Figure 5.12 shows the R-value variation for various values of M. Obviously the curves pass the correct values in 0°, 45° and 90°. An observation is that the maximum value does not appear at 45° and that the dependency on M is relatively limited; the largest difference appears for angles between 10° and 40°. Figure 5.13 shows the yield stress variation as function of the angle to rolling direction. This figure indicates a very strong dependency on the M-value: Going from M=2 to M=18 leads to a raise from ≈ 0.57 to ≈ 0.89 in the relatively yield stress. This means that analysing a tensile test performed in 45° will lead to very different conclusions with regard to the stress necessary to cause plastic deformation.

Figure 5.12 and 5.13 correspond to curves given by Barlat et al. [14], [136].

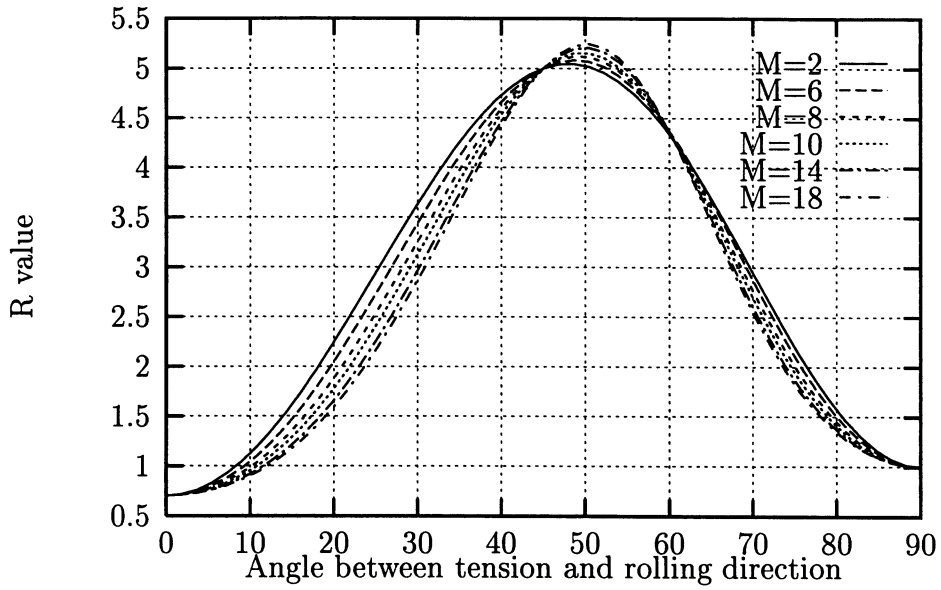

Figure 5.12: *R-value predicted with Barlat's 2D criterion for various values of the exponent M. The values used for generating the curves are:* $R_{00} = 0.7$, $R_{45} = 5.0$, $R_{90} = 1.0$, *values and variations which may be obtained for materials as brass and titanium.*

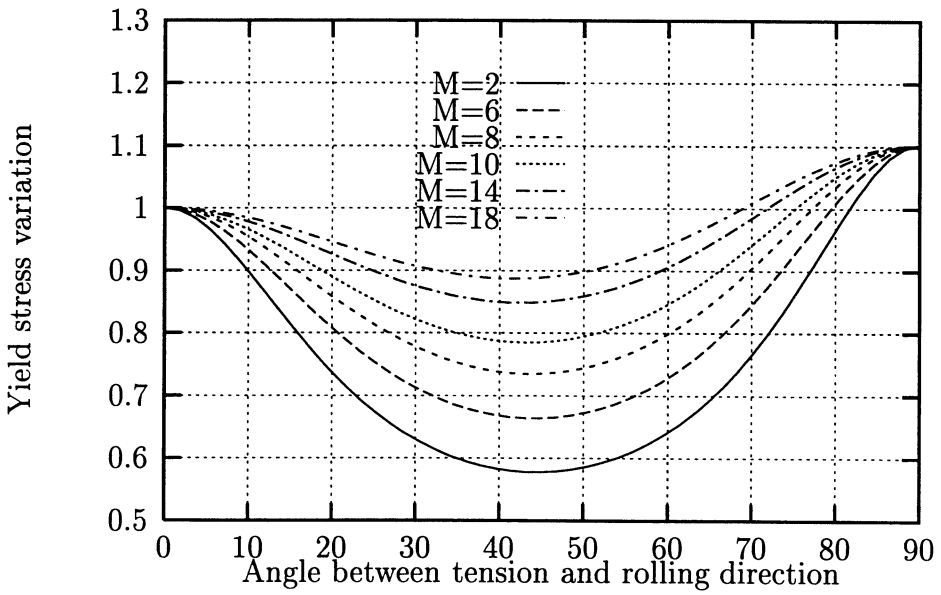

Figure 5.13: *Variation of yield stress predicted with Barlat's 2D criterion for various values of the exponent M. The values used for generating the curves are:* $R_{00} = 0.7$, $R_{45} = 5.0$, $R_{90} = 1.0$

As this thesis primarily deals with mild steel, a comparison between the R-value and yield stress variation obtained experimentally and with Barlat's 2D criterion may be appropriate. In figures 5.14 and 5.15 are shown the predicted variation and the experimentally obtained variation (see section 7.1.2). Figure 5.14 shows the experimentally obtained R-

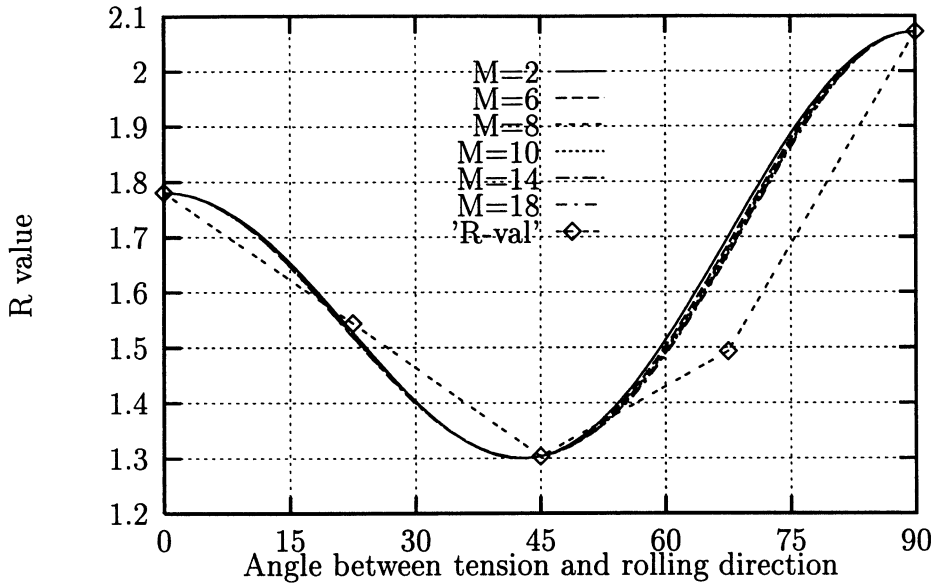

Figure 5.14: *R-value predicted with Barlat's 2D criterion for various values of the exponent M. The values used for generating the curves are:* $R_{00} = 1.781$, $R_{45} = 1.303$, $R_{90} = 2.072$.

values (with marks) compared to the variation predicted with Barlat's criterion for various values of M. The value at 22.5° is in a reasonable agreement whereas the value at 67.5° is poorer estimated. The judgement is that the M-value has no significant influence on the R-vale variation for a typical mild steel (when parameters are determined from R_{00}, R_{45} and R_{90}) and that the overall predicted values seem to be in a good agreement. Figure 5.15 shows the variation on yield stress obtained experimentally and with Barlat's criterion. The experimental yield stress in various directions are calculated from the yield stress fit (Hollomon-Swift) for the actual direction at 4 levels of plastic straining (5, 10, 15 and 20 per cent). It is found quite reasonable to include this dependency on plastic straining as the R-values are determined within the same range. The values are normalized with the value at 0°.

The relation between experimentally obtained yields stresses in 0° and 90° seems to be rather constant as the strain level is increased, but at 45° a larger variation can be seen; the relative value goes from ≈ 1.07 to ≈ 1.04. One may state that $\sigma_{Y,45} \rightarrow \sigma_{Y,0}$ as the strain is increased.

The analytically calculated values do not depend on the plastic straining - one way to obtain a similar behaviour for the yield criterion could be to let M depend on the effective plastic strain. This will not affect the relatively yield stress in 0° and 90°, but it opens the possibility to vary the value in 45°.

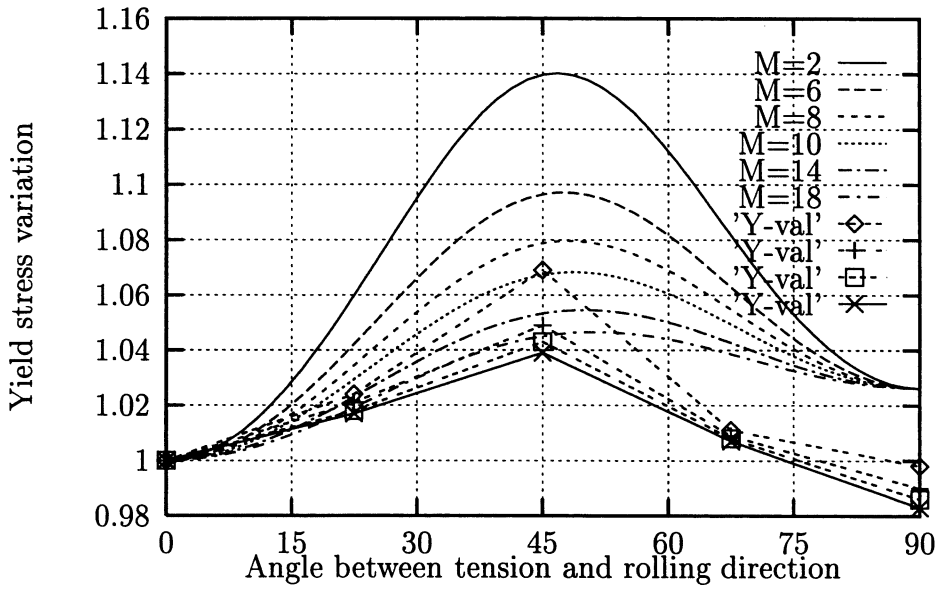

Figure 5.15: *Variation of yield stress predicted with Barlat's 2D criterion for various values of the exponent M. The values used for generating the curves are:* $R_{00} = 1.781$, $R_{45} = 1.303$, $R_{90} = 2.072$.

The anomalous behaviour can be seen in figure 5.15 where the yield stress at 90° is overestimated - the analytic values are higher than the values at 0° whereas the experiments show lower values.

5.10 Implementation of material models

This section deals with implementation of material models in LS-Dyna3d. The models are implemented as so-called user-materials, where the rotations of stresses and strain increments are performed exterior to the material subroutine. This makes the implementation of new material models easier, because transformations into the local coordinate system do not have to be dealt with in the material routine.

In section 5.6 there is a brief discussion about numerical integration schemes and reasons for the choice of integration scheme are given in this section as well. As the implemented models are intended to be used in future research regarding material models the same integration scheme has been used for the four implemented models and an extension to include more yield criteria should be straight forward.

The criteria which have been implemented are:

- von Mises' criterion
- Hill's transverse anisotropic criterion
- Hill's in-plane anisotropic criterion
- Barlat's 2'd criterion

5.10.1 Implementation procedure

Below the procedure used for the standard part of the material routine is given. The basis is given for Barlat's criterion, but the procedure for the other implemented criteria is identical.

To characterize the size of a plastic strain increment $\dot{\epsilon}^p$ with a single scalar, we have to define the equivalent strain increment. For a final increment in strains it becomes:

$$\Delta\epsilon^p_{eq} = \frac{\sigma_{ij}\Delta\epsilon^p_{ij}}{\sigma_{eq}} \tag{5.159}$$

In connection with Barlat's 2D criterion, also denoted as the superquadratic yield function (see section 5.9), the equivalent stress σ_{eq} can be calculated as:

$$\sigma_{eq} = \left\{ \frac{a}{2}\left|K_1 + K_2\right|^M + \frac{a}{2}\left|K_1 - K_2\right|^M + \frac{2-a}{2}\left|2K_2\right|^M \right\}^{\frac{1}{M}} \tag{5.160}$$

where the coefficients, a, K_1 and K_2 are defined in section 5.7.9. The formulation of the equivalent stress follows directly from the yield function. Due to the exponent M (which in principle can be chosen freely) the representation with $1/M$ is more appropriate than the representation in section 5.7.9 in order to avoid numerical problems (these problems have also been reported by Peric et al. [176]). Now using the flow rule for associated flow:

$$\Delta\epsilon^p_{ij} = \Delta\lambda\frac{\partial f}{\partial\sigma_{ij}} \tag{5.161}$$

we get:

$$\Delta\epsilon_{eq}^{p} = \Delta\lambda \frac{\sigma_{11}\frac{\partial f}{\partial \sigma_{11}} + \sigma_{22}\frac{\partial f}{\partial \sigma_{22}} + 2\sigma_{12}\frac{\partial f}{\partial \sigma_{12}}}{\left\{\frac{a}{2}|K_1 + K_2|^M + \frac{a}{2}|K_1 - K_2|^M + \frac{2-a}{2}|2K_2|^M\right\}^{\frac{1}{M}}} \tag{5.162}$$

To achieve an easier way of writing the equations a function $B(\sigma_{ij})$ is introduced:

$$\Delta\epsilon_{eq}^{p} = \Delta\lambda B(\sigma_{ij}) \tag{5.163}$$

If we also introduce $H = \frac{\partial \sigma_Y}{\partial \epsilon_{eq}}$ the consistency condition can be rewritten as:

$$\Delta f = \frac{\partial f}{\partial \sigma_{ij}}^{T} \Delta\sigma_{ij} - H\Delta\epsilon_{eq} = 0 \tag{5.164}$$

which corresponds to 5.44. The first step is to make an elastic prediction of the stress, here designed by indices B. By using the values at point B in the stress space some computational efforts are spared compared to for example a midpoint algorithm. The computational steps are illustrated in figure 5.16 (figure 5.8 repeated). From point B the next point C is

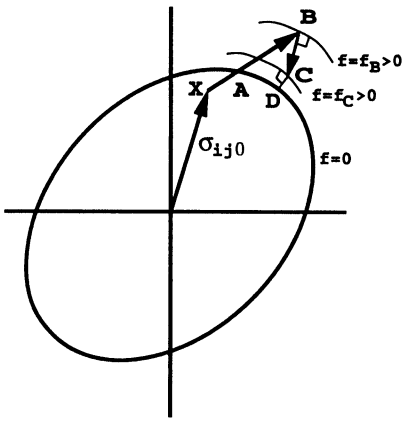

Figure 5.16: *Illustration of the backward Euler procedure.*

calculated by performing a plastic relaxation (according to equations 5.76 and 5.77):

$$\sigma_{ijC} = \sigma_{ijB} - \Delta\lambda_B \frac{\partial f_B}{\partial \sigma_{ij}} \tag{5.165}$$

The scaling of the stresses by using $\frac{\partial f}{\partial \sigma_{ij}}$ calculated at B means that computation of intersections with the yield surface is avoided.

The formulation can easily be transformed to include work hardening instead of strain hardening as described in section 5.4.1. $\Delta\lambda$ is calculated as:

$$\Delta\lambda = \frac{f_B}{\frac{\partial f_B}{\partial \sigma_{ij}} D_{ijkl} \frac{f_B}{\frac{\partial f_B}{\partial \sigma_{kl}} + A_B}} = \frac{f_B}{\frac{\partial f_B}{\partial \sigma_{ij}} D_{ijkl} \frac{\partial f_B}{\partial \sigma_{kl}} + H_B B(\sigma_B)} \tag{5.166}$$

Based on the value for $\Delta\lambda$, the change in stresses, plastic strains and effective plastic strains are calculated. This will return the stresses, but this will normally not produce a set of

stresses and plastic strains corresponding to a position on the yield surface. To improve the predicted stress state the operator splitting method (section 5.6.4) is used:

$$\sigma_{ijD} = \sigma_{ijC} - \delta\lambda_C D_{ijkl} \frac{\partial f_C}{\partial \sigma_{kl}} \tag{5.167}$$

with the multiplier calculated at C:

$$\delta\lambda_C = \frac{f_C}{\frac{\partial f_C}{\partial \sigma_{ij}} D_{ijkl} \frac{\partial f_C}{\partial \sigma_{kl}}} \tag{5.168}$$

If the resulting value of f is not close enough to 0 further relaxation is applied by repeating the equations 5.167 and 5.168 by using the values at D (stress and plastic strain) for evaluation of f and $\frac{\partial f}{\partial \sigma_{ij}}$.

The procedure is as follows:

- Elastic predictor
- Check yield criterion
- Initialize variables (step n+1)
- Evaluate residuals
- Calculate $\Delta\lambda_C$
- Calculate $\sigma_C, \epsilon^p_C, \epsilon^p_{eqC}$
- Calculate $\dot{\lambda}$
- Calculate $\sigma, \epsilon^p, \epsilon^p_{eq}$
- Evaluate yield function
- Eventually apply further relaxation (set $B \leftarrow C$)

The actual coding of the basic material subroutine is given in appendix A. Most of the examples to be given in the remaining part of the thesis have been analysed using the implemented model.

5.11 Summary of the implemented material model

In the following the material routine implemented options are summarized.

5.11.1 Implemented hardening options

In the material subroutine the four hardening laws given below are included:

- a1 $\sigma_Y = \sigma_{Y0} + H\epsilon^p_{eff}$
- b1 $\sigma_Y = K{\epsilon^p_{eff}}^n$, it is plastic deformation from the start of loading.
- c1 $\sigma_Y = K(1 - Ae^{B\epsilon^p_{eff}})$
- $\sigma_Y = K(\epsilon_0 + \epsilon^p_{eff})^n$ where A: (d1) $\epsilon_0 = \left(\frac{E}{K}\right)^{\frac{1}{n-1}}$ or B: (e1) $\epsilon_0 = e^{(\frac{1}{n} ln(\frac{\sigma_0}{K}))}$

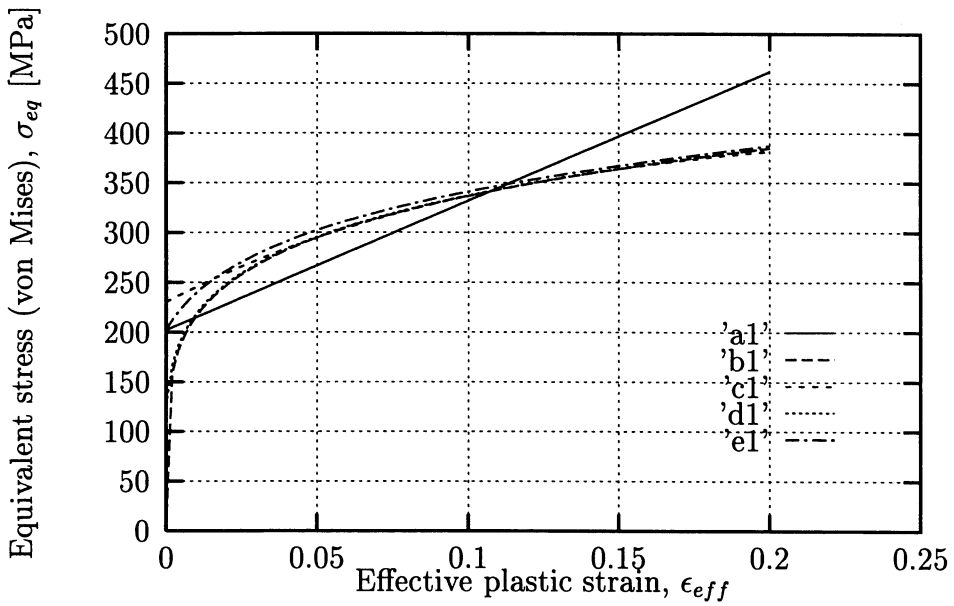

Figure 5.17: *Response obtained with the implemented material model.*

Figure 5.17 shows the predicted relation between effective plastic strain and equivalent yield stress obtained with the implemented material model (Barlat's 2D criterion reduced to von Mises). The parameters used to describe the material behaviour are given in table 5.1. The elastic parameters are a Young's modulus of 210.000 MPa and a Poisson's ratio of 0.3. The data are obtained by fitting to the same experimental curve, however, subjected to some additional conditions, which may make the fit different from the optimum fit. The

Hardening law			
Linear	H [MPa]	σ_0 [MPa]	
hardening	1298	202	
Hollomon	K [MPa]	n	
hardening	524	0.192	
Voce	K [MPa]	A	B
hardening	449.5	0.4363	-5.5352
Hollomon-Swift	K	n	ϵ_0
hardening	524	0.192	0.060%/0.698%

Table 5.1: *Parameters used to describe hardening behaviour.*

linear hardening was forced to start in the initial yield strength (202 MPa) which led to the modulus on 1298 MPa. The Hollomon curve starts with $\sigma_Y = 0$ which is obviously a poor initial estimate. The Voce hardening is fitted over the range up to 0.2 effective plastic strain leading to an initial yield stress of $\approx$ 230 MPa. This estimation of initial yield stress is relatively good compared to the Hollomon and the Hollomon-Swift with ϵ_0 determined from option A. Option B in the Hollomon-Swift relation does of course lead to the correct initial σ_Y. In general the curves are (apart from the linear) very similar after a straining of $\approx$ 0.05. However, it is obvious that forming problems dominated by low effective strains (less than 0.05) can be influenced strongly by the choice of hardening law.

In connection with the hardening description it is possible to choose between strain hardening and work hardening.

5.11.2 Implemented yield criteria

Four yield criteria have been implemented:

- von Mises' yield criterion.
- Hill's 48 criterion with $R_{00} = R_{45} = R_{90}$.
- Hill's 48 criterion reduced to plane stress (in-plane anisotropy).
- Barlat's 2D criterion.

5.11.3 Strain rate effects

It is possible to include strain rate effects with the implemented material routine. Rate effects are included by using multiplicative yield functions (see section 5.5.5). The two implemented models are the Norton and the Wagoner-Swift model:

$$F = (\Delta\dot{\epsilon}^p_{eff})^m \qquad F = \left(\frac{\Delta\dot{\epsilon}^p_{eff}}{\Delta\dot{\epsilon}^p_{ref}}\right)^m \tag{5.169}$$

F is used to scale the quasi-static hardening curve by multiplication. The notation $\Delta\dot{\epsilon}^p_{eff}$ is used for the effective strain rate to clarify that the strain rates arise from final increments (corresponding to the use of Δ in connection with integration of constitutive equations in section 5.6). The two implemented models are in principle identical and can lead to identical results, however, as tensile testing is performed with a certain strain rate the most sound approach is in my opinion, to include the reference strain rate (as it is done with the Wagoner-Swift relation).

The implementation is simplified in order to reduce the number of operations. Firstly, it is assumed that the effective plastic strain increment can be expressed as:

$$\Delta\dot{\epsilon}^p_{eff} = \sqrt{\frac{2}{3}\Delta\dot{\epsilon}^p_{ij}\Delta\dot{\epsilon}^p_{ij}} \tag{5.170}$$

This means that anisotropic effects are omitted in the evaluation of strain rate effects. Secondly, it is assumed that the plastic strain increment $\Delta\epsilon^p_{ij}$ is the deviatoric part of the total strain increment. The yield stress is hereby influenced in case of a pure elastic loading.

When entering the material routine we may have $\sigma_{33} \neq 0$ due to rotation. Taking this into account, we can express the transversal strain increment $\dot{\epsilon}_{33}$ by assuming elasticity as:

$$\Delta\epsilon_{33} = -\frac{1}{E}\left(\sigma_{33} + \nu(\Delta\sigma_{11} + \Delta\sigma_{22})\right) \tag{5.171}$$

The stress increments (elastic) are found to be:

$$\Delta\sigma_{11} = \frac{E}{(1+\nu)(1-2\nu)}[(1-\nu)\Delta\epsilon_{11} + \nu(\Delta\epsilon_{22} + \Delta\epsilon_{33})] \tag{5.172}$$

$$\Delta\sigma_{22} = \frac{E}{(1+\nu)(1-2\nu)}\left[(1-\nu)\Delta\epsilon_{22} + \nu(\Delta\epsilon_{11} + \Delta\epsilon_{33})\right] \tag{5.173}$$

Inserting the stress increments in equation 5.171 and subsequently solving for $\Delta\epsilon_{33}$ leads to:

$$\Delta\epsilon_{33} = -\frac{\Delta\sigma_{33} + \lambda(\Delta\epsilon_{11} + \Delta\epsilon_{22})}{\lambda + 2\mu} \tag{5.174}$$

where λ and μ are the Lame' constants ($\lambda = \frac{\nu E}{(1+\nu)(1-2\nu)}$ and $\mu = \frac{E}{2(1+\nu)}$). After having estimated the transversal strain increment and assuming that the deviatoric strain increment is plastic we find:

$$\Delta\epsilon^p_{ij} = \Delta\epsilon_{ij} - \delta_{ij}\frac{\Delta\epsilon_{kk}}{3} \tag{5.175}$$

In case the increment is a plastic loading from a point on the yield surface this approximation will be reasonable, but if the increment primarily leads to elastic deformation the approximation is somewhat poorer. Reexpressing the effective plastic strain increment leads to:

$$\Delta\epsilon^p_{eq} = \sqrt{\frac{2}{3}\left((\Delta\epsilon^p_{11})^2 + (\Delta\epsilon^p_{22})^2 + (\Delta\epsilon^p_{33})^2 + 2(\Delta\epsilon^p_{12})^2\right)} \tag{5.176}$$

The strain rate is then calculated as $\Delta\dot{\epsilon}_{eq} = \frac{\Delta\epsilon^p_{eq}}{\Delta t}$ for use in the multiplicative yield function.

5.11.4 Correction for loading rate scaling

In general it is necessary to increase the loading rate compared to the physical process in order to obtain a reasonable computational efficiency. To take strain rate effects into account in the simulations it is then necessary to perform a "reverse" scaling of the strain rate sensitivity in the constitutive modelling. In this project most examples have been modelled with the loads prescribed using a sine profile (the punch velocity follows a sine curve with a period equal to twice the loading time, leading to low disturbances at initial contact and also a low level of kinetic energy at the end of loading). Using more advanced profiles will in principle not lead to increased complications and in the following we therefore limit the discussion to loading rate (punch velocity) scaled with a sine profile.

Assuming a constant punch velocity, C, for the process the load scaling as function of analysis time can be expressed as:

$$s = \frac{v_F}{v_P} = \frac{Ksin(\frac{\pi}{T}t)}{C} = \frac{K}{C}sin(\frac{\pi}{T}t) \tag{5.177}$$

where K is a scaling factor. Assuming that the overall response is in good agreement with the physical process we must, during the analysis, also have a good agreement with the strain increment in the analysis apart from the scaling of load. Defining the effective plastic strain rate as above, we obtain the strain rate (physical strain rate in the process) to be employed in the multiplicative yield function:

$$\dot{\epsilon}_{pro} = \frac{C\dot{\epsilon}^p_{eq}}{Ksin(\frac{\pi}{T}t)} \tag{5.178}$$

This approach is based on the assumption that the strain rates follow the development in the load directly. This may in some cases lead to errors as simulations in some cases are altered due to velocity (or mass) scalings.

Another type of scaling may be achieved, e.g. for an excenter press the physical punch velocity may be rather close to a sine shaped variation. In this case it may be reasonable to scale the strain rate directly with the inverse of velocity scaling.

In the material subroutine these two scalings are included as well as the standard case where the loading rate in the simulation is assumed to be the physical loading rate.

Chapter 6

Analysis of Instability Problems and Wrinkling Behaviour

Formation of wrinkles is, as indicated in section 1.1, a very typical cause of failure in sheet metal forming processes. The present chapter gives a discussion on different aspects on wrinkling in connection with the use of explicit finite element methods for the process simulation.

A number of methods for indication of different types of bifurcation and/or limit points in structures analysed with an explicit finite element formulation are proposed. Although the primary goal is to indicate/predict instabilities in sheet metal forming the methods may be found useful in other kinds of analysis performed with an explicit finite element code.

Some examples on deep drawing of circular cups and square boxes are given in the last part of the chapter. These process types have been studied in more detail and the numerical results are compared to experimental results for drawing under conditions which do not lead to wrinkling, see section 9.1 and 9.2. In these sections it is concluded that strains, thickness, shape, etc can be predicted with a good accuracy.

As it can be expected that simulations yield accurate results as long as the deformation is stable it is judged that proceeding with analysis of instability events seems reasonable. Most instability phenomena are strongly related to geometry and in order to analyse these phenomena it is necessary that the analysis results up to onset of instability is modelled with a sufficient accuracy, otherwise we cannot expect accurate results for the wrinkling behaviour.

The main purpose of the project is to analyse sheet metal forming with explicit finite element methods rather than to perform analysis of general structural instability. However, in order to perform these process analyses efficiently, information which is present during the simulation has been used utilized for judgement of either 1) the risk of failure and/or 2) for indication of whether or not an instability has occured in the simulated process. (the already present information has been used to avoid spending CPU and disk resources on performing more traditional analyses.) In some cases it is rather hard to detect instabilities when evaluating the global analysis results. If the considered process

is locally unstable at some stage it is of importance to be able to detect it easily during postprocessing of the FE-results.

The chapter includes a short discussion of some approaches to predict wrinkling together with a very short discussion of finite element approaches to treat instability in more general cases of structural instability.

Three methods are proposed for use within the frame of explicit finite element methods: 1) The current stiffness parameter, CSP, 2) an estimation based on the Rayleigh coefficient and 3) a method based on Hill's uniqueness criterion [92]. The methods are tested in relatively simple examples where a comparison with analytical solutions is possible. In subsequent sections the methods are used for some examples involving plastic deformation. Finally the methods are illustrated by analysing instability events for more complicated examples where wrinkling is likely to occur during the process.

The CSP method is essentially based on a previously often used measure ot the stiffness within implicit codes; the current stiffness parameter (CSP). The CSP is normally calculated as function of time or some pseudo time describing the evolution of the load. The CSP was introduced by Bergan and Söreide, [29] to characterize the type of bifurcation and to guide the choice of step lengths in implicit solution schemes for static or quasi-static non-linear problems. The purpose of the present collection of examples is to illustrate possibilities for indication and/or prediction of the loss of stability, global or local, for non-linear systems, which in practice relates to all structures when instability appears.

The Rayleigh method is similar to the CSP method. The Rayleigh method presented approximates the Rayleigh coefficients by the use of internal forces instead of the traditional use of a stiffness matrix; whereby the method becomes much more suitable in connection with explicit time integration.

The third method is based on Hill's uniqueness criterion. However, in order to avoid integration over a part of the structure only the actual value in the integration point is considered. This makes the method very quick - actually the value is calculated in all the integration points throughout the simulation.

6.1 Traditional approaches to instabilities in sheet metal forming

It has been chosen to focus on structural instability , which in connection with sheet metal forming primarily is the formation of wrinkles. Another instability type commonly seen in sheet metal forming is related to necking behaviour and this is discussed in more detail in chapter 8.

Flange wrinkling in a cup has been analysed by a number of authors using either analytical or experimental methods. If we restrict ourselves to the analytical methods four different analytical approaches exist according to Jimma and Kuwabara (in [34]):

- Set up the differential equations for an asymmetric buckling problem of an annulus and solve for the critical load directly.
- The energy method.
- The moment equilibrium method.
- The method based on Hill's uniqueness criterion.

Another categorization is made by Kaftanoglu [112], who lists a number of theoretical and experimental approaches in a small review where he distinguishes between energy methods and static equilibrium methods. In general it can be noticed that most of the methods given in the literature are based on simple geometries and in most cases the methods are much too difficult to use in connection with more general analyses of sheet forming operations.

As sheet metal forming is very complex seen from a computational point of view, it is often necessary to use numerical techniques in order to solve the equations describing the problem. Zhang, Yu and Wang [226] utilize the "modified adaptive dynamic relation" method to model the conical die cup test. In this case a finite difference approach is used and the method proposed by Lyaponoff [11, 122] for detecting bifurcation points is utilized. The results reported are rather good, but due to the simplifications made in the model it is hard to use the method for more general problems.

Ellagoune and Boivin [70] analyse a process very similar to the one analysed by Zhang et al.: Conical deep drawing with blank hold. In their analyses a rectangular element is analysed analytically and when the elastic strain energy due to membrane stresses equals the energy to form a wrinkle, the wrinkling limit is found. This analysis has the disadvantage that simplifications must be made for the constitutive relations in order to obtain a solution with analytical methods. In principle the method can be used for more general parts as long as they remain plane during the deformation until the onset of instability, and the method may appear usable for flange wrinkling. For the situation where we have second order wrinkles similar calculations are much more complicated: The blank is then normally in a (single or double) curved configuration whereby the analysis of the deformation itself is difficult - but the main problem may be to predict the wrinkling mode (typically a sine shaped configuration is assumed).

Another aspect which should be mentioned is that very often the wrinkles seem to start from the die shoulder zone. Most analytic methods assume that the blank is deforming in an uniform way up to the formation of wrinkles. This is in contrast to the fact that almost all sheet forming operations lead to a very non-uniform deformation; this is caused by geometry or material anisotropy, and this non-uniformity may cause onset of wrinkles under the blank hold at a very early stage of the process.

Several attempts have been made to extend the FLD concept to cover the area with compressive stresses. Such a diagram principle is illustrated in figure 6.1. Unfortunately it seems to be impossible to state these limits with sufficient reliability. This is mainly due to that tearing and splitting failures mainly are related to material properties, whereas the wrinkling is dependent on both local sheet geometry and material properties. Both failure types are, however, strongly influenced by tool contact and it must be realized

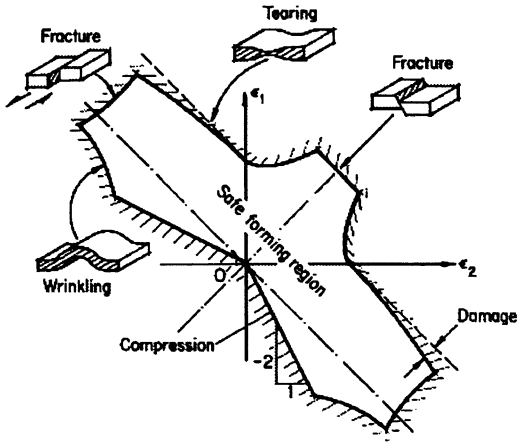

Figure 6.1: *Illustration of a total forming limit concept (from Marciniak and Duncan, [141]).*

that the use of both the traditional FLD as well as a possible extended version do have this limitation. Neale and Tugcu [158] and Hayashi et al. [88] have tried to establish the wrinkling limit numerically and experimentally, respectively. However, approaches to find a wrinkling limit similar to the fracture limit seems to fail as it is evident that wrinkling formation is strongly related to curvature of the sheet during forming, tool contact, etc. Yoshida developed a tensile test to simulate wrinkling and buckling in thin sheets. The test principle has been investigated by Hayashi [87], Gerdeen et al. [76] and Nordlund [164].

Dealing with instability of plastic deformed sheets a study of the accuracy with which the onset and development of wrinkles can be modelled should be performed. In section 6.6 a number of analyses for an elastic Euler beam are presented and discussed with regard to discretization and loading conditions. In section 6.13 an anisotropic cup is analysed with regard to prediction of wrinkle pattern and some conclusions are drawn from a comparison with experiments.

6.2 Instabilities simulated with explicit methods

When using an implicit solution procedure for highly non-linear problems, either quasi-static or dynamic, it turns out that the load increment for each step must be determined/corrected during the analysis as the stiffness of the system changes. The methods discussed will all refer to the finite element method (other methods as the finite difference method, etc can from a theoretical point of view be used too). One way to choose load increments can as proposed by Bergan and Söreide [29] be to require that the change in incremental stiffness must be close to constant in all the steps. The measure used by Bergan and Söreide is the current stiffness parameter. Section 6.3 gives the basic theory for the static, non-linear problem and the following sections illustrate the use of the current stiffness parameter in simulation of sheet metal forming with explicit codes.

Bifurcation predictors based on extrapolation are described by Bjaerum [33] for quasi-static analyses of buckling and post buckling of shell structures. Similar attempts have

been made using the CSP-measure to forecast the loss of stability, but for the present they do not seem to be very informative.

6.2.1 Explicit FE used in connection with instability problems

Let us first recapture the explicit FE-technique. Starting with the equation of dynamic equilibrium for the FE-discretized system we have:

$$\mathbf{M}\ddot{\mathbf{u}}(t) + \mathbf{C}\mathbf{u}(t) + \mathbf{f}_{int}(\mathbf{u}, t) = \mathbf{f}_{ext}(t) \tag{6.1}$$

When using the explicit time integration it is assumed that $\mathbf{M}$ is diagonal; otherwise the computational efficiency will be drastically reduced. Omitting artificial damping we have the relation which controls the time integration:

$$\ddot{\mathbf{u}}(t) = \mathbf{M}^{-1}(\mathbf{f}_{ext} - \mathbf{f}_{int}) \tag{6.2}$$

Performing a first order approximation leads to velocity:

$$\dot{\mathbf{u}}^{t+\frac{\Delta t}{2}} = \dot{\mathbf{u}}^{t-\frac{\Delta t}{2}} + \Delta t \ddot{\mathbf{u}}^{t} \tag{6.3}$$

and hereby we find the updated displacements:

$$\mathbf{u}^{t+\Delta t} = \dot{\mathbf{u}}^{t} + \Delta t^{t+\frac{\Delta t}{2}} \dot{\mathbf{u}}^{t+\frac{\Delta t}{2}} \tag{6.4}$$

The above presentation of the explicit technique is of course very schematic, a more detailed discussion is given in section 3.3.1. What is important is that no stiffness matrices are used and all stiffness information is contained in $\mathbf{f}_{int}$. This leads to lack of information compared to an implicit solution, at least when the implicit methods are based on the tangential stiffness matrix.

6.2.2 Implicit static solution of instability problems

In section 3.1 different solution methods are discussed; here we recapture the implicit, static solution in connection with instability problems. Traditionally implicit methods have been used to treat non-linear and/or instability problems in examples which are regarded quasi-static. It is assumed that a static equilibrium is established at a load level (pseudo time) λ.

$$\mathbf{f}_{ext}(\lambda, \mathbf{u}) = \mathbf{f}_{int}(\mathbf{u}) \tag{6.5}$$

If we introduce the residual Φ we can express the problem via the out of balance force:

$$\Phi(\lambda, \mathbf{u}) = \mathbf{f}_{ext} - \mathbf{f}_{int} \tag{6.6}$$

Assuming we know the residual for $\mathbf{u}^R$, an improved solution can be obtained by solving:

$$\Phi(\lambda, \mathbf{u}^R + \Delta\mathbf{u}) = \Phi(\lambda, \mathbf{u}^R) + \frac{\partial \Phi}{\partial \mathbf{u}} \Delta\mathbf{u} = \mathbf{0} \tag{6.7}$$

From the precedent equation we can define the tangential stiffness matrix:

$$\mathbf{K}_T = -\frac{\partial \Phi}{\partial \mathbf{u}} = \frac{\partial \mathbf{f}_{int}}{\partial \mathbf{u}} - \frac{\partial \mathbf{f}_{ext}}{\partial \mathbf{u}} \tag{6.8}$$

If we introduce:

$$\lambda = \lambda(s) \qquad \mathbf{u} = \mathbf{u}(s) \tag{6.9}$$

and write differentiation with respect to s as:

$$\frac{\partial}{\partial s} = (\dot{}) \tag{6.10}$$

we can write the variation of Φ as:

$$\dot{\Phi} = \frac{\partial \Phi}{\partial \mathbf{u}}\dot{\mathbf{u}} + \frac{\partial \mathbf{F}}{\partial \lambda}\dot{\lambda} = -\mathbf{K}_T\dot{\mathbf{u}} + \mathbf{P}\dot{\lambda} = \mathbf{0} \tag{6.11}$$

as $\dot{\Phi} = \mathbf{0}$ along the equilibrium path. The solution of 6.11 is unique as long as $\mathbf{K}_T$ is regular. An instability occurs when $\mathbf{K}_T$ becomes singular, and at such points the solution cannot be uniquely determined.

Let ψ_0 be the eigenvector associated with the zero eigen-value:

$$\mathbf{K}_t\psi_0 = \mathbf{0} \quad \rightarrow \quad \psi_0^{\mathbf{T}}\mathbf{K}_{\mathbf{T}} = \mathbf{0} \tag{6.12}$$

Premultiply 6.11 with ψ_0^T

$$-\psi_0^T\mathbf{K}_T\dot{\mathbf{u}} + \psi_0^T\mathbf{P}\dot{\lambda} = 0 \tag{6.13}$$

Which reduces to:

$$\psi_0^T\mathbf{P}\dot{\lambda} = 0 \tag{6.14}$$

The possible solutions of the equation is either a limit point:

$$\dot{\lambda} = 0 \tag{6.15}$$

or a bifurcation point:

$$\psi_0^T\mathbf{P} = 0 \tag{6.16}$$

Using explicit FE-technique we can of course introduce the tangent stiffness matrix in the same manner as for the implicit methods (provided that the inertial effects have limited influence):

$$\mathbf{K}_T = \frac{\partial \mathbf{f}_{int}}{\partial \mathbf{u}} - \frac{\partial \mathbf{f}_{ext}}{\partial \mathbf{u}} \tag{6.17}$$

but as mentioned above $\mathbf{K}_T$ is never evaluated directly. An alternative to the traditional evaluation of $\mathbf{K}_T$ could be to use numerical differentiation:

$$\mathbf{K}_T \approx \frac{\Delta \mathbf{f}_{int}}{\Delta \mathbf{u}} = \frac{\mathbf{f}_{int}^{t+\Delta t} - \mathbf{f}_{int}^{t}}{\mathbf{u}^{t+\Delta t} - \mathbf{u}^{t}} = \frac{1}{\Delta t}\frac{\mathbf{f}_{int}^{t+\Delta t} - \mathbf{f}_{int}^{t}}{\dot{\mathbf{u}}^{t+\frac{\Delta t}{2}}} \tag{6.18}$$

Which could be rewritten as:

$$K_T(m,n) = \frac{\Delta f_{int,m}}{\Delta t \ddot{u}_n^{t+\frac{\Delta t}{2}}} \tag{6.19}$$

This approach may be relatively cheap compared to the traditional FE calculation of $\mathbf{K}_T$, but in the present the approach is judged to be too costly and also too inaccurate. One of the main reasons why explicit methods can compete with implicit methods is the avoidance of calculation and not least storage of the stiffness matrix. At the same time a traditional analysis will demand additional analysis of the stiffness matrix in order to obtain the information wanted.

6.3 The current stiffness parameter

In 1977 Bergan and Söreide [29] proposed a simple measure of stiffness for a FE-discretized system. In this section a brief review of the original paper is given. The stiffness of a system is the relation between a force increment $\mathbf{\Delta F}$ and the corresponding displacement increment $\mathbf{\Delta u}$, popularly written as:

$$\text{"}\frac{\mathbf{\Delta F}}{\mathbf{\Delta u}}\text{"} \tag{6.20}$$

This operation is only valid for the one-dimensional case and to make this expression a scalar it is postmultiplied with the force increment and hereby the "current stiffness" is obtained:

$$CS = \frac{\mathbf{\Delta F^T}}{\mathbf{\Delta u^T}} \frac{\mathbf{\Delta F}}{\mathbf{\Delta F}} \tag{6.21}$$

This value is scaled with an initial stiffness:

$$CSP = \frac{\frac{\mathbf{\Delta F^T}}{\mathbf{\Delta u^T}} \frac{\mathbf{\Delta F}}{\mathbf{\Delta F}}}{\frac{\mathbf{\Delta F_0^T}}{\mathbf{\Delta u_0^T}} \frac{\mathbf{\Delta F_0}}{\mathbf{\Delta F_0}}} = \frac{\Delta \mathbf{u}_0^T \Delta \mathbf{F}_0}{\Delta \mathbf{u}^T \Delta \mathbf{F}} \frac{\|\Delta \mathbf{F}\|^2}{\|\Delta \mathbf{F}_0\|^2} \tag{6.22}$$

The measure CSP has the initial value of 1 and for increasing stiffness the value increases and vice versa for decreasing stiffness. Passing a value of 0 corresponds to passing a point of "zero stiffness" - an instability point. The method can be further refined, e.g. with the bifurcation index, but for the present this is not done.

6.3.1 Proposed use of the CSP-method

Based on the above procedure a similar technique is proposed for problems analysed with explicit FEM. Choosing an arbitrary simply connected part of the blank a similar measure of stiffness is introduced:

$$CSP = \frac{\Delta \mathbf{u}_0^T \Delta \mathbf{f}_{int0}}{\Delta \mathbf{u}^T \Delta \mathbf{f}_{int}} \frac{\|\Delta \mathbf{f}_{int}\|^2}{\|\Delta \mathbf{f}_{int0}\|^2} \tag{6.23}$$

here $\Delta \mathbf{f}_{int}$ expresses the change in internal forces calculated for the region and $\Delta \mathbf{u}$ the corresponding displacements. This approach yields a significant advantage; in a very simple way we can characterize the stiffness for an area ranging from a single element to major parts of the blank. This is convenient as instability onset very often is of a local nature which in general cannot be detected on a global level. Another advantage is that the method can be used for wrinkle formation analysis as well as necking behaviour. The necking behaviour is of course limited to diffuse instability and without further changes of a standard code we cannot simulate the localization effect directly. Writing the measure in an alternative way leads to the expression:

$$CSP = \frac{constant}{\frac{\Delta \mathbf{u}^T[\Delta \mathbf{f}_{ext} - \mathbf{M}(\ddot{\mathbf{u}}^{k+1} - \ddot{\mathbf{u}}^k) - \mathbf{C}(\dot{\mathbf{u}}^{k+1} - \dot{\mathbf{u}}^k)]}{\|\Delta \mathbf{f}_{ext}{}^i - \mathbf{M}(\ddot{\mathbf{u}}^{k+1} - \ddot{\mathbf{u}}^k) - \mathbf{C}(\dot{\mathbf{u}}^{k+1} - \dot{\mathbf{u}}^k)\|^2}} \tag{6.24}$$

It becomes obvious that the CSP measure proposed here is dependent on the dynamic effects when an explicit analysis method is used, but as long as the overall response is in good agreement with the physical process both the internal forces as well as the displacements must represent the problem fairly well. If the simulation is sufficiently close to the quasi-static behaviour a negative value of the CSP indicates that a point of instability has been passed. We cannot expect the measure to indicate the risk of a bifurcation/load limit before the switch in deformation takes place. The measure should of course be capable of judging a steady decrease in stiffness.

6.4 The Rayleigh coefficient

Inspired from the expressions for the CSP measure, which in its mathematical nature is similar to the Rayleigh coefficient, it is chosen to include some discussion on the Rayleigh coefficient. If we instead of postmultiplying with the increment in forces in equation 6.21 postmultiply with the increments in displacement an expression very similar to the Rayleigh coefficient is obtained. Starting out from a linear system we can write the Rayleigh coefficient as:

$$\lambda = \frac{\mathbf{d}^T \mathbf{K} \mathbf{d}}{\mathbf{d}^T \mathbf{M} \mathbf{d}} \tag{6.25}$$

where $\mathbf{d}$ is an arbitrary vector. If $\mathbf{d}$ approximates an eigenvector the value for λ will be close to an eigen-value for the system. But when the system is non-linear, and especially for explicit methods where we do not want to establish the stiffness matrix, some manipulations have to be made. As the choice of $\mathbf{d}$ is arbitrary we can choose $\Delta \mathbf{u}$, and if $\Delta \mathbf{u}$ is close to an eigen-mode at the current state we obtain an approximation of the lowest eigen-value.

$$\lambda = \frac{\Delta \mathbf{u}^T \mathbf{K} \Delta \mathbf{u}}{\Delta \mathbf{u}^T \mathbf{M} \Delta \mathbf{u}} = \frac{\Delta \mathbf{u}^T \Delta \mathbf{f}_{int}}{\Delta \mathbf{u}^T \mathbf{M} \Delta \mathbf{u}} \tag{6.26}$$

Using the latter part of the expression we can avoid the calculation of $\mathbf{K}$ and hereby the estimation is relatively cheap seen from an computational point of view.

Using a time step, either bounded by element time step or related to some loading increment, the right part of equation 6.26 can be rewritten:

$$\lambda = \frac{\Delta \mathbf{u}^T \Delta \mathbf{f}_{int}}{\Delta t \mathbf{v}^T \mathbf{M} \Delta t \mathbf{v}} = \frac{\Delta \mathbf{u}^T \Delta \mathbf{f}_{int}}{\Delta t^2 \mathbf{v}^T \mathbf{M} \mathbf{v}} = \frac{\frac{\Delta \mathbf{u}^T}{\Delta t} \frac{\Delta \mathbf{f}_{int}}{\Delta t}}{2W_k} \tag{6.27}$$

If $\Delta\mathbf{u}$ is close to or indeed represents an eigen-mode it should be possible to detect the onset of the instability by monitoring the value of λ. If we rewrite 6.26 the resemblance with the CS measure becomes obvious:

$$\lambda = \frac{\Delta\mathbf{f}_{int}^T}{(\mathbf{M}\Delta\mathbf{u})^T}\frac{\Delta\mathbf{u}}{\Delta\mathbf{u}} \tag{6.28}$$

which indeed leeds to the one-dimensional definition $\lambda = \omega^2 = \frac{K}{M}$. For the one-dimensional case the only difference between the CSP and the Rayleigh measure is that a normalization with regard to the mass is performed. Later on some examples on the use of the Rayleigh coefficient for judging structures analysed with explicit FE are given.

The above presented should not be mistaken with the Rayleigh method used by Meier and Reissner, [147],[112] who consider the critical level between energy needed for formation of a wrinkle and energy released due to the decrease in membrane load.

6.4.1 The implemented scheme for calculation of CSP and the Rayleigh coefficient

The first attempts made to calculate the CSP-value for a number of problems were based on an estimation of internal forces from stress values dumped during FE-analyses. This approach turned out to be too inaccurate due to the number of digits used when saving stresses in an ascii-file.

In order to improve the accuracy of the analysis with the proposed approaches a facility was implemented in LS-Dyna3d to make it possible to dump the internal forces on an element by element basis (transformed to the global coordinate system) with a specified time interval. The values of CSP and the Rayleigh coefficient are then to be calculated by postprocessing FE-results.

A future work to be performed could be to implement the method more directly in LS-Dyna3d. In connection with the present work, three in principle identical programmes were programmed, one for analysis of regions consisting of four elements, one for nine elements and one for arbitrary but simply connected regions. The structure of the programme is given below:

1: Read file specifying region, centre node or centre element.

2: Read nodal point coordinates from the input deck to LS-Dyna3d.

3: Read element data from the input deck.

4: Search for elements specified.

5: Determine nodal points for the region.

6: Read nodal forces (internal) and nodal displacements from output files from LS-Dyna3d.

7: Calculate for each specified time step $CS_i = \frac{\|\Delta\mathbf{f}_{int_i}\|^2}{\Delta\mathbf{u}_i^T\Delta\mathbf{f}_{int_i}}$

8: Calculate the Rayleigh coefficient $\lambda_i = \frac{\Delta\mathbf{u}_i^T\Delta\mathbf{F}_{int_i}}{\mathbf{u}^T\mathbf{M}\mathbf{u}}$

9: Calculate $CSP_i = \frac{CS_i}{CS_0}$ and $RAYLEIGH_i = \frac{\lambda_i}{\lambda_0}$

10: Save values for the CSP and Rayleigh measure for each state calculated.

In the calculation of the Rayleigh coefficient nodal masses of 1 are assumed. The measures can be calculated for translational degrees of freedom only or taking all degrees of freedom into account. The experience from the use of the measures is that the clearest picture is obtained by monitoring the values calculated from translational degrees of freedom only.

6.5 A method based on Hill's uniqueness criterion

Another interesting way to indicate loss of stability in local regions has been investigated by Nordlund [164] in 1995. In the following a similar method will be discussed. The idea is to start out from Hill's condition for uniqueness of a solution:

$$\int_V \left(\dot{\sigma}^*_{ij}\dot{\epsilon}^*_{ij} - \sigma_{ik}\dot{\epsilon}^*_{jk}\dot{\epsilon}^*_{ij} + \sigma_{ij}\dot{\epsilon}^*_{kk}\dot{\epsilon}^*_{ij} \right) dV > 0 \tag{6.29}$$

A star denotes the difference between the current (stable) solution and any other kinematically admissible solution. If we use the actual increments in strains and stresses we can calculate the above given integral directly; the value is the second order work of stresses associated with variation in displacements. If a structure is stable this value will be positive for all admissible variation of displacements. If the value is zero we have a critical state and a negative value indicates an unstable configuration.

Nordlund implemented the method on an element basis, that is, performed the integration over one element. The last term in equation 6.29 was omitted in his implementation which I think is dangerous as the switching from membrane deformation to out of plane modes normally will include an elastic unloading which can be significant. Nordlund argues that the deformation is dominated by plastic deformation and hereby conserve volume, however, in my opinion the loss of stability will to a high degree be influenced by elastic unloading.

Instead of performing the integral over each element it is proposed to use the method in each integration point giving a value of the second order incremental work per unit volume. This has been chosen as the absolute value is of minor interest - it is the passing from positive to negative values which indicates that the solution path is unstable.

We start out from Hill's criterion written for the actual path:

$$\int_V \left(\dot{\sigma}_{ij}\dot{\epsilon}_{ij} - \sigma_{ik}\dot{\epsilon}_{jk}\dot{\epsilon}_{ij} + \sigma_{ij}\dot{\epsilon}_{kk}\dot{\epsilon}_{ij} \right) dV > 0 \tag{6.30}$$

Assuming vanishing stress in the z-direction and only taking the in-plane shear stress into account leads to the expression:

$$\begin{aligned} \int_V (& \dot{\sigma}_{11}\dot{\epsilon}_{11} - \sigma_{11}\dot{\epsilon}_{11}\dot{\epsilon}_{11} - \sigma_{12}\dot{\epsilon}_{12}\dot{\epsilon}_{11} + \sigma_{11}(\dot{\epsilon}_{11} + \dot{\epsilon}_{22} + \dot{\epsilon}_{33})\dot{\epsilon}_{11} \\ & + \dot{\sigma}_{22}\dot{\epsilon}_{22} - \sigma_{21}\dot{\epsilon}_{21}\dot{\epsilon}_{22} - \sigma_{22}\dot{\epsilon}_{22}\dot{\epsilon}_{22} + \sigma_{22}(\dot{\epsilon}_{11} + \dot{\epsilon}_{22} + \dot{\epsilon}_{33})\dot{\epsilon}_{22} \\ & + 2\dot{\sigma}_{12}\dot{\epsilon}_{12} - \sigma_{11}\dot{\epsilon}_{21}\dot{\epsilon}_{12} - \sigma_{12}\dot{\epsilon}_{22}\dot{\epsilon}_{12} + 2\sigma_{12}(\dot{\epsilon}_{11} + \dot{\epsilon}_{22} + \dot{\epsilon}_{33})\dot{\epsilon}_{12} \\ & - \sigma_{21}\dot{\epsilon}_{11}\dot{\epsilon}_{21} - \sigma_{22}\dot{\epsilon}_{12}\dot{\epsilon}_{21})dV > 0 \end{aligned} \tag{6.31}$$

Expression 6.32 can be reduced to:

$$\int_V \dot{\epsilon}_{11}(\dot{\sigma}_{11} - \sigma_{11}\dot{\epsilon}_{11} - \sigma_{12}\dot{\epsilon}_{12} + \sigma_{11}\dot{\epsilon}_{ii}) + \dot{\epsilon}_{22}(\dot{\sigma}_{22} - \sigma_{12}\dot{\epsilon}_{12} - \sigma_{22}\dot{\epsilon}_{22} + \sigma_{22}\dot{\epsilon}_{ii}) \quad (6.32)$$
$$+\dot{\epsilon}_{12}(2\dot{\sigma}_{12} - \sigma_{11}\dot{\epsilon}_{12} - \sigma_{12}\dot{\epsilon}_{22} + 2\sigma_{12}\dot{\epsilon}_{ii} - \sigma_{12}\dot{\epsilon}_{11} - \sigma_{22}\dot{\epsilon}_{12})dV > 0$$

The evaluation of the integrand in equation 6.33 is implemented in the material routine and the value is calculated during the analysis. No volume integration is performed and the routine returns the actual value of the integrand in the Gauss points.

6.6 Analysis of buckling of linear elastic Euler beams

Instability phenomena is, when analysed with the FE-method, dependent on the level of discretization, size of imperfection, etc. However, using an explicit time integration raise additional aspects such as loading rate and artificial damping which must be taken into account. In this section buckling of an elastic beam column is considered.

The characteristics of the beam analysed are: Length 200 mm, width 20 mm and thickness 4 mm. In the analyses BLT-shell elements are used with an Young's modulus of 200000 MPa and with Poisson's ratio equal to zero in order to obtain beam theory using shell elements.

The normal Euler analysis of a column does not include dynamic effects but is only dependent on the stiffness of the column. Using an explicit finite element code means that the mass must be included in order to make the dynamic simulation.

Intending to perform an analysis of an instability problem gives raise to some additional considerations in order to obtain a reliable FE-model. The most important aspects in this example are considered to be: Loading rate, size of the imperfection, amount of exterior damping and the discretization.

In the following some results are given for a hinged-hinged column analysed using a displacement controlled load and using imperfections at the mid-nodes to force the beam not to follow the primary unstable path. If no imperfections are utilized the beam will just shorten and the problems when reaching the instability limit are not recognized. The problem is illustrated in figure 6.2. The beam is modelled by a single row of elements and the loading is modelled by the displacement of the upper point which follows a ramp function. In table 6.1 is given the characteristics of a number of analysis.

6.6.1 Influence from the discretization

To investigate and illustrate the influence from the degree of discretization a number of analyses are performed with various number of elements. The loading is a prescribed displacement equal to 1.25 times the critical and two different loading rates were employed. The damping corresponded to 10 per cent of the critical damping and the imperfection was 0.01 mm. In figure 6.3 is shown the predicted horizontal displacement of a node placed at the middle of the column. The predicted displacements are nearly linear up to approxi-

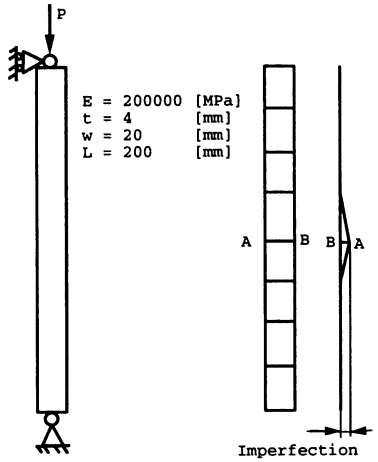

Figure 6.2: *Hinged-hinged beam with imperfections and the principle of discretization.*

Time [msec]		125	250	375	500
Imperfection [mm]	0.1	0.01	0.001	0.0001	0.00001
Damping factor		1%	10%	100%	200%
Number of elements		4	8	12	16

Table 6.1: *The analyses are performed with various values for the loading rate, imperfection, damping factor and discretization.*

mately 80 msec and the time after is followed by a rather rapid growth. As expected the response becomes stiffer concurrently with the coarseness of the mesh. An improvement can be seen when going from 8 to 16 elements and it is concluded that 16 elements are sufficient to accurately model the deflection. The curves for 16 and 24 elements yield almost identical responses.

In figure 6.4 is shown the longitudinal stresses (at the reference surface) in elements with a boundary up to the midpoint. From figures 6.3 and 6.4 it can be seen that the loading rate corresponding to 125 msec analysis time results in an overshoot in the stresses which is not seen for an analysis time of 500 msec. Although the predicted response is a good characterization of the behaviour of the system, it is often easier to evaluate the stresses directly in order to evaluate the loss of stability.

After reaching the load carrying capacity the example loaded over 125 msec (figure 6.4, left) indicates that the response is overlaid with a vibration, whereas the examples loaded over a time of 500 msec seem to deform in a more stable manner, the same vibration modes should be present, but the amplitudes are so small that they cannot be detected from the figure. The only discrepancy between the examples is the loading rate which can be concluded to be of importance for the structural response.

When comparing the results with the analytical value (-65.8 MPa) it is seen that the response for the models with 16 and 24 elements are almost identical and corresponds very well with the analytically obtained critical stress (-65.8 MPa). With 4 and 8 elements the

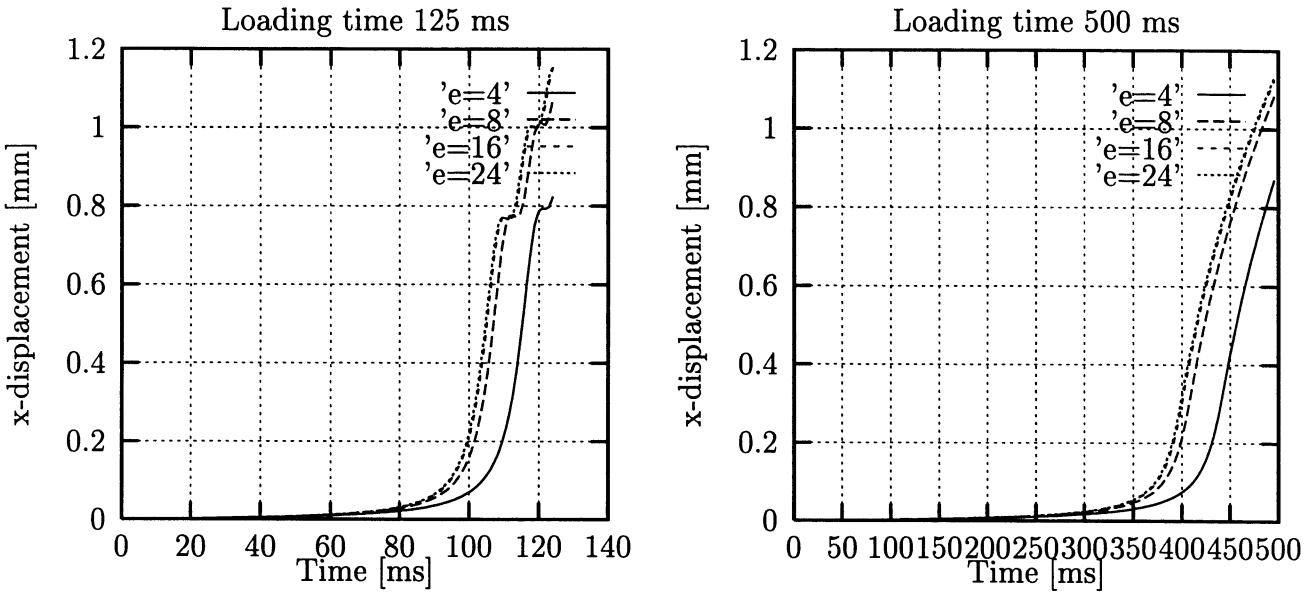

Figure 6.3: *Predicted x-displacement for two different loading rates and 4 different discretizations.*

model over-estimates the critical stress.

The beams were given a small initial imperfection by moving one of the mid-nodes a small distance (in the range from 0.00001 to 0.1 mm). The effect of the size of the imperfection is shown in figure 6.5. The loading time was 125 msec, the damping 10 per cent of the critical and the number of elements in the beam 16. The predicted response is seen to heavely depend on the imperfection. From the predicted displacement it can be seen clearly that the imperfection on 0.1 mm is far too high and regarding the stress response it seems to be most adequate to utilize an imperfection in the order of 0.01 mm to obtain the correct maximum value of the normal stress. However, the smaller the imperfection the closer the response is to the nature of Euler buckling where no transversal displacement should be seen before reaching the instability limit. Figure 6.6 shows the predicted displacement and development of stress for four different discretizations. The analyses are performed using a critical damping of the system. Comparing figure 6.5 and 6.6 (the only difference being the level of damping) it can be noticed that increasing the artificial damping does delay the onset of buckling.

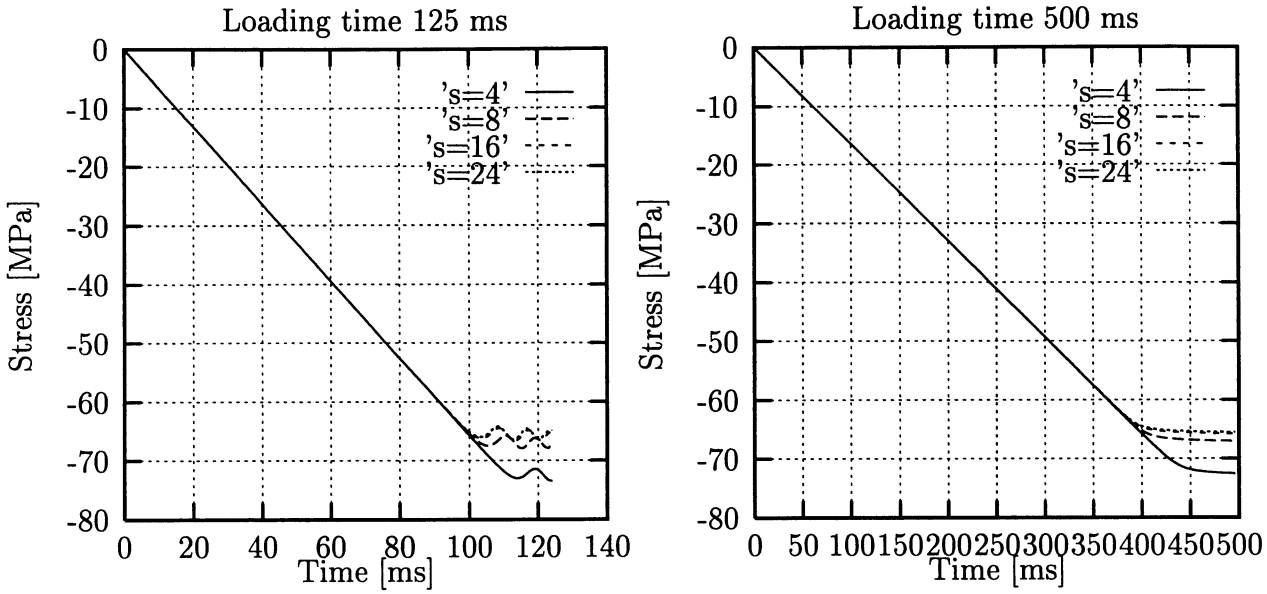

Figure 6.4: *Predicted longitudinal stress for two different loading rates and 4 differentiation discretizations.*

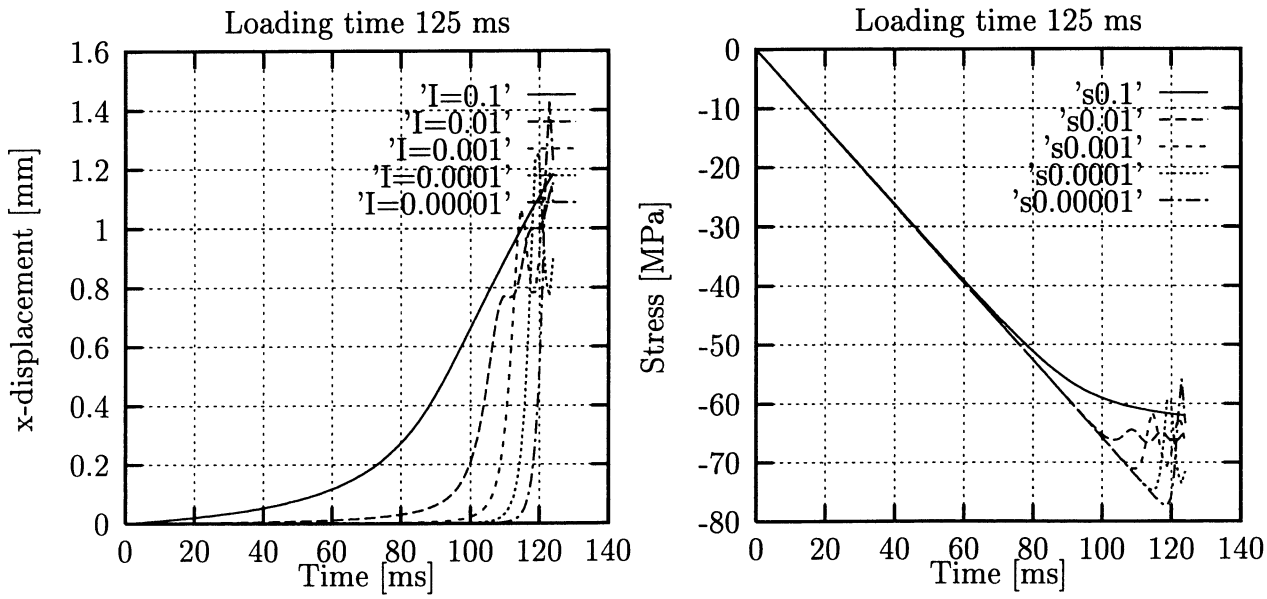

Figure 6.5: *Predicted displacement and stress for different imperfections in the range from 0.00001 to 0.1 mm.*

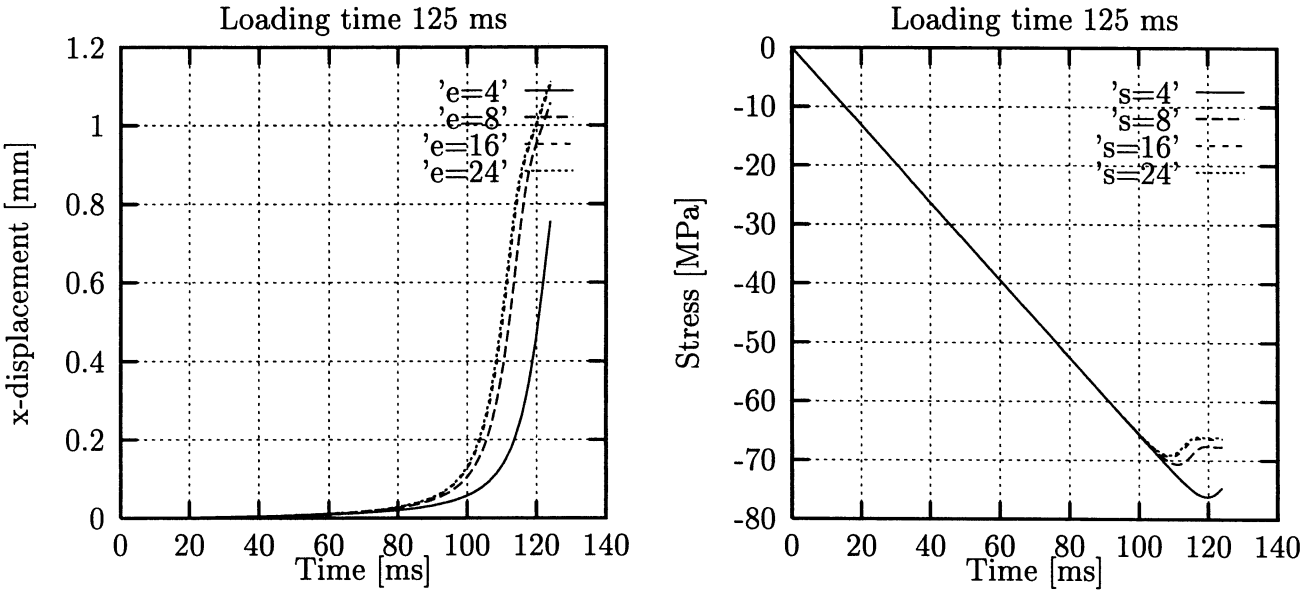

Figure 6.6: *Predicted displacement and stress for an imperfection on 0.01 mm, critical damping and various degrees of discretization.*

6.7 Beam instability analysis using CSP

In the following results for the CSP method discussed in section 6.3.1 are given. A beam consisting of 16 elements, damped 10 and 100 per cent of the critical damping, loading time 125 msec and an imperfection of 0.01 mm is used in the analyses, identical to the beam in the previous section. In figures 6.7 and 6.8 are shown the values for the CSP-measure calculated for a region with four elements (label E4) and for a region with 16 (all) elements (label E16). For the analysis with 10 per cent of the critical damping an instability point is detected a time of $\approx$ 104 msec. This is a short delay compared to the analytical value, (100 msec), but regarding the response shown in figure 6.6 it can be seen that the value corresponds very well with what can be extracted from the stress response. For the critical damped system the post-buckling behaviour is a bit more steady. The response is further delayed and loss of stability is found at a loading time of $\approx$ 110-112 msec, but the detected loss of stability corresponds to the FE-predicted.

Summarizing the beam example it can be stated, that if the FE-predicted response is in a good agreement with the quasi-static nature of the buckling problem, the loss of stability can be detected using the CSP-measure.

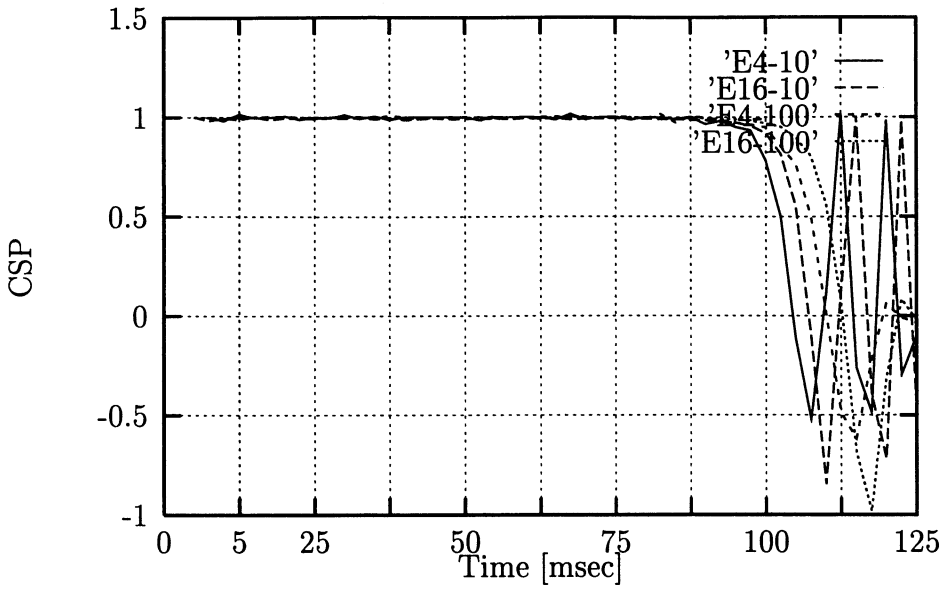

Figure 6.7: *The CSP-value for a hinged-hinged beam. The curves indicate analysis performed with 10 and 100 per cent of the critical damping. Curve indicated with 4 is the CSP-value calculated for 4 elements placed at the centre of the beam, 16 indicate that all elements are included in the calculation of the CSP-value.*

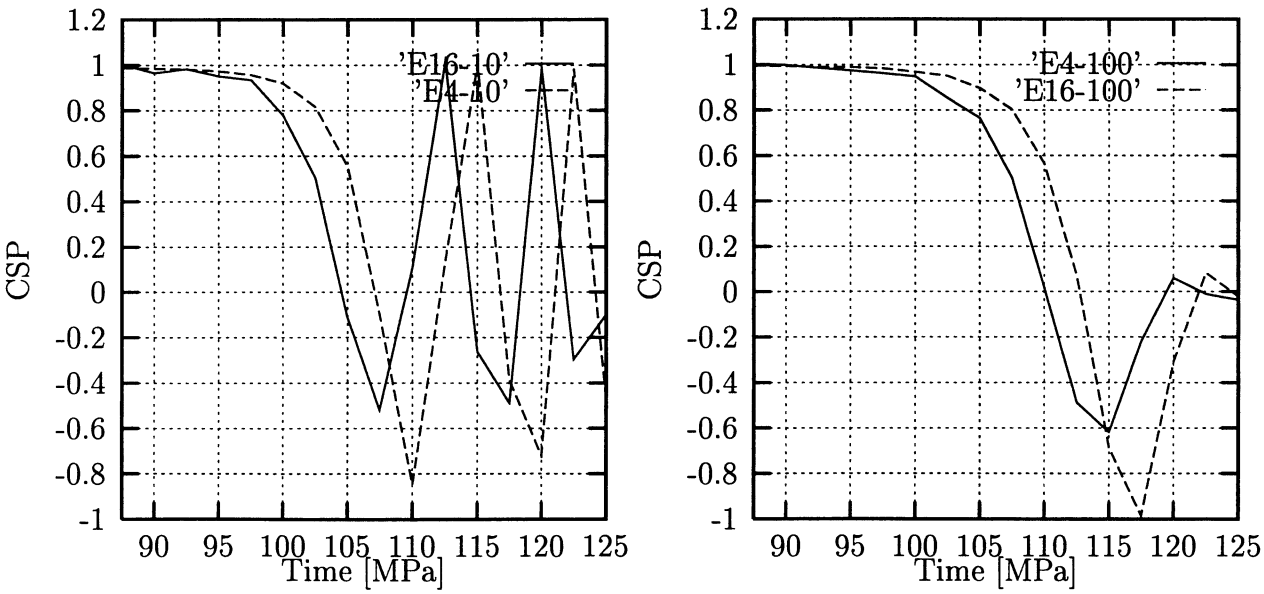

Figure 6.8: *Calculated value of the current stiffness. Left is given the example with 10 per cent of critical damping and right the critical damped case (for regions of 4 and 16 elements, respectively), only the loading steps close to the loss of stability are included.*

6.8 One degree of freedom system

In the following a one-degree of freedom system is considered. The system (illustrated in figure 6.9) consists of a bar and a linear spring and is loaded with a force P resulting in a displacement w. Assuming small strain gives the following relation between displacement

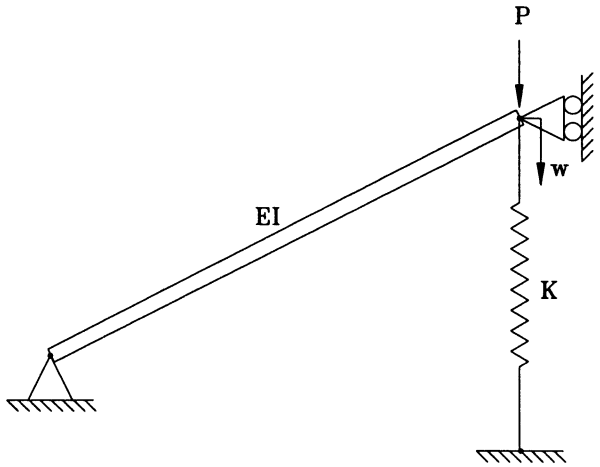

Figure 6.9: *Illustration of one-dimensional problem.*

and external load:

$$P = Kw + AE\frac{H-w}{L_A}\frac{L_A - L_I}{L_I} \tag{6.33}$$

where P is the load, K the spring stiffness, H the initial height of the right point of the bar, L_I and L_A are the initial and actual length of the bar ($L_A = \sqrt{(H-w)^2 - L_I^2}$). In figure 6.9 is shown the force P as function of the vertical displacement w. From the relationships illustrated in figure 6.10 it can be noticed that for zero spring stiffness (k=0) a snap-through behaviour is present. By applying an additional stiffness it is possible to make the system stiffen and hereby the problem can be analysed as a force driven problem. Otherwise it is necessary to use displacement control. If no spring is present most methods will fail when coming close to the local maximum, either leading to lack of convergence in the solution or leading to a sudden jump in displacement from $w \approx 0.4mm$ to $w \approx 2.2mm$.

If we apply a spring with a stiffness sufficient to give the system an overall stiffness which is positive it is interesting to note that we for the system have parts for which the stiffness contribution is tending first to zero and following to a negative value indicating a local unloading.

This could also be the case in a sheet metal operation where a local region looses stability and/or stiffness contribution due to the formation of wrinkles or due to a local onset of necking. But if the overall response still is of a character similar to the two systems stiffened with springs (k=120 N/mm and k=240 N/mm) it can be hard to detect the problem performing traditional postprocessing.

Turning to the one-dimensional problem we can write the tangential stiffness as:

$$K_T = \frac{\partial P}{\partial w} \tag{6.34}$$

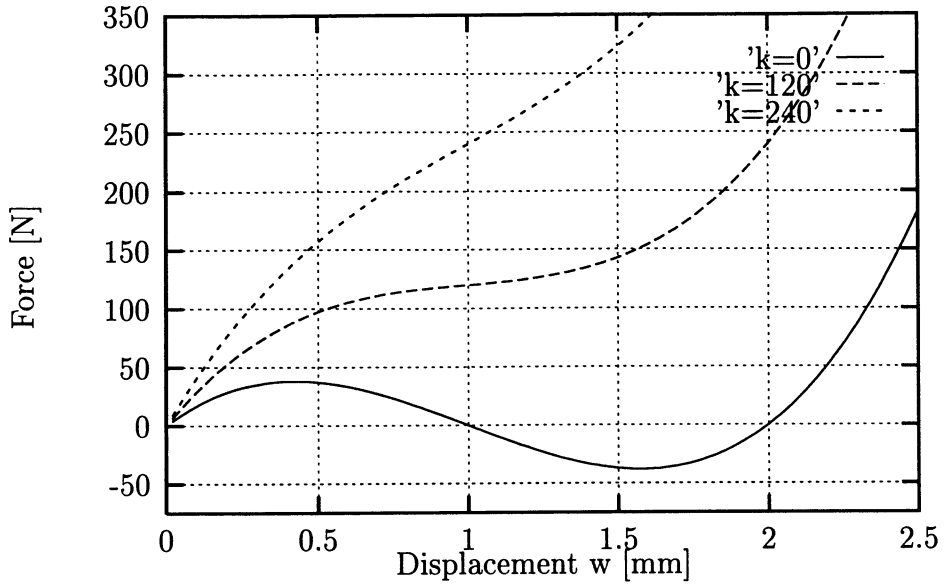

Figure 6.10: *Relation between load and displacement for A=1 mm^2, E=200000 MPa and K equal to 0, 120 and 240 N/mm, respectively. The initial inclination H for the truss was 1 mm.*

The occurrence of a load instability appears for $K_T \rightarrow 0$. Very often one will use some techniques which linearize the problem and solve the response in an incremental way, typically expressed on the form:

$$\Delta F = [K_{T_{k \rightarrow k+1}}] \Delta w \tag{6.35}$$

going from one state of equilibrium k to state k+1. After linearization we can solve the problem up to the point where $K_T \rightarrow 0$, but then multiple solutions can exist and it is necessary with special algorithms in order to follow a path as the one illustrated in figure 6.10 for k=0.

6.8.1 Elastic truss

Two typical problems in connection with sheet metal forming are snap-through and limit point problems. In order to test and describe the proposed methods the example discussed in section 6.8 is analysed with LS-Dyna3d. The problem is analysed with an inclination H on 10 mm and the initial beam length L_I equal to 100 mm. The displacement w is prescribed and reaches a maximum value of 20 mm. In figure 6.11 is shown the analytic solution to the problem: Left the relation between force and displacement which is characterized by a load maximum followed by a unloading phase until a load minimum is reached. After the load minimum the truss becomes stretched and the stiffness increases again. The stiffness shown in the right part of figure 6.11 reaches a minimum for a displacement w=H.

In the FE-analysis one shell element is used to model the truss. In order to obtain the truss like behaviour Poisson's ratio is set to 0. In figure 6.12 is illustrated the results using the CSP method proposed (section 6.3.1). The behaviour of the CSP is plotted for two examples: Left where only translational displacement (and related force increments) are

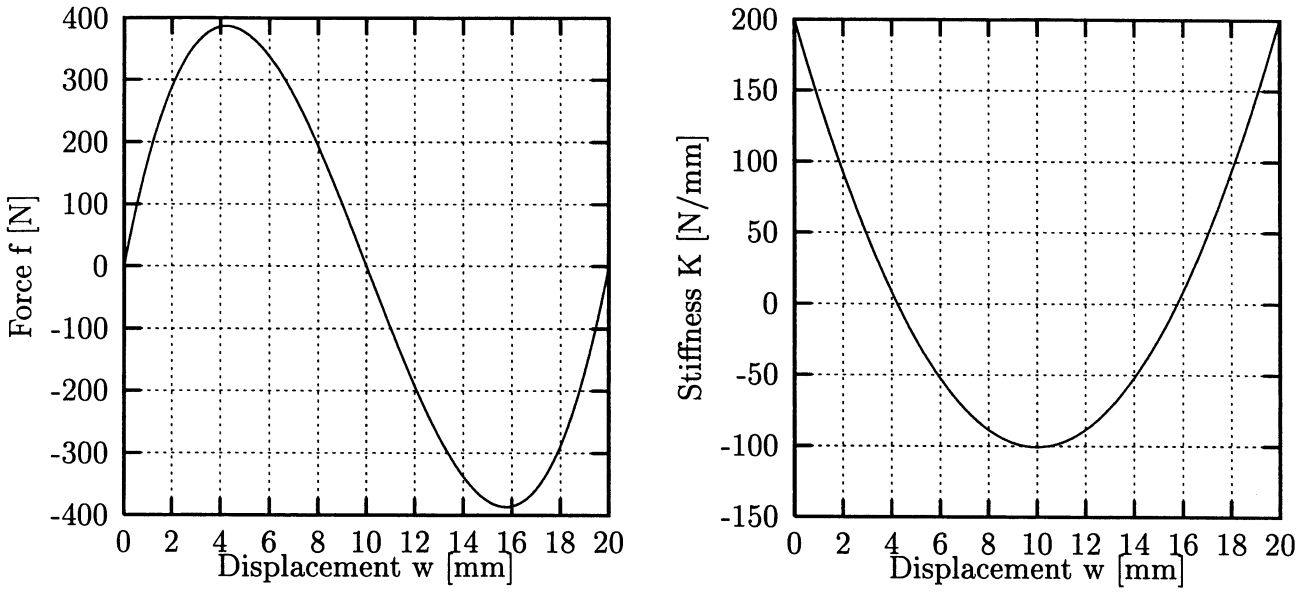

Figure 6.11: *Left is shown the force development as function of displacement w. Right is shown the corresponding stiffness.*

taken into account. Right is given the same measure now calculated using generalized forces (includes rotation and moments). It is clear from figure 6.12 that at two points a significant change takes place: The first point corresponds to the load maximum and the second to the point where the force reaches a minimum (the shift from negative to positive stiffness). In both curves two points leading to infinite values have been left out. Between the points of instability the CSP value is negative which is in accordance with the calculated stiffness in figure 6.11.

In figure 6.13 is shown the variation of the Rayleigh coefficient using only translational degrees of freedom (left) and using generalized degrees of freedom (right). The Rayleigh coefficient calculated from translational degrees of freedom indicates the same variation of the stiffness as the analytic distribution. The only variable in connection with translations is the vertical displacement and the related force. Taking the expression of the Rayleigh coefficient and reducing to a one-degree of freedom system:

$$\lambda = \frac{\Delta \mathbf{u}^T \mathbf{K} \Delta \mathbf{u}}{\Delta \mathbf{u}^T \mathbf{M} \Delta \mathbf{u}} = \frac{K}{M} \tag{6.36}$$

As the mass can be considered constant the Rayleigh coefficient should follow the nature of the stiffness. The right side of figure 6.13 shows the development of the Rayleigh coefficient including rotational effects. This figure indicates the eigen-value variation of the system and indicates a clear minimum at the displacement w=H=10 mm, this value can be seen to remain positive over the entire range of displacement. Both values shown have been normalized with an initial value determined close to beginning of the loading (at a displacement of approximately 0.2 mm). The curves in figure 6.13 start with a value around 1, drop to values of -0.5 and almost zero, respectively, whereupon the values are increasing and reach the initial level at a displacement of 2H. This behaviour can also be noticed for the CSP-curves which more or less can be mirrored around the line w=H=10 mm.

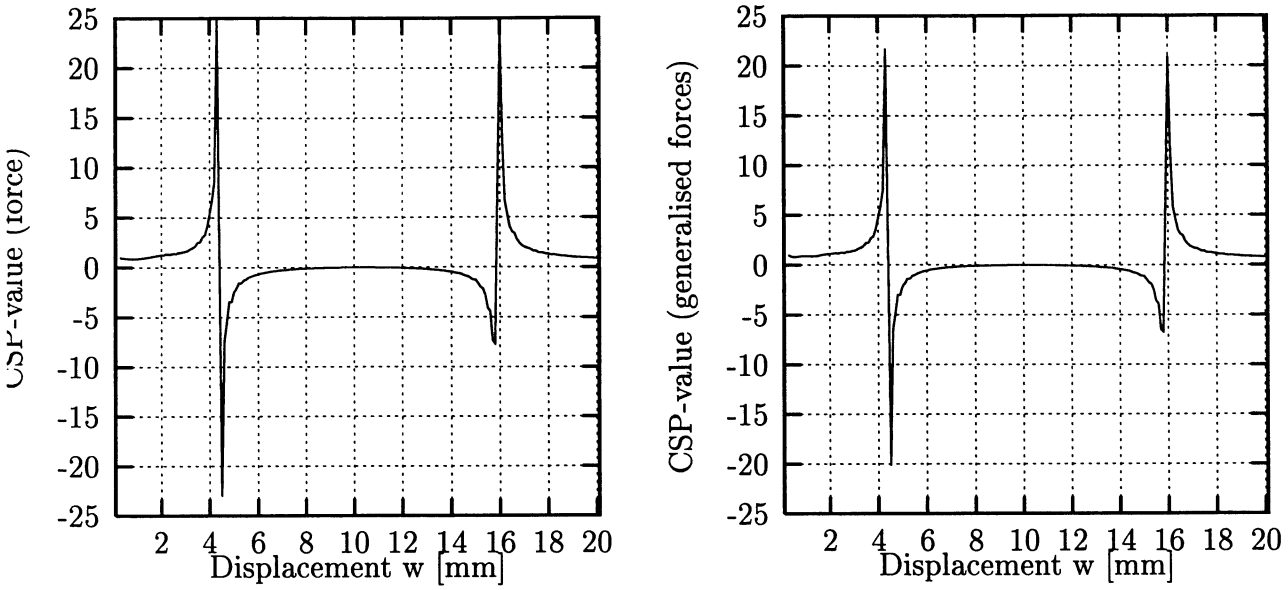

Figure 6.12: *Left is shown the calculated value of CSP based on translations and forces. Right the similar expression including contributions from rotations and internal moments.*

The uniqueness criterion proposed by Hill has been implemented in the material routine for continuous calculation (for each Courant time step). However, as dumps for postprocessing only are performed with a specified interval some options regarding the value to be dumped are included in the material routine: The first option is to dump the current value at dump time, the second option is to filter the values to values between -1 and 1, if the value is above 1 the value is set to 1 and values below -1 is set to -1, values in between keep the current value. The third option accumulates the minimum value experienced during simulation, $(if\ H_{current} < H_{min} \rightarrow H_{min} = H_{current})$.

The variation of the current value is shown in figure 6.14. Figure 6.14 shows the actual value of the Hill criterion calculated for a unit volume (the value in the integration point). The left figure gives the variation with a linear scale and the right gives the value using a logarithmic scale. The left figure shows that very low values are achieved around $u = h$, but the minimum value is hard to judge directly. The right figure shows more clearly that a dramatic change takes place: The value becomes as low as ≈ 0.05 which seen with regard to initial values well above 10000 is a dramatic decrease. However, the shape of the curve is more informative than the actual values - the logarithmic scaling leads to an indication of a behaviour which is only first order continuous.

The variation of the filtered value is illustrated in figure 6.15 where it can be seen that one single value goes below 1 indicating a point in time where, for a more complicated analysis, we should check the structural behaviour. The method seems to work in the present example, but for other analyses it may not.

In the right side of figure 6.15 the last option is illustrated: As the value is continuously calculated the minimum value experienced during the analysis is kept and the "actual" minimum value is then dumped for postprocessing. Here it can be seen that the curve is decreasing to the displacement w=H=10 mm whereupon the curve becomes constant.

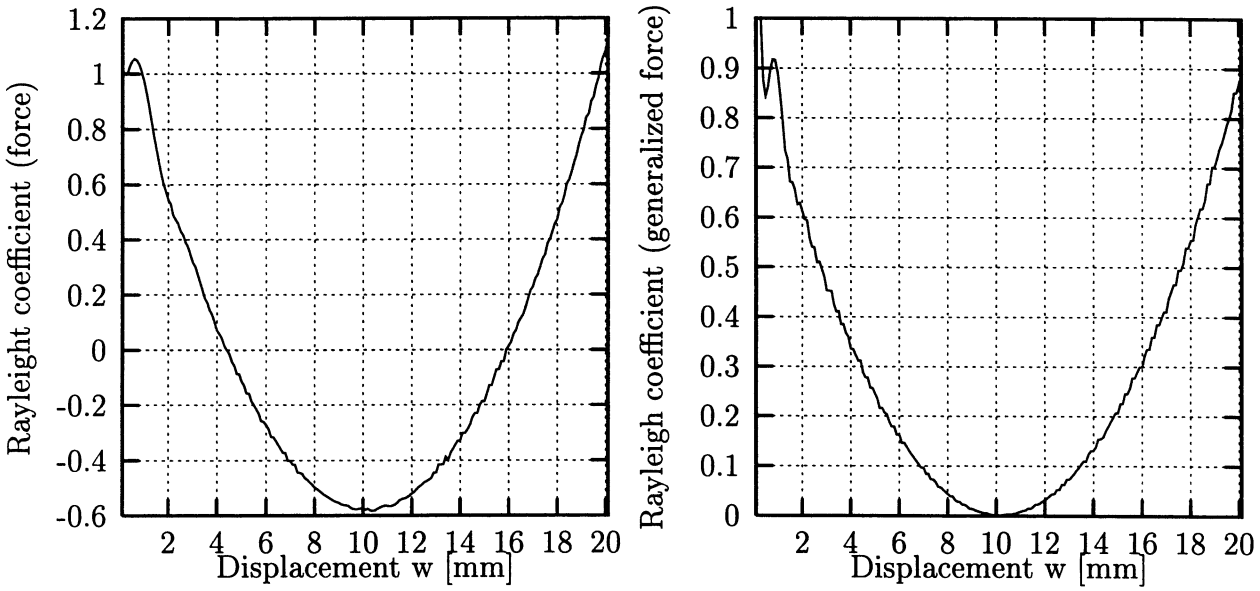

Figure 6.13: *Left is shown the variation of the Rayleigh coefficient based on translations and forces. Right the similar expression including contributions from rotations and internal moments.*

Also it should be noticed that using this approach leads to a minimum value slightly less than zero. This was not discovered using the two previous dump options.

To use the value in more general examples it is therefore suggested to combine two methods: Plotting the log value for the values at dump time together with a check of the minimum value experienced during the analysis. This simple example illustrates some of the possibilities to (in an easy way) investigate the stability of a system analysed using explicit finite element. Some conclusions can be drawn at this stage: The CSP method seems very effective to indicate load maximum as well as minimum - the global snap-through is not so clearly indicated, but it may be possible to better evaluate the CSP value. The Rayleigh coefficient seems capable of indicating almost the same characteristica, at least for this simple example. The uniqueness criterion clearly indicates the point of an unstable configuration.

One of the problems using the above methods seems to be the evaluation of the actual value: It seems to be necessary to take the development of the value into account.

Figure 6.12 does not seem to indicate the snap-through behaviour as accurately as the two other methods. This is, however, primarily due to the plot scale. In figure 6.16 is plotted the absolute value of the CSP using a linear scale (left) and a log scale (right). The left part of figure 6.16 does clearly show the two peaks indicating local extrema. It can also be noticed that the level around w=10 mm is very low, however, the behaviour seems stable. The right figure does in contrast to this clearly indicate an abrupt behaviour at the time of zero stiffness.

Also for the CSP-measure it is hard to use the absolute value directly, again it seems necessary to take the historical development into account in order to judge the current

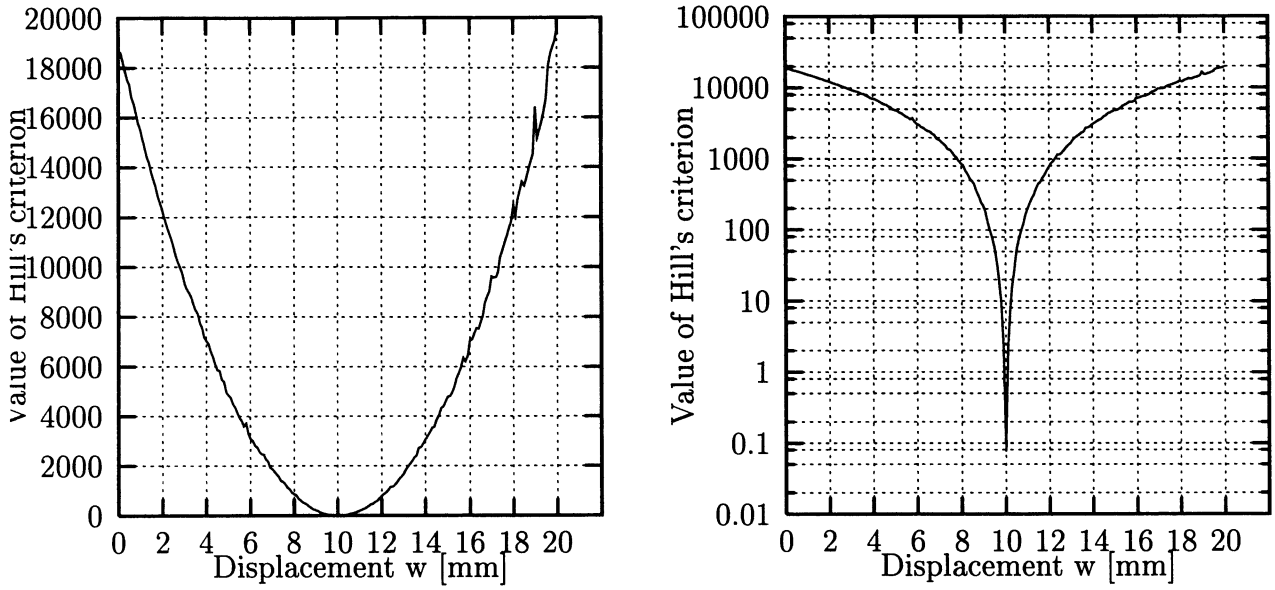

Figure 6.14: *The current value of Hill's instability criterion at specified times for saving data during analysis (200 times during the analysis). Right is plotted the same data using a log-scale for the ordinate.*

behaviour.

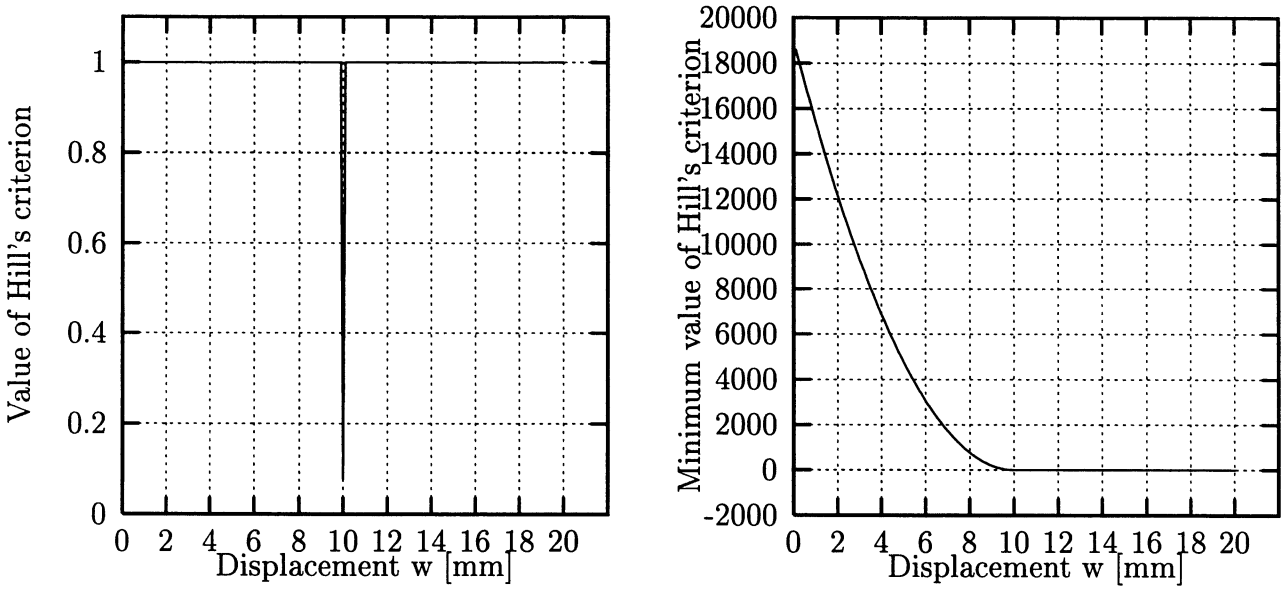

Figure 6.15: *Left: The value of Hill's instability criterion filtered using a filter which limits the absolute values to be less than 1. Right the minimum value of Hill's criterion experienced during the analysis.*

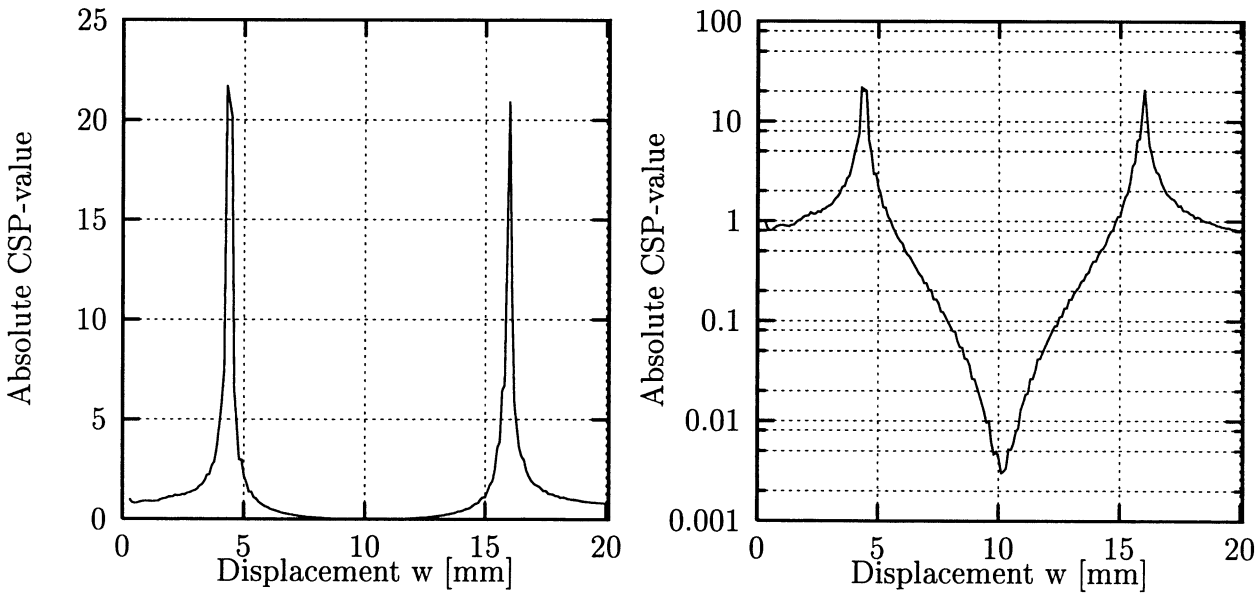

Figure 6.16: *The absolute value of CSP plotted using linear and logarithmic scales for the elastic truss problem.*

6.8.2 Plastic truss

In the following results for the same example as in the previous section are given, but here with a truss reaching the plastic state before the local load maximum.

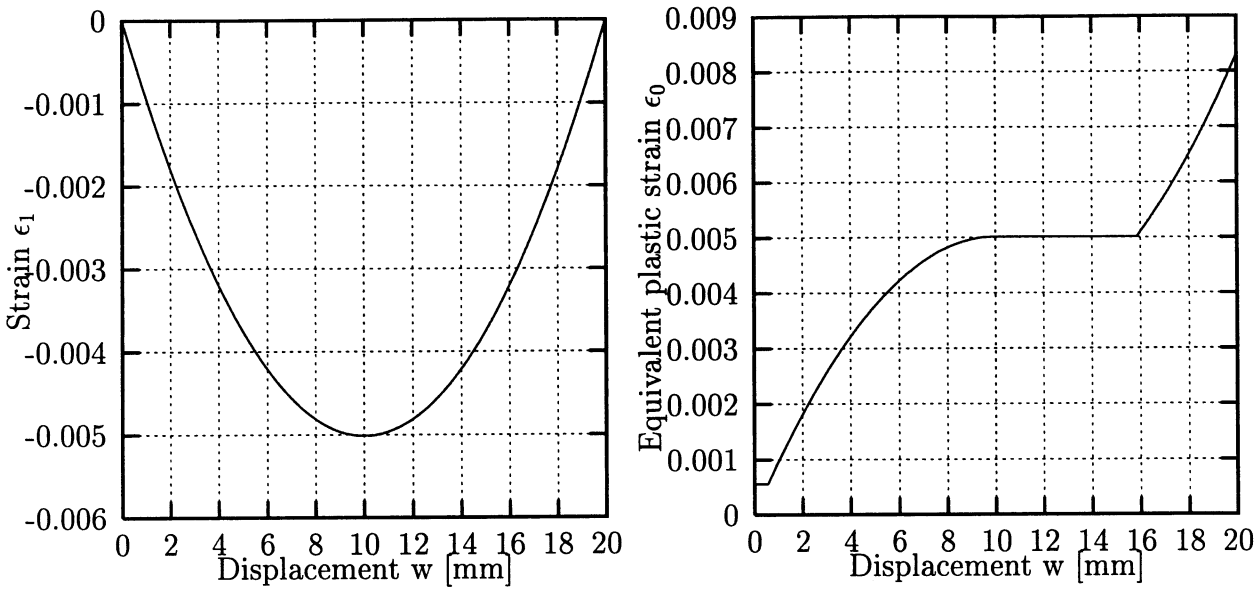

Figure 6.17: *Left is shown the analytical calculated development of strain as function of displacement, and right is shown the growth in equivalent plastic strain. Note that in the figure the plastic strain includes* ϵ_0 *used in the Hollomon-Swift relation.*

Figure 6.17 shows left the analytic relation between strain and displacement w and right is given the relation between plastic strain and displacement. As the truss element is unloaded after passing w=H=10 mm the level of effective plastic strain is constant up to a time of 16 msec. Figure 6.18 shows left the longitudinal stress in the truss as function of

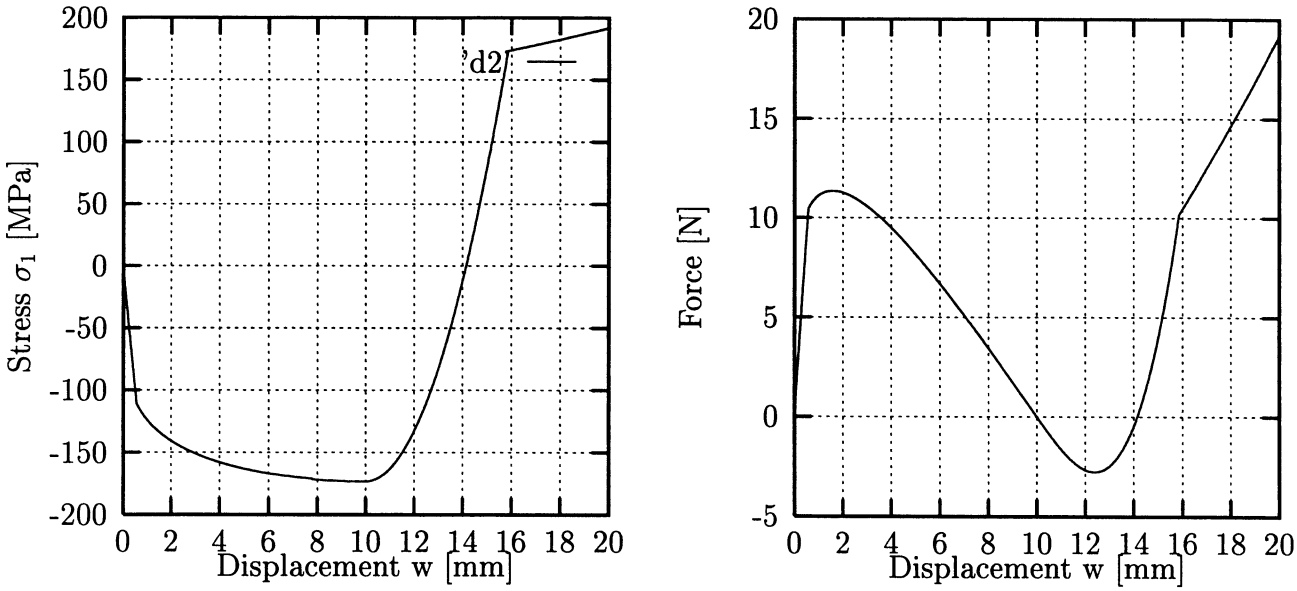

Figure 6.18: *Left is shown the development in stress as function of displacement, right is shown the development in force.*

displacement, right is given the relation between force P and displacement. Although the same geometry is used it can be seen that the local maximum and local minimum occur earlier than in the case with the elastic truss. The local maximum is reached around a displacement of $\approx$ 1.6 mm and the minimum at $\approx$ 12.5-13 mm. In figure 6.19 is shown the

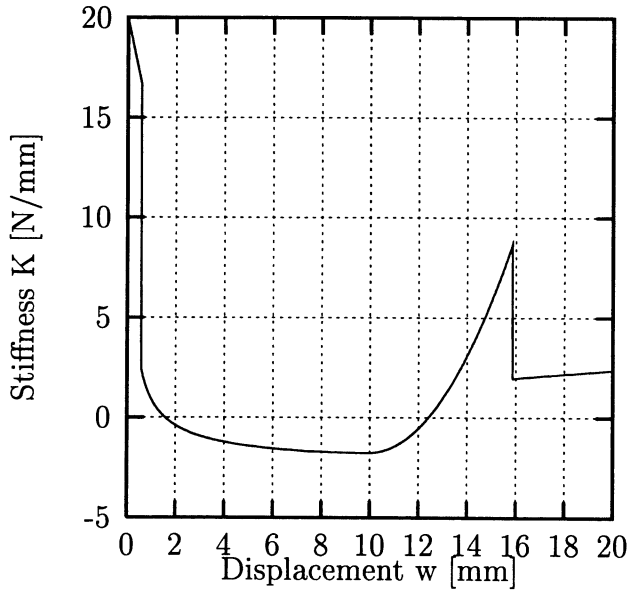

Figure 6.19: *Illustration of the evolution of stiffness calculated by analytical means.*

development in the stiffness of the system as function of displacement. A rapid drop can

be seen for w $\approx$ 0.5-0.8 mm when the truss goes from elastic to plastic deformation. A similar effect can be seen at a displacement of $\approx$ 16 mm. Figure 6.20 illustrates the relation

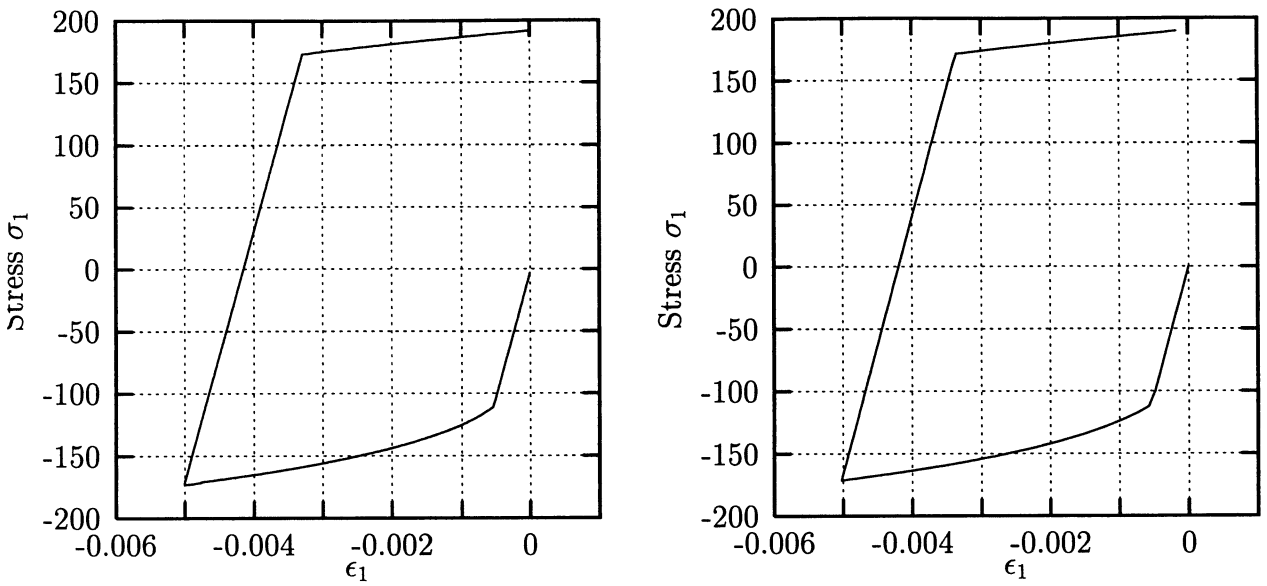

Figure 6.20: *Illustration of the relation between stress and strain in the truss element. Left predicted analytically, right the corresponding results obtained using explicit FE and the implemented material model.*

between longitudinal strain and longitudinal stress for the truss. Left is given the response predicted using analytical calculations and right the corresponding values obtained with the material routine. The analytical approach does not take transverse effects due to incompressibility into account in the plastic part in contrast to the FE-modelled approach. The strains are limited and the simplifications made for the analytic approach are not significant for the behaviour. The primary difference is that the analytic response reaches a state of zero strain whereas the FEM predicts a final strain of approximately 0.0001 due to the use of strain increments calculated on the basis of actual length. In the analytic response strain increments are calculated as engineering strain increments related to the initial length of the beam. Figure 6.21 shows the development in Hill's instability criterion as function of displacement w plotted with a linear scale (left) and with a logarithmic scale (right). When plotted with a logarithmic scale a clear indication of the passing a point of zero stiffness appears. Also the switching from elastic to plastic (or reverse) can be detected from the curve at a displacement of $\approx$ 0.8, 10 and 16 mm. Figure 6.22 shows the development in Hill's criterion using the other dump facilities: Filtered values left and minimum experienced value right. Both methods can be used to detect the point where the truss passes a horizontal position. An advantage of the minimum experienced value is that the absolute minimum discovered is taken into account. In this example we reach the first negative value around w=10 mm which indicates an unstable system. The other dump options do not lead to negative values for the dump interval used in the simulation. Figure 6.23 shows left and right the variation of the CSP-value obtained using either only translational or generalized degrees of freedom, respectively. Both curves clearly indicate the drop in stiffness when going from elastic to plastic deformation at $\approx$ 0.8 mm. Also the load minimum is found at $\approx$ 1.8 mm where the CSP-value goes from positive to negative values. The CSP-value does also very clearly show the load minimum: The switch from

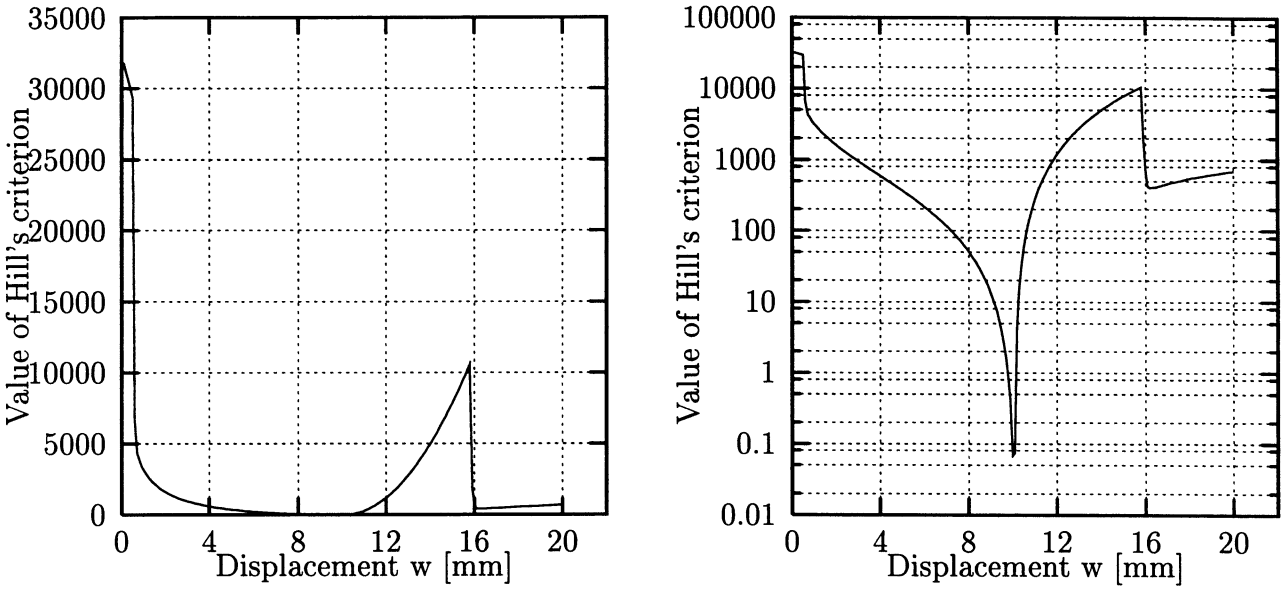

Figure 6.21: *Left: The value of Hill's instability criterion at the time when dumping data for postprocessing (200 times during the analysis). Right is plotted the same data using a log-scale for the ordinate.*

negative to positive values around 12.5 mm. Finally the switch from elastic to plastic deformation is well recorded at 16 mm. In figure 6.24 is plotted the absolute value of the CSP-variation (left). Right is given the same variation plotted in a logarithmic scale. In this case the instability point at w=10 mm is discovered - as it was the case for the elastic truss. Figure 6.25 shows left and right the variation in the Rayleigh measure calculated for translational and generalized degrees of freedom, respectively. If we look at the right part of figure 6.25 and compare with figure 6.13 it can be noticed that the Rayleigh coefficient predicted for a displacement in the range 10-16 mm seems to be almost identical. It is quite obvious that this behaviour also should be expected. The plastic truss is deforming plastically for a displacement less than 10 mm. After 10 mm the straining of the truss is reversed and up to a displacement of approximately 16 mm the loading is purely elastic and as the total elongations are relatively small this loading should correspond to the elastic truss. Here it can (as for the elastic truss) be concluded that the Rayleigh measure calculated for translational degrees of freedom gives a very good estimation of the structural stiffness.

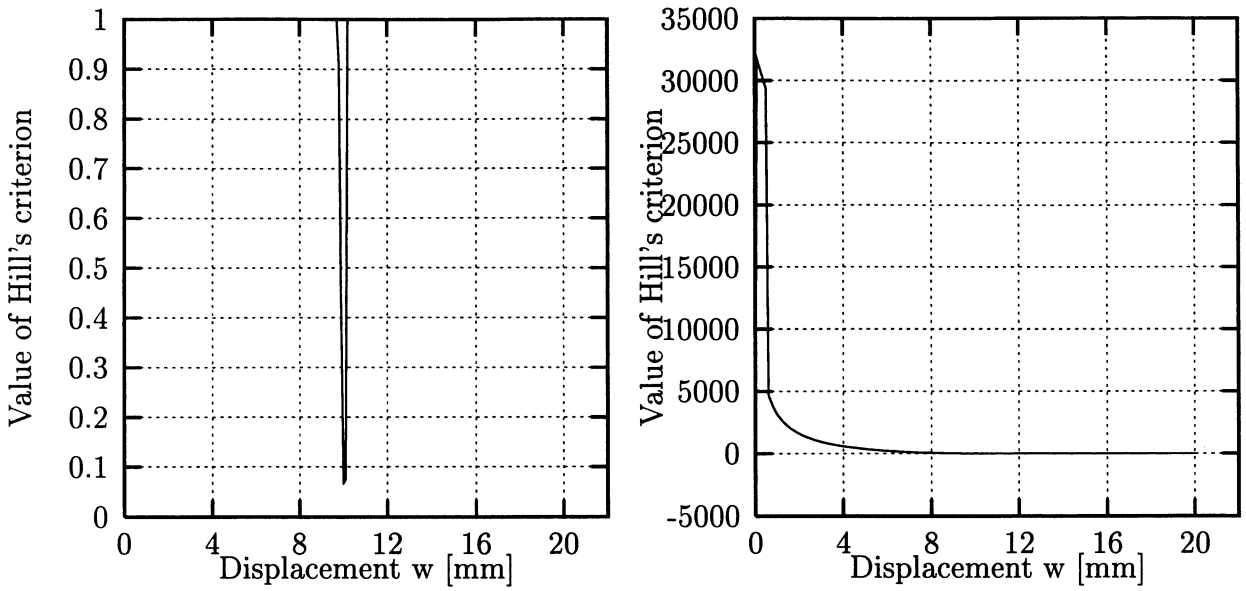

Figure 6.22: *Left: The value of Hill's instability criterion during analysis using a filter which limits the absolute values to be less than 1. Right the minimum value of Hill's criterion experienced during the analysis.*

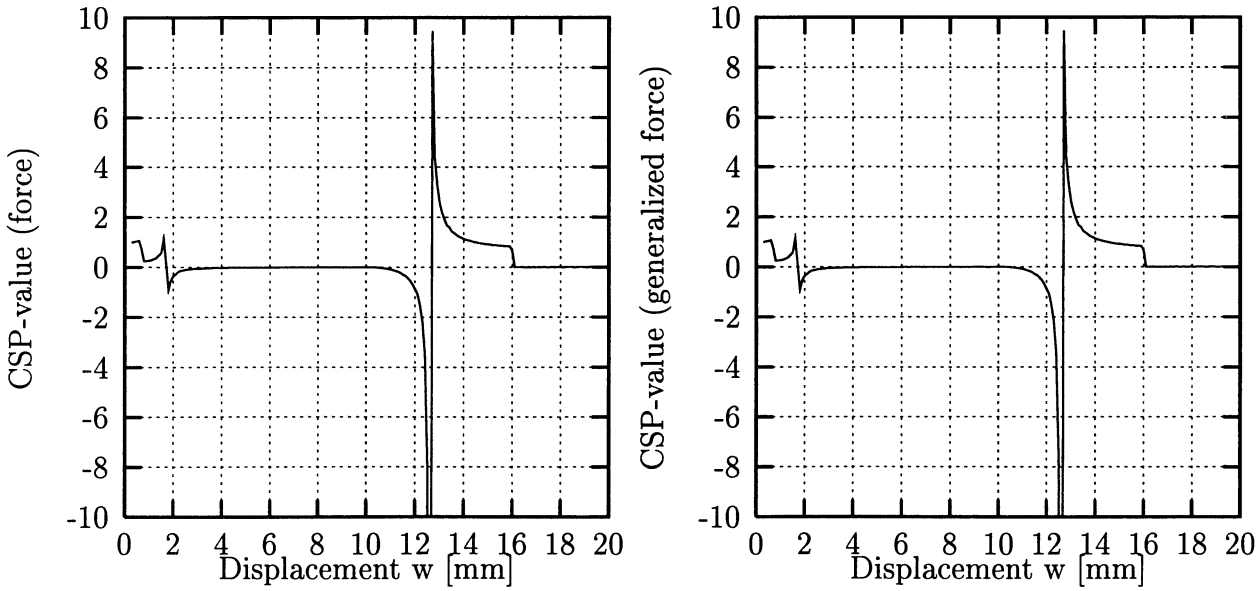

Figure 6.23: *Left is shown the calculated value of CSP based on translations and forces. Right the similar expression including contributions from rotations and internal moments.*

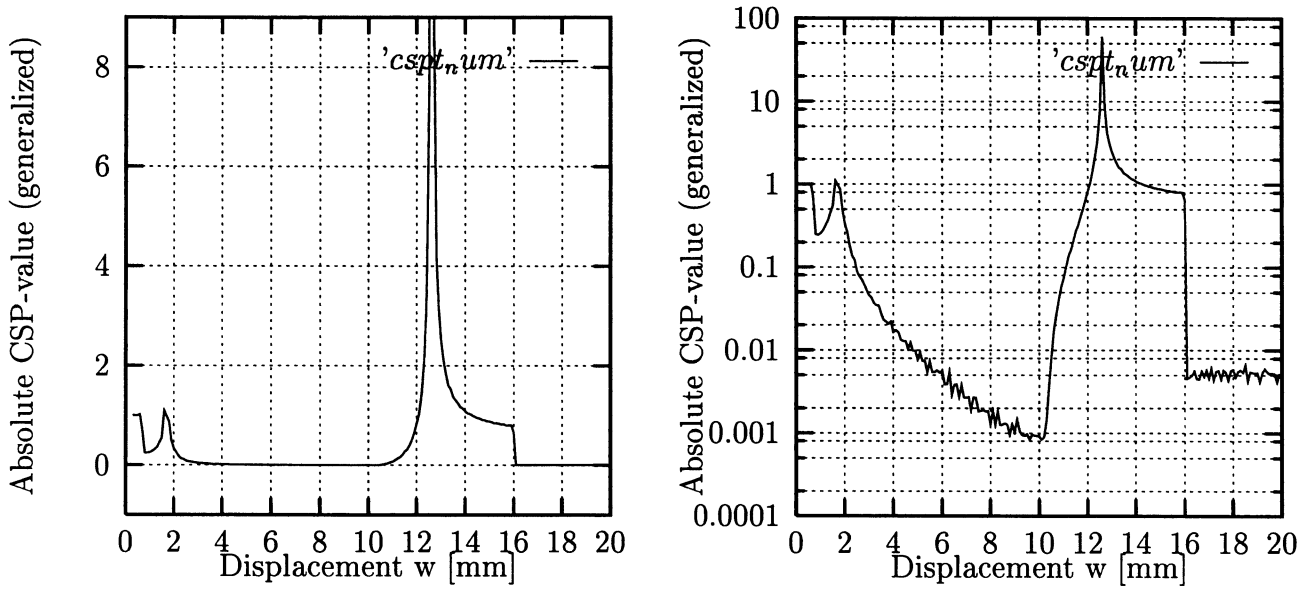

Figure 6.24: *The absolute value of CSP plotted using linear and logarithmic scales for the plastic truss problem.*

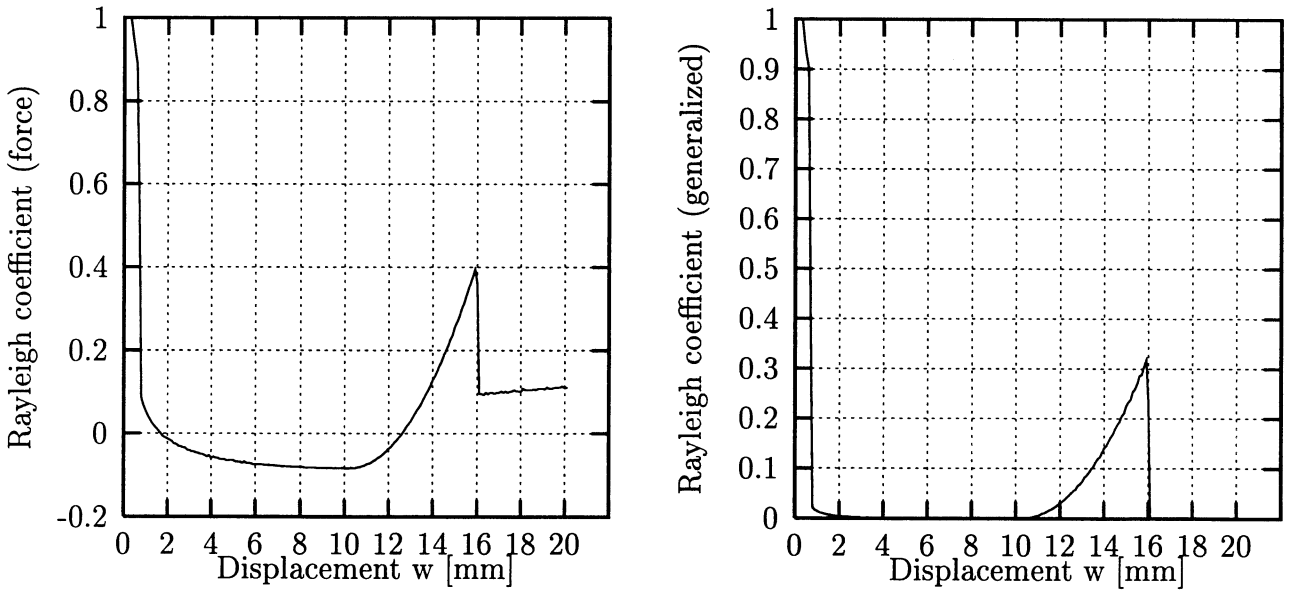

Figure 6.25: *Left is shown the variation of the Rayleigh coefficient based on translations and forces. Right the similar expression including contributions from rotations and internal moments.*

6.9 Elastic beam

The behaviour analysed in the previous example is somewhat simplified compared to the sheet metal forming process. To move towards a more advanced example a problem very similar to the truss example is analysed: The truss is substituted by a beam. For the present example the beam has a length of 100 mm and the inclination is 8.72 mm. The thickness of the beam is set to 4.175 mm and the beam is 10 mm wide. Young's modulus is set to 206200 MPa and Poisson's ratio to 0.3.

The beam is only modelled with four elements but it opens up the possibility to experience an additional instability: Buckling of the beam element. When only four elements are used it leads to a too high buckling resistance. However, in the present context it is just wanted to include the buckling behaviour and to document whether the buckling behaviour can be recorded using the proposed methods.

The analysis is again controlled by a forced displacement of the right end of the beam. To provoke the instability artificial damping is employed so that the solution depends on both loading rate and degree of damping. In figure 6.26 is given the predicted strain

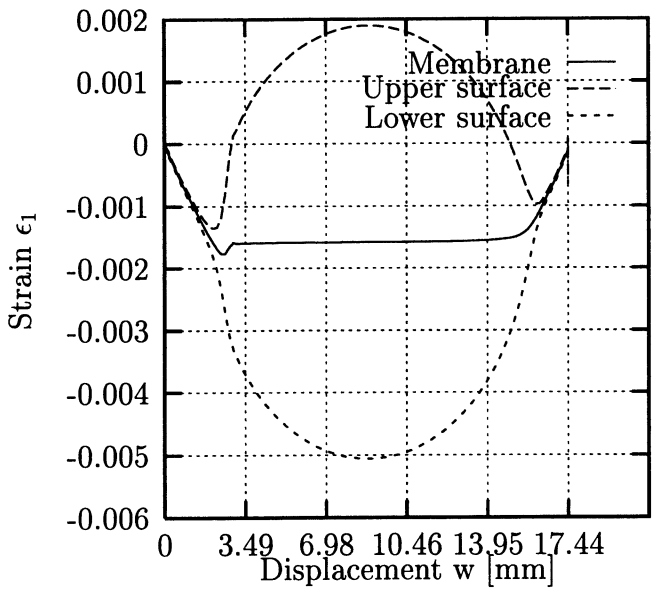

Figure 6.26: *Strain development as function of the displacement. Strains are plotted for the reference surface as well as for the surfaces.*

development and the figure shows the development in membrane and surface strains, respectively. The strains develop to start with in a very stable manner followed by a growth in the outer surface strain and a decrease of the inner surface strain. The point where the strains start to deviate from the membrane strain corresponds to the onset of buckling. As the end of the beam is forced down the strains develop and reach a maximum straining level at w=8.72 mm, corresponding to the point where a horizontal position is passed. After this point the difference in strains decreased and around w=16 mm the same level for membrane and skin strains is reached. At this point the membrane strain starts decreasing which means that the system is stiffening. In figure 6.27 are shown the values of Hill's criterion for element 1 and 2. From the figure it can be seen that the buckling

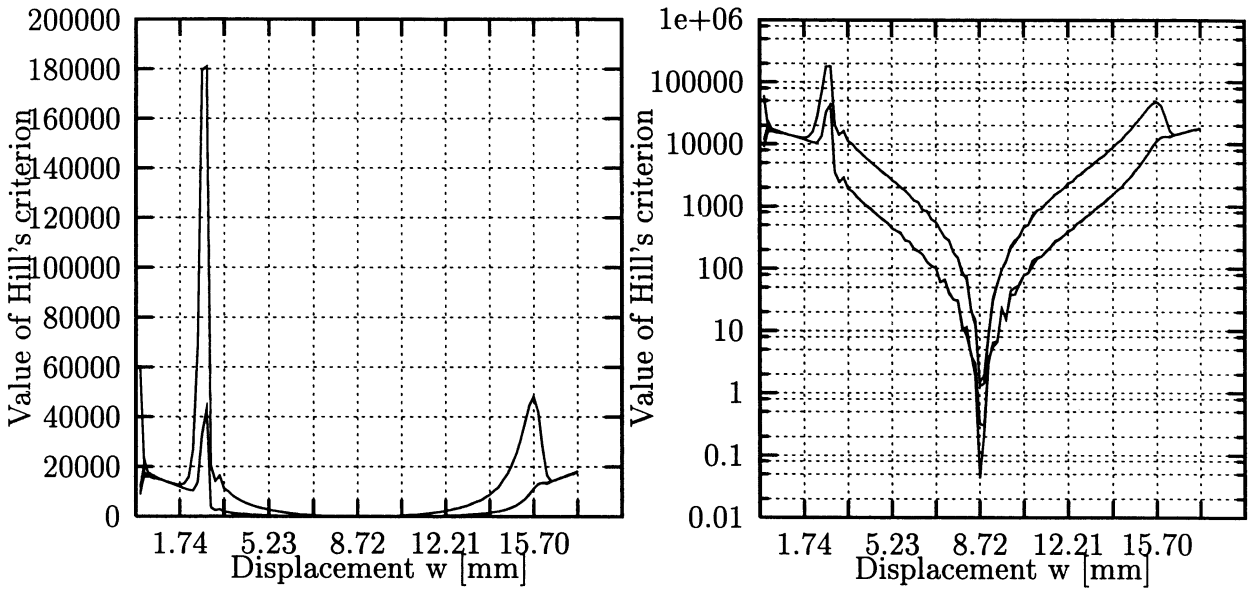

Figure 6.27: *The curves show the predicted values of Hill's criterion for two elements (1 and 2). Left plotted in a linear diagram and right the same data presented in a logarithmic diagram.*

behaviour is not detected using Hill's criterion for the elastic beam example - instead of reaching negative values peak values are discovered. Figure 6.28 shows the variation for element 2 plotted in a scale similar to the one used in figure 6.14. Relating figure 6.28 to figure 6.14 indicates a similar behaviour, the starting level is around 17000 and the value drops almost to zero at w=8.72 mm (see right figure 6.27). However, at a displacement of approximately 2.5 mm and at 16 mm a marked difference can be seen: These are the points where the beam element looses and gains its compressive strength. This can also be seen on the shape of the curve in figure 6.28 compared to 6.14: After buckling the drop in the Hill coefficient takes place much faster for the beam compared to the truss element.

The Hill criterion implemented for use within each element seems to be a strong tool to analyse a rather complicated situation: It does clearly indicate the overall loss of stiffness due to geometric changes (at w=8.72 mm). The method does not seem capable of detecting the pass of a local extrema which should be discovered around a displacement of $\approx$ 5 mm. Figure 6.29 shows the predicted variation of the CSP-measure. In the left part (the value calculated on basis of translations) a drop towards a value of zero can be seen around w=2.5 mm followed by a small peak value. Before reaching a displacement of w=5.2 mm the value drops below zero which indicates an unstable system. Around 16 mm a very abrupt behaviour can be seen corresponding to going from an unstable system to a stable system with a finite stiffness. A similar behaviour can be seen for the value calculated from generalized forces: Here 3 peaks are evident indicating buckling, geometric loss of stiffness and regaining of stiffness.

The information from the CSP-value seems to be accurate and it is reasonably easy to decipher the meaning of the value. In figure 6.30 is given the variation in the Rayleigh measure calculated on basis of forces and generalized forces, respectively. Also this value gives a clear indication of the the buckling, the local maximum and the stiffening in the

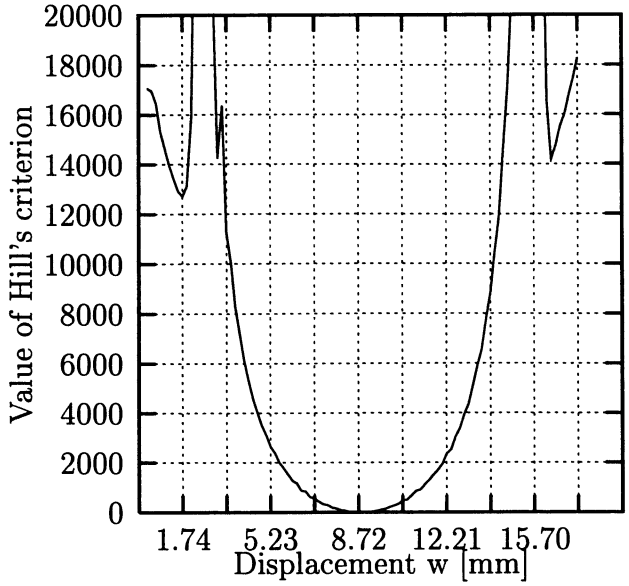

Figure 6.28: *The data from figure 6.27 plotted in a scale similar to figure 6.14.*

latter part of the process. The Rayleigh measure calculated from translational degrees of freedom is very informative: The initial level is around one until buckling, the value then drops to a rather low value, however, still positive. But after the local maximum the value drops to negative values until the system reaches a stable level.

6.10 Plate example

The second example concerns elastic buckling of a square plate. Analysis of the same plate with various algorithms can be found in Bjaerum [33] and analytical analysis can be found in Timoschenko [205]. The plate is loaded in compression in one direction, simply supported and free to move in x and y direction along edges as illustrated in figure 6.31 where also the material parameters can be found. The theoretical stability limit is reached for a normal stress of 29.12 N/mm^2. In order to obtain the buckling a pseudo load is applied to the mid node at the time where a load of 0.8 times the critical load is reached. A number of tests are made varying the size of the pseudo load. This is in general a difficult task, when performing instability analysis of geometric perfect structures. If choosing a geometric imperfection or a disturbance force, one must take care, that the results obtained are not due to a higher bifurcation mode. Figure 6.32 shows left the discretization used for a quarter of the plate and right the predicted normal stress in element number one. In the figure is given the stress at the reference plane and at the outer and inner surface. To get a more clear view of the membrane stress this component is also plotted using absolute values. The stresses are plotted as function of normalized load with 1 being equal to the critical load. It appears that the surface stresses start to deviate from the membrane stress closely after passing the critical load. However, if we consider only the membrane stress one may easily get the impression that the instability is first met for a loading of 1.10-1.15 times the critical load. The stress curves indicate that instability can be accurately modelled using the explicit FE-method. Figure 6.33 shows left the relation between out-of-plane displacement of point A and normalized load. From this curve it

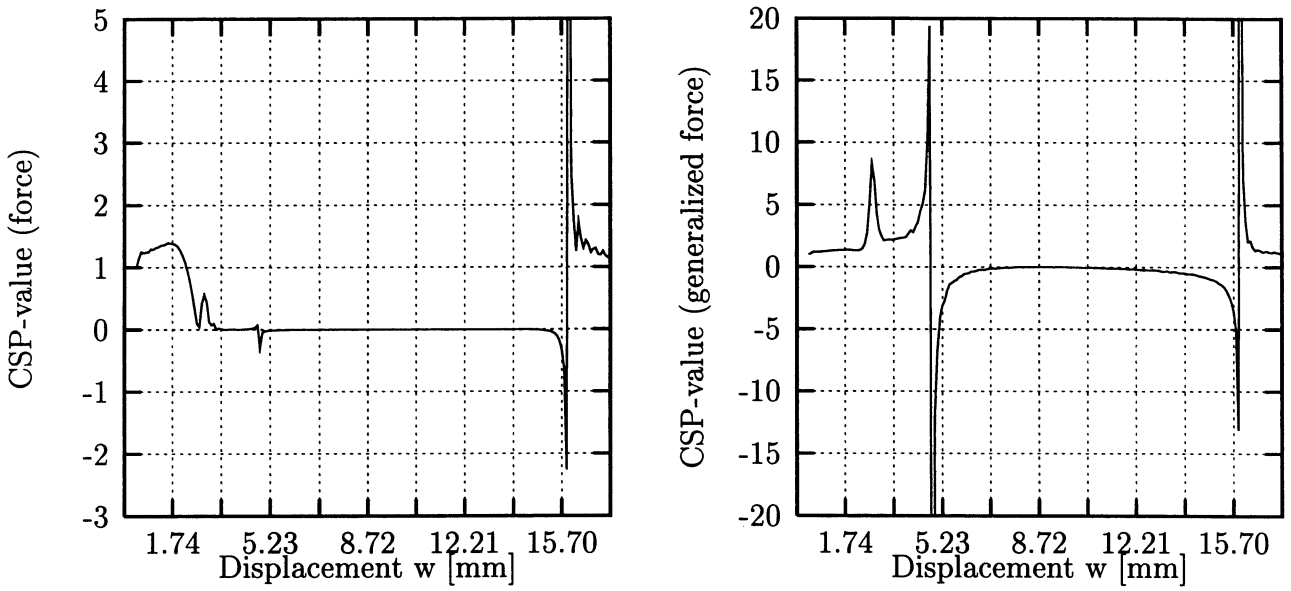

Figure 6.29: *The curves show the predicted variation of the CSP-value calculated for the beam example. Left is given the value calculated from translational displacements and forces, right from generalized forces.*

appears that until the critical load is reached we have an in-plane deformation. The right part shows the relation between the x-displacement of point B and the load level. This curve indicates a linear relation up to the point of critical loading. Figure 6.34 shows the predicted variation of the CSP-value. To calculate the CSP-value two regions are utilized; one with 6 elements (1-6) and one with 36 elements (1-6, 9-14, 17-22, 25-30 and 41-46). The curves shown left are calculated with forces and displacements and the curves shown right are calculated using generalized forces and displacements. The CSP-curves show essentially the same behaviour: The value is steady at a level of one until the critical load is reached. When the critical load is reached we see a drop to a level around zero. After the critical load a small difference can be seen between the region with 6 elements and the region with 36 elements; the small region indicates a more scattered response compared to the large region. The small region indicates also smaller values than the large region. Figure 6.35 gives the variation of the Rayleigh coefficient calculated on the same basis as the CSP-value in figure 6.34. The behaviour is essentially the same for the Rayleigh coefficient as for the CSP-value, however, the Rayleigh coefficient seems to be slightly more influenced by dynamic effects in the period up to the critical load. It can also be noticed that the Rayleigh coefficient calculated from forces and displacements indicates negative values whereas the one based on generalized forces and displacements does not.

As regard the CSP-value and the Rayleigh coefficient a conclusion can be drawn from the plate example: Both the CSP-measure and the Rayleigh coefficient can be used to accurately detect the instability loss. It is obvious that the loss of stability can be found by investigating the stress response, however, if one only consider the membrane stress one may reach a wrong estimate of the instability limit and here the methods may be a tool to ensure that instability points are detected.

Bjaerum [33] investigates the same example and reports figures directly comparable to

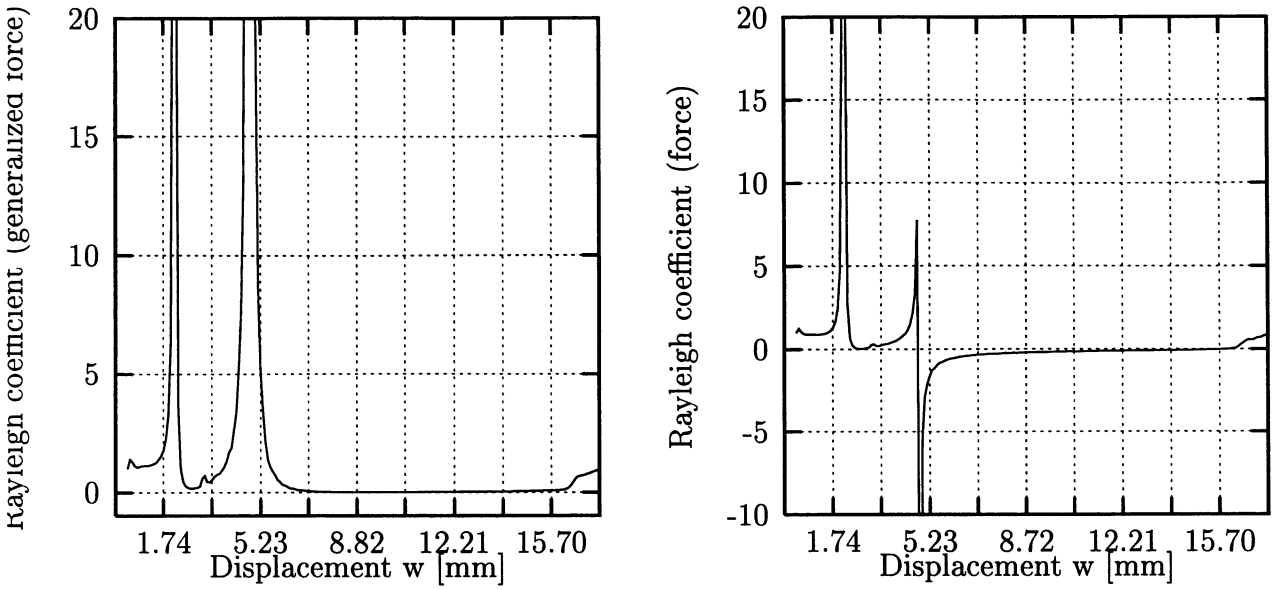

Figure 6.30: *Left is shown the variation of the Rayleigh coefficient based on translations and forces. Right the similar expression including contributions from rotations and internal moments.*

figures 6.33 and 6.34. There is a good agreement between figure 6.33 and Bjaerum's results, however, the displacement curve for point A differs in shape. Bjaerum has a curve which has a horizontal tangent at the critical load, which is different from the results obtained with explicit FE, however, the relation between displacement and load at ≈ 1.2 times the critical load agrees quite well. Also the curve for displacement of point B is rather accurate apart from the region where instability is met.

Bjaerum reports the CSP-value obtained with implicit FE; at the critical load he finds a singularity. Using the explicit FE we indicate a rapid drop, however, due to the artificial damping and inertia effects the singularity is not as clear as the one reported by Bjaerum. In the analysis a damping corresponding to critical damping is specified. After the critical load Bjaerum reports a relatively stable level of the CSP-value of $\approx$ 0.2-0.3. The CSP-curves given here indicate a level of ≈ 0. This is due to the dynamic effects: If the problem is analysed as a quasi-static problem a configuration of equilibrium must be obtained whereas the explicit approach may take a certain time to reach the corresponding configuration. As a matter of fact this can also be obtained with the presented method provided that the loading rate is sufficiently low.

The previous examples show how accurate, the method can be used for detecting buckling points. In the case with the square plate one would hardly notice the onset from stress or displacement curves early enough. This feature of the methods seems to be general to a certain point.

The plate example has also been analysed using Hill's instability criterion. Even though many loading rates, densities, degrees of damping and perturbating forces have been employed, it does not seem possible to predict negative values. This is, however, reasonable: If the problem is modelled with a too low perturbation force no buckling appears and the de-

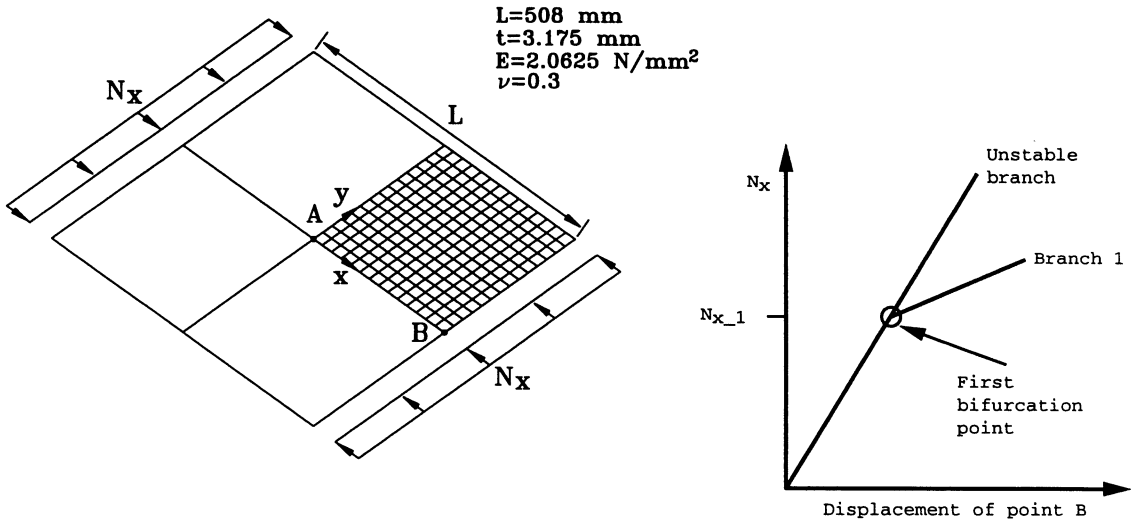

Figure 6.31: *Illustration of elastic plate loaded with in-plane compression. Right is shown the principle of the response for point B either following the primary unstable branch or following branch 1 after bifurcation.*

formation follows the primary (instable) branch. If the perturbation is sufficient to switch the deformation from the instable branch to branch 1 the results is a response similar to the principle shown in figure 6.31. However, although we are passing a bifurcation point this does not in this example lead to a direct unloading for point B.

The conclusion so far for the Hill criterion is that analysis of a bifurcation problem will not be detected if the bifurcation does not lead to an unloading.

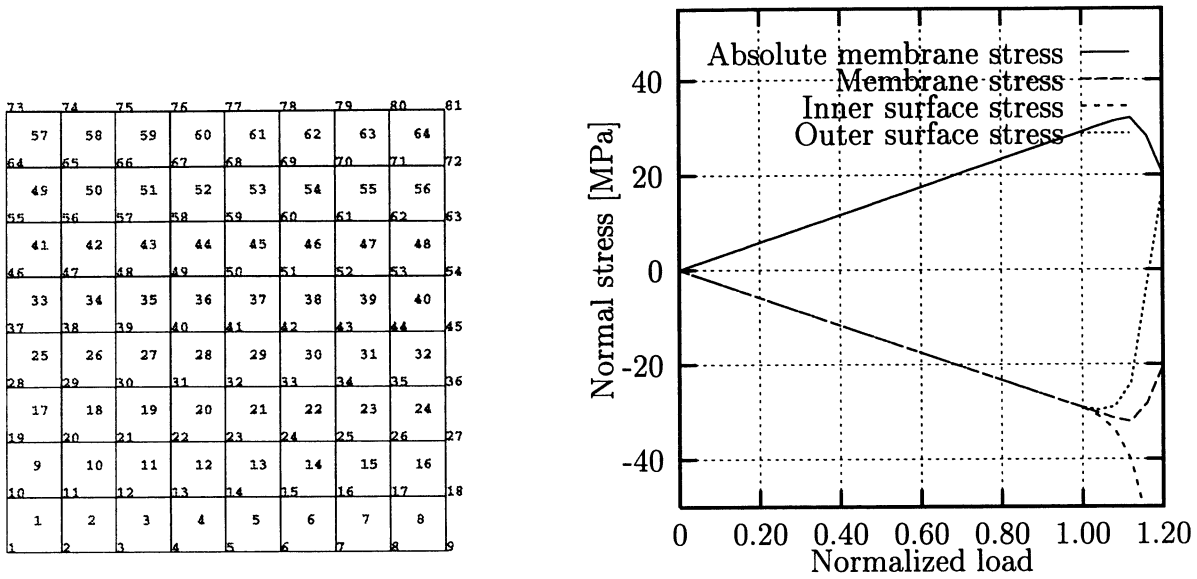

Figure 6.32: *Left: The discretized plate with node and element numbers. Right: The stress response of element 1 (loading direction) at the reference plane and at outer and inner surface, respectively. The normal stress at the reference plane is also plotted using absolute values.*

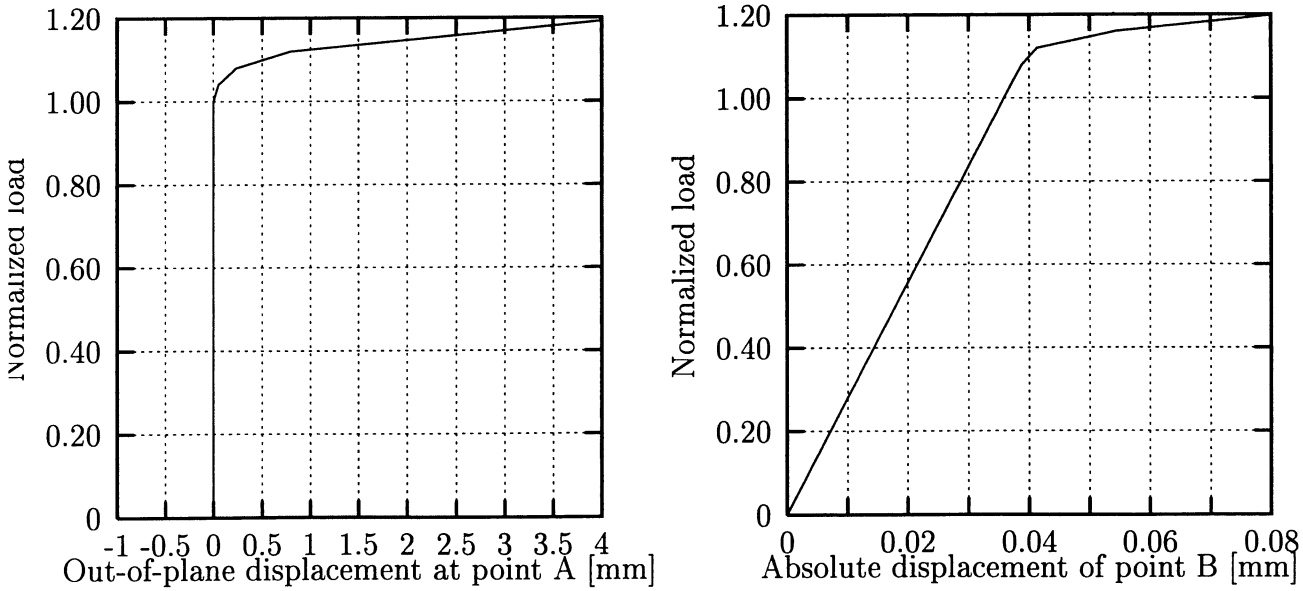

Figure 6.33: *Left: The predicted out-of-plane displacement at point A. Right: Load-displacement curve at point B.*

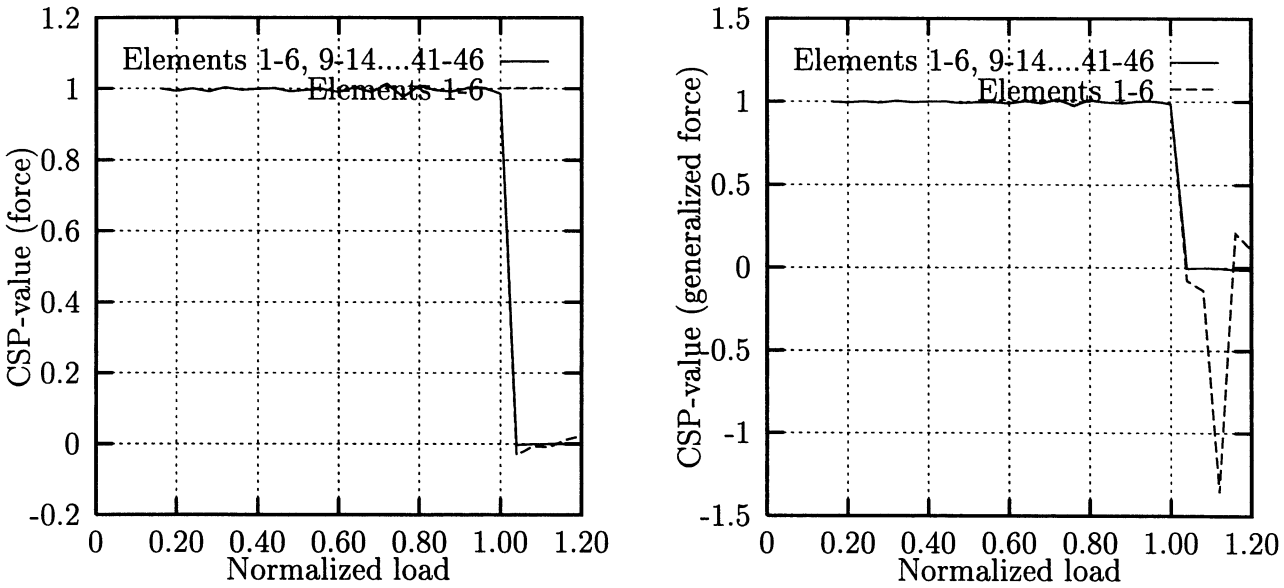

Figure 6.34: *The curves show the predicted variation of the CSP-value calculated for the plate example. Left is given the value calculated from translational displacements and forces, right from generalized displacements and forces. The values are calculated from two regions; one with the elements from 1-6 and one including element numbers: 1-6, 9-14, 17-22, 25-30, 33-38 and 41-46.*

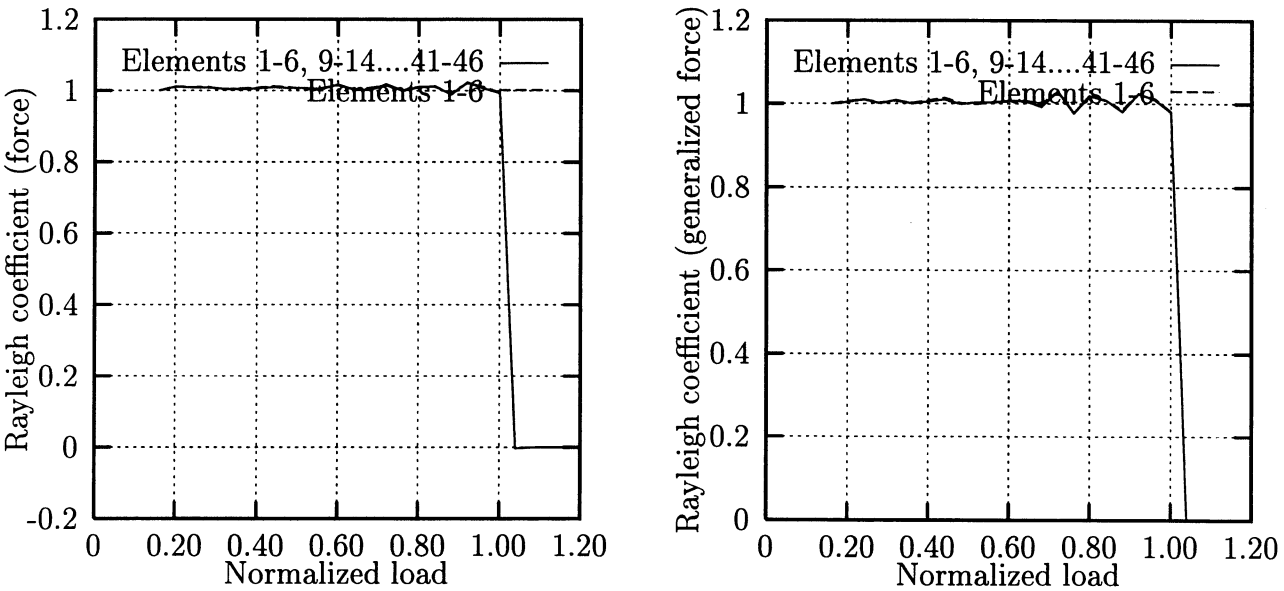

Figure 6.35: *The curves show the predicted variation of the Rayleigh coefficient calculated for the plate example. Left is given the value calculated from translational displacements and forces, right from generalized displacements and forces. The values are calculated from two regions; one with the elements from 1-6 and one including element numbers: 1-6, 9-14, 17-22, 25-30, 33-38 and 41-46.*

6.11 Analysis of wrinkle formation for an isotropic cup

It is often argued that the explicit finite element method is the most reliable in connection with investigations of wrinkle formation. This is in my opinion more related to the fact that explicit finite element handles formation of wrinkles without problems with convergence. The formation of wrinkles can often lead to problems when using an implicit approach. But one may ask the question - how reliable are the explicit methods and how accurate are the predicted wrinkle formations? In this and the following section a summary of a numerical investigation of cup drawing is given and the two aspects discussed are loading rate and anisotropy and their influence on the predictive capability.

The loading rate used in connection with explicit methods is raised significantly compared to most practical loading rates. In this connection one can expect that a sort of limit exists beyond which the solution becomes so severely influenced by impact and inertial effects that the solution is far from the quasi-static behaviour. At least we can see this influence for elastic problems and it should not be expected to be of less importance for problems involving plastic deformation. Dealing with the wrinkle behaviour this may be even more important than for a stable process. Regions which start wrinkling decrease significantly in stiffness and the importance of inertial effects may increase many fold compared to a stable process running without the appearance of instability problems.

Bazant and Cedolin [21] argue that instability events combined with unloading always will be influenced by dynamic effects as it is hard to imagine that phenomena like for example the buckling of a beam can be analysed correctly assuming a quasi-static behaviour.

6.11.1 FE-discretization

In the following sections a discussion is given on analyses of cups. These analyses are performed using the discretization shown in figures 6.36 and 6.37. Material behaviour is

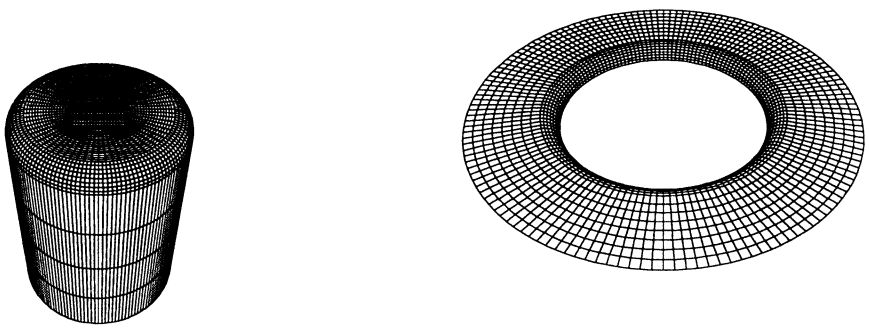

Figure 6.36: Discretization of punch and die used for simulation of the deep drawing of cylindrical cups.

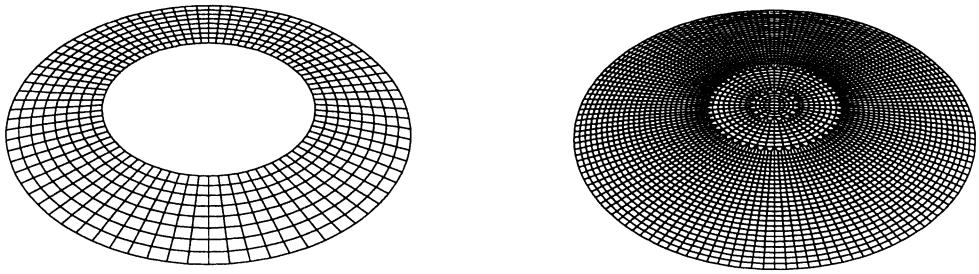

Figure 6.37: Discretization of blank holder and blank used for simulation of the deep-drawing of cups.

modelled as isotropic elastic-plastic and hardening is following a Hollomon-Swift hardening curve.

6.11.2 Analysis without blank hold

In order to evaluate the effect of loading rate three analyses are performed using different loading rates. The process modelled is a cup drawing using an isotropic material. The process time is set to 10 msec in the three analyses and a sine shaped velocity profile is used for prescribing the punch displacement leading to a total punch displacement of 43 mm at 10 msec. The loading rate is changed through variation in the mass properties for the blank.

The analyses are identical apart from changes in the base density and minimum time step (used in the mass scaling). The conditions used in the analysis are:

- Conditions 1: $\rho = 8.1e^{-9}\ ton/mm^3$ and $\Delta t = 0.3\ \mu$sec.
- Conditions 2: $\rho = 4.05e^{-9}\ ton/mm^3$ and $\Delta t = 0.15\ \mu$sec.
- Conditions 3: $\rho = 2.025e^{-9}\ ton/mm^3$ and $\Delta t = 0.075\ \mu$sec.

Figure 6.38 shows the predicted flange height for three analyses performed under conditions 1, 2 and 3. From figure 6.38 a very clear difference is seen between the three loading rates. The fastest analysis (1.00) leads to a much smaller flange height and what may be more important (and also the reason for the first observation) is that a higher wrinkle mode is predicted. Another aspect which can be noticed is that the flange height in 0° and 90° do differ in each of the analyses. This deviation should not be expected as the model is made axi-symmetric, the only non-symmetry included is due to the discretization of the blank. The discretization of the blank is, however, symmetric around the line y=x so the non-symmetric effects of the mesh should not be detectable as a difference between values in 0° and 90°. Figure 6.39 shows the predicted punch force for the three loading conditions. Looking at figure 6.39 one may at first glance get the impression that the process is stable up to a level around 3 msec. However, from figure 6.40, which shows the z-displacement of the flange, it can be seen that there is a clear formation of wrinkles already at 2 msec.

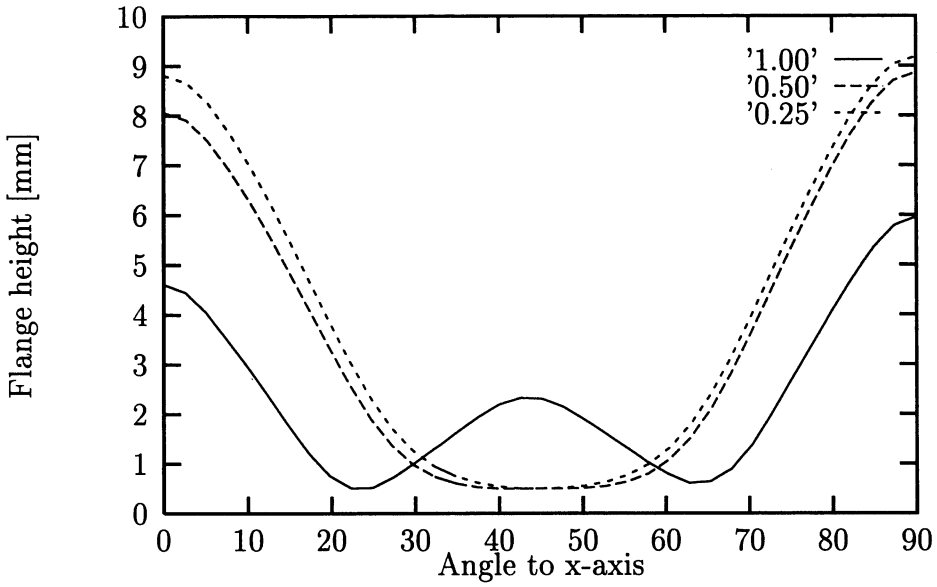

Figure 6.38: *The calculated flange height for three different loading rates. Label 1.00 corresponds to condition 1, 0.50 and 0.25 to conditions 2 and 3, respectively. The analyses have been performed using material 18 in LS-Dyna3d (isotropic, power-law hardening). The flange height is initially 0.5 mm (half the plate thickness) which should be subtracted from the actual values in the figure.*

In the right part of figure 6.39 the punch force is plotted in a close view and it can be seen that at 1.7 msec there seems to be a variation in the development of punch forces. It is postulated that this point corresponds to the wrinkle onset for analyses with condition 2 and 3 (the analyses with the highest loading rate). However, effects of this type could easily be overlooked in the postprocessing, especially for problems where the wrinkling do not lead to overall loss of carrying capacity.

In section 4.10.1 it is proposed to check the inertial effects by monitoring the resulting force on the blank. In this case it turns out (very clearly) that this check does not indicate whether the loading rate is sufficiently slow or not. In figure 6.41 is shown the contact forces arising from punch and die for the analysis under condition 1. Figure 6.41 indicates a very limited deviation between the forces and using this deviation as criterion for whether the analysis is run too fast or not fails here in connection with formation of wrinkles - the predicted flange height shown in figure 6.38 indicates that there is a significant difference between the predicted response for condition 1 compared to the response for conditions 2 and 3.

Formation of wrinkles can in this case not be considered a global instability and two possibilities remain: The formation of wrinkles is a stable process or the formation is due to local loss of stability, a loss which is not detected in a more global measure as for instance the punch force.

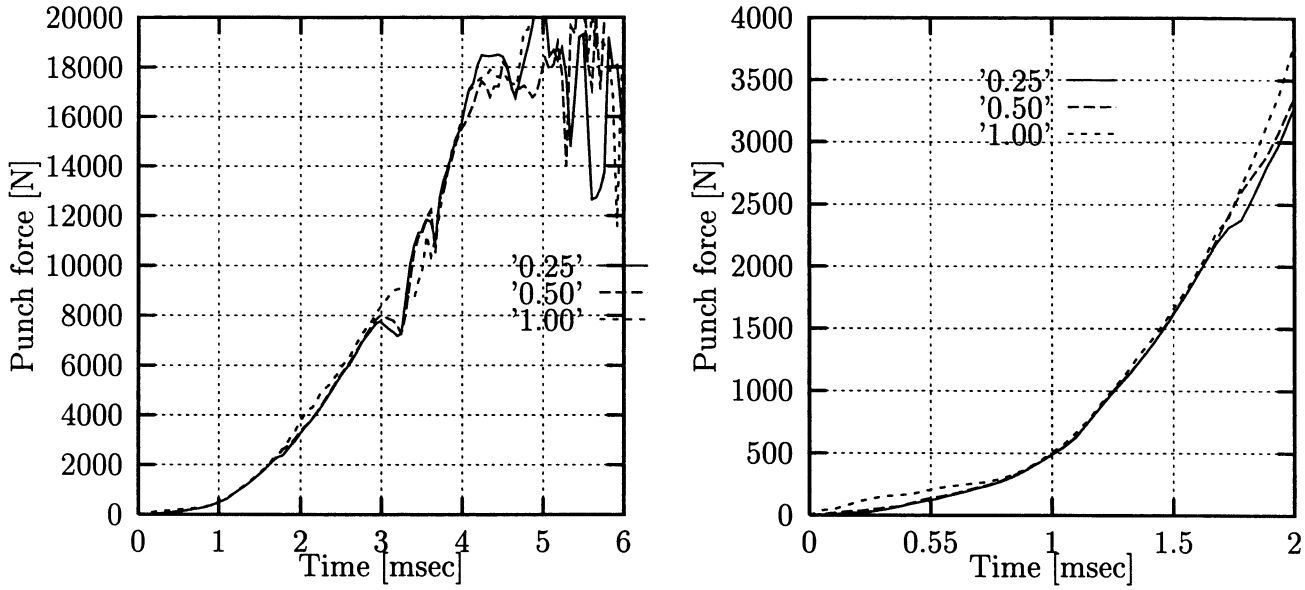

Figure 6.39: *The predicted punch force plotted for three loading rates. Left seen over an analysis time of 6 msec, right over 2 msec.*

6.11.3 Analysis with 4 kN blank hold

As a major variation could be seen for the example without blank hold a similar study is performed for the example where a blank hold of 4 kN is applied during the process. The material is still modelled as isotropic.

Here two variations of density/time step are analysed, 1) full density ($\rho = 8.1e^{-9}\ ton/mm^3$) and a time step of 0.3 μsec, 2) half density ($\rho = 4.05e^{-9}\ ton/mm^3$) and a time step of 0.15 μsec corresponding to analysis conditions 1 and 2, respectively, in the previous section.

Looking at the two cups at a process time of 4.5 msec only a limited difference can be seen for the overall geometry, as shown in figure 6.42, where the deformed meshes are shown for condition 1 and 2 (left and right). Based on figure 6.42 one may claim that the results are in a reasonable agreement with regard to the formation of wrinkles. In figure 6.43, which shows the predicted z-displacement at 3 msec, a marked difference in the formation of wrinkles can be seen. Under condition 1 12 wrinkles appear (left part of figure 6.43, but condition 2 leads to a formation of 16 folds (right part). The folding arising here is, however, the result of an even earlier formation where only 8 wrinkles formed; this is illustrated in figure 6.44. The same conclusion as drawn from the example without blank hold can be made: Raising the load rate may lead to a too high wrinkling order. However, in this example the resulting number of folds becomes the same, which is the 16 folds also found from experiments (see perhaps figure 6.48).

Another observation which should be mentioned: It is very important to postprocess the results accurately in order not to overlook events which indeed are present in the numerical results at an intermediate stage, but which cannot be detected from the final geometric configuration.

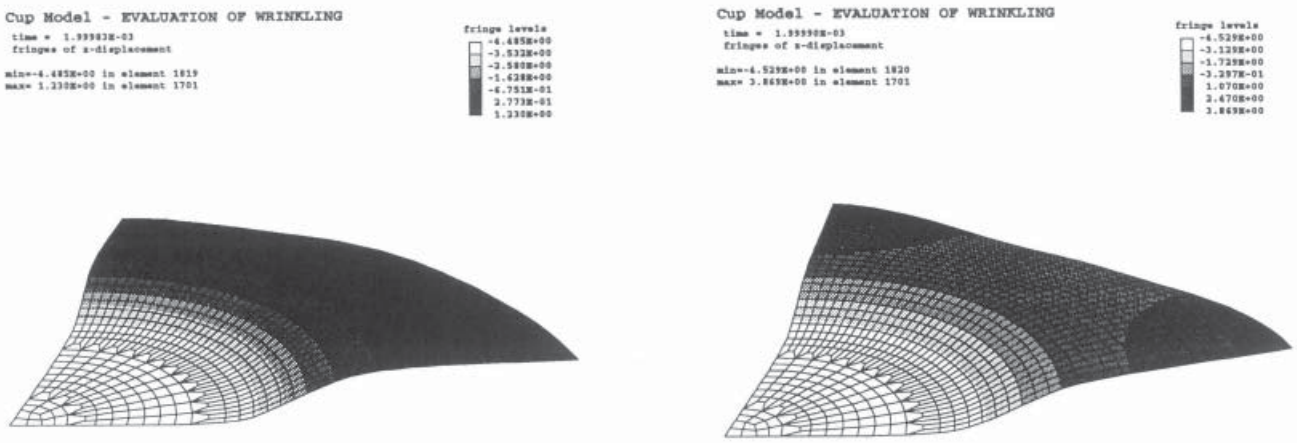

Figure 6.40: *The predicted z-displacement at 2 msec under condition 1 (left) and under condition 2 (right).*

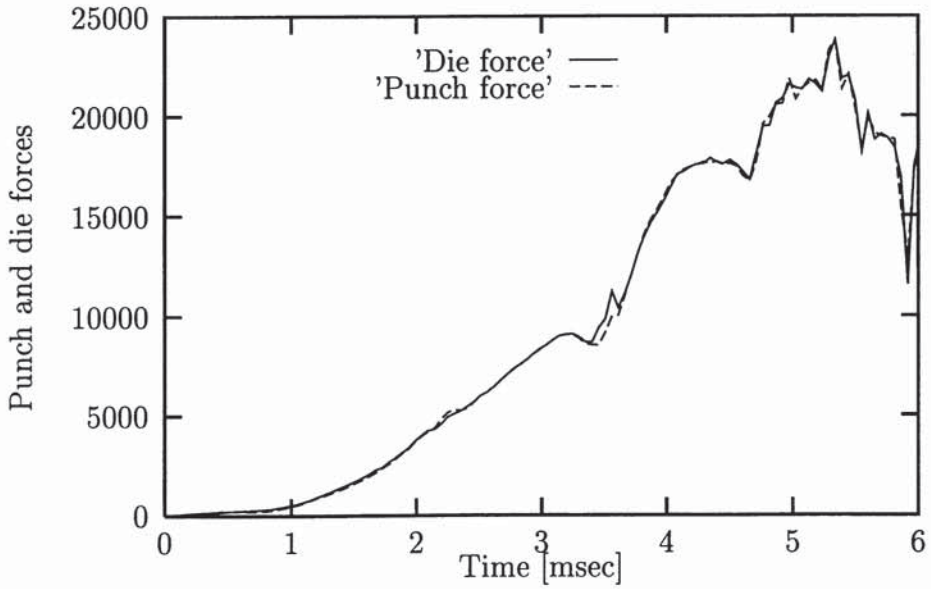

Figure 6.41: *Contact forces (z direction) between punch and blank and between die and blank for the simulation with condition 1. No blank holder is used which for a quasi-static analysis means that the die and punch force should be equal.*

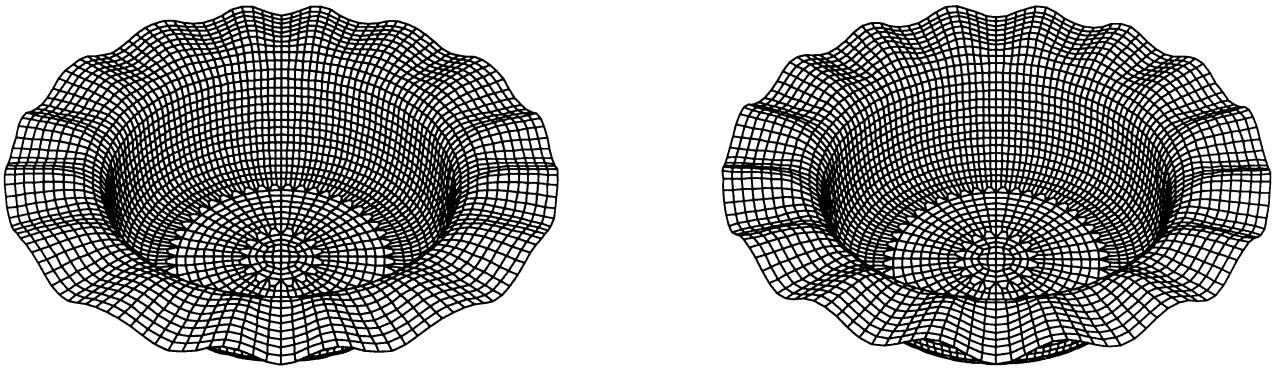

Figure 6.42: *The predicted shape at 4.5 msec predicted with condition 1 (left) and with condition 2 (right). The applied blank hold is 4 kN.*

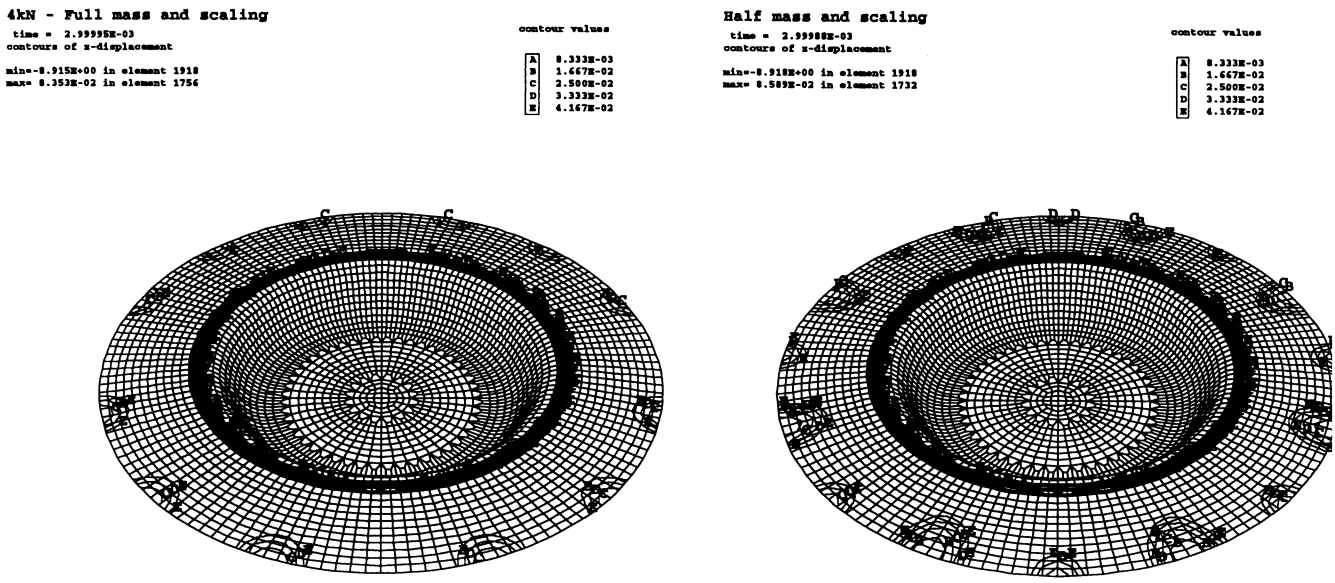

Figure 6.43: *The predicted z-displacement at 3 msec using condition 1 (left) and condition 2 (right). The applied blank hold is 4 kN.*

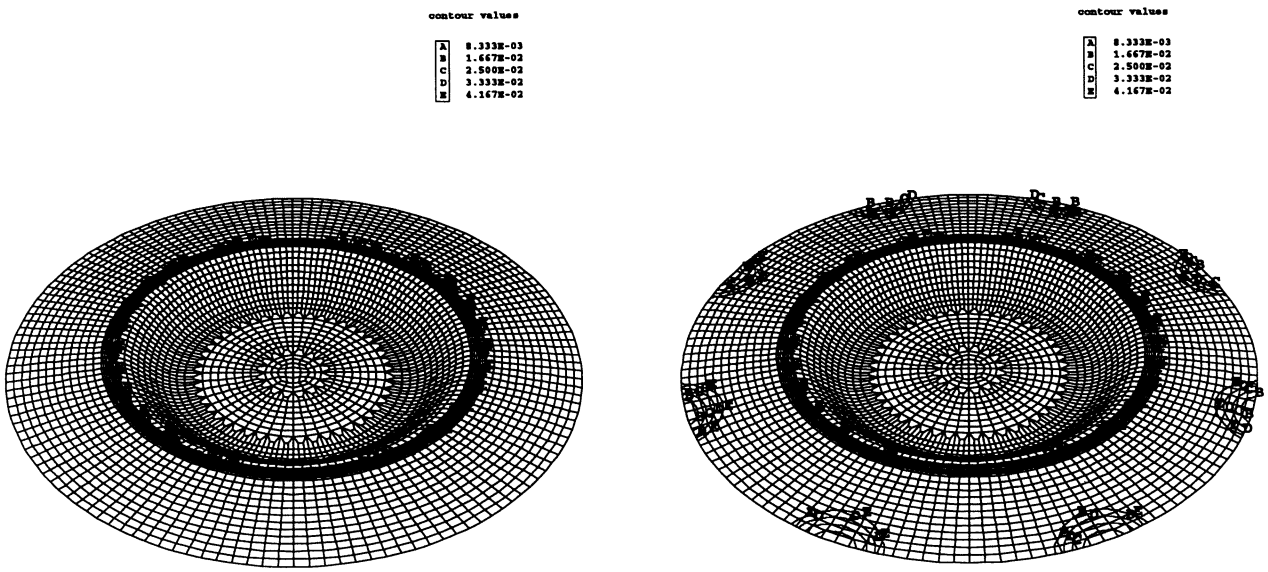

Figure 6.44: *The predicted z-displacement at 2.5 msec with condition 1 (left) and condition 2 (right). The applied blank hold is 4 kN.*

6.12 Analysis of wrinkle formation for anisotropic cups

The analyses in section 6.11.3 are for a cup with isotropic material, but most metal sheets show a pronounced anisotropy and this is most likely to influence the wrinkling behaviour. In this section the example examined in the previous section is analysed taking anisotropy into account in the constitutive modelling. The material is modelled using Barlat's 2-D criterion, the exponent M is set to 8 and remaining parameters in the yield criterion are calculated from Lankford coefficients. The discretization is the same as shown in section 6.11.1. The process is simulated for various blank holder forces and the numerical predicted folding is compared to experiments.

As base for the analyses the results obtained by Damborg and Jensen [49] for deep drawing of stainless steel cups have been chosen. In figure 6.45 is shown the tool geometry and table 6.2 lists the most important parameters for the analyses as well as the material parameters. Depending on the level of blank hold various wrinkle modes are formed. A higher blank

Steel type	E[MPa]	ν	C[MPa]	n	R_{00}	R_{45}	R_{90}	$\bar{R}$	ΔR
DIN 1.4301	200000	0.3	1358	0.41378	0.85	0.99	0.92	0.94	-0.11

R_p	R_{pn}	R_d	R_{ds}	R_{bla}	t_{bla}
23 mm	6 mm	25 mm	4 mm	46 mm	1 mm

Table 6.2: *Geometry and material data used for the simulation of deep drawn stainless steel cups, values are from Damborg and Jensen [49].*

hold leads to a higher wrinkle mode. In figure 6.46, 6.47, 6.48 and 6.48 are shown the resulting geometries when using blank holder forces of 0, 1.6, 4.0 and 7.0 kN, respectively. Figure 6.46 shows a cup drawn without blank hold. A very good relation between experiment and analysis can be seen. The results are similar to the analysis performed with an isotropic material. Applying a blank hold of 1.6 kN leads to the results shown in figure 6.47. Here 9 wrinkles are formed in the experiments whereas 12 wrinkles are formed in the

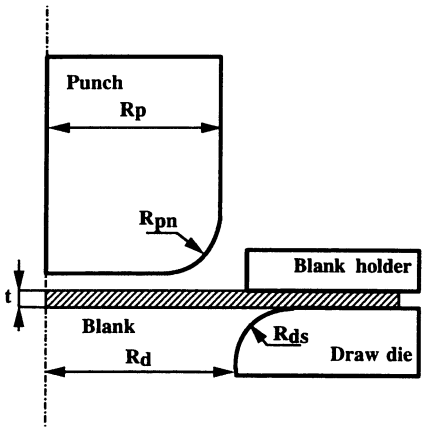

Figure 6.45: *Illustration of geometry for the stainless steel cup drawing.*

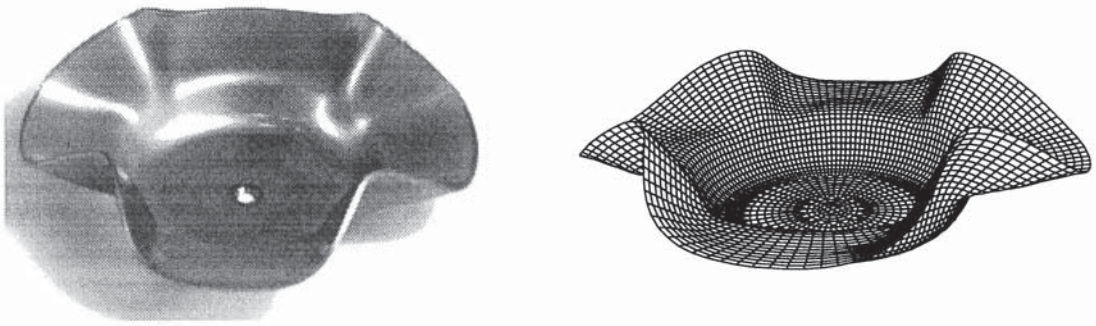

Figure 6.46: *Cup drawn without blank hold.*

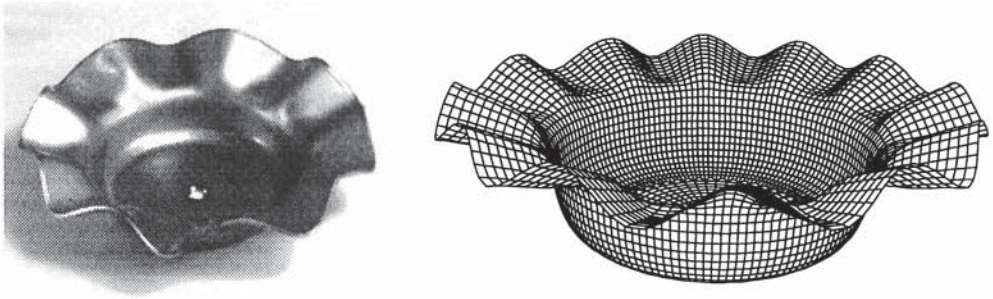

Figure 6.47: *Cup drawn with a blank holder force on 1.6 kN.*

simulation. The overall impression is that there seems to be a reasonable agreement of the size of folds. As only a quarter of the cup was modelled in the simulation a mode with 9 folds cannot be predicted due to the boundary condition arising. Raising the blank hold

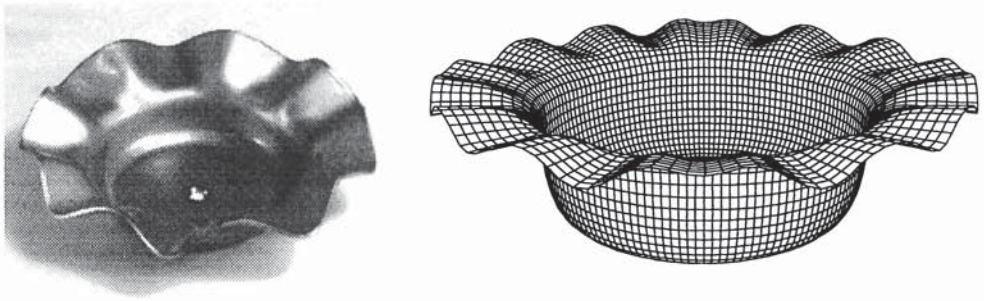

Figure 6.48: *Cup drawn with a blank holder force on 4.0 kN.*

to 4.0 kN leads to the results shown in figure 6.48. Here both experiment and analysis indicate 16 wrinkles. This example corresponds to the one analysed with isotropic materials in section 6.11.3 where 16 wrinkles are also predicted. The experimental cup does clearly show variation of the size of the wrinkles. This is also found from the numerical analysis with anisotropic material behaviour where a similar variation can be found. The isotropic cup analysis does not indicate any variation of the same type. Figure 6.49 shows left the cup processed experimentally and right the corresponding cup from the analysis at a slightly earlier stage in the process. Again an influence from the non-uniformity caused

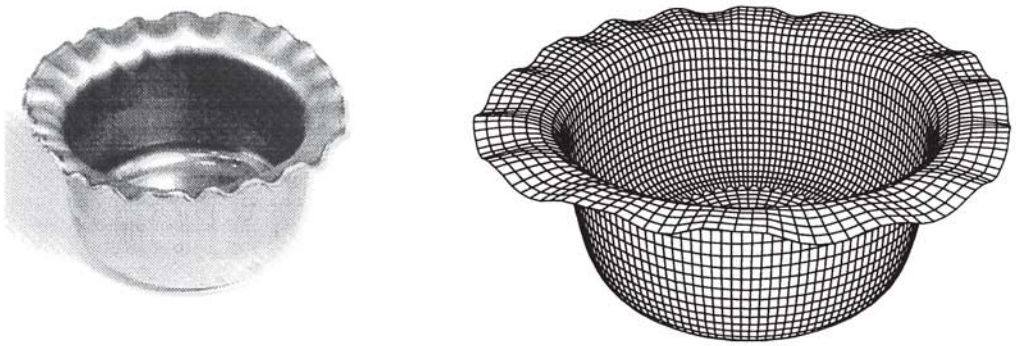

Figure 6.49: *Cup drawn with a blank holder force on 7.0 kN.*

by material anisotropy can be seen in the analysis results. The analysis predicts fewer wrinkles compared to the experiments. Two reasonable explanations can be that the blank hold in the experiments has either been slightly higher than 7 kN or the flange is hardened so severely that the utilized Hollomon-Swift model gives a wrong estimate of the yield stress as function of plastic strain. If the analysis is continued more wrinkles develop, but this mode is judged to be too severely affected by the relatively coarse mesh to give reasonable results with regard to an evaluation of the influence from anisotropy on the wrinkling behaviour.

The figures 6.46 to 6.49 do clearly indicate how accurate the post-wrinkling can be predicted. It is clear from both the experiments and the analysis that the number of wrinkles is strongly influenced by the level of blank hold; this effect has been found by several authors using experimental and analytical approaches, respectively. It can also be seen from both the experiments and the analysis that anisotropic material behaviour has a strong influence on the resulting wrinkles. Especially figures 6.48 and 6.49 illustrate how inhomogeneous the formation of wrinkles can be.

To better illustrate the development of the wrinkled rim the analysis with anisotropic material and a blank hold of 4 kN is considered. When deep drawing an anisotropic cup the anisotropy will lead to a non-uniform stress distribution relatively early in the process and it should be expected that this variation affects the wrinkling at least to some degree.

Using the Barlat criterion leads to formation of 4 relatively thick zones and also 4 relatively thin zones. Apparently one should expect the possibility that a formation of 4 wrinkles is initiated by material anisotropy - this seems to be the case for the present example.

In figure 6.50 is shown the predicted flange height for a quarter blank as function of the angle to rolling direction at various stages in the process, left is given the flange variation at 5 stages between 1.5 and 3.5 msec. Right is given four stages from 3.5 to 5.0 msec. The curve for 3.5 msec is included in both the left and the right part of the figure. Early in the process (at 2 msec) two regions are slightly lifted - this may purely be due to the anisotropic deformation leading to a non-uniform distribution of thickness. At 3 msec two zones are lifted (approximately at 10° and 45° - this mode is a shift compared to the mode at 2.5 msec. The mode at 2.5 msec may be explained from the thickness variation. When

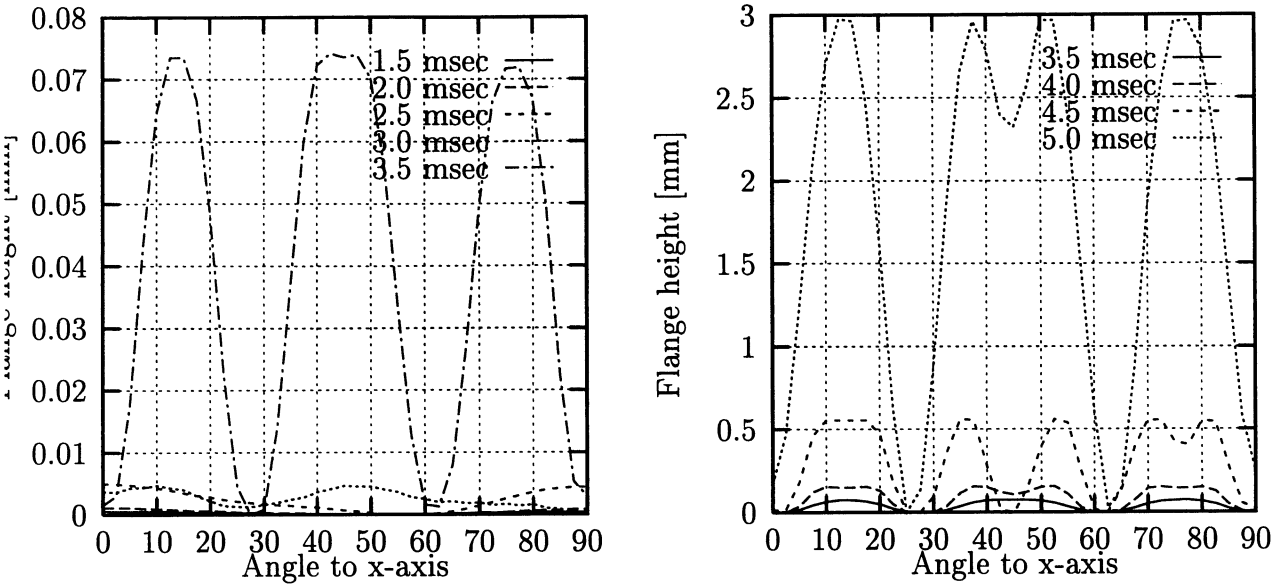

Figure 6.50: *The predicted flange height at various stages in the process.*

a simulation time of 3.5 msec is reached it is clear that three wrinkles are formed over 90°, but at 4.0 msec four folds are present (forms in 45°) followed by the formation of a fifth fold (at 75°) at 4.5 msec. The latter, however, is not visible in the final flange height, whereas the fourth fold can be seen.

This formation of wrinkles shifting from one number of folds to another is believed to be very typical for the formation of wrinkles for anisotropic material. This is also supported by the experiment where a non-homogeneous distribution of folds, see figures 6.48 and 6.49, can be found.

6.12.1 Conclusion drawn from analysis of cup wrinkling

Based on the analyses it is concluded that if wrinkle formation is to be predicted in a reliable manner it is important to check the influence from inertia. It is clear that if a too high instability mode is predicted to be the lowest then erroneous interpretation of results may arise.

It can be concluded that explicit FE can model the onset and formation of wrinkles. But it is also shown that the predicted wrinkling mode to a high degree is dependent on the mass scaling used. In other words - just looking at the interface forces in order to evaluate whether the rate of scaling is reasonable or not may lead to a wrong conclusion - it is necessary to perform sensitivity analysis to evaluate if the loading rate/mass scaling does influence the results and eventually check whether the lowest mode has been predicted or not. A bad FE-model (regarding mesh size, element shape, etc) and/or a too high loading rate may yield results for the wrinkling behaviour which are quite different from the results obtained using a "good" FE-model and a slow loading rate.

Another interesting observation is that there seems to be a strong relation between anisotropy and formation of wrinkles. Looking at the punch forces it is indicated that the folding onset

may be much more stable than the traditional treatments claim. This postulate is also supported by illustrations of flange height during the process. The predicted flange height variation indicates the formation of wrinkles at a much earlier stage than predicted using the "traditional" methods. One may argue that the formation of wrinkles is not necessarily connected to loss of load carrying capacity - which is easily detected by monitoring the punch force.

Based on the observations from this section it is again strongly emphasized that the material behaviour must be modelled as accurately as possible.

It can also be noticed that for elastic buckling of beams it seems to be necessary with 10-16 elements in order to predict the instability limit whereas we for the present deep drawn cup can predict the deformed shape and the deformation mode with a very good accuracy with relatively few elements for each wave. However, even the resulting deformations seem reliable one may expect that the predicted load limit is too high due to a too coarse discretization.

6.13 Anisotropic cups - predicted loss of stability

The same cup drawing process as the one in section 6.12 with a blank hold of 4 kN is considered. The material is modelled as anisotropic with Barlat's criterion and the purpose is to illustrate the use of Hill's uniqueness criterion as discussed in section 6.5 with regard to prediction of instabilities.

The analyses performed for beams indicated that even a rather complicated structural behaviour could be well predicted/described by dumping the current value of Hill's criterion during an analysis. Coming to a more realistic plastic forming operation gives some limitations: Firstly, the loading rate is high and secondly, the loading is dominated by a biaxial strain/stress state which may change significantly during deformation leading to effects as thickening followed by thinning (or reverse). These two aspects make the predicted response much more difficult to decode. It has therefore been chosen only to look at the minimum value of Hill's criterion experienced during the simulation. This has the advantage that all negative values encountered are shown. Figure 6.51 shows the regions

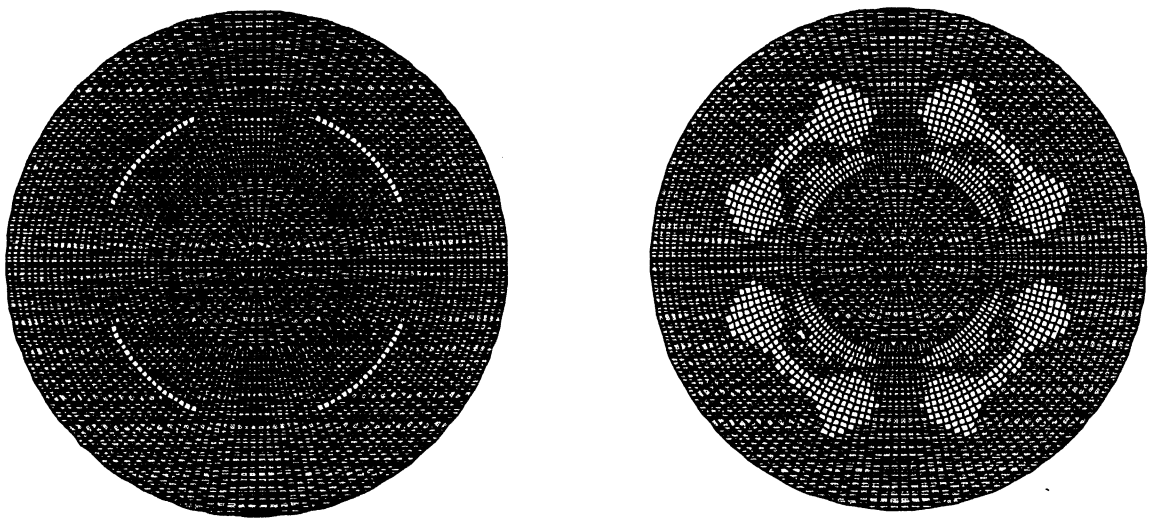

Figure 6.51: *Distribution of the Hill criterion at 1.25 and 2 msec (accumulated minimum value).*

which have experienced negative values in Hill's criterion. The light zones indicate negative values whereas a darker grey region indicates positive values. The left figure shows that only four rows of elements have experienced loss of stability in the time span 0-1.25 msec. These regions are placed directly over the start of the die shoulder. The direct interpretation of this pattern is that loss of stability is initiated at the die shoulder and furthermore I interpret this mode as the one leading to four folds. Later in the process (at 2 msec, right part of the figure) a shift in the pattern can be noticed - the instable regions are split up in 8 areas. This shift may indicate a shift from a wrinkle mode with four wrinkles to a mode with 8 wrinkles. Another aspect which should be noticed is that the zone over the punch nose is predicted to loose stability as well. This may very well be the case as we early in the process do have negative hoop stresses for this zone. However, for a cylindrical shape the wrinkling mode will be directed inwards - a mode with outward wrinkles would demand a significant straining of the material. However, before the wrinkles reach critical levels the

growth of this mode is constrained by the punch. In figure 6.52 is given similar plots of

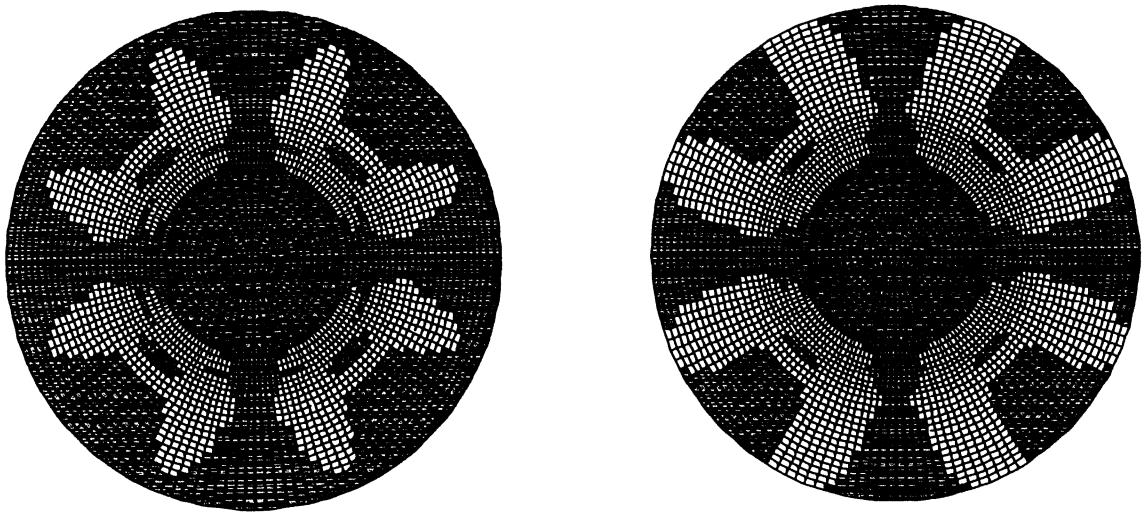

Figure 6.52: *Distribution of the Hill criterion at 2.25 and 2.5 msec (accumulated minimum value).*

Hill's criterion at 2.25 and 2.5 msec. The left part shows a continued growth of the regions with negative values, but the overall pattern is the same as for 2 msec (figure 6.51). At 2.5 msec the regions have grown to reach the outer flange and one may expect this limit to be important for the overall behaviour: When reaching the edge the region looses some of the stabilizing effect from the surrounding material. Figure 6.53 shows left the continued

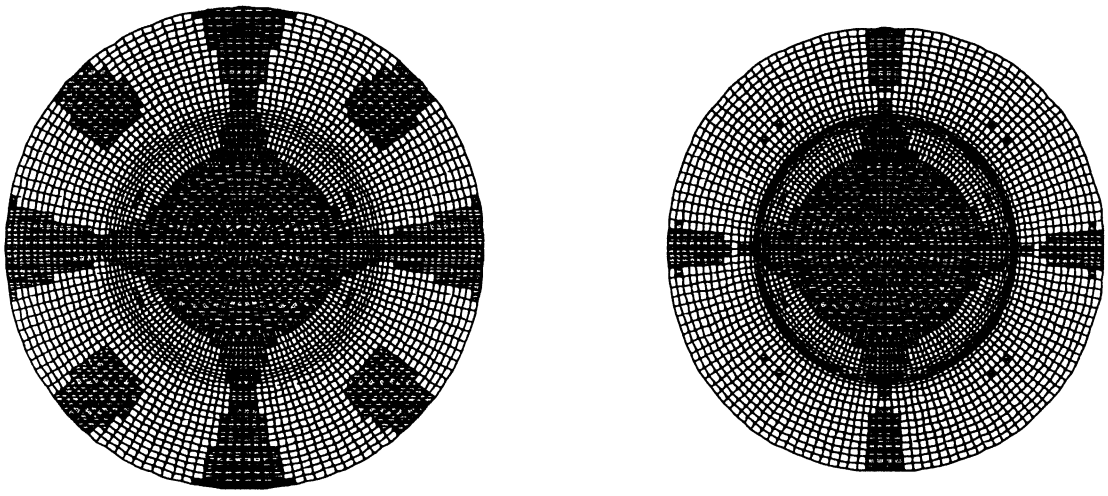

Figure 6.53: *Distribution of the Hill criterion at 3.0 and 3.95 msec*

development of the areas with negative values with the same pattern as is obvious at 2 msec. The right part shows the situation at 3.95 msec - at this stage we can see that the regions have grown together. Here it can also be noticed that this effect appears right over the start of the die shoulder. Figure 6.54 shows the predicted z-displacements (orthogonal to the die surface) at 2.5 and 3.0 msec, respectively. Here we can see that a clear shift takes place from one mode to another: At 2.5 msec we see 8 regions at the outer flange with low

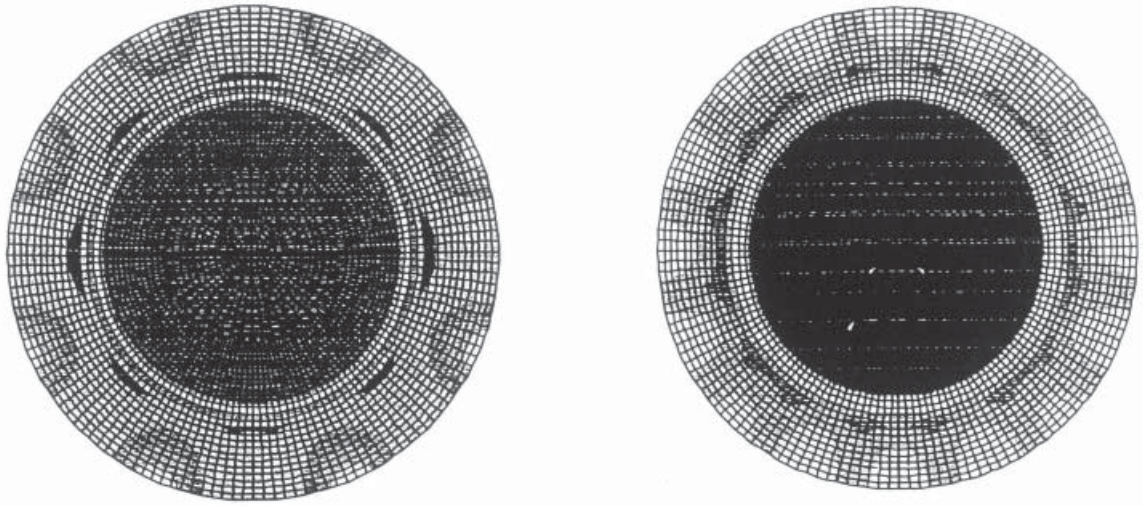

Figure 6.54: *Fringes of z-displacements plotted for the range 0 to 0.2 mm at time 2.5 and 3.0 msec.*

values (light zones are close to a displacement of 0) and for 3 msec we see a clear pattern of 16 wrinkles. From the left figure we can also see that the regions with major displacement (dark zones close to 0.2 mm) indicates a periodicity of 8, however, looking closely at the figure reveals that the dark regions (at 90° and 270° to the rolling direction) seem to have started splitting up. This effect is more clear in the right figure where 16 dark regions with high values are clearly seen, but we can still see that these regions originate from the 8 dark regions indicated in the left figure. These observations indicate that the formation of resulting wrinkles not is due to a bifurcation switching from a membrane loading to the wrinkled configuration. Another observation is that the earlier modes seem to arise from the die shoulder. Whether the shift from 8 to 16 wrinkles is initiated from the outer flange or from the die region cannot be detected from the presented results - however, Hill's criterion do with the current implementation indicate that loss of stability occurs initially at the die shoulder. In figure 6.55 is shown the effective plastic strain distribution. At

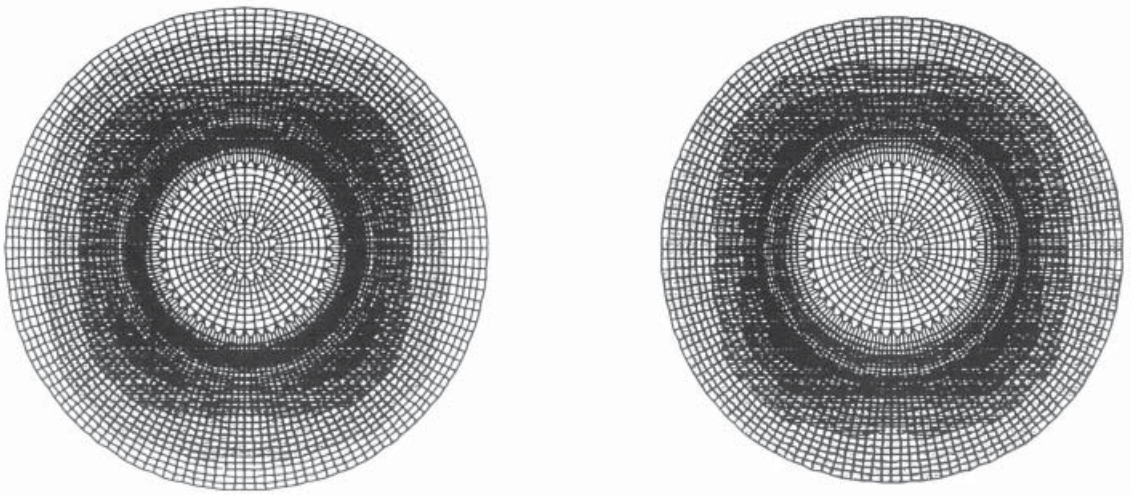

Figure 6.55: *Distribution of effective plastic strain at outer surface at time 3 and 3.5 msec.*

3 msec we can see that at the outer part of the flange a periodicity of more than 4 does exist. For the part closer to the draw die the periodicity is 4 and judged to be primarily due to anisotropy. Figure 6.56 gives the plastic strain distribution at 3.7 and 3.75 msec.

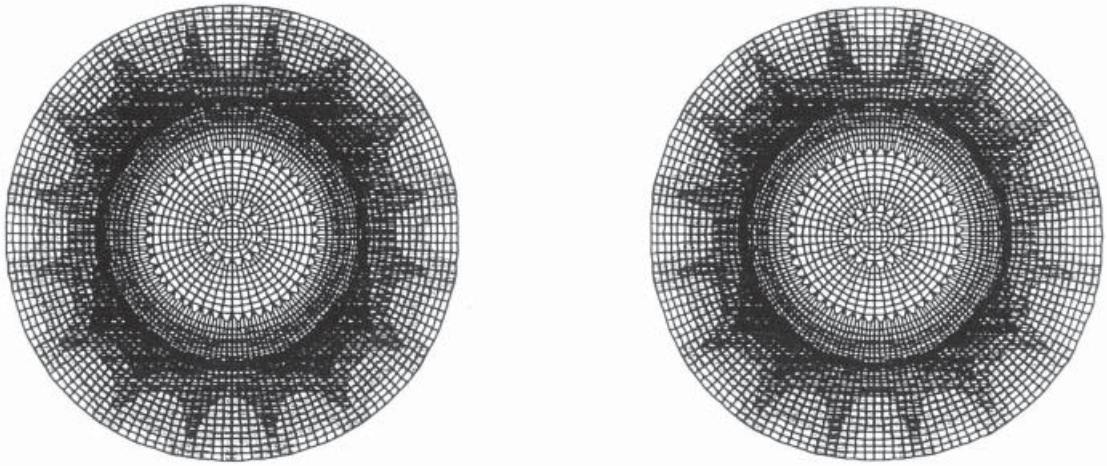

Figure 6.56: *Distribution of effective plastic strain at outer surface at time 3.7 and 3.75 msec.*

At 3.7 msec we have the highest effective strain over the die region due to bending. The next level of strains do have a periodicity of 4 with a tendency of 8 corners indicating a periodicity of 8 but the flange does clearly show 16 wrinkles. The picture at 3.75 msec has more or less the same characteristica, however, the periodicity of 8 is less pronounced. The 16 wrinkles have grown and are dominating the major part of the flange. Another aspect which should be mentioned is that the strain variation is significant: The maximum value for the plastic strain at 3.7 msec is 0.25 and the difference between fringe values is 0.04. Figure 6.57 shows the circumferential stress (at the outer shell surface) in the flange

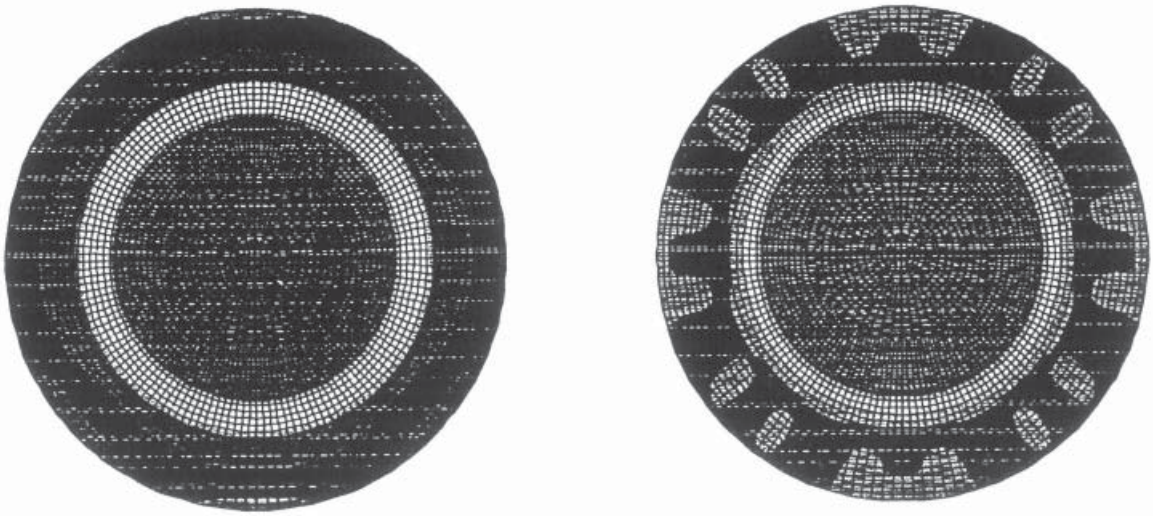

Figure 6.57: *Distribution of circumferencial stress at outer shell surface at time 2.0 and 2.5 msec.*

at 2 and 2.5 msec: The dark zone shows the minimum stresses and the grey zone shows

regions with slightly higher stresses. The left figure shows that a small variation does exist at 2 msec and this variation may be due to anisotropy of the sheet, at least the variation corresponds to the variation that should be expected from the variation in the R-values. The right figure (at 2.5 msec) shows a quite different picture. The variation now follows a pattern with a periodicity of either 8 or 16. It seems that the regions caused by anisotropic deformation at 0°, 90°, 180° and 270° are splitting up in two regions and at the same time 8 regions do exist at regions in between the original four regions with slightly higher stresses. This may indicate that the anisotropy has a strong influence on the folding behaviour: The regions at 0°, 90°, 180° and 270° may start from the edge of the flange whereas the folding between these areas seems to start from the interior part of the flange (this effect is similar to the effect discussed from figure 6.50 showing the development of wrinkles). Figure 6.58

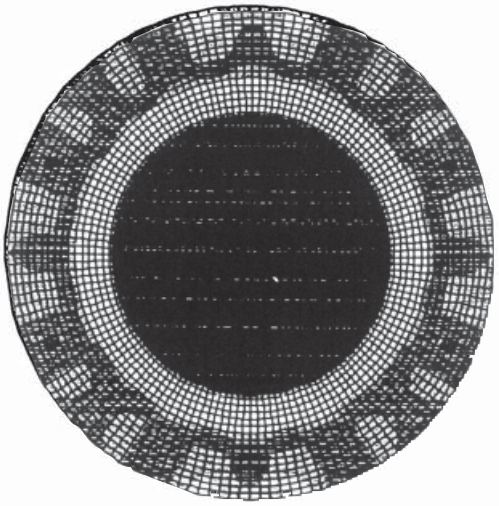

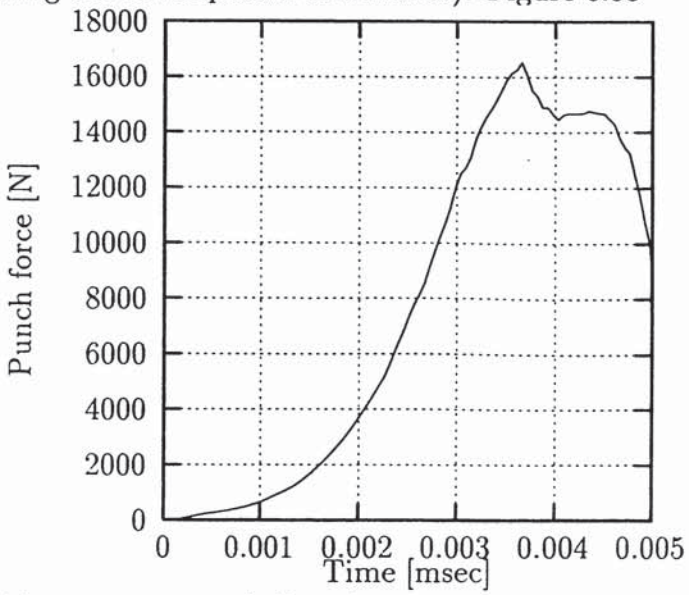

Figure 6.58: *Distribution of circumferencial stress at outer shell surface at time 2.75 msec and right: The predicted punch force.*

shows left the circumferential stresses at 2.75 msec. We do now have a very clear periodic distribution of the stresses indicating 16 wrinkles. In the right part is shown the predicted punch force (for a quarter blank). From the curve some characteristics can be seen: At 3 msec a shift in slope can be seen and at 3.7 msec we find the maximum force followed by an abrupt drop indicating what traditionally has been considered the instability limit.

However, even before the loss of global instability occurs (at time $\approx$ 3.7 msec), a very inhomogeneous strain distribution is present in the flange due to the formation of small wrinkles, and it is believed that this inhomogeneous strain distribution will influence the remaining deformation even if the blank hold is increased at say time $\approx$ 3.5 msec in order to avoid the global loss of instability at $\approx$ 3.7 msec.

6.13.1 Isotropic cup

In the following the cup from the previous section is considered, the only difference here is that the material is modelled as isotropic. The reason to rerun the problem is to get conditions which can be simulated with an older version of LS-Dyna3d where the option for dump of internal forces is available. Figure 6.59 shows the negative regions of Hill's cri-

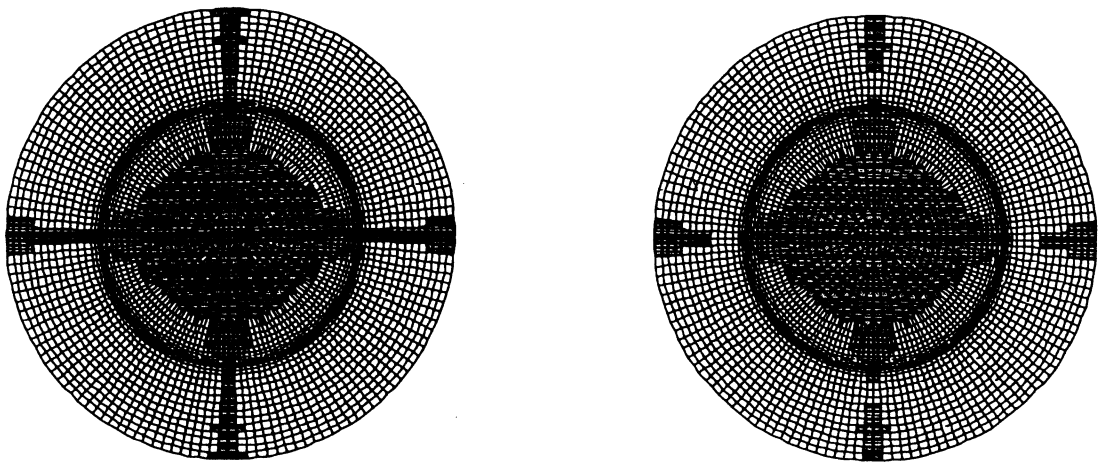

Figure 6.59: *Distribution of Hill criterion at 3.9 and 4.0 msec*

terion experienced in the time span 0-3.9 msec and 0-4.0 msec (left and right, respectively). Looking at figure 6.59 and the right part of figure 6.60 one may reach the conclusion that the instability limit predicted by monitoring the punch force (figure 6.60) corresponds to the time where regions which have lost stability grow together. This can be seen from figure 6.59: The left part of the figure shows the minimum value experienced of the Hill criterion at a time of 3.9 msec (the light gray area corresponds to negative values). The negative areas are dominating the blank, but the areas are not connected. The right part shows the situation at a time of 4.0 msec. Now the four isolated regions have grown together. This event does for this example correspond well with the time of maximum force.

This example has also been analysed with the CSP and Rayleigh approach discussed in section 6.3.1. In figures 6.61, 6.62, 6.63 and 6.64 are given the results predicted at various position in the blank. The positions are indicated in figure 6.60: Figure 6.61 shows the calculated variation of the CSP-measure for row 1 to 6, it is the regions closest to the edge. The behaviour is very typical: Up to a time slightly over 1.0 msec we have a relatively steady level of the CSP-measure. At 1 msec a drop can be seen, this drop corresponds to the time where plastic deformation starts in the outer part of the flange. Following there is a long period up to 3.8 msec with a steady behaviour of the measure. At $\approx$ 3.85 msec an abrupt drop can be seen which indicate loss of stability; the time corresponds very well with the predicted maximum force. Some of the curves (for region 5 and 6) experience a peak value of $\approx$ 0.2-0.3 before reaching negative values. After the indication of loss of stability a very scattered response can be seen indicating that the response is strongly influenced by dynamic effects. Figure 6.62 shows the variation for row 7-12. Compared to the first 6 rows a much more scattered response can be seen. At time $\approx$ 1 msec we can still see the drop due to the switch from elastic to plastic deformation followed by

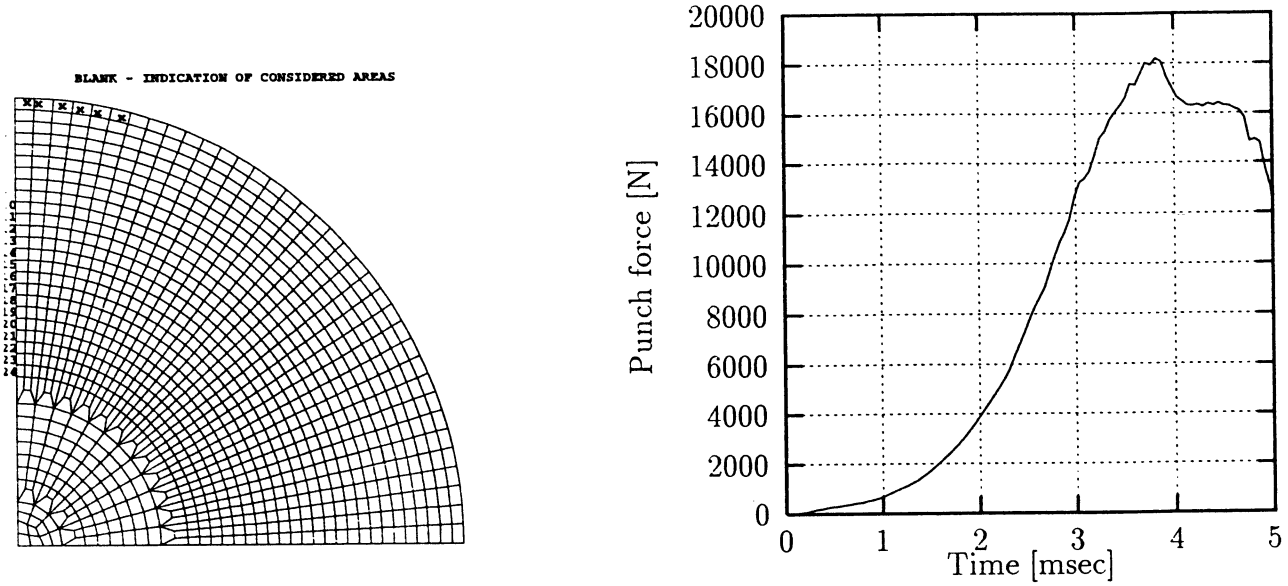

Figure 6.60: *Left: Illustration of the blank and the position of regions to be analysed. The regions considered consist of 6 elements, for example region 1 is indicated by 'x'. Right: The predicted punch force for a isotropic material.*

a period with a relatively steady behaviour. However, row 12 does indicate local loss of stability at 3.5 msec. An effect of this type was in the first analysis performed with the CSP-measure interpreted as an effect arising from noise in the simulation, but after the analysis with Hill's criterion it is evaluated to be caused by a deformation mode leading to local unloading due to formation of a wrinkle. Figure 6.64 shows the variation of the CSP-measure for row 13-18. These regions lead to a much more scattered response than the previous 12 rows discussed. These rows are plastically deformed at an early stage of the process and we do only for row 13 see the characteristic drop due to the switch from elastic to plastic deformation. Row 16 indicates loss of instability at a time of 1.3 msec. This corresponds reasonably with the results for the anisotropic cup. For the anisotropic cup a single row of elements indicates negative values of Hill's criterion, the position of this row corresponds to row 15 in the present section and the deviation (here it is row 16 which reaches instability) may be explained from the difference in material modelling. Figure 6.64 shows the predicted CSP-measure for row 19-24. Here the response indicates loss of stability at a time of 1 msec for row 24. This mode is not predicted using Hill's criterion. Row 19 to 21 indicate a loss of stability around 2.5-2.5 msec. The behaviour of these curves is similar to the behaviour seen for row 1 to 12. The curves (19 to 21) may seem more scattered but this is partly due to the scaling; the CSP-values for these curves are normalized with initial values which are determined when the regions already experience plastic deformation.

For the anisotropic cup analysed with the Hill criterion we see an effect of the instable regions growing: This effect can also be partly decoded from the presented CSP-curves. The CSP-measure indicates an early loss of stability for the interior part of the blank. Moving from the interior part to the outer part (from row 24 to 1) a delay of the onset of instability can be seen. However, due to the present coding used to calculate the CSP-measure, it is difficult to present the results in a way more directly comparable to the Hill criterion discussed in section 6.13.

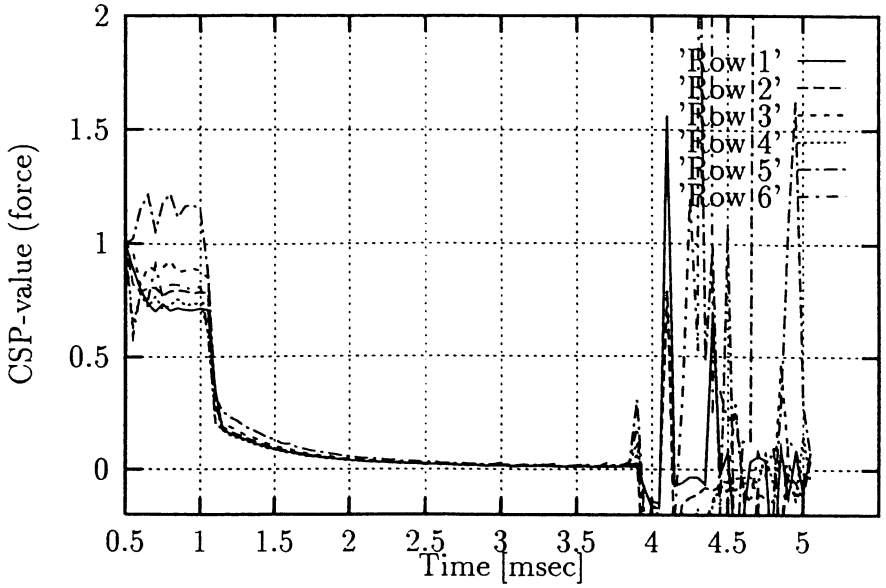

Figure 6.61: *Variation of the CSP measure for row 1-6.*

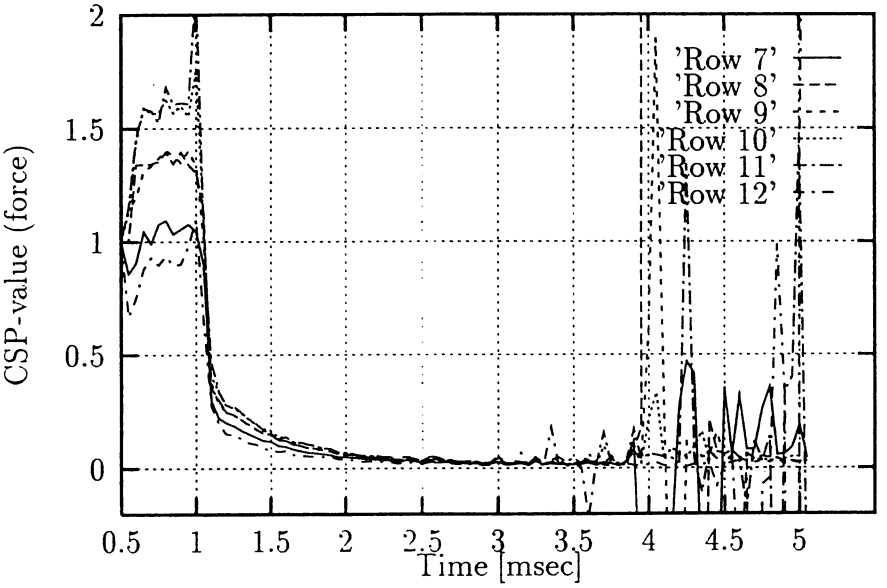

Figure 6.62: *Variation of the CSP measure for row 7-12.*

The same regions as analysed with the CSP-measure are analysed using the Rayleigh measure. In figure 6.65 is given the variation to the Rayleigh measure. The overall behaviour is very similar to the behaviour found using the CSP-measure. Loss of stability at the outer part of the flange is also found to occur at 3.8 msec. The primary differences are 1) that the steady drop which is found using the CSP-measure has a more dynamic nature now and 2) that the response after loss of stability is much less scattered. Figure 6.66 shows the variation in Rayleigh coefficient for row 7 to 12 and the general picture is very much the same as for row 1 to 6. From figure 6.66 loss of stability is also predicted to occur at 3.8 msec. A slight difference can be seen compared to the CSP-measure. The CSP-measure indicated a negative value for row 11. This is not the case for the Rayleigh measure. Figure 6.67 shows the variation for row 13 to 18. Now the general picture is quite different compared to the previous 12 rows. The values have been normalized with the value at a time of 0.5 msec; for row 16, 17 and 18 values well above 1 can be seen. This may indicate a stiffening behaviour not discovered using the CSP-measure. The Rayleigh

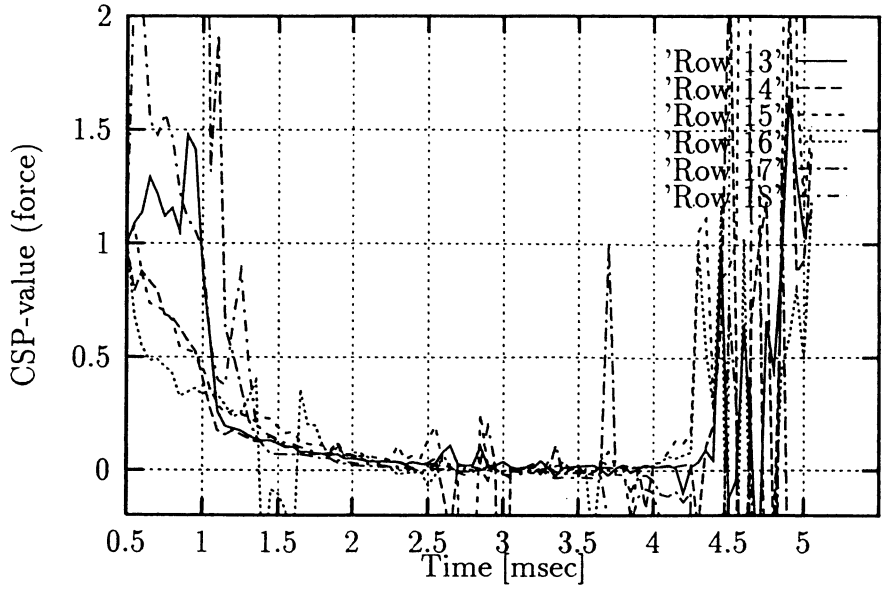

Figure 6.63: *Variation of the CSP measure for row 13-18.*

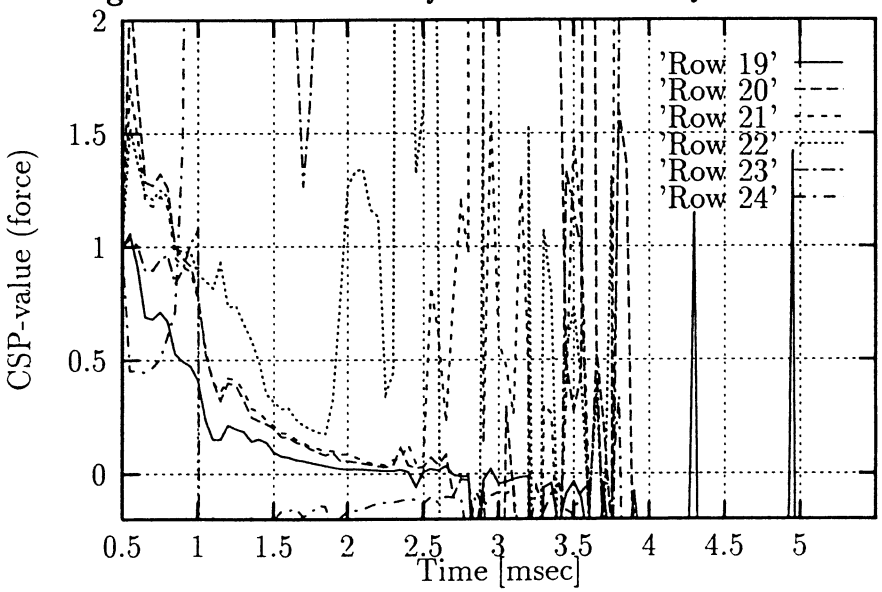

Figure 6.64: *Variation of the CSP measure for row 19-24.*

variation for row 16 does, however, indicate loss of stability at the same time as the CSP-measure. The curves for row 19 to 24 are shown in figure 6.68. The curve predicts loss of stability at $\approx$ 1 msec for row 23 and 24 which is similar to the results predicted using the CSP-measure. Row 19 and 20 are predicted to loose stability at 2.5 msec which is also in good agreement with the CSP-measure. Plotting the CSP and Rayleigh measure for row 1 and 2 in the same figure (6.69) does indicate a very good relation between the two measures. The predicted loss of stability (negative value) is indicated at the same time using the two methods. One may note that the Rayleigh measure seems to be stronger influenced by the dynamic effects: Where the CSP seems to be at a stable level from 0.5 to 1.0 msec followed by a significant drop (due to the switch from elasticity to plasticity) the Rayleigh measure indicates a more dynamic behaviour. After reaching a state of steady plastic loading the vibrations seem to be damped out leading to a response just as steady as the CSP measure.

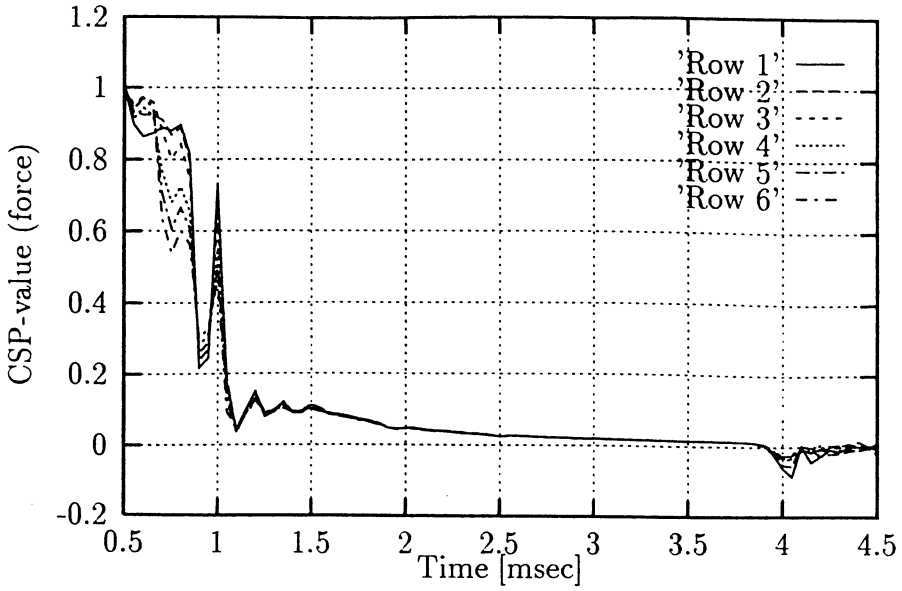

Figure 6.65: *Variation of the Rayleigh measure for row 1-6.*

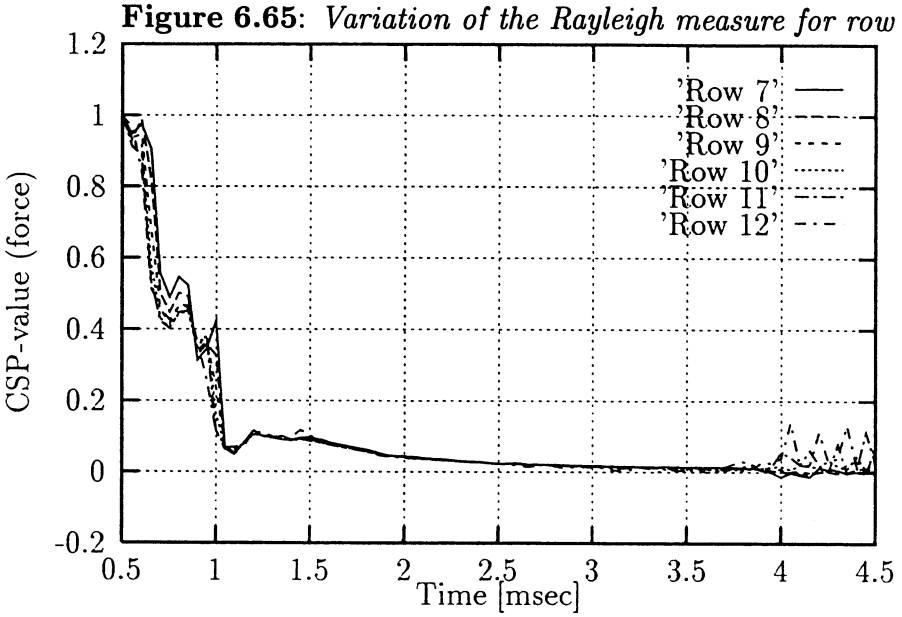

Figure 6.66: *Variation of the Rayleigh measure for row 7-12.*

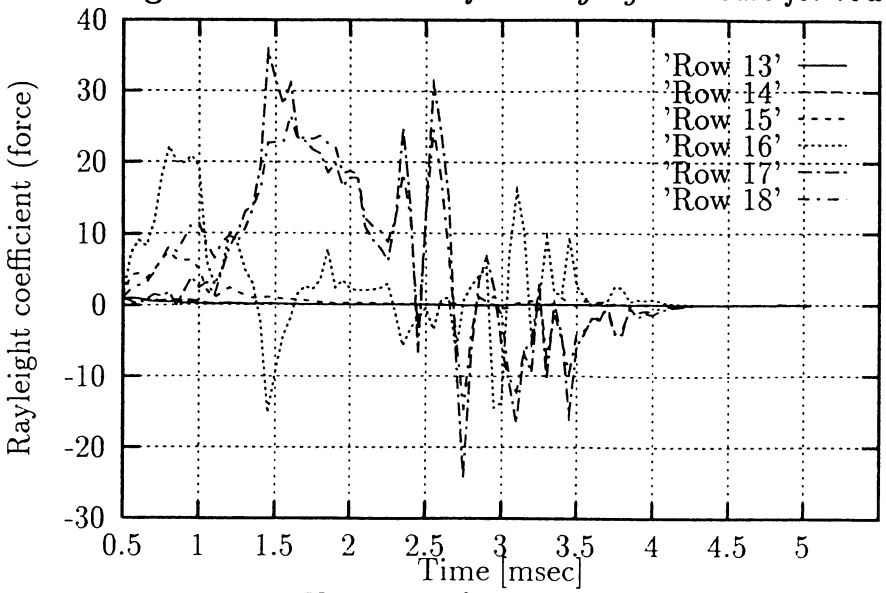

Figure 6.67: *Variation of the Rayleigh measure for row 13-18.*

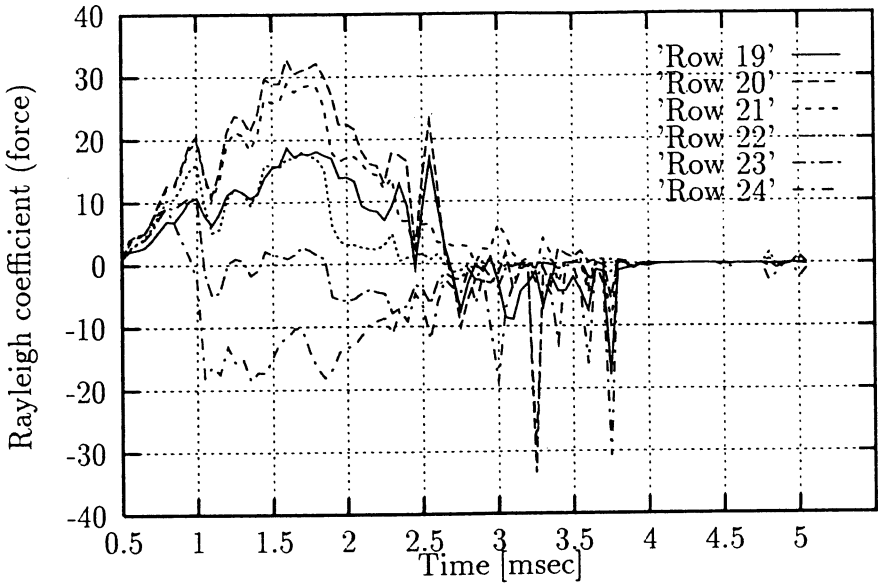

Figure 6.68: *Variation of the Rayleigh measure for row 19-24.*

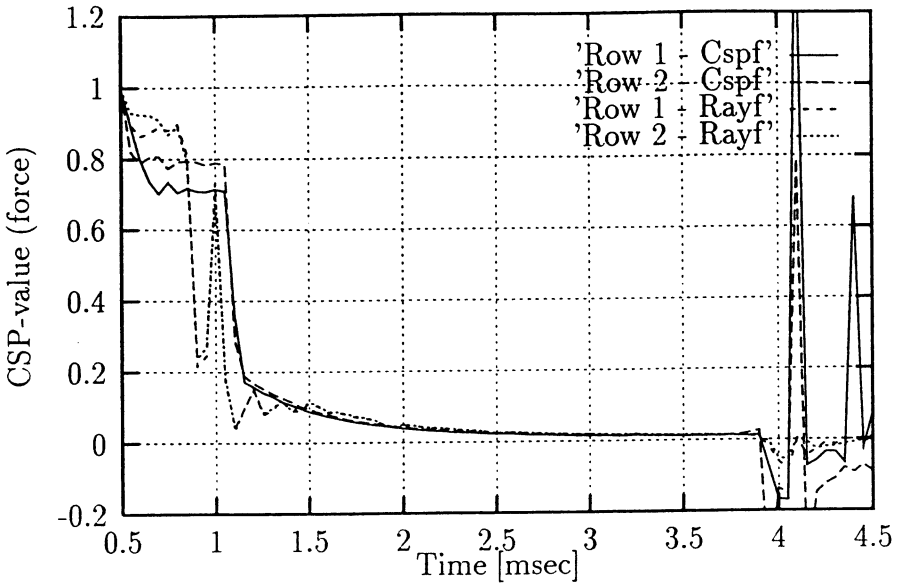

Figure 6.69: *Comparison between the CSP and Rayleigh measure for row 1 and 2.*

6.14 Deep drawing of a bar sink

In the present, another typical example of a deep drawn product, a bar sink made of stainless steel is considered, the tool dimensions are given in figure 6.70. A typical goal for this

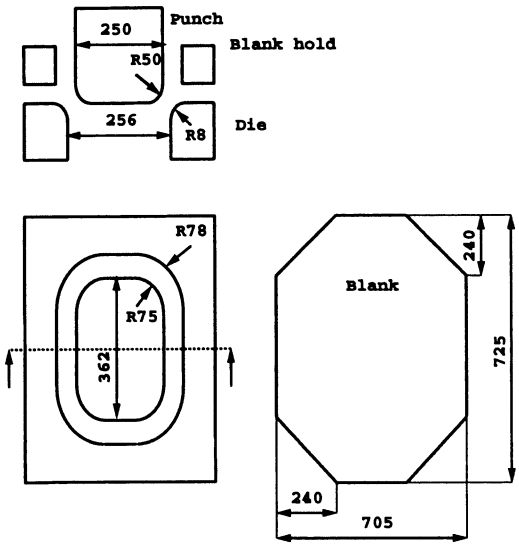

Figure 6.70: *Geometry for tools and blank for deep drawing of a bar sink.*

kind of products is to become able to produce higher and higher sinks with smaller and smaller radii of punch nose, die should and corner. In this connection FE-simulations are very valuable in order to predict whether a given tool geometry is feasible or not. However, in the present the purpose of the example is to illustrate a wrinkling behaviour different from typical first and second order wrinkles.

The first attempts with this example is to check whether a 1 mm thick stainless steel sheet could be used for the production. Here only two analyses are documented, one analysis with a relatively low blank hold leading to wrinkles and a high blank hold sufficient to avoid wrinkles. However, both examples lead to fracture later in the process due to localization.

In figures 6.71 to 6.76 are shown the development of the Hill criterion. As in the previous section the results are presented as the regions which have experienced negative values. These negative values are indicated by a dark region, light regions indicate regions which have had positive values for the Hill criterion during the entire analysis. The left part of the figure is from the analysis with a high blank hold, the right part is the lower blank hold. Figure 6.71 shows the distribution of negative values experienced (dark zones) up to a time of 8.0 msec for a quarter of the blank. Although the blank hold differs significantly the two analyses give almost the same distribution. The negative elements are grouped in two regions which may be slightly connected for the lower blank hold. Figure 6.72 gives the regions for which Hill's criterion indicates loss of stability (on a local level) at 9.3 msec. The pattern is very similar to the situation at 8.0 msec apart from one aspect: A few elements located over the straight part of the die shoulder indicate loss of stability - this effect seems to be the same for the two blank holds. Figure 6.73 shows the situation at 10.7 msec. The two major regions have grown and the elements placed at the lower

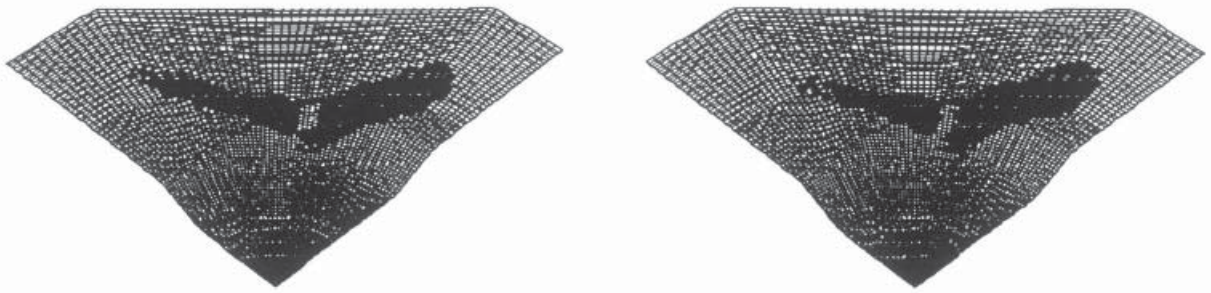

Figure 6.71: *Distribution of the Hill criterion at 8.0 msec for a high blank hold (left) and a lower blank hold (right).*

part of the straight die shoulder (some of the elements were at the top of the die shoulder at 9.3 msec) give an indication of some effects: There seems to be a repetitious pattern with 4 or 5 regions along the die shoulder, this pattern seems to be the same for both blank holds. Looking at the distribution at the upper part of the blank we do see some difference between the low and high blank hold: For the low blank hold more elements have experienced a deformation history leading to negative values of Hill's criterion. Figure 6.74 shows the distribution at 12 msec. The regions close to the die shoulder have grown for both blank holds and again the primary difference is for the upper flange region where the stable region is slightly less for the low blank hold. Figure 6.75 shows the situation at 13.3 msec. Now the regions have clearly grown together leaving a small interior zone which remains stable. Still, there is an indication of a repeated pattern along the die shoulder. Figure 6.76 shows the variation of the minimum value of the Hill criterion experienced in the time span 0-14.7 msec. From the figure it can be seen that most of the flange has experienced negative values. To summarize on figure 6.71 to 6.76 it can be concluded that the measure gives results which can be hard to decipher. There can be seen some influence from the blank hold, but one may expect a larger difference - at least that is what one will expect considering flange wrinkling and the relation to blank hold.
Figure 6.77 shows the thickness distribution for the flange region at 14.7 msec. The thinnest regions correspond reasonable with the regions for which the Hill criterion predicts loss of stability.

If we compare the thickness distribution with the stable regions at 13.3 and 14.7 msec we can refind the thick area (the almost circular contour in figure 6.77) as the interior stable area. Also the stable regions at the outer flange correspond very well with the thick regions found here.

It also seems reasonable that it is the growth of the instable region (this growth takes place in the regions with the lowest thickness) which causes the formation of wrinkles later in the process.

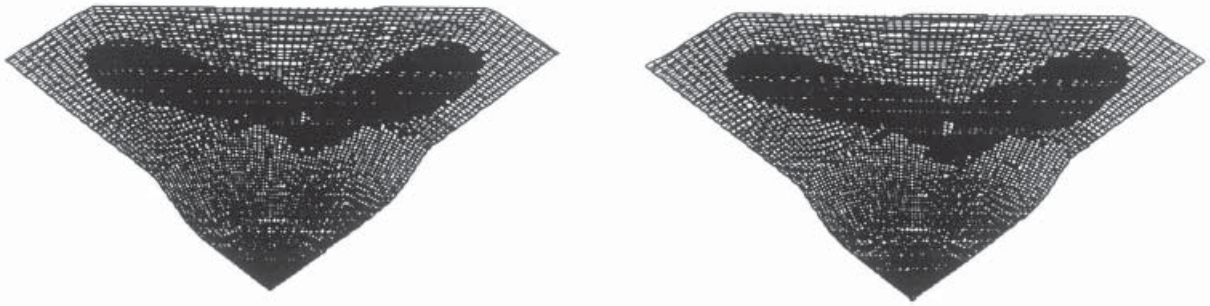

Figure 6.72: *Distribution of the Hill criterion at 9.3 msec for a high blank hold (left) and a lower blank hold (right).*

Although the flange wrinkles are apparent at full punch stroke (at 40 msec) the onset is hard to detect by postprocessing. However, choosing a plot range between -0.0475 and 0.0275 mm we obtain the patterns for the z-displacements shown in figure 6.78 at 14.7 and 16.0 msec. These patterns correspond well with the final wrinkle pattern. Although the wrinkling mode seems to be detectable it should be mentioned that the displacements of the flange are of the same order as the thickness changes. This example does indicate that although we are far from wrinkle formation which can be detected on the punch force or a formation which is visible, we are capable of detecting the pattern using Hill's criterion.

Another effect which could be detected with the Hill criterion is the pattern which seems to arise at the straight part of the die shoulder zone. In order to check whether we do have some deformation pattern which can explain this apparent repeated loss of stability a number of plots for the long side of the bar sink are shown in the following. As the mesh is poorly aligned with the tools it has been chosen to plot the hydrostatic pressure. Figure 6.79 shows the level of hydrostatic pressure at 5.3 and 6.7 msec. The left part indicates some variation along the straight part of the die shoulder, but at this level the process is in its very early stage and hereby we have also a relatively low hydrostatic pressure. At 6.7 msec the deformation has spread to the flange region and the contour plot of the hydrostatic stresses does not indicate any disturbance from wrinkles. Figure 6.80 gives the hydrostatic pressure at 8.0 and 9.3 msec. At 8.0 msec we have almost the same picture as for 6.7 msec. Two contour lines are now placed aligned with the die shoulder and the contours are less smooth than the corresponding lines at 6.7 msec. At 9.3 msec there is an indication of a stronger variation along the draw die shoulder. Figure 6.81 shows the distribution at 10.7 and 12.0 msec. Now a pattern similar to the one obtained with the Hill criterion becomes more clear. As we saw at 10.7 msec for the Hill criterion there seems to be a pattern of 8 to 10 zones along the straight part of the die shoulder (for a mirrored part as shown in figure 6.81). If we repeat the plot at 12.0 msec with a more distant view the periodicity of the distribution becomes more clear. In figure 6.82 is repeated figure

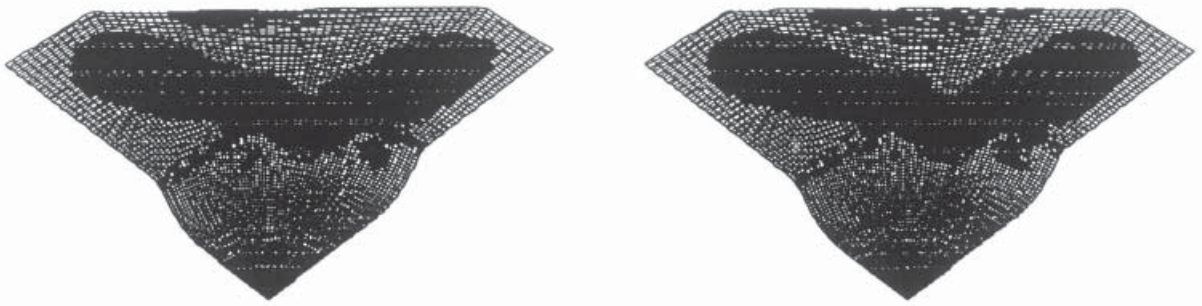

Figure 6.73: *Distribution of the Hill criterion at 10.7 msec for a high blank hold (left) and a lower blank hold (right).*

6.81 right with a more distant view. Figure 6.82 left is identical to figure 6.81 left apart from the geometric scale. Here we see a very clear pattern which corresponds to the one predicted with the Hill criterion.

At a time of 9.3 msec we see the first significant variation in pressure - this corresponds very well with the prediction from figure 6.72 where at 9.3 msec we have an indication of loss of stability for a few elements in the region. Figure 6.83 shows a shaded view of the bar sink drawn with the high blank hold. Here it is very clear that we have the wrinkles in the final part. Raising the blank hold leads to fracture so the conclusion from this study is that the blank thickness should be increased or the die design altered.

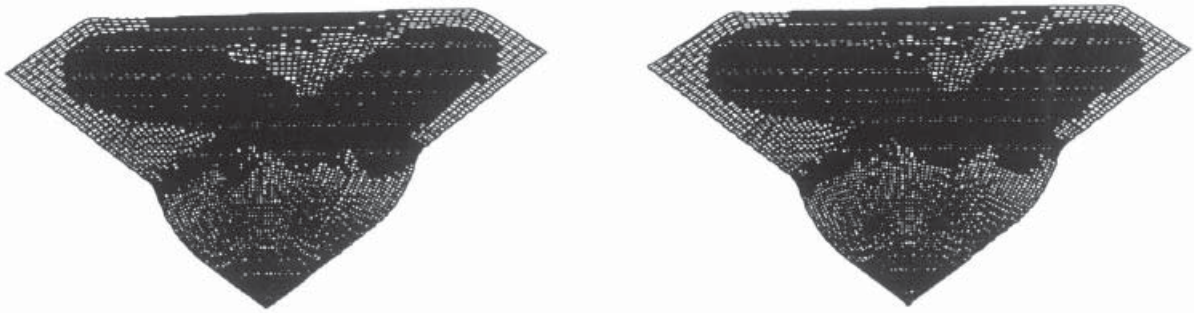

Figure 6.74: *Distribution of the Hill criterion at 12.0 msec for a high blank hold (left) and a lower blank hold (right).*

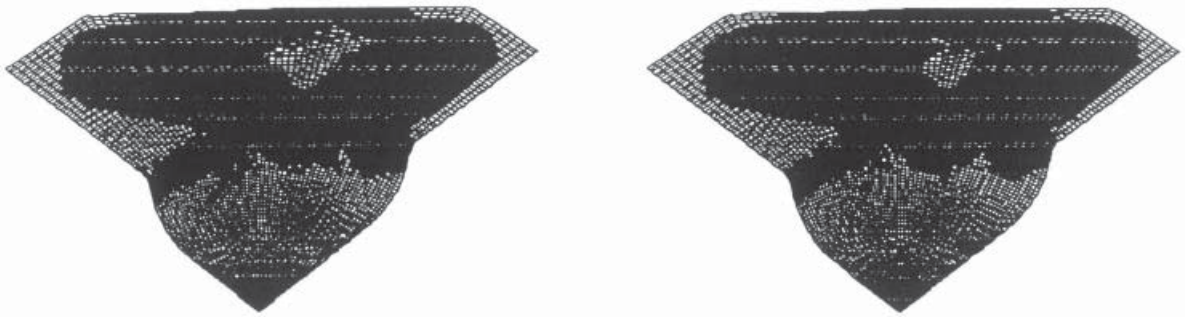

Figure 6.75: *Distribution of the Hill criterion at 13.3 msec for a high blank hold (left) and a lower blank hold (right).*

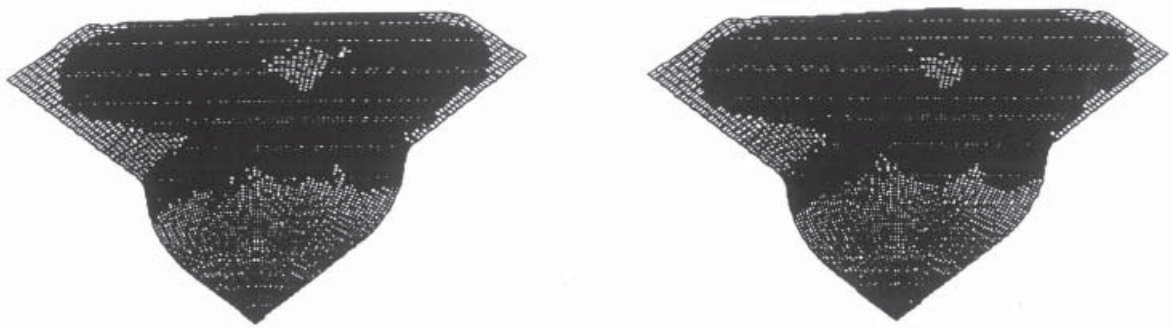

Figure 6.76: *Distribution of the Hill criterion at 14.7 msec for a high blank hold (left) and a lower blank hold (right).*

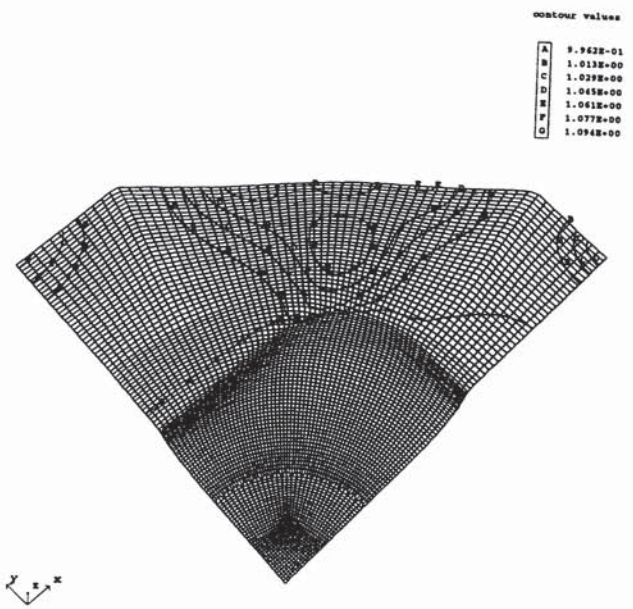

Figure 6.77: *Thickness variation for the flange region for the example with low blank hold at 14.7 msec.*

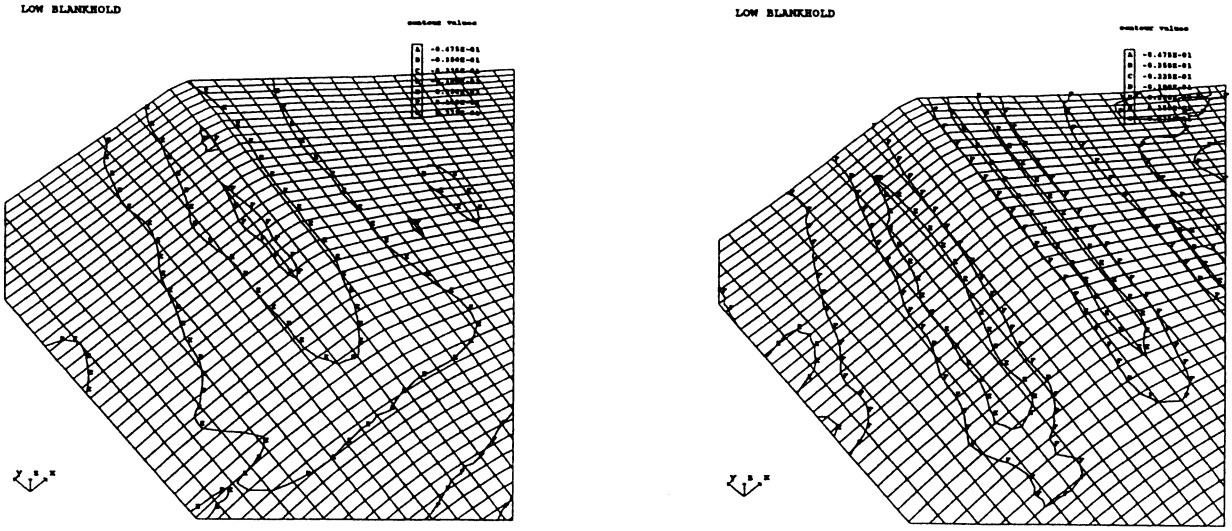

Figure 6.78: *Predicted variation of z-displacement at times of 14.7 and 16.0 msec for the low blank hold where formation of wrinkles are clear later in the process. Only the flange part above the straight part of the die is shown.*

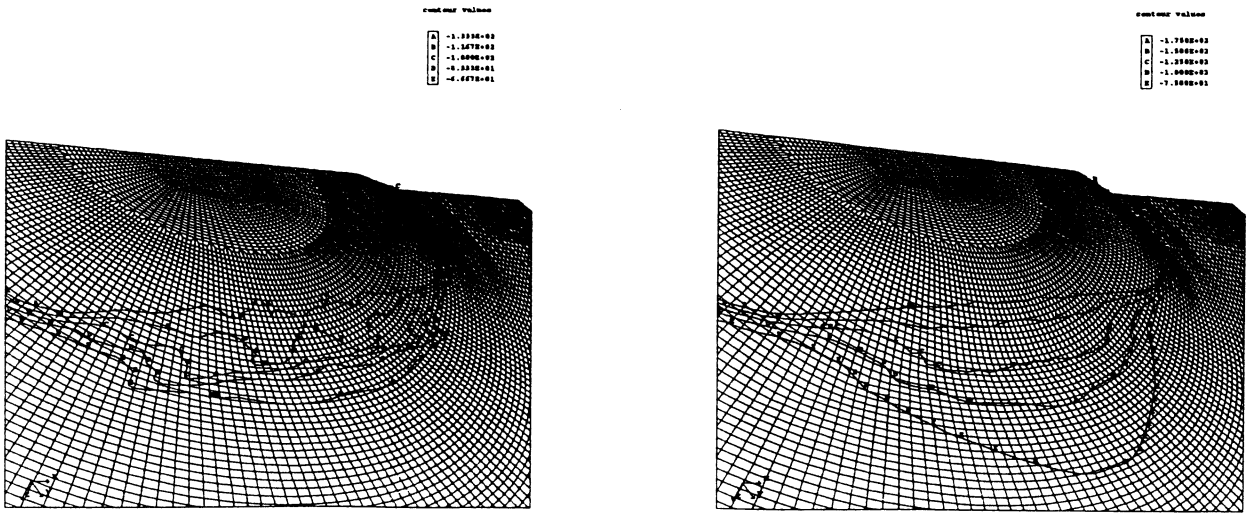

Figure 6.79: *Distribution of hydrostatic pressure at a time of 5.3 and 6.7 msec for the high blank hold. The figure shows a closeup of the part mirrored.*

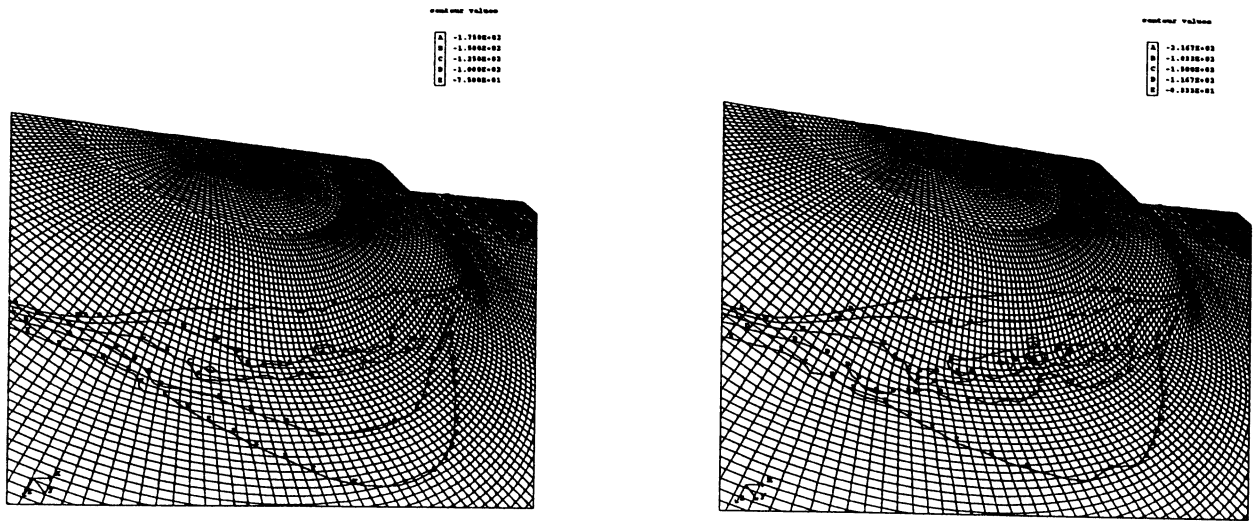

Figure 6.80: *Distribution of hydrostatic pressure at a time of 8.0 and 9.3 msec.*

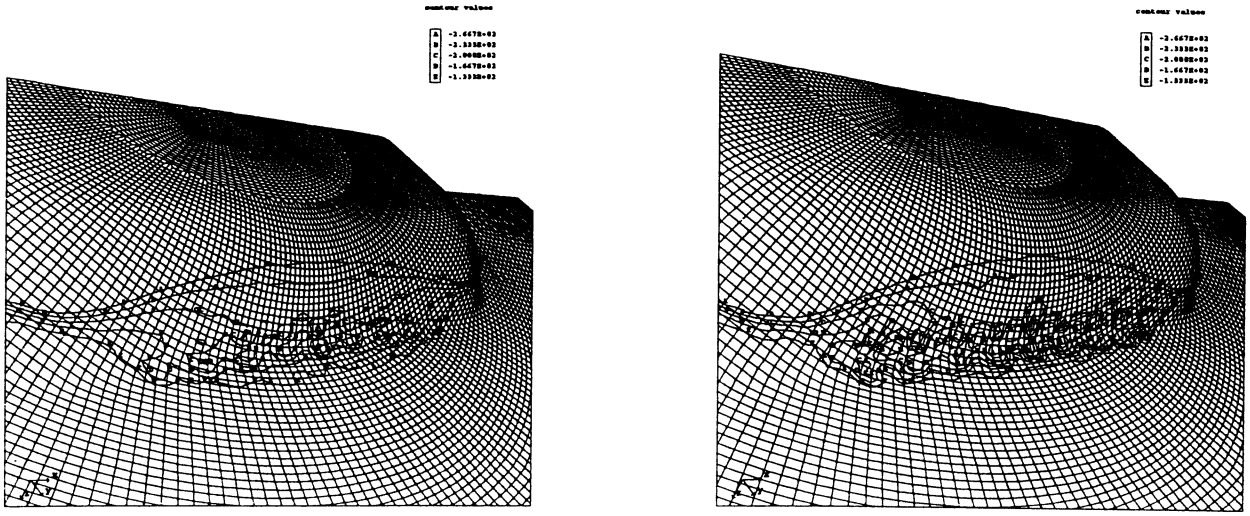

Figure 6.81: *Distribution of hydrostatic pressure at a time of 10.7 and 12.0 msec.*

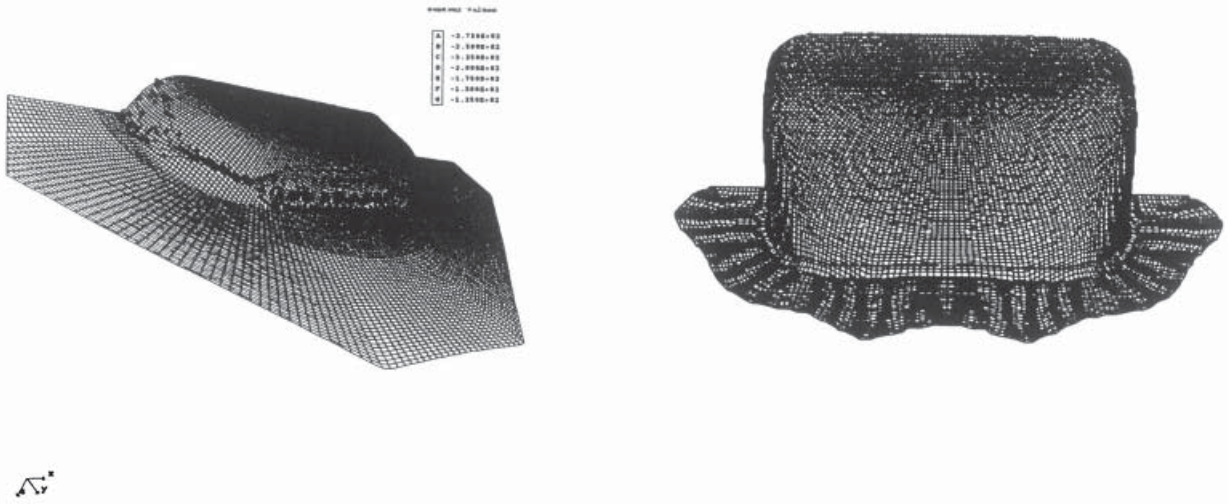

Figure 6.82: *Left: The same hydrostatic pressure distribution as shown in figure 6.81. Right: The wrinkle configuration, the dark fringe levels indicate positive z-displacements.*

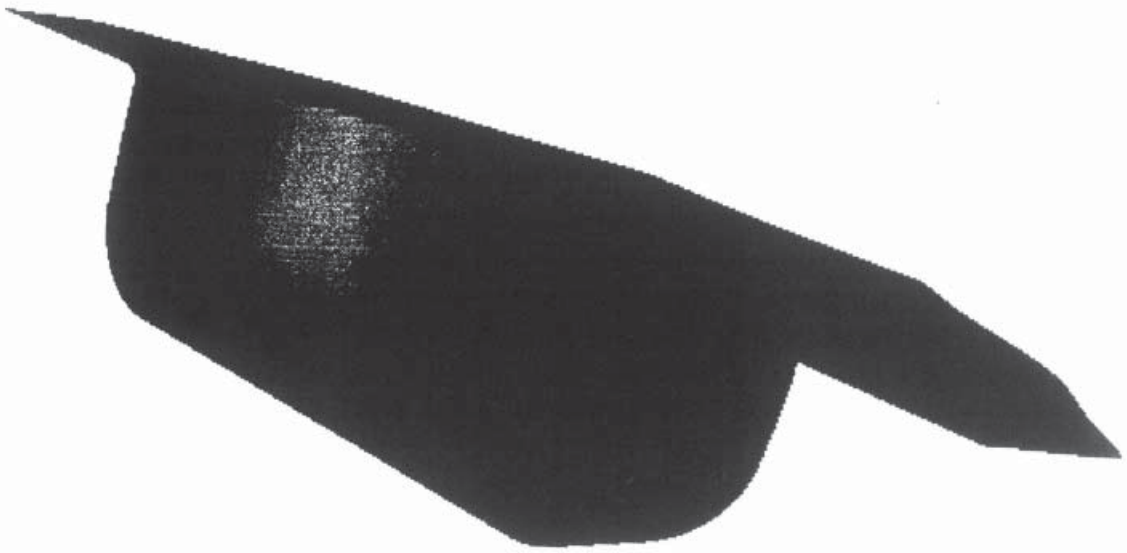

Figure 6.83: *Shaded view of the bar disk after development of wrinkles in the wall side.*

6.15 Conclusion drawn from the instability analyses

From the precedent two examples, deep drawing of circular cups and the bar sink, it can be concluded that the proposed methods seem to work out reasonably. However, the results are much more difficult to decipher than for the truss and beam examples in the previous section. One reason for this is of course that the behaviour cannot be explicitly predicted in advance as it was the case for the beam and truss.

One thing which can be concluded is that the traditional approaches to predict instability for deep drawing of cups seem to be far too simplified. They may represent a limit which can be of use in connection with prediction of forming heights, etc, but I am convinced that they do not discover the event of instability build up: Both for the cup as well as the sink the results strongly indicate that the cause of instability arises from the draw die shoulder.

The proposed CSP method seems to be functional, however, occasionally one can find results which are impossible to decipher. In section 9.4 is given an example where the method is used on a forming operation performed under conditions leading to a successful and an unsuccessful part, respectively. The alternative method (based on the Rayleigh coefficient) gives more of less the same results as the CSP measure. However, due to its use of force increments to produce a scalar, it seems to be more sensitive, especially with regard to the behaviour after the instability or load maximum. Here one should remember that instability events will almost always lead to a dynamic behaviour, for example as pointed out by [21], and we must of course take this aspect into consideration when talking sheet metal forming - this aspect is not included in the traditional predictions of instability where one normally considers the possibility for two configurations for a given load (after bifurcation), or one considers the limit where release of energy is sufficient to form a wrinkled configuration. As illustrated in section 6.11.2 the loading rate used in the analysis and hereby the inertial effect plays a significant role.

The proposed way to utilize Hill's criterion seems to be of some interest, especially for the beam and truss example it seems to work out very well. For the more complicated examples the results presented have only been the experienced minimum value in each element (if the values are plotted at an instant time the resulting pictures are even harder to decipher). In the previous examples some preliminary interpretations were given which combined with the results obtained with the CSP and Rayleigh measure seem to be reasonable.

When an interior region (of negative values) expands to the edge of the blank it influences the formation of wrinkles. It is also indicated that when two regions with negative values grow together one has an indication of loss of stability. At least the two examples can be interpretated that way.

Future work should include a more detailed discussion on the proposed measures - it should especially be investigated whether a limit can be found which not only gives an indication of loss of stability, but which can estimate the risk of growth of wrinkles. The findings documented in this section do indicate that the loss of stability may appear earlier than

part failure due to growth of wrinkles.

Based on the examples shown in the previous sections it is concluded that explicit FE can be used with a good accuracy for analysis on instability problems.

It can also be concluded that the predicted geometry after folding for plastic forming problems seems to be rather good even when the FE-models primarily are made in order to obtain good analysis in the case of a successful forming. So far it seems as if it is unnecessary to take special precautions in order to provoke the type of instabilities with wrinkles of first and second order. This is perhaps the most convincing reason why explicit FE has become so popular in the field of sheet metal forming during the last decade.

The use of the three proposed methods are evaluated to be efficient tools for indicating the onset of instability. However, this indication demands that the FE-simulation is correct and here some problems are recognized for the elastic problems as a delay of the onset can be seen in many cases where a relatively coarse mesh is utilized. This delay seems to be less important for the processes analysed, but based on the examples it cannot be concluded how crucial the effect is for the plastic forming processes.

Chapter 7

Sheet Metal Testing and Formability

The purpose of this section is to give a brief overview and a short discussion on some well known test methods which are used to describe the formability of a given material. The methods will not be discussed in detail, only some disadvantages and advantages will be mentioned. It is concluded that the Marciniak double blank method seems to have some advantages compared to the other methods in connection with determination of a forming limit diagram (FLD). Through the years many attempts have been made to characterize the formability of sheet materials. Some general tests are the Erichsen test, the Swift test, the Fukui test and the LDH-test (Nakazima test).

Unfortunately many of the test methods are very dependent on the test process wherefore it may be difficult to obtain results which are reproductive from one laboratory to another as friction conditions, tool surface quality, etc may vary and hereby influence the measured quantities. Another problem is that it is difficult to compare the results from different test principles and finally it can be discussed whether the measured results, e.g. Erichsen Index, Limiting Drawing Height and Diameter of Fracture, are material properties characterizing formability or just a characterization of the actual test process.

The chapter deals primarily with experimental methods used for the determination of formability with regard to sheet metal forming. This chapter includes a number of FE-analyses which have either been performed in order to investigate or illustrate the characteristics of the test methods or alternatively, have been performed in order to check modelling assumptions. The presentation will focus on the forming limit diagram which is widely accepted (despite its weaknesses) in the academic as well as in the industrial world today. The concept of a forming limit diagram (FLD) where the major principal strain at fracture is plotted as function of the minor principal strain was proposed by Keeler [117] and Goodwin [78]. Keeler investigated the right side of the FLD ($\epsilon_2 > 0$) and Goodwin the left side of the diagram. This type of diagrams is often called the Keeler-Goodwin diagram. Other popular designations are forming limit diagram and forming limit curve (FLC). Figure 7.1 shows an example of a Keeler-Goodwin diagram. The principle of using the major and minor strains in the plane of the blank to characterize formability is very convenient in connection with stretching and deep drawing processes, however, for other processes e.g. ironing and multistep forming where curvatures and/or abrupt changes in strain paths are significant, the FLD-concept seems to be an insufficient tool for judgement of the process severity. The "direct" use of FLDs is limited to processes where strain paths

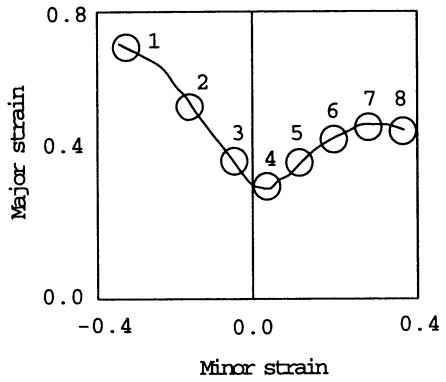

Figure 7.1: *Typical Keeler-Goodwin diagram for mild steel. The indicated 8 zones correspond to an example of testing procedures given by Boyer [35]*

are "reasonably" linear. However, some theories may be used to evaluate the severity of a forming process even for non-linear paths (discussed further in chapter 8). Figure 7.1 indicates 8 zones which relate to zones with strain ratios that can be obtained by using various experimental approaches. The test methods covering the various strain ratios indicated in figure 7.1 are according to Boyer [35]:

- 1: Tensile testing. The method is used for estimation of fracture strains for a strain ratio of $\approx$ -0.5. The method can be refined by cutting out regions so that strain ratios of $\approx$ -0.5 to -0.1 can be obtained.
- 2: Square box drawing. Deep drawing of square boxes can be used for obtaining fracturing strains for negative strain ratios. This strain state is reached for a fracture at the shoulder zone. If the fracture occurs at the punch corner instead, the limiting strain will be closer to zone 4 or 5.
- 3: Swift redraw test
- 4: Erichsen test. The Erichsen test can be used to obtain strain paths close to plane strain at the fracture. However, the sheet area considered is relatively small leading to problems with the measurement of limiting strains due to large strain gradients.
- 5: Draw fracture testing. Fracture at region 5 can be obtained with a number of draw operations, typically tests are performed by using sheet strips clamped in cylindrical tools, e.g. the Nakazima test.
- 6: Swift test. The test is a standard cup drawing process and the limiting drawing ratio, which can be obtained, is used to characterize the sheet formability (the limiting drawing ratio, LDR). When the test is used to obtain fracturing strains, positive strain ratios are obtained (6) around the punch nose.
- 7: Hemispherical punch testing. The principle is similar to the Swift test, however, the sheet is normally clamped. When using a hemispherical punch the process is more dominated by stretching leading to fracture strains at ratios slightly larger than for the Swift test (where the punch has a nose radius smaller than the punch radius).
- 8: Hydraulic bulging. The test can be used to obtain fracture under balanced stretching conditions. The method can be refined by using rectangular or elliptic matrices leading to strain ratios covering most of the right side of the FLD.

Some of the methods are capable of covering a wider range of strain paths than indicated in figure 7.1. In order to obtain a FLD for a given sheet it is necessary to perform a number of experiments, however, depending on the material it may be possible to limit the number of experiments by performing extrapolations based on theoretical analyses. Most of the analytic methods have both weaknesses and strong sides which must be considered before relying too heavily on these methods. A discussion of a number of theoretical approaches is given in chapter 8. The rest of this chapter will focus on experimental methods utilized for characterizing sheet metal formability.

During the last years some attention has been paid to the Marciniak Double Blank Method (see section 7.5). This test method has compared to the above mentioned methods the clear advantage that all strain ratios described in a FLD can be tested by using the same equipment.

7.1 Uniaxial tensile test

This test method is of particular interest in connection with the determination of elastic and plastic properties to describe material behaviour in more complex loading histories. The measured stresses and strain are normally fitted to an analytic expression in order to describe the hardening behaviour. In connection with simulation of forming processes this hardening curve is used to describe the hardening in connection with three dimensional stress states. Tensile testing gives only homogeneous plastic deformation up to a level where $\epsilon_{eq} \approx n$ (the exponent used in a Hollomon hardening law, $\sigma_Y = K\epsilon_{eq}^n$). To establish hardening curves from measurements in the range from 0 to n and then using these in forming problems, where effective strains as high as 100 per cent often are achieved, may be a very drastic extrapolation (to me it is surprising how good results can be obtained using this approach).

However, tensile testing must still be regarded as the most important material test as most reported material values (elastic parameters, hardening description, R-values) are based on this test method. Another reason why other test methods are not widely used is due to problems in connection with obtaining a relation between load and deformation. In many of the proposed alternative methods for material testing contact arises during the test and the relation between load (stress state) and deformation (plastic straining) is hard to obtain. In many tests problems arise due to non-uniform stress and strain distributions which makes an analytic analysis almost impossible. In order to overcome these problems and to estimate more material parameters a strong interest in inverse techniques is seen today, where numerical analysis is combined with experiments in order to determine material parameters.

Use of tensile test is a very convenient way of testing materials, and as long as the deformation is homogeneous it is easy to obtain information about the material behaviour as the relation between load and deformation is easy to measure.

The typical measures of formability (or ductility) are the elongation after fracture for a reference length of 50 or 80 mm and (not least) the hardening exponent n. Based on n

a very good characterization of the formability can be made for mild steel, but for other materials, e.g. aluminum and high strength steel, the relation between formability and n-value is not so strongly related (the knowledge of the behaviour of mild steel cannot be transferred directly to other materials).

Regarding the formability strain paths with a ratio $\rho = \frac{\dot{\epsilon}_{22}}{\dot{\epsilon}_{11}}$ of approximately -0.5 can be obtained. The deviation from -0.5 will depend on the degree of plastic anisotropy.

7.1.1 Tensile test with cut-outs

One way to utilize tensile tests to obtain a wider range of strain paths is to use tensile specimens with cut-outs. According to Kleemola [124] and Hecker [89] it is possible to obtain strain ratios in the range from approximately -0.5 to -0.1 by using tensile specimens with various cut-outs. This way to determine limiting strains may be of interest as it is both faster and somewhat cheaper than for example the Marciniak double blank method, see section 7.5. An important aspect is the relatively small area in which the main deformation takes place and that is why experimental results are strongly affected by the adopted measuring technique. Figure 7.2 shows left an example of geometries capable of

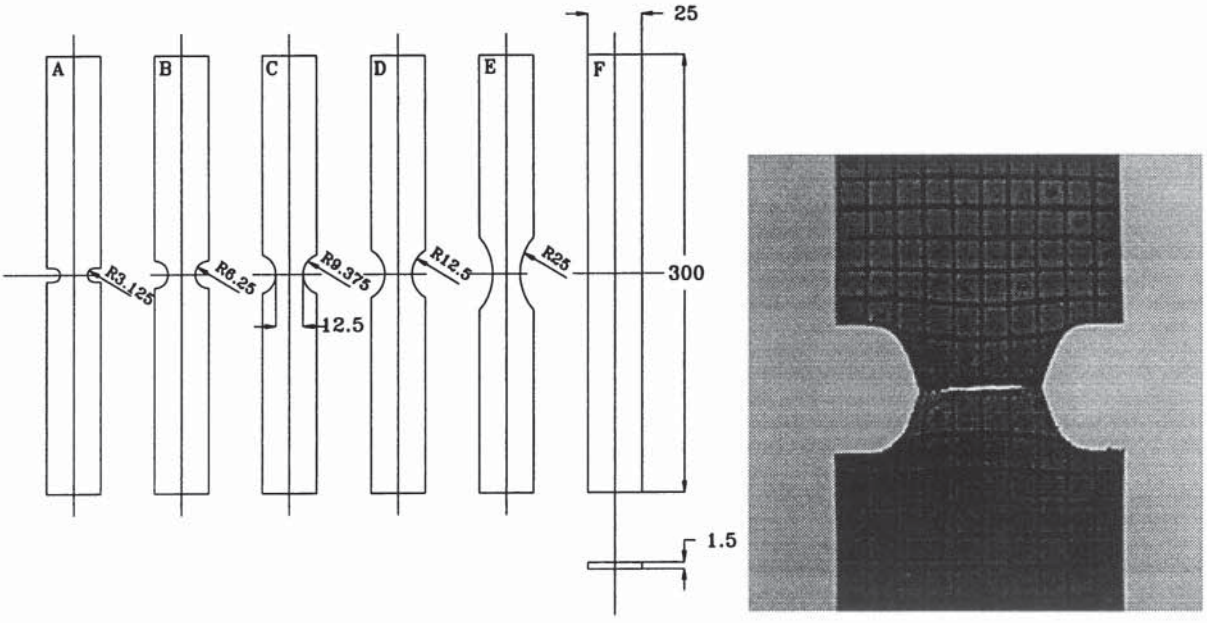

Figure 7.2: *Left: Example of specimen geometries which can give the strain paths for the left-hand side of a FLD. Right: Specimen type A after fracture. The illustrated fracture is very typical for tensile specimens with cuttings: Fracture initiates at the symmetry point and grows towards the edges.*

covering almost the entire left-hand side of the FLD and the right part shows the specimen type A after fracture. The fracture only affects a very limited zone of material. As the strain across the fracture zone will be far from uniform and strong strain gradients exist in the longitudinal direction, the measured values for the current examples are far from what can be found by using e.g. the Marciniak double blank method (discussed in section 7.5).

During testing the total elongation is recorded together with the tensile force. With intervals (typically 12-20 during a test) pictures are recorded and stored for later image processing. Figure 7.3 shows strain paths for specimen type A to E. The strain was recorded

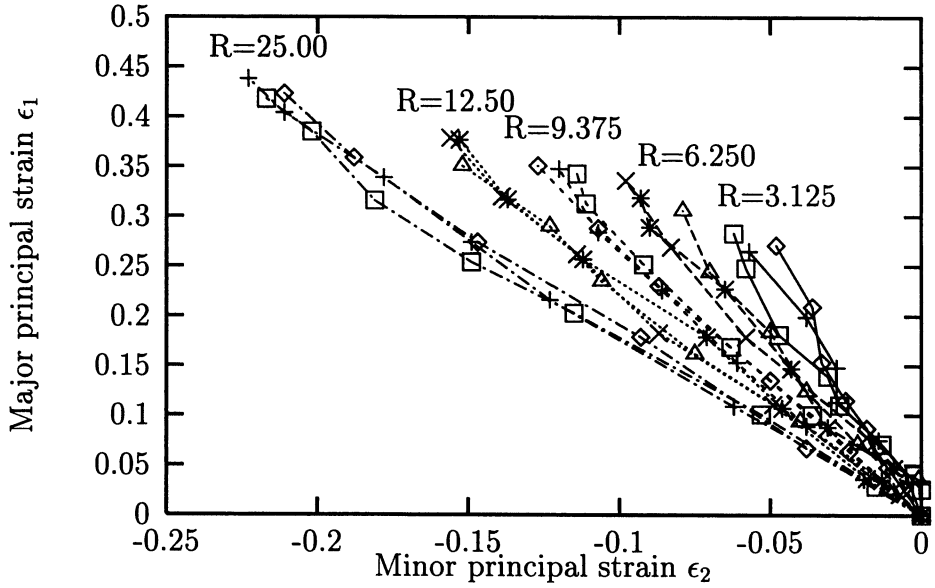

Figure 7.3: *Strain paths recorded for the tensile specimens with cuttings. 3 specimens for each geometry were tested.*

by using the ASAME system, [213], and the reported values are average values of 4 grid elements placed symmetrically around the point of double symmetry. From figure 7.3 it can be seen that the paths are strongly influenced by the cut-outs. The strain paths cover approximately the strain ratio range from -0.45 to -0.15.

Although the strain paths appear linear, it must be judged that the use of tensile specimens with cut-outs leads to so large strain gradients that the measurement of limiting strains is difficult.

7.1.2 Determination of material parameters using tensile test

In the following section the results of a tensile test series are shown together with a discussion on the measured parameters. Tests are conducted with specimens cut in an angle of 0°, 22.5°, 45°, 67.5° and 90° to the rolling direction. The material tested is a mild steel (FE P03) with a nominal thickness of 1.5 mm. The purposes of the test series are:

- To determine material parameters
- To check the reproducibility of the tests
- To document the procedure used in the treatment of experimental data
- To obtain information concerning the variation of R-values and yield stresses as function of the angle to the rolling direction

7.1.3 Specimen geometry

The free length of the specimens were 245 mm and a 50 mm gauge length extensometer was used to measure the longitudinal elongation. Transverse strains were measured by using a modified extensometer. The transverse extensometer has 3 points (marked with A) of contact as illustrated in figure 7.4. The longitudinal extensometer is guaranteed to

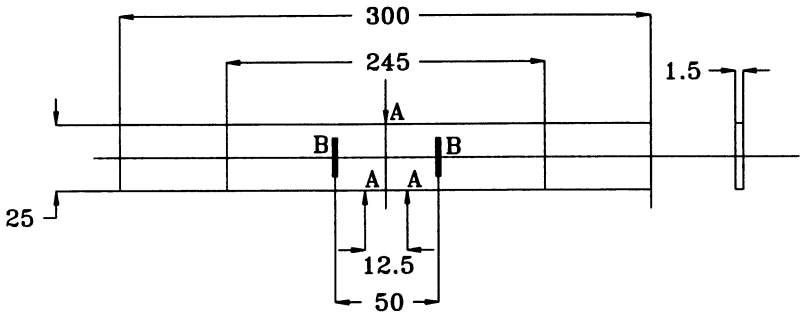

Figure 7.4: *Geometry for tensile specimen and position of extensometers. The points A indicate points of contact for the measurement of transverse strains and the points B the position of longitudinal extensometer. The figure is not scaled according to dimensions.*

have a maximum relative error less than 0.5 per cent. In order to verify the measurements performed with the transverse extensometer a test measurement was conducted. The width of a tensile specimen was measured manually and at the same time with the extensometer. Only the homogeneous deformation is taken into account. The result of the comparison is shown in figure 7.5 where the difference in transversal engineering strain when using the two above mentioned ways of measuring is plotted as function of transversal strain. The figure shows a very good agreement, and the agreement is even better than what

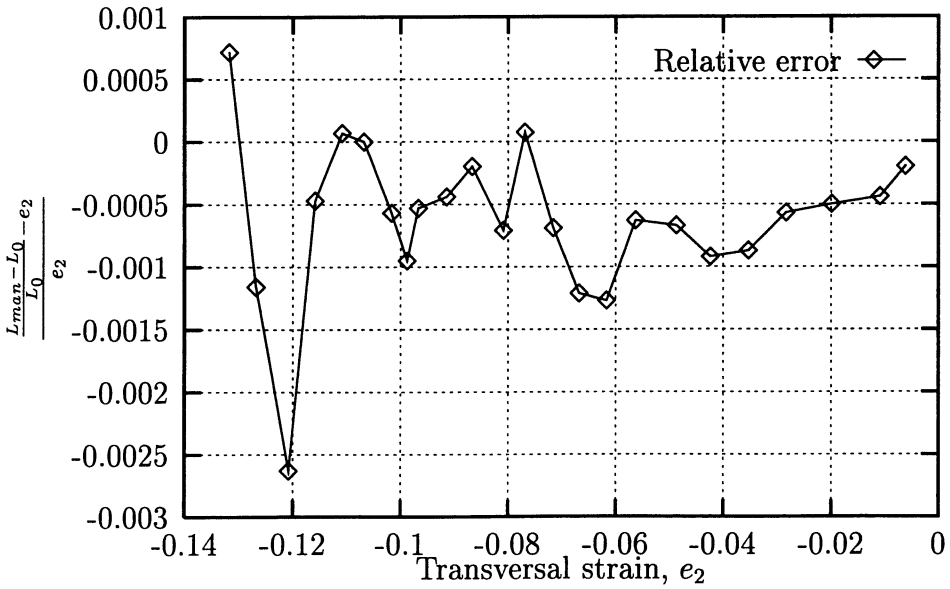

Figure 7.5: *The recorded difference between manually measured transverse engineering strain and the engineering strain recorded by the extensometer. The values are normalized with the transverse engineering strain e_2 measured with extensometer.*

is guaranteed by Instron for the "not modified" extensometer: Instron reports that the

extensometer is linear within 2 per cent for extensions in the range ±5 mm using a gauge length of 20 mm. The testing is performed on an Instron testing machine and the data are recorded by using the software delivered together with the testing machine.

7.1.4 Determination of hardening behaviour

Figure 7.6 shows the nominal stress curves for the different directions. The curves illustrate an excellent correlation between the 3 tests for each direction as the curves are nearly coincident up to the onset of necking. The primary difference arises for the localization where it can be seen that the specimen localizes at different strain levels. This is due to the fact that the position of localization with regard to the gauge position influences the recorded elongation. Although the maximum strain does not necessarily express the ultimate straining we may note that the specimens in 0° lead to maximum strains over 0.3 (nominal) whereas the specimens in 90° localize between strains from 0.25 to 0.3 which indicates a lower formability transverse to the rolling direction than along the rolling direction. The formability is normally lowest for loadings transverse to the rolling direction, but e.g. some aluminum sheets show the lowest formability when the major loading is parallel to the rolling direction. The conclusion, which is drawn from the nominal stress versus engineering strain plots, is that the stress-strain curve can be reproduced and it can also be concluded that the measured initial thickness and width are correct with a satisfactory accuracy.

The normal way to obtain the relation between the true stress and the logarithmic strain is to assume conservation of volume during the plastic deformation and neglect elastic deformations, these assumptions lead to the following relations:

$$\epsilon = ln(1+e) \qquad \sigma = \sigma_{nom}(1+e) \tag{7.1}$$

The resulting curves: True stress as a function of logarithmic strain is given in figure 7.7. It it obvious that the curves are as reproductive as the nominal curves because they are based on exactly the same information. According to EN 10 130 the values of n and K in the Hollomon expression:

$$\sigma = K\epsilon^n \tag{7.2}$$

should be determined for longitudinal strains in the range of 10 to 20 per cent. Using the least square method the expression for the exponent becomes:

$$n = \frac{N\Sigma_{i=1}^{N} x_i y_i - \Sigma_{i=1}^{N} x_i \Sigma_{i=1}^{N} y_i}{N\Sigma_{i=1}^{N} x_i^2 - \left(\Sigma_{i=1}^{N} x_i\right)^2} \tag{7.3}$$

where $x_i = ln(\sigma_i)$, $y_i = ln(\epsilon_i)$ and N is the number of points measured. Figure 7.7 shows a very good agreement between the measured results and the fitted curves. In the region between 0 and 5 per cent strain there is some deviation which should be expected as these points are not taken into account in the fitting. It can also be seen that there is a very good agreement for the region over 20 per cent straining. The problem is more likely to be extrapolation to strain levels higher than 20 per cent.

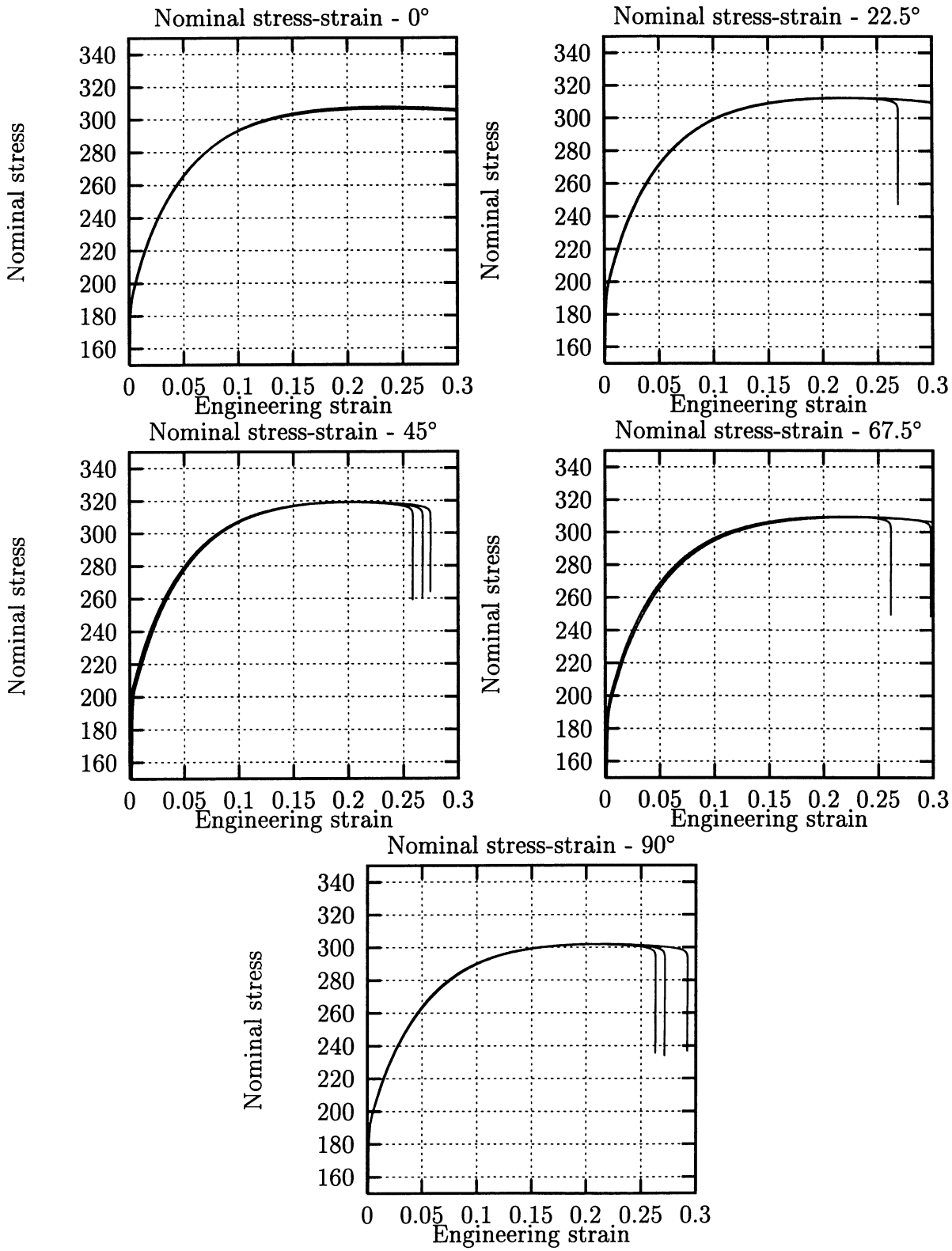

Figure 7.6: *Nominal stress plotted as a function of engineering strain (measured with extensometer) for 3 specimens for each of the directions to the rolling direction: 0, 22.5, 45, 67.5 and 90°, respectively.*

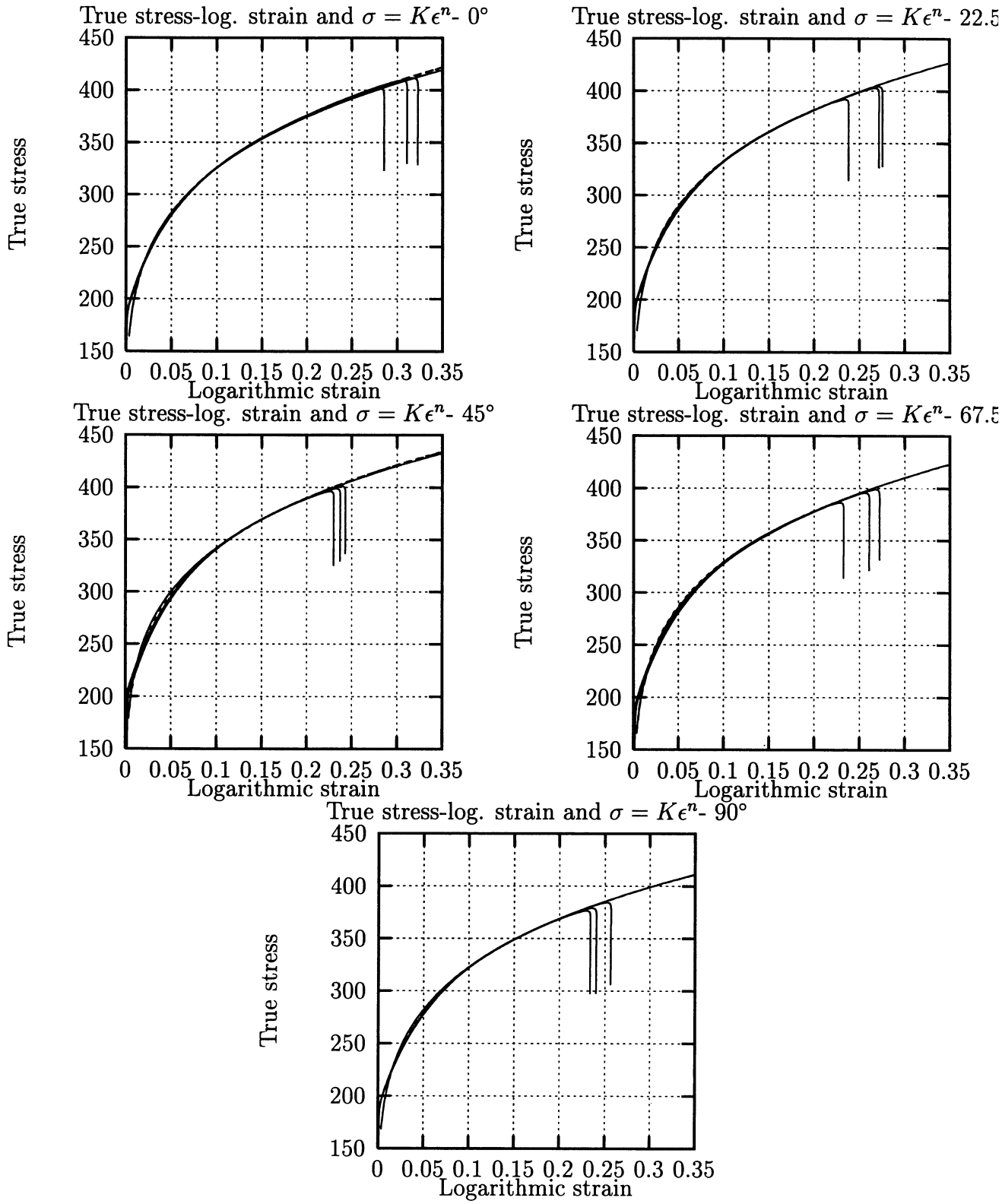

Figure 7.7: *The curves illustrate the relation between measured true stress-logarithmic strain compared to plots using the estimated values of K and n. The full line that reaches a strain of 0.35 is the standard fit to a Hollomon hardening. The dotted line indicates the fit when elastic strains are eliminated (almost overlaying the standard fit).*

Parameter	Spec./Angle	0°	22.5°	45°	67.5°	90°
	1	0.2023	0.2003	0.1879	0.2015	0.1934
n	2	0.2054	0.1987	0.1899	0.2042	0.1929
	3	0.2057	0.1995	0.1931	0.1989	0.1945
	mean	0.2045	0.1995	0.1903	0.2015	0.1936
	1	518.5	526.7	527.0	522.9	503.8
K [MPa]	2	523.4	526.0	529.7	524.4	503.2
	3	523.2	526.2	532.1	521.0	504.1
	mean	521.7	526.3	529.6	522.8	503.7

Table 7.1: The values of n and K determined for each of the specimens used.

The values for K and n utilized in figure 7.7 are listed in table 7.1. The mean values are calculated to $K = 522.9\ [MPa]$ and $n = 0.1976$ according to the principle:

$$n = \frac{n_0 + 2n_{22.5} + 2n_{45} + 2n_{67.5} + n_{90}}{8} \tag{7.4}$$

The principle is similar to the procedure recommended by EN 10 130. It can be discussed whether this procedure is reasonable for the parameters utilized in simulations that use anisotropic material models. These procedures are normally based on the hardening behaviour in the rolling direction (x-direction). But in this case the deviation between the average values and the values in 0° are rather small, 0.2 per cent and -3.4 per cent for K and n, respectively. From the curves it can be noticed that the recorded instability limits seem to differ from specimen to specimen. This is partly due to the placement of the extensometer and partly to the position of the instability zone relative to the fixation in the jaws.

One may discuss the method used to obtain the true stress-strain curves. The calculation of transverse strains is entirely based on the longitudinal strain combined with the assumptions of plastic incompressibility and that elastic strains can be neglected, however, it is evident that some elastic deformation is present during the testing. Below some simple considerations are made concerning the determination of the "true stress". The true stress is expressed as:

$$\sigma = \frac{F}{A_{actual}} \tag{7.5}$$

Splitting the total strain into an elastic part and a plastic part we have:

$$\epsilon_{ij} = \epsilon^e_{ij} + \epsilon^p_{ij} \tag{7.6}$$

Considering the material as isotropic elastic (which might be a wrong assumption) and assuming that only normal straining is present in the specimen, we can write:

$$\begin{Bmatrix} \epsilon_{11} \\ \epsilon_{22} \\ \epsilon_{33} \end{Bmatrix} = \begin{Bmatrix} \epsilon_{11} \\ -\nu\epsilon_{11} \\ -\nu\epsilon_{11} \end{Bmatrix} + \begin{Bmatrix} \epsilon^p_{11} \\ \epsilon^p_{22} \\ \epsilon^p_{33} \end{Bmatrix} \tag{7.7}$$

Assuming that the stress state is uniaxial and assuming that we can express the elastic strain parts from linear theory of elasticity we have:

$$\begin{Bmatrix} \epsilon_{11} \\ \epsilon_{22} \\ \epsilon_{33} \end{Bmatrix} = \begin{Bmatrix} \frac{\sigma_{11}}{E} \\ \frac{-\nu\sigma_{11}}{E} \\ \frac{-\nu\sigma_{11}}{E} \end{Bmatrix} + \begin{Bmatrix} \epsilon_{11}^p \\ \epsilon_{22}^p \\ \epsilon_{33}^p \end{Bmatrix} \tag{7.8}$$

If we now impose the condition of plastic incompressibility we can eliminate the plastic thickness straining (when using logarithmic strains).

$$\epsilon_{33}^p = -\epsilon_{11}^p - \epsilon_{22}^p \tag{7.9}$$

Leading to:

$$\begin{Bmatrix} \epsilon_{11} \\ \epsilon_{22} \\ \epsilon_{33} \end{Bmatrix} = \begin{Bmatrix} \frac{\sigma_{11}}{E} \\ \frac{-\nu\sigma_{11}}{E} \\ \frac{-\nu\sigma_{11}}{E} \end{Bmatrix} + \begin{Bmatrix} \epsilon_{11}^p \\ \epsilon_{22}^p \\ -\epsilon_{11}^p - \epsilon_{22}^p \end{Bmatrix} \tag{7.10}$$

The current area is expressed as a function of the transversal strains:

$$A_{actual} = W_0 T_0 e^{(\epsilon_{22}+\epsilon_{33})} \tag{7.11}$$

with T_0 and W_0 as the initial thickness and width, respectively. Expressing the true stress and eliminating ϵ_{33}:

$$\sigma = \frac{F}{W_0 T_0} e^{-(\epsilon_{22} - \frac{\nu\sigma_{11}}{E} - \epsilon_{11}^p - \epsilon_{22}^p)} \tag{7.12}$$

Which can be rewritten as:

$$\sigma = \sigma_{Nom} e^{-(-\epsilon_{11} + \frac{\sigma_{11}}{E}(1-2\nu))} \tag{7.13}$$

Using nominal stress in the right side of the expression (it is assumed that ϵ_{11} is large compared with $\frac{\sigma_{11}}{E}$):

$$\sigma = \sigma_{Nom} e^{-(-\epsilon_{11} + \frac{\sigma_{Nom}}{E}(1-2\nu))} \tag{7.14}$$

If we compare this expression to the traditional approach we may find the discrepancy shown in figure 7.8. The deviation is very limited and in case of a mild steel it must be judged that the influence is of minor importance, the discrepancy is in the strain range from 5 to 25 per cent far below 1 per cent. In other cases, for example aluminum, the situation may be different. The stress level can for aluminum be of the same magnitude as for steel, but Young's modulus will be approximately one third. Is the ductility at the same time lower, ϵ_{11} will be smaller than in case of mild steel and the effect of elastic strains can be more significant.

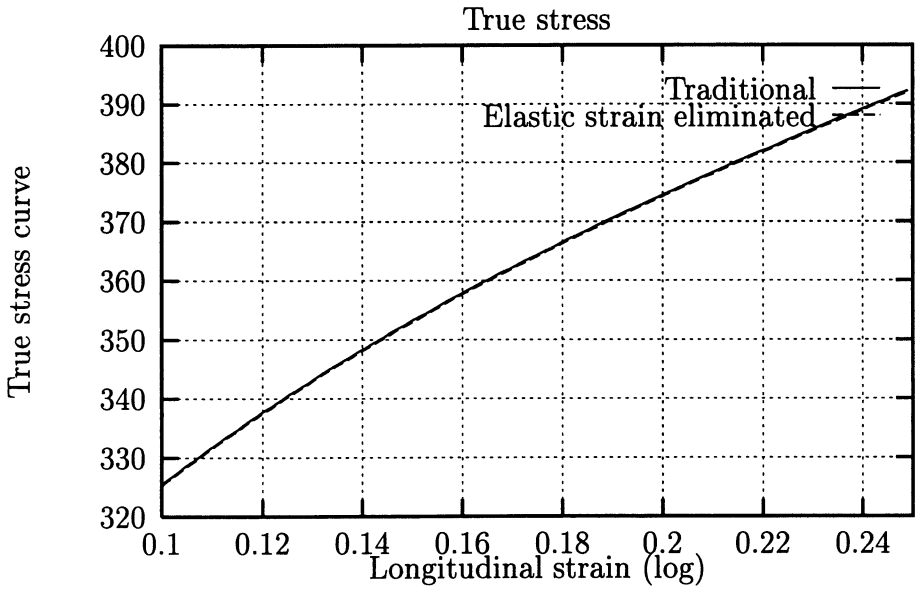

Figure 7.8: *Relation between traditional calculated true stress and the method described.*

7.1.5 Determination of R-values

In order to determine R-values (Lankford coefficients) it is necessary that the relations between the measured strains ϵ_{11} and ϵ_{22} can be recorded correctly. Figures 7.9 and 7.10 show the relation between the strains. Figure 7.10 indicates that the relation is close

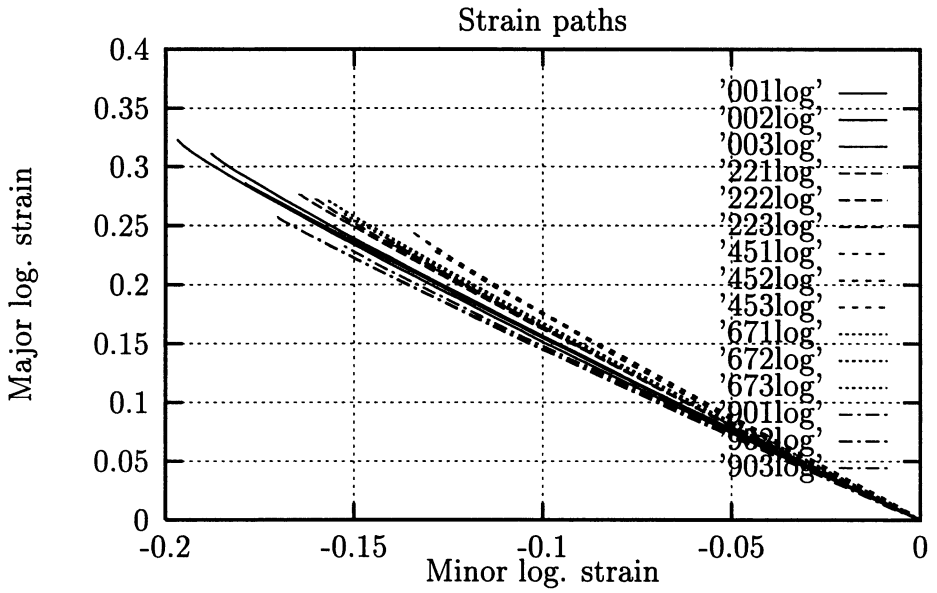

Figure 7.9: *Relation between measured major and minor strain for tensile test specimens taken in 0°, 22.5°, 45°, 67.5° and 90° to the rolling direction. The first two letters in the label identify the direction, the third identifies the specimen number of the actual direction.*

to linear, but for each of the directions (each direction is plotted with the same linetype for the three specimens) some variation can be seen as the slope differs slightly from one specimen to another.

To characterize the anisotropy of sheet metal it is common practise to use the Lankford coefficients. These coefficients are obtained from uniaxial tensile tests where the specimens are cut in an angle α to the rolling direction. The coefficients are defined as:

$$R_\alpha = \frac{\epsilon_{22}^p}{\epsilon_{33}^p} \tag{7.15}$$

ϵ_{22}^p and ϵ_{33}^p are the true plastic strains in the width and thickness direction, respectively. The R-value is to be determined, when the specimen has been subjected to an elongation strain ϵ_{11} of 20 per cent according to EN 10 130 [71] and Stahl-Eisen Prüfblatt 1126 [197]. However, when the anisotropy coefficients are used in connection with FE-simulation it is common practise to use the anisotropy factors to control the relation between plastic strain increments:

$$R_\alpha = \frac{\dot{\epsilon}_{22}^p}{\dot{\epsilon}_{33}^p} \tag{7.16}$$

This approach was used in sections 5.8 and 5.9.1. This means that in many constitutive models based on a rate formulation material parameters are used in a context which differs

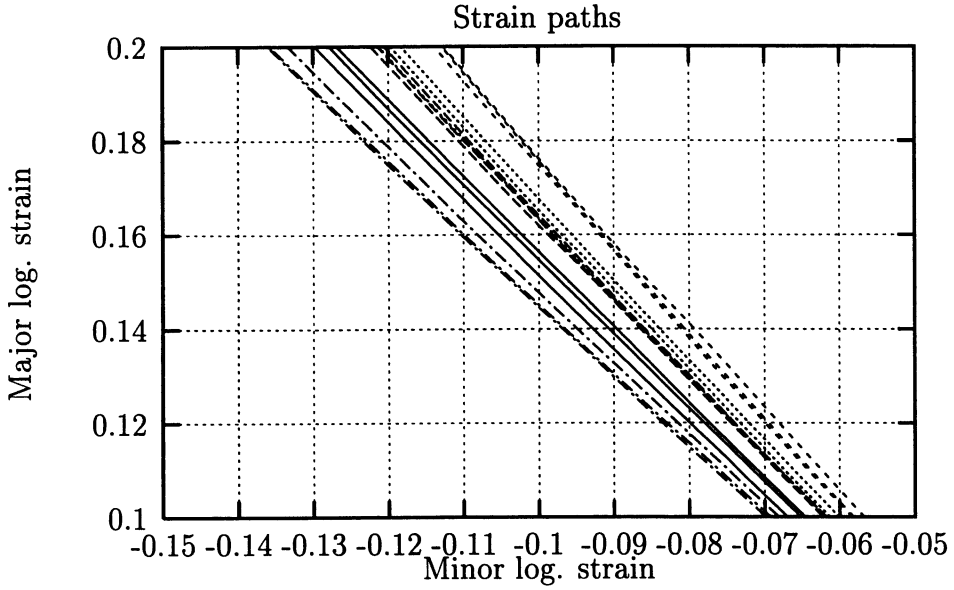

Figure 7.10: *Close view of figure 7.9.*

from the definition used for the determination the material parameters. It is evident that this can lead to discrepancies between the modelled and the physical behaviour. Below some issues concerning the experimental determination and the treatment of measured data are discussed.

The typical way to obtain the thickness strain (which is difficult to measure directly) to be used in equation 7.15 or 7.16, is to assume that the material is plastic incompressible leading to the incremental relation:

$$\dot{\epsilon}^p_{33} = -\dot{\epsilon}^p_{22} - \dot{\epsilon}^p_{11} \tag{7.17}$$

And when using logarithmic strains:

$$\epsilon^p_{33} = -\epsilon^p_{22} - \epsilon^p_{11} \tag{7.18}$$

Using this approach to determine the thickness strain equations 7.15 and 7.16 can be rewritten as:

$$R_\alpha = \frac{\epsilon^p_{22}}{-\epsilon^p_{22} - \epsilon^p_{11}} \qquad R_\alpha = \frac{\dot{\epsilon}^p_{22}}{-\dot{\epsilon}^p_{22} - \dot{\epsilon}^p_{11}} \tag{7.19}$$

If the R-values are determined from strains measured on an unloaded specimen, the definition is reasonably easy to obtain, but today most laboratories use automatic test equipment and in order to obtain the correct values of R from the measured strains (ϵ_{22} and ϵ_{11} are measured when the specimen is loaded) these must be corrected to take the elastic strains into account.

One way to eliminate the elastic strains is to use the previously discussed method (see equation 7.10) where elastic strains are determined from the nominal stress. Below a slightly different approach is given.

If the load F on the tensile specimen is released we can find the change in gauge length ΔL_e (due to elasticity) as:

$$\Delta L_e = L\frac{F}{EA} = L\frac{\sigma_{nom}}{E}\frac{A_0}{A} = L^2\frac{\sigma_{nom}}{EL_0} \tag{7.20}$$

where L is the gauge length and A the cross section area of the specimen after unloading. The elastic situation is referred to the unloaded configuration. In equation 7.20 it is assumed that plastic incompressibility can be used ($L_0A_0 = LA$) which is an approximation. If we denote the gauge length for the loaded specimen L^* we can alternatively express the change in gauge length as:

$$\Delta L_e = L^* - L \tag{7.21}$$

If equation 7.21 is divided by L_0 and combined with 7.20 we obtain:

$$\left(\frac{L}{L_0}\right)^2\frac{\sigma_{nom}}{E} + \frac{L}{L_0} - \frac{L^*}{L_0} = 0 \tag{7.22}$$

If we introduce $e^*_{11} = \frac{L^*-L_0}{L_0}$ (the actual measured engineering strain) and solve the second order equation we can find the unloaded gauge length to be:

$$L = L_0\frac{-1 + \sqrt{1 + 4(1 + e^*_{11})\frac{\sigma_{nom}}{E}}}{2\frac{\sigma_{nom}}{E}} \tag{7.23}$$

The engineering width strain is determined by:

$$e^e_{22} = -\nu e^e_{11} = -\nu\frac{\Delta L_e}{L} = -\nu\frac{\sigma_{nom}}{E}\frac{L}{L_0} \tag{7.24}$$

The width after unloading can then be determined to:

$$W = W_0\frac{1 + e^*_{22}}{1 - \nu\frac{L}{L_0}\frac{\sigma_{nom}}{E}} \tag{7.25}$$

Stahl-Eisen Prüfblatt 1126 gives a method where L and W (the unloaded values) can be found from:

$$L = L_0\left(\frac{L^*}{L_0} - \frac{\sigma_{nom}}{E}\right) \qquad W = W_0\left(\frac{W^*}{W_0} + \nu\frac{L}{L_0}\frac{\sigma_{nom}}{E}\right) \tag{7.26}$$

These equations are different from the equations derived in equations 7.23 and 7.25, and equation 7.26 leads to a higher value of L (which is believed to be an over-estimation) than equation 7.23.

The determination and use of R-values in connection with constitutive modelling have been thoroughly discussed in course of time and although most researchers agree that it causes problems to use the R-values due to their variation with straining, difficulties in measuring them, and so on, no realistic alternatives exist today. At least not when it comes to a compromise between information and the cost of performing the tests. In the present context the main interest has been to obtain reasonably accurate R-values to be

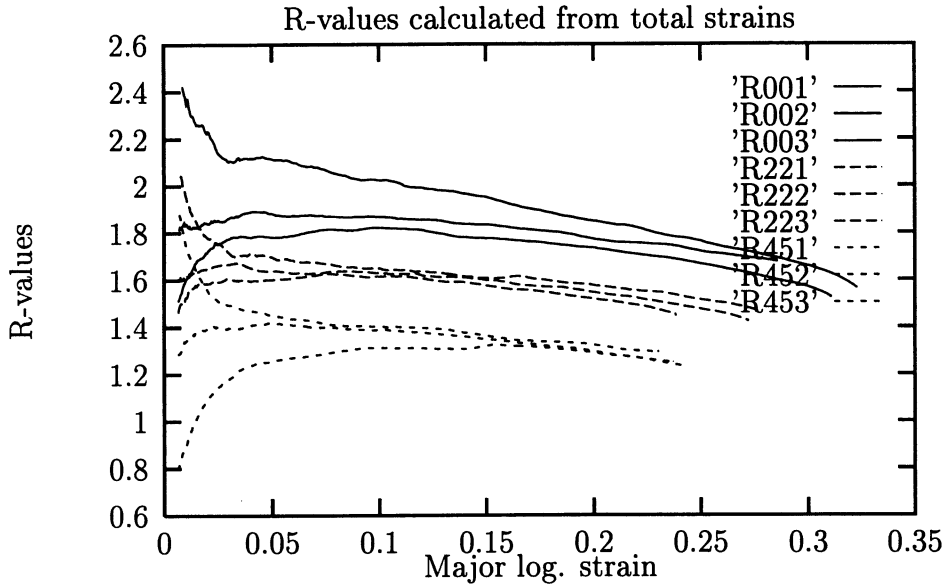

Figure 7.11: *Illustration of R-value development as function of major logarithmic strain for directions 0°, 22.5° and 45° to the rolling direction. The values are calculated from total strains.*

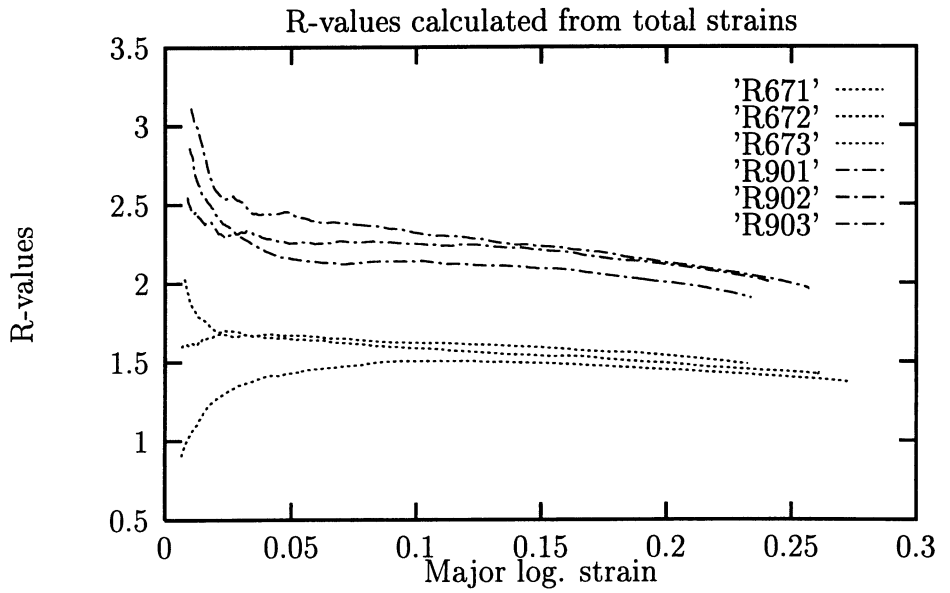

Figure 7.12: *Illustration of R-value development as function of major logarithmic strain for directions 67.5° and 90° to the rolling direction. The values are calculated from total strains.*

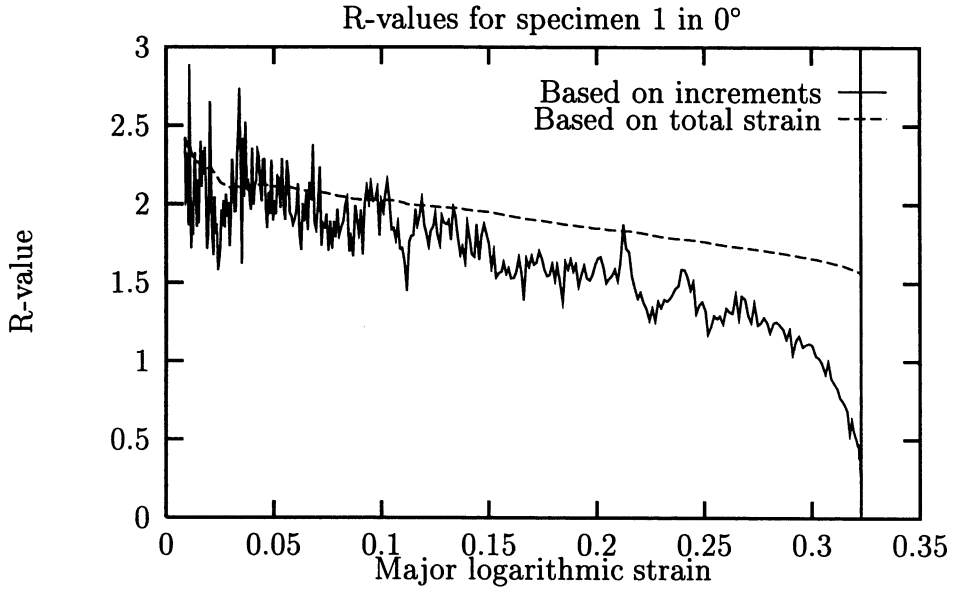

Figure 7.13: *The predicted R-value variation calculated from either total strains or from increments in strain for specimen 1 (0°).*

used in connection with various yield criteria.

The following pages show a number of figures illustrating the variation between various methods used for determining the R-value. From figures 7.11 and 7.12 it can be noticed that there is a strong connection between the strain level and the R-value. It can also be noticed that the values predicted at a low strain level indicate a somewhat peculiar behaviour. This is due to the way in which the R-value is calculated, which is strongly influenced from even very small errors in the measured values of ϵ_{11} and ϵ_{22}.

When modelling anisotropic plasticity, the constitutive behaviour is normally based on a relation between strain increments rather than total strains. If we instead of basing the values on total strains use increments in strain (approximately $\Delta\epsilon_{11} = 0.001$) a somewhat different behaviour can be seen as illustrated in figure 7.13. Figure 7.13 shows the difference between R-values predicted from total strains and from measured increments in strain. The R-value determined from increments is very scattered compared to the R-value based on total strains, and it must be judged that the applyed technique may lead to a wrong estimate. A way to avoid the scatter could be to fit the measured strains (ϵ_{11} and ϵ_{22}) to an analytic expression and then find the incremental values by analytic differentiation of the resulting expressions. There seems to be a clear discrepancy between the two values and seen from a computational point of view the latter should be the most correct. If increments are used the decrease in R-value for increasing strain seems to be slightly more pronounced.

7.1.6 Variation of yield stress and R-values

One of the purposes of the tests has been to obtain information concerning the variation of R-values as well as yield stresses as function of the angle to the rolling direction. Figure

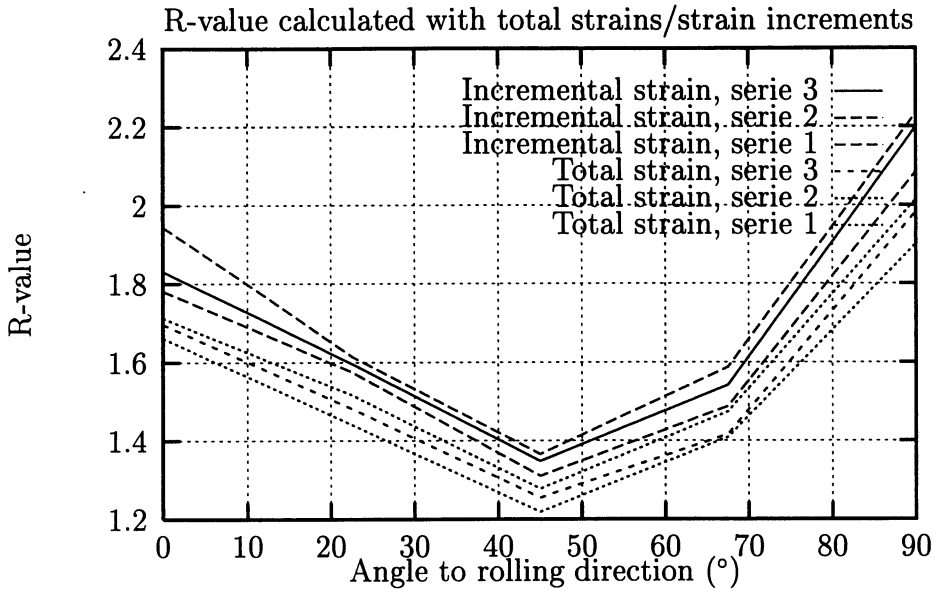

Figure 7.14: *Variation of the R-value with respect to the angle to rolling direction. The values are found using total strains (the three upper curves) and using incremental strains (the three lower curves). The values are not corrected for the elastic strain present during measurements.*

7.14 shows the variation of R-values related to the angle to the rolling direction. The R-value variation is very much the same no matter whether the determination is based on the total or incremental strains, the difference is primarily that the incremental values lead to a lower R-value (obtained by smoothing the R-curves of the type shown in figure 7.13) at a straining of 20 per cent. The figure illustrates also another characteristic of the determination of R-values: Though the strains are measured with a high accuracy, there seems to be some variation from one specimen to another. If a mean value is calculated for each direction the variation ΔR is ≈ 0.1. Table 7.2 shows some characteristics: If the R-values calculated from total strains are corrected to exclude the elastic strains, a slight increase can be seen (≈ 2 per cent). The elastic strains do also influence the R-values when the R-values are determined from incremental strains (with the used technique where $\Delta\epsilon_{11} \approx 0.001$), this influence is significantly lower than when the measurement is based on total strains. The increase in R-values when eliminating elastic strains is ≈ 0.5 per cent for the method based on increments.

If we compare the R-values determined from total strains to the values calculated from incremental values a more marked difference can be seen. Here the difference is in the order of ≈ 10 per cent.

When discussing the correction techniques that are used for eliminating the elastic strains, one should not, as mentioned above, forget the variation that arises from specimen to specimen. This variation is for the present test series just as high or even higher than the

Direction	Spec.	Total No correction	Inc. No correction	Total Corrected	Inc. Corrected
R_{00}	1	1.996	1.811	2.053	1.821
	2	1.790	1.742	1.835	1.751
	3	1.848	1.761	1.896	1.771
	mean	1.878	1.771	1.928	1.781
$R_{22.5}$	1	1.611	1.540	1.648	1.547
	2	1.591	1.517	1.626	1.524
	3	1.637	1.554	1.675	1.562
	mean	1.613	1.537	1.650	1.544
R_{45}	1	1.389	1.299	1.416	1.304
	2	1.370	1.279	1.396	1.284
	3	1.300	1.316	1.323	1.321
	mean	1.353	1.298	1.378	1.303
$R_{67.5}$	1	1.573	1.466	1.608	1.472
	2	1.482	1.479	1.513	1.485
	3	1.610	1.516	1.646	1.523
	mean	1.555	1.487	1.589	1.493
R_{90}	1	2.223	2.113	2.292	2.126
	2	2.291	2.078	2.366	2.091
	3	2.105	1.988	2.167	2.000
	mean	2.206	2.060	2.275	2.072

Table 7.2: *Predicted R-values using total strains and incremental strains. The first two columns show R-values calculated from total strains and incremental strains, respectively. Column 3 and 4 show the corresponding values after correction for elastic strains.*

variations due to the employed numerical technique.

7.1.7 Conclusion drawn from the tensile tests

From the tensile tests we can conclude that the test method is reliable with regard to the hardening behaviour. The reproduction is also very good for the parameters K and n.

The determination of Lankford coefficients is more difficult than the determination of hardening parameters, and it is harder to reproduce the values. This is due to the test principle where only ϵ_{11} and ϵ_{22} are measured, and it is obvious that the term $\frac{\Delta\epsilon_{22}}{\Delta\epsilon_{33}}$ (where ϵ_{33} is calculated from the assumption of volume constancy) will lead to a much higher sensitivity to small errors in the measured strains compared to values determined directly from total strains.

The R-value is sensitive to the approach used in the calculations, that is whether increments in strains or total strains are used and whether the strains are corrected for the elastic contributions or not.

Another aspect which may be discussed is the variation of the R-values as function of the straining. A characteristic drop is seen for the steel tested and e.g. the curves given by Arrieux [8] indicate a variation just as big. This effect is seldom included in the material models employed for sheet metal forming simulations. But if the variation is as big as indicated one of the most beneficial ways to improve simulation results may be to develop constitutive models which are capable of dealing with these phenomena. Another aspect which may lead to a direct improvement can be to determine a new standard for the determination of R-values. Instead of using the plastic strains at an elongation of 20 per cent, the R-values could be determined on the basis of increments in strains, this method is at least more consistent with the numerical modelling of material behaviour that is typically employed today.

7.2 The Erichsen test

The principle of the Erichsen test is rather simple: A square blank is clamped between a cylindrical draw die and a blank hold and a spherical punch is used to load the sheet up to fracture. The Erichsen test is standardized in DIN 50101 and the norm specifies the tool geometry shown in figure 7.15. One major advantage of the Erichsen test is that it is

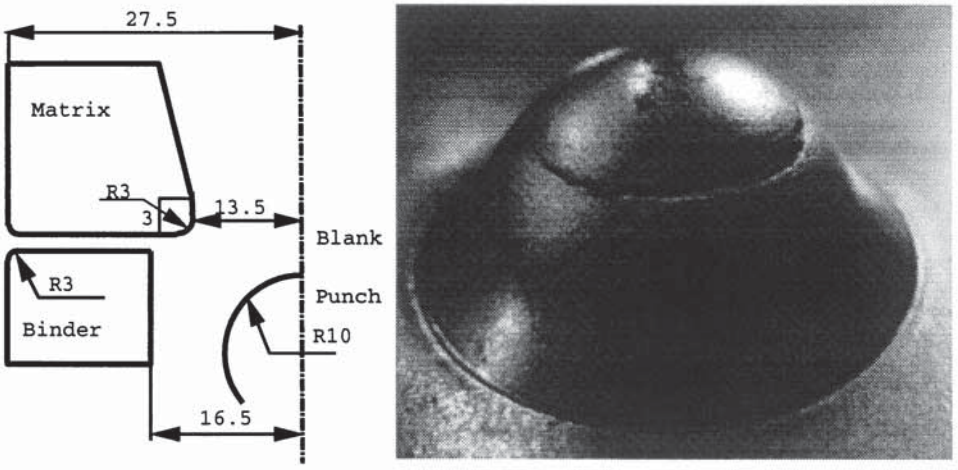

Figure 7.15: *Left: Geometry for the die, binder and punch in the standardized Erichsen test with 20 mm punch. Right: Typical fracture mode for the Erichsen test.*

very easy and cheap to perform. Unfortunately the test has some weak points; it is often argued that the test is sensitive to variation in friction and the fracture limit might be difficult to determine accurately as the punch diameter is relatively small compared to the sheet thickness, at least for thicknesses from about 1 mm and up. When through thickness fracture is visible the related punch depth is taken as the characteristic material property: The Erichsen Index (EI). DIN 50101 gives an alternative to the visible judgement: To take the point where a marked drop in punch force can be seen.

The test has been analysed in order to evaluate the effect of variations in friction conditions. Figure 7.16 shows the discretization used in the analyses. The punch was modelled

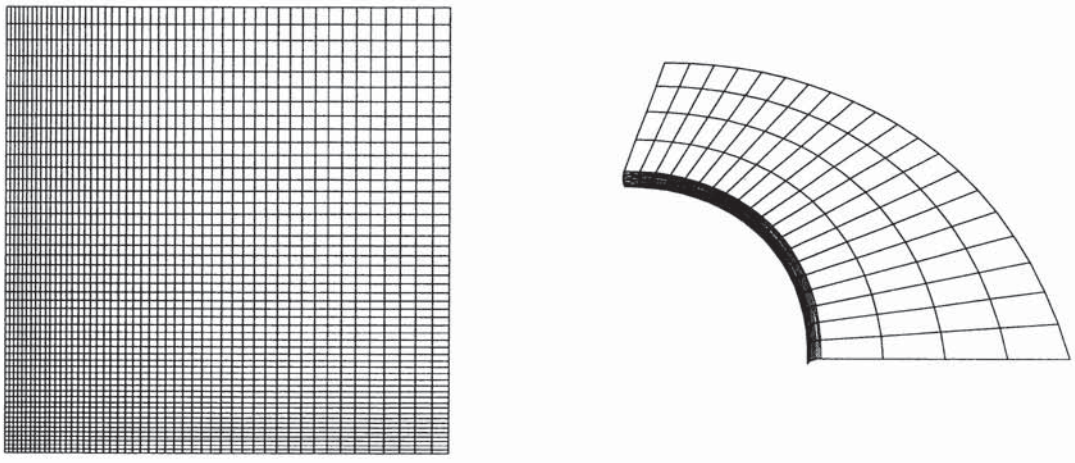

Figure 7.16: *The discretization used for the blank and die for the Erichsen test.*

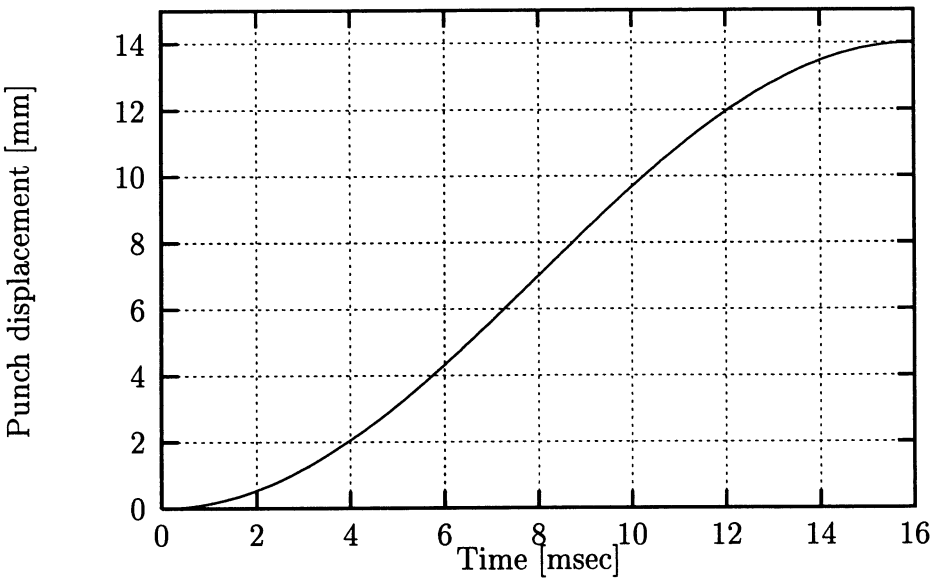

Figure 7.17: *The displacement of the punch as function of process time.*

as rigid by using a so-called stone wall (an analytical representation of the punch surface). Hardening is described with a Hollomon expression with K=554.5 MPa and n=0.22. The punch displacement is prescribed as a cosine profile and is illustrated in figure 7.17.

7.2.1 Frictional effects

It is often claimed that the Erichsen test is significantly affected by frictional conditions. In order to evaluate how severely the coefficient of friction influences the overall results, a total of 5 analyses are performed with various Coulomb friction coefficients. As the base point it was chosen to use $\mu_{tools} = 0.10$ and $\mu_{punch} = 0.04$, around this point four variations were included: (0.08,0.04) (0.12,0.04) (0.10,0.02) and (0.10,0.06). These analyses are performed assuming isotropic material behaviour (von Mises) with a Hollomon hardening with the parameters given above. Figure 7.18 gives the resulting thickness variation at a punch displacement of 9.75 mm. From figure 7.18 it can be seen that the friction between punch and blank has a more marked influence on the process than the friction between die and blank. Going from $\mu_{punch} = 0.06$ to $\mu_{punch} = 0.02$ leads to an additional thinning of ≈ 0.075 mm, whereas a variation in μ_{tool} from 0.08 to 0.12 only leads to an additional thinning of 0.01 mm. For material 4 to 5 mm away from the pole there is no significant variations in thickness due to the variation in friction coefficients. Figure 7.19 shows the predicted load on the die for various combinations of friction coefficients between blank and punch and between blank and die, respectively. It is characteristic that almost up to the maximum force the curves are close to one another which indicates that only limited sliding takes place compared to the performed plastic work. After maximum the difference is more marked and the punch friction has a higher influence on the remaining part of the test. The figure also shows that the maximum punch force is predicted to occur for almost the same punch stroke. However, the curve for $\mu_{punch} = 0.02$ gives the maximum force slightly earlier than the remaining variations. Another observation is that the friction between blank and die influences the force after localization: Up to maximum force the three curves marked with (0.08,0.04), (0.10,0.04) and (0.12,0.04) are very close to each

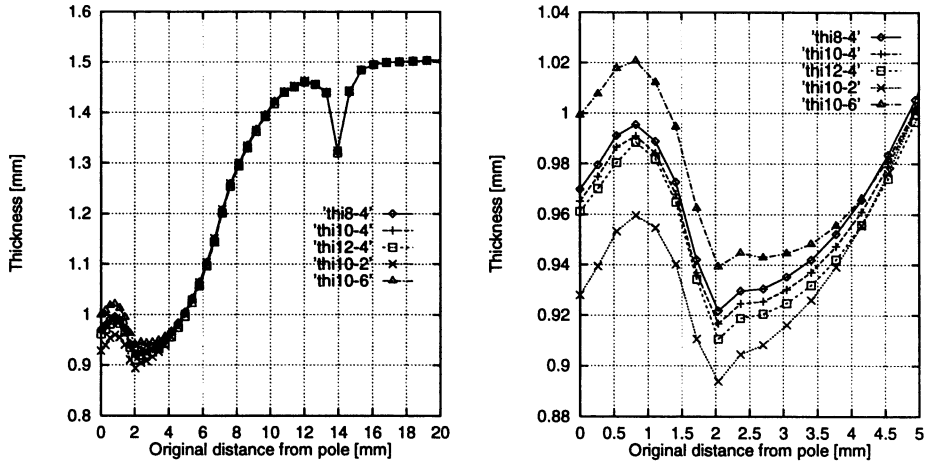

Figure 7.18: *Thickness distribution for a symmetry line as function of original distance to the centre of the blank at a punch stroke of ≈ 9.75 mm (10 msec).*

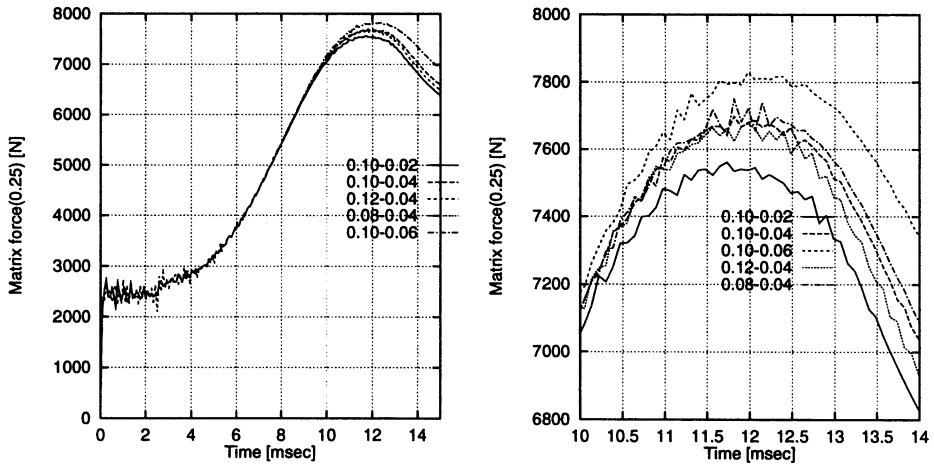

Figure 7.19: *Left: Predicted load on the die, it is both binder and punch force. Right: A closer view of the same curves.*

other, but after maximum the curve for the highest friction coefficient drops faster than the curves for the lower friction.

DIN 50101 prescribes that the punch depth should be determined with an accuracy of 0.1 mm. The present analyses indicate that the punch displacement, where maximum force is reached, is only slightly influenced by friction and with the variations included in the analyses it seems possible to stay within the accuracy of 0.1 mm on the punch stroke. This leads to the proposal that maximum force is used to characterize the formability measure IE instead of using visible fracture. To use this approach makes the measurement more stable as the other fracture limit is more difficult to determine accurately and it also offers the advantage that the influence from variations in friction conditions seem to be very limited compared to the influence after the maximum load as it is believed that the fracturing process is influenced by the friction. Figure 7.20 shows on the left side the process signatures at 8 msec obtained with a higher variation in friction coefficients (0.04, 0.10 and 0.15 between punch and blank). Process signatures is the concept proposed by Karima

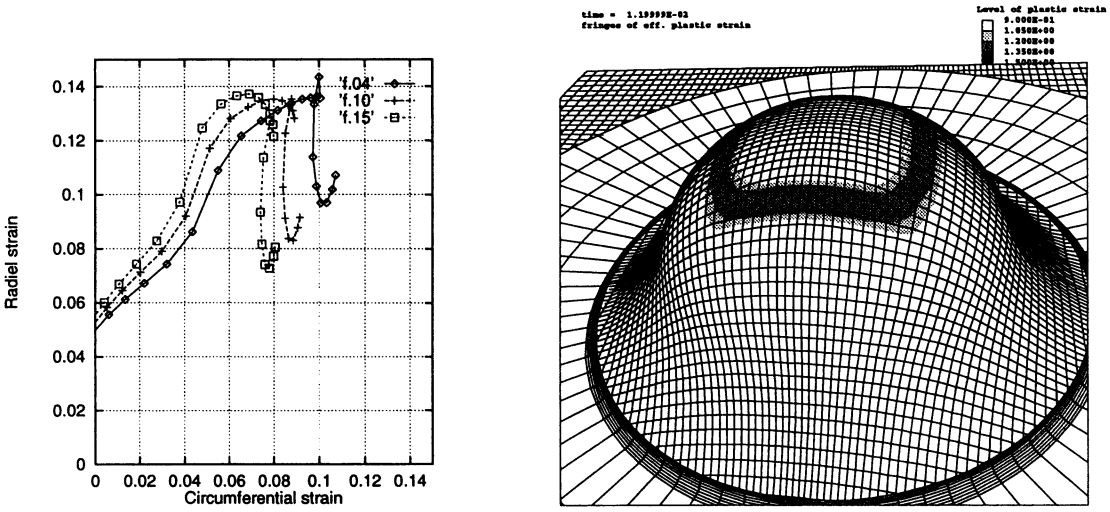

Figure 7.20: *Left: Process signatures for friction coefficients of 0.04, 0.10 and 0.15 between punch and blank.Right: Illustration of localization via the plastic strain level. The dark zone indicates elements which have reached the maximum load carrying capacity and the following deformation is concentrated to these elements. The die is also shown in order to get a clear indication of the position compared to figure 7.15.*

et al. [114] and the idea is that a process can be characterized with one or more lines in the plane of the blank (typically originating from the symmetry line) by plotting the major principal strain as function of the minor principal strain along the given line. The lower the friction coefficient the higher the stretching over the punch (the pole is in balanced biaxial stretching). As regards the lower friction coefficient there is a lower stretching away from the punch. The variations shown in figure 7.20 are due to essentially higher variations in friction coefficients than those used for generating figures 7.18 and 7.19. It can here be noticed that although the stretching over the punch is affected significantly, the maximum ϵ_r is almost the same. The change is that the maximum ϵ_r is reached at a lower ϵ_θ for a higher friction between punch and blank. The variation in strain ratio at maximum ϵ_r is from $\rho \approx 0.5$ to $\rho \approx 0.64$. If we compare this with the diffuse instability criterion proposed by Moore and Wallace (see section 8.1) it can be noticed that this variation in ρ only leads to a slight difference in the limiting strain. This is a very possible explanation of why the maximum force is only slightly influenced by the variations in friction.

The right side of figure 7.20 shows the distribution of effective plastic strain after localization. The predicted fracture mode is similar to the experimental one shown in figure 7.15 (sheet thickness 1 mm), however, the predicted localization seems to be somewhat affected by the mesh and does not show the same circular fracture.

7.2.2 Model of the Erichsen test using Barlat's 2D criterion

This section deals with the influence of material anisotropy modelled using Barlat's 2D criterion and the results are compared with the results obtained assuming isotropic material behaviour. It is investigated how the exponent M in Barlat's criterion influences the deformation and the predicted maximum force.

The material parameters are taken from the course material [5] and apply to a typical mild steel (FE P04 with thickness 1.5 mm). The R-values are reported to be $R_{00} = 1.52$, $R_{45} = 1.15$ and $R_{90} = 1.95$ and the hardening is described with the parameters also used for the isotropic analyses (K=554.5 MPa, n=0.22). The average Erichsen Index (IE) is 12.1 mm using load maximum as the formability limit and the experimental values has a scatter less than 0.1 mm (12.1 mm corresponds to a process time of 12.16 msec in the following analyses). Figure 7.21 shows left thickness variations at two stages in the process; at 10

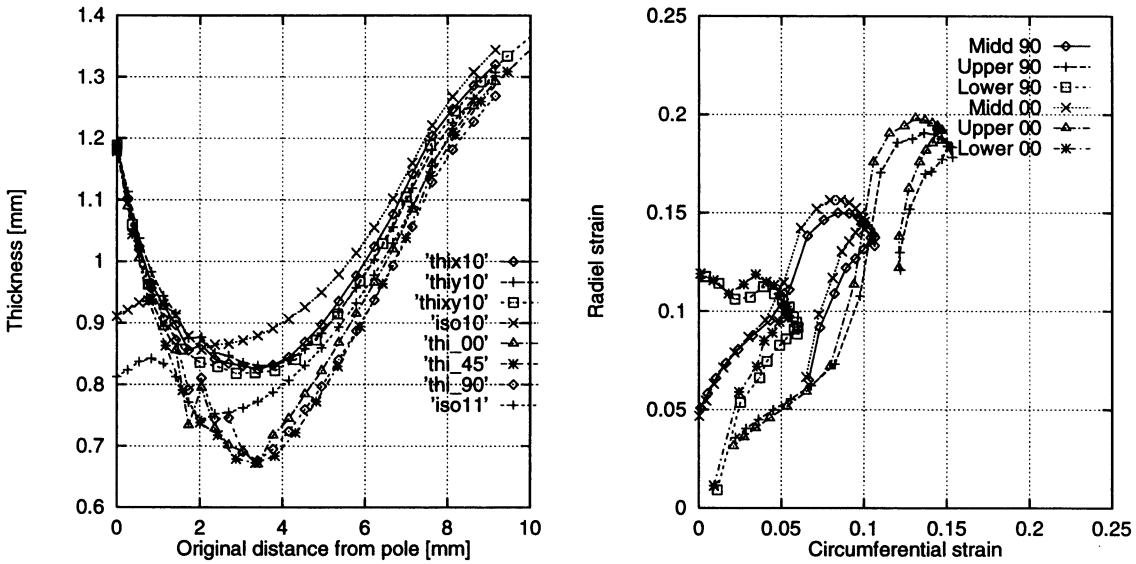

Figure 7.21: *Left: Thickness distribution predicted with finite element at 10 and 11 msec, respectively. The figures show the distribution for the anisotropic and the isotropic situation. Right: Process signatures for the anisotropic case at 8 msec plotted at the middle, upper and lower surface in two directions, 0° and 90° to the rolling direction.*

and 11 msec. In the figure four curves are given for each stage: The thickness variation along a line in 0°, 45° and 90° to the rolling direction and finally the thickness distribution for an isotropic material. Right is shown the process signatures for a line in 0° and 90° to the rolling direction; here are given the variation at the midd plane, at outer and at inner surface. It can from these curves be seen that there is a small variation depending on the orientation to the rolling direction and it is also evident that bending effect is significant. Figure 7.22 shows on the left side the predicted profiles of the sheet (in 0°) at a punch displacement of 6.25 mm. The profiles have been generated with assumptions of isotropic and anisotropic material behaviour, respectively. Close to the pole the profiles are almost identical, but for a distance of $\approx$ 5 mm or more from the pole a difference can be seen (the marks indicate nodal coordinates). However, it is obvious that the straining over the pole is different, but this effect must be integrated over a distance before it becomes visible in the nodal coordinates. The right side of figure 7.22 shows the corresponding punch forces.

Based on figure 7.22 one conclusion can be drawn directly: The interface forces are identical up to an analysis time of approx. 3 msec indicating that the elastic part in the implemented material model behaves exactly as the corresponding material model in LS-Dyna3d (number 18, power-law hardening) which is used for modelling isotropic behaviour.

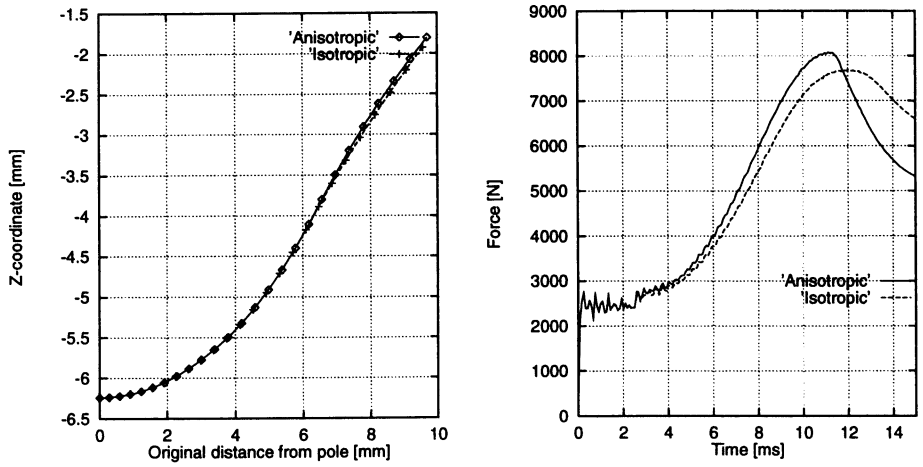

Figure 7.22: *Left: Predicted shape at a punch displacement of 6.25 mm illustrated with the Z-coordinate as function of original distance from the pole. Right is given the corresponding predicted forces. The analyses were identical apart from the constitutive modelling using von Mises and Barlat yield criterion (M=8), respectively.*

The maximum punch force is obtained earlier (less punch travel) for the anisotropic material. This behaviour seems to be reasonable: As the strain field is generally stretching one should expect a lower strain limit as the transverse anisotropy increases, at least that is what is predicted when using the Marciniak-Kuczynski approach, see section 8.4. The anisotropic material leads to higher forces compared to the isotropic material (at the same punch displacement) which agrees with expectations as the average R-value is well above one.

To illustrate the effect of the exponent M the resulting force on the die is shown in figure 7.23 for various values of M (2,5,6,7 and 8). Figure 7.23 shows that the values of

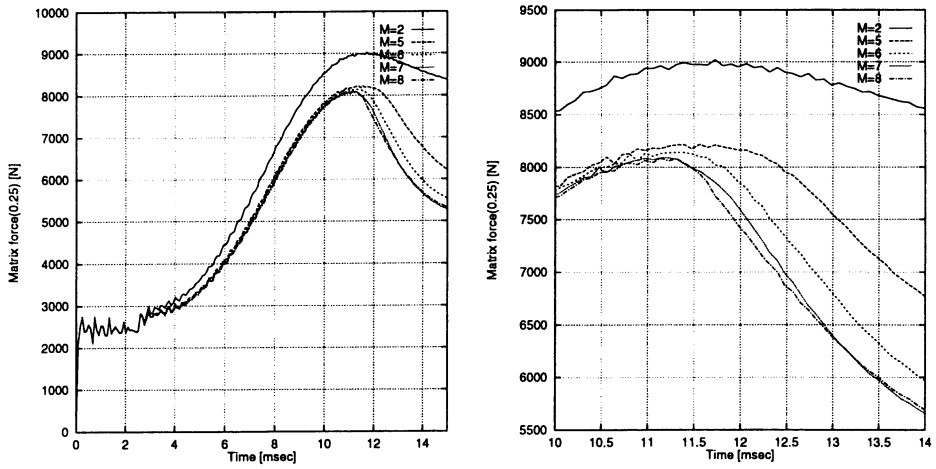

Figure 7.23: *Left: Predicted force on the die for various values of M (2,5,6,7 and 8). Right: Close view of the predicted forces.*

M have a marked influence on the overall behaviour. The lower the M value, the higher the maximum force and the later the maximum force appears. Low M-values increase the

stresses necessary to cause yielding for stress states close to balanced stretching and hereby a higher load can be carried (see figure 5.11), and as stretching is dominating this process the overall behaviour should clearly be affected. The example shows a marked variation when going from a M value of 2 to a M value equal to 5 or higher.

The first analyses performed for the Erichsen test were made by using a discretized surface for the punch. Contrary to expectations the use of an analytical surface (stone wall) in the analysis does not seem to be any improvement with regard to noise in the punch force, this fact can, however, be related to lack of possibility to employ damping in that kind of contact interfaces. Figure 7.22 shows some scatter in the predicted punch force up to a simulation time of $\approx$ 4 msec. After this time the process is dominated by plastic deformation, which leads to an effective damping.

From figure 7.21 it can be concluded that the strain distribution as well as the strain level are severely influenced by the normal anisotropy; increasing the R-values leads to much less thinning over the pole. However, when the material is more constrained over the punch the free area between punch and die becomes thinner for the anisotropic material (at $\approx$ 3.3 mm) for the same punch position. So the strain that leads to fracture (maximum force) is apparently higher for the anisotropic material (at the same punch displacement). At first glance one would estimate that a lower Erichsen index also indicates a lower formability. However, the different distribution of strains may lead to a wrong conclusion: Due to a low EI a material is judged to be less formable than a material with a higher EI, but if the material with the low EI has relatively high R-values the maximum strains at load maximum may be higher than for the material with the high EI. If the strain level is taken into account, one may argue that the fracture limit appears at higher strains and hereby indicates a higher formability. One way to improve the Erichsen test would be to report the diameter of the free skullcap and hereby get an impression of where the fracture occurs - most processes fail in the zone between full contact and no contact (at punch slip or at die slip) and the diameter of the skullcap may be a good way to characterize the failure in the Erichsen test.

It is clear that the strain distribution in the Erichsen test is affected by material anisotropy; this effect can also be expected in other test principles and I am convinced that it is important to incorporate this possible variation when comparing material formability from tests which are based on some process limitation, e.g. the Swift test.

It should also be realized that the Erichsen test is rather severe compared to many industrial sheet forming processes. Figure 7.24 shows process signatures for the Erichsen test plotted at the middle, upper and lower surfaces. The left side shows the behaviour of isotropic material and the right side the behaviour of anisotropic material. Looking at the curves for the middle surface it can be noticed that the strain level at the pole is lower for the anisotropic material. The straining for the isotropic material is $\approx$ 0.11 at the pole but drops for the following four elements slightly to $\approx$ 0.1. This effect can also be seen in figure 7.21 where the thickness increases when going from a distance of 0 up to 1.5 mm to the pole. This variation is not seen for the anisotropic case.

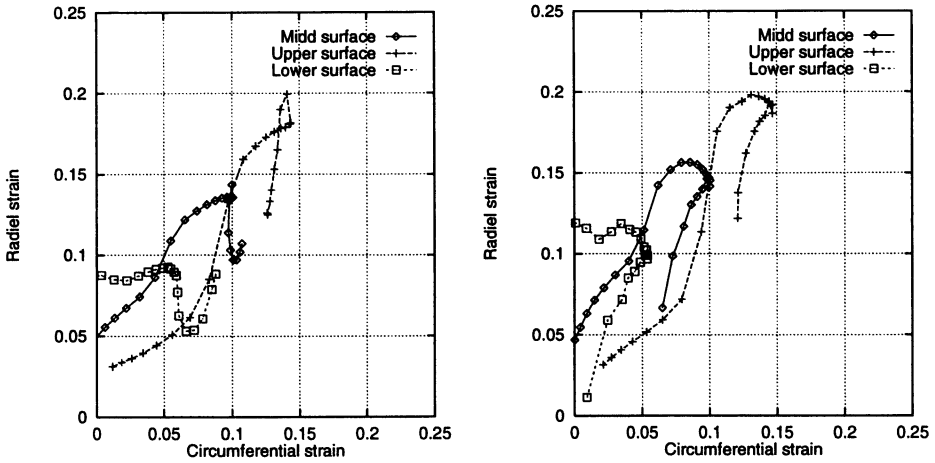

Figure 7.24: *The figure shows process signatures at 8 msec for inner, middle and upper surfaces. Left: Isotropic material behaviour. Right: Anisotropic material behaviour (Barlat's 2D criterion, M=8).*

7.2.3 Conclusion drawn from the Erichsen test

From the simulations of the Erichsen test we can conclude that the friction seems to play a minor role until the maximum force is reached. After reaching maximum force the deformation primarily takes place in the localized area and the punch force seems to become more affected by the friction condition (due to sliding between punch and material). These observations lead to the proposal that the maximum force should be used when specifying the IE.

The analyses performed with Barlat's criterion indicate a very strong influence from the M-value on the overall behaviour. Especially, the difference between the values M=2 and M=5 is significant for the predicted punch force. The M-value influences also the behaviour after the maximum force strongly, but it is to be noticed that the discretization may influence this behaviour, too. The higher the value of M, the earlier the maximum force is reached.

Based on the simulation it may also be noticed that one or two aspects can easily be improved. A slight draw-in of a corner point did exist and can be avoided just by increasing the binder force. In the norm a minimum force is specified; this value has been used in the reported analyses. Another way to almost eliminate the draw-in effects is to use a larger blank than the minimum blank shape specified in the norm.

The test method is cheap and easy to perform, but it can be concluded from the presented analyses that one cannot rely on the IE as a direct measure of the formability when comparing a particular sheet to another.

7.3 Nakazima test principle

Figure 7.25 shows a sketch of the Nakazima test. This test method has the advantage that

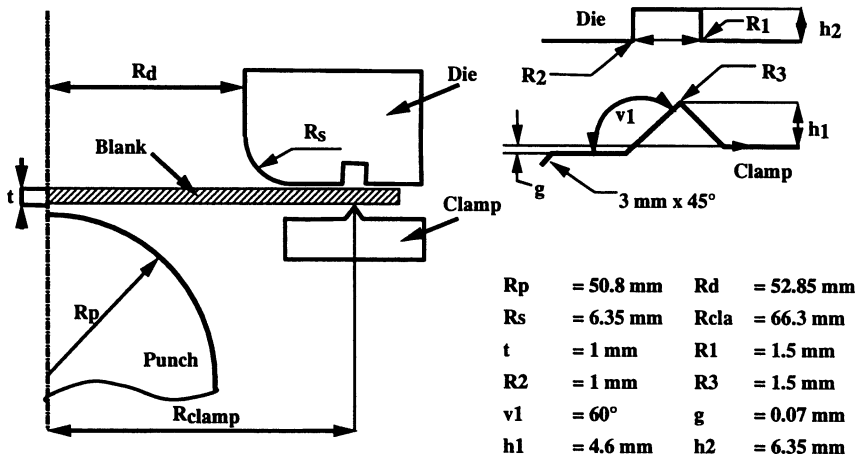

Figure 7.25: *Sketch of the Nakazima test principle. The geometric values correspond to the Numisheet'96 Benchmark.*

strain ratios in the range from -0.5 to 1 can be obtained by changing the geometry of the test blanks. The disadvantage is that the limiting strains are influenced by both frictional and bending effects, however, bending effects are much less pronounced than the bending effects in an Erichsen test.

7.3.1 FE-analysis of the Nakazima test

The analysis reported for the Nakazima test corresponds to the benchmark tests for Numisheet'96. Only one test strip geometry with the dimensions 180 x 100 mm is analysed. The discretization level for the tools is the same as the one used for the Marciniak Double Blank Method, see section 7.5. In the analyses three different materials are included for which the material parameters can be found in table 7.3. Figure 7.26 shows left a sketch

Direction to rolling	Yield strength	Tensile strength	n	K	R	m	Coulomb coeff.μ	Thickness
IF 0	152	294	0.239	526	1.85	0.015		
45	159	301	0.231	530	1.52			
90	163	292	0.231	516	2.37			
mean	158	297	0.233	526	1.82	0.015	0.11	1.0
HS 0	358	468	0.162	739	0.72	0.008		
45	369	465	0.157	728	1.21			
90	384	480	0.149	741	1.03			
mean	370	470	0.156	734	1.04	0.008	0.11	0.92
AL 0	161	278	0.232	498	0.64	0	0.13	
45	153	272	0.232	484	0.65	0		
90	152	270	0.233	481	0.61	0	0.06-0.08	
mean	155	273	0.232	488	0.64	0	0.10	0.92

Table 7.3: *Material data for the Nakazima test according to the Numisheet'96 Benchmark.*

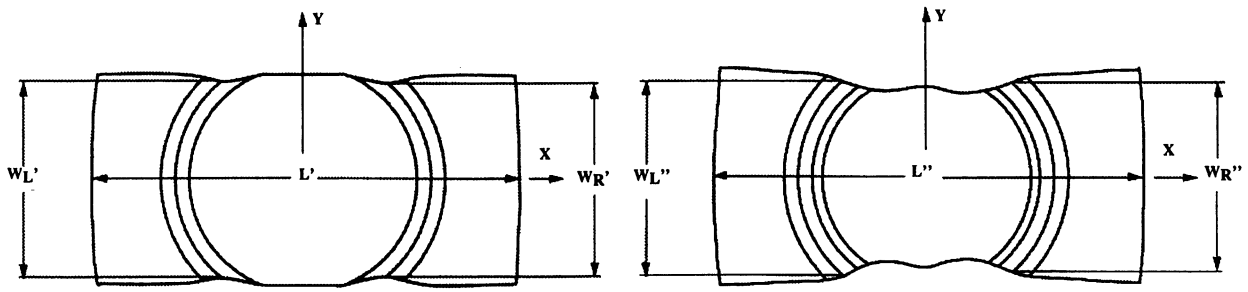

Figure 7.26: *Critical geometric parameters. Left is given the measures W'_L and W'_R which should be kept within a difference less than 1 mm to insure symmetric conditions. Right: The measure L" for which (L'-L") should be less than 0.25 mm.*

of the test blank after clamping and right is shown the test blank after testing. In order to ensure that the test is performed correctly the measure L'-L" should be less than 0.25 mm, otherwise the test should be repeated with a new test blank.

To model the anisotropic material behaviour Barlat's 2D criterion is used in the simulation. Seen from a theoretical point of view the exponent M should be set to 6 or 8 depending on the crystallografic structure of the material [12, 14]. Other authors suggest that the exponent M is used as a fourth material parameter which is to be fitted for the best correlation between experiments and simulations. In the present analyses values of 8, 2 and 12 have been used for mild steel, high strength steel and aluminum, respectively. As shown previously the localization of strains depends strongly on the value of M, and the values have been chosen to obtain a reasonable agreement between the predicted fracture limit and the behaviour that is normally expected of the actual material types. A value of 8 for the exponent has turned out to give good results for mild steel and with this as reference the M-value is increased for aluminum (as the same level of n is given for the hardening behaviour) in order to reach localization at an earlier process stage (which is indicated from the preliminary FLDs for the Numisheet Benchmark, see figure 8.18). Analysis with the aluminum sheet indicates almost the same formability limit as mild steel when analysed with the value of M equal to 8. This is no matter for surprise as the n-values for the two materials are almost identical. The value for high strength steel has been set to 2 as it was judged that localization occurred too early when using a M-value of 8. Figure 7.27 shows left the major strain distribution and right the minor strain distribution along the symmetry line with Y=0 at a punch displacement of 30 mm (20 mm for aluminum). Figure 7.28 shows major and minor strain distribution along the symmetry line with X=0. Figure 7.29 shows major and minor strain along the outer line with the initial position Y=50 mm. The strain distributions given in figures 7.27 to 7.28 corresponds to the results which were reported to the Numisheet'96 conference. Figure 7.30 shows left the calculated punch force as function of punch displacement and right is shown the preliminary FLDs given together with the Benchmark material.

For high strength steel two very characteristic peaks for the major strain can be seen in figure 7.27; these peaks are caused by beginning localization which clearly have been initiated at the particular punch stroke. The fracture is, however, first evaluated to occur at a punch stroke of 33.1 mm (see figure 7.30) where maximum load is found. The statement

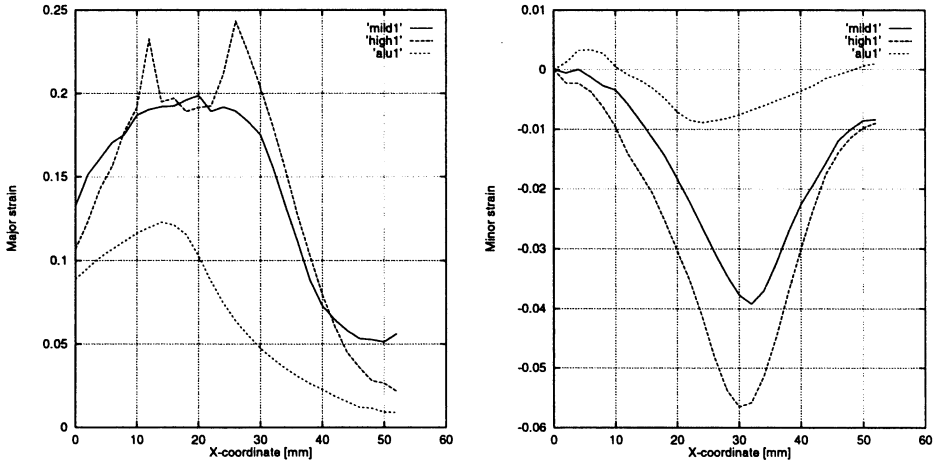

Figure 7.27: *Major and minor strain along the line: Y=0 for the Nakazima (LDH) test corresponding to the Numisheet'96 Benchmark. The values for steels are reported for a punch stroke of 30 mm and for aluminum 20 mm.*

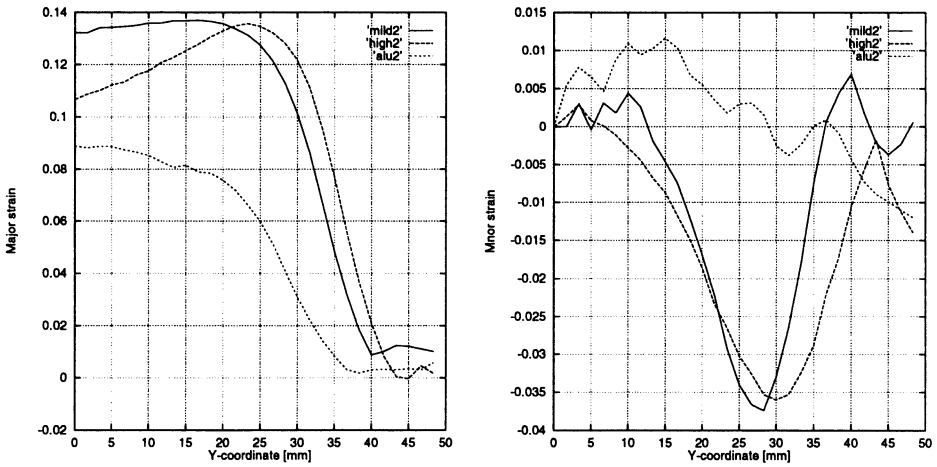

Figure 7.28: *Major and minor strain along the line X=0. The values for steels are reported for a punch stroke of 30 mm and for aluminum 20 mm.*

that maximum force can be used to determine the process limitation is maybe troublesome: The strain distribution shown in figure 7.27 indicates that localization can be detected at a punch displacement of 30 mm whereas the maximum force first appears at 33.1 mm. The reason is that the onset of instability starts from the symmetry plane and the localization must propagate over the entire section before the punch force reaches the maximum.

This discrepancy between mild steel and high strength steel is believed to be partly related to the n-value. Several authors report that for an increasing n-value there is a better distribution of strain. For instance Boyer [35] gives the following description: "The major strain, ϵ_1, in the critical region of a formed part is more uniform distributed for steel having the higher value of n".

The punch forces in figure 7.30 give an idea of the predicted formability (the punch stroke cannot be related directly to the strain level), mild steel reaches the maximum point at 37.6, high strength steel at 31.3 mm and aluminum at 31.3 mm, too. This impression is to

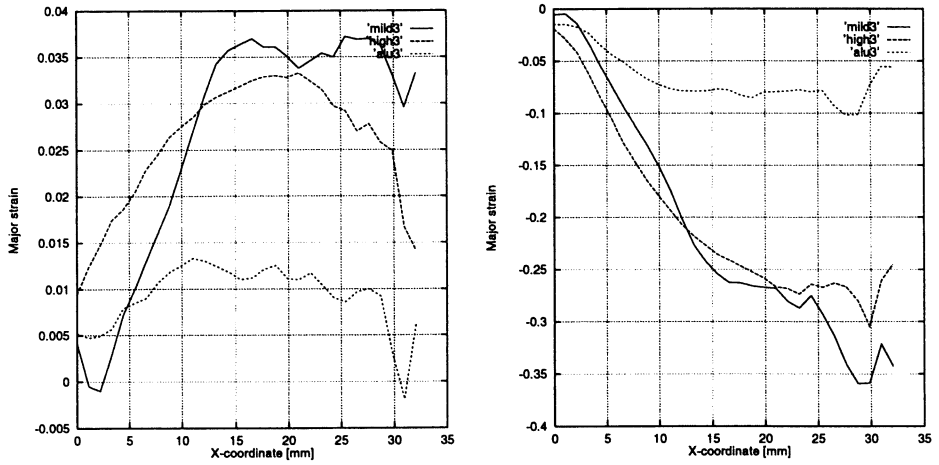

Figure 7.29: *Major and minor strain along the line Y=50. The values for steels are reported for a punch stroke of 30 mm, for aluminum 20 mm.*

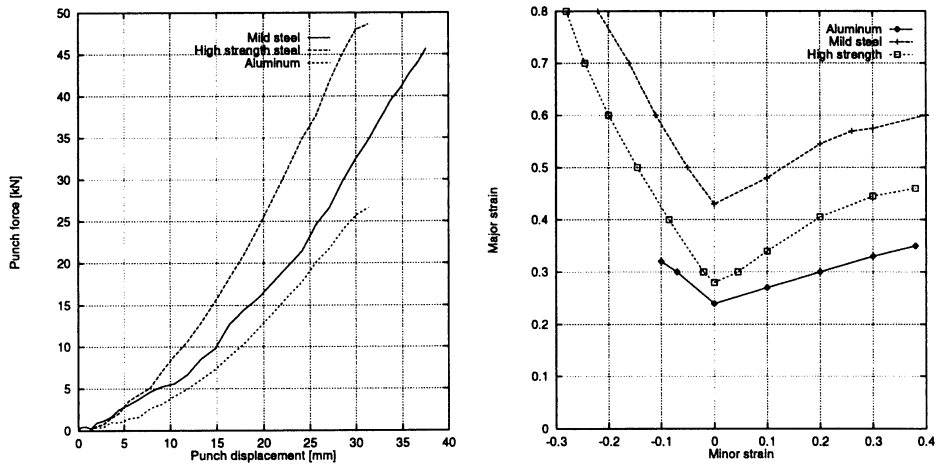

Figure 7.30: *Calculated punch force as function of punch stroke. Right is given the preliminary FLDs reported in the Numisheet'96 Benchmark material.*

some degree in contrast with the FLDs given on the right side of figure 7.30. The variation between mild steel and high strength steel obtained numerically may seem reasonable - but it is obvious that the formability, which is predicted for aluminum, is too high. It can be concluded from this observation that dealing with fracture in sheet metal forming is rather complicated and that we cannot in general expect to model the fracturing limit accurately just by using the hardening description according to e.g Hollomon and yielding behaviour by using von Mises, Barlat and Hill type criteria. In other words: It is not sufficient to have a reasonable description of hardening and of anisotropy in order to investigate process limitations. It is obvious that more complicated constitutive modelling should either be considered or FLDs should be incorporated in the FE-codes. These matters are discussed in detail in the subsequent chapter, which deals with theoretical determination of FLDs.

Another interesting aspect is the correction which has been sent to the Benchmark participants: It had been observed that a too heavy clamping of the sheet leads to fracture in the die contact area. This aspect was also found with the present analyses; if the condition $((L' - L'') < 0.25\ mm)$ given in figure 7.26 is fulfilled fracture occurs in the die zone,

but when reducing the clamping force so $(L' - L'') \approx 0.4\ mm$ the fracture occurs close to the punch contact zone instead. The phenomenon was especially pronounced for the high strength steel. Figure 7.31 illustrates the mesh after a clear localization at the die region(left) and at the punch region (right). The only difference between the two examples is that the clamping was relaxed in the simulation leading to the strain distribution shown right. Figure 7.32 shows various clamping force profiles which are tested in order to avoid

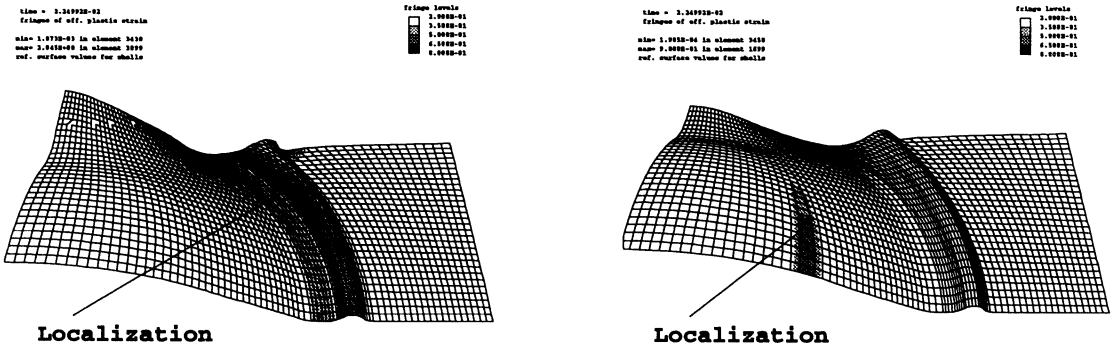

Figure 7.31: *Illustration of the fracture zone at high (left) and medium (right) clamping force. The dark grey zones indicates regions which have experienced an effective plastic strain over 0.5.*

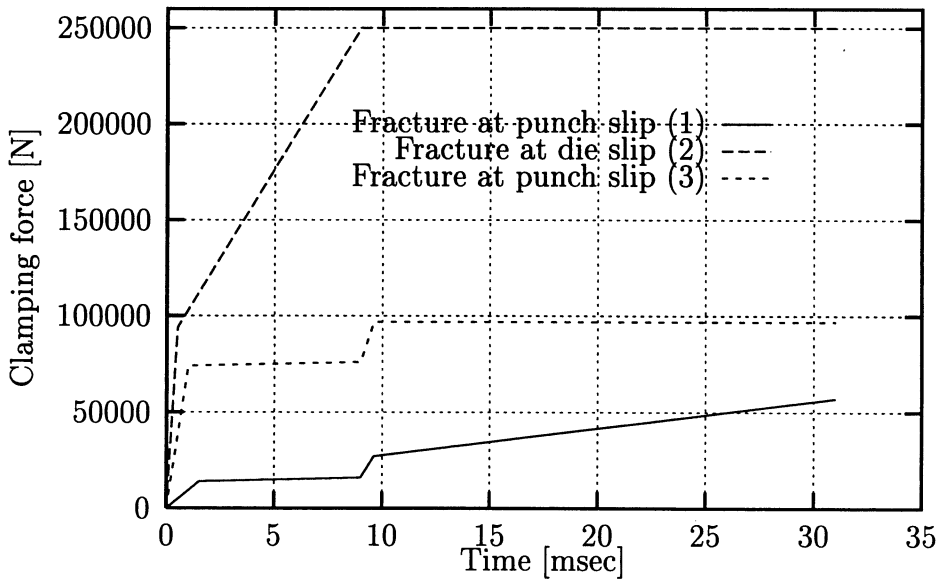

Figure 7.32: *Clamping forces used for the LDH test. Curves 1 and 3 lead to fracture at punch slip (curve 3 is very close to fracture at the die zone early in the process), curve 2 allows almost no draw-in after clamping.*

fracture at the die zone. The curves 1 and 3 lead to fracture in the zone where the blank gets in contact with the punch. Curve 2 leads to fracture at the contact zone between die and blank. Use of a clamping force following curve 3 leads to a deformation which is

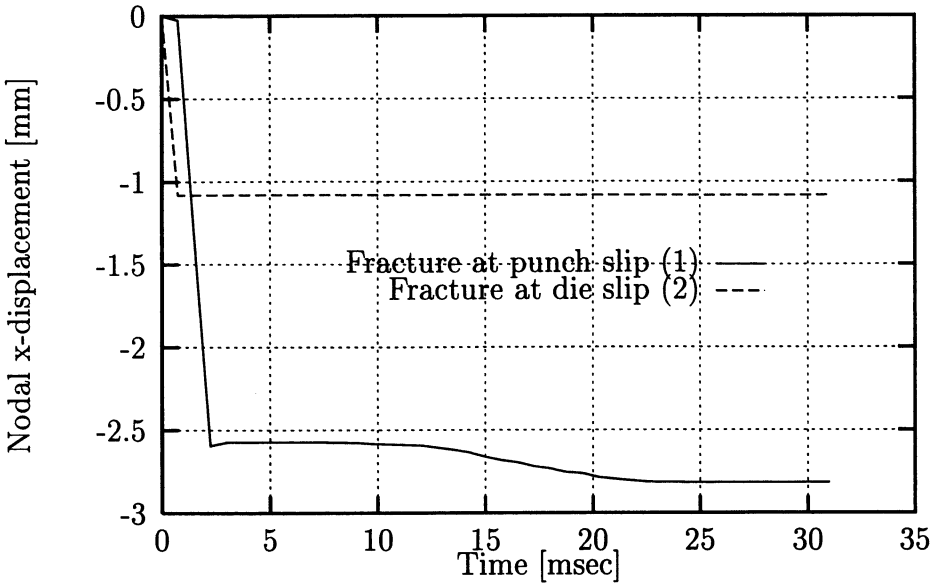

Figure 7.33: *Displacement as function of analysis time for the node initially placed at X=90, Y=0 when the clamping force is specified with the curves given in figure 7.32 with labels 1 and 2, respectively.*

very close to localization at the die zone. Figure 7.33 gives the displacement history of the node initially placed at X=90, Y=0 under two clamping force profiles. The curve (label 1) indicates that no sliding takes place after the initial clamping whereas the curve (label 2) indicates a sliding of $\approx$ 0.2 mm over a time interval from 12 to 23 msec. This small sliding is sufficient to avoid fracture at the die zone.

From this it appears that the boundary conditions have a crucial effect on the predicted overall response for this model: It is evident that it becomes very important to model the correct behaviour of blank to tool interaction accurately when dealing with more complex sheet forming operations. From the previous discussion it becomes obvious that the Nakazima test principle (LDH) has some drawbacks. As shown above, the method is highly influenced by the clamping force and it is expected that the method will lead to some scatter in the experimental results from one laboratory to another. Several other aspects might influence the results such as variations in temperature, lubrication, etc, but these have not been considered in more detail. It is, however, expected that friction will have a more pronounced effect in this method than in the Erichsen test as the geometry and hereby the overall displacements are much larger. On the other hand it must be realized that the test conditions are much closer to the sheet metal operations typically used in the automotive industry.

7.4 The Hemispherical Punch Test

To perform the Nakazima test with a full blank is identical to the Hemispherical Punch test. This example has previously been investigated by Peric & Owen [177] and by Brännberg [36] by using implementations of Barlat's 2D criterion. Peric & Owen use an implicit FE-approach and Brännberg uses explicit finite element to simulate the forming operation. Figure 7.34 shows the discretization of the blank and die which I have used. Figures 7.35

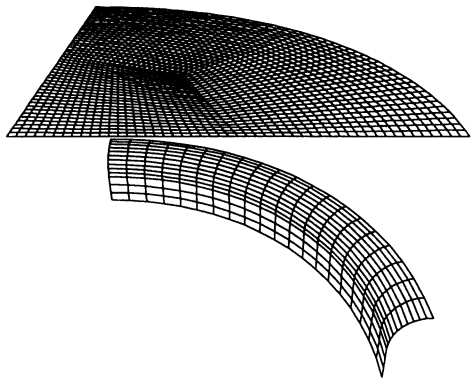

Figure 7.34: *Discretization of the blank and sheet used for the hemispherical punch stretching. The die consists of 260 elements and the blank consists of 1875 elements.*

and 7.36 show the predicted radial strain at 30 and 35 mm punch displacement, respectively. In figure 7.35 the curve for M=4 cannot be seen, because it coincides with the curve for M=2. The predicted distribution in figures 7.35 and 7.36 agrees very well with the results reported in [177] and [36], however, the maximum predicted radial strain is slightly higher than the strain predicted by the other authors; the reason is that smaller elements are used in the present simulations. For the zone away from the localization the same levels and variations are predicted. The position of the fracture (at 31.5 mm) agrees very well with Peric and Owen, but differs slightly from Brännberg's results (predicted at 29-30 mm). It is believed that this is due to the modelling of the punch; Brännberg uses a relatively coarse discretization of the punch whereas Peric and Owen use a very fine discretization. In the present the punch is modelled by using an analytical surface and we hereby eliminate the effects of the inevitable facetted surface when using plane elements.

From the simulations and the comparison with Brännberg's and Peric and Owen's results it can be stated that the level of discretization is important: If the discretization is too coarse the contact forces cannot distribute correctly. A too coarse mesh leads to less sliding than a fine mesh and in the present example it seems to be sufficient to move the zone where fracture occurs. Combining these observations with the observations made for the Marciniak Double Blank Method and the Nakazima test it becomes clear that in order to make the correct modelling of boundary conditions it is not sufficient to describe the friction and clamping correctly - it is of importance also to include the aspect of discretization.

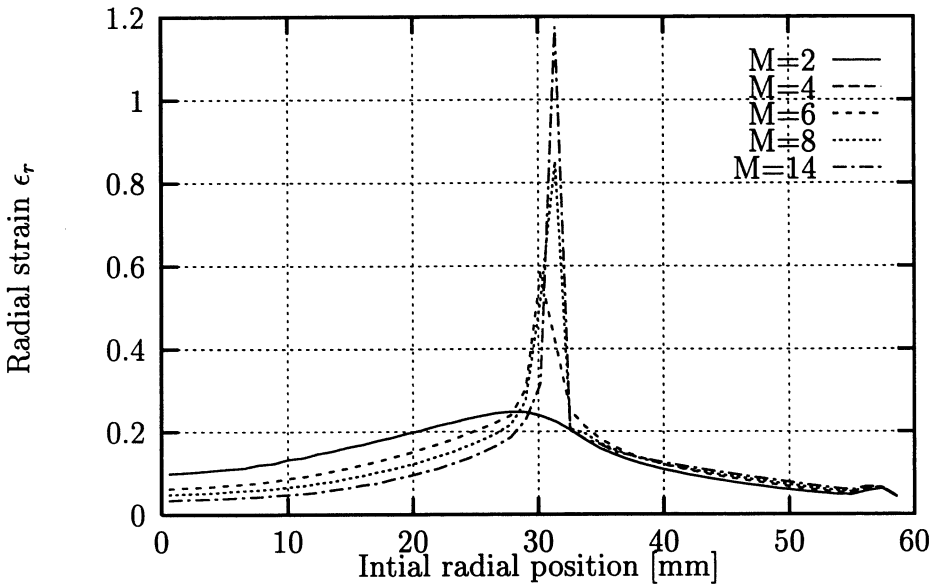

Figure 7.35: *Radial strain predicted for the Hemispherical Punch stretching at a punch stroke of 30 mm using Barlat's 2D criterion on an isotropic material with various values of the coefficient M (M=2,4,6,8,14) and with a sheet thickness of 1.0 mm.*

As regards the Erichsen test (section 7.2) a strong influence from the exponent M can be seen for the predicted punch force. Figures 7.39 and 7.40 show the predicted punch forces for various values of exponent M, and sheet thicknesses of 1.0 and 1.5 mm, respectively. The punch forces shown in figures 7.39 and 7.40 are taken as the interface forces between die and blank. The figures show, for the 1.0 mm blank thickness especially, that the force response is overlaid with a vibration in the first part of the process. At the beginning of the process the major part of the blank is only loaded elastically and the vibrations are hereby not damped out effectively. A more steady response can be obtained by applying artificial damping, however, the use of such a technique will affect the force transmitted to the die and should in the general case be avoided.

From a comparison between the responses shown in figures 7.39 and 7.40 and the response obtained for the Erichsen test (see figure 7.23), it appears that the influence from the exponent M is much less for the Hemispherical Punch example than in the Erichsen test, where M=2 leads to a somewhat higher punch force at an early stage in the process. On the other hand a much clearer delay of the maximum force (as the M-value is decreased) can be seen in the Hemispherical Punch examples.

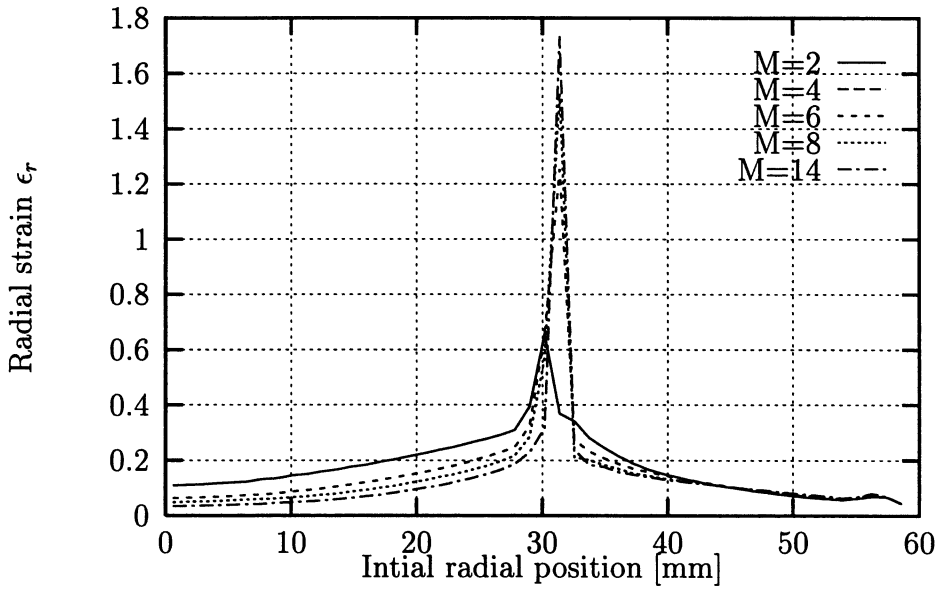

Figure 7.36: *Radial strain predicted for the Hemispherical Punch stretching at a punch stroke of 35 mm using Barlat's 2D criterion on an isotropic material with various values of the coefficient M (M=2,4,6,8,14) and with a sheet thickness of 1.0 mm.*

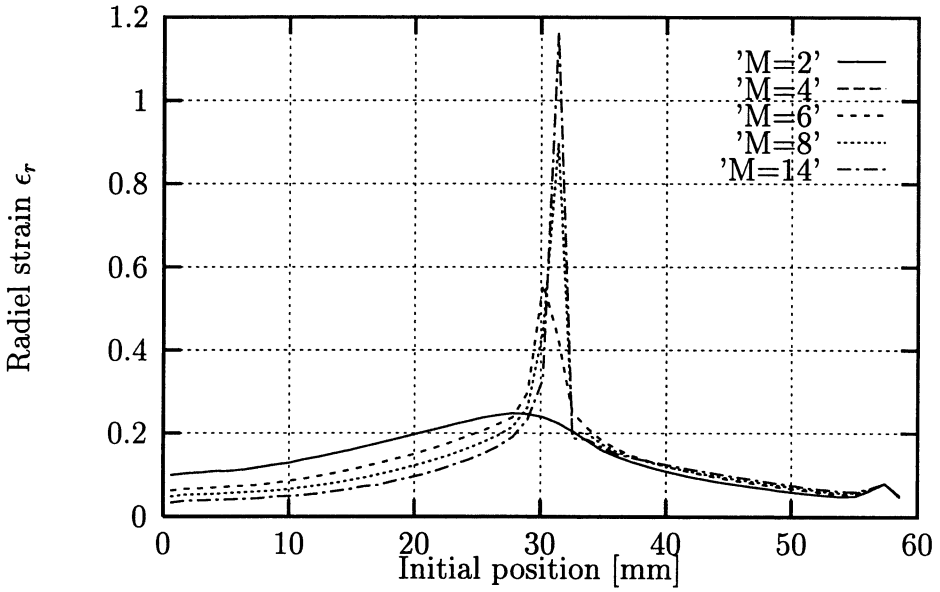

Figure 7.37: *Radial strain predicted for the Hemispherical Punch stretching at a punch stroke of 30 mm using Barlat's 2D criterion on an isotropic material with various values of the coefficient M (M=2,4,6,8,14) and with a sheet thickness of 1.5 mm.*

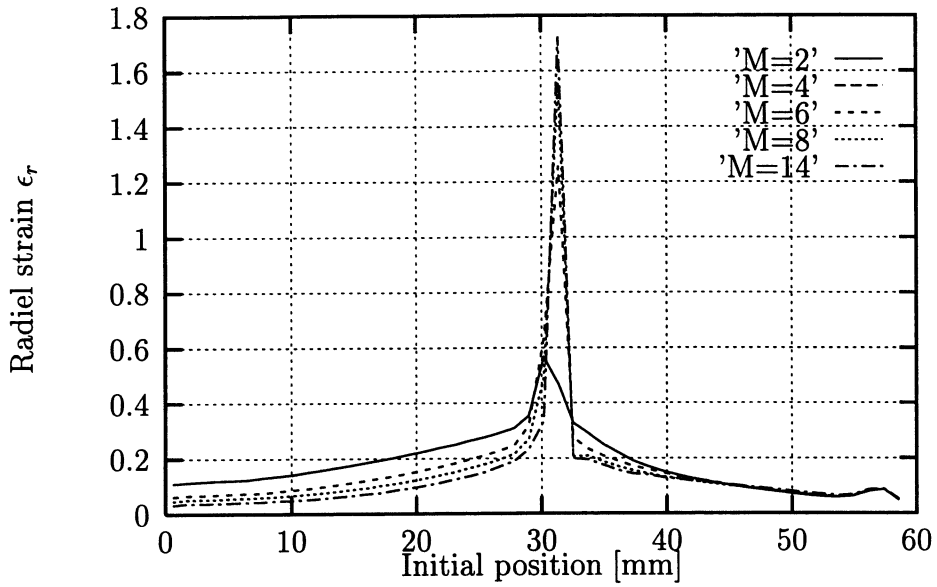

Figure 7.38: *Radial strain predicted for the Hemispherical Punch stretching at a punch stroke of 35 mm using Barlat's 2D criterion on an isotropic material with various values of the coefficient M (M=2,4,6,8,14) and with a sheet thickness of 1.5 mm.*

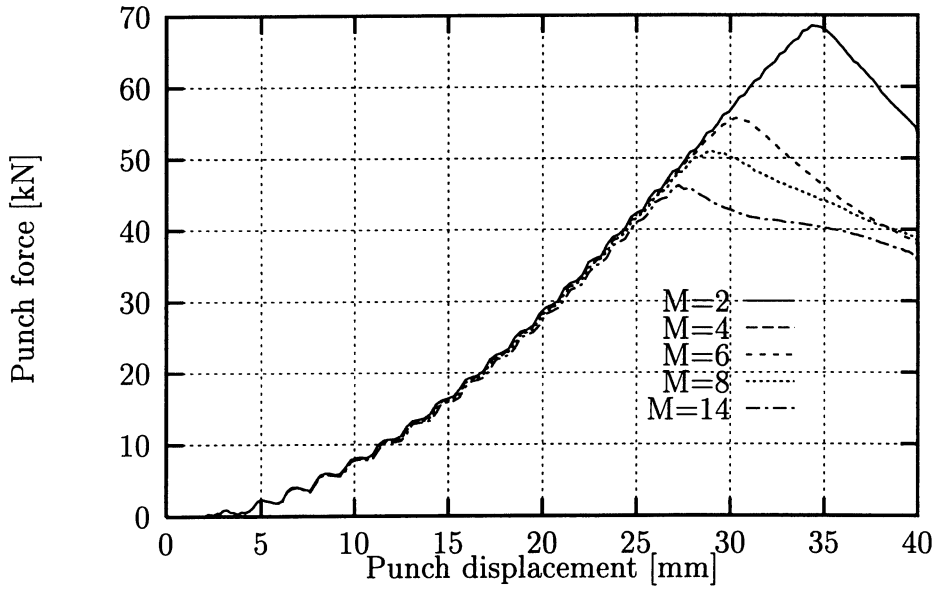

Figure 7.39: *Predicted punch force for the Hemispherical Punch stretching using Barlat's 2D criterion on an isotropic material with various values of the coefficient M (M=2,4,6,8,14) and a sheet thickness of 1.0 mm.*

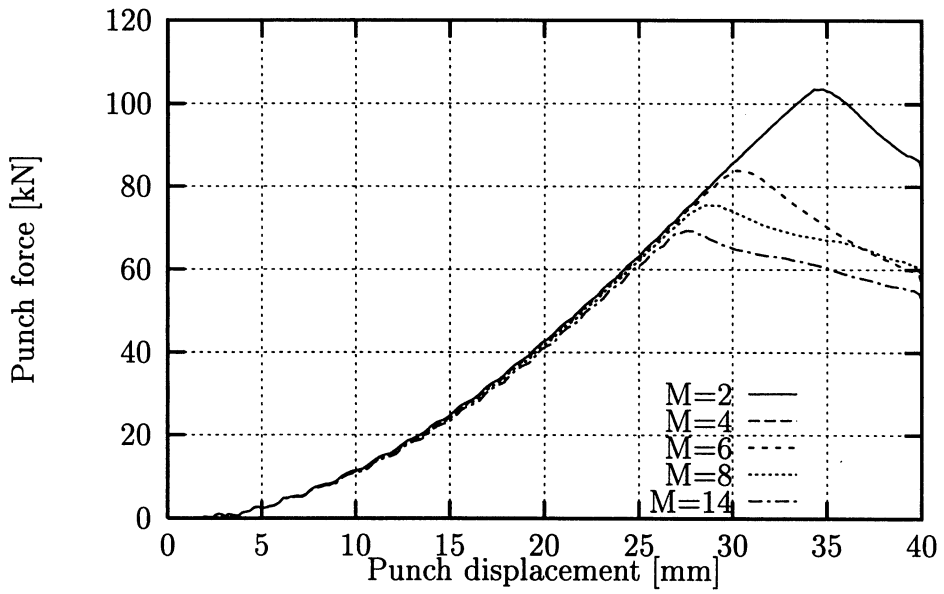

Figure 7.40: *Predicted punch force for the Hemispherical Punch stretching using Barlat's 2D criterion on an isotropic material with various values of the coefficient M (M=2,4,6,8,14) and a sheet thickness of 1.5 mm.*

7.5 The Marciniak Double Blank Method

Figure 7.41 shows a sketch of the tool geometry used for the Marciniak Double Blank Method (Mdbm). The process principle of the Mdbm is similar to the Nakazima test,

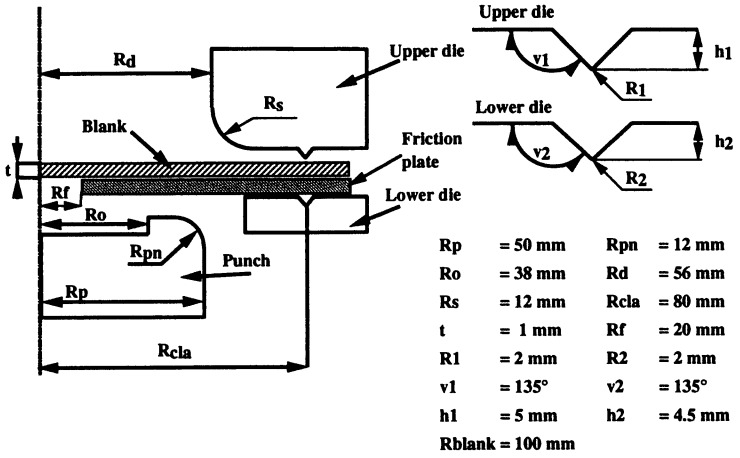

Figure 7.41: *Sketch of the Marciniak Double Blank test principle. The geometric values correspond to values reported by Albrektsen, [4]. The blank diameter is 200 mm.*

however, the punch geometry differs significantly and furthermore an additional blank, the friction blank, is used in the Mdbm. The Mdbm test is performed by clamping a test blank and a friction blank between the upper die and the lower die. After clamping, the punch is moved upwards to expand the sheets. The punch is cylindrical (radius 50 mm) with a nose radius (12 mm), but it differs from a traditional punch used for deep drawing by an opening (radius 38 mm). The punch gets into contact with the friction plate which for increasing punch higth expands. By using the friction plate it is possible to unload the test blank over the punch nose and the typical fracture at the punch corner region can hereby be avoided. Instead of fracturing at the punch nose the test blank fractures in the free zone over the hole in the friction blank (above R_f which increases as the friction blank and the test blank expand). To ensure that fracture occurs in the free zone it can be necessary to choose R_f different from the 20 mm given in the figure - if the material is sufficiently formable the hole in the friction blank may expand so much that the test blank gets in contact with the punch.

An important difference between the Nakazima test and the Mdbm is that the examined area remains flat. As the fracture occurs in a plane and unsupported part of the blank another advantage is the fact that the fracturing is unaffected by friction - here not stating that the Mdbm is unaffected by friction. However, the purpose of the principle is not to measure any process characteristica - instead it is the strain path leading to fracture which is of interest. This leads to measured values which are closer to what may be considered a material property; the formability limit. An advantage of the Mdbm is, when compared to the methods given in the first part of this chapter, that strain paths which cover the entire FLD can be followed up to fracture. Figure 7.42 shows the geometry of the test blank. A full test blanket is a eight-sided polygon with equal side length (this geometry is due to geometrical constrains established by the experimental equipment utilized - in principle a circular or square shape can be used instead). To obtain strain ratios ranging from uniaxial tension to balanced biaxial stretching two sides are cut away from the test blank leaving a

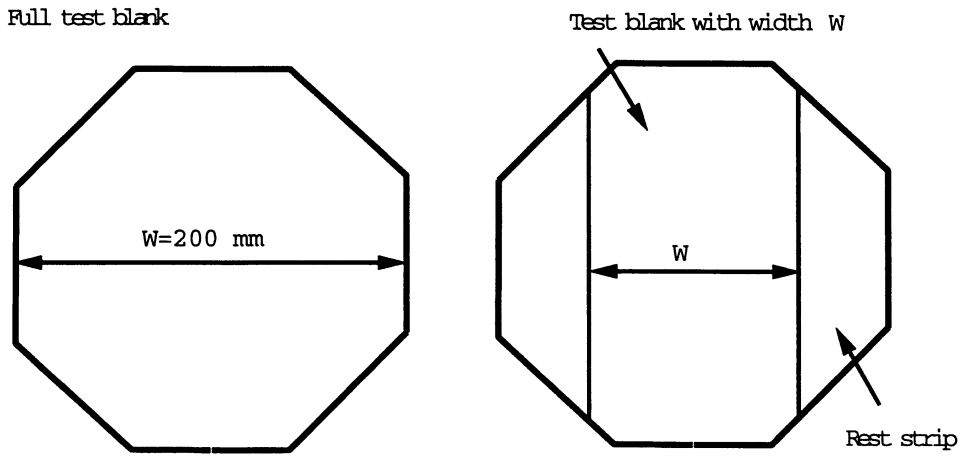

Figure 7.42: *Left: Geometry for a full test blank. Right: Geometry for a test blank with a width of W. Depending on W strain paths ranging from balanced straining (W=200 mm) to uniaxial loading (W≈60 mm).*

width W in the range from 60 to 200 mm (200 mm being the full test blank). This gives for widths below 200 mm two rest pieces which together with the rest blank are clamped between the upper die and the friction blank. If the test pieces are omitted a too severe clamping is the result, and this leads to fracture at the die instead of fracture in the free zone. This principle may be a way to overcome the problems with the LDH test discussed in section 7.3.1 where it was found necessary to relax clamping conditions; if two rest pieces are clamped together with the test blank, the test blank will be unloaded and it may be sufficient to avoid fracture at the die.

7.5.1 Experimental results

The Mdbm has been subject to investigation at the Department of Production, Aalborg University, and a special test rig for performing Mdbm tests has been built, [4]. By using this test rig Albrektsen has determined FLDs for two steel sheets: Docol 300 RP-X and St 14.03. Table 7.4 shows the material parameters for the two steels. Table 7.5 repeats

Steel	A_{80}	A_{50}	$R_{p0.2}$	R_m	C	n	R_0	R_{45}	R_{90}
Docol 300 RP-X	33.1	38.0	317	433	675	0.165	1.16	1.28	1.68
St 14.03	40.8	48.0	202	316	524	0.192	1.62	1.37	2.02

Table 7.4: *Material parameters used in the simulations (see Albrektsen [4])*

the strain ratios determined by Albrektsen, [4]. It can be noticed when looking at the experimental results in table 7.5 that for blank widths of 130, 140, 145 and 150 mm there are big differences in the obtained strain ratios for the two steels. This discrepancy is so big that it cannot be explained by the difference in material parameters.

One factor that may partly explain the discrepancy between the strain ratios obtained experimentally is that the friction plate employed was made from mild steel and hereby

Width [mm]	60	80	100	120	130	140	145	150	200
Principal strain ratio (Docol)	-0.52	-0.49	-0.40	-0.24	-0.13	0.12	0.44	0.69	0.99
Principal strain ratio (St 14.03)	-0.55	-0.51	-0.43	-0.22	-0.05	0.43	0.58	0.81	0.99

Table 7.5: *Experimentally obtained strain ratios reported by Albrektsen [4]*

has a considerably in-plane anisotropy. From the reported experimental results it is not clear whether the orientation of the test blank and the friction blank coincides or not. As the friction plate is strained to a considerable level, the orientation of the friction blank may cause a significant variation in the strain ratio as the friction blank is considerably thinned (and hereby influenced by anisotropy), however, this issue is not investigated further.

Albrektsen [4] reports also another problem in connection with the determination of the FLDs for the two materials; some of the strain paths seem to be slightly curved and this may influence the recorded limiting strain. The two FLDs are given in section 8.8 in connection with the forming limit stress concept.

7.5.2 FE-analyses of the Marciniak test

In the following section a FE-model corresponding to the test set up used by Albrektsen [4] is presented. The purposes of the analyses are 1: To find an explanation of why so big differences are found in the experimentally obtained strain ratios, 2: To evaluate the capability of Barlat's 2D criterion to predict the material behaviour for an anisotropic steel sheet typically used for deep drawing operations and 3: To determine whether the results of the FE-analyses are sufficiently accurate so that the method can be used in connection with determination of an improved tool geometry in order to obtain linear strain paths.

In the analyses it was realized at an early stage that the lock bead geometry could not be satisfactorily modelled as the height h_1 was bigger than h_2 (see figure 7.41). This leads to a penetration close to half a mm when closing the tools which again leads to severe contact problems in the simulation. This is due to the use of shell elements in a contact zone, which is dominated by stresses transversal to the sheet. Due to these difficulties the reported analyses are performed with a slightly changed geometry where h_1 is reduced to 3 mm. It is believed that this change does not significantly influence the results as the sheet also is clamped between the plane parts of the dies.

All the analyses are performed with the same discretization of the tools. Figure 7.43 illustrates left the models of the punch, the lower and the upper die, the friction plate (in between the dies), and right the test blank (width 140 mm) and the rest strip. The punch, upper and lower die are modelled as rigid and are discretized with 1080, 960 and 690 elements, respectively. The friction blank consists of 2040 BLT elements and is modelled as isotropic elastic-plastic because the actual orientation in the experiments is unknown.

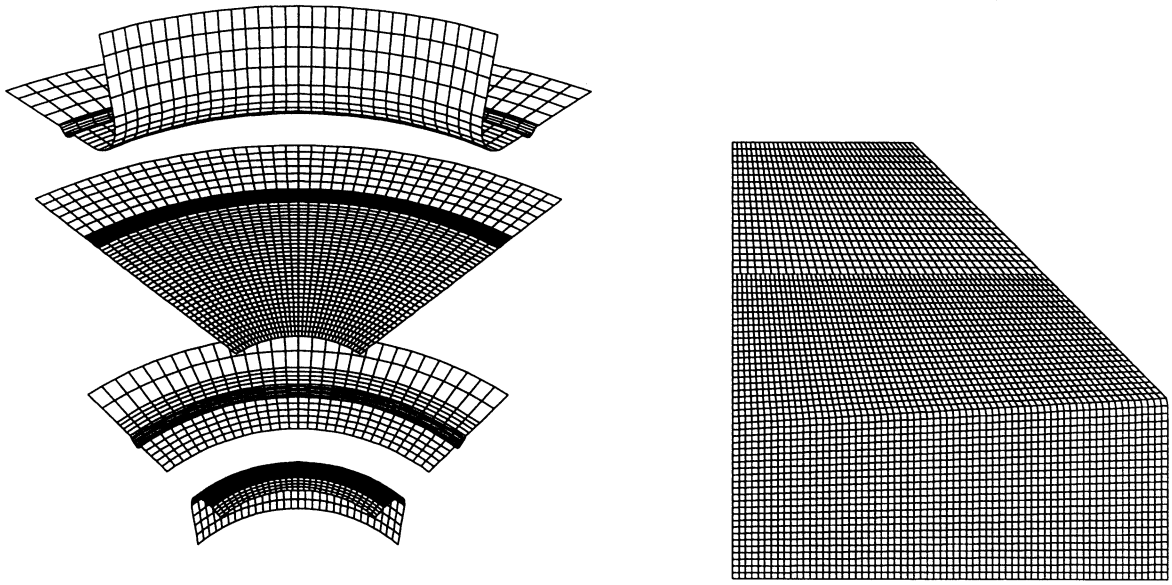

Figure 7.43: *Left: The discretized models used for punch, upper and lower die and friction plate. Right: Discretization of the blank with a width of 140 mm and the rest strip; the typical side length of an element is 1.5 mm. The border between test and rest strip can be seen from the change in discretization. In the analysis there is initially a gab of 0.01 mm between the rest and the test strip.*

The blank is modelled with a relatively fine mesh in order to obtain a mesh capable of following the curvature of the tools. In figure 7.43 is illustrated the mesh utilized for a blank width of 140 mm (the mesh consists of 3948 BLT elements). The remaining blank widths are meshed in a similar way, apart from the full blank (width 200 mm) where no cuttings are made; the full blank is discretized with a mesh similar to the friction blank (see figure 7.43); a fine discretization in the region of the lock bead and a somewhat coarser mesh outside the lock bead area.

The punch movement is prescribed with a sine shaped velocity profile and the blank holder force is modelled by a ramped curve. The principle is illustrated in figure 7.44. Figure 7.44 illustrates that the first millisecond of the total simulation time is used for the clamping in order to obtain the full clamping effect before the punch starts to move.

The geometry and the contact conditions are rather complicated in this example where contact occurs 1) between punch and friction plate, 2) between friction plate and test blank and rest strips, respectively, 3) between test blank and rest strips and upper die and 4) between friction plate and lower die. It was necessary to tune the model with regard to relatively many aspects.

Due to the complicated contact is was evaluated that the clamping force and the friction coefficient used were important for the response. In order to limit the number of analyses a series of analyses was first performed in order to determine a sufficient clamping force which was capable of eliminating draw-in of the flange after the binding phase. After

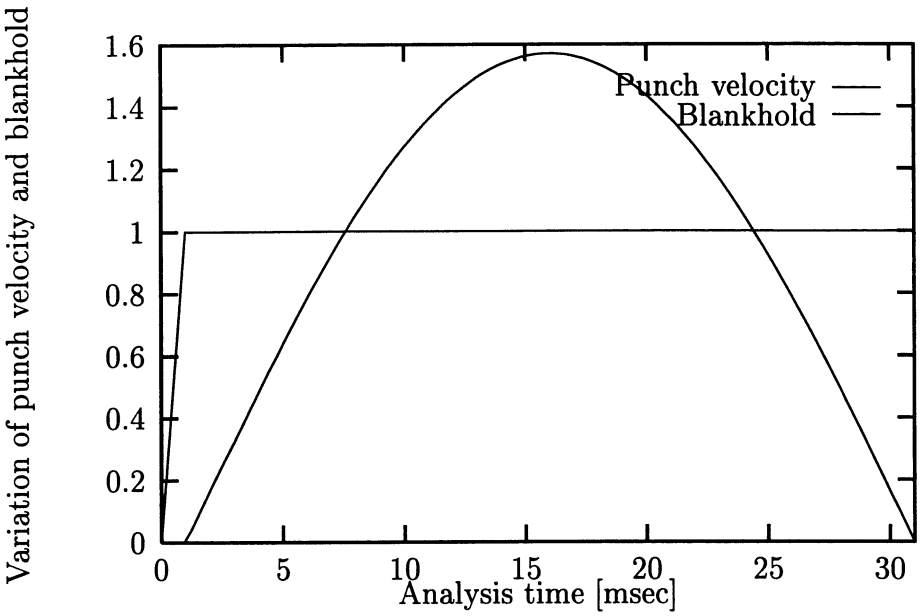

Figure 7.44: *Variation of the punch velocity and blank holder force. The curves are scaled in order to obtain the total punch stroke and the clamping force.*

having reduced the uncertainty concerning the clamping force two blank geometries were examined in more detail in order to obtain a good correlation between experiments and numerical results for the St 14.03 steel (the material parameters given in table 7.4) by fitting friction coefficients. After this sequence of analyses the remaining geometries were analysed without any further tuning of the model and conclusions were drawn.

7.5.3 Evaluation of a necessary clamping force

As discussed in section 7.3 the clamping condition can influence the overall response significantly; therefore a number of analyses with variation in the clamping force were performed. Another reason for a more detailed investigation of the effect of clamping force is that the modelling of the lock bead (different from the tool geometry sketched in figure 7.41) may have lead to a too high clamping pressure on the flat parts between the upper and lower die (for radius less than 80 mm).

Figure 7.45 shows the shapes predicted for various clamping forces. For a clamping force of 75 kN (upper left) there is a clear draw-in of the corner of the test blank (leading to a visible gab). For the higher clamping forces the draw-in is small for the part of the blank outside the lock bead region. For a clamping of 150 kN (upper right) there can still be seen a small draw-in of the outer corner of the test blank. With clamping forces of 225 and 300 kN no draw-in can be seen for the material outside the lock bead. However, a difference can be seen in the gab between the rest strip and the test blank at the symmetry plane for each of the illustrated geometries; the higher the clamping force the smaller the gab. This can influence the results significantly as the blank is constrained against draw-in in the transverse direction and it is obvious that a visible variation in the overall behaviour will influence the recorded strain.

In figure 7.46 is given the strain paths for the element at the center for clamping forces of

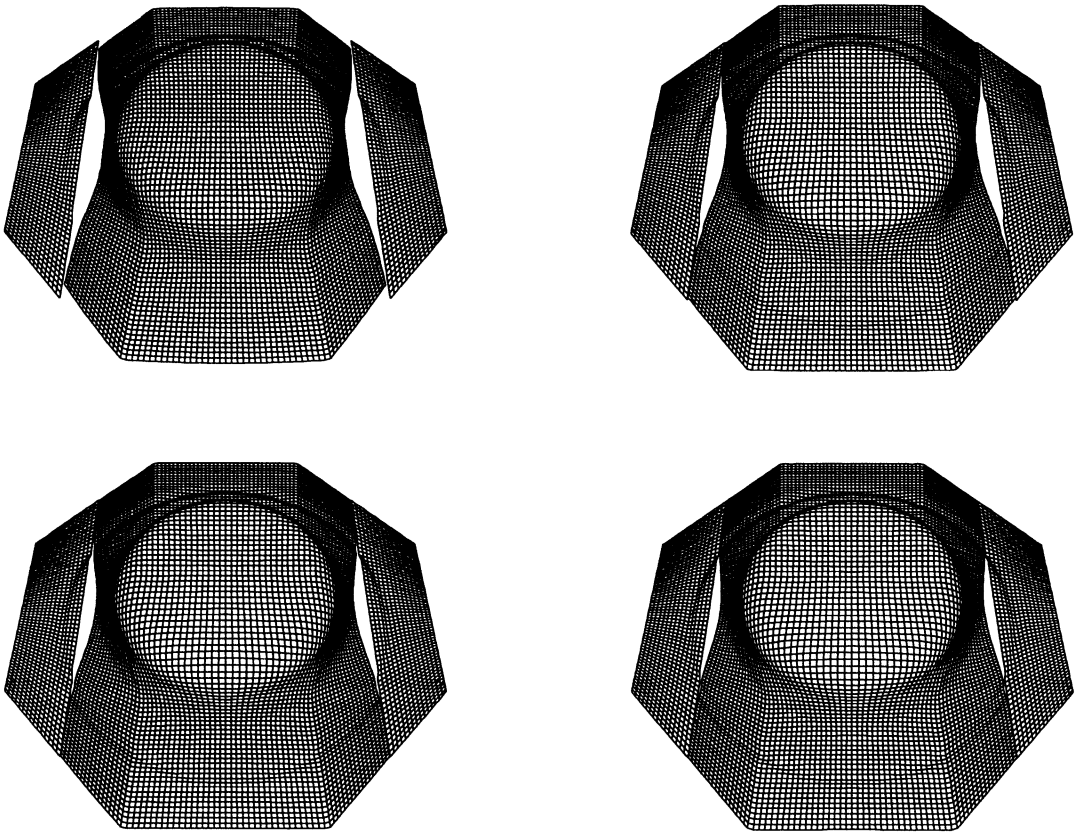

Figure 7.45: *The test blank and the rest strips shown at the same punch stroke for clamping forces of 75 kN (top left), 150 kN (top right), 225 kN (bottom left) and 300 kN (bottom right).*

75, 150, 225 and 300 kN, respectively. The loading situations correspond to the loading situation for which the resulting geometries are shown in figure 7.45. From figure 7.46 strain ratios can be found to vary between 0.16 and 0.65. This variation is sufficient to explain the variation in strain path ratios reported by Albrektsen [4]. Based on this series of analyses for the 140 mm blank width it was decided to run the analyses with a clamping force of 300 kN as the experiments show that no draw-in appears after clamping.

7.5.4 Comparison between numerical and experimental results

In order to evaluate how accurate the straining response is modelled, a comparison to a number of strain paths reported by Albrektsen [4] is performed in figure 7.47. Figure 7.47 shows the strain paths predicted with FE compared to experimental results. In the figure the results for 6 test blanks with widths of 60, 80, 130, 145, 150 and 200 mm, respectively, are given. The path predicted (dotted line) for the full blank ($\rho = 0.98$) almost coincides with the experimental results (line with points). For the widths 145 ($\rho = 0.58$) and 150 mm ($\rho = 0.81$) a slight deviation between the FE-results and the experiments can be seen, however, the trend with curved strain paths is very clear for these two geometries. A blank width of 130 mm leads to a response close to plane strain and there is here a good

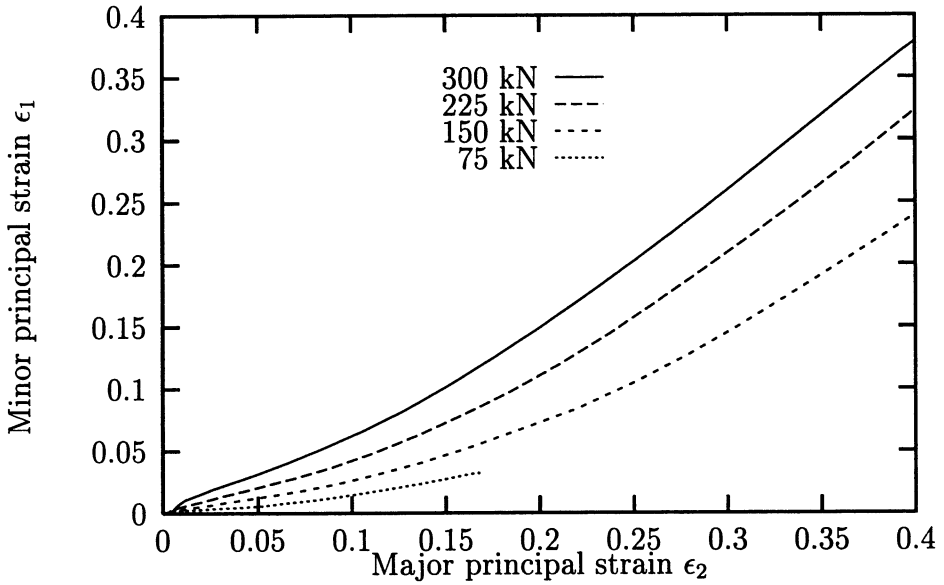

Figure 7.46: *The centre element's strain path at clamping forces of 75, 150, 225 and 300 kN.*

agreement between analysis and experiment. For the smallest width ($\rho = -0.55$) there is a very good agreement for the first part of the strain path, but for strains where $\epsilon_1 > 0.45$ a deviation of the same order as for test widths of 145 and 150 mm can be seen. For the test blank width of 80 mm ($\rho = -0.55$) the same characteristics can be seen as for a width of 60 mm, the primary difference is that the deviation appears at a lower level of straining. As the results obviously are closest to the experiments for the full test blank it may indicate that the estimated friction coefficient between friction blank and test blank (or between punch and friction blank) is a bit too low. An increased friction will lead to a higher ϵ_2 for the width equal to 145 and 150 mm, and it will also improve the results for the two smallest widths.

If we judge the responses obtained with these analyses it can be concluded that a good correlation to the experimental results is found. The trends with curved strain paths for relatively small positive strain ratios pointed out by Albrektsen also appear clearly in the analysis. It can be concluded that good results can be obtained for a forming operation as complex as the Marciniak Double Blank Method. On the other hand it is also clearly demonstrated how crucial the modelling of boundary conditions is, and in the case where no experimental results are available for tuning the model it is advisable to be cautious before one relies on the quantitative results.

7.5.5 Summary of the Marciniak Double Blank Method

Based on the results it is concluded that the implemented material model is indeed capable of predicting the behaviour of mild steel including a pronounced anisotropy. The analyses also illustrate that even complicated contact conditions can be modelled with success using the explicit finite element method.

However, the analyses also show that it may require a tuning effort to obtain good re-

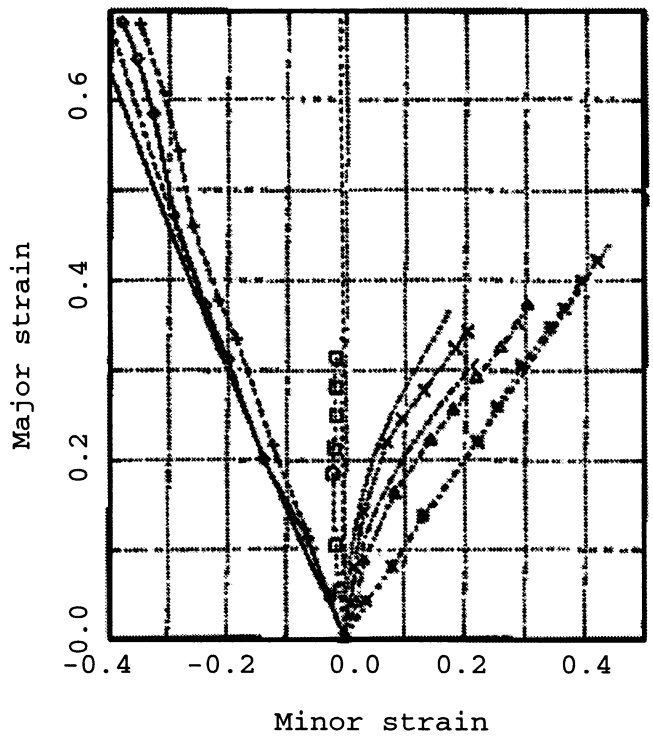

Figure 7.47: *Comparison between numerically and experimentally obtained strain paths for St 14.03. The material behaviour was modelled by using Barlat's 2D yield criterion and experimental results are from Albrektsen [4]. The lines with points are experimental values and the dotted lines the corresponding numerical results.*

sults. In this particular case one of the first analysis did indicate completely wrong results (due to the modelling of lock beads). It must be emphasized that when the forming operation is complex there is a higher risk of overlooking parameters of crucial importance. It is evident that aspects as discretization and loading rate play an important role, but moving to a complicated model many other aspects must necessarily be investigated carefully. If we reverse the problem and instead of refinding a behaviour experimentally found now want to judge a complicated process in advance - then we must be careful that possible errors in the modelling (due to estimated constitutive parameters, process conditions, etc) must be eliminated before the evaluation of the quantative response.

The Mdbm has some advantages compared to the other methods for determining FLDs discussed in the thesis. The main advantage is the fact that the strain field up to instability is much more uniform and that the bending effects are eliminated. However, as illustrated by the analysis there is, due to a more complicated test setup (for instance compared to a bulge test), a relatively high risk that clamping and friction conditions may vary due to minor variations in lubrication etc. It is believed that the big variations in strain paths obtained experimentally (table 7.5) are due to variations in friction and clamping conditions between the tests, but on the other hand, as long as the strain paths are recorded up till fracture it is possible both to find the limiting strain and at the same time obtain

information regarding the linearity of the strain path. The influence from anisotropy can also be rather big - to use friction blanks that show a significant anisotropy may influence the strain path significantly, and it is proposed in order to make the test more standardized to use the same material for test strip and friction blank and that the strips and friction plate are identically aligned with regard to the rolling direction. Scatter in experimental results may hereby be reduced from one laboratory to another.

7.6 Bulge Test

One of the most popular ways to determine limiting strain for positive strain ratios has been hydrostatic bulging of diaphragms. This test principle has the advantage that it is almost unaffected by friction. When bulging the sheet, the sheet obtains a curvature and hereby bending, however, it is believed that these effects are so limited that they are of no importance for the predicted strain limit. It is obvious that the sheet is exposed to a transversal stress component, however, this component is so small compared to the in-plane stresses that it can be neglected. The pressure is typically reported in the range from 2 to 10 MPa which compared to the yield stress typically obtained in sheet forming is very limited.

Another advantage of this test principle is that a relation between equivalent stress and equivalent strain can be obtained for biaxial loading. However, in order to obtain this relation it is necessary that the expression for the yield function is chosen. Using a traditional analytic approach the following relation between stress and strain can be obtained for a material with in-plane isotropic behaviour in the case where a circular die is used, [125].

$$\sigma_{eq} = \sigma_y \sqrt{\frac{3}{R+2}} \qquad \epsilon_{eq} = -\epsilon_z \sqrt{\frac{R+2}{3}} \tag{7.27}$$

where σ_y is determined from the relation:

$$\sigma_y = \frac{p\rho}{2t} \tag{7.28}$$

It is necessary to experimentally measure the curvature ρ and the thickness t related to the actual pressure p. t is normally determined from the thickness strain ϵ_z which is obtained by measuring surface strains and assuming volume constancy.

The use of elliptic or rectangular tools makes it possible to obtain positive strain ratios and hereby strain paths covering most of the right hand side of a FLD. In the following sections a discussion on FE-analysis of bulging is given and a number of geometries and materials are analysed and the results are compared to reported experimental results.

7.6.1 FE-analysis of bulge testing.

Analysis of the bulge test is seen from a computational point of view interesting as it can be modelled as a load driven process. However, this is only possible up to maximum pressure: If maximum pressure in the simulation exceeds the maximum pressure which can be sustained by the sheet it will lead to significant disturbances from dynamic effects. Reaching a load limit point will in practise normally lead to a drop in fluid pressure because the experimental setup normally is controlled by the fluid flow rather than by the pressure (see section 7.7.1).

In the analyses the load is applyed as a normal pressure increasing with time; this means that after reaching a load limit the system becomes dynamic and the response can be severely influenced. This effect can to some degree be limited by applying external damping to the system (see section 4.11 where the same example is used in connection with the

discussion on solution methods).

Hydrostatic bulging is of interest in connection with the determination of FLDs, however, there are additional reasons for investigation of the test principle: The computational effort to perform the analyses is limited and at the same time the example is found suitable for verifying material models and solution approaches as many experimental results are available from literature.

The hydrostatic bulging has been analysed by a number of authors, among others Bate [16] who uses various implicit FE-approaches and compares numerical results with experiments. However, his numerical results deviate significantly from the experimental results. Iseki et al. [107] perform similar analyses and reach reasonable agreement between simulations and experiments. Duncan and Johnson [67, 66, 68] make analytical analyses and also FE-analyses and they obtain good results for pressure versus deflection, strain distribution, instability limit and maximum pressure when comparing with experiments. Kim and Yang [123, 223] also obtain good results with an implicit FE-approach.

It is believed that the results of Bate [16] mainly differ from the experiments due to major simplifications in the FE-formulation; he uses a simple static explicit FE-solution technique without equilibrium iterations together with a coarse mesh. Bate concludes that he obtains better results the smaller the load steps, a conclusion which seen with regard to the utilized static explicit technique is obvious.

The geometry and material parameters used in the simulations of the bulging of rectangular diaphragms are taken from Duncan and Johnson [67, 66] who published a number of articles in 1968 with description of experiments with bulging of rectangular diaphragms. In the following a comparison between analyses and experiments for elliptic diaphragms is also given where geometry and material parameters are obtained from the well documented articles published by Iseki et al. [107, 108]. Results from these articles have also been used by Yang and Kim [123, 223] for comparison with FE-results.

The purpose of the analysis in the present context is two-fold: To evaluate the test principle with regard to obtaining linear strain paths and to verifying the implemented material model.

7.6.2 Rectangular diaphragms

The geometry was generated from the principle shown in figure 7.48. The mild steel used by Duncan and Johnson has an anisotropy in the plane of the sheet given by $R_{00} = 1.78$, $R_{45} = 1.04$ and $R_{90} = 1.95$ leading to a mean R-value of 1.45. Additionally they used another expression for the determination of the mean anisotropy:

$$R = 2\left[\frac{\sigma_b}{\frac{1}{4}(\sigma_0 + 2\sigma_{45} + \sigma_{90})}\right]^{(\frac{2}{n+1})} - 1 \tag{7.29}$$

where n is the slope of the stress-strain curves when plotted logarithmically. The yield stresses used in expression 7.29 are taken for an effective plastic straining of 15 per cent.

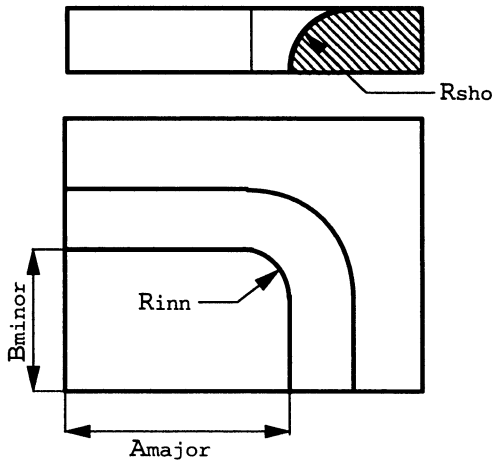

Figure 7.48: *Geometry for a quarter of the die used for bulging of rectangular diaphragms. The measures are:* R_{inn} = 6.35 *mm,* R_{sho} = 6.35 *mm,* $2A_{major}$ = 152.4 *mm and* $2B_{minor}$ = 152.4, 114.15, 76.2 *and* 38.1 *mm leading to aspect ratios of 1:1, 4:3, 2:1 and 4:1, respectively.*

In section 7.1.2 determination of Lankford coefficients were discussed and some problems regarding measurement was mentioned. The above approach may be used in order to get a better estimation of the R-value, at least influence from a biaxial balanced yield stress is included in contrast to the determination of R-values from tensile tests. In 7.29 a mean n-value is used and it may be noticed that the n-value often depends on the angle to the rolling direction (see e.g. sections 7.1.2 and 7.3.1 where 7 and 11 per cent variation of the n-value can be found for mild steel and aluminum, respectively, when varying the angle to the rolling direction).

The material hardening is modelled as: $\sigma_{ref} = 592.5(0.02 + \epsilon_{eff})^{0.275}$ $[MPa]$. The analyses are performed using Barlat's 2D criterion with M=8. Pressure is applied as an increasing load following a cosine profile. The choice of principle is discussed in more detail in section 4.11 where computational aspects are in focus.

FE-discretization of rectangular diaphragms

Figure 7.49 shows the discretization of the die and blank. Between the die and the blank contact was taken into account. To simulate the clamping between tool parts the in-plane displacements of the boundary nodes were set to zero. The simulation time was specified to 20 msec.

In the first analyses it was attempted to omit the die and only use boundary constraints on the blank: This approach turned out to give results that were in a bad correlation to the experimental results. It was tested to constrain all translational degrees of freedom along the boundary which lead to a too soft response. On the other hand constraining the rotation around a line following the boundary leads to a too stiff response and fracture at the outer row of elements on the side with length A_{major} (see figure 7.48).

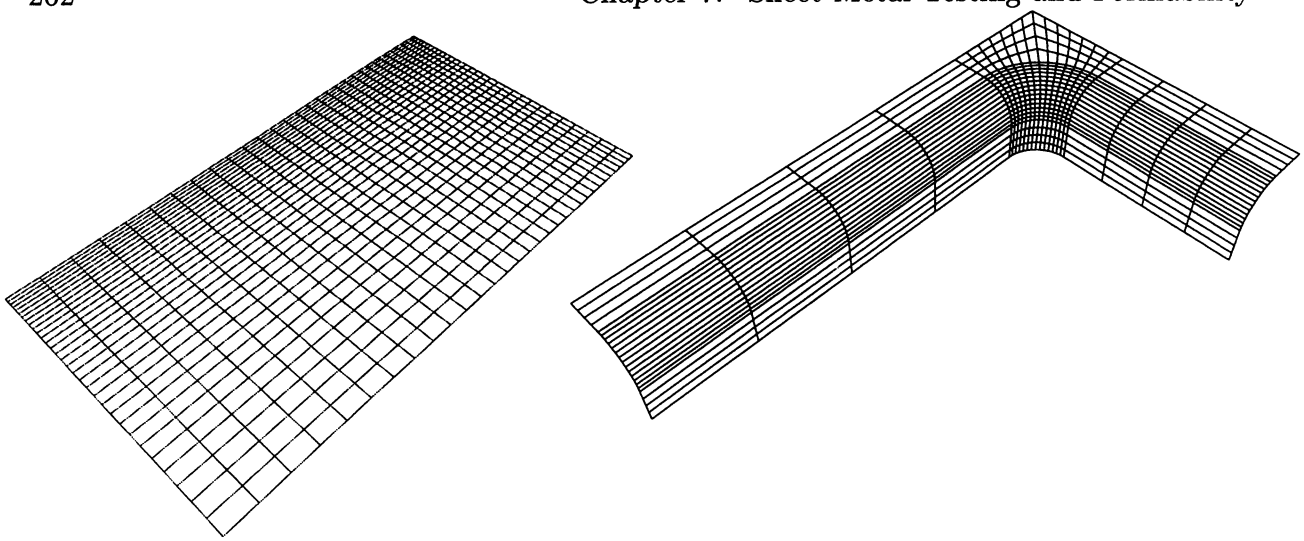

Figure 7.49: *FE-discretization used for the modelling of bulging rectangular diaphragms.*

7.6.3 Numerical results

In order to evaluate the results, some of the experimental results from Duncan and Johnson are compared to numerical results. Figure 7.50 shows the predicted relation between pole

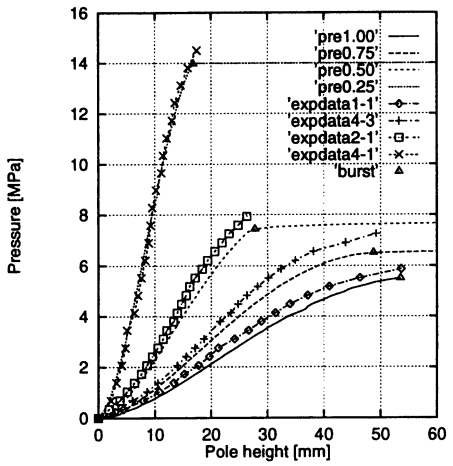

Figure 7.50: *Predicted relation between displacement of centre node and fluid pressure compared with experimental results.*

height and pressure (lines). Lines with points are experimental results from [67, 66]. In figure 7.50 some characteristics may be noticed. In the case where the ratio between minor and major die aperture length is 0.25 an extremely good relation between experiments and analysis is obtained. The three other aspect ratios lead to somewhat poorer estimations; the FE-analyses indicate a too flexible response. One way to improve the result may be to decrease the M-value: By decreasing the M-value the shape of the yield criterion is changed so that higher stresses are resisted for balanced stretching. Figure 7.51 shows left the predicted strain paths at the pole for the four aspect ratios analysed. Right is shown the stress paths corresponding to the strain paths. The strain paths predicted, shown in figure 7.51, are very linear and should at first glance be well suited for the prediction of formability based on linear strain paths. However, only the square die aperture leads to fracture at the pole and the three remaining aspect ratios are hereby of minor interest in

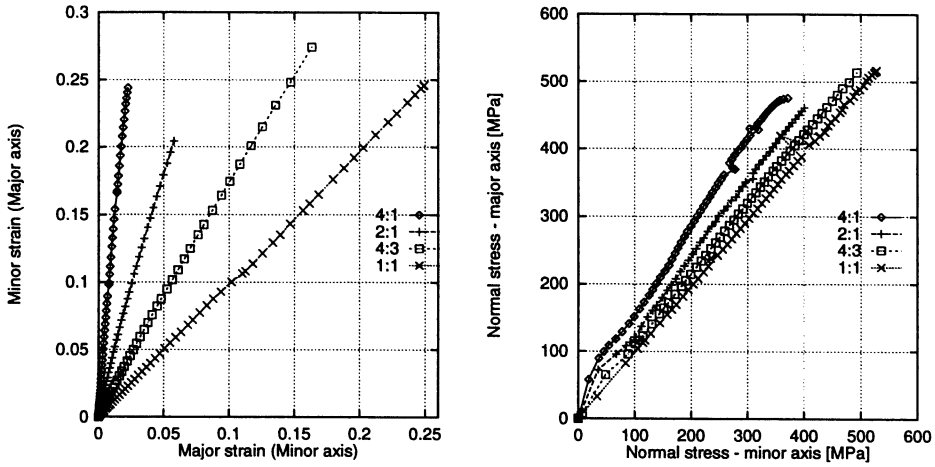

Figure 7.51: *Predicted strain and stress paths for the corner element limited by the two symmetry planes.*

connection with determination of limiting strains.

It can be noticed that the limiting strain point ($\approx (0.25, 0.24)$) seems reasonable when compared to typical values reported for mild steel. It can also be noticed that although the strain paths give an impression of a very stable deformation, the stress paths indeed indicate some disturbances. Figure 7.52 shows the predicted interface force between die and blank. According to the specified pressure profiles the interface forces should sum up to the same force for aspect ratios of 1:1 and 4:3 and for 4:1 and 2:1. However, the curve for 4:3 appears to be slightly delayed compared to 1:1; this indicates that the system damping is so high that it may have influenced the response. For a aspect ratio of 4:1 it can be seen that the analysis it tending to become unstable (the interface force is dropping at the end of the analysis time). The aspect ratios of 2:1 and 4:3 leads first to a localization of deformation followed by a very rapid dynamic growth which leads to elements with a negative Jacobiant that causes the programme to stop.

In the stress paths some disturbances are seen; similar effects can also be registered for the interface forces given in figure 7.52. This effect is judged to appear due to spurious unloading caused by noise introduced by the application of load which leads to a small structural vibration sufficient to cause unloading.

In the paper of Duncan and Johnson it is noticed that for the aspect ratios of 4:1, 2:1 and 4:3 fracture occurs at the die (at the end of the minor axis) for all the materials tested. For the square aperture fracture is also initiated at the edge for isotropic material, but the anisotropic material moves the fracture zone to the pole. The article concludes (from experiments) that anisotropy can move the instability point from the edge to the pole. These observations are in fully agreement with what is found from the present analyses. Another aspect which can be noticed is that the fracture limit reported by Duncan and Johnson is in a good agreement with the stability limit predicted with Barlat's 2D criterion; the deviation is around 4 per cent both for the predicted pressure and the predicted polar height.

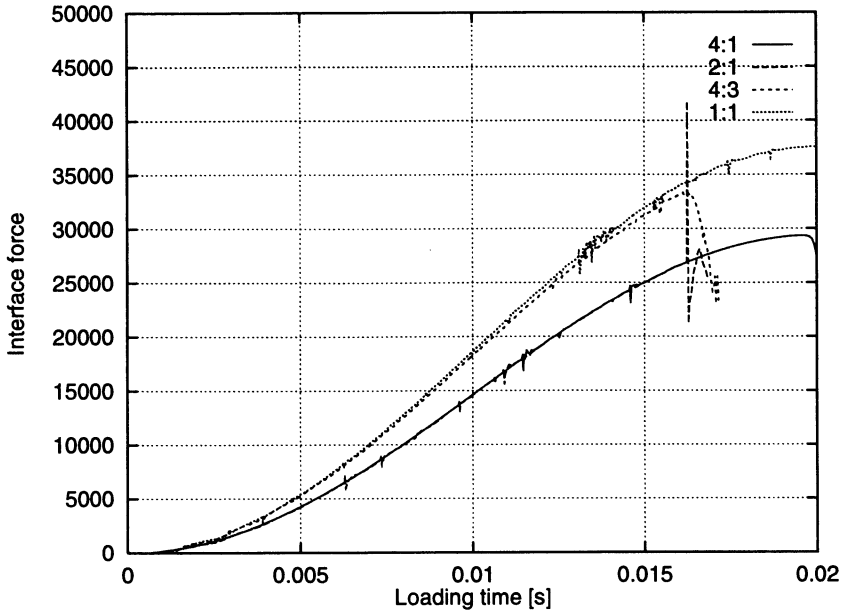

Figure 7.52: *Interface forces for a quarter of the bulge test for 4 aspect ratios.*

7.7 Elliptic Diaphragms

In this section elliptic diaphragms with three aspect ratios are analysed. A sketch of the die and the geometric parameters are given in figure 7.53 (geometry and material parameters are taken from Iseki et al. [107]). The material is modelled as isotropic with

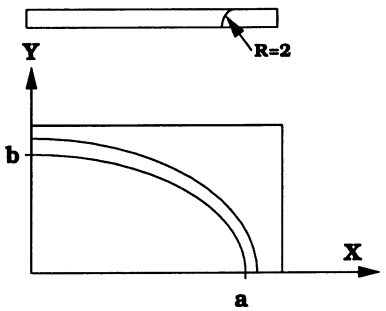

Aspect ratio	2a [mm]	2b [mm]
1.00	48.6	48.6
0.66	61.9	41.1
0.37	88.8	32.7

Figure 7.53: *Geometry for the elliptic diaphragms analysed (from Iseki et al. [107]).*

E=7000 kg/mm^2, Poisson's ratio 0.314 and a hardening curve: $\sigma_{eq} = 18(0.000769 + \epsilon_{eq})^{0.29}$ kg/mm^2. It has been chosen to use the same units as Iseki et al.

FE-discretization of elliptic diaphragms

Figure 7.54 shows the discretization used for the three aspect ratios. The dies were modelled with a level of discretization corresponding to the level used for modelling the dies used in bulging of rectangular diaphragms. The loading is applyed as a normal pressure following a cosine profile and a loading time of 20 msec have been used.

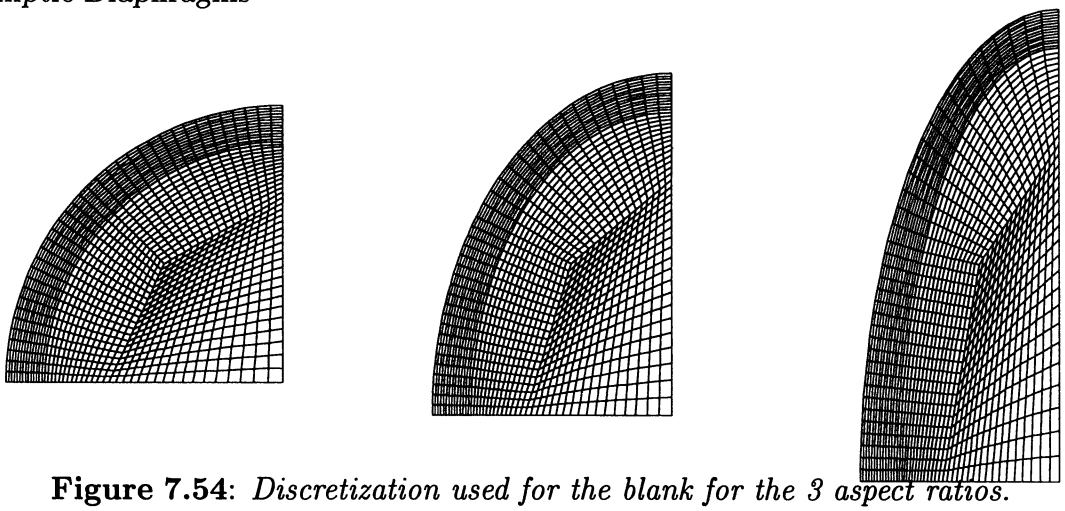

Figure 7.54: *Discretization used for the blank for the 3 aspect ratios.*

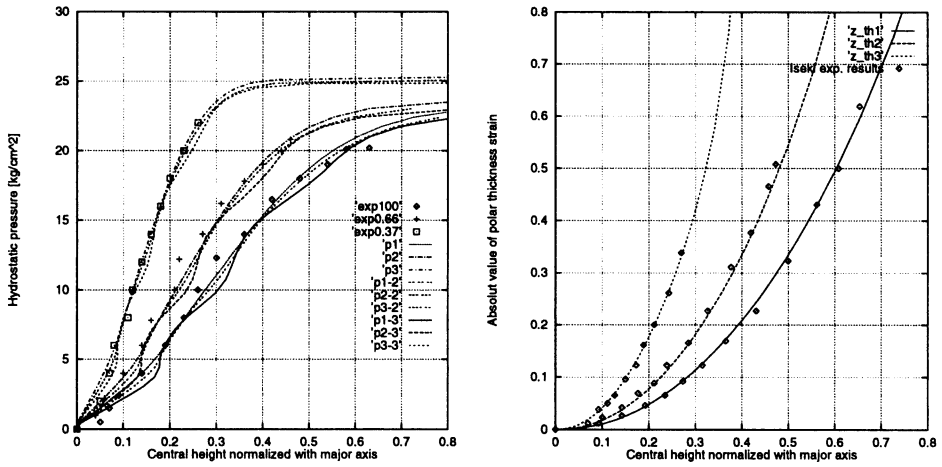

Figure 7.55: *Left is given the calculated relation between polar deflection and hydrostatic pressure. Three situations were analysed: No viscous damping and viscous damping with damping coefficients of 500 and 1000, respectively. The experimental results are from the article of Iseki et al. Right is given the relation between polar height and thickness strain at the pole.*

Numerical results

Figure 7.55 shows left the predicted relation between pole height (normalized) compared to experimental results reported by Iseki et al. Right is given the predicted relation between pole height and thickness straining at the pole compared to experimental results for the three aspect ratios. In the left part is given the results of various damping conditions; each aspect ratio has been analysed without damping, with c=500 sec^{-1} and with c=1000 sec^{-1}. The curves for the undamped curve show that the response is overlaid with a structural vibration, however, applying system damping is sufficient to eliminate this vibration. Similar effects of structural vibration are seen for the Hemispherical Punch stretching discussed in section 7.4. The analyses are in a good agreement with the experimental results.

The right part of figure 7.55 indicates a very good correlation between the predicted and the experimentally found relation between strain and displacement at the pole for all aspect ratios. In figure 7.56 a more steady response in the stress path for the centre element can be seen compared to the response obtained for the rectangular diaphragms (see figure

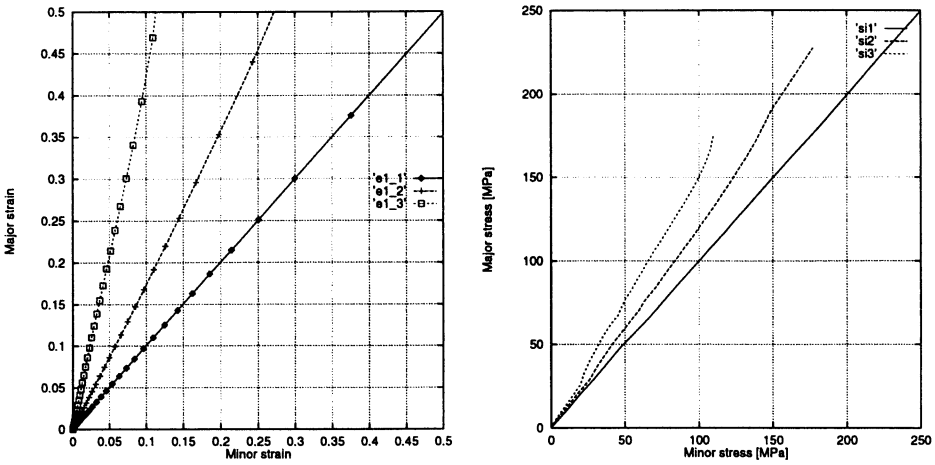

Figure 7.56: *Left is given the strain paths for the centre element, right the corresponding stress paths.*

7.51). This difference is mainly caused by the number of times where results are saved during the analysis: The fewer states saved the higher is the risk to overlook a variation. Here it is also clear that by specifying additional damping it is possible to avoid the structural vibration: The specified damping seems to be sufficient to avoid the dynamic effects. This can also be seen in figure 7.55: When applying a sufficient damping to the system, the overlaid vibration due to the lowest eigen-frequency is avoided.

Most analytical/semi-analytical methods to predict FLDs are based on the assumption that strain paths are linear. In figure 7.56 are given the strain paths obtained for the centre element. As can be seen from the results rather straight paths are obtained, however, the paths have a slight tendency to move closer to plane strain conditions at larger strain levels (for the two curves generated with non-cylindrical die aperture). However, the deviation is small and indicates that the limit points obtained using this test method to establish points on a FLD seems to be very good.

If the maximum stable pressure is taken as the pressure corresponding to maximum interface force between die and blank we obtain numerical 24.5 kg/cm^2 versus an experimental value of 22 kg/cm^2, 20.8 versus 22.7 and 20.2 versus 21.2 for the three aspect ratios. These findings are in a reasonable agreement with the experiments and the deviations are 11.5, 8.9 and 4.7 per cent, respectively. However, the resolution of the pressure steps in the experiments are relatively high especially for the 0.37 aspect ratio wherefore it may be guessed that the pressure limit can be somewhat higher leading to an even better agreement.

Iseki reports fracture to occur at the pole for the aspect ratio of 1 and 0.66. For the ratio of 0.37 fracture occurs at the edge. In the analysis it was found that fracture occurred at the pole in all situations. This example does not lead to the same accurate prediction of position of failure as the case was for the square diaphragms in the previous section.

Kleemola [124] reports strain paths obtained from a number of bulge tests with elliptic

masks. In his results very similar strain paths are obtained. Unfortunately Kleemola's results are not completely documented wherefore it was chosen to use the experimental results from Iseki et al. [108, 107] for the verification purpose.

It is interesting to note that the deviation between the present reported numerical results and numerical results obtained by Iseki et al. in 1977 and later on in the article by Kim and Yang [123] in 1984 is quite significant although the same basis was used for the modelling. The deviation consists mainly of two things: The fracture estimated by Kim and Yang is over-predicted and also both articles list FE-results which indicate a far too stiff response. Taking the present numerical results which seem to be in a very good accordance with Iseke's experimental results, one might conclude that their approach based on an incremental technique without overall equilibrium iterations in combination with a tangential stiffness approach without taking changes in hardening behaviour into account can lead to significant deviation between simulations and real behaviour. It can also be noticed that this is a typical improvement obtained during a relatively short period of time, from midd-seventies to midd-nineties, as one would today hardly rely on a finite element code in which out-of-balance forces are not taken into account or in which the modelling of hardening behaviour is not based on e.g. the consistent tangent modulus or similar approaches.

Another important conclusion might be that if the process is "pressure controlled" the fracture limit predicted just by using standard BLT elements (or another suitable shell element) combined with a proper constitutive model including a reasonable integration strategy and a loading rate suitable for the problem does indeed lead to surprisingly good results.

This process class where a hydro-static pressure is used to drive the deformation will when the critical pressure level (corresponding to diffuse instability) is reached indicate fracture (uncontrolled growth in the simulation) very quickly after reaching this maximum load situation. This effect may be a weakness of the modelling technique used: Pressure is applied as an increasing load - passing maximum load for the process will naturally lead to problems in the simulations (as there in principle is no static solution) - however, a real process may differ from this and be volume controlled rather that pressure controlled.

7.7.1 Flow versus pressure driven bulging of a sphere

Hosford and Caddell [100] consider a spherical shell subjected to internal pressure. If the material is considered isotropic, power-law hardening process instability (load maximum) will occur for $\epsilon_{eq} = \frac{2}{3}n$ but material instability (maximum wall force) will occur at $\epsilon_{eq} = 2n$. In figure 7.57 is shown the discretization used for an analyses where internal pressure is applied. Hardening is modelled as Hollomon hardening with K=500 MPa and n=0.2 and the analytic relation between equivalent plastic strain and internal pressure is given by [100]:

$$P = 2K\epsilon_{eq}^{n}\frac{t_0}{r_0}e^{-\frac{3}{2}\epsilon_{eq}} \tag{7.30}$$

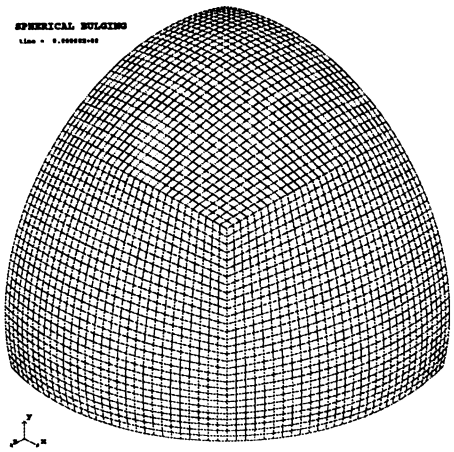

Figure 7.57: *Discretization used for modelling a sphere with nominal diameter 240 mm, sheet thickness 0.7 mm. Symmetry conditions are applied for the xy-, yz- and zx-planes*

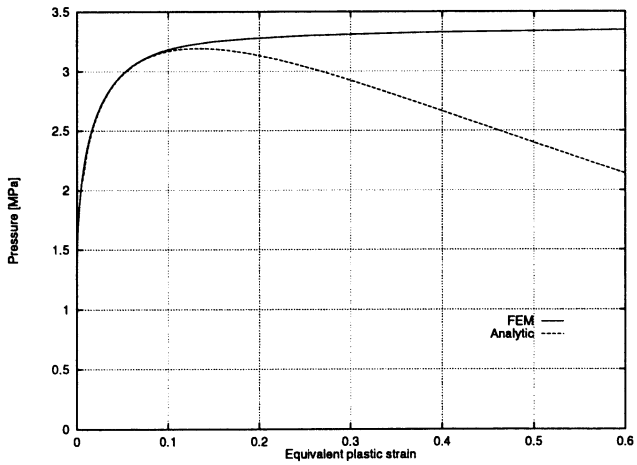

Figure 7.58: *Comparison between response predicted with explicit FE and the analytic solution.*

In the FE-model pressure is applied as a normal pressure increasing with time. Figure 7.58 shows the curve obtained with the analytic expression together with the response predicted using explicit FE. From figure 7.58 it can clearly be seen how crucial the passing of a load carrying capacity can be. Almost up to the maximum allowable pressure (at $\frac{2}{3}n$) a good correlation can be seen between the static analytical solution and the FE solution. The reason why the analytic solution and the FE-solution differ is primarily due to the fact that the discretized model does not lead to an exact homogeneous distribution of strains. After this point a very rapid growth of plastic strain can be seen in the FE-results (which very fast leads to uncontrolled growth in the simulation). Knowing the analytic response it is possible to obtain a more reasonable prediction using system damping, but in the more general case one has no idea about the load carrying capacity in advance, wherefore analysis of force controlled processes of this type is difficult to perform with explicit FEM (this is also the case using implicit FEM which probably will fail due to convergence problems for this particular example).

For processes with this type of loading characteristica difficulties are likely to occur if

the load is applied as an increasing load. However, for the bulge problem considered the experimental results reported indicate fracture at load maximum.

Again it should perhaps be stated that use of artificial damping can lead to severe overestimation due to the fact that the response can be delayed. In cases where materials are strongly influenced by strain rate effects care should be taken, especially when scaling the loading rate.

7.8 Summary of test methods

To sum up some of the conclusions in the chapter is can be stated that the Erichsen test seems to be only slightly influenced by friction if the maximum force is considered the characterizing parameter and it is proposed to use the punch displacement at maximum force instead of visible fracture (which is more subjective and harder to measure).

Taking more advanced tests, e.g. the Nakazima and the Mdbm, it must on the other hand be concluded that the use of an global parameter, e.g. punch movement at fracture to characterize the formability of materials, is so strongly influenced by boundary conditions that results may be difficult to reproduce.

Based on FE-analyses of the test methods previously mentioned and the results obtained by a number of authors it is concluded that the most promising method for testing the forming limits is the MDBM. This is mainly due to the following points:

- The test area remains flat.
- The area considered in the test is unaffected by friction.
- The area where necking occurs is during the plastic loading strained in a more uniform way than in the other methods mentioned.
- It is possible to determine the entire FLD using the same test principle.

If it is postulated that the FLD can be considered a material property it must be concluded that the Marciniak-double blank method is the most suitable test method available today (as it is unaffected by bending and friction) despite the weakness that strain paths are sensitive towards variations in boundary conditions. However, even if the strain paths may vary due to e.g. frictional variations, the actual limiting strain is recorded and the experimental results is though not sensitive to variations in boundary conditions. The only problem in this connection is that the strain paths may be non-linear and this may influence the fracture strains.

Hydrostatic bulging is in my opinion also very suitable as regards prediction of limiting strains. However, the findings from the precedent examples and from the sources indicate that it may be a problem to ensure that fracture occurs at the pole. It is believed that this problem can be eliminated by choosing other die geometries - the shoulder radii used for the two geometries are relatively small compared to the sheet thickness.

To conclude on the implemented material model it can be stated that very accurate results

can be achieved in comparison with reported experimental results. The yield criterion seems to give reasonable predictions of load maxima; these maxima are, however, also shown to be strongly influenced by the exponent M.

Another conclusion (and perhaps the most important) is that many of the analyses given in this chapter show a very strong dependency of the boundary conditions - this is of course important when judging the test methods, - but it may be more important to bear this in mind when performing process analyses, which often are of a so high complexity that it is unrealistic to perform these more detailed investigation of the influence from boundary conditions.

As regards pressure driven problems is seems possible to estimate the fracture by assuming that fracture occurs when maximum force is transmitted to the die, however, the example with spherical bulging indicates a large discrepancy between the analytical solution and the FE-solution after reaching the load maximum. The reason why this example turns out poorly compared to the other bulging examples is the fact that the spherical bulging leads to an homogeneous distribution of strains - in the other examples of bulging the strain distribution varies and the deformation in the FE-results will hereby localize and this is also the situation in the experiments.

Chapter 8

Theoretical Determination of Forming Limit Diagrams

As discussed in section 7.3 failure can be difficult to predict reliably using FEM, and this complicates the judgement based on the FE-results alone as to whether the process will be safe or not in the workshop. With the advanced simulation tools available today it is possible to obtain quite accurate information with regard to strain paths, etc, as well as information regarding the influence from tool geometries and process parameters. If this information is combined with knowledge about the FLD of the material, it may be possible to judge the severity of the stamping process.

Some of the primary purposes of using simulation tools are to produce parts which improve the exploitation of the material and to obtain processes which do not cause problems in the workshop. In fact, today it seems even more important to be able to evaluate severity of the process as well as the remaining formability in order to produce cost effective parts - if the severity cannot be determined with sufficient accuracy it is impossible to take the full advantage of the more and more advanced presses and simulation tools available.

In FE-analysis it is also interesting to use the FLDs as a control parameter to avoid unnecessary spending of computer resources. In cases where cpu-costs are high it is relevant to end the analysis when reaching a certain risk of fracture. The analysis results after indication of fracture are normally of minor interest seen from a production point of view. Another interesting area is the usage of failure criteria implemented in the codes to control the process parameters adaptively, for instance Cao et al. [41] use this approach in a cup drawing and conclude that it can be advantageous to include severity evaluations in numerical simulations to optimize pressing operations (focusing on the determination of an optimal blank holder force).

One reason why the use of FLDs is relatively limited is the fact that the experimental determination is expensive. A cost-effective way to obtain a complete FLD can be to combine experiments with analytical/numerical predictions - hereby it may be possible to reduce the experimental work needed. This is interesting in connection with simulation of processes - but also in connection with the traditional use of FLDs (as a helping tool for productional purposes).

Since the 1950s a number of methods for predicting FLDs have been proposed. Although the FLD approaches do not always present very accurate results, the approaches can be used for evaluating sheet metals and their expected properties in a forming operation. In the following a number of criteria are given together with the theoretical derivation. The reason for including the theory is that the theoretical approaches give a good understanding of some mechanisms involved in sheet metal failure.

8.1 The diffuse instability limit

One of the first criteria made in order to evaluate diffuse instability and hereby (to some degree) evaluate formability of sheet material was proposed by Swift in 1952. He estimates diffuse necking to occur for an isotropic material when the major principal strain reaches the value:

$$\epsilon_1^* = \frac{2n(1+\rho+\rho^2)}{(1+\rho)(2\rho^2-\rho+2)} \tag{8.1}$$

when the loading is proportional with a constant strain ratio $\rho = \frac{\epsilon_2}{\epsilon_1}$.

According to Albrektsen [4] the criterion proposed by Swift was in principle already touched upon by Considere in 1885 who considered uniaxial tensile testing. His criterion corresponded to maximum load P_{max}, it is the point characterized by:

$$\delta P = 0 = \delta(\sigma A) = A\delta\sigma_1 + \sigma_1\delta A \tag{8.2}$$

Assuming incompressibility this criterion can be rewritten to:

$$\frac{\delta\sigma_1}{\delta\epsilon_1} = \sigma_1 \tag{8.3}$$

where index 1 indicates the loading direction (the major principal direction). For a Hollomon hardening material, $\sigma_Y = K\epsilon_{eq}^n$ equation 8.3 yields the limit $\epsilon_{eq} = \epsilon_1 = n$.

Derivation of the Moore and Wallace criterion

Swifts criterion is limited to isotropic material. To overcome this limitation Moore and Wallace [149] expanded the criterion to take into account anisotropic behaviour using Hill's 48 yield criterion.

If the criterion proposed in 1964 by Moore and Wallace [149] is reduced to a material with in-plane isotropy the following expression is obtained:

$$\frac{H'(\epsilon_{eq})}{\sigma_Y(\epsilon_{eq})} = \sqrt{\frac{3}{2(2+R)}}\frac{(1+R)^2\alpha^3 - (2+R)R\alpha^2 - (2+R)R\alpha + (1+R)^2}{[(1+R)\alpha^2 - 2R\alpha + (1+R)]^{\frac{3}{2}}} \tag{8.4}$$

where H' denotes the work-hardening rate, $\frac{d\sigma_Y}{d\epsilon_{eq}}$, α the stress ratio $\frac{\sigma_1}{\sigma_2}$ and R the mean value for the transversal anisotropy. The criterion is proposed for uniform stretching and can be

considered to extend Swift's criterion to include anisotropy (Hill's 48 criterion).

In the following a rather detailed derivation of the relations between strain and stress ratios is given to be used in the instability criterion proposed by Moore and Wallace in 1964.

The starting point is the associated flow rule, which can be expressed as:

$$\frac{\delta\epsilon_1}{(G+H)\sigma_1 - H\sigma_2} = \frac{\delta\epsilon_2}{(F+H)\sigma_2 - H\sigma_1} = \frac{-\delta\epsilon_3}{G\sigma_1 + F\sigma_2} \tag{8.5}$$

The yield criterion can be expressed as:

$$\frac{3}{2}\left\{\frac{(G+H)\sigma_1^2 - 2H\sigma_1\sigma_2 + (F+H)\sigma_2^2}{F+H+G}\right\} = \sigma_{eq}^2 \tag{8.6}$$

With the above representation of the yield function the increment in equivalent strain can be expressed as:

$$\delta\epsilon_{eq} = \sqrt{\frac{2}{3}\frac{F+G+H}{FG+GH+HF}(F\delta\epsilon_1{}^2 + G\delta\epsilon_2{}^2 + H\delta\epsilon_3{}^2)} \tag{8.7}$$

Providing that the axes of strain do not rotate and that the ratios of principal strains remain constant, the equivalent strain can be expressed as:

$$\epsilon_{eq} = \sqrt{\frac{2}{3}\frac{F+G+H}{FG+GH+HF}(F\epsilon_1{}^2 + G\epsilon_2{}^2 + H\epsilon_3{}^2)} \tag{8.8}$$

Introducing the stress ratio $\alpha = \frac{\sigma_1}{\sigma_2}$ the yield criterion can be rewritten to:

$$\sigma_{eq} = \sigma_2\sqrt{\frac{3}{2}\frac{(G+H)\alpha^2 - 2H\alpha + (F+H)}{F+G+H}} \tag{8.9}$$

The increase in equivalent stress due to a variation in stresses is found by differentiation to:

$$\begin{aligned}\delta\sigma_{eq} &= \sqrt{\frac{3}{F+G+H}}\left\{\frac{((F+H)\sigma_1 - H\sigma_2)\delta\sigma_2 + ((G+H)\sigma_2 - H\sigma_1)\delta\sigma_1}{\sqrt{(G+H)\sigma_1^2 - 2H\sigma_1\sigma_2^2 + (F+H)\sigma_2}}\right\} \\ &= \sqrt{\frac{3}{F+G+H}}\left\{\frac{((F+H) - H\alpha)\delta\sigma_2 + ((G+H)\alpha - H)\delta\sigma_1}{\sqrt{(G+H)\alpha^2 - 2H\alpha + (F+H)}}\right\}\end{aligned} \tag{8.10}$$

Swift's instability condition claims that when the thinning due to a increase in load is balanced by the plastic hardening we have the diffuse instability limit. This can be expressed as:

$$\frac{\delta\sigma_1}{\sigma_1} = \delta\epsilon_1 \qquad \frac{\delta\sigma_2}{\sigma_2} = \delta\epsilon_2 \tag{8.11}$$

Rewriting we can express $\delta\sigma_1$ as:

$$\delta\sigma_1 = \sigma_1\delta\epsilon_1 = \frac{\delta\epsilon_1}{\delta\epsilon_2}\delta\epsilon_2\frac{\sigma_1}{\sigma_2}\sigma_2 = \frac{(G+H)\alpha - H}{(F+H) - H\alpha}\alpha\sigma_2\delta\epsilon_2 \tag{8.12}$$

The variation in equivalent stress can now be rewritten:

$$\delta\sigma_{eq} = \left\{ \frac{(F+H) - H\alpha - \alpha\left[\frac{(G+H)\alpha - H}{(F+H) - H\alpha}\right]^2}{\sqrt{((G+H)\alpha^2 - 2H\alpha + (F+H)}} \right\} \frac{\sqrt{3}\sigma_2 \delta\epsilon_2}{\sqrt{F+G+H}} \tag{8.13}$$

The strain increment $\delta\epsilon_2$ is related to the equivalent strain increment as (following from 8.8 and 8.5):

$$\delta\epsilon_{eq} = \sqrt{\frac{2(F+G+H)}{3}} \frac{[(G+H)\alpha^2 - 2H\alpha + (F+H)]^{\frac{1}{2}}}{(F+H) - H\alpha} \delta\epsilon_2 \tag{8.14}$$

The expression for variation in equivalent stress can then be written as:

$$\delta\sigma_{eq} = \frac{\sqrt{3}\left[(G+H)^2\alpha^3 - (H+2G)H\alpha^2 - (H+2F)H\alpha + (F+H)^2\right]}{\sqrt{2(F+G+H)}\left[(G+H)\alpha^2 - 2H\alpha + (H+F)\right]^{\frac{1}{2}}} \delta\epsilon_{eq} \tag{8.15}$$

By claiming that the increment in equivalent stress shall be equal to the increase due to hardening we obtain:

$$\frac{d\sigma_{eq}}{d\epsilon_{eq}} = \frac{\sigma_{eq}}{\frac{\sqrt{\frac{2}{3}\left(\frac{F}{H}+\frac{G}{H}+1\right)}\left[\left(1+\frac{G}{H}\right)\alpha^2 - 2\alpha + \left(1+\frac{F}{H}\right)\right]^{\frac{3}{2}}}{\left[\left(1+\frac{G}{H}\right)^2\alpha^3 - \left(1+\frac{2G}{H}\right)\alpha^2 - \left(1+\frac{2F}{H}\right)\alpha + \left(1+\frac{F}{H}\right)^2\right]}} \tag{8.16}$$

For an in-plane isotropic material ($R = \frac{H}{F} = \frac{H}{G}$) the stability limit can be reduced to:

$$\frac{d\sigma_{eq}}{d\epsilon_{eq}} = \frac{\sigma_{eq}}{\sqrt{\frac{2(2+R)}{3}} \frac{[(1+R)\alpha^2 - 2R\alpha + (1+R)]^{\frac{3}{2}}}{[(1+R)^2\alpha^3 - (2+R)R\alpha^2 - (2+R)R\alpha + (1+R)^2]}} \tag{8.17}$$

Figure 8.1 shows limiting curves for various values of R and n. For each value of n (0.1, 0.2, 0.3 and 0.4) curves are given for four values of R (0.5, 1.0, 1.5 and 2.0). It is characteristic that the predicted instability limit for balanced stretching is reached at (ϵ_1,ϵ_2)=(n,n) and for plain strain at ϵ_1=n and according to the model variation of the R-value has no effect on the limits at these points.

The model predicts a quite strong relation between limiting strains and the n-value. A doubling of n leads to a doubling in limiting strain for a given strain ratio. The model predicts that variation in Lankford coefficients only has a very slight effect on the formability in the stretching area, but a relatively large effect for negative strain ratios. A lower R-value decreases the formability in stretching but increases the limit for negative strain ratios.

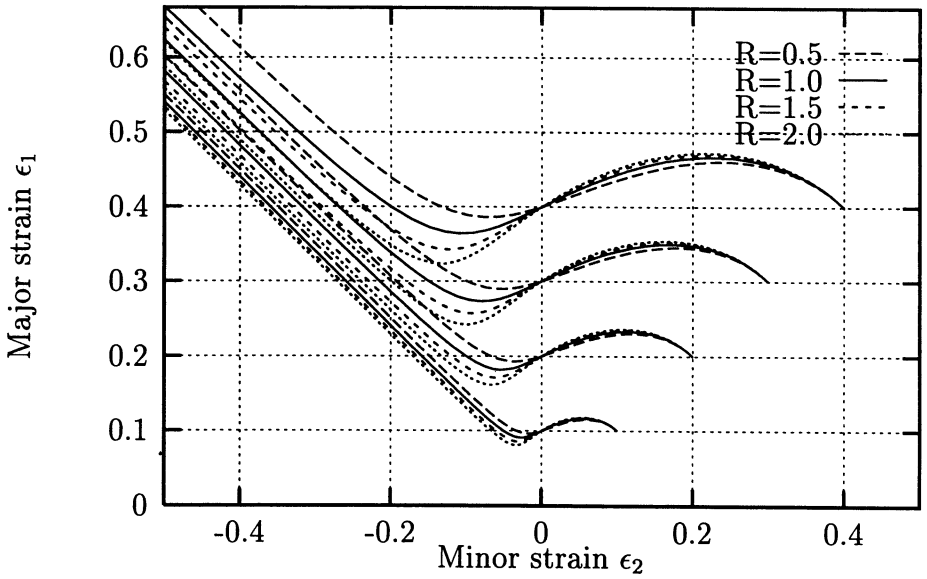

Figure 8.1: *Diffuse instability limits according to the criterion by Moore and Wallace for n-values of 0.1, 0.2, 0.3 and 0.4 for various R-values. The curves for same n-value pass the point (0,n).*

8.2 Hill's localization criterion as presented by Hosford and Caddell

In the following a brief discussion on the stability criterion proposed by Hill in 1952 is given. Practise shows that the forming limits predicted by the diffuse instability condition underpredict the forming capability, especially for negative strain ratios, it is in the left-hand side of a forming limit diagram.

To overcome this disagreement it is common to utilize the criterion proposed by Hill. In his approach it is stated that a local instability can occur only after the formation of a diffuse instability. Further the condition for a local instability is that in the plane of the sheet we have a direction of plane strain:

$$\epsilon_\theta = \epsilon_1 cos^2(\theta) + \epsilon_2 sin^2(\theta) = 0 \tag{8.18}$$

provided that the loading is without shear components ϵ_{12}. This leads to the angle in which the instability can occur:

$$tan^2(\theta) = -\frac{\epsilon_1}{\epsilon_2} \tag{8.19}$$

Assuming proportional loading and by using the relation between strain and stress ratio the above can (for Hill's 48 criterion reduced to in-plane isotropy) be rewritten:

$$tan^2(\theta) = -\frac{(1+R)\alpha - R}{1+R-R\alpha} \tag{8.20}$$

with $\alpha = \frac{\sigma_1}{\sigma_2}$. For uniaxial straining $\alpha \to \infty$ and the local instability zone will form in the angle θ to the loading direction:

$$tan^2(\theta) = \frac{1+R}{R} \tag{8.21}$$

The condition that local instability can appear is that $\epsilon_2 \leq 0$ (as $tan^2(\theta) \geq 0$) and it is provided that $\epsilon_1 > 0$. This leads to:

$$\epsilon_2 \leq 0 \quad \to \quad (1+R) - R\alpha \leq 0 \quad \to \quad \alpha \geq \frac{1+R}{R} \tag{8.22}$$

This local instability condition can only be used for non-positive strain ratios. If the strain ratios are positive we cannot find a direction of plane strain, and instead a Marciniak and Kuczynski approach may be used (discussed in detail in section 8.4).

First we consider an uniaxial stress state and we have the stability criterion proposed by Hill:

$$d(\sigma_{\theta+90} A_\theta) = 0 \quad \to \quad d\sigma_{\theta+90} A_\theta + \sigma_{\theta+90} dA_\theta = 0 \quad \to \quad \frac{d\sigma_{\theta+90}}{\sigma_{\theta+90}} = -\frac{dA_\theta}{A_\theta} \tag{8.23}$$

where $\sigma_{\theta+90}$ is the stress perpendicular to the plane strain direction and A_θ is the area on which this stress component acts. The condition for a local instability is that the straining along θ is zero and we can rewrite the left part of 8.23:

$$\frac{dA_\theta}{A_\theta} = \frac{dt}{t} = d\epsilon_3 \tag{8.24}$$

With $\sigma_2 = 0$ we have, from the yield criterion, the relation:

$$d\epsilon_2 = -\frac{Rd\epsilon_1}{1+R} \tag{8.25}$$

where t is the thickness of the sheet. Assuming incompressibility leads to:

$$d\epsilon_3 = -d\epsilon_1 - d\epsilon_2 = -\frac{d\epsilon_1}{1+R} \tag{8.26}$$

The stress perpendicular to the instability zone can be expressed as:

$$\sigma_{\theta+90} = \frac{\sigma_1+\sigma_2}{2} + \frac{\sigma_1-\sigma_2}{2}cos(2[\theta+90]) = \sigma_1\left(\frac{1}{2} - \frac{cos(2\theta)}{2}\right) \tag{8.27}$$

The variation of equation 8.27 leads to:

$$d\sigma_{\theta+90} = d\sigma_1\left(\frac{1}{2} - \frac{cos(2\theta)}{2}\right) \tag{8.28}$$

Using the information in equation 8.23 we obtain:

$$\frac{d\sigma_1}{\sigma_1} = \frac{d\epsilon_1}{1+R} \tag{8.29}$$

For the uniaxial stress state the above can be rewritten:

$$\frac{d\sigma_{eq}}{\sigma_{eq}} = \frac{d\epsilon_{eq}}{1+R} \rightarrow \frac{d\sigma_{eq}}{d\epsilon_{eq}} = \frac{\sigma_{eq}}{1+R} \tag{8.30}$$

In case of biaxial stretching the same procedure can be used. The instability criterion now leads to:

$$\frac{d\sigma_{\theta+90}}{\sigma_{\theta+90}} = -\frac{dA_\theta}{A_\theta} = -d\epsilon_3 = d\epsilon_1 + d\epsilon_2 = (1+\rho)d\epsilon_1 \tag{8.31}$$

The stress increment perpendicular to the instability line can be written as:

$$d\sigma_{\theta+90} = \frac{[1+\frac{1}{\alpha} - (1-\frac{1}{\alpha})cos(2\theta)]d\sigma_1}{2} \rightarrow \frac{d\sigma_{\theta+90}}{\sigma_{\theta+90}} = \frac{d\sigma_1}{\sigma_1} \tag{8.32}$$

The ratio between stresses can, as α is constant, be written.

$$\frac{d\sigma_1}{\sigma_1} = \frac{d\sigma_{eq}}{\sigma_{eq}} \tag{8.33}$$

Rewriting with the strain ratio we obtain:

$$\frac{d\sigma_{eq}}{\sigma_{eq}} = (1+\rho)d\epsilon_1 \tag{8.34}$$

The relation between the strain in the principal direction and the equivalent strain can be rewritten using the stress ratio:

$$d\epsilon_1 = \frac{1+R-R\frac{1}{\alpha}}{\sqrt{1+R}\sqrt{1+R-2R\frac{1}{\alpha}+(1+R)\frac{1}{\alpha^2}}}d\epsilon_{eq} \tag{8.35}$$

The relation between stress and strain ratio is given by:

$$\rho = \frac{d\epsilon_2}{d\epsilon_1} = \frac{1 + R - R\alpha}{(1 + R)\alpha - R} \tag{8.36}$$

The stability condition can then be rewritten:

$$\frac{d\sigma_{eq}}{\sigma_{eq}} = \frac{1 + \frac{1}{\alpha}}{\sqrt{1 + R}\sqrt{1 + R - 2R\frac{1}{\alpha} + (1 + R)\frac{1}{\alpha^2}}} d\epsilon_{eq} \tag{8.37}$$

or alternatively:

$$\frac{d\sigma_{eq}}{d\epsilon_{eq}} = \frac{1 + \frac{1}{\alpha}}{\sqrt{1 + R}\sqrt{1 + R - 2R\frac{1}{\alpha} + (1 + R)\frac{1}{\alpha^2}}} \sigma_{eq} \tag{8.38}$$

The limit strain for various stress ratios can now be expressed as:

$$\epsilon_1 = \frac{1 + R - R\frac{1}{\alpha}}{\sqrt{1 + R}\sqrt{1 + R - 2R\frac{1}{\alpha} + (1 + R)\frac{1}{\alpha^2}}} \frac{\sqrt{1 + R}\sqrt{1 + R - 2R\frac{1}{\alpha} + (1 + R)\frac{1}{\alpha^2}}}{1 + \frac{1}{\alpha}} n \tag{8.39}$$

$$\epsilon_2 = \frac{(1 + R)\frac{1}{\alpha} - R}{\sqrt{1 + R}\sqrt{1 + R - 2R\frac{1}{\alpha} + (1 + R)\frac{1}{\alpha^2}}} \frac{\sqrt{1 + R}\sqrt{1 + R - 2R\frac{1}{\alpha} + (1 + R)\frac{1}{\alpha^2}}}{1 + \frac{1}{\alpha}} n \tag{8.40}$$

If the hardening curve is expressed as $\sigma_{eq} = K\epsilon_{eq}^n$, the above expressions can be reduced to:

$$\epsilon_1 = \frac{1 + R - R\frac{1}{\alpha}}{1 + \frac{1}{\alpha}} n \qquad \epsilon_2 = \frac{(1 + R)\frac{1}{\alpha} - R}{1 + \frac{1}{\alpha}} n \tag{8.41}$$

The stress ratio is related to the strain ratio through:

$$\alpha = \frac{1 + R + R\rho}{R + (1 + R)\rho} \tag{8.42}$$

which used in 8.41 gives:

$$\epsilon_1 = \frac{1 + R - R\frac{R + (1 + R)\rho}{1 + R + R\rho}}{1 + \frac{R + (1 + R)\rho}{1 + R + R\rho}} n = \frac{n}{1 + \rho} \tag{8.43}$$

The relations between major and minor strain predicted by Hill's criterion are illustrated in figure 8.2 for various values of the hardening exponent n. The criterion indicates a strong dependency on the n-value. Another conclusion which can be drawn from the criterion is that the limit is independent of the R-value.

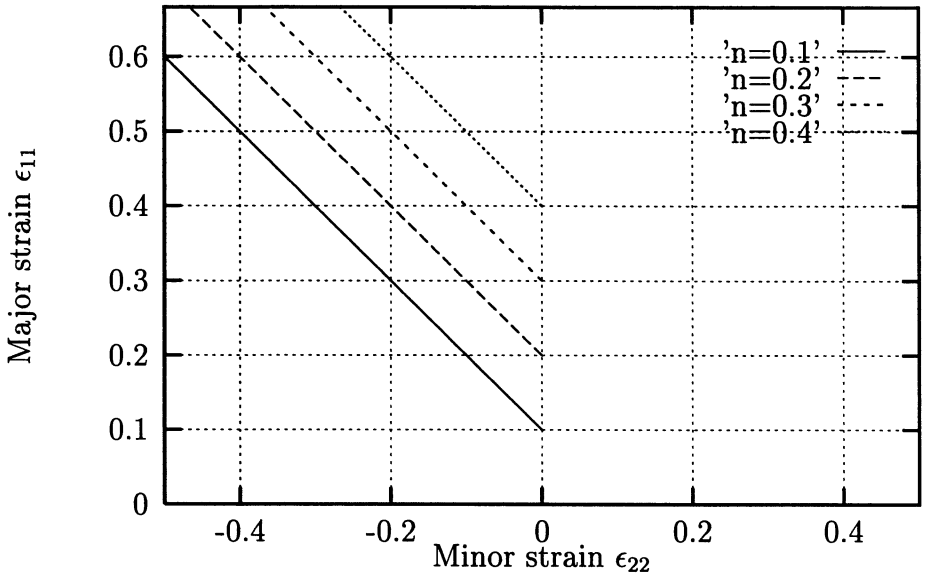

Figure 8.2: *Local instability limits for negative strain ratios according to the criterion proposed by Hill.*

8.3 Hill's instability criterion compared to the diffuse instability criterion

If we compare the diffuse instability limits to the limits predicted by Hill's criterion some differences can be found which is illustrated in figure 8.3. Figure 8.3 shows the limits predicted when using the two criteria proposed by Moore and Wallace and by Hill, respectively. The limiting strains predicted by Hill's criterion are much higher than the diffuse limits. The criterion by Moore and Wallace predicts a large variation in the limits for negative strain ratios when varying the R-value for high n-values. In contrast to this Hill's criterion is unaffected of variations in the R-value. Characteristic of this is that the two methods predict the same limit for plane strain ($\epsilon_1 = n$).

A popular way to determine a complete FLD is to combine the two approaches and use Hill's criterion for negative strain ratios. Both criteria show a strong relation to the n-value - this relation may be used as a rule of thumb, however, as it appears from figure 7.30 it gives a severe under-estimation for the mild steel, but a good characterization for the aluminum sheet - the materials have almost identical n-values but a marked difference in the FLDs. Both criteria have the advantage that knowledge of only n and R-values is needed. On the other hand, it has been demonstrated by various authors that the predicted limits are not reliable. However, the criteria may be used for giving an explanation of the effects of the various material parameters. Also, in the context of discussing hardening characteristics the criteria can be useful; several authors have pointed out that the predicted FLDs are strongly related to the hardening characteristic, and that the choice of the mathematical description of hardening has a large impact on the predicted results.

The limiting curves obtained by Moore and Wallace (diffuse instability) are significantly lower that the curves obtained with Hill's criterion, however, this does not necessarily in-

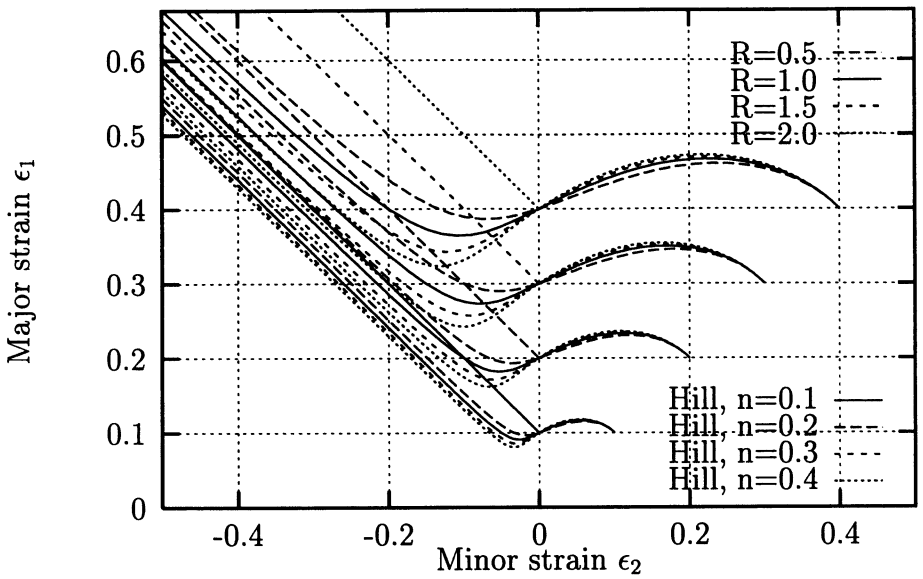

Figure 8.3: *Diffuse and local instability limits according to the criteria by Hill and Moore and Wallace, respectively.*

dicate a contradiction between the two methods. One may state that diffuse instability is not a direct process limitation whereas localization leads directly to a fractured part.

8.4 The Marciniak-Kuczynski approach to determine limiting strains

In 1967 Marciniak and Kuczynski [142] proposed a model for the understanding of sheet metal failure in biaxial tension, which was often described with Swift's instability criterion (diffuse instability) previously. The main idea of their approach is to assume that an imperfection or defect is present in the sheet considered. This defect is typically assumed to be a variation in thickness; the sheet with nominal thickness t_a has a local region with a thickness t_b, and the defect is characterized by the imperfection factor $F = t_b/t_a$. The defect may just as well be due to variations in constitutive parameters, etc.

The model has attracted quite a number of authors and below only a few are listed: Hutchinson and Neale [105], Lee and Zaverl [129], Lege et al. [133], Lian et al. [136], Rasmussen [179] and Lu and Lee [138] and Nie and Lee [160]. One common feature of the above mentioned attempts to predict the limiting strains is the fact that the material is assumed to deform only plastically; elastic effects are disregarded.

The two subsequent sections give the necessary steps for a numerical determination of the limit strains calculated using the Marciniak-Kuczynski approach [142] originally proposed in 1967. First the original approach is given which only makes it possible to determine limiting strains for positive strain ratios, second the theory of an extended version is given. Both principles have been programmed. The structure of the programme is based on the usermaterial subroutine implemented in LS-Dyna3d. The purpose of the programme is

to be able to obtain estimated FLDs which are consistent with the constitutive modelling used in the FE-programme. Attempts have been made in order to ease analyses of more complex strain paths; e.g. to evaluate remaining formability by using strain paths determined with LS-Dyna3d. The routine can also be used as a tool for evaluating the effect of various parameters, for instance the effect of various hardening laws.

8.5 The original model of Marciniak and Kuczynski

In the programme a special option exists which can be used in order to investigate the formability according to the original model proposed by Marciniak and Kuczynski. The primary reason for including this model has been to ensure that the material subroutine is stable enough to be used in connection with the determination of unknown strain increments in an imperfected zone. A short description of the theory is given in the following, it is mainly based on Marciniak and Duncan [141].
A sheet loaded in biaxial tension is considered. Perpendicular to the major loading (x-direction) an initial imperfection in the form of a thinner region (the hatch area) is assumed as shown in figure 8.4:

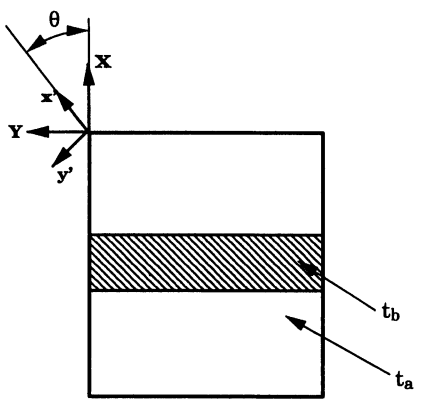

Figure 8.4: *An imperfection B in a region A of uniform strain. The imperfection is perpendicular to the direction of the major principal stress. The system X-Y denotes the loading system, coordinate system x'-y' is used for describing the material properties.*

During loading we have the condition of static equilibrium normal (nn) to the imperfection:

$$\sigma_{nnA} t_A = \sigma_{nnB} t_B \tag{8.44}$$

and a condition of compatibility tangential (tt) to the imperfection:

$$d\epsilon_{ttA} = d\epsilon_{ttB} \tag{8.45}$$

When strain increments are prescribed in region A, the corresponding strain increments can be found for region B using the conditions of equilibrium and compatibility. In the programme the unknown strain increments are found using an iterative technique based on an optimization scheme. Below the scheme for the overall programme is given:

- Initialize all variables. Input all material parameters including orientation of material coordinate system (θ), t_A and t_B and finally specify strain path.

- II: Prescribe new major strain increment $\dot{\epsilon}_{11}^{A}$ in region A and calculate $\dot{\epsilon}_{22}^{A}$ based on the prescribed strain path.
- Calculate local strain increments, $\dot{\epsilon}_{11}^{\prime A}, \dot{\epsilon}_{22}^{\prime A}, \dot{\epsilon}_{12}^{\prime A}$
- Calculate the local stress increments $(\dot{\sigma}_{ij}^{\prime A})$ and update local stresses, local strains and thickness t_A (materialroutine).
- Solve equilibrium equations using optimization technique (minimize the error): $ERR(\dot{\epsilon}_{11}^{\prime B}) = (\sigma_{nn}^{A} t^{A} - \sigma_{nn}^{B} t^{B})^2 < \delta$
- Control $\frac{\dot{\epsilon}_{11}^{B}}{\dot{\epsilon}_{11}^{A}}$ - if the fraction is larger than some limiting value, write limiting strain state in region A, otherwise return to II.

An extended version of the Marciniak and Kuczynski model

The original MK-approach has, as pointed out by Rasmussen [180], some limitations due to the assumption that the groove is aligned perpendicular to the principal stress direction. In order to overcome these limitations an extension of the original model has been proposed and used by a number of authors. The model is almost identical to the original but the groove is now allowed to appear in an arbitrary angle ϕ to the Y-axis. Hereby it is possible to predict the limit strains for negative strain ratios, it is the left-hand side of the FLD. The geometry is illustrated in figure 8.5. The routine used for arbitrary orientations

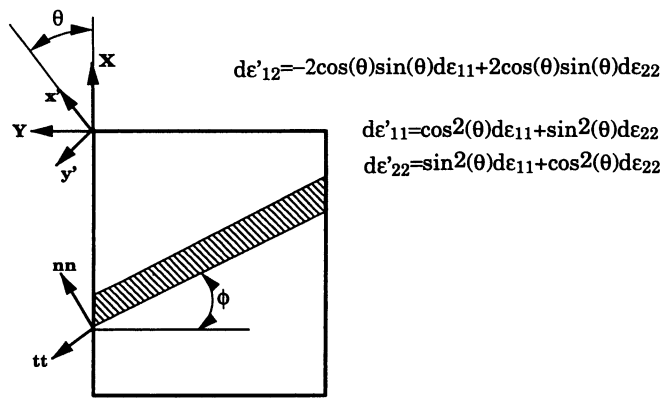

Figure 8.5: *Illustration of the imperfection line (B) in a region (A) of uniform thickness and the relations between prescribed strain increments and increments in the material coordinate system (x',-y'). The imperfection is aligned an angle ϕ to the direction of greatest principal stress. The initial inclination ϕ_0 can be chosen arbitraily.*

of the groove is:

- Initialize all variables. Input all material parameters including orientation of material coordinate system (θ), t_A, t_B and ϕ_0 and specify strain path.
- II: Prescribe new strain increment $\dot{\epsilon}_{11}^{A}$ in region A and calculate $\dot{\epsilon}_{22}^{A}$ based on the prescribed strain path.
- Calculate local strain increments, $\dot{\epsilon}_{11}^{\prime A}, \dot{\epsilon}_{22}^{\prime A}, \dot{\epsilon}_{12}^{\prime A}$
- Calculate the local stress increments $(\dot{\sigma}_{ij}^{\prime A})$ and update local stresses, local strains and thickness t_A.
- Update principal total strains $(\epsilon_{11}^{A}, \epsilon_{22}^{A})$ and calculate the orientation of the band: $tan(\phi) = tan(\phi_0) e^{(\epsilon_{11A} - \epsilon_{22A})}$.

- Calculate the straining aligned with the groove:

$$\dot{\epsilon}_{tt}^{A} = sin^2(\phi-\theta)\dot{\epsilon}'_{11} + cos^2(\phi-\theta)\dot{\epsilon}'_{22} - 2cos(\phi-\theta)sin(\phi-\theta)\dot{\epsilon}'_{12} \tag{8.46}$$

- Solve equilibrium equations using optimization technique (minimize the error):

$$ERR(\dot{\epsilon}'^{B}_{11}, \dot{\epsilon}'^{B}_{22}) = (\sigma^{A}_{nn}t^{A} - \sigma^{B}_{nn}t^{B})^2 + (\sigma^{A}_{nt}t^{A} - \sigma^{B}_{nt}t^{B})^2 < \delta \tag{8.47}$$

  Design variables are $\dot{\epsilon}'^{B}_{11}, \dot{\epsilon}'^{B}_{22}$, the shear component is calculated from the compatibility condition:

$$\dot{\epsilon}'^{B}_{12} = \frac{-\dot{\epsilon}^{A}_{tt} + sin^2(\phi-\theta)\dot{\epsilon}^{B*}_{11} + cos^2(\phi-\theta)\dot{\epsilon}^{B*}_{22}}{2cos(\phi-\theta)sin(\phi-\theta)} \tag{8.48}$$

- Control $\frac{\dot{\epsilon}^{B}_{11}}{\dot{\epsilon}^{A}_{11}}$ - if the fraction is larger than some limiting value, write limiting strain state in region A, otherwise return to II.

Implemented options

The programme consists in principle of three parts: The first part is just the material routine described previously: The routine is used for updating stresses in region A and the routine is also used for determining the stress states in region B for the iterative solution of equilibrium conditions. The second part is the solution algorithm used for solving the equilibrium and compatibility conditions with regard to strain increments in the imperfection zone. This second part controls the optimization technique and uses sensitivity analysis to find the unknown strain increments. The third part is the main routine controlling input, output and the description of strain increments in region A. Figure 8.6 shows the options included and the analysis types available in the programme.

The first column is used for determining the limiting strain for various strain paths. With these options only one path is used in the analysis. The types of paths which can be prescribed are:

- A linear strain path ($\dot{\epsilon}_2 = C_1\dot{\epsilon}_1$).
- A broken linear strain path made of 2 linear segments. ($\dot{\epsilon}_2 = C_1\dot{\epsilon}_1$ for $\epsilon_1 \leq \epsilon_0$ and $\dot{\epsilon}_2 = C_2\dot{\epsilon}_1$ for $\epsilon_1 > \epsilon_0$)
- A curved path specifying the relation between $\dot{\epsilon}_2$ and $\dot{\epsilon}_1$ as: $\dot{\epsilon}_2 = C_1\dot{\epsilon}_1 + C_2\dot{\epsilon}_1^2$.
- An arbitrary strain path specified through a number of points (<100).

The second column gives the implemented options regarding determination of a complete FLD. This is determined through a number of strain paths and a number of initial inclinations (ϕ_0) of the groove: For each groove orientation a limiting curve is found, and the FLD is constructed by using the minimum values for each strain path. Furthermore, it is possible to specify that various imperfection factors F are to be analysed, and it is possible to specify different constitutive parameters in region A to B (even the constitutive model can differ from region A to B, e.g. region A could follow von Mises criterion with linear hardening and region B could follow Barlat's 2D criterion with a Hollomon hardening).

The orientation of the material coordinate system can also be specified (angle θ).

Column three gives the options for determining a complete FLD when the material has been prestrained. One option is to give an initial equivalent plastic strain - the effect of prestraining is then taken into account by initializing the history variables in the material routine (just by setting the equivalent plastic strain). The second option is to specify an arbitrary strain path - a FLD is then determined by following this strain path whereupon a number of linear paths (see figure 8.10) are investigated up to the limiting strain. Using the first option for a prestrained material corresponds to the standard determination with a slightly changed hardening curve.

Column four offers the original MK-approach (these analyses can also be performed with the standard FLD determination by analysing only the groove orientation $\phi_0 = 0$). It is possible to dump strain relations, determine a standard original FLD (positive strain ratios only) and finally it is possible automatically to examine a range of F-values.

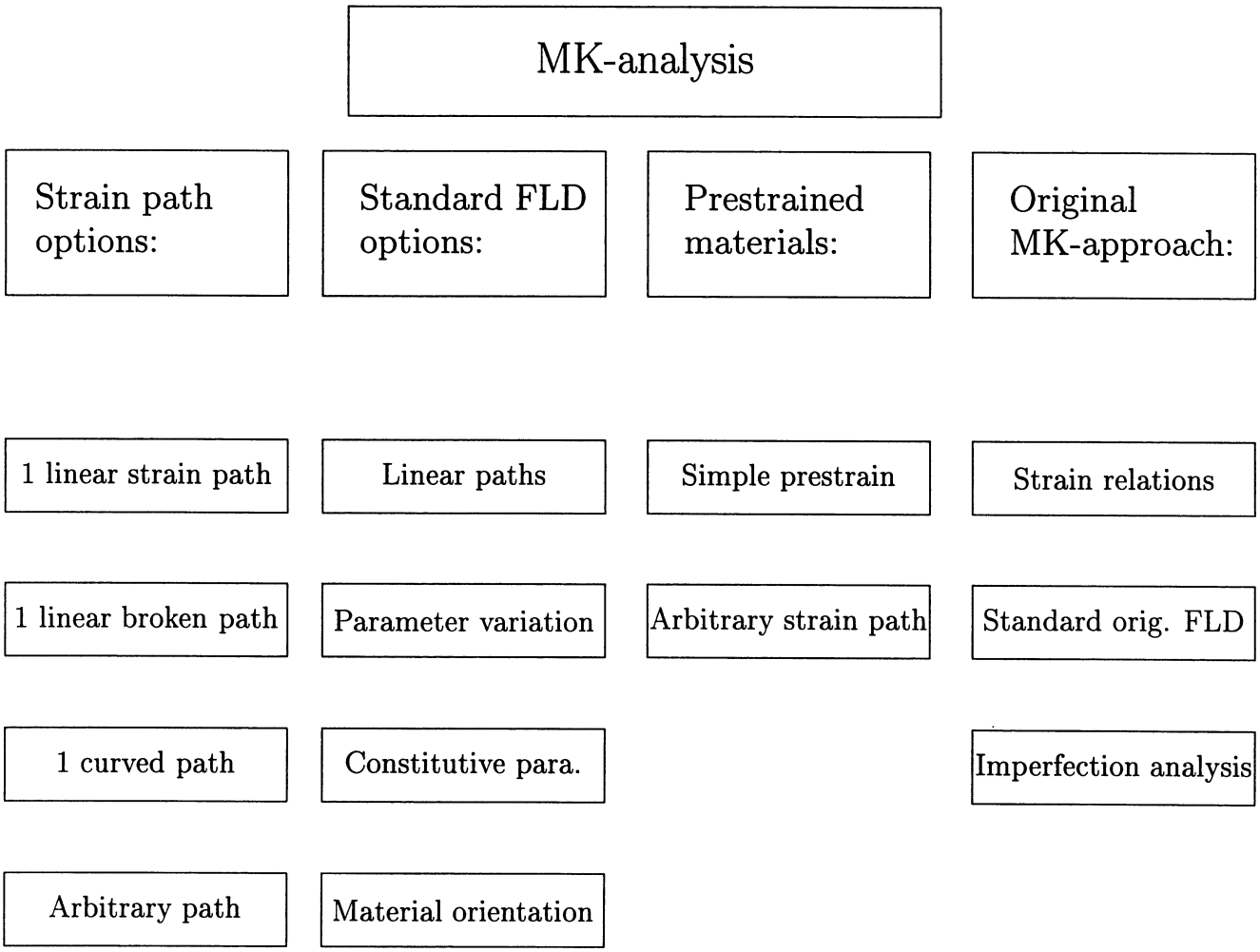

Figure 8.6: *The structure of the implemented programme: The main routine handles 4 different types of analysis: 1) Different types of strain paths, 2) Determination of standard FLDs for linear paths, variations in imperfection parameters and constitutive parameters and finally the possibility to use an arbitrary material orientation, 3) Takes prestraining of materials into account either by specifying initial effective plastic strain or an arbitrary initial strain path and 4) The original MK-approach with the groove perpendicular to the major principal stress.*

In the following some examples are given of the types of strain paths which can be specified. For some of the strain paths the corresponding stress paths are given (calculated with Barlat's 2D criterion with parameters corresponding to Hill's 48 criterion reduced to in-plane isotropy). The curves are primarily included in order to illustrate the response obtained with the material routine. Examples of path types are given in figures 8.7, 8.9 and 8.10. Figure 8.7 gives examples of paths which can be specified for analyses with a

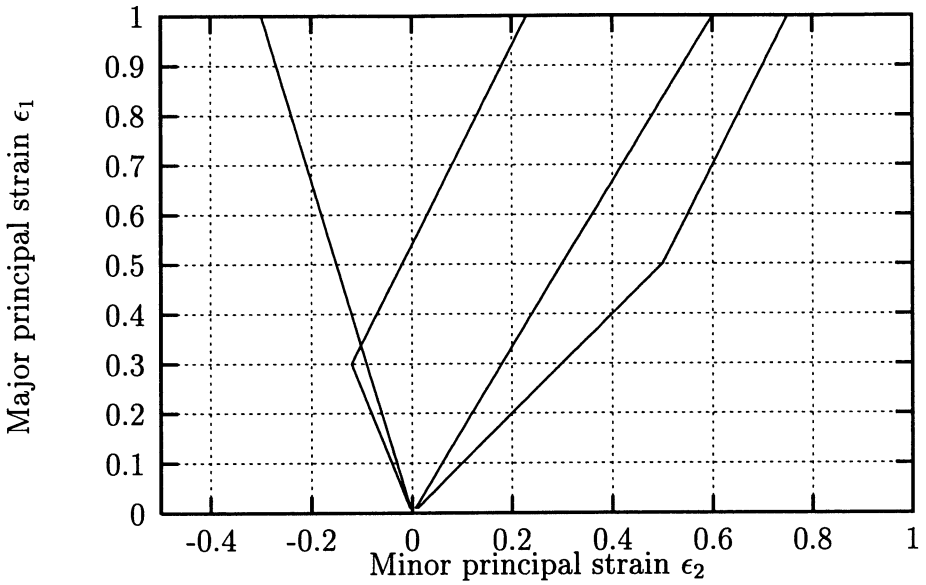

Figure 8.7: *Illustration of linear and linear broken strain paths.*

single path. For broken strain paths it is assumed that the second strain ratio is constant up to the limiting strain. Figure 8.8 shows the stress paths corresponding to the broken

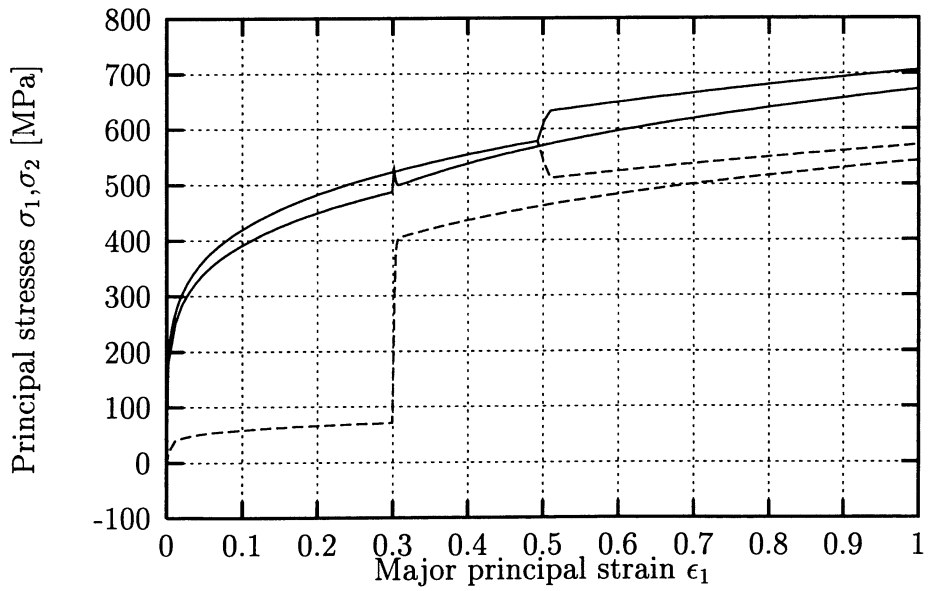

Figure 8.8: *Stress response for broken linear strain paths corresponding to figure 8.7*

strain paths in figure 8.7. This figure and the following figures illustrate the stress response, full lines represent the major principal stress and dotted lines represent the minor

principal stress. The stresses reported belong to the homogeneously strained part of the sheet (A). The first strain path has initially $\rho = 1$ and when $\epsilon_1 = 0.5$ ρ is changed to 0.5. This means that when the material is in-plane isotropic the two principal stresses will for the first part of the loading be overlaid. When the strain ratio changes a change in stresses due to elasticity can be seen (effects which are taken into account in the current implementation). The second strain path has initially $\rho = -0.5$ which switches to 0.5 at $\epsilon_1 = 0.3$. This switch does also lead to elastic effects, a small peak in the major principal stress can be seen. Another aspect is the fact that the minor principal stress differs from 0 for $\rho = -0.5$; this is due to the inclusion of elastic effects and the fact that $\rho = -0.5$ does not correspond to uniaxial tension when R is different from 1 (when elasticity is taken into account the values $\rho = -0.5$ and R=1 will not lead to an uniaxial stress response).

The standard determination of FLDs is based on linear strain paths which are illustrated in figure 8.9 in the case where 7 paths are utilized. Figure 8.9 shows a set of strain paths

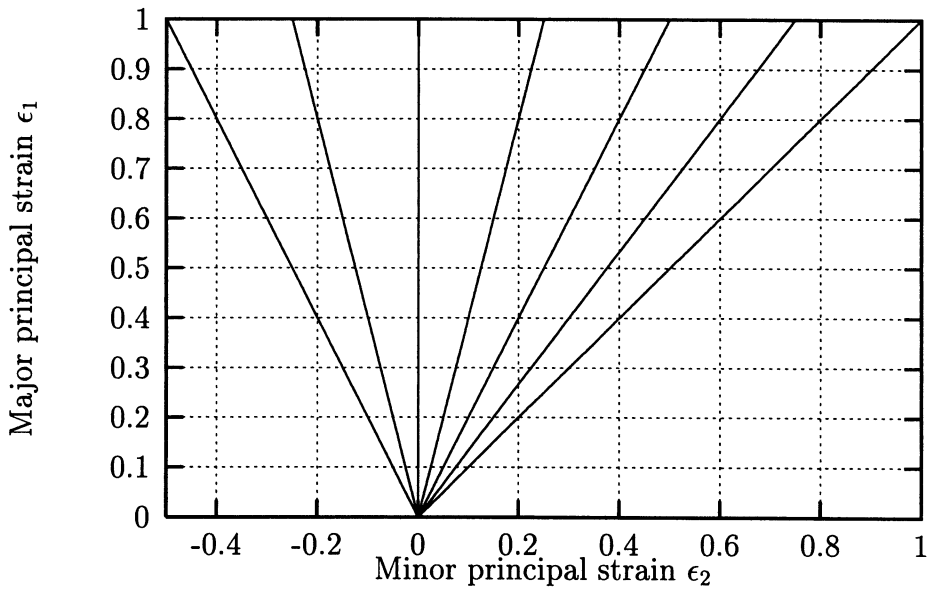

Figure 8.9: *Illustration of strain path principle used for a standard determination of a FLD.*

typically used for the determination of a FLD. The programme uses a number of paths varying from the minimum strain ratio $\rho = -0.5$ to the maximum ratio$\rho = 1.0$. Figure 8.10 shows the principle used for specifying strain paths when it is required to include an arbitrary straining history. For the actual example the strain path is given up to $\epsilon_1 \approx 0.5$ after which the strain path is assumed to be linear. This approach is flexible, but with the current implementation there are some limitations; the principal strain paths must be aligned with the coordinate system (X,Y) used for prescribing the loading situation. Figure 8.11 shows the predicted stress response for the strain paths given in figure 8.10. These curves do also indicate that an influence from elasticity is present when changing the strain ratio.

The conclusion drawn from this section is that the material subroutine provides good and robust results for the strain path options included in the MK-analysis.

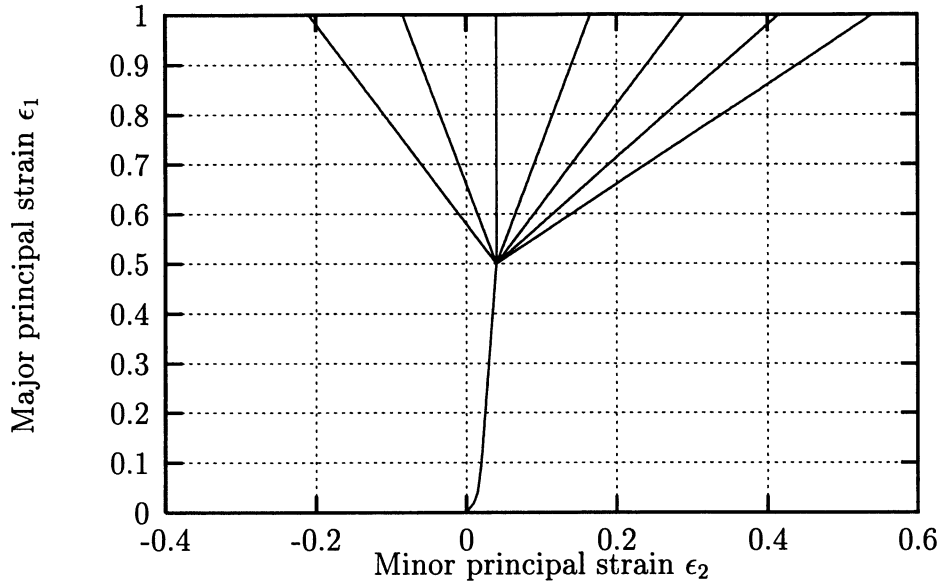

Figure 8.10: *Illustration of strain path principle used for the determination of a FLD for a prestrained material.*

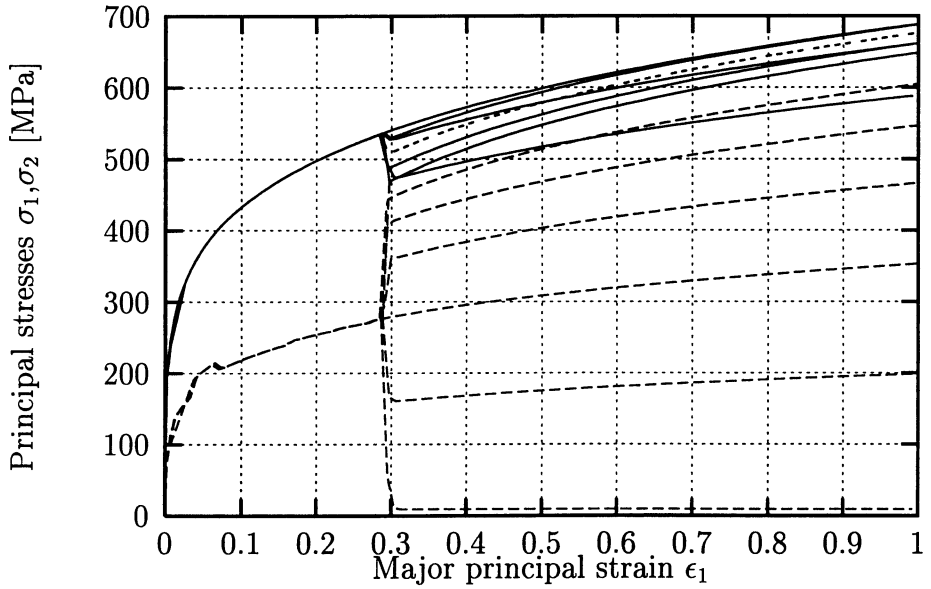

Figure 8.11: *Stress response for arbitrary strain paths obtained with LS-Dyna3d corresponds to the paths given in figure 8.10. The variation seen in the first part (between 0 and 5 per cent strain) is due to different number of points in the curves.*

Numerical example

In order to verify the implementation a number of FLDs have been determined. Figure 8.12 gives the results of an in-plane isotropic material and linear strain paths. Figure

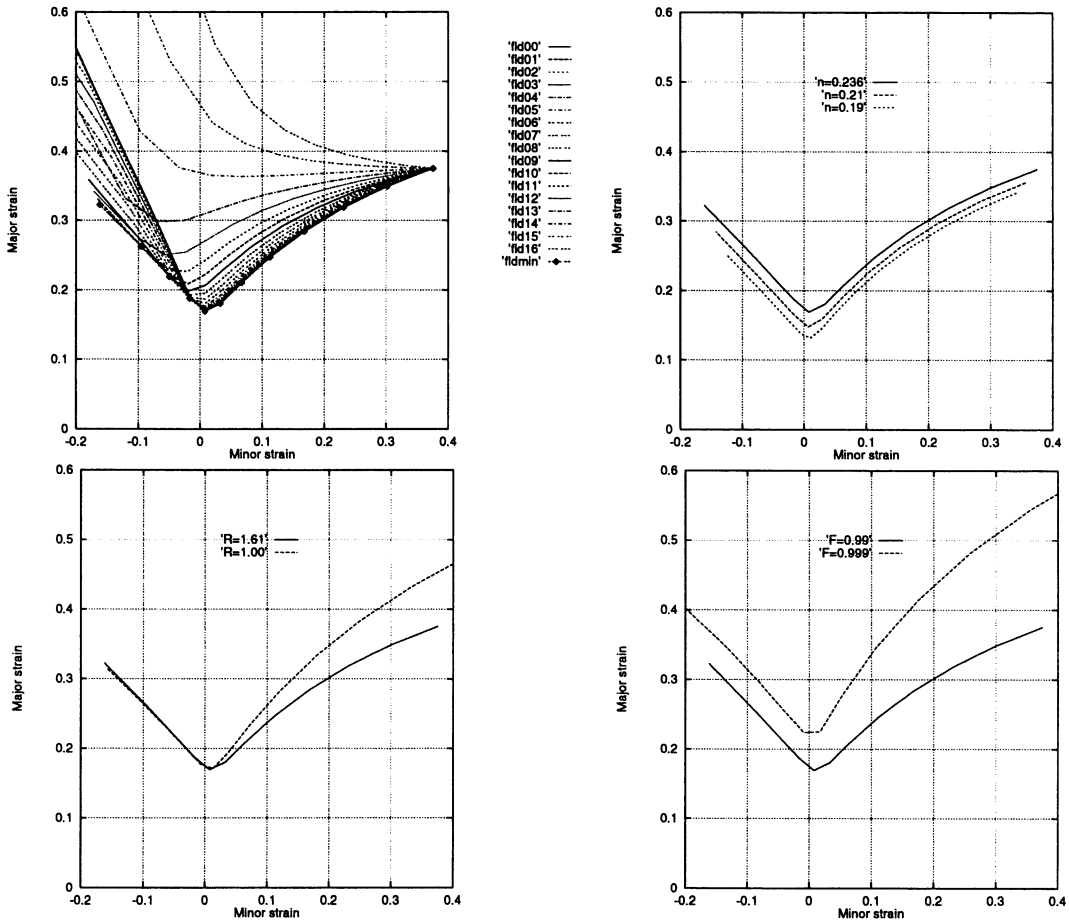

Figure 8.12: *Predicted FLDs using the material data available in the paper by Lu and Lee [138]. Top left-hand shows the limit strain curves predicted for various angles of the imperfection. The following three figures show the effect of variation in hardening exponent n, R-value and imperfection F.*

8.12 shows the predicted forming limits in a number of situations. In the top left-hand corner is shown the predicted limit (solid line with marks) for a material with n=0.236, R=1 and imperfection F=0.99. The routine checks a number of orientations of the groove, and the limiting strain point is taken from the orientation leading to the lowest value. In the right-hand side of the FLD the curve fld00 (corresponding to a groove perpendicular to the major principal stress) leads to the lowest values (the resulting FLD is indicated by the line with point marks). This is in good agreement with what is found by numerous authors. By increasing the angle of the groove (increased number on the curve label) the limiting curves are lifted for positive strain ratios. For balanced biaxial straining all curves pass the same point indicating that this situation is unaffected by groove orientation, which also should be expected. For negative strain ratios a dependency on the angle can be seen. Each negative strain ratio reaches the lowest predicted strain point for a given direction.

In the top right-hand corner is shown the predicted FLDs for the material with R=1 and n values of 0.19, 0.21 and 0.236, respectively. The MK-approach indicates a very strong influence from the n-value. This value is often taken as one of the "formability quality factors". One characteristic of the MK-approach which can be found from the curves is the fact that the instability limit in plane strain cannot exceed the n-value (even for F values very close to 1 this will be the case). Experimental reported FLDs often indicate higher values for the limiting strains in the region around $\epsilon_2 = 0$, thus this limiting value in the MK-approach does not seem too accurate. One way to improve the behaviour in this region is to include strain rate effect whereby the limit can be raised. These effects are included in the MK-approach developed, but no further investigation of strain rate effects has been performed. Another explanation to the fact that the limiting strain often is predicted to be relatively low for plane strain loading may be that the use of a power law hardening with a fixed exponent is not sufficiently accurate to describe the material behaviour. This problem has also been mentioned by e.g. Stören and Rice [200].

In the bottom left-hand corner in figure 8.12 is shown the effect of variations in R-values. For positive strain ratios a lower limiting strain can be seen for larger R-values; this is in good agreement with observations made by numerous authors using the MK-approach.

If we compare the results obtained with the MK-programme to results obtained with Hill's and Moore and Wallace's criteria it can be noticed that the limit predicted at plane strain is close to the n-value for all criteria, however, the MK-predicted limit is also influenced by the imperfection factor. The FLD-variation due to R-value variations is much larger for the MK-analysis than what is seen from the diffuse instability predictions (see section 8.1). The Erichsen test simulated in section 7.2.2 using Barlat's 2D criterion indicates the same effects for localization - however, one should expect localization in an element (or a row of elements) to be more related to the diffuse instability limit. In my opinion this indicates that the MK-approach is more suitable for explaining effects for positive strain ratios than to predict the absolute limit. The MK-approach does predict a behaviour for negative strain ratios which are very similar to the behaviour predicted with Hill's criterion - the left hand side of the (MK)FLD curve is almost linear and almost unaffected by variation in the R-value.

One of the reasons for developing the programme is to be able to take elastic effects into account. However, in figure 8.12 no effects of elasticity can be seen if the results are compared to results obtained by Lu and Lee [138]. Lu and Lee give FLDs which are directly comparable to the results given in figure 8.12 and no difference can be seen on the predicted limits. This is due to the proportional loading used for generating the curves, and it is believed that the elastic effects can influence the predicted limit in some cases where strain paths are broken.

At the time when the MK-programme was developed the plan was to make several numerical investigations of FLDs. However, during my study of formability predictions I became more and more sceptical with regard to the practical use of the MK-approach. One reason is that the physical quantities should correspond to the quantities existing in practice and this is not the situation as the imperfection parameter typically must be cho-

sen different from the thickness variations which can be measured. Another reason is that the predicted limit strain at plane strain is relatively low (below the n-value) compared to experiments.

In the programme the determination of strain increments in region B is based on an optimization strategy. This strategy turns out to give a relatively high CPU-use for the overall solution as it was found necessary to utilize relatively small prescribed strain increments in region A in order to obtain a sufficiently stable response from the material model. However, using very small increments imply that problems with numerical accuracy can arise when determining the sensitivities (by numerical differentiation).

8.6 A short deriviation of Jun's method

In the following the deriviation of an instability criterion presented in 1982 by Bressan and Williams [38] and developed further by Jun [111] is given.

The idea of the method is that necking is caused by localized shear deformation. In the original approach given by Bressan and Williams it is assumed that shear deformation will take place in the 1-3 plane (1-2 is the loading plane). The orientation of the plane is determined by finding a direction of plane strain, and instability onset is reached when the shear stress acting on this plane reaches a critical value τ_{cr}.

The approach given by Jun is similar, however, he reaches his criterion in a slightly different way: He finds the orientation of the plane where shear deformation will lead to localization from considerations of the stress state. Following the instability onset will be reached when the shear stress reaches a critical value. The orientation of the plane is found by assuming that pure shear deformation will take place when the stress state can be described by a normal stress equal to the mean stress ($\sigma_m = \frac{1}{3}(\sigma_1 + \sigma_2 + \sigma_3)$) and a shear stress. When the shear stress on this plane reaches the critical value τ_{cr} the localized necking will take place.

The approaches can be considered as extensions of Hill's method, which is based on the assumption of zero extension in the plane of the sheet (the 1-2 plane). Hill's assumption that plane strain occurs in the plane of the sheet makes his criteria valid only for non-positive strain ratios, this applies for the left-hand side of a FLD. Furthermore, the present methods deviate from Hill's criterion as the instability limit occurs when the critical value of the shear stress is reached. This is distinct from Hill's approach which is based on a maximum load (see section 8.2).

One main difference between the methods presented and the methods proposed by for example Marciniak and Kuczynski [142], Stören and Rice [200] and Moore and Wallace [149] is the fact that information obtained from a limiting strain point is included in order to estimate the necessary parameter τ_{cr}. The other methods are based on the material parameters used to describe plastic deformation and on an initial defect in the case of a MK-approach.

Information concerning the forming limit is included in the criterion in the following method and in my opinion this should be a sound approach. The following is to some extent based on the papers by Bressan and Williams [38], Jun [111] and Albrektsen [4]. The papers all include the principle of the method, the primary difference being the yield criterion, hardening rule, etc. Jun obtains very good relations between experimental and theoretical predicted FLDs, Bressan and Williams comparisons are less favourable and they conclude that their method gives a lower bound for the FLD.

In the present the material is assumed to obey Hill's 48 criterion reduced to in-plane isotropy and to follow a hardening curve: $\sigma_Y = K\epsilon_{eff}^n$. The equivalent stress can be expressed as:

$$\sigma_{eq} = \sqrt{\sigma_1^2 - \frac{2R}{1+R}\sigma_1\sigma_2 + \sigma_2^2} = \sigma_1\sqrt{1 - \frac{2R}{1+R}X + X^2} \tag{8.49}$$

where X is the principal stress ratio $(\frac{\sigma_2}{\sigma_1})$. The associated flow rule leads to the following relation between strain increment for a given stress state:

$$\frac{d\epsilon_1}{1+R-RX} = \frac{d\epsilon_2}{(1+R)X-R} = -\frac{d\epsilon_3}{1+X} = \frac{d\epsilon_{eq}}{(1+R)\frac{\sigma_{eq}}{\sigma_1}} \tag{8.50}$$

The effective strain is defined as:

$$d\epsilon_{eq} = \frac{(1+R)\sqrt{1 - \frac{2R}{1+R}X + X^2}}{1+R-RX}d\epsilon_1 \tag{8.51}$$

The principal stress ratio is related to strain increment ratio $\rho = \frac{d\epsilon_2}{d\epsilon_1}$:

$$X = \frac{R+(1+R)\rho}{1+R+R\rho} \tag{8.52}$$

In figure 8.13 examples on strain increments and stresses represented in Mohr circles are illustrated. The angle for which no elongation takes place is characterized by the angle θ:

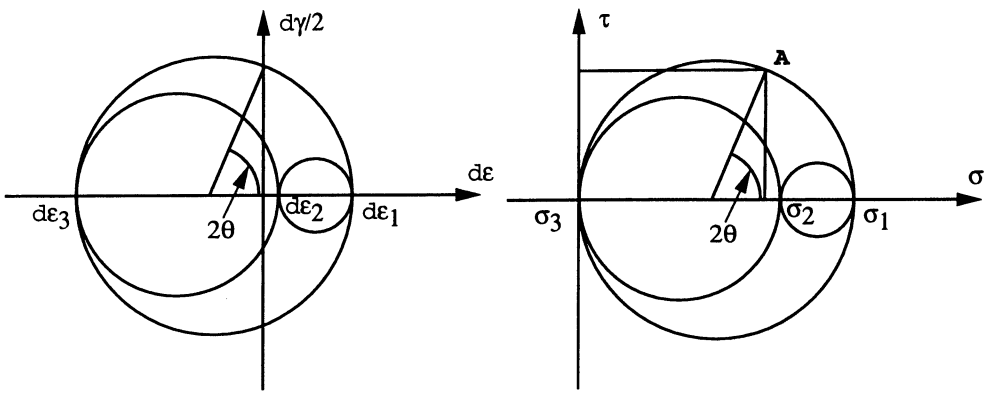

Figure 8.13: *Mohr's circles for strain increments and for the state of stress at the onset of local necking shown left and right, respectively.*

$$cos(2\theta) = -\frac{\frac{d\epsilon_1+d\epsilon_3}{2}}{\frac{d\epsilon_1-d\epsilon_3}{2}} \tag{8.53}$$

θ characterizes the angle between a normal to the sheet and the direction in the 1-3 plane where a state of pure incremental shear deformation exists. Equation 8.53 can, assuming plastic incompressibility for the plastic strain increment, be expressed:

$$cos(2\theta) = -\frac{d\epsilon_1 - d\epsilon_1 - d\epsilon_2}{d\epsilon_1 + d\epsilon_1 + d\epsilon_2} = \frac{d\epsilon_2}{2d\epsilon_1 + d\epsilon_2} = \frac{\rho}{2+\rho} \tag{8.54}$$

From Mohr's circle the relation between stresses is found to:

$$sin(2\theta) = \frac{2\tau_{cr}}{\sigma_1} \tag{8.55}$$

Combining equations 8.54 and 8.55 the relation between the major principal stress and the critical shear stress is found to be:

$$\tau_{cr} = \sigma_1 \frac{\sqrt{1+\rho}}{2+\rho} \quad or\ alternatively \quad \sigma_1 = \tau_{cr} \frac{2+\rho}{\sqrt{1+\rho}} \tag{8.56}$$

If the critical shear stress is known it is possible to determine the principal stress at localization for a given strain ratio and hereby the limiting strain can be determined. The above is essentially the basic of the approach given by Bressan and Williams.

The method by Jun is somewhat different. If we start out with a given strain ratio we can determine σ_1 and σ_2. Jun claims that the stress situation that leads to pure shear deformation appears for the orientation where the normal stress (σ_n) equals the mean stress:

$$\sigma_n = \frac{1}{3}(\sigma_1 + \sigma_2) = \frac{\sigma_1}{2} + \frac{\sigma_1}{2} cos(2\theta) \tag{8.57}$$

Using the stress ratio equation 8.57 can be rewritten to:

$$cos(2\theta) = \frac{2X - 1}{3} \tag{8.58}$$

The corresponding shear stress is $\tau = \frac{\sigma_1}{2} sin(2\theta)$ which combined with equation 8.58 leads to:

$$\tau = \frac{\sigma_1}{3}\sqrt{2 - X^2 + X} \tag{8.59}$$

When the shear stress reaches the value τ_{cr} we have reached the limit. For a given stress ratio we find the critical major stress:

$$\sigma_1 = \frac{3\tau_{cr}}{\sqrt{2 - X^2 + X}} \tag{8.60}$$

In order to use the criterion we must determine τ_{cr} and in the following three methods are given to determine τ_{cr} from experiments. Normally the criterion is established using the limiting strain in either plane strain ($\rho = 0$) or balanced biaxial straining ($\rho = 1$). As an alternative to these methods the results from an uniaxial tension test ($\rho = -R/(1+R)$) can be applied. The last method seems to be the easiest way to obtain information on the instability strain, however, the measuring of ϵ_1 is difficult at fracture in a tensile test.

Plane strain

First we consider plane strain ($\rho = d\epsilon_2 = 0$). If we in 8.59 substitute σ_1 with σ_{eq} (from 8.49) we obtain:

$$\tau_{cr} = \frac{\sigma_{eq}}{3} \frac{\sqrt{2 + X - X^2}}{\sqrt{1 - \frac{2R}{1+R}X + X^2}} \tag{8.61}$$

The stress ratio X is found to be $X = \frac{\sigma_2}{\sigma_1} = \frac{R}{1+R}$. If we take $\epsilon^*_{1,ps}$ at fracture the effective plastic strain at fracture can be expressed:

$$\epsilon^*_{eq} = \frac{(1+R)\sqrt{1 - \frac{2R}{1+R}X + X^2}}{1 + R - RX} \epsilon^*_{1,ps} = \frac{1+R}{\sqrt{1+2R}} \epsilon^*_{1,ps} \tag{8.62}$$

The critical shear stress τ_{cr} for a Hollomon hardening material is then given by:

$$\tau_{cr} = \frac{K\left\{\frac{1+R}{\sqrt{1+2R}}\epsilon^*_{1,ps}\right\}^n}{3} \frac{\sqrt{2 + \frac{R}{1+R} - \frac{R^2}{(1+R)^2}}}{\sqrt{1 - \frac{2R}{1+R}\frac{R}{1+R} + \frac{R^2}{(1+R)^2}}} = \sqrt{2+R}\frac{K\left\{\frac{1+R}{\sqrt{1+2R}}\epsilon^*_{1,ps}\right\}^n}{3} \tag{8.63}$$

Using the above equation as the left-hand side of 8.61 we obtain:

$$\sqrt{2+R}\frac{K\left\{\frac{1+R}{\sqrt{1+2R}}\epsilon^*_{1,ps}\right\}^n}{3} = \frac{\sigma_{eq}}{3} \frac{\sqrt{2 + X - X^2}}{\sqrt{1 - \frac{2R}{1+R}X + X^2}} \tag{8.64}$$

Eliminating common coefficients the following expression is obtained for the effective plastic strain at onset of necking for a given stress ratio (proportional loading):

$$\epsilon^*_{eq} = \epsilon^*_{1,ps} \left(\frac{1+R}{\sqrt{1+2R}}\right) \left(\frac{(2+R)\left(1 - \frac{2R}{1+R}X + X^2\right)}{2 + X - X^2}\right)^{\frac{1}{2n}} \tag{8.65}$$

Balanced biaxial straining

In case of balanced biaxial straining we have $\rho = X = 1$ leading to:

$$\tau_{cr} = \frac{K(\sqrt{2+2R}\epsilon^*_{1,bs})^n}{3}\sqrt{1+R} \tag{8.66}$$

From the major strain $\epsilon^*_{1,bs}$ at fracture the plastic strain is found to be:

$$\epsilon^*_{eq} = \epsilon^*_{1,bs} \left(\sqrt{2+2R}\right) \left(\frac{(1+R)\left(1 - \frac{2R}{1+R}X + X^2\right)}{2 + X - X^2}\right)^{\frac{1}{2n}} \tag{8.67}$$

Uniaxial stress

Using a tensile test to determine the critical shear stress we have a stress ratio $X = 0$ and a strain ratio $\rho = -\frac{R}{1+R}$ which lead to:

$$\tau_{cr} = \frac{K\epsilon_{1,us}^{*\,n}}{3}\sqrt{2} \tag{8.68}$$

Leading to the plastic strain where the critical shear stress is reached:

$$\epsilon_{eq}^{*} = \epsilon_{1,us}^{*}\left(\frac{2\left(1 - \frac{2R}{1+R}X + X^2\right)}{2 + X - X^2}\right)^{\frac{1}{2n}} \tag{8.69}$$

When the effective straining is determined for a given stress ratio using one of the above methods, the limiting strains can be found as:

$$\epsilon_1^{*} = \frac{1 + R - RX}{(1+R)\sqrt{1 - \frac{2R}{1+R}X + X^2}}\epsilon_{eq}^{*} \quad \textit{and} \quad \epsilon_2^{*} = \rho\epsilon_1^{*} = \frac{1 + R - RX}{(1+R)X - R}\epsilon_1^{*} \tag{8.70}$$

In figures 8.14 and 8.15 Jun's method, Moore and Wallace's and Hill's criteria are compared. Figure 8.14 shows the limit curves predicted with Jun's compared to Hill's and

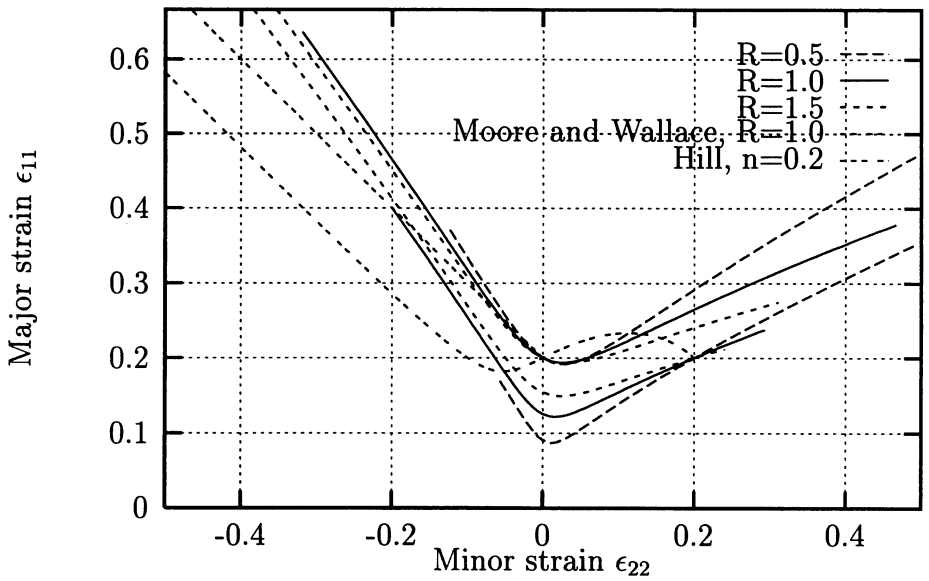

Figure 8.14: *Forming limit diagrams predicted using Jun's method (n=0.2) for R-values of 0.5, 1 and 1.5. The 3 lowest FLDs are established using the biaxial strain limit predicted by Moore and Wallace (n,n). The 3 upper curves are predicted using the plane strain limit (0,n). Also the curves obtained for an isotropic material using Hill's criterion and Moore and Wallace's criterion are shown.*

Moore and Wallace's criteria. The curves predicted with Jun's criterion are generated from R-values of 0.5, 1 and 1.5 and a hardening exponent n=0.2. To generate the curves two approaches are utilized: 1) the equivalent strain is predicted using the limit at plane strain, $\rho = 0$, (here set to coincide with the n-value) or 2) predicted using the value given by Moore and Wallace's criterion for $\rho = 1$, ($\epsilon_1^{*} = n$, $\epsilon_2^{*} = n$). Thus, by utilizing three R-values we end up with 6 curves for Jun's method where the three upper curves pass (0,n) and the lower curves pass the point (n,n). In the figure is also shown the curves based

on Moore and Wallace's criterion (with R=1 and n=0.2) and based on Hill's criterion for n=0.2 (only covering negative strain ratios).

The nature of the curves are quite different from the curve which shows Moore and Wallace's criterion for positive strain ratios. The characteristic curvature appearing with Moore and Wallace's criterion is substituted with a shape which is almost linear for positive strain ratios. For negative strain ratios the predicted limit strains are larger when predicted by Jun's method compared to the limits predicted with the diffuse instability criterion. With regard to variations in the R-value the strains predicted using Jun's method are much more sensitive than the variation predicted for the diffuse instability (see figure 8.1). It is clear from the figure that when the point of plane strain is used for determining τ_{cr} the sensitivity towards variation in the R-value are most pronounced for the larger strain ratios. When τ_{cr} is predicted using the limit at balanced biaxial strain the variation appears for the limits around the region close to plane strain. For the smallest strain ratios it seems as if there is no significant influence on the predicted limits when varying the R-values. If we compare the observations made for the MK-approach the trends are essentially the same: By increasing the R-value the result is a reduced formability for positive strain ratios. Jun's method is affected somewhat for negative strain ratios, however, this cannot be seen in figure 8.12 (the MK-approach). Figure 8.15 has been generated as figure 8.14 the only

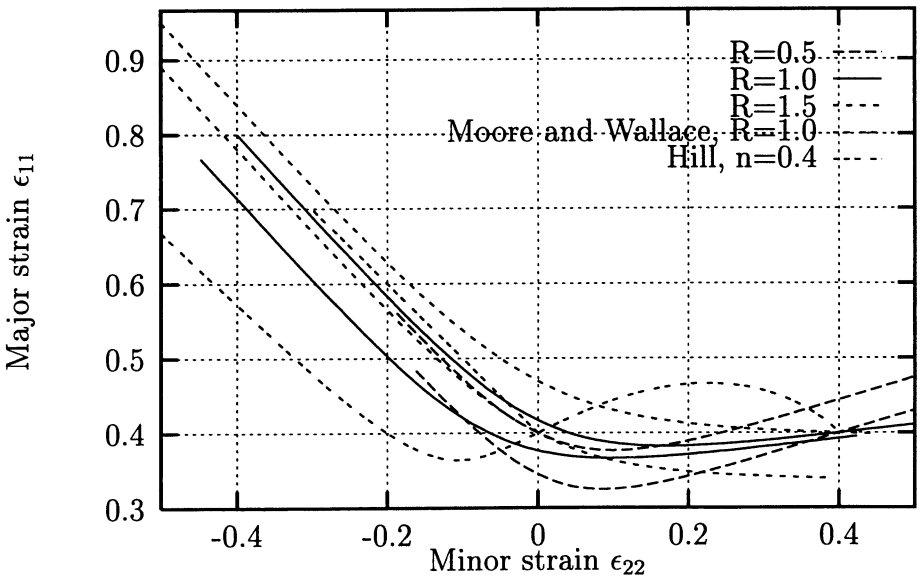

Figure 8.15: *Forming limit predicted using Jun's method (n=0.4). The values used are either plane strain (n,0) or balanced straining (n,n) corresponding to the limits predicted by Moore and Wallace. Also the curves obtained for an isotropic material using Hill's criterion or Moore and Wallace's criterion are shown.*

difference is that n=0.4 (and hereby the limit used for plane strain is 0.4 instead of 0.2 and (0.4, 0.4) is used for balanced straining). Again, a very poor correlation between the diffuse instability criterion and Jun's method can be seen. The slope of the limiting curves are similar to the slope predicted with Hill's criterion for negative strain ratio. The effects of variations in the R-value seem to be less pronounced for n=0.4 than for n=0.2 - this effect is opposite the effect predicted by using Moore and Wallace's criterion: Here, due to variations in R-value the largest variation is seen for the larger values of n (however, still

relatively small).

Based on figures 8.14 and 8.15 it is obvious that the hardening exponent has a significant effect on the predicted FLD. This can also apply to the previously discussed methods, but for these methods a variation in n does not lead to changes in the nature of the predicted curves. FLDs predicted by Jun's method are in general lifted when the n-value is increased, but at the same time the curves become more flat. This effect may make the criterion suitable in connection with materials where the limit in plane strain is well above the n-value (this is often the case for mild steel).

From the figure 8.14 it can be noticed that the use of the balanced biaxial strain limit leads to a very low predicted formability for negative strain ratios when the R-value is low. This may lead to the suggestion that the plane strain limit should be used for determining the entire FLD. Yet another advantage of the method is the fact that it is relatively easy to utilize more advanced yield criteria and thus the flexibility can be extended further.

8.7 The criterion proposed by Stören and Rice

In 1975 Stören and Rice [200] proposed a method for determining forming limit curves. Their method was developed based on the fact that localized modelling under biaxial stretching of a uniform and homogeneous sheet is impossible when flow theory of plasticity is used.

In 1967 Marciniak and Kuczynski [142] proposed their method in order to overcome this problem by assuming an initial inhomogeneity in the sheet. Stören and Rice argue that the model of Marciniak and Kuczynski leads to unrealistic values for the imperfection when their predicted results are in reasonable agreement with experiments. On the contrary Barlat et al. [133, 14] claim that the use of the MK-approach leads to imperfections which are reasonable in relation to thickness variation for commercial aluminum sheets.

The approach by Stören and Rice is instead based on the assumption that a band inclined some angle to the major stress direction may exist over which an inhomogeneous flow field can exist. In the following the principle of the theory is given as reported in Stören and Rice [200].

Condition for the onset of localized necking in plane stress

We consider uniform quasi-static deformation of a homogeneous plane sheet loaded in plane stress and with current thickness H. The purpose of the method is to find the condition for which further loading may result in an incipient non-uniform flow field which varies across a band but remains uniform outside the band. The situation is illustrated in figure 8.16.
A unit vector n_α normal to the band can be described by the angle ψ:

$$n_1 = cos\psi, \qquad n_2 = sin\psi \tag{8.71}$$

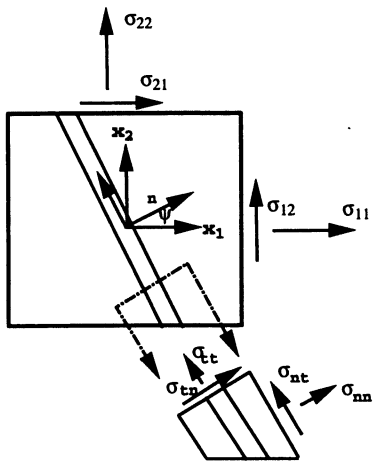

Figure 8.16: *Coordinate system and direction of the localization band. The cut illustrates the stress components normal and parallel to the band.*

As in the original paper we denote the difference between the values of the field variables inside and outside of the band by Δ. The flow field is restricted to vary perpendicular to the band and hereby the difference in velocity Δv_α becomes:

$$\Delta v_\alpha = v_{\alpha,inside} - v_{\alpha,outside} = f_\alpha(x_1 cos\psi + x_2 sin\psi) = f_\alpha(n_\beta x_\beta) \tag{8.72}$$

with $\alpha = 1, 2$ describing the components of the velocity lying in the plane of the sheet. $v_{\alpha,outside}$ is the homogeneous velocity field. Based on this variation in the velocities we have a variation in rate of deformation:

$$\Delta\left(\frac{\partial v_\alpha}{\partial x_\beta}\right) = \frac{\partial(\Delta v_\alpha)}{\partial x_\beta} = f'_\alpha(n_\gamma x_\gamma) n_\beta = g_\alpha n_\beta \qquad (\alpha, \beta, \gamma = 1, 2) \tag{8.73}$$

where

$$g_\alpha = f'_\alpha(n_\beta x_\beta) \qquad (\alpha, \beta = 1, 2) \tag{8.74}$$

From figure 8.16 we have the condition for equilibrium in the plane of the sheet:

$$\frac{\partial(H\sigma_{\alpha\beta})}{\partial x_\alpha} = 0 \qquad (\alpha, \beta = 1, 2) \tag{8.75}$$

H denotes the current thickness of the sheet. For the rate of change of the stress-resultants at a fixed point in space we have:

$$\frac{\partial}{\partial x_\alpha}\left[\frac{\partial(H\sigma_{\alpha\beta})}{\partial t}\right] = \frac{\partial}{\partial x_\alpha}\left[\dot{(H\sigma_{\alpha\beta})} - v_\gamma\left[\frac{\partial(H\sigma_{\alpha\beta})}{\partial x_\gamma}\right]\right] \tag{8.76}$$

where $\dot{(...)}$ denotes the instantaneous material derivative, and $\sigma_{\alpha\beta}$ $(\alpha, \beta = 1, 2)$ are the true stress components in the plane of the sheet. From 8.75 it follows that 8.76 can be reduced to:

$$\frac{\partial}{\partial x_\alpha}(\Delta\dot{\sigma}_{\alpha\beta} + \sigma_{\alpha\beta}\Delta\dot{\epsilon}_{33}) = 0 \tag{8.77}$$

where $\Delta\dot{\sigma}_{\alpha\beta}$ is the difference in stress-rate corresponding to the incipient flow field given by 8.71 and 8.72. The variation in deformation gradient is given by:

$$\Delta\dot{\epsilon}_{33} = \Delta\left(\frac{\dot{H}}{H}\right) \tag{8.78}$$

it is the difference in thickness strain rate inside and outside the band. As it is stated that the flow field is only varying over the band, 8.77 can be written as:

$$n_\alpha \Delta\dot{\sigma}_{\alpha\beta} + n_\alpha \sigma_{\alpha\beta} \Delta\dot{\epsilon}_{33} = 0 \tag{8.79}$$

In order to relate the variation in stress rates and thickness-strain rate it is necessary to use the constitutive equations. If it is assumed that the following linear strain rate relations are valid:

$$\dot{\sigma}_{\alpha\beta} = L_{\alpha\beta\gamma\delta}\left(\frac{\partial v_\gamma}{\partial x_\delta}\right) \qquad \dot{\epsilon}_{33} = M_{\gamma\delta}\left(\frac{\partial v_\gamma}{\partial x_\delta}\right) \tag{8.80}$$

where the components of $\mathbf{L}$ and $\mathbf{M}$ are some functions of current stress state and the constitutive parameters and if $\mathbf{L}$ and $\mathbf{M}$ remain the same inside and outside the band at the point of inception, then the following differences may be formed:

$$\Delta\dot{\sigma}_{\alpha\beta} = L_{\alpha\beta\gamma\delta}\Delta\left(\frac{\partial v_\gamma}{\partial x_\delta},\right) = L_{\alpha\beta\gamma\delta} n_\delta g_\gamma \tag{8.81}$$

$$\Delta\dot{\epsilon}_{33} = M_{\gamma\delta}\Delta\left(\frac{\partial v_\gamma}{\partial x_\delta},\right) = M_{\gamma\delta} n_\delta g_\gamma \tag{8.82}$$

By substitution of 8.81 and 8.82 into 8.79 a set of linear homogeneous equations in g_1, g_2 are obtained:

$$(n_\alpha L_{\alpha\beta\gamma\delta} n_\delta + n_\alpha \sigma_{\alpha\beta} M_{\gamma\delta} n_\delta) g_\gamma = 0 \tag{8.83}$$

The condition for the onset of necking is met if 8.83 is satisfied for some non-zero g_1 and/or g_2, that is, if:

$$det(n_\alpha L_{\alpha\beta\gamma\delta} n_\delta + n_\alpha \sigma_{\alpha\beta} M_{\gamma\delta} n_\delta) = 0 \tag{8.84}$$

However, the increment in strain vector will be normal to the yield surface due to the normality condition for flow theory. This condition has, as pointed out by Stören and Rice, a stabilizing effect on the flow as a sudden change in stress rate does not change the flow pattern instantaneously. If equation 8.84 is solved using the flow theory of plasticity the resulting stress is of the same order as the shear modulus G. (As a matter of fact, I have reached the same solution from personal experience). By relaxing the normality condition it becomes possible to obtain a rapid change in flow direction - this relaxation can be obtained by using deformation theory or by using flow theory with a pointed vertex at the current stress state. Stören and Rice use a simplified constitutive model of a pointed vertex on subsequent yield loci so that the equations of deformation theory of rigid-plastic solids apply for fully active stress increments, and thus they predict the onset of localized necking under biaxial stretching.

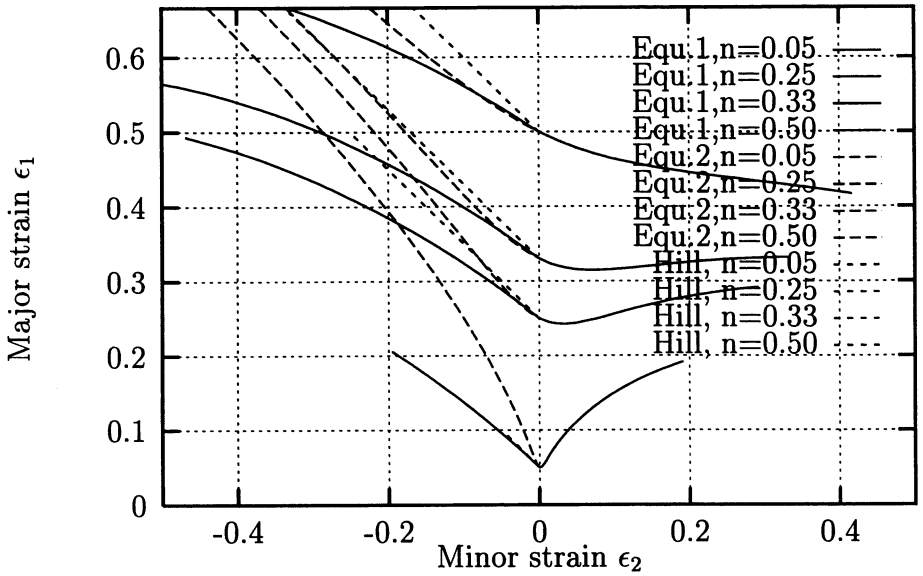

Figure 8.17: *Instability limits for isotropic materials with various hardening exponents (n=0.05, 0.25, 0.33 and 0.5) calculated using the analytic expressions given by Stören and Rice [200]. For comparison the limits predicted using Hill's instability criterion is included (straight dotted lines).*

Stören and Rice give analytical solutions for an isotropic, work hardening material described with a power-law hardening with index n. In order to obtain a analytic solution they make assumptions regarding the neck orientation. If it is assumed that the neck will form in the direction of minimum extension ($\psi = 0$) they obtain the following expression:

$$\epsilon_1^* = \frac{3\rho^2 + (2+\rho)^2 n}{2(2+\rho)(1+\rho+\rho^2)} \tag{8.85}$$

where $-1 \leq \rho \leq 1$ and $\psi = 0$. If it is assumed that the neck can form in plane strain, it is with zero extension along the neck (corresponding to Hill's assumptions) Stören and Rice find the analytical expression:

$$\epsilon_1^* = \frac{n}{1+\rho}\left\{\frac{1-n}{2} + \sqrt{\frac{(1+n)^2}{4} - \frac{\rho n}{(1+\rho)^2}}\right\}^{-1} \tag{8.86}$$

where $(-1 \leq \rho \leq 0)$ and $\psi = arctan(\sqrt{-\rho})$. For both equations hardening is assumed as $\sigma_Y = K\epsilon_p^n$ and ψ is the angle between ϵ_1 direction and the normal to the localized necking line. Figure 8.17 shows the limits predicted using Stören and Rice's criterion. Some common features can be seen for the criterion: For plane strain we obtain the limit at the point (0,n) - the same point as for diffuse instability and also what is found using Hill's criterion. If the imperfection factor in the MK-approach is very close to one the same limit can be reached. In the figure curves found by using equations 8.86 and 8.85 are given, the curves are marked as equation 1 and equation 2, respectively. In the figure the limit predicted with Hill's criterion (negative strain ratios only) is also given.

For the higher n-values there is a reasonable agreement with Hill's criterion and the limits

found based on the equation marked 2, but for a n-value of 0.05 the curve marked with 1 so to speak coincide with Hill's criterion. Another characteristic is the fact that the shape of the curves is strongly related to the n-value: A low n-value leads to a V-shaped FLD but the higher values indicate a much smoother curve. The n-value of 0.5 leads to a curve which is monotonicly decreasing which is quite different from the results obtained using methods discussed previously (apart from Jun's method).

One advantage of the criterion is the fact that we do not need to estimate additional parameters such as the imperfection factor in the MK-analysis. If necking behaviour really is caused by instability an approach based on instability analysis may be the way to proceed.

8.8 Consideration concerning the forming limit stress concept

Another interesting approach used in order to evaluate the risk of failure is the forming limit stress concept(FLSD). This concept was initially proposed by Gronostajski [81, 80] and Arrieux [8]. The basic idea in the FLSD is that the relation between principal stresses at fracture is calculated from a standard FLD. It has been found that, in contrast to the forming limit strain concept, the limiting stresses seem to be nearly unaffected by prestrain, strain path, etc. This means that having established a FLSD (a diagram where the major stress at fracture is plotted as function of the minor strain) it is much simpler to evaluate the remaining formability seen from a computational point of view. In the following a short presentation of the method is given and it is illustrated how the approach may be used in connection with FE-simulations.

The steps in the procedure are given below:

- Determine experimental FLD
- Calculate FLSD (here using Barlat's 2D criterion)
- Option 1: Use calculated stress points in an evaluation of the direct risk of fracture (to be dumped during FE-analysis)
- Option 2: Post process data: Choose element from the FE-analysis and obtain the strain path, add linear strain paths to the final strain state until the limiting stress state is reached in order to evaluate the remaining formability.

This approach can be used in the planning of for example the layout of multi step operations, e.g. by optimizing the tool geometry used in the first step in order to obtain the maximum allowable deformation in the subsequent operations.

In order to evaluate the method a number of FLDs available from literature have been chosen as basis for an evaluation of the characteristics of the methods. Three FLDs from the Numisheet'96 Benchmark Material and the two FLDs including the recorded strain paths reported by Albrektsen [4] are used in the following.

One of the first characteristics which is noticed reading the articles by Arrieux [10, 8]

is that the limiting stresses show almost the same value for the major principal stress regardless the value of the minor principal stress. This also turns out to be the case for the Numisheet FLDs. Figure 8.18 shows left the FLDs reported in the Numisheet'96 Bench-

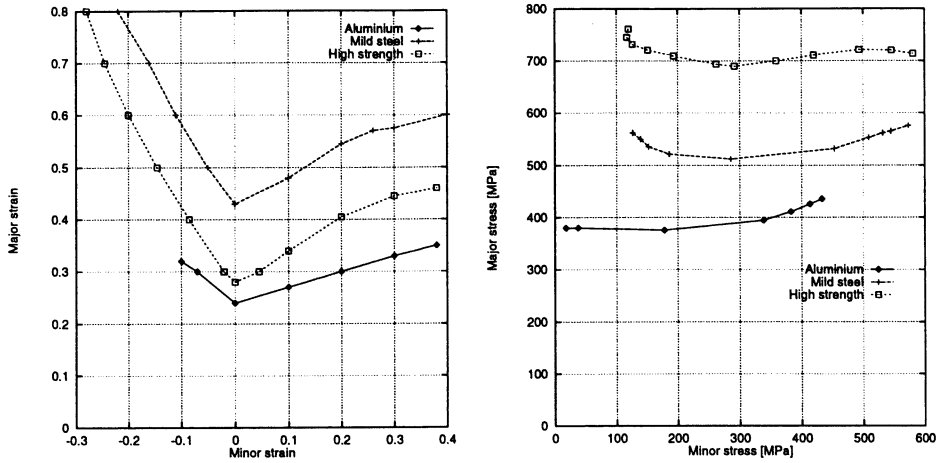

Figure 8.18: *Left: Forming limit diagrams reported in the Numisheet'96 Benchmark Material. Right: The corresponding forming limit stress diagrams.*

mark material. If it is assumed that the limiting strain has been obtained from linear strain paths the FLSDs shown in the right part of the figure can be obtained (here using Barlat's 2D criterion). Curves are given for three materials; an aluminum sheet, a mild and a high strength steel sheet. The FLSD curve for the high strength steel indicates a somewhat peculiar shape for strain paths close to uniaxial tension; this is due to the fact that the highest limiting strain (0.8) is reached with a strain ratio slightly higher than the ratio leading to the limiting point with $\epsilon_1 = 0.7$. Figure 8.19 gives a FLD obtained for a mild steel (St 14.03). The dotted lines in the figure indicate the strain paths. The right-hand side gives the corresponding stress paths calculated with Barlat's 2D criterion. The strain path for $\rho \approx -0.5$ leads to a stress response with some stress points including negative minor stresses. This is hardly the true situation - it is more a result of the uncertainty under which the intermediate strain points are determined. Figure 8.20 gives the FLD and strain paths for another mild steel, Docol 300 RP-X, reported by Albrektsen [4]. The right-hand side shows the corresponding stress paths. It is characteristic that the strain paths reported by Albrektsen lead to a somewhat scattered response in the forming limit stress curves as well as in the stress paths. For some of the reported strain paths the last strain point reported has been omitted in order to make the FLDs correspond to the maximum principal stress calculated. Although the strain paths appear reasonably linear, the stress response becomes much more scattered as a relatively small change in strain ratio can lead to elastic unloading. In figure 8.21 the FLSDs for the 5 materials shown in the precedent figures are given. Each curve can to some degree be assumed to be at a constant level of σ_1 - this may be surprising when one considers that the materials have been subject to rather different levels of plastic straining depending on the strain ratio. The FLSD for Docol 300RP-X shows a somewhat peculiar behaviour for the fourth stress path (counted from the left-hand side in the FLD), maybe the last point in the strain path should have been left out when calculating the limiting stress points.
Looking at figure 8.21 a conclusion might be drawn: If the FLDS were calculated for the major stress perpendicular to as well as aligned with the rolling direction there ought to be

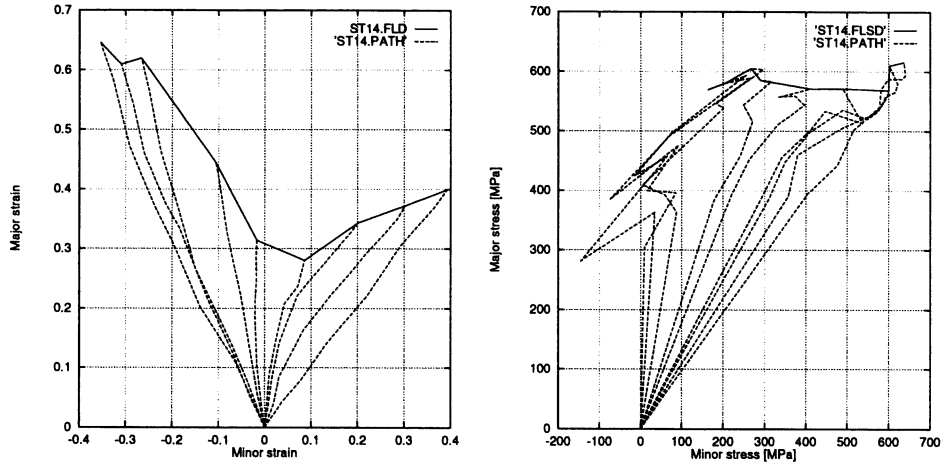

Figure 8.19: *Left: Forming limit diagram reported by Albrektsen for a mild steel (St 14.03). Right: The corresponding forming limit stress diagram.*

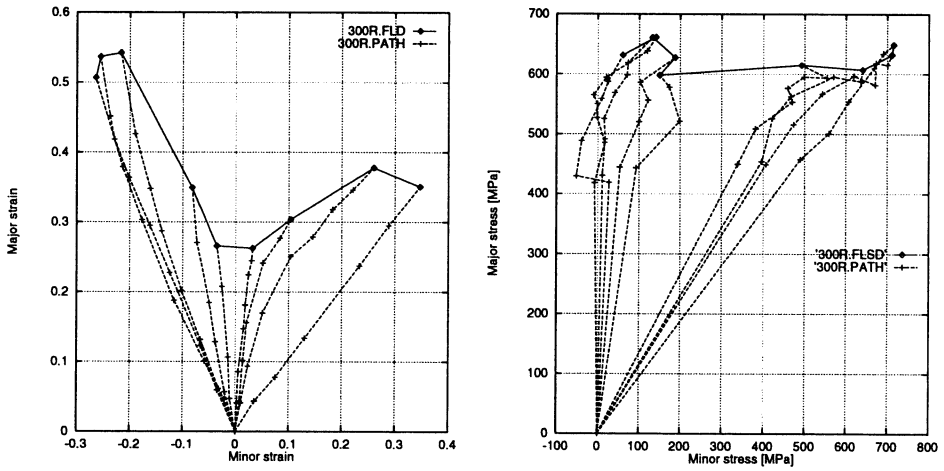

Figure 8.20: *Left: Forming limit diagram reported by Albrektsen for a mild steel (Docol 300 RP-X). Right: The corresponding forming limit stress diagram.*

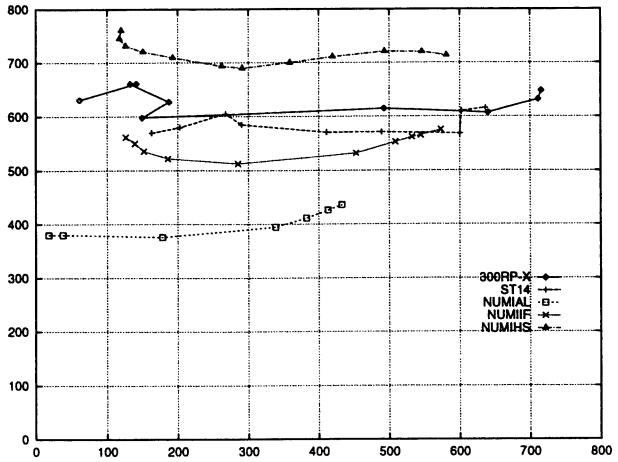

Figure 8.21: *Forming limit stress diagrams for the materials used in the previous figures.*

a second order continuity in the stress curves, however, the shapes in figure 8.21 indicate a formation of a sharp corner. Such a sharp corner is illustrated in figure 8.22 where the limiting curve is plotted for both σ_1 and σ_2 being the major principal stress. The typical

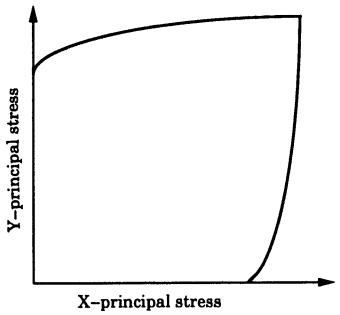

Figure 8.22: *Typical forming limits stress diagram found in the literature in the case where fracturing strains have been found for loading direction along and transverse to the rolling direction.*

forming limit stress variation indicated in figure 8.22 can be found for FLSD-curves reported by Arrieux [10] which are calculated from experimental FLDs for tension along and perpendicular to the rolling direction.

The FLSD can to some degree be used directly in order to evaluate the risk of failure in a FE-simulation, however, it should be noticed that relatively small variation in stress can lead to large variation in strain level depending on the hardening behaviour. Figure 8.23 gives the FLSD for St 14.03. In the figure stress contours for constant equivalent strain (ϵ_{eq}=0.1, 0.2, 0.3 and 0.4) are also given. Obviously a relatively small variation in σ_1 can correspond to a relatively large strain and this means that it is hard to judge the severity directly from the stress state.

Despite the lack of a direct information of the remaining stretchabilty the principle can be used: If we have simulated a forming operation it is simple to plot the stress path in a FLSD diagram, and depending on the position of the stress path it is possible to judge in what way the process should be altered in order to reduce risk of fracture. In some cases it

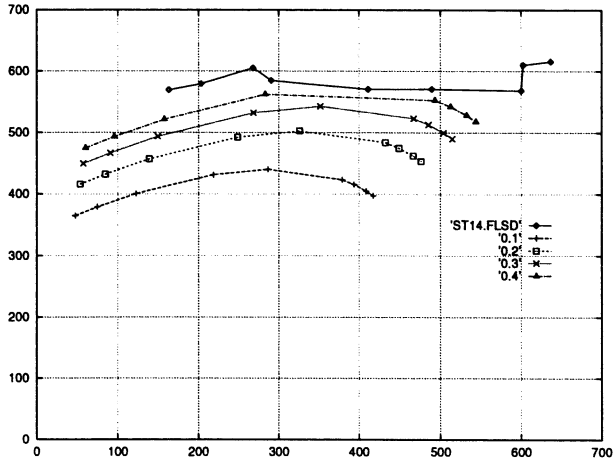

Figure 8.23: *Forming limit stress diagrams for St 14.03 plotted together with curves of constant effective plastic straining calculated for the same strain path as the related FLSD value.*

may be beneficial to constrain the process further in order to increase the minor principal stress, in other cases a release is an opportunity. The presses become more and more advanced, especially with regard to controlling the blank hold, and due to this development we have improved possibilities to control the process.

Another advantage of the FLSD concept is the fact that when the strain path varies drastically during the forming it is possible directly to take this effect into account. For example, a biaxial stretching followed by plane straining will often lead to a limiting strain which is lower than the limit which may be reached with a linear strain path. To evaluate this kind of effects the FLSD concept is quite suitable and simple to employ compared to e.g. the MK-approach.

Fracture criterion

Some authors [4], [80] use the approximation that the limiting stress can reasonably be represented by a straight line of the form:

$$\sigma_1^* = \sigma_0 + a\sigma_2^* \tag{8.87}$$

Assuming this relation is valid and although the mathematical representation is of minor importance for the principle, the assumption is used in the following for evaluation of the risk of fracture. First, determine the fraction between the two principal stresses:

$$b = \frac{\sigma_1}{\sigma_2} \tag{8.88}$$

Then calculate the risk as the remaining distance from the point to the FLSD, it is along the line

$$\sigma_1^* = b\sigma_2^* \tag{8.89}$$

Finally, intersection leads to:

$$RISK = \frac{\sigma_2}{\sigma_2^*} = \frac{\sigma_2}{\frac{\sigma_0}{b-a}} \tag{8.90}$$

This method of fracture evaluation has been published by Arrieux et al. [9], who implemented the option in a FE-code taking the FLSD variation with the angle to the rolling direction into account.

The above given risk evaluation is implemented in the material routine. One may argue that this primarily is suitable for the judgement: fracture - no fracture, as it is not directly visible how large remaining deformation a risk of say 80 per cent indicates. Another aspect which should be remembered is the fact that if only one stress state is taken into account it is necessary to carefully investigate the process development. In other words, it is not sufficient to dump the maximum values of σ_1 and σ_2 experienced during the forming operation. To make the measure meaningful it is necessary to investigate the path so that stresses are evaluated pairwise.

However, when postprocessing FE-results it might be suitable with a more direct measure of the remaining formability. This can very easily be obtained with the FLSD approach and a procedure is given in the following section.

Determination of remaining formability using the FLSD concept

Having established a FLD a FLSD can easily be obtained and with the process signature for a material point, a procedure very similar to the procedure used for calculating the standard FLSD can be used.

The first point is to calculate the stress response related to the simulated strain path (ending at ϵ_1^P, ϵ_2^P); these stresses may be taken from the FE-analysis. If the resulting stress point is above the FLSD we have detected direct failure but in the opposite case a number of strain paths (with strain ratios from -0.5 to 1) are assumed to follow the deformation. For each of these paths the stress path is calculated up to the point where the FLSD is reached. This point defines the major and minor strain (ϵ_1^*, ϵ_2^*) at estimated fracture for the actual strain ratio. The remaining formability is then estimated to be:

$$\epsilon_1^R = \epsilon_1^* - \epsilon_1^P, \quad \epsilon_2^R = \epsilon_2^* - \epsilon_2^P \tag{8.91}$$

8.9 The method proposed by Müschenborn and Sonne

An approach very similar to the forming limit stress concept was proposed by Müschenborn and Sonne [155] in 1975. Their approach is based on a pure empirical treatment, but as later shown by Rasmussen [180] identical results can be found using the FLSD approach given by Arrieux.

The idea of the method is the fact that for a given deformation there is an equivalent plastic strain: $\epsilon_{eq}^* = \frac{2}{\sqrt{3}}\sqrt{\epsilon_1^2 + \epsilon_2^2 + \epsilon_1\epsilon_2}$. Subsequently, an elliptic curve is generated by setting $\epsilon_{eq}^* = f(\rho) = constant$. Plotting this elliptic curve together with the standard FLD obtained for linear strain paths the remaining formability is found by measuring the length from 0,0 to the limiting strain minus the length of the strain path up to intersection with the ellipse of constant equivalent plastic strain. Figure 8.24 shows two examples of

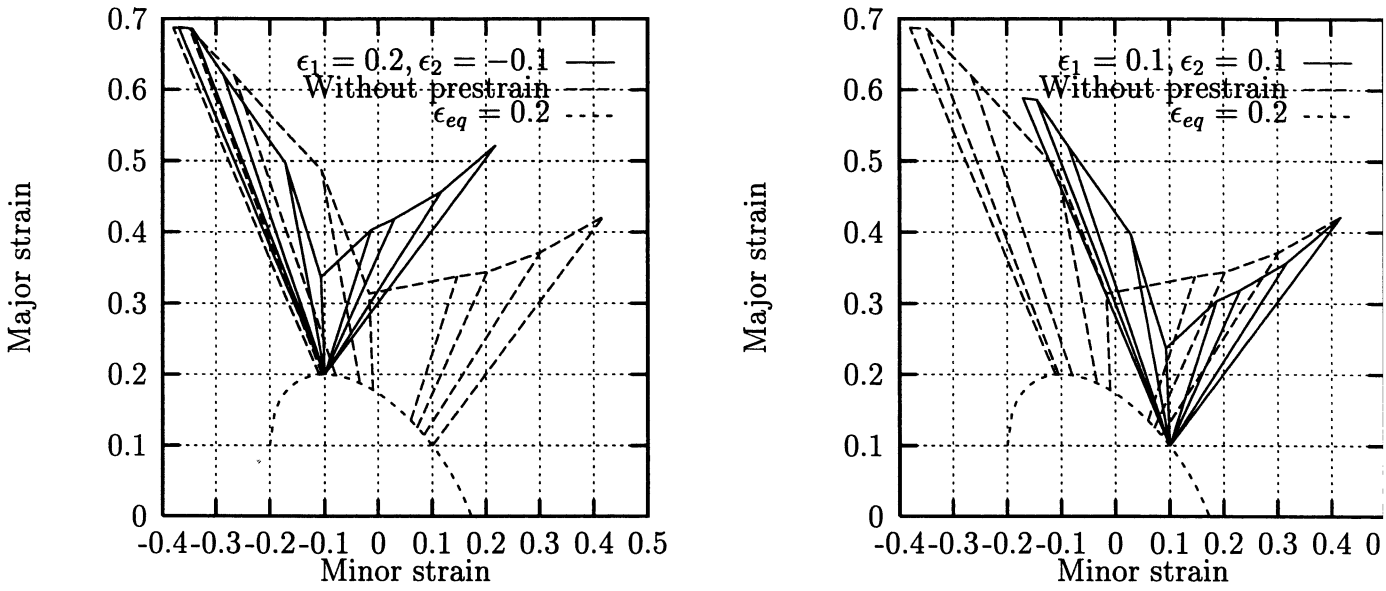

Figure 8.24: *Forming limit diagrams for St 14.03. Left the effect of uniaxial prestraining (-0.1,0.2), right the effect of a balanced prestraining (0.1,0.1) using the method of Müschenborn and Sonne.*

determined formability after prestraining. Left an example is given where the material is strained up to the point (-0.1, 0.2) and right an example of balanced straining up to (0.1, 0.1) is given. To find the remaining formability, for example for the situation where uniaxial straining is followed by balanced straining the procedure is: First we find the limit in balanced strain (0.42, 0.42). From this limit we subtract the value where the elliptic curve intersects $\epsilon_2 = \rho\epsilon_1$ ($\rho = 1$) and finally we add the value for the prestraining:

$$(\Delta\epsilon_1,\ \Delta\epsilon_2) = (0.42 - 0.1, 0.42 - 0.1) + (0.2,\ -0.1) = (0.52,\ 0.22) \tag{8.92}$$

For the situation where we load up to (0.1, 0.1) and continues with $\rho = -0.5$ we obtain:

$$(\Delta\epsilon_1,\ \Delta\epsilon_2) = (0.68 - 0.2,\ -0.38 - (-0.1)) + (0.1,\ 0.1) = (0.58,\ -0.18) \tag{8.93}$$

The method is implemented in the developed material subroutine and the remaining formability is characterized by the values of uniaxial straining, plane strain and balanced straining. This is very convenient, though in the current implementation it is not optimal as the orientation of the remaining formability cannot be directly visualized.

8.10 Bulk forming criteria

Throughout the years in the area of bulk forming a number of fracture criteria have been proposed. In the following a number of these criteria are given and the behaviour of these criteria for plane stress is illustrated.

These criteria are included because sheet metal parts often fail due to ductile fracture and, in principle, there ought to be a reasonable conformity with the ductile fracture criteria typically used in connection with bulk forming. The criteria included in the discussion

Author	Year	Criterion	Parameters
Rice and Tracey(1)	69	$\int_0^{\epsilon_{eq}^f} 0.283 e^{\frac{3\sigma_m}{2\sigma_{eq}}} d\epsilon_{eq} = C_2$	C_2
Oyane(2)	78-80	$\int_0^{\epsilon_{eq}^f} \left(1 + \frac{\sigma_m}{A\sigma_{eq}}\right) d\epsilon_{eq} = C_3$	C_3, A
Ghosh(3)	76	$\frac{\sigma_1+\sigma_2+\sigma_3}{2} \frac{\sigma_1-\sigma_3}{2} = C_4$	C_4
Freudenthal(4)	50	$\int_0^{\epsilon_{eq}^f} \sigma_{eq} d\epsilon_{eq} = C_5$	C_5
Cockcroft and Latham(5)	68	$\int_0^{\epsilon_{eq}^f} \sigma_1 d\epsilon_{eq} = C_6$	C_6
Brozzo et al.(6)	72	$\int_0^{\epsilon_{eq}^f} \frac{2\sigma_1}{3(\sigma_1-\sigma_m)} d\epsilon_{eq} = C_7$	C_7
Norris et al.(7)	78	$\int_0^{\epsilon_{eq}^f} \frac{1}{1-D\sigma_m} d\epsilon_{eq} = C_8$	C_8, D
Atkins(8)	87	$\int_0^{\epsilon_{eq}^f} \frac{2+\frac{d\epsilon_1}{d\epsilon_2}}{2(1-D\sigma_M)} d\epsilon_{eq} = C_9$	C_9, D
Lemaitre(9)	85	$\int_0^{\epsilon_{eq}^f} \left[\frac{2}{3}(1+\nu) + (3-6\nu)\frac{\sigma_m^2}{\sigma_{eq}^2}\right] d\epsilon_{eq} = C_{10}$	C_{10}, ν

Table 8.1: *A list of ductile failure criteria as given by Cescotto and Zhu [42]. The number in parenthesis in the first column is used for references in the text and subsequent figure 8.25.*

are listed by Cescotto and Zhu [42] and are given in table 8.1. Table 8.1 gives nine criteria which have been proposed from 1950 to 1987. The first column lists the originator, the second column lists the year of publication, the third lists the failure criterion and finally the fourth column lists the parameters needed to utilize the criterion. In table 8.1 $\sigma_1, \sigma_2, \sigma_3$ are the principal stresses in decreasing order, ϵ_1, ϵ_2 are the principal strains, (ϵ_3 is the thickness strain), σ_m the hydrostatic stress, ϵ_{eq} the equivalent strain and ϵ_{eq}^f the equivalent strain at fracture. Cescotto and Zhu point out that none of the existing fracture criteria(1-8) can provide reliable predictions for all of the tested specimens in [42] whereas it is possible with the damage model(9). The first impression obtained from the listed criteria is that they are relatively simple and that only few additional parameters (1 or 2) need to be determined.

In order to get an idea of the behaviour of these criteria for a loading in plane stress figure 8.25 shows the relation between minor and major stress (left) and the corresponding relation between minor and minor strain calculated for proportional loading. The curves have been generated using the material routine for a von Mises material with a Hollomon hardening. Parameters C_i have been determined so that the limiting strain point for balanced loading is (0.4, 0.4). Parameters ν, A and D have been set to 0.3, 1 and 0.001, respectively. One conclusion which can be drawn from figure 8.25 is the fact that the shapes of the predicted strain limit curves deviate substantially from those classically established as well as experimentally obtained FLDs. The values for balanced stretching (used for estimation of parameters C_i) and uniaxial tension seem to be reasonable, but for all values in between it seems to be a strong over-prediction of failure strains. For all the criteria convex strain curves are obtained apart from curve cr3 (the criterion proposed by Ghosh).

For the FLSD curves given in section 8.8 which are based on experimentally obtained FLDs there seems to be a concave relation for σ_1 as function of σ_2 - for the criteria based

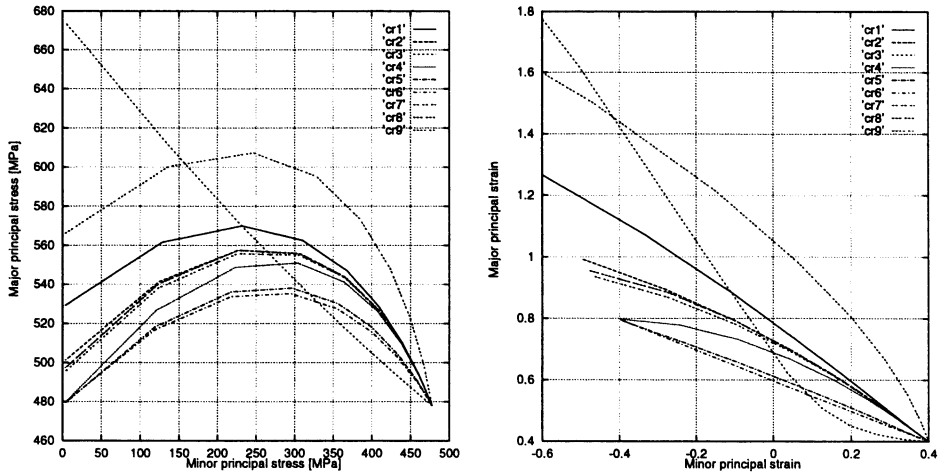

Figure 8.25: *Left the limiting stress diagrams calculated for various fracture criteria as listed in table 8.1. Right is given the corresponding limiting strains. To estimate parameters the same balanced stress state (corresponding to the strain point (0.4, 0.4)) has been used for all criteria. Additional parameters A and D (for criteria number 2, 7 and 8) have been set to 1 and 0.001, respectively.*

on forming consideration we experience the opposite effect - eight of the stress curves are convex.

This obvious discrepancy can be explained reasonably: Bulk forming operation will often fail due to formation of internal cracks (leading very fast to part failure) whereas sheet metal parts contrast as they are very often evaluated on "a visual" basis; localization or rotation of grains are considered as failure. Another aspect is the measurement of the limiting strain: Methods most popular for determining the limiting strain are based on grid analysis and the choice of grid size is of outmost importance for the size of the recorded limiting strain. Among people working in the area this has been subject of discussion for several years. Veerman [212] and Hecker [89] proposed methods in order to predict the fracture strain more accurately. Veerman's method is to plot the major principal strain for the fracturing zone as function of the major principal strain outside the fracture zone. When the slope of this line (which before localization should be 1) increases the limiting strain is assumed to be present. Hecker interpolates the predicted strain at fracture by taking the principal strain predicted by a line of circles crossing the fracture (three at each side) into account. The most popular method is to use the "nearest circle to fracture" (or square grid), but in my opinion this limit is very diffuse; e.g. some authors report that the limit is found by using the principle: Select the circle (square grid) closest to the fracture but still unaffected by the fracture. In my opinion the fracture strain cannot be measured exactly using grid techniques as the reference length cannot be made sufficiently small to capture the localization. One way to overcome this is to measure the strain field which is unaffected of the fracture; this approach seems very valid seen from a productional point of view - but it is believed that this kind of discrepancies is one of the reasons why the area, in my opinion, has not been able to really succeed. To develop better theoretical approaches it is believed that the behaviour should be modelled on a more detailed level and, if necessary, more constitutive parameters should be included.

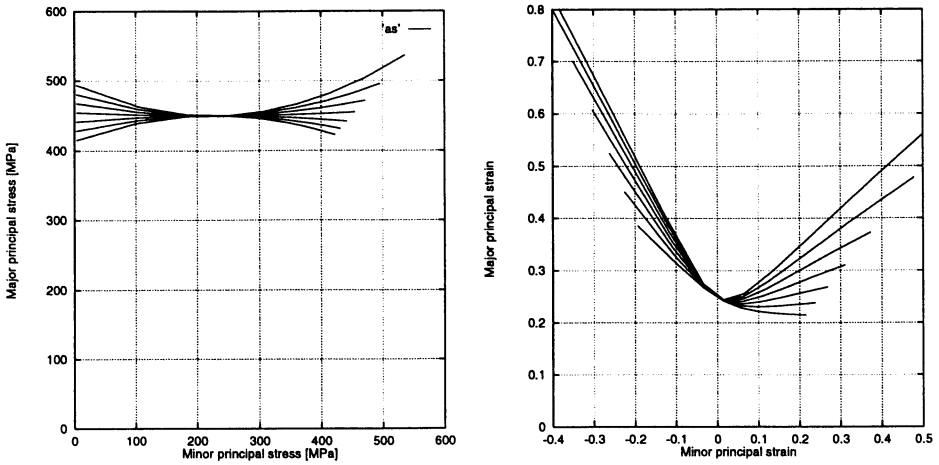

Figure 8.26: *Left: The limiting stress diagrams where the major principal stress varies parabolic as function of the minor stress. Right: The corresponding limiting strains. The curves pass the same point for plane strain.*

8.11 The relation between bulk criteria, FLSDs and FLDs

To indicate how variations in the FLSD curve influence the FLD, figure 8.26 shows the effect of describing σ_1 as a parabolic function of σ_2. The value of σ_1 in plane strain is kept constant in all curves. As can be seen from figure 8.26 the shape of the FLDs strongly depend on the shape of the FLSDs. The curves predicted for the most convex FLSDs indicate shapes tending towards the trends of the FLDs predicted by the bulk criteria.

Returning to the discussion on FLSDs with regard to figures 8.19, 8.20 and 8.21, it can be noticed that the tangential direction at balanced stress for the bulk criteria is in a much better agreement with the continuity demand discussed previous.

One way to proceed with prediction of failure in sheet metal forming may be to establish a forming limit stress criterion which is very similar to an yield criterion. It seems as if it is possible to obtain FLD-shapes with a convex limiting stress curve which are in a reasonable agreement with those predicted by for example Stören and Rice's criterion, the MK-approach and Jun's method.

8.12 The concept of damage mechanics

The approach used for obtaining equation 9 in table 8.1 is based on damage mechanics, however, the expression is of a very simple nature and the damage approach can be refined significantly. In many of the classical approaches it is assumed that fracture is due to some localization process and it may be appropriate to combine the damage mechanics with either bifurcation analysis or imperfection analysis. It may be possible to use the MK-approach and by using damage mechanics obtain more realistic values for the imperfection factor.

The following is primarily based on the book of Lemaitre [134], where a more complete discussion on damage mechanics can be found. The section will focus on plane stress and situations relevant for sheet metal forming and should be seen in continuation of the more classical approaches to predict failure discussed in the previous sections. The discussion is somewhat simplified; a more rigorous discussion on damage and instability in plasticity can be found in Stein et al. [199] who present a survey of a number of methods. Their article gives a good overview and many references.

The primary reason for including this section is to illustrate a much more "integrated" approach to the prediction of forming limits, but also to give some aspects which are well-known in the field of damage mechanics and which do not, for the time being, seem to be given a sufficiently high priority in the field of sheet metal forming. A recent publication using a similar approach, however much more advanced, has been given by De souza Neto et al. [58]; the article gives an example on the implementation and use of Lemaitre's elasto-plastic damage theory. The authors conclude that including damage in the modelling can improve numerical predictions of strain distribution and demonstrate clearly how large the impact is on the hemispherical punch stretching example.

8.12.1 The effective stress concept

Rabotnov proposed in 1968 to use an effective stress concept in connection with damage of materials. If we consider the usual uniaxial stress:

$$\sigma = \frac{F}{S} \tag{8.94}$$

where F is the force and S the current area, we can if the material is damaged (and all defects open) introduce the effective stress:

$$\tilde{\sigma} = \frac{\sigma}{1 - D} \tag{8.95}$$

where D indicates the degree of damage ($0 \leq D \leq 1$) which is determined as $D = \frac{S_D}{S}$. The (effective) surface that resists the load is $S - S_D$. Typically the damage of material is developing from nucleation of cavities due to decohesions between inclusion and the matrix followed by their growth and their coalescence through the phenomenon of plastic instability. These effects are only true for tensile loading; if the stress increment leads to compression closure effects ought to be taken into account. This issue has been left out in the following discussion on the modelling of damage.

8.12.2 The strain equivalence principle

This approach has been introduced by Lemaitre [134] in 1971 in order to postulate a principle at the mesoscale. Lemaitre states the principle as: "Any strain constitutive equation for a damaged material may be derived in the same way as for a virgin material except that the usual stress is replaced by the effective stress."

With Lemaitre's approach we have for an undamaged material:

$$D = 0 \qquad \epsilon = f(\sigma, ...) \tag{8.96}$$

and for a damaged material:

$$0 < D < 1 \qquad \epsilon = f(\frac{\sigma}{1-D}, ...) \tag{8.97}$$

If we as an example take elastic material behaviour:

Undamaged material	*Damaged material*
$D = 0$	$0 < D < 1$
$\epsilon^e_{11} = \frac{\sigma}{E}$	$\epsilon^e_{11} = \frac{\sigma}{E(1-D)}$
$\epsilon^e_{22} = \epsilon^e_{33} = -\nu\epsilon^e_{11}$	$\epsilon^e_{22} = \epsilon^e_{33} = -\nu\epsilon^e_{11}$

It is normally assumed that the Poisson's ratio ν is unaffected by damage. The elasticity modulus of the damaged material is defined by the ratio

$$\tilde{E} = \frac{\sigma}{\epsilon_{11}} = E(1-D) \tag{8.98}$$

This indicates a clear drop in modulus of elasticity when the material is damaged. Lemaitre gives examples published by Dufailly for copper, where a reduction from 99000 MPa to 33000 MPa is found experimentally and another example for copper where the E-modulus is reduced with 80 per cent. The two above-mentioned degrees of reduction in elasticity appeared for an effective plastic straining of around 100 per cent. In my opinion these effects are of outmost importance when discussing simulation of spring back. During the simulation the elasticity does not normally play any significant role for the overall behaviour. But when the part is allowed to spring back the actual modulus of elasticity is the most important material parameter. Depending on the position in a formed part different levels of plastic straining can be found and a corresponding variation of Young's modulus can thus be expected. At IDDRG 1994 is was decided to pay special attention to this problem, e.g. Usuda et al. [211] pointed out at the Working Group meeting that they found this effect experimentally. Also at the Numisheet'93 conference many problems seemed to arise during the unloading phase (spring back). Many authors, including myself, obtained for the 2-D Draw Bending Example geometries which after spring back obviously were wrong. This was a pronounced problem for the participants who used explicit finite element, but also many of the analyses based on implicit approaches seemed to have problems with the spring back simulation.

It is suggested that instead of initiating too much activity in the sheet metal forming society, one should make a more detailed study in the areas of fracture and damage mechanics, where the problem is well-known and the theoretical methods are directly available. Evaluating the above given degrees of reduction it must be evaluated that the determination of effects such as; tolerances after spring back, residual stresses, elastic behaviour of the part, etc must be conducted with greatest care.

8.12.3 Plasticity and damage

To model plastic behaviour two types of hardening are normally included in the constitutive equations: Isotropic and kinematic hardening of the material. If σ_y is the initial yield stress, R the stress due to isotropic hardening and X the back stress, the latter two considered to be functions of the plastic strain, we find the one-dimensional criterion defining the current threshold of yield:

$$\sigma = \sigma_y + R(\epsilon_p) + X(\epsilon_p) \qquad or: \qquad f = |\sigma - X(\epsilon_p)| - R(\epsilon_p) - \sigma_y = 0 \tag{8.99}$$

where f is the yield function from which the kinetic constitutive equations are derived. Increments in plastic strain are related to the yield criterion:

$$\dot{\epsilon_p} \neq 0 \ if \ f = 0 \ and \ \dot{f} = 0 \qquad \dot{\epsilon_p} = 0 \ if \ f < 0 \ or \ \dot{f} < 0 \tag{8.100}$$

If damage occur, the yield criterion must take the damage into account which according to the principle of equivalence can be written:

$$f = |\frac{\sigma}{1-D} - X| - R - \sigma_y = 0 \tag{8.101}$$

Lemaitre claims that experiments show that the damage equally decreases the yield stress, the isotropic strain hardening and the back stress according to a function of the type:

$$\sigma = (\sigma_y + R + X)(1 - D) \tag{8.102}$$

One should expect that fracture corresponds to D=1, but for many materials the fracture is to some degree an unstable process (for instance unstable crack propagation) wherefore it is more realistic to introduce a critical value of D, D_c. The final fracture is characterized by a critical value of the effective stress σ_∞ acting on the resisting area. This stress cause decohesion of atoms and this stress should correspond to the critical level of D:

$$\sigma_\infty = \tilde{\sigma} = \frac{\sigma}{1 - D_c} \tag{8.103}$$

In practice the value of σ_∞ may be taken as the ultimate stress σ_u, however, this stress is always smaller.

$$D_c \approx 1 - \frac{\sigma}{\sigma_u} \tag{8.104}$$

If D_c is close to 0 the fracture is brittle, and D_c close to 1 indicates ductile fracture. Lemaitre claims that typical values are in the range from 0.2 to 0.5. For a tensile test 8.104 corresponds to

$$D_{1c} = 1 - \frac{\sigma_R}{\sigma_u} \tag{8.105}$$

where σ_R is the true stress at fracture. D_{1c} is considered a material constant.

Another characteristica, which must be incorporated is the effect that below a certain level of straining (ϵ_{pD}) no damage seems to occur; it may be stated as:

$$\epsilon_p < \epsilon_{pD} \ \rightarrow \ D = 0 \tag{8.106}$$

The above stated may be summarized to give the basis for damage mechanics:

$$\epsilon_e = \frac{\sigma}{1-D} \tag{8.107}$$

$$|\frac{\sigma}{1-D} - X| - R - \sigma_y = 0 \text{ as the plastic yield criterion} \tag{8.108}$$

$$\epsilon_p < \epsilon_{pD} \rightarrow D = 0 \text{ as the damage threshold} \tag{8.109}$$

$$D = D_{1c} \rightarrow \text{crack initiation} \tag{8.110}$$

Lemaitre gives a number of experimental approaches to determine the parameters necessary to establish the background for the constitutive modelling; these methods will not be discussed in the present context. Lemaitre gives examples on material constants where ϵ_{pD} equals 0.44, 0.1 and 0.0 for mild steel and stainless steel at 20 and at 600°C, respectively. The corresponding values of D_{1c} are 0.2, 0.15 and 0.5. These limits are inside the ranges of practical importance for sheet metal forming.

8.12.4 Strain-damage coupled constitutive equations

The previous discussion can be extended to three dimensions for a relatively general material behaviour. In the following only elastic-perfectly plastic and damageable material is considered. This limitation is, however, not that restrictive.

The presentation closely follows the presentation given by Lemaitre. One of the first postulates is that no damage occur below a certain threshold of the accumulated plastic strain ϵ_{pd}:

$$\epsilon_p < \epsilon_{pD} \rightarrow \dot{D} = 0 \tag{8.111}$$

Lemaitre states that this threshold value is so high that for many materials saturation of kinematic and isotropic hardening has been achieved:

$$\epsilon_p > \epsilon_{pD} \rightarrow \begin{cases} \dot{X}_{ij}^D = 0 \\ \dot{R} = 0 \end{cases} \tag{8.112}$$

This means that the assumption of perfect plastic deformation is not so strict as it may appear af first glance. The plasticity criterion becomes:

$$f = \tilde{\sigma}_{eq} - \sigma_s = 0 \tag{8.113}$$

where σ_s is the (constant) threshold in consideration. The choice of σ_s is somewhat subjective, but is has to be bounded by σ_y and σ_u:

$$\sigma_y \leq \sigma_s \leq \sigma_u \tag{8.114}$$

Taking $\sigma_s = \sigma_u$ is according to Lemaitre often a good choice; it is to determine σ_s from:

$$\frac{d\sigma}{d\epsilon} = 0 \tag{8.115}$$

for a tensile test. The increments in plastic strains and damage may be expressed:

$$\dot{\epsilon}_{ij}^p = \frac{\partial f}{\partial \sigma_{ij}} \dot{\lambda} \quad if \quad \begin{cases} f = \frac{\sigma_{eq}}{1-D} - \sigma_s = 0 \\ \dot{f} = 0 \text{ with } \dot{\lambda} = \dot{\epsilon}_p(1-D) \end{cases} \tag{8.116}$$

$$\dot{D} = \frac{Y}{S}\dot{\epsilon}_p \quad if \quad \epsilon_p > \epsilon_{pD} \quad with \quad Y = \frac{\sigma_{eq}^2 R_\nu}{2E(1-D)^2} = \frac{\tilde{\sigma}_{eq}^2 R_\nu}{2E} \tag{8.117}$$

where R_ν is the triaxiality function:

$$R_\nu = \frac{2}{3}(1+\nu) + 3(1-2\nu)\left(\frac{\sigma_H}{\sigma_{eq}}\right)^2 \tag{8.118}$$

with σ_H the mean stress and S a material parameter. Knowing the critical value for one stress combination gives the equivalent damage criterion.

8.12.5 Plane stress and the damage equivalent stress criterion

The stress situation can be characterized by σ_1 and σ_2, which leads to $\sigma_H = \frac{1}{3}(\sigma_1 + \sigma_2)$. The deviatoric component are expressed as:

$$\sigma_{ij}^D = \frac{1}{3}\begin{bmatrix} 2\sigma_1 - \sigma_2 & 0 & 0 \\ 0 & 2\sigma_2 - \sigma_1 & 0 \\ 0 & 0 & -(\sigma_1 + \sigma_2) \end{bmatrix} \tag{8.119}$$

The von Mises equivalent stress is:

$$\sigma_{eq} = \left(\sigma_1^2 + \sigma_2^2 - \sigma_1\sigma_2\right)^{\frac{1}{2}} \tag{8.120}$$

The damage equivalent stress criterion becomes:

$$\sigma_{eq}^* = \left(\sigma_1^2 + \sigma_2^2 - \sigma_1\sigma_2\right)^{\frac{1}{2}} \left[\frac{2}{3}(1+\nu) + \frac{1}{3}(1-2\nu)\frac{(\sigma_1+\sigma_2)^2}{\sigma_1^2 + \sigma_2^2 - \sigma_1\sigma_2}\right]^{\frac{1}{2}} \tag{8.121}$$

which defines the one-dimensional stress σ_{eq}^* which, for the same value of damage, yields same the value of the elastic strain energy as the three-dimensional state (the above expression only illustrates two-dimensional loading). If we take equation 8.121 we can generate the damage equivalent stress for various values of the Poisson's ratio ν. This is illustrated in figure 8.12.5 for plane stress. Figure 8.12.5 illustrates the effect of Poisson's ratio on the damage equivalent stress criterion. It is interesting to notice the dramatic effect of Poisson's ratio.

If we return to the expression for plastic strain increments we can from the yield criterion obtain:

$$\frac{\partial f}{\partial \sigma_{ij}} = \frac{3}{2}\frac{\sigma_{ij}^D}{\sigma_{eq}}\frac{1}{1-D} \tag{8.122}$$

where σ_{ij}^D is the deviatoric stress tensor. Y is found to:

$$Y = \frac{\sigma_s^2}{2E}R_\nu \tag{8.123}$$

The demand of consistence leads to:

$$\dot{f} = \frac{\dot{\sigma}_{eq}}{1-D} + \frac{\sigma_{eq}}{(1-D)^2}\dot{D} = 0 \qquad \rightarrow \qquad \dot{\sigma}_{eq} + \sigma_s \dot{D} = 0 \tag{8.124}$$

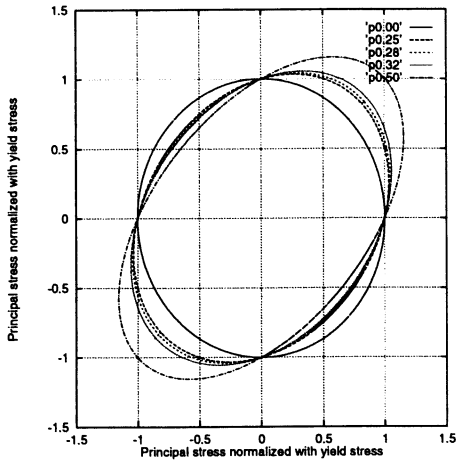

Figure 8.27: *The damage equivalent criterion plotted for plane stress for various values of Poisson's ratio ν (0, 0.25, 0.28, 0.32 and 0.50).*

leading to the expression for the damage increment expressed from the increment in effective plastic strain (from 8.117):

$$\dot{D} = \frac{\sigma_s^2}{2ES} R_\nu \dot{\epsilon}_p = \frac{\sigma_{eq}^2}{2ES(1-D)^2} R_\nu \dot{\epsilon}_p \tag{8.125}$$

and the increment in plastic strains:

$$\dot{\epsilon}_{ij}^p = \frac{3}{2} \frac{\sigma_{ij}^D}{\sigma_s} \frac{\dot{\epsilon}_p}{1-D} \tag{8.126}$$

If $\epsilon_p > \epsilon_{pD}$ we can express the increment in effective plastic strain from the increment in damage:

$$\dot{\epsilon}_{ij}^p = \frac{3ES}{\sigma_s^3} \frac{\sigma_{ij}^D}{1-D} \frac{\dot{D}}{R_\nu} \tag{8.127}$$

This illustrates that for a perfectly plastic material the plastic strain is directly related to the damage. From the consistency condition another relation arises:

$$\dot{D} = -\frac{\dot{\sigma}_{eq}}{\sigma_s} \tag{8.128}$$

As the damage rate must be positive we have that the equivalent stress rate is negative owing to the softening damage process. With the above assumptions another interesting result appears. If we write the plasticity criterion in terms of elastic strains:

$$\epsilon_{ij}^e = \epsilon_{ij}^{eD} + \epsilon_H^e \delta_{ij} \quad with \quad \epsilon_H^e = \frac{1}{3} \epsilon_{kk}^e \tag{8.129}$$

the stresses can be expressed:

$$\sigma_{ij} = \sigma_{ij}^D + \sigma_H \delta_{ij} \quad with \quad \sigma_H = \frac{1}{3} \sigma_{kk} \tag{8.130}$$

The elastic strain can be expressed as:

$$\epsilon_{ij}^{eD} = \frac{1+\nu}{E(1-D)}\sigma_{ij}^{D} \qquad \epsilon_{H}^{e} = \frac{1-2\nu}{E(1-D)}\sigma_{H} \tag{8.131}$$

Rearranging leads to:

$$\sigma_{eq} = \left(\frac{3}{2}\sigma_{ij}^{D}\sigma_{ij}^{D}\right)^{\frac{1}{2}} = \frac{E(1-D)}{1+\nu}\left(\frac{3}{2}\epsilon_{ij}^{eD}\epsilon_{ij}^{eD}\right)^{\frac{1}{2}} \tag{8.132}$$

and

$$f = \frac{\sigma_{eq}}{1-D} - \sigma_s = \frac{E}{1+\nu}\left(\frac{3}{2}\epsilon_{ij}^{eD}\epsilon_{ij}^{eD}\right)^{\frac{1}{2}} - \sigma_s \tag{8.133}$$

which with f=0 leads to:

$$\left(\epsilon_{ij}^{eD}\epsilon_{ij}^{eD}\right)^{\frac{1}{2}} = constant \tag{8.134}$$

In tension we have:

$$\frac{\sigma_{eq}}{1-D} = \frac{\sigma}{1-D} = E\epsilon_e \tag{8.135}$$

$$E\epsilon_e - \sigma_s = 0 \tag{8.136}$$

$$\epsilon_e = \frac{\sigma_s}{E} = constant \tag{8.137}$$

which means that we for the elastic perfectly plastic and damageable material have a constant elastic strain. To summarize we have a complete set of equations:

$$\epsilon_{ij} = \epsilon_{ij}^{e} + \epsilon_{ij}^{p} \qquad \epsilon_{ij}^{e} = \frac{1+\nu}{E}\tilde{\sigma}_{ij} - \frac{\nu}{E}\tilde{\sigma}_{kk}\delta_{ij} \tag{8.138}$$

$$\dot{\epsilon}_{ij}^{p} = \frac{3}{2}\frac{\tilde{\sigma}_{ij}^{D}}{\sigma_s}\dot{\epsilon}_p \; if \; \tilde{\sigma}_{eq} - \sigma_s = 0 \qquad \dot{D} = \frac{\sigma_S^2}{2ES}R_v\dot{\epsilon}_p \; if \; \epsilon_p \geq \epsilon_{pD} \tag{8.139}$$

where R_ν can be expressed as a function of the strain

$$R_\nu = \frac{2}{3}(1+\nu) + \frac{3}{1-2\nu}\left(\frac{E\epsilon_H}{\sigma_s}\right)^2 \tag{8.140}$$

as:

$$\frac{\sigma_H}{\sigma_{eq}} = \frac{\frac{E(1-D)}{1-2\nu}\epsilon_H^e}{\sigma_s(1-D)} \tag{8.141}$$

and $\epsilon_H^e = \epsilon_H$ since the plastic strain increment is deviatoric.

8.12.6 Localization of damage

Lemaitre also discusses localization of damage. In the following is given his version of the instability analysis first given by Billardon et al. The reason for including this section is not to discuss in detail localization problems for damage - the purpose is to illustrate the connection to the instability analysis proposed by Stören and Rice, see section 8.7.

Considering a body loaded by a uniform stress σ_{ij} leading to a strain ϵ_{ij} and a damage D. The displacement of the body is described with u_i. We want to find the conditions for the existence of a inhomogeneous zone, it is a zone where a quantity X differ across a surface:

$$(X^+ - X^-) = \Delta X \tag{8.142}$$

Further we must demand that:

$$\Delta(\dot{u}_i) = 0 \qquad \Delta(\dot{\sigma}_{ij} n_j) = 0 \tag{8.143}$$

Starting out from the constitutive equation on rate form:

$$\dot{\sigma}_{ij} = H_{ijkl}\dot{\epsilon}_{ij} \tag{8.144}$$

where H_{ijkl} is the tangent stiffness tensor which in this context is a function of damage as well as the stress and strain state. Using Maxwell's compatibility equation for the general shape of the discontinuity of a second order tensor gradient:

$$\dot{\epsilon} = \frac{1}{2}[grad(\vec{u}) + (grad(\vec{u}))^T] \tag{8.145}$$

which can be written:

$$\Delta\dot{\epsilon}_{ij} = \frac{1}{2}(g_i n_j + n_i g_j) \tag{8.146}$$

where g_i is a vector to be determined. If $g_i = 0,\ i = 1,3$ we have no discontinuity. Reexpressing 8.143:

$$0 = \Delta(\dot{\sigma}_{ij} n_j) = \Delta(\dot{\sigma}_{ij}) n_j = \Delta(H_{ijkl}\dot{\epsilon}_{kl}) n_j \tag{8.147}$$

If we assume that the tangent stiffness tensor has no discontinuity across the surface we can rewrite 8.147:

$$0 = \Delta(H_{ijkl}\dot{\epsilon}_{kl}) n_j = H_{ijkl}\Delta(\dot{\epsilon}_{kl}) n_j = H_{ijkl}\Delta(\frac{1}{2}(g_k n_l + n_k g_l)) n_j = 0 \tag{8.148}$$

The tangent stiffness tensor has a number of minor symmetries which may be used to simplify 8.148:

$$H_{ijkl}\Delta(\frac{1}{2}(g_k n_l + n_k g_l)) n_j = (n_j H_{ijkl} n_l)\Delta g_k = 0 \tag{8.149}$$

But g_i must differ from the zero vector in order to have a variation in strain rates corresponding to the requirement that the matrix:

$$n_j H_{ijkl} n_l \tag{8.150}$$

is singular, it is the determinant should equal 0:

$$det(n_j H_{ijkl} n_l) = 0 \tag{8.151}$$

If we follow the derivation closely we do in fact have the same analysis as the analysis performed by Stören and Rice. The only difference is that here we include damage in the constitutive modelling. Also another difference should be noticed; even when we have localization of damage this does not mean fracture - the fracture will first appear when D reaches the critical value for fracture.

It is shown by Stören and Rice that localization of deformation will only take place for negative strain ratios when using flow theory of plasticity. But instead of relaxing the normality condition one may introduce damage in the flow theories in order to overcome this apparent difficulty.

8.12.7 Prediction of forming limits using master curves of ductile fracture

Another way to evaluate the severity of a stress state is to use master curves of ductile fracture. Lemaitre gives master curves which can be used to predict failure for both brittle and ductile materials. In the following is repeated the deriviation for ductile damage of metals. Lemaitre states the general damage law as:

$$\dot{D} = \frac{Y}{S}\dot{\epsilon}_p H(\epsilon_p - \epsilon_{pD}) \tag{8.152}$$

where D is the damage, Y energy release per unit area, S a constant related to fracture, H is the heavyside function. Considering only proportional loading, it can be shown that for a given strain path we have:

$$\frac{\sigma_H}{\sigma_{eq}} = const \tag{8.153}$$

In the three dimensional case we find by integration of the kinetic law [134]:

$$\frac{p_R - p_D}{\epsilon_{pr} - \epsilon_{pD}} = \left[\frac{2}{3}(1+\nu) + 3(1-2\nu)\left(\frac{\sigma_H}{\sigma_{eq}}\right)^2\right]^{-1} \tag{8.154}$$

where p_R is the accumulated plastic strain and p_D the damage threshold plastic strain and ϵ_{pr} and ϵ_{pD} the corresponing values for pure tension. Letting the damage develop from the very start of loading, $\epsilon_{pD} = 0$, and setting $D_c = 1$ leads to:

$$\frac{p_R}{\epsilon_{pr}} = \left[\frac{2}{3}(1+\nu) + 3(1-2\nu)\left(\frac{\sigma_H}{\sigma_{eq}}\right)^2\right]^{-1} \tag{8.155}$$

The results for both the master curves of ductile failure as well as the responding FLDs are shown in figure 8.28. Figure 8.28 indicates the importance of Poisson's ratio in damage mechanics. A Poisson's ratio of 0.5 (ideal plasticity) leads to much higher limits than realistic values of Poisson's ratio. A drop to 0.49 leads to a significant drop. A value of 0.49

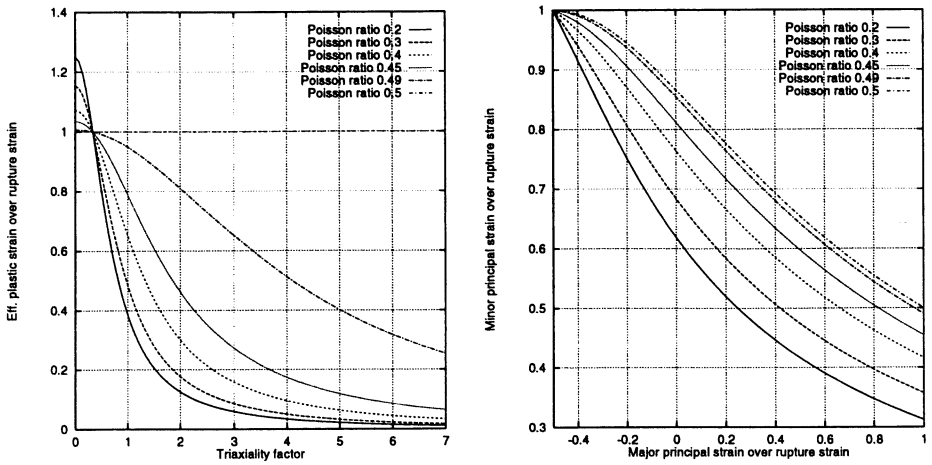

Figure 8.28: *Left is given the master curves of ductile failure, right the corresponding FLDs plotted for strain ratios in the range -0.5 to 1.*

is close to the "effective Poisson's ratio" when an isotropic elastic-plastic material (steel) is loaded in uniaxial tension. However, the high values of Poisson's ratio are only inclosed to illustrate the effect as it must not be forgotten that the relation goes back to release of energy at fracture, an effect which is treated from assumptions of elasticity.

From figure 8.28 it can clearly be seen how crucial the triaxiality factor is on the possible deformation. From this type of curves it can be explained why a sharp notch makes a material behave more brittle: A notch can give a triaxiality factor up to 5 or 6 according to Lemaitre. - That is the material does not become more brittle, instead it is the hydrostatic stresses that causes early fracture.

It should be noticed that the Poisson's ratio is important when talking master curves - the same effects is found for the damage equivalent stress criterion discussed in section 8.12.5. This is perhaps the most important difference between the damage approach and the traditional approaches given in previous sections. The classical approaches are based on a continued plastic deformation away from the localization zone where damage criteria instead are related to release of energy.

8.12.8 Summary of damage mechanics

The purpose of including a brief discussion on damage mechanics has not been to perform a complete description of the issue. The theory discussed is to some degree oversimplified leading to an approach not directly applicable to practical use, but it was found important to include the topic when discussing the traditional approaches to evaluate formability. Also the trends in evolution of modulus of elasticity should be given some attention among researchers and engineers operating in the field of sheet metal forming simulations. An area where it may be of importance to have correct elastic parameters is when analyzing for instance car structures with regard to strength and deflection, vibrational properties, etc. If the variation of the E-modulus is so strongly related to the plastic deformation as reported by Lemaitre it means that in the past 20 years structural analysis has been performed with so significant variation in elastic properties that many conclusions and

verifications on real structures should be reconsidered.

It is believed that in order to better predict the formability of metals damage mechanics is one of the most promising approaches, which at the same time gives the possibility to integrate process severity more directly in the constitutive modelling used in FE-simulations.

Also damage mechanics open the possibility to evaluate final parts better with regard to low and high cycle fatigue taking the forming history (and the damage developed during forming) into account. This subject has, however, been completely left out in this report. Here I found the book of Lemaitre [134] to be good as an introduction to the subject.

8.13 Conclusion of the estimation of formability

It is judged that valuable information can be obtained from the classical methods concerning evaluation of specific effects: How crucial is a change in material parameters, will a change in strain path have any effect, and in the confirming case how much, how big is the process window, etc. However, it is judged that a quantitative evaluation of formability is more troublesome.

From the presented analysis types it is evaluated that a reliable prediction of FLDs from pure analytical means is unrealistic with the current state of art. The method presented by Jun seems to be good for the estimation of the entire FLD and the estimation can be made from just one experimentally determined limiting strain point.

When discussing more general problems it is evaluated that damage mechanic is the most promising way to establish a better description of the mechanisms leading to fracture. This is not only interesting in regard to formability but also when talking spring back behaviour. In order to obtain a overall good estimation of part tolerances it becomes of outmost importance to be able to model the elastic behaviour after forming. Also the aspect that release of elastic energy when fracture occurs is included is in my opinion an advantage compared to a treatment based on assumptions of pure plastic deformation.

The FLSD concept seems (for the examples examined) to indicate a concave relation ($\sigma_1 = f(\sigma_2)$) where the fracture criteria investigated indicate a convex relation. It is illustrated how crucially the variation of a forming limit stress curve can influence the forming limit strain.

Another problem is that there seems to be a strong tradition within the area of FLDs - the first approaches were purely experimental. The fracture strain obtained with damage mechanics is related to the "real strain state" - a state which will never be recorded using the experimental methods used today. One may of course ask the question whether the fracture strain is of interest in practical forming. A part is often characterized as failed long before reaching the limiting strains predicted with damage theories.
To sum up: It seems that there still is quite a difference between approaches: I am convinced that none of the discussed methods are really capable of predicting the forming limits from constitutive parameters alone. Some of the methods seem to indicate that

reasonable results can be obtained from relatively few experiments - however a feeling still remains: To what degree can one trust the limit - is it fool proof of just within say 90 per cent?

For more complex strain paths the FLSD approach seems in my opinion to be the most promising, especially when taking the computational effort needed into account. Similar prediction concerning the remaining formability may be obtained using the MK-approach, but the computational effort will increase. The FLSD approach demands determination of the FLD for the material under consideration and the results found using the FLSD approach will of course be strongly influenced by the theories and/or the experimental methods used for the establishment of the FLD.

For isotropic materials the method proposed by Müschenborn and Sonne is straight forward to implement when a FLD for linear strain paths is known. The method proposed by Müschenborn and Sonne can be expanded to include material anisotropy by calculating ϵ_{eq} from an anisotropic yield criterion.

Chapter 9

Examples on Process Analysis using Explicit FEM

This chapter deals with examples which are related more directly to common industrial sheet forming operations. The overall purposes of the chapter are to illustrate results obtainable by FE-simulation and to show effects of process velocity scaling, effects of anisotropy, examples of the use of the proposed CSP and Rayleigh approaches and the judgement of process severity.

9.1 Deep drawing of cylindrical cups

One of the main topics in the thesis is the modelling of anisotropic behaviour of metal sheet. The purpose of the following section is to illustrate and evaluate the prediction of anisotropic behaviour in a cup drawing process with a number of steel sheets ranging from mild steel to high strength steel.

The section deals with deep drawing of rotational symmetric cups, and the geometries and types of steel correspond to those experimentally investigated by Andersen [6]. The reported material parameters are given in table 9.1. Table 9.1 gives parameters K and

Steel type	K [MPa]	n	R_{00}	R_{45}	R_{90}	$\bar{R}$	ΔR	t [mm]
E275	610	0.165	0.80	0.95	1.07	0.94	0.02	1.11
E420	641	0.139	0.84	1.11	1.09	0.93	-0.15	1.00
E420	782	0.141	0.60	1.14	0.84	0.93	-0.43	1.00
220 RP	611	0.186	1.62	1.44	2.16	1.66	0.45	1.00
300 RP-X	675	0.165	1.16	1.28	1.63	1.34	0.12	1.00
St 14.03	524	0.192	1.62	1.37	2.02	1.60	0.45	1.00

Table 9.1: *Material parameters used in the simulation of cup drawing. The values are from Andersen [6].*

n for describing the hardening and Lankford coefficients are given to describe anisotropy,

finally the nominal thickness of the sheet is given. Young's modulus is set to 200.000 MPa and Poisson's ratio to 0.3 in all the analyses. Figure 9.1 gives the tool geometry and the

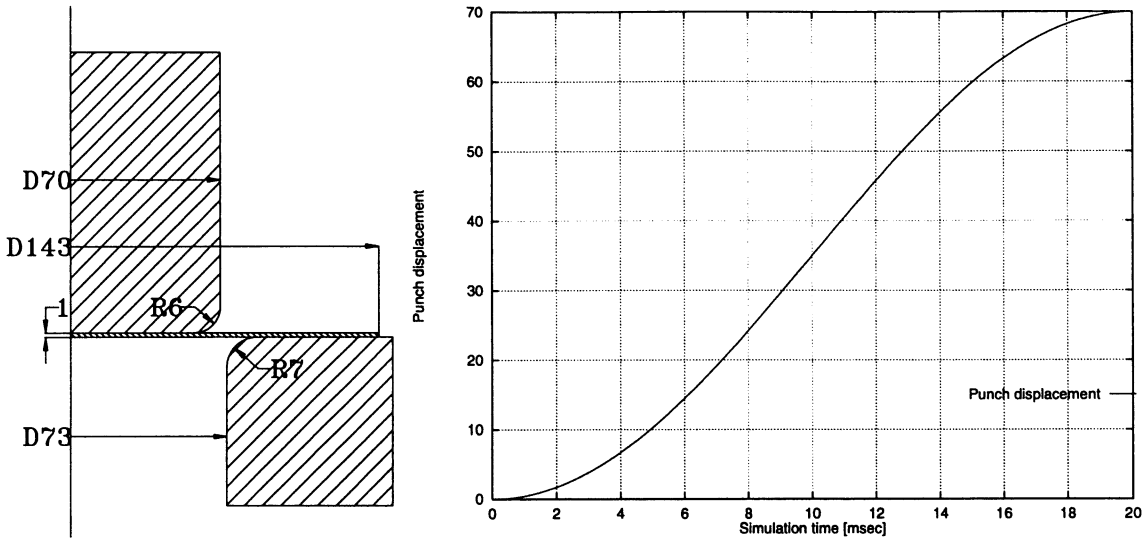

Figure 9.1: *Left: The geometry of punch, die and blank used by Andersen [6]. Right: The punch displacement as function of simulation time.*

prescribed displacement of the punch as function of the analysis time. In the process blank hold is force controlled and as in the experiments a blank hold of 16 kN is utilized.

9.1.1 FE-model of the cup drawing process

Figure 9.2 shows the discretized models of the punch, die, blank holder and blank which are used in the analyses. Only one quarter is modelled in the analyses due to symmetry. The material behaviour is modelled with Barlat's 2D criterion and with M=2, apart from the analysis discussed in section 9.1.5 where an exponent of 8 is used. Hardening is modelled with a Hollomon-Swift relation using the above given parameters. Friction between all surfaces is described as Coulomb friction with $\mu = 0.1$.

9.1.2 Comparison between numerical results for M=2 and experiments

Figure 9.3 and 9.4 show the numerical predicted thickness distributions compared to experimentally measured values for the 6 types of steel (listed in table 9.1). The experimental values are all results given by Andersen [6]. Figure 9.3 gives the thickness distribution for E275, E315 and E420 along lines at 0, 45 and 90° to the rolling direction. These steels are characterized by a relatively low n-value and also a relatively low R-value. The absolute ΔR value is low for the two first steels and relatively high for E420, however, in my opinion ΔR does not give any real information concerning the in-plane anisotropy. For E275 and E315 a typical behaviour can be seen: The numerically predicted thinning is too low for cupwall height between $\approx$ 20 to $\approx$ 30 mm. It is also characteristic for the shown curves that the upper part of the cup wall is estimated to become thicker than what is found from experiments. For E420 the thickness distribution agrees better, however, the tendency that

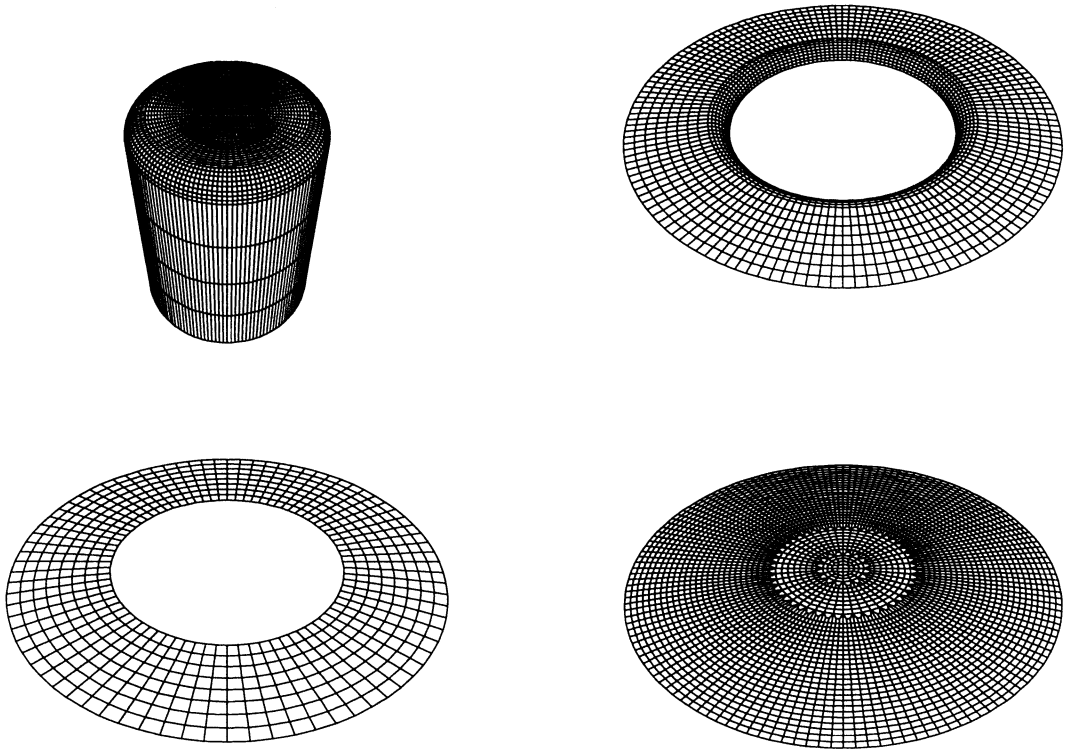

Figure 9.2: *Discretization of punch, die, blank holder and blank.*

the upper cup wall becomes too thick in the simulations is still present. Figure 9.4 shows the predicted thickness of the cup wall compared to experiments for the three latter materials. Here the same trends with over-prediction of thicknesses can be seen. These steels are characterized by higher values of n and R compared to the three previously discussed steels (E275 and 300 RP-X have the same n-value). From the figure it is characteristic that the thickness distribution predicted in 0° is in much better agreement than in 45° and 90°. This may indicate that when the material modelling is based on the hardening curve at 0° it can lead to a poorer estimate for other direction, however, this cannot be concluded as we cannot directly transfer the uniaxial behaviour used for determination of material parameters to the much more complicated straining situation of deep drawing. To draw a conclusion from the predicted thicknesses some characteristics are observed: Almost all of the curves in the figures from 9.3 to 9.4 show that the numerical predicted thicknesses for heights between 10 and 30 mm are reasonably predicted. It is also concluded that the upper wall thickness is predicted to become larger than what is seen from the experiments. This effect has also been observed by Mortensen [150] and Damborg and Jensen [49] using von Mises' yield criterion in 2-D analysis (and hereby including transverse stresses in the flange part). Thus, the discrepancy between numerical and experimental results cannot be explained from the assumption of plane stress in the shells used in the present analyses.

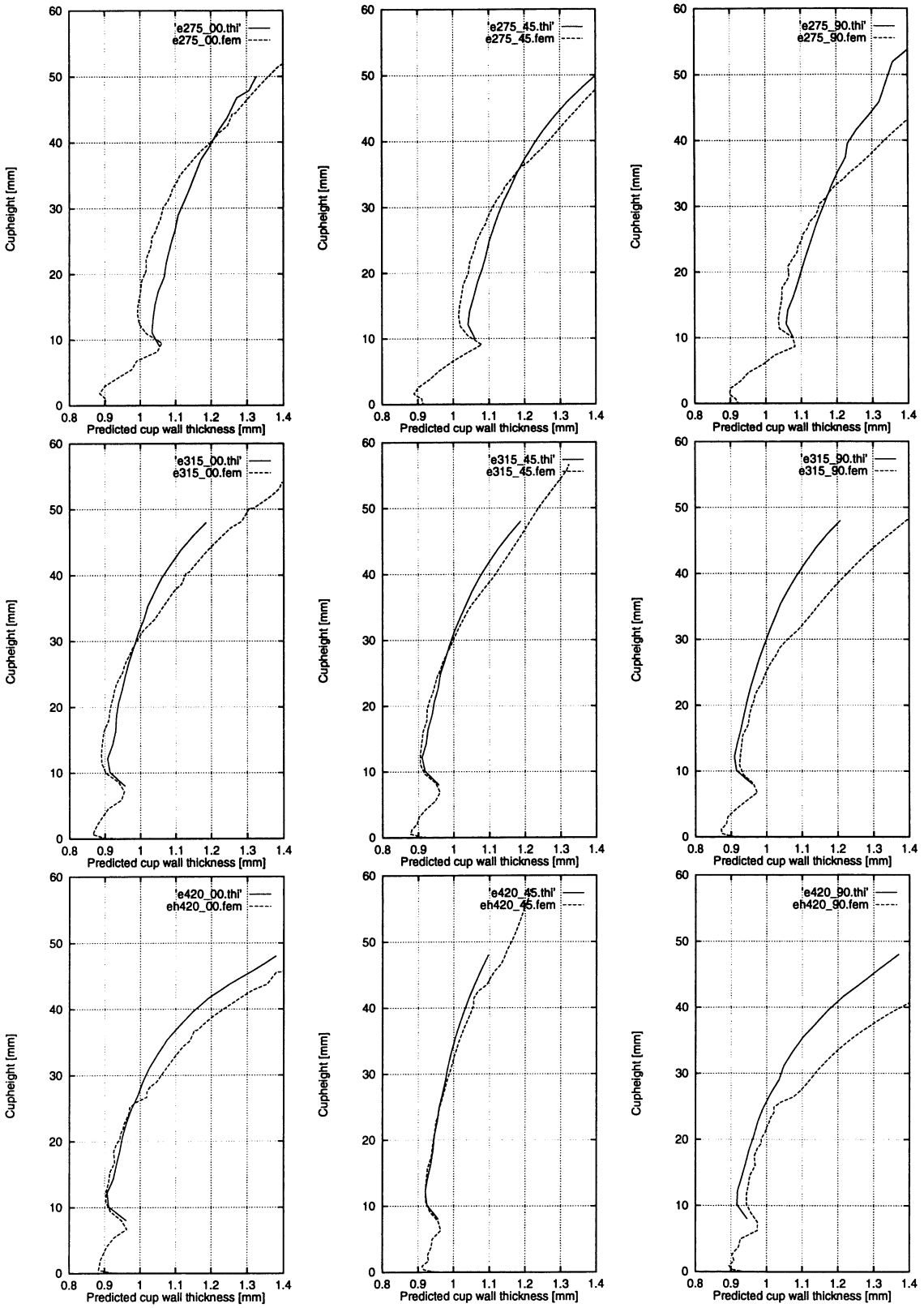

Figure 9.3: *Comparison between numerical and experimental measured cup wall thickness related to cup height for E275, E315 and E420 at angles of 0°, 45° and 90° to the rolling direction.*

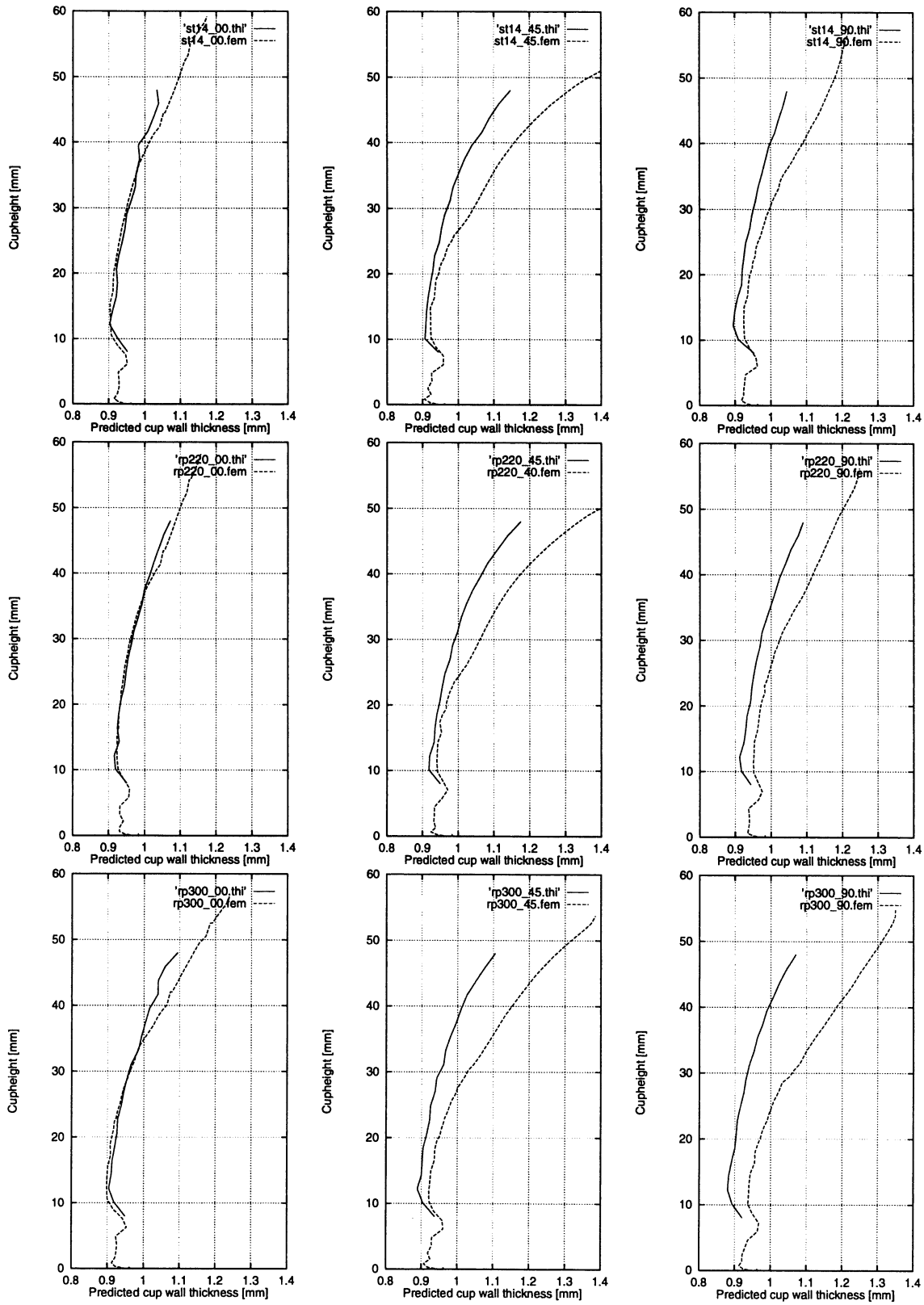

Figure 9.4: *Comparison between numerically and experimentally measured cup wall thickness related to cup height for St 14.03, 220 RP and 300 RP-X at angles of 0°, 45° and 90° to the rolling direction.*

The flange is deformed to an equivalent plastic strain level well above the level obtained in a tensile test and this may indicate that the hardening description is not correct for a so high level of straining. This is in agreement with observations made for the theoretical determination of FLDs where it is mentioned that the use of a power law hardening with a constant coefficient may be insufficient.

Andersen reports that the thickness of the sheets with nominal thickness vary from 0.97 to 1.01 mm, however, all simulations are performed using a nominal thickness of 1 mm apart from E275 (1.11 mm). These variations should be kept in mind when comparing the results of the thickness variation.

The effect of the die impact line is very clear in the analyses as well as in the experiments. Due to difficulties when measuring the corner region the experimental results are only reported for cup heights above $\approx$ 8 mm. The punch impact line can be seen clearly in the numerically predicted thickness distributions.

The cups are only measured up to a cup height of 48 mm to ensure that formation of a valley between ears does not interrupt the measurement. Some of the cups also show tendencies to wrinkle at the top of the cup wall which makes the measurement of thickness by using the 3D-coordinate measuring machine unreliable due to the employed probe size.

9.1.3 Shape tolerances

For two types of the steels, St 14.03 and E420, contact surfaces are eliminated when reaching full punch stroke and the analyses are continued to damp out vibrations in order to obtain the shape after spring back. For comparison it was chosen to use the predicted ear height variation as function of the angle to the rolling direction and the radius variation at a cup height of 40 mm. Figure 9.5 shows the predicted ear height variation for steel E420

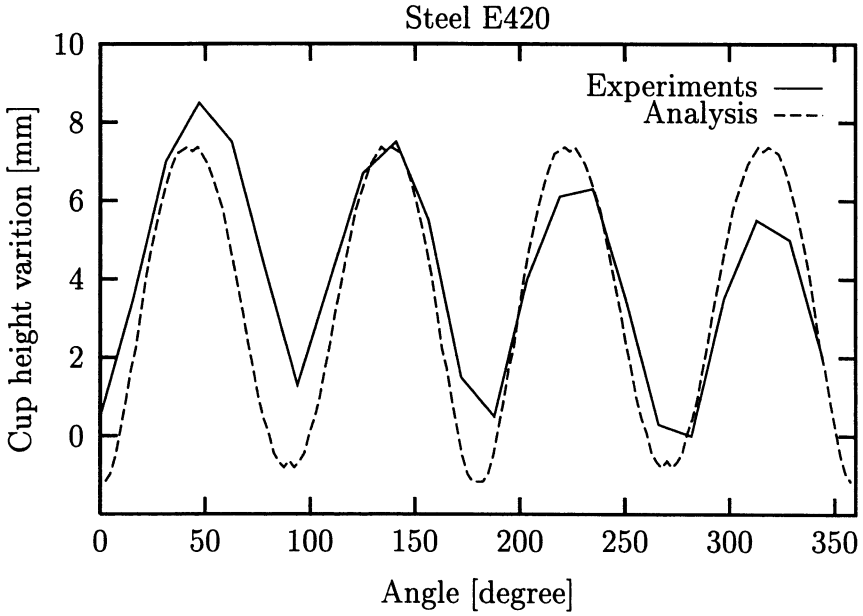

Figure 9.5: *Cup height as a function of the angle relative to the rolling direction.*

compared to experiments. From the figure it appears that a good relation can be found between geometric parameters such as the ear height variation. If we compare this correlation with the correlation between wall thickness given in figure 9.3 the predicted ear height indicates a better agreement between experiments and simulation than the agreement indicated by thickness distributions. Figure 9.6 gives the numerically and experimentally found ear height variation for St 14.03. This figure indicates a correlation with the same accuracy as the relations obtained for E420. Figure 9.7 shows the predicted radius variation after spring back compared to the radius variation found experimentally. The radius variation is measured at a cup height of 40 mm. In the figure the numerical prediction is plotted for the reference surface and the experiments are given as the radius variation for the inner and outer surface. It appears from the figure that this variation is predicted with a high accuracy, the accuracy being higher than the accuracy one would expect if only the thickness distribution is taken into account. The tendency in the analysis results is that the variation is slightly over-estimated; at 0° and 90° the radius is above the experiments and at 45° beyond the experiments. The effect that the radii found experimentally reach a higher level at 0° than at 90° is not found in the analysis. Figure 9.8 shows the comparison between radii for St 14.03. The predicted level seems very reasonable, but the variation found experimentally is not found in the analysis. The experiments lead to two local minima (over 360°) whereas the analysis leads to four. The numerically predicted variation does, however, indicate a lower radius in 0° than at 90° - this variation was not found in the analysis for E420 where experiments show this effect.

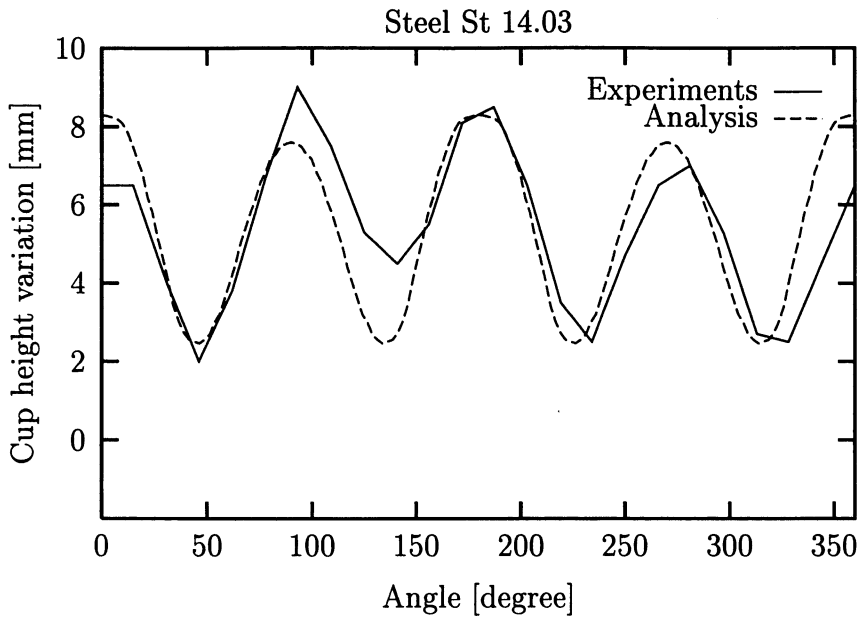

Figure 9.6: *Cup height as a function of the angle relative to the rolling direction.*

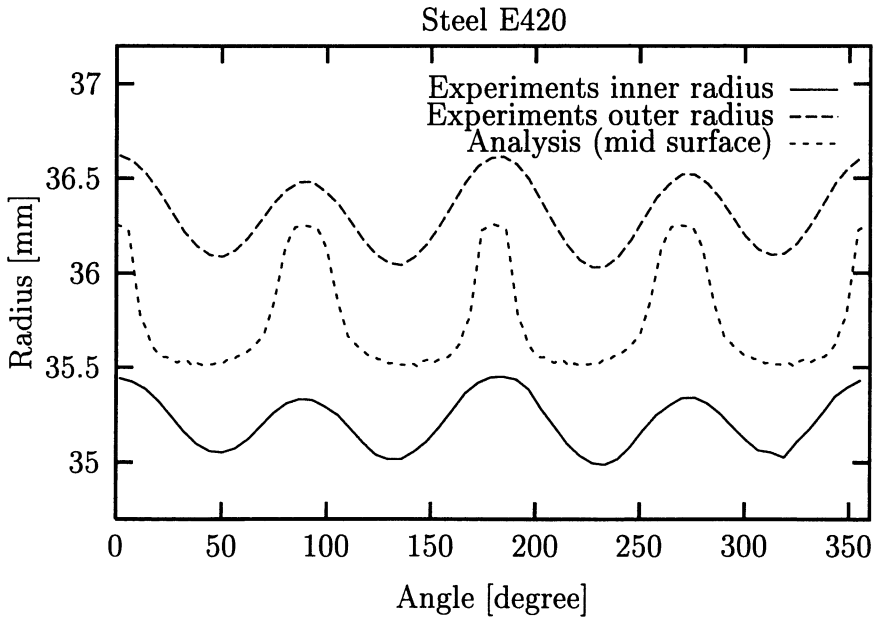

Figure 9.7: *Radius at a cup height of 40 mm as a function of the angle relative to the rolling direction.*

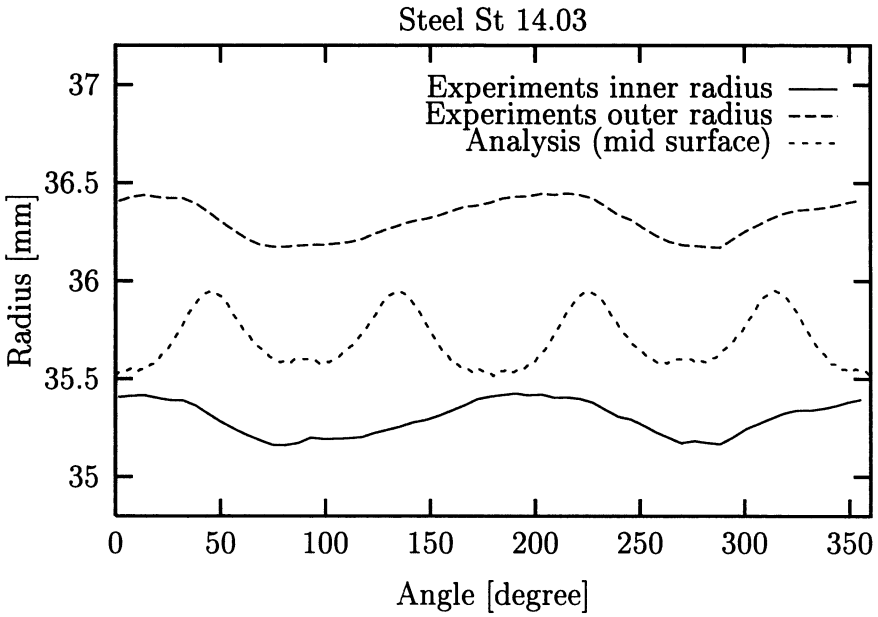

Figure 9.8: *Radius at a cup height of 40 mm as a function of the angle relative to the rolling direction.*

To conclude on the predicted shape tolerances it can be stated that results which are reasonably accurate can be obtained. However, it must also be realized that there seems to exist mechanisms which are not included in the analysis.

9.1.4 Process signatures for the cup drawing

A very effective way to obtain an overview of the process is to plot process signatures for selected lines. This section presents examples of process signatures for the cup made from St 14.03 and gives a brief discussion. Figure 9.9 shows the process signatures for a

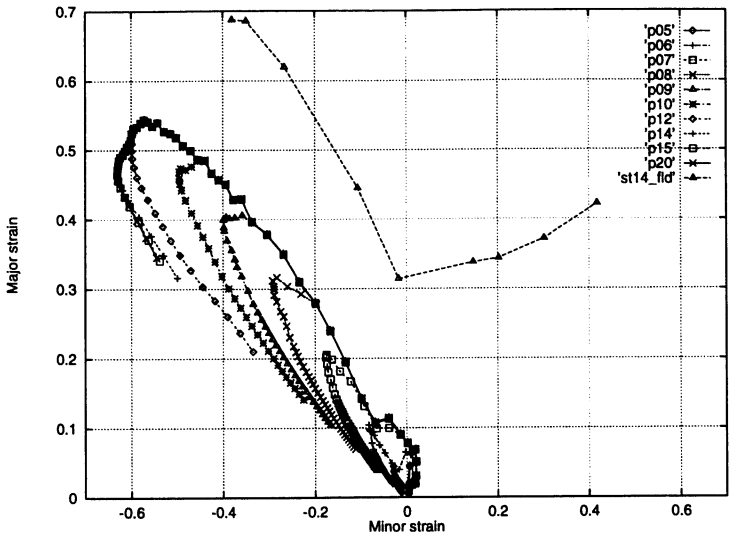

Figure 9.9: *Process signatures in the rolling direction plotted at various stages in the cup drawing for St 14.03 together with a forming limit curve. The number of the curve label corresponds to the time in the analysis, see figure 9.1.*

line at 0° to the rolling direction at various stages in the process together with a forming limit diagram for St 14.03 (from [4]). It is to be expected that this process is in the absolutely safe range, however, if the process severity is only judged from a plot like figure 9.9 one will be out of touch with the sensitivity towards variations in the process conditions.

To be able to distinguish between the curves the process signatures from figure 9.9 are plotted in figure 9.10 without point marks and using a larger scale. To obtain results which can better be judged with regard to severity one may try variation of various parameters. From the process signatures it can also be noticed that the strain level in the bottom region is reached relatively early in the process. The curves given in figure 9.10 show that for process times above 8 msec the curves are almost identical in the region of the sheet which is formed around the punch nose. This matches our expectations as a traditional cup drawing reaches the maximum punch force around one third of the punch stroke.

Figure 9.11 shows the resulting process signatures for analyses made with different values of the blank holder force; the normal blank hold of 16 kN and a high blank hold of 83.5 kN. In this situation it is apparent that it is possible to increase the blank hold significantly without reaching a critical level of strains. Figure 9.11 illustrates that the most significant changes in process signatures take place in the outer part of the flange. At 10 msec the two process signatures are rather close to one another; the absolute difference ≈ 0.02. The radial strain is generally higher for the high blank hold for the material close to the symmetry line. For material in the flange the difference is primarily that the minor principal strain is smaller for the high blank hold - or in other words: At 10 msec the

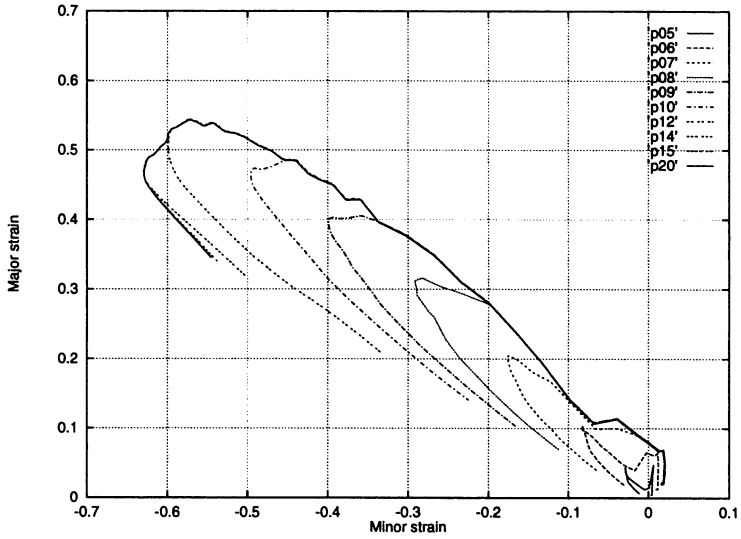

Figure 9.10: *Process signatures in the rolling direction plotted at various stages in the cup drawing for St 14.03. The number of the curve label corresponds to the time in the analysis, see figure 9.1.*

blank has been drawn to a smaller radius when using the low blank hold. It can also be noticed that even though the blank hold is considerably increased the biaxial straining over the punch does not change. This indicates that with the employed punch geometry the resulting strain distribution at the bottom of the cup is unaffected of variations in blank hold. If the the punch nose radius is increased more stretching will occur over the punch bottom and this will probably lead to a higher sensitivity towards changes in the blank hold.

For the process signatures at 20 msec the picture is similar for the material initially close to the punch, but for the outer part of the flange a considerable variation can be seen when going from a blank hold of 16 kN to 83.5 kN. This may be one explanation for a so high difference can be seen between numerical analysis and the experiments; If the blank hold utilized in the experiments is higher than reported this may partly have caused the difference, however, other sources report the same effect with a too severe thickening for a fixed blank holder gab.

In my opinion it is necessary to perform an analysis of this type for parameters (and/or process options) in order to get a safe indication of the process severity - the information which is directly obtained from a comparison with a FLD and with the strain paths obtained by simulation does not give an impression of the real process stability. The parameters which are most likely to vary, e.g. material properties from batch to batch, friction conditions, etc should be checked and following the process parameters leading to the safest set up should be found.

9.1.5 Influence from the exponent M

It has in previous sections been shown that the exponent M has an influence on the strain distribution. These examples are dominated by stretching, whereas the cup drawing process results in process signatures primarily placed in the left-hand side of a FLD.

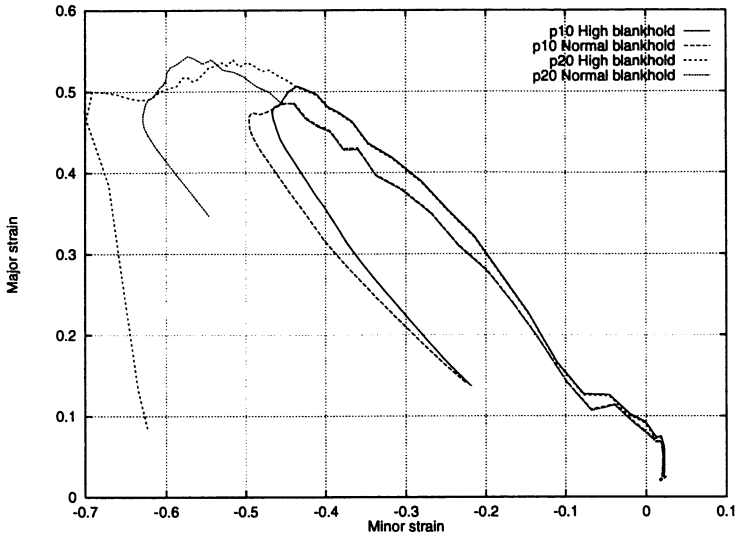

Figure 9.11: *Process signatures in the rolling direction plotted at two stages (10 and 20 msec) in the cup drawing for St 14.03 for a blank hold of 16 kN (normal) and 83.5 kN (high).*

Only the mild steel (St 14.03) is considered in order to clarify if simulation results can be improved by including M as a fitting parameter. Figure 9.12 shows the predicted thick-

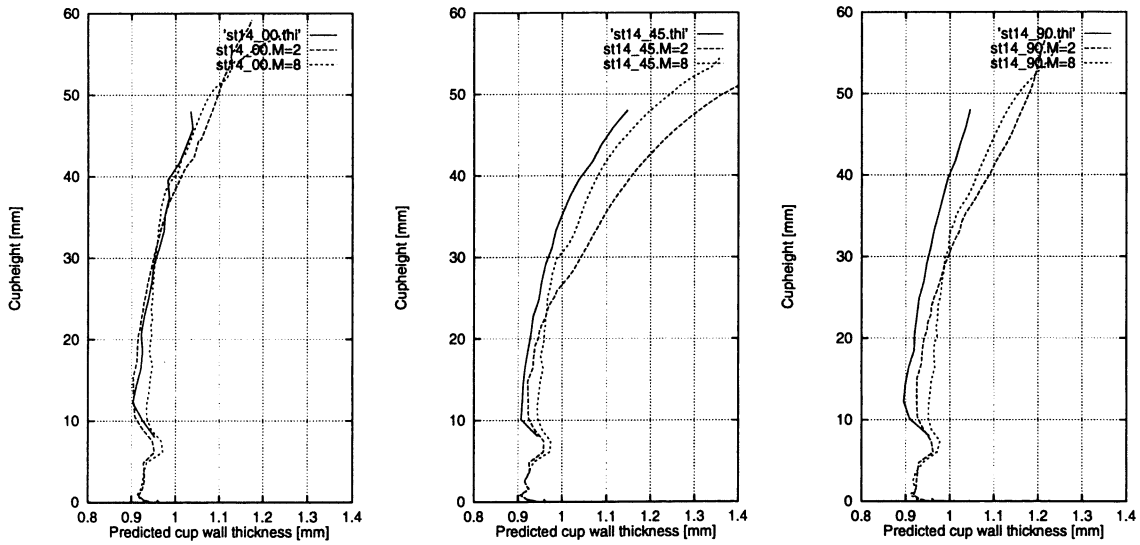

Figure 9.12: *Comparison between numerically obtained and experimentally measured cup wall thickness related to cup height for St 14.03 at angles of 0°, 45° and 90° to the rolling direction. Numerical results are obtained by using exponents of M equal to 2 and 8.*

ness variation as function of cup height when modelling the material behaviour of St 14.03 with Barlat's yield criterion and M=2 and M=8, respectively. In the figure the corresponding experimentally obtained curves are also given.

By increasing the M-value it appears that the predicted shape of the curve can be improved, especially for 45° and 90°. However, this improvement in shape leads to a predicted

thicknes which in general is too high for the lowest part of the cup wall. In 0° the curve for M=2 seems to be in a better agreement with experiments than the curve for M=8. The analysis may indicate that the initial thickness has been more than 1 mm for the sheet used in the experiments. Figure 9.13 shows the process signatures in 0° to the rolling direction.

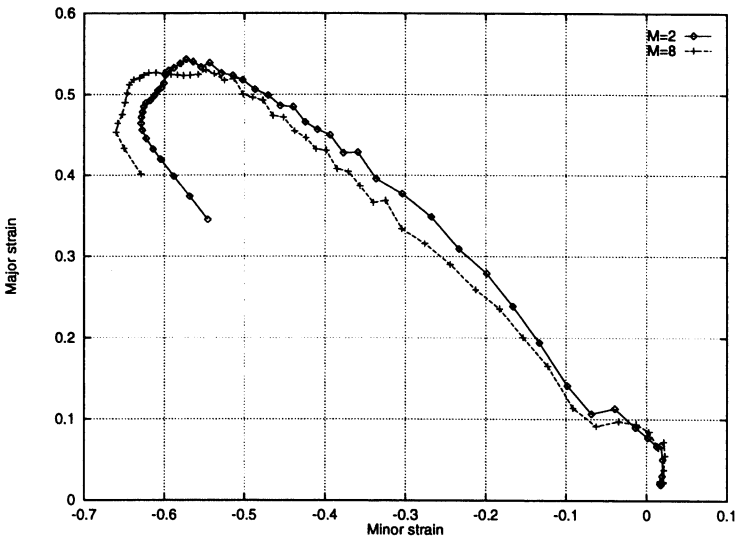

Figure 9.13: *The process signatures obtained for the rolling direction for the cup made of St 14.03 by using an exponent M=2 and M=8, respectively.*

It appears that the changes are limited, however, the same characteristics as found for the thickness distribution can be seen: For the lower part the thickness increases and the major part of the upper flange decreases in thickness, however, the last 4-5 elements indicate a larger thickening for M=8 than for M=2 (if the strains are assumed to be plastic, a line with a slope of -1 indicates a contour line with constant thickness strain, e.g. the line passing 0,0 and having a slope of -1 indicates that no thickness changes occur).

9.1.6 Summary of cup drawing

The implemented material model seems able to predict aspects which also can be found for the reported experiments. However, for the upper part of the cup it is significant that thicknesses are over-predicted. It is believed that this discrepancy is found due to mechanisms not included in the material model. To improve the predictions it is proposed to let M depend on the equivalent strain level or to expand the hardening description so that deformation strongly influenced by compressive stresses ($\sigma_{\theta\theta}$ in the flange region) can be modelled different from e.g. stretching; this may be done by defining two equivalent strain measures - one being active when the two normal stresses are positive, the other when the minor principal stress is negative.

9.2 Deep drawing of square boxes

Geometries which are often used in practice are square and rectangular boxes, for instance kitchen sinks, roasting tins and parts for electronical devices. Many other more complex deep drawn parts can be considered to be an extension of the square box deep drawing. In connection with experiments the geometry is also suitable as the tools are relatively cheap to produce and the resulting parts are easy to measure.

In the following a discussion is given of the possible speed-up of analysis and aspects as interface damping is illustrated. The section also gives a comparison between numerical and experimental results. Finally examples are given on the use of the CSP-method.

9.2.1 Geometry and loading conditions

The process, which is considered here, corresponds to one of the benchmark tests from the Numisheet'93 Conference: Square cup deep drawing where a traditional deep drawing with force controlled blank hold is considered. Figure 9.14 shows the tool geometry.

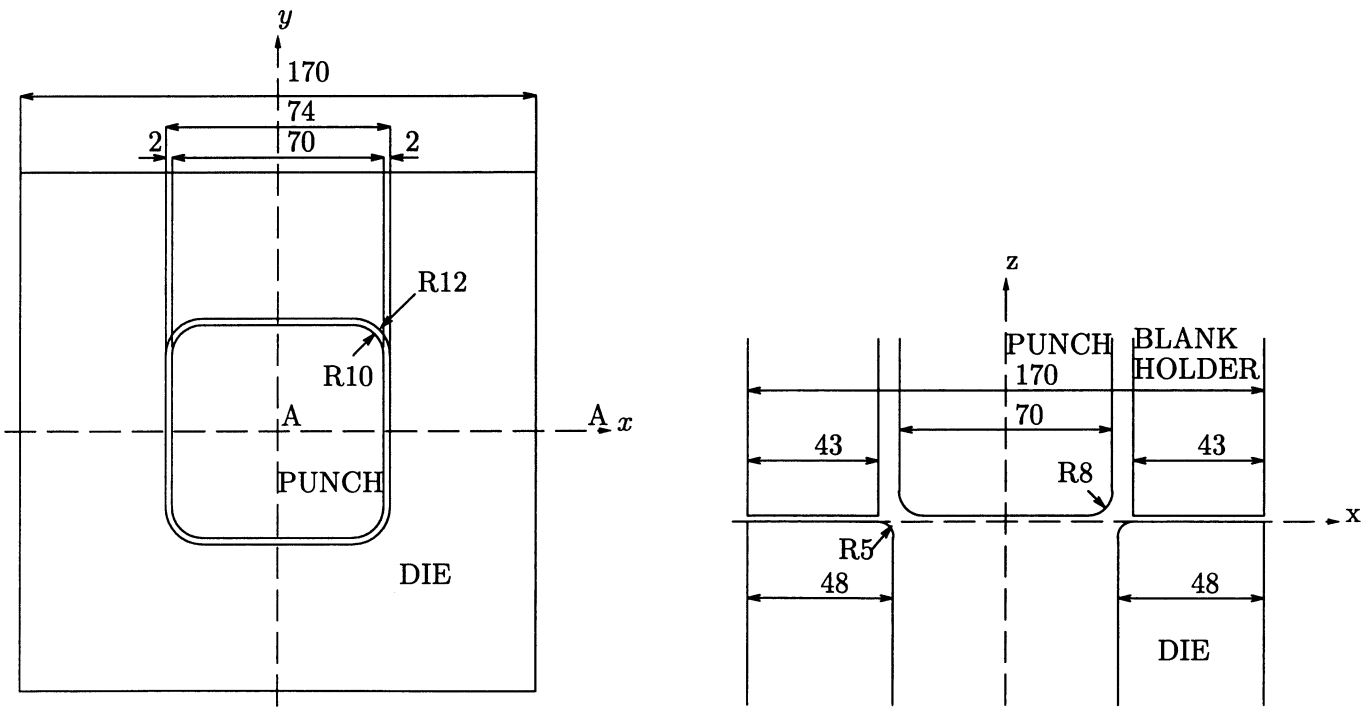

Figure 9.14: *Geometry of the square cup deep drawing example. Left: The top view. Right: The side view. The geometry corresponds to the Numisheet'93 Benchmark: Square cup deep drawing [94].*

9.2.2 Mass scaling

This section illustrates the influence of mass scaling through a number of simulations and a loading rate is chosen for the subsequent analyses on the basis of these simulations. The section also shows the effect of contact damping on the contact forces. All simulations are made with the same discretization. Figure 9.15 shows the discretization used for the

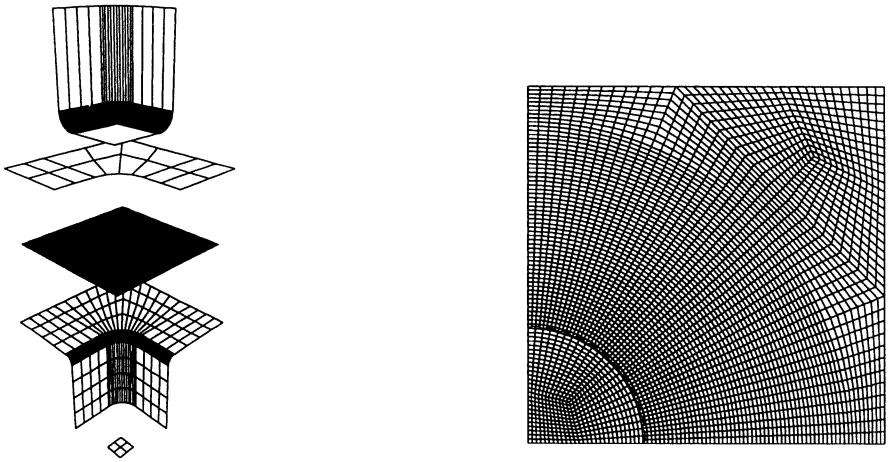

Figure 9.15: *The discretized model consisting of punch, blank holder, blank and die. The small part shown in the bottom is made to ensure the position of the drawn workpiece when eliminating the remaining contact surfaces. The right part shows the discretization of the blank.*

square box deep drawing. The tools are modelled as rigid and the blank as elastic-plastic using the implemented material model, see chapter 5.10. Only a quarter of the square box is analysed due to the symmetry, and the quarter of the sheet consists of 1969 Belytschko-Tsai shell elements. The full blank measures 150 × 150 mm and it is made of mild steel with a nominal thickness of 0.78 mm. The mesh may seem a bit untraditional; it was developed in connection with my participation in the Numisheet'93 Benchmark to obtain a smooth sliding between tools and blank. It was found that if a mesh consisting of equally sized square elements was used it led to "noise" in the deformation of elements positioned in a zone aligned around a line in 45° to the x-axis as the deformation led to rhomb shaped elements; the elements were here primarily deformed along diagonals, one diagonal being compressed, the other stretched. These effects are limited when the mesh illustrated in figure 9.15 is used; the primary deformation is then better aligned with the element sides.

When using discretized surfaces for tools parts one should also carefully check that the predicted material flow is not influenced by the discretization (in some cases it is directly visible, for example in the plastic strain distribution). In the latest versions of LS-Dyna3d it has become possible to use an analytical representation of the tool surfaces and it is believed that using analytical description of tool surfaces can reduce, but not eliminate, the problem with noise.

Figure 9.16 shows the punch displacement as a function of the process time used in the analyses. The punch velocity was modelled with a sine shaped profile in order to avoid impact effects and to obtain a final punch velocity of zero. The use of a sine shaped ve-

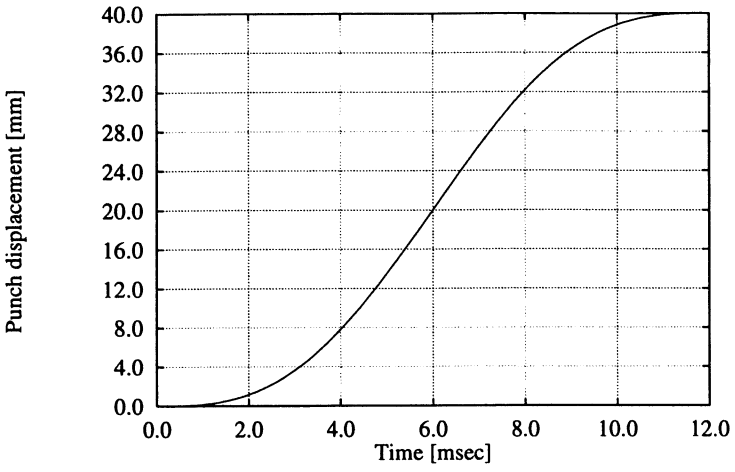

Figure 9.16: *The displacement of the punch as a function of time for the 40 mm punch travel.*

locity profile leads to a relatively low level of kinetic energy at 12 msec, the time from when the cup is exposed to artificial damping in order to damp out vibration and hereby obtain the geometry after spring back. The spring back phase was performed over 6 msec which was found sufficient. The relatively short time of damping also indicates that the final part is relatively stiff as the time needed to damp out vibrations is bounded by the lowest eigen-value. After reaching the final punch stroke (12 msec) contact between blank and die, blank hold and punch sides, respectively, was eliminated, leaving only two contact surfaces towards the blank: The punch bottom and the small part (the small part can be seen in figure 9.15). These contact surfaces combined with symmetry conditions are sufficient to keep the drawn cup in place.

Another benefit from using the sine shaped punch velocity is the fact that the imposition of higher order vibrations due to discontinuity in the derivative of the specified punch velocity is avoided. My experience with simulation of processes which are quasi-static of nature is that loading functions which follow a sine shape with the half periods equal to the forming period (in simulation time) gives a stable response. This is also what could be expected: Using a loading function, for example made up by linear pieces, will lead to introduction of noise with a higher frequency. A piecewise linear function can be represented by a Fourier expansion and in order to get a close representation many terms must be included. The more terms the higher frequencies will be present in the loading function and influence the simulation. The optimal choice as regards avoiding high frequencies is thus a trigonometric function with the longest possible period: Twice the entire simulation period (loading period).

Blank holder force is applied as a constant pressure on the blank holder. To avoid initial penetration between tool parts and the blank it is necessary to have a minor gab between the parts. Although the gab is small (0.001 mm) it is sufficient to give the blank hold a small acceleration and hereby a final velocity at the time when the first contact is made.

In order to limit oscillations in connection with contact, a contact damping of 80 per cent of the critical damping was specified according to section 4.5. Figure 9.17 shows the

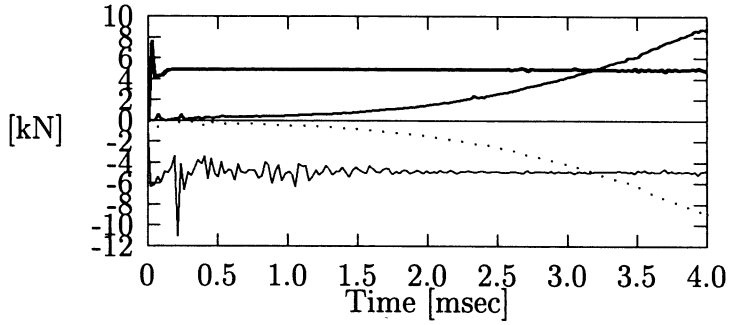

Figure 9.17: *Blank holder force for mass scaled solutions without interface damping and with 80 per cent interface damping, using negative and positive values, respectively . The punch forces are also shown. The figure only shows 4 msec of the total process time (simulation) of 12 msec.*

predicted interface forces between punch and blank and between blank holder and blank. The figure represents an analysis with an interface damping of 80 per cent and an analysis without interface damping. As regards the first mentioned analysis the forces are represented by positive values and as for the last mentioned negative values are used. The curve which increases is the punch force and the blank holder force is almost constant. As it will appear from the figure the use of contact damping can be quite effective. The damped blank holder force curve (the thickest line) is much less scattered than the corresponding undamped curve. The effect on the punch force does not seem that significant, however, the line representation used for the undamped punch force may have smeared out some noise. The figure also illustrates the influence of the blank holder which has a velocity at the time of initial contact as an overshoot can be seen clearly.

9.2.3 Material and friction modelling

The hardening is modelled as $\sigma_Y = K(\epsilon_0 + \epsilon_{eq})^n$ without taking strain rate effects into account. Friction is modelled as Coulomb friction and values for the constitutive behaviour is given in table 9.2.3. R-values are used for determining the parameters used in Barlat's 2D criterion and resulting values for the parameters are given in table 9.2.3. The analyses in this section are all carried out by using the implemented material model using Barlat's 2D criterion apart from section 9.2.4, which discusses load scaling, where an isotropic model (material 18 in LS-Dyna3d) is used. In all the simulations that employ Barlat's 2D criterion the exponent M is set to 8. Section 9.2.5 treats the Numisheet'93 Benchmark and the comparison of results is based on the experimental results reported by Danckert [53] (as part of the corresponding experimental Numisheet'93 Experimental Benchmark).

Direction to rolling	Yield strength	Tensile strength	Elon-gation	Lankford coef. R	Coefficient C	Hardening coef. n	Initial straining
[°]	[MPa]	[MPa]	%	(at 20%)	[MPa]		%
0	167.0	308.5	47.3	1.79	567.29	0.2637	0.007127
45	176.5	316.0	44.0	1.51	578.00	0.2589	0.007450
90	172.5	305.0	46.0	2.27	554.38	0.2543	0.006444
mean	173.1	311.4	45.3	1.77	565.32	0.2589	0.007117

Table 9.2: *Material data for mild steel used in the Numisheet'93 Square Cup Benchmark [94]. Young's modulus, E=206 GPa, Poisson's ratio ν=0.3 and material thickness is 0.78 mm. The coefficient of friction is reported to 0.144.*

Exponent M	Parameter a	Parameter c	Parameter h	Parameter p
2	0.665270	1.334730	0.961358	0.879085
3	0.665270	1.334730	0.961358	0.871341
4	-	-	-	0.888337
6	-	-	-	0.911582
8	-	-	-	0.925425

Table 9.3: *Coefficients a,c,h and p calculated from R-values for various exponents in Barlat's 2D criterion (only p varies with the exponent). In the analyses M=8 is the only value used.*

9.2.4 Evaluation of possible speed-up

When performing sheet metal forming simulations one of the critical aspects with regard to accuracy is, as shown in section 4.11, the speed-up. It has in this case, as a rather non-uniform mesh is utilized, been decided to choose the simulation time to 12 msec, followed by an investigation of the effect of mass scaling. In this section von Mises elasto-plastic material with an exponential hardening law $\sigma_f = K\varepsilon^n$ with $K = 565.32$ MPa and the hardening parameter $n = 0.2589$, is utilized. Figure 9.18 shows the relation between specified minimum time step and speed-up of solutions and total mass of the blank, respectively. The relation between specified time step and speed-up is as expected almost linear (note the use of a log scale). The total mass changes more drastically and in some cases it may influence the lowest eigen-frequency so severely that what is gained due to increase in time step is lost due to the need of a longer simulation time (for example in order to damp out vibrations). The mass scaled solution, which uses a time step of 0.3 μsec, leads to a scaling of 5.27 of the minimum time step and hereby to a decrease in the CPU time of approximately 80 per cent compared to the unscaled solution. As the process time is set to 12 msec the total increase in efficiency is very high compared to the unrealistic situation: To perform the analysis over the real process time span (in the order of tenth of seconds).

Figure 9.19 illustrates how severe the effect of mass scaling can be. The figure shows the contour lines of the thickness distribution at various mass scalings with minimum time

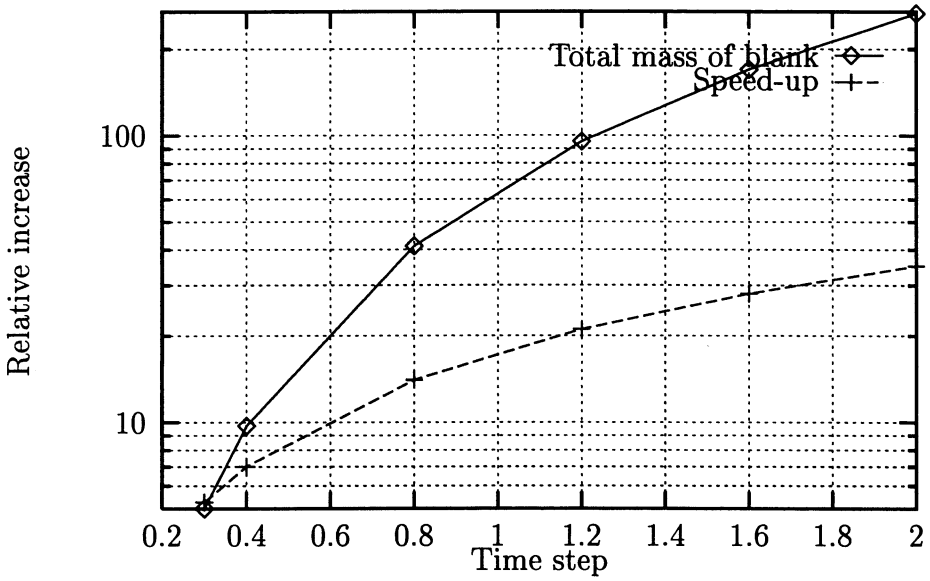

Figure 9.18: *Relative increase in total mass of the blank and the relative speed-up compared to an unscaled simulation of mass scaled solutions with time steps in the range 0.3 to 2.0 μsec.*

steps of 0.3, 0.4 0.8, 1.2, 1.6 and 2.0 μsec, respectively. As regards the two first scalings (0.3 and 0.4 μsec) the distribution is almost identical, but when moving to the third scaling (0.8 μsec) a minor discrepancy can be noted, e.g. the contour level D (in the punch corner region) covers a slightly larger area, indicating slightly more thinning, compared to the upper two figures.

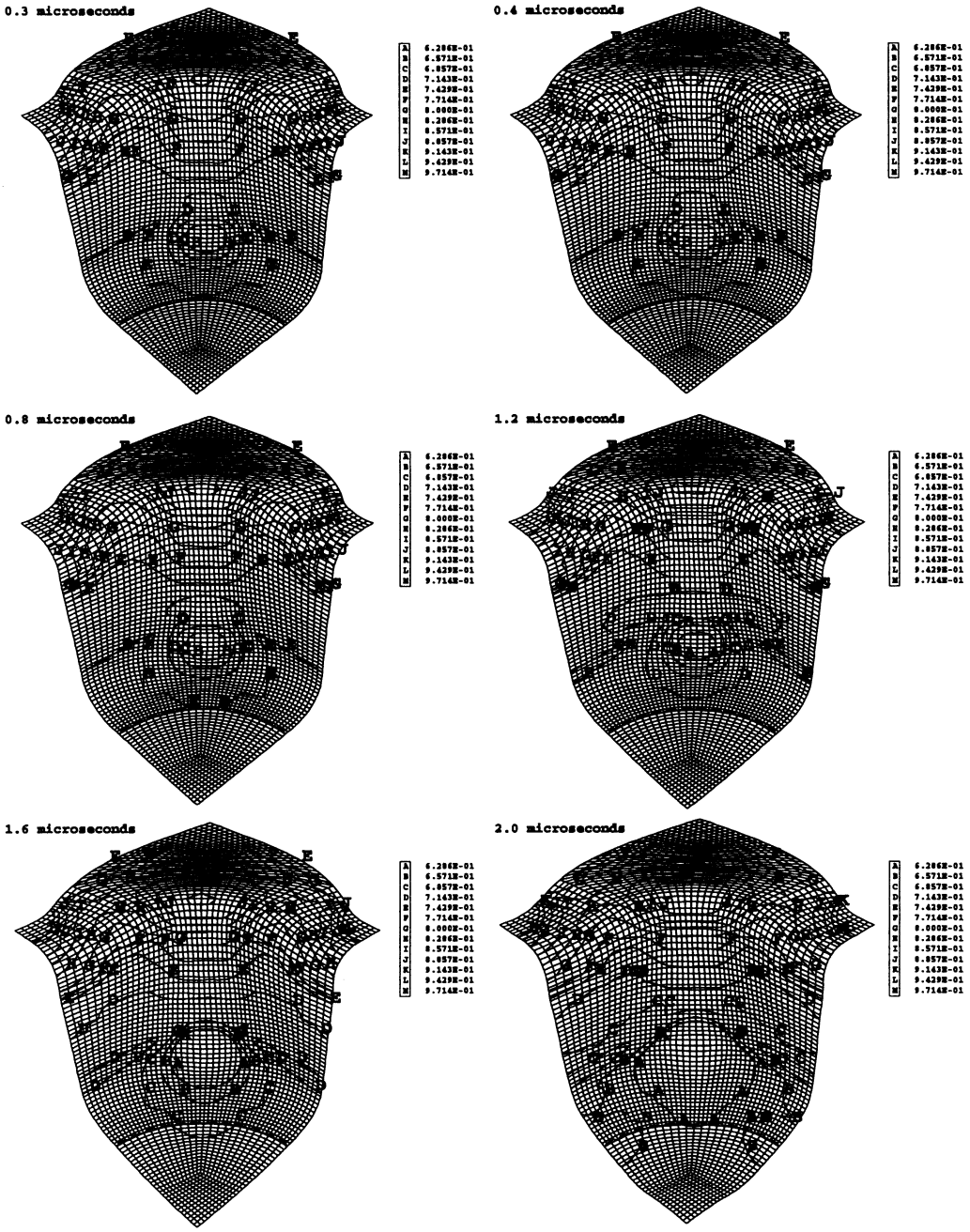

Figure 9.19: *Thickness strain distribution at various rates of mass scaling.*

One conclusion is that the strain distribution in a quite large range of time steps (0.3 to 0.8 μsec) is almost unaffected by the mass-scaling.

Another good measure of the resulting geometry is the draw-in DX and DD at A and B, respectively, (originally placed at (x,y=75,0) and (x,y=75,75)) as shown in figure 9.20. Figure 9.21 shows the draw-in obtained using various time steps in the mass scaling. The

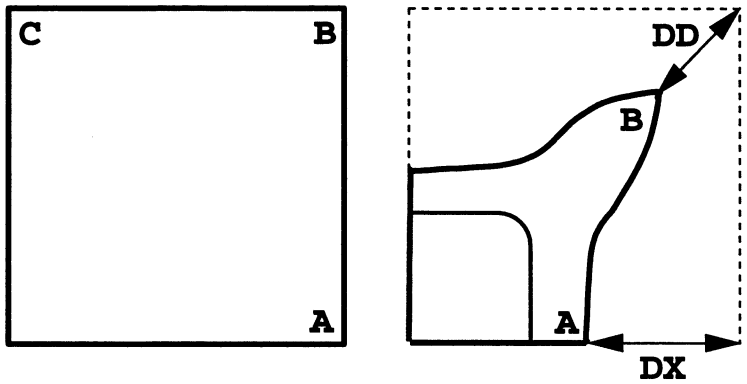

Figure 9.20: *Illustration of the blank before and after drawing. Properties DX and DD refer to the displaments of midspan and corner node, respectively.*

values of DD and DX have been normalized with the values obtained with the time step of 0.3 μsec. Figure 9.21 illustrates more clearly the effect of mass scaling than the contour plots given previously. When using a minimum time step of 0.8 μsec, a decrease around one per cent in displacement can be noticed for point A, point B is almost unaffected.

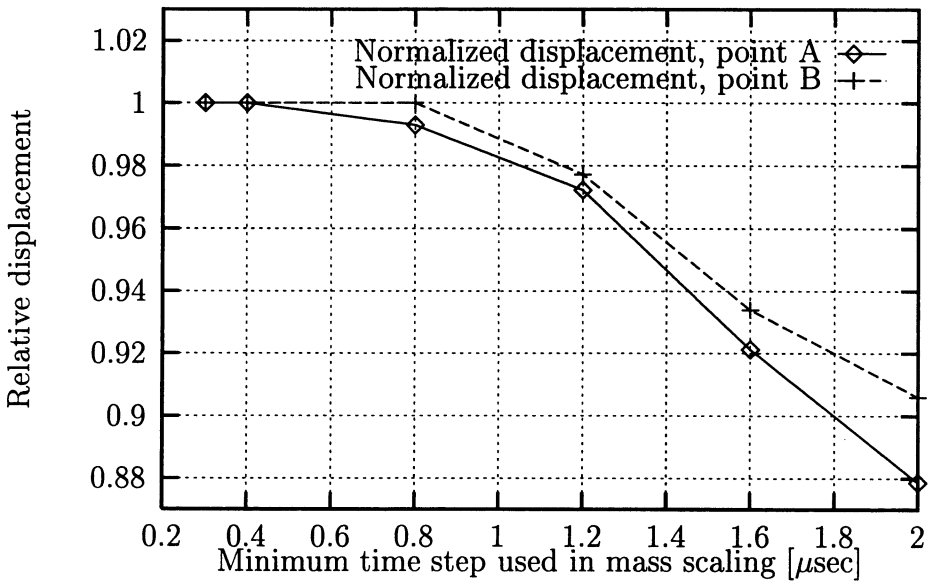

Figure 9.21: *Relative x-displacement $\frac{u_{\Delta t}}{u_{0.3}}$ for point A and B as a function of the time step used in mass scaling. The displacements for a time step of 0.3 μsec were 28.85 and 15.54 mm, respectively.*

In Nielsen, Brännberg and Nilsson [162] it is found that a very high loading rate can be utilized. In the paper the same geometry is analysed with a discretization almost identical to the one used in the present. The analyses in [162] led to the thickness strain distribution shown in figure 9.22. The figure illustrates that the thickness strain distribution is almost identical both with a mass scaling that leads to a 11.3 times higher total mass of the plate and without mass scaling. This corresponds to the results from figure 9.21 in which an increase in mass of approximately 5 (0.3 μsec) leads to identical results of the draw-ins at A and B compared with a mass increase of approximately 9.5 (0.4 μsec).

Figure 9.22 shows that the influence on the thickness distribution is very limited even when the mass scaling leads to a mass of the workpiece of 11.3 times the unscaled mass. It appears that the difference between these solutions only amounts to a few per cents.
Figure 9.23 shows the predicted punch forces (also from [162]) which differ very little,

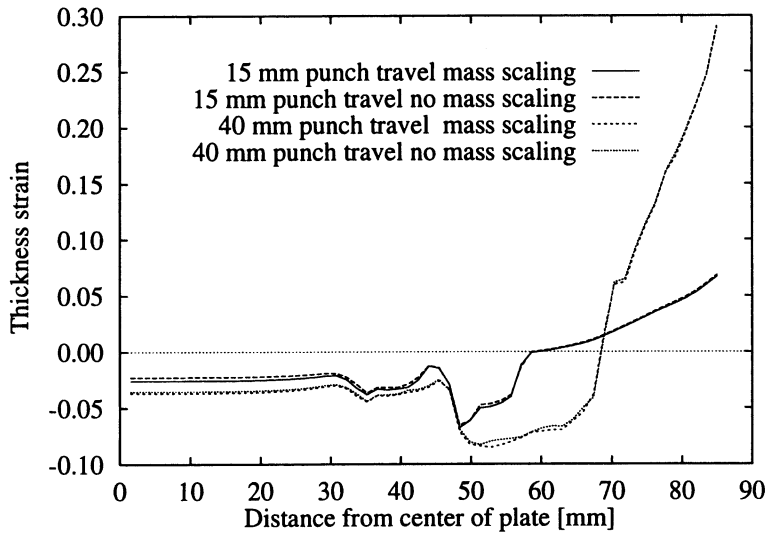

Figure 9.22: *The thickness strain distribution along the x-axis for simulations run without and with a mass scaling that leads to a total mass of 11.3 times the unscaled solutions.*

although the total mass of the plate after scaling is increased 11.3 times. However, it appears from the punch forces that a slight increase arises from the mass scaling. In figure 9.24 the thickness strains from the simulation with and without mass scaling are overlaid. The figure indicates clearly that the solutions are almost identical: The boundary of the cups are placed so close to one another that there is almost no difference between them. The only difference in the thickness distributions is for the material in the zone which has just passed the draw die radius: The contour levels F and G differ a little, the remaining contour lines coincide. From this it is evident that the conclusion so far is that a reasonable time step of 0.75 μsec can be used in connection with a loading time of 12 msec. This choice leads to a mass increase of approximately 25 times the unscaled mass and an improvement in computational efficiency of 1200 per cent compared to the solution without mass scaling (it is a reduction to 0.08 times the analysis time needed for an unscaled solution).

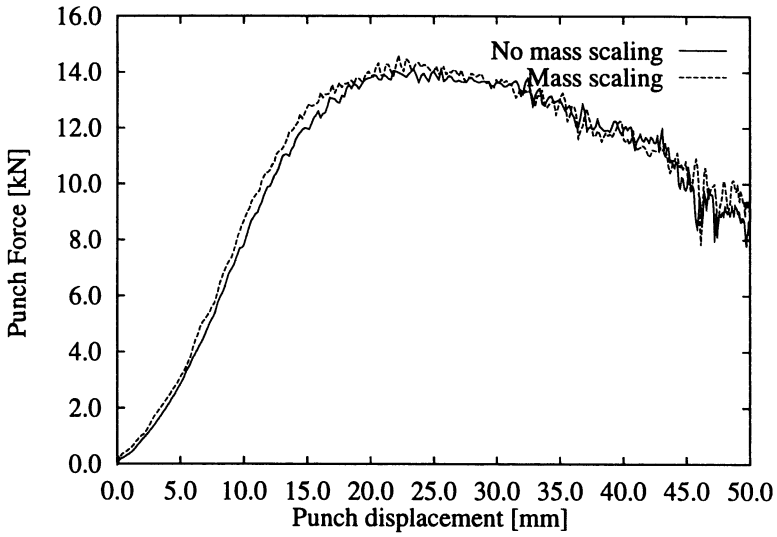

Figure 9.23: *Punch force on a quarter of the plate.*

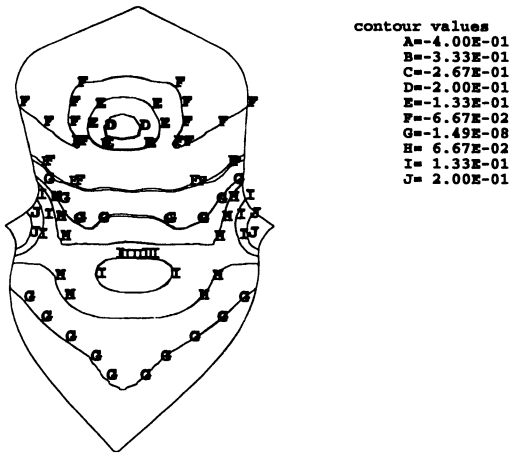

Figure 9.24: *Plot of overlaid contours of thickness strain obtained for simulations with and without mass scaling, the punch travel is 40 mm.*

9.2.5 Comparison between numerical and experimental results

Figure 9.25 shows the resulting strains that are obtained using Barlat's 2D criterion. As it appears there is a very good correlation for lines OA and OC (x- and y-axis, respectively). For the direction OB (diagonal) slightly smaller ϵ_{11} strains are predicted for the punch corner zone (the material which is at an initial distance of 50 to 65 mm to the centre of the blank). It is reasonable to assume that the discrepancy is related to the measurement of strains which is performed on the surface by using grid technique (see Danckert [53] for more details of the measurements) whereas the FE-results are reported for the mid-surface. The discrepancy in ϵ_{11} (line OB) is also found for the thickness strain ϵ_{33} as the experimental values for ϵ_{33} arise from the assumption of plastic incompressibility,

From the comparisons it can be concluded that there is a very good correlation between geometries obtained from experiments and from analyses. However, a reason why this example seems to turn out more successful than the cylindrical cups discussed in section 9.1 may be the fact that the strain level is much lower for the square box that is under consideration. Figure 9.26 shows process signatures for direction OB and OC with strains obtained numerically and experimentally, respectively. It is my opinion that by using the process signatures it is possible to get a better overview of the relation between results obtained from analysis and experiments (or when varying parameters in either analyses or experiments) than when the individual strains are plotted e.g. as function of original position along a line. The figure indicates that for line OB there are a few points in the FE-analysis where the the strain level is under-estimated and for line OC there is a small over-estimation. The point which differs significantly at (-0.65,0.4) is not included in the reported experimental results.

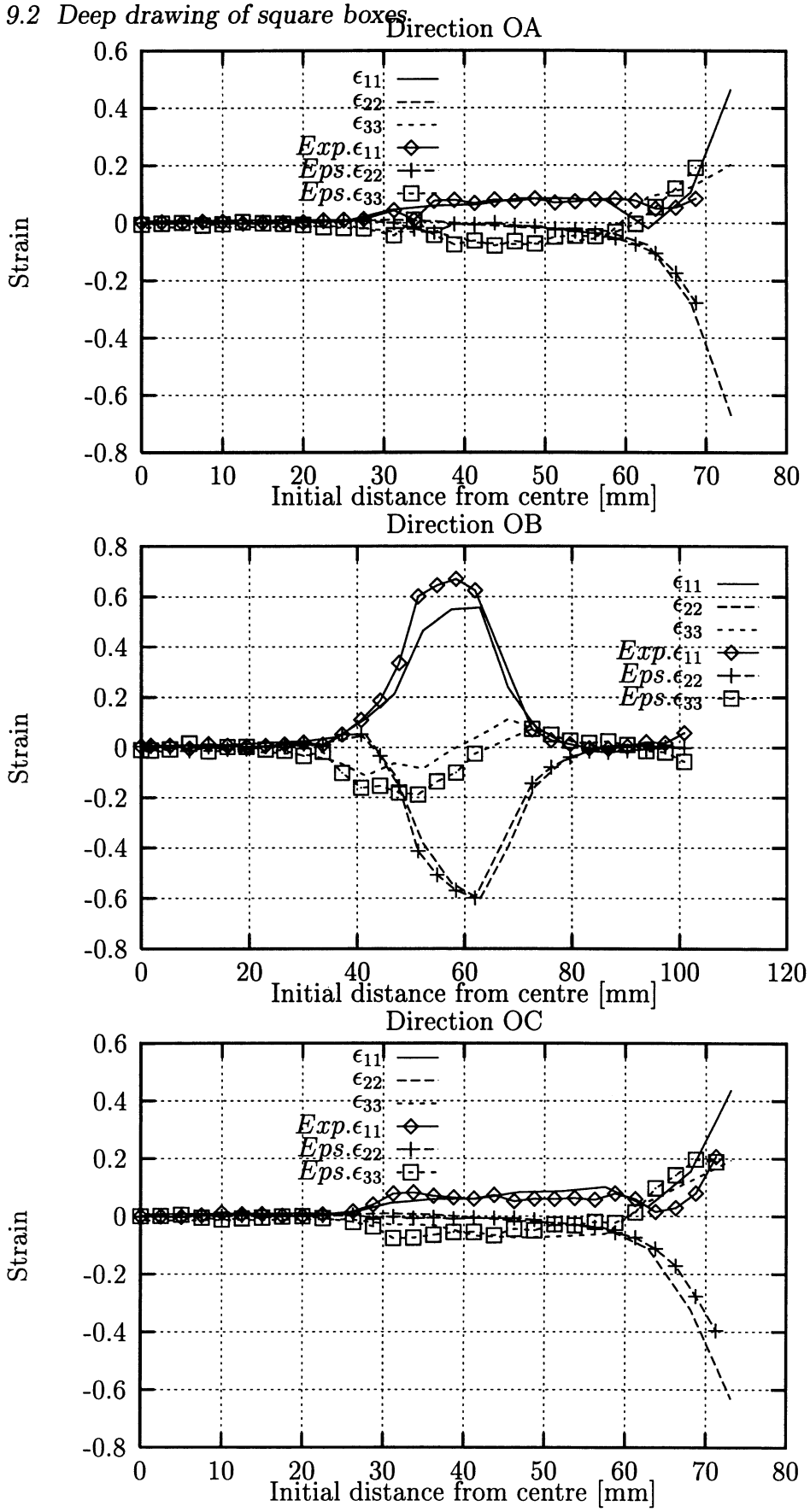

Figure 9.25: *The curves show the predicted strains ϵ_{11}, ϵ_{22} and ϵ_{33} compared to experimental results obtained by Danckert [53]. Direction OA corresponds to the x-axis, OB to the diagonal axis and OC to the y-axis (90° to the rolling direction).*

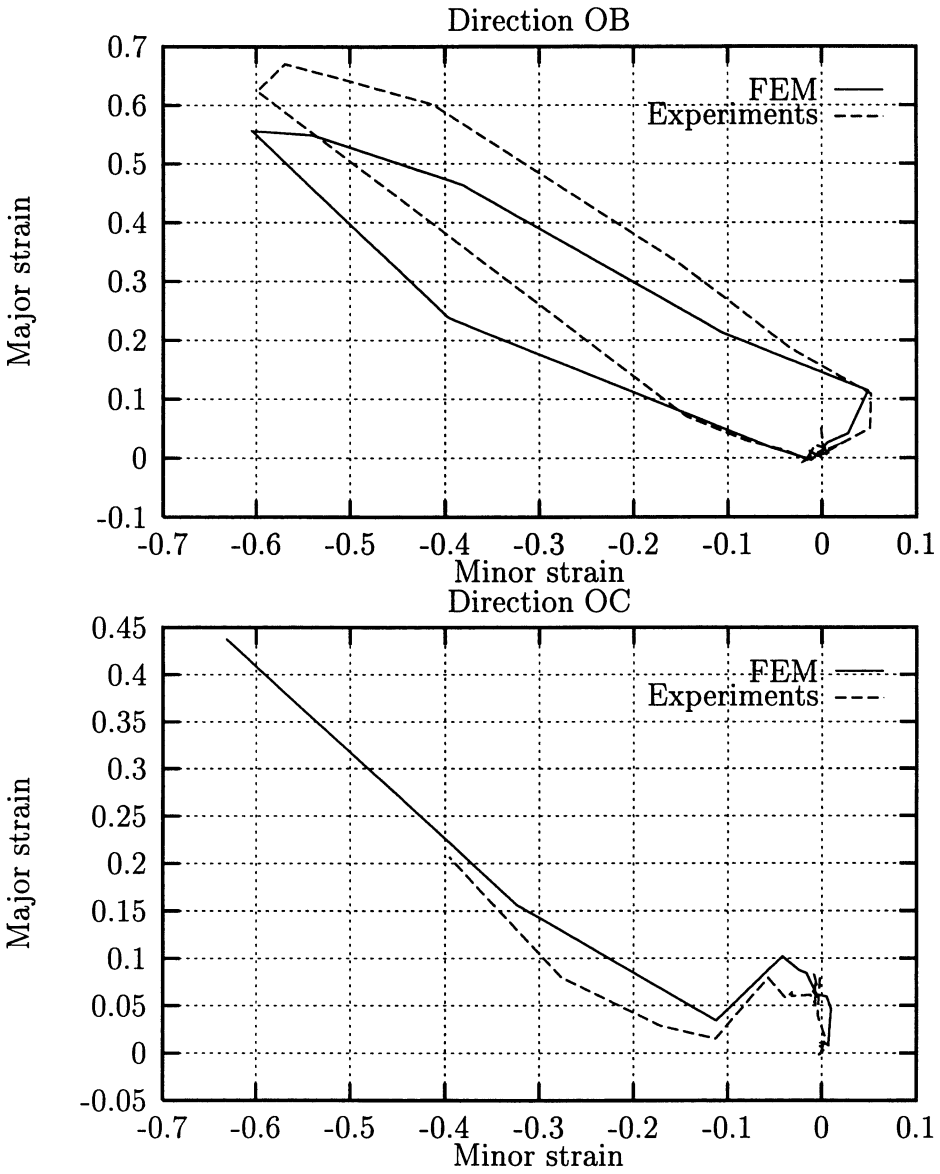

Figure 9.26: *Process signatures obtained by using Barlat's 2D criterion compared to experimental results for directions OB and OC.*

9.2.6 Simulation of wrinkling and necking

In order to provoke wrinkling and diffuse instability, two different blank holder forces were used: 0.25 and 8 times the original force. Both examples are included in the curves for the CSP-value given in figure 9.28. Figure 9.28 shows the calculated CSP values of two situa-

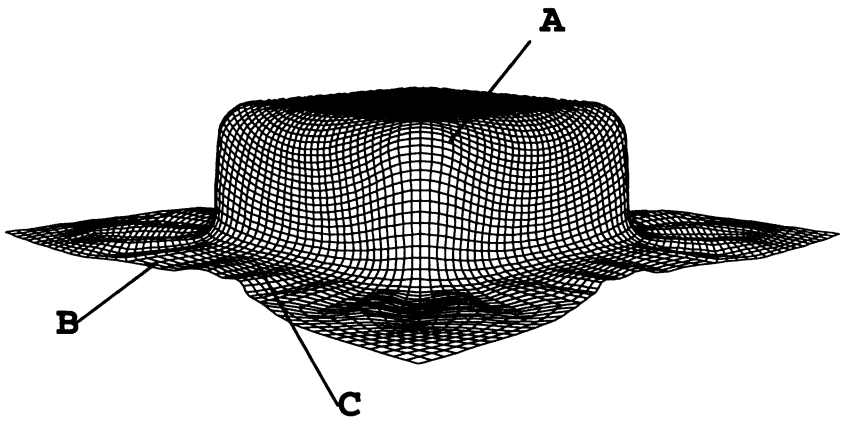

Figure 9.27: *Intermediate state where the wrinkling effect is obvious.*

tions. Firstly, the case in which the blank hold is increased to provoke necking in the zone around A in figure 9.27. The proposed CSP approach detects here diffuse instability, which is illustrated with the curve CSP_A. The predicted limit corresponds reasonably to the limit which can be predicted by using the Swift/Moore and Wallace criterion (see section 8.1). Although the predicted limit seems reasonable the discrepancy between the actual forming and the assumption of plane stress in the Moore and Wallace approach should be noticed. The zone, in which the fracture (localization) is initiated, experiences bending, for which reason, the strain and stress distribution is resulting from a non-homogeneous loading and furthermore the strains and stresses will vary over the thickness. This type of fracture is believed to be reasonably predicted from the constitutive modelling - however, in cases where materials such as high strength steel and aluminum are used, it is believed that the diffuse instability will appear too late to indicate the fracture which is experienced in the workshop. It may be possible that the direct fracture appearing due to localization can be regarded as an upper bound - however, this is in contradiction with the argument used when Hill's localization criterion was established.

Secondly, the case in which a low blank hold is specified: The predicted wrinkling at the points C and B (see figure 9.27) occurs at times corresponding closely to what can be found from postprocessing of the results. The wrinkling modes can be detected in the postprocessing by plotting node velocities parallel to the punch movement. These velocities are, however, very small compared to the punch velocity and can easily be overlooked in the postprocessing, especially if the process is close to the final stage.

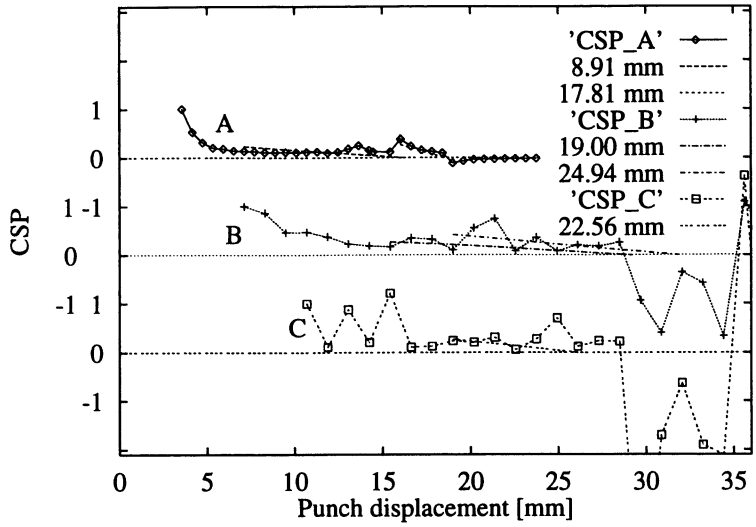

Figure 9.28: *CSP for the square box example where either wrinkling (B and C) or necking (A) arise during the simulation. Note that the figure includes 3 zero lines for the CSP value.*

From figure 9.28 it also appears that when necking takes place in the region under consideration the response remains stable at a level close to zero. This is due to the continuous dissipation of plastic work for the elements. The curves CSP_B and CSP_C indicate a much more scattered response; after onset of wrinkling both negative and positive values can be seen as the sheet starts folding which leads to both elastic and plastic deformation. It can also be noticed that a flange zone is more strongly influenced by dynamic effect than the corner region which is considered in the curve CSP_A. The corner zone is more severely deformed during the process leading to a more stable dissipation of energy - the flange zone is deformed to a much lower level. As the process progresses the flange develops zones with different thickness which opens up the possibility that small amplitudes of vibration can exist (and hereby influence the CSP value) which explains the more dynamic behaviour before the onset of winkling. These findings agree with the trends predicted for the bar sink discussed in section 6.14.

If the simulation is carried on for some time the wrinkles become obvious, see figure 9.27. However, seen from a production point of view it is valuable to be able to indicate the onset of wrinkling and in connection with the square box that is being analysed the method seems valid. The possibility of determining the onset of wrinkling sufficiently early may make it possible to adjust the blank hold so damage of the part can be avoided.

9.2.7 A typical problem drawing square boxes

Figure 9.29 illustrates a typical problem with drawing of square boxes; a total punch displacement of 50 mm is used instead of the displacement of 40 mm used in the previous examples. It is normally desirable to obtain a cup with as straight sides as possible, but

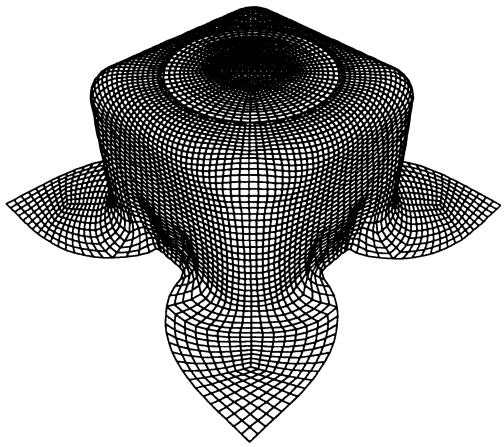

Figure 9.29: *Shape at 50 mm punch travel.*

as figure 9.29 shows this is far from obtained. To change the initial blank geometry, to vary the blank hold or to use draw beads are the best ways to improve the quality of the resulting part.

This typical behaviour where wall sides are compressed is related to the wrinkling mode discussed in section 6.14.

9.2.8 Summary of the square box example

An increase in the loading rate, which is necessary in order to perform a sheet metal forming simulation using an explicit formulation, may yield good results even when it is scaled with factors of thousands. To make this possible it is necessary to smooth the loading functions to decrease impact effects. Solutions can be obtained with substantially less computational effort if mass scaling is used and combined with an increased loading rate.

The interface damping is in this example very effective to reduce the scatter in contact forces.

The comparison between numerical and experimental results indicates a good agreement; this agreement is better that what was found for the cylindrical cups discussed in the previous section. This is believed to be due to the fact that the strain level is relatively low for the square box example and also that the process is more influenced by stretching than the cylindrical cup drawing.

The results obtained with the CSP-methods seem reasonable, however, the response is scattered, the scatter is believed to be partly due to the rate with which the simulation is performed. In this connection one may discuss whether it can be justified to focus on

strain distribution when estimating the proper loading rate. In section 6.11.2 the wrinkling behaviour was found to be influenced by the loading rate and this indicates that when wrinkles are appearing in a simulation, the results should be examined in order to determine whether the deformation mode is influenced by the scaling rate of not.

9.3 Flexible forming

Figure 9.30 shows the principle in flexible forming. The figure illustrates the process at the

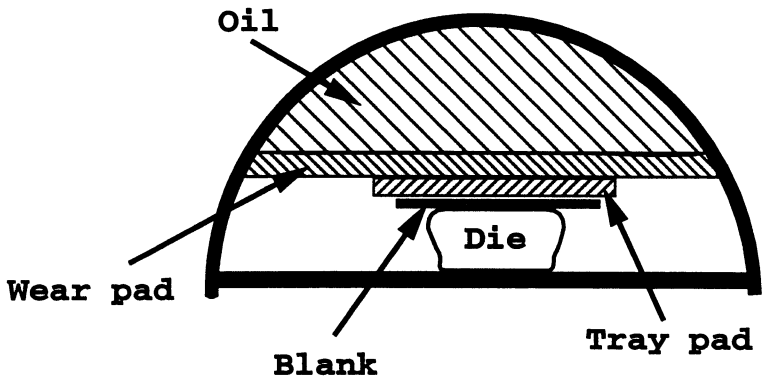

Figure 9.30: *Sketch of a rubber pad forming operation. The process is driven by control of the volume of oil and it hereby expands the pads in order to perform the forming of the blank over the die part.*

starting point. By controlling the oil volume it is possible to perform the forming operation and in order to obtain reasonable tolerances the process is normally ended by overlaying a relatively high pressure to assure that the blank is pressed firmly against the die part. The fluid cell press consists of a rubber membrane bag filled with oil. When the pressure is increased, the oil expands the bag which acts as a deformable punch that forms the sheet onto a rigid die. There are several layers of rubber membranes between the rubber bag and the sheet in the actual process.

The process is normally used in connection with low series production for example in the aircraft industries. The advantage of the process is that only one tool part needs to be manufactured and in many cases sufficiently accurate parts can be produced by using tools made of wood. This advantage is also used in the automotive industry where the process is used for prototype production and sheet parts for car models produced in a low number. A limitation to the process is that the formation of wrinkles is hard to control as a relatively large part of the blank is normally unsupported by tool parts. The forming operation is quite different from traditional deep drawing as the process is controlled by load instead of controlled by displacement.

The example given in this section shows to some degree a wrinkling tendency. These tendencies are analysed with the method described in section 6.3.1. This example has been published previously in coorperation with Brännberg et al. [162]. Nordlund [164] has also analysed this process focusing primarily on formation of wrinkles.

9.3.1 Flexible forming of a shrink formed flange

To model the process in LS-Dyna3d it is only the first rubber membrane that is included in the analysis. The rubber membrane is placed on top of the sheet. The material of the sheet is aluminum (AISI 2024-0) and it is modelled using an elasto-plastic material model

which follows the Hollomon-Swift hardening rule (material 18 in LS-Dyna3d). The rubber membrane is modelled using the Blatz Ko rubber model (material 7 in LS-Dyna3d). The remaining materials are modelled by using rigid parts. Figure 9.31 shows the FE model of the flexible forming example. The sheet consists of 960 shell elements, the rubber membrane of 2520 brick elements, and the die of 540 rigid shell elements. The pressure is first

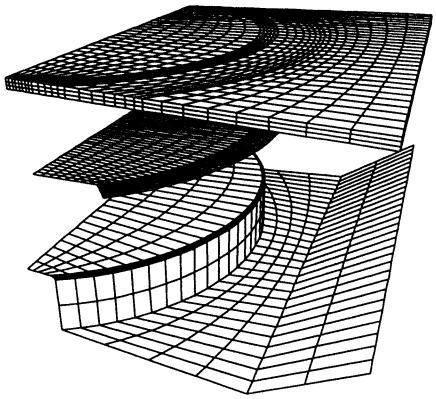

Figure 9.31: *The FE model of the flange including the rubber membrane, blank and die*

increased to 0.3 MPa during the first 10 msec and then raised to the final pressure of 10 MPa after 20 msec. Figure 9.32 shows the sheet in its initial state, in two intermediate states, and in its final state. The final configuration is shown in figure 9.33, where the

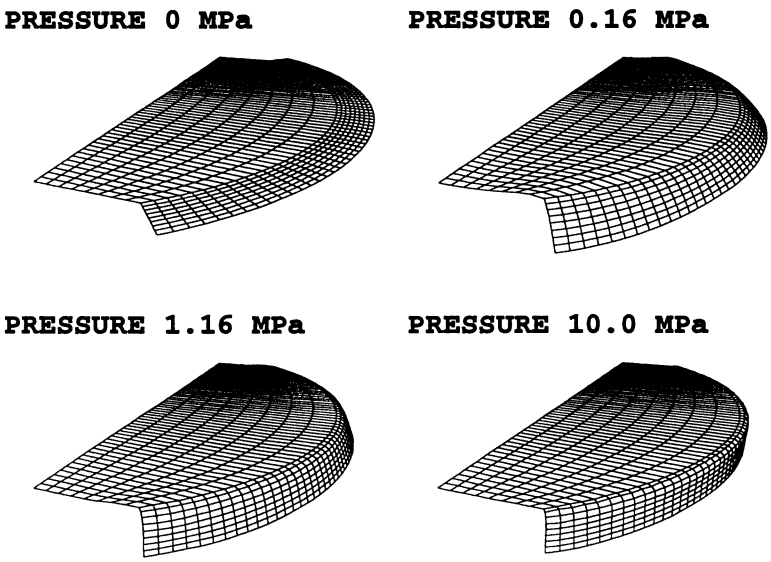

Figure 9.32: *Deformation of the sheet during pressing*

rubber sheet is included. The example is analysed both with and without mass scaling. In order to evaluate the differences between the two solutions we have compared the thickness distribution along the centre of the sheet, see figure 9.34. In this example we have obtained a speed-up of a factor of three and the results both with and without mass scaling agree well. We have also analysed an example using a higher flange, see figure 9.35. As it

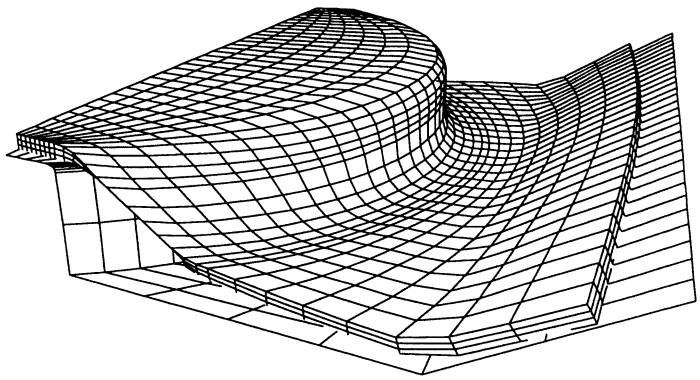

Figure 9.33: *Illustration of the predicted final configuration illustrating the position of the part of the rubber pad included in the analysis.*

appears from figure 9.35 the wrinkling becomes obvious for the higher flange. Figure 9.36 shows some curves for the CSP value for the two areas (A and B see figure 9.35), each area consists of 4 elements. A clear indication of the loss of stability is noticed in all CSP curves. In order to check whether the loss of stability can be predicted from the history of the CSP an estimation was made on the basis of linear regression. The regression is based on 4 points and 3 regression lines corresponding to various stages of the process are included in figure 9.36. The loss of stability seems to be predicted with reasonable accuracy. This example indicates that regression methods may be used in connection with the proposed CSP method in order to predict instabilities in advance. Although the curve for position A has a relatively high peak at 2.25 MPa the instability point predicted agrees quite well with the latter development in CSP value. As it appears from most of the CSP examples included in this thesis there is normally some scatter in the CSP value and it can apparently be an improvement to fit the values to a straight line. The last of the 4 points used for each regression is indicated by the line type label in figure 9.36, for instance 2.75 MPa indicates the use of points between 2 and 2.75 MPa.

As it appears from figure 9.36, region B looses its stability after a pressure of 3 MPa has been applied. For region A the loss occurs a bit later - between 4 and 4.25 MPa, however, looking at figure 9.35 the folding at region A is invisible but it develops later on. Figure 9.35 also shows that although a pressure of 10 MPa is applied at maximum load the shape is clearly influenced by the folds formed at an earlier stage in the process. This effect is characteristic of most sheet metal forming processes: If wrinkles have been introduced it is almost impossible to squeeze them out later in the process. Even if the wrinkles can be squeezed out the product will suffer from the inhomogeneous deformation which arises due to wrinkling.

Brännberg [36] has a more detailed discussion on the simulation of this process. He also compares numerical and experimental results obtained at the Sheet Metal Laboratory, Aalborg University and concludes that good correlations between the strains are obtained. The shape after spring back is also discussed and the shape corresponds well with with experimental findings.

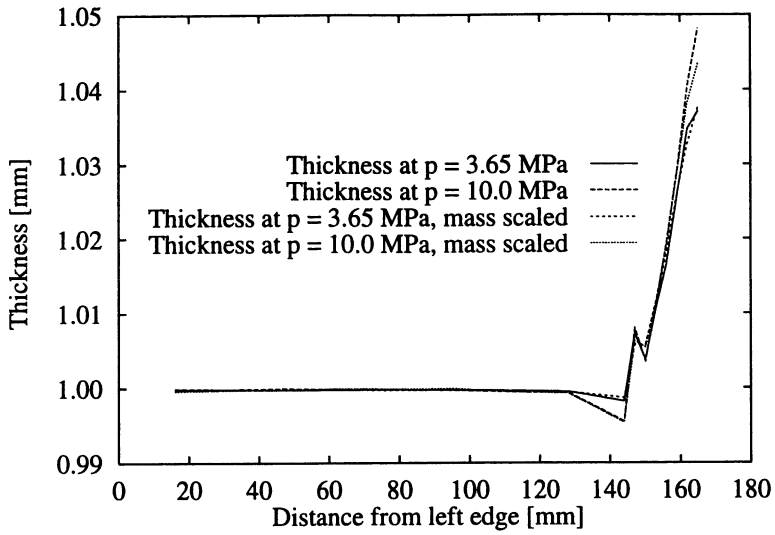

Figure 9.34: *Sheet thickness distribution in the flexible forming example.*

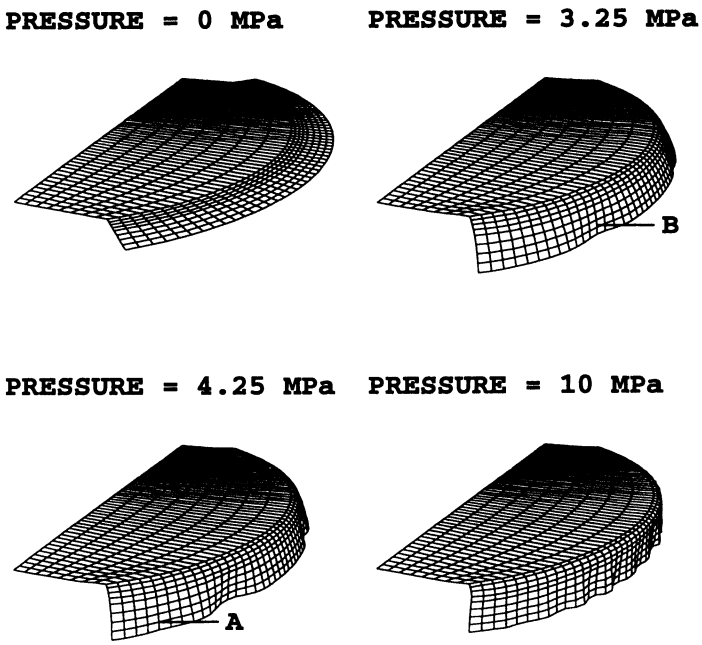

Figure 9.35: *Deformation of the sheet during pressing. The flange height has been increased to provoke wrinkling.*

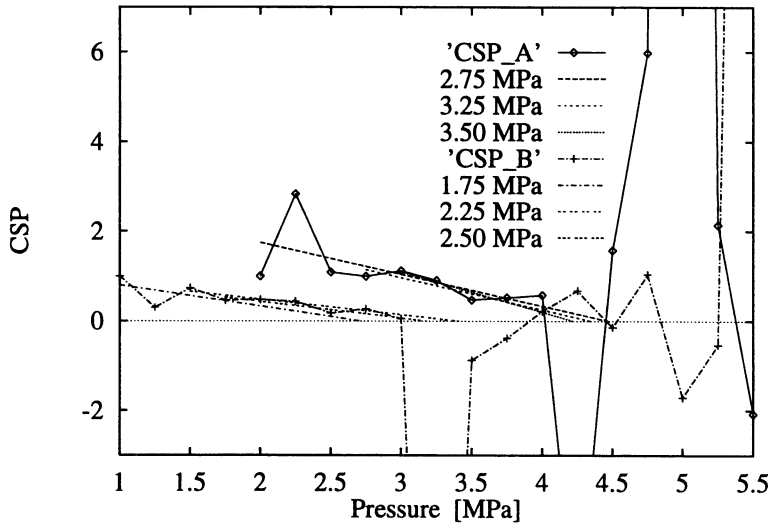

Figure 9.36: *Calculated CSP for the flexible forming process including predictions for loss of stability.*

9.4 Simulation of tube bending

The purpose of the following section is to illustrate how effectively the explicit FE-method can be used to clarify problems occurring in a tube bending process. Many companies struggle with problems related to specific processes. The resulting quality may be too poor or the failure rate too high, etc. Many approaches are used for solving these problems or at least reduce them from trial and error experiments to more sophisticated methods based on data registration and statistics. However, when using this type of analyses it is not always guaranteed that the cause of the problem is correctly identified or that the improved result is really related to the parameter which has been adjusted. In connection with the above approaches FE-simulations can give additional valuable information - it is possible to check whether a given parameter really has the suggested effect and in many cases the simulations make it possible to explain the mechanism which leads to the improvement.

A Danish company discovered that one of their bending processes led to severe problems. Although the problems were well-known in the company no systematic approach had been tried out in order to eliminate the problem. The problems could be separated in two: a) occasionally problems due to the occurrence of buckles and b) the cross section of the bend profile became oval rather than circular. The approach utilized in the company was to change tool geometry in an attempt to improve shape tolerances when the problem was so pronounced that something had to be done.

This particular pipe bending process was investigated by a group of students [50] who came to the conclusion that the buckling which sometimes occurs was due to variations in the material parameters. Figure 9.37 shows a tube with buckles. Firstly the tube bend-

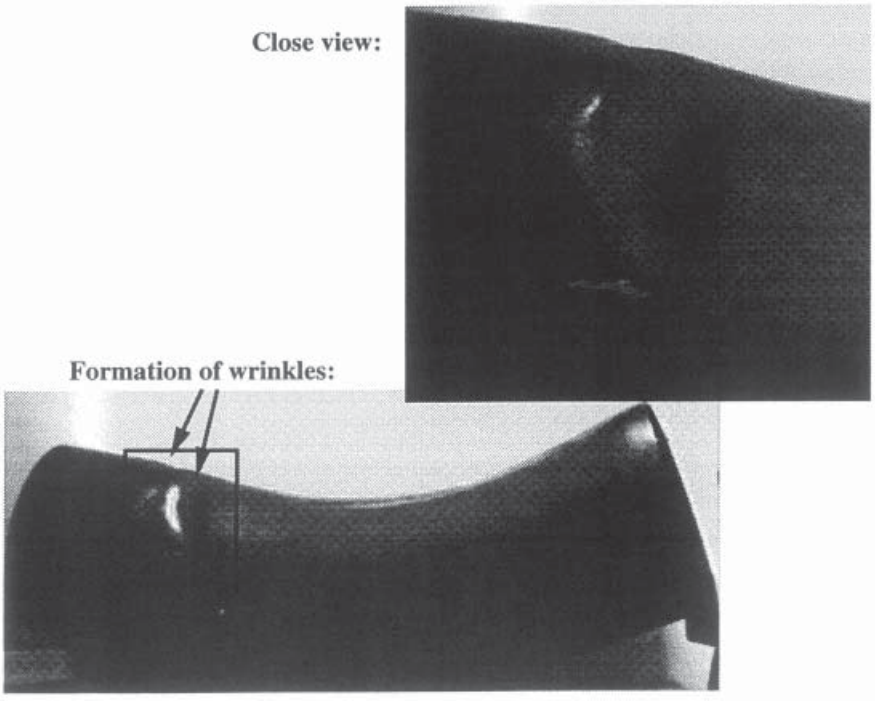

Figure 9.37: *Photos of the bend tube. The typical formation of wrinkles consists of two wrinkles as indicated in the figure.*

ing process is simulated in order to clarify whether the buckling problem really is related to variations in material parameters, secondly the problem is analysed with the proposed methods for detecting onset of instability, and thirdly FE-simulations are combined with an optimization scheme to reach an optimal tool geometry. The example is very illustrative and demonstrates clearly some of the benefits which can be obtained by using FE to simulate processes.

9.4.1 The pipe bending process considered

The considered bending process is a so-called draw bending operation. Figure 9.38 shows the principle of draw bending. Other commonly used methods for bending tubes are

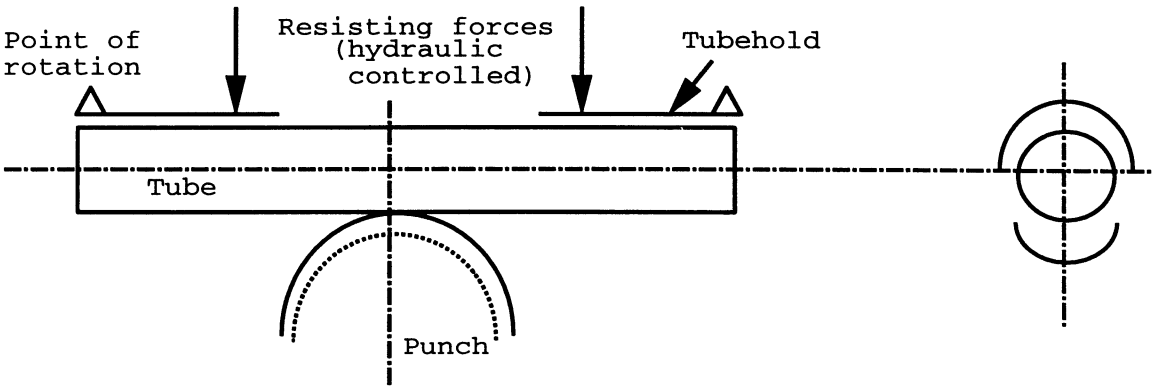

Figure 9.38: *Illustration of the stretch bending process. The tube holds are free to rotate around a fixed point, the only adjustable process parameters are speed and tube hold.*

stretch bending and compression bending. These processes are in principle almost identical, the only difference is the fact that the two may be considered an improvement of the draw bending process. The improvement is obtained by overlaying tensile or compressive stresses during the bending process.

The most common problem in tube bending is the collapse of the tube (at least for ductile tubes), and it can be necessary to use internal mandrels or to fill the tubes with for instance sand. Is the pipe made of less formable material fracture due to necking can also be a problem.

As regards the given problem it was a demand that internal mandrels and fillings should be avoided. This demand gives a limiting ratio between the bending radius and the tube diameter in order to avoid collapsing of the tube. To control the bending process the two rotating tool parts are connected to hydraulic controlled pistons.

9.4.2 The buckling problem

The primary process problem is as mentioned related to batches where a marked difference in the material behaviour appears. Figure 9.39 shows the typical material behaviour of materials belonging to batches of tubes where buckles occur and to batches where no buckles occur. The figure shows the relation between load and extension, and it is obvious

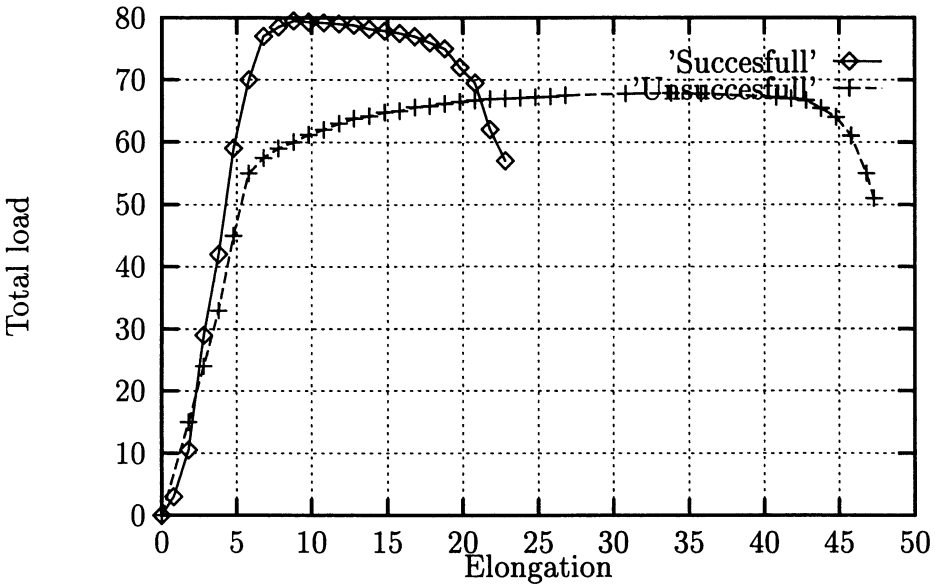

Figure 9.39: *Typical behaviour of materials which could be bend successfully and unsuccessfully, respectively. Data is taken from [50].*

that the elastic region is over-predicted either due to elastic deformation of the testing machine or due to sliding between the grips and test specimen. Hardness measurement of the tubes indicated a significant difference in yield stress. Although this discrepancy in material behaviour is clear, it can be difficult to judge whether the buckling problem is related to this difference or to some other variations. To investigate the effect of variation in material properties a FE-model is made as described in 9.4.3 and it is proved that variation in material parameters has a significant effect on the tendency to buckle.

9.4.3 The FE-model

To model the bending process which is described above, double symmetry is assumed. Later on it was verified with a complete model without symmetry conditions that no buckling modes seem to be constrained when using this approach. The results which are reported below concern the same model apart from the constitutive parameters.

At first the stress strain curve was fitted to Hollomon's expression $\sigma = K\epsilon_{eq}^n$ and material type 18 in LS-Dyna3d was used. When using material type 18, the initial yield stress is determined as:

$$\sigma_0 = K\epsilon_0^n \quad with \quad \epsilon_0 = \left(\frac{E}{K}\right)^{\frac{1}{n-1}} \quad or \quad \epsilon_0 = e^{(\frac{1}{n}ln(\frac{\sigma_0}{K}))} \tag{9.1}$$

The expression in 9.1, however, under-estimates severely the initial yield stress of the material. To model a process where it is critical to capture the transition from elastic to plastic deformation correctly, a good description of the material behaviour for small strains is essential. The material model, developed in this work, was slightly modified, which made is possible to describe the material behaviour with an initial yield stress combined with hardening following the Hollomon-Swift rule. No mass scaling was used as the mesh was very homogeneous. It was instead chosen to scale the velocity.

9.4.4 Numerical results with regard to material property variation

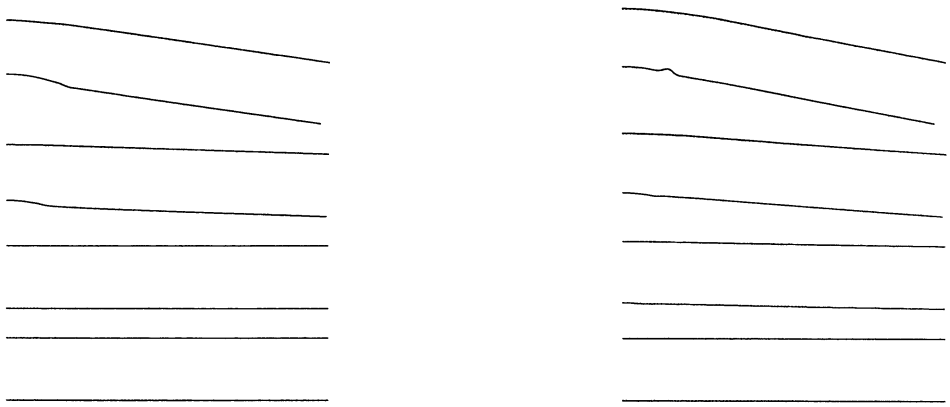

Figure 9.40: *Process evolution seen at four stages for the symmetry lines in the plane of the bending. Right: The successful bending. Left: The unsuccessful bending. (Bottom: The unbent tube, Top: The tube at a stage where the unsuccessful bending clearly shows the formation of a buckle.)*

Figure 9.40 shows the symmetry section at various stages in the process for pipes bent without formation of buckles (left) and for the pipes which buckled (right). The two upper left figures show clearly how the diameter is reduced on a relatively early stage in the process. The upper right figure shows clearly a buckle. The only discrepancy between the two simulations is the modelling of yield stress as a function of plastic straining.

The buckling of the tube is to some degree similar to the formation of wrinkles in a more traditional sheet forming operation and the methods proposed in sections 6.3.1 and 6.4 have been tried out on both the successfully and the unsuccessfully bent tubes in order to clarify whether reliable predictions are achieved. Figure 9.41 shows on the left side a quar-

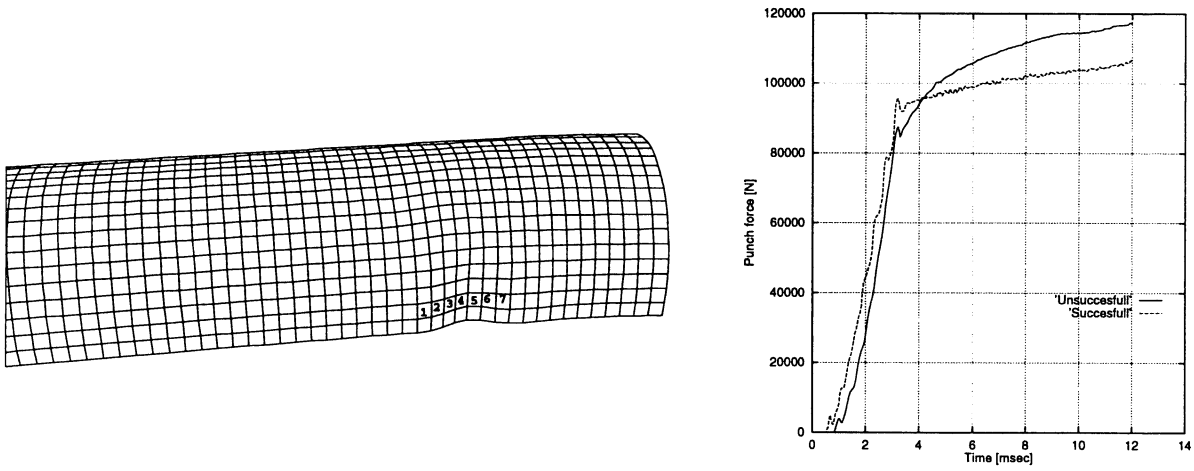

Figure 9.41: *Right: Position of the considered elements, Left: Punch forces predicted numerically for the successful and unsuccessful bending, respectively.*

ter of the deformed tube with an identification of 7 elements which are investigated closer in connection with the CSP method and the Rayleigh coefficient based method. The right side shows the predicted punch forces using the two material descriptions corresponding to buckling and no buckling, respectively. It can be noticed that the evolution of punch force is almost the same in the two examples - from this it can be concluded that although some buckling takes place it is not of the same drastical nature as for instance flange wrinkling in a cup drawing process, where there normally is an abrupt drop in punch force as the resistance towards draw-in almost drops to zero. If we look very carefully at figure 9.41 it may be possible to detect the onset of buckling; from a process time of approximately 0.009 to 0.0105 seconds the punch force for the unsuccessful material is positioned at an almost constant level eventually indicating a load maximum, but according to my judgement one will not at first glance consider this type of punch force critical. Figures 9.42 and 9.43 show

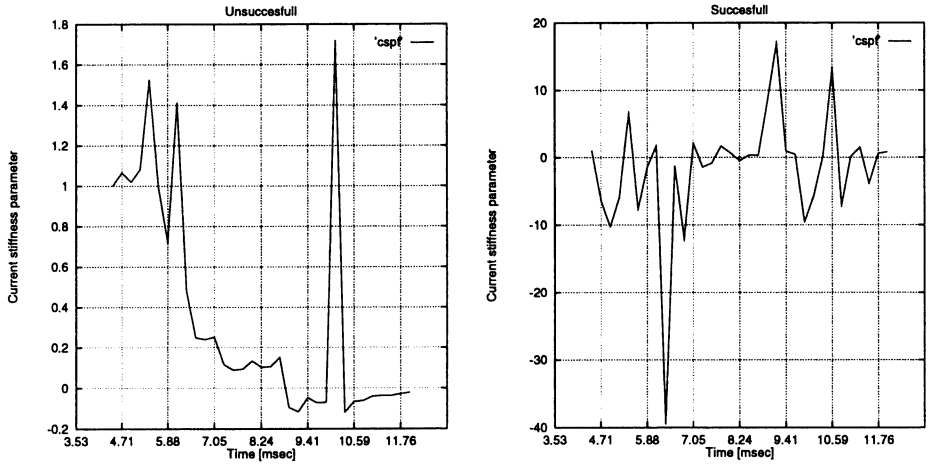

Figure 9.42: *Example of the CSP value variation for identical regions (element 2-6) for the unsuccessful and successful bending.*

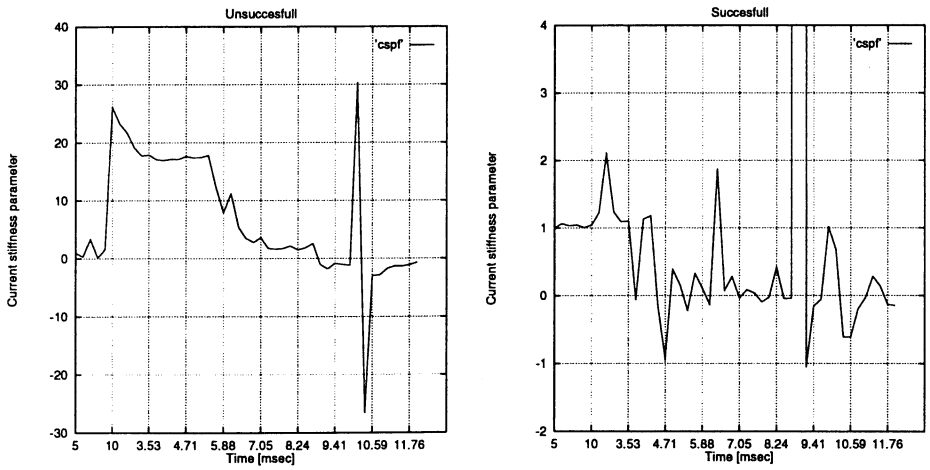

Figure 9.43: *Example of the CSP value variation for identical regions (element 1-7) for the unsuccessful and successful bending.*

the variation in the CSP value for regions consisting of 5 and 7 elements, respectively. The considered elements are shown in figure 9.41. In the figures 9.42 and 9.43 the left curves

show the results of the buckling tube. These curves show a behaviour very similar to the sheet forming operations analysed earlier, see sections 6.13.1 and 9.2.6. Both of the regions indicate the same point of loss of stability. The right sides of the figures 9.42 and 9.43 show the variation in CSP in the successful bending for corresponding regions. However, these values are much more scattered and the line where CSP equals zero is passed several times during the period. A CSP value equal to zero should indicate a loss of stability, a loss which cannot be found from the postprocessing of results . This can be explained by the fact that if we have a steady plastic deformation which leads to folding, we can detect the point of loss of stability. However, in the case where the structure remains stable and hereby the region becomes dominated by elastic loading it is evident that dynamic effects are present which destroy the reliability of the CSP method. One way to improve the behaviour may be to give a threshold for the CSP value; e.g to consider that if the loading on a region is insufficient to cause a given level of deformation (the limit may be set to plastic deformation) over the time step then the CSP value should be kept constant.

As the process progresses the actual zone of bending is moving away from the symmetry section, and an explanation of the scatter in the CSP value can be the fact that the considered region reaches a maximum bending load followed by a decrease whereby no further dissipation of energy due to plastic deformation takes place. If this is the situation the variation in internal forces will be strongly influenced by elastic stress waves which with a more random nature may cause the scatter; elasticity will also cause the response to be influenced by significantly higher frequencies. It is obvious that when the CSP approach is based on assumptions of static behaviour, then the inertial effects of the structure may influence the measure so much that the measure becomes meaningless - the demand that the investigated problems show a sufficiently high accuracy of the geometric configuration (compared to the quasi-static problem) may not be sufficient: If the structure is exposed to overlaid vibrations, these vibrations may cause a shift in the sign of the CSP-value.

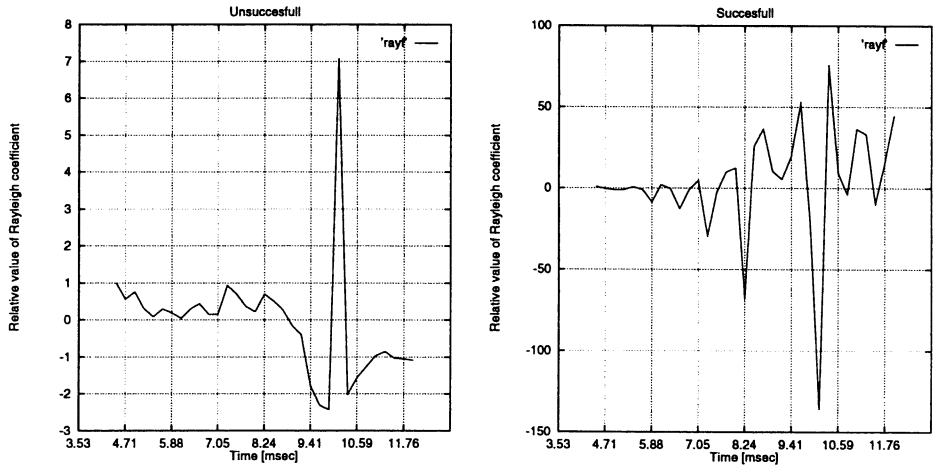

Figure 9.44: *Example of the the variation in the relative value of the Rayleigh coefficient for identical regions (element 2-6) for the unsuccessful and successful bending.*

Figures 9.44 and 9.45 show the variation of the Rayleigh coefficient for the same regions as used for determination of the CSP-variation. The Rayleigh coefficient if calculated from forces and displacements. The left side of the figures gives the situation where the pipe buckles during bending and the right side gives the results for the pipe successfully bent.

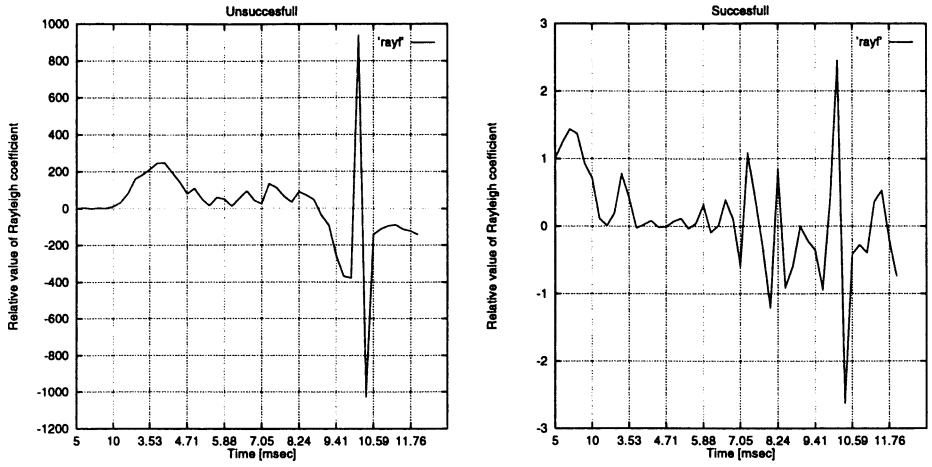

Figure 9.45: *Example of the the variation in the relative value of the Rayleigh coefficient for identical regions (element 1-7) for the unsuccessful and successful bending.*

For the pipe which fails a very clear indication of the loss of instability appears. However, for the successfully bent pipe the results are just as hard to decipher as the CSP-results. The Rayleigh coefficient does also indicate a behaviour which is influenced by elastic deformation. Figure 9.46 shows the development of longitudinal stresses for element number 4,

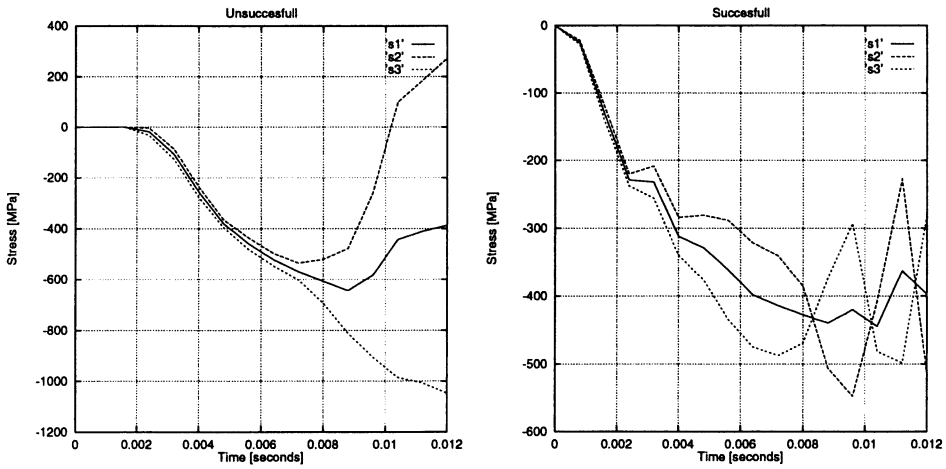

Figure 9.46: *Development of local stress σ_{11} for the element with number 4 in figure 9.41 for the unsuccessful and successful bending. The stresses are plotted for three points; s3 at the outer surface, s1 at the middle plane and s2 at the inner surface.*

see figure 9.41, for the unsuccessfully and the successfully bent tube left and right, respectively. The above mentioned explanation to the fact that the CSP value is very scattered seems to be confirmed by the development in the stresses. The buckling tube shows a steady increase in stress up to approximately 7 msec followed by a decrease in the outer surface point (s2), an increase in the inner surface point (s3) and as regards the value at the middle plane (s1) a drop appears at approximately 9 msec, which is in good agreement with the predicted loss of stability at 8.7 msec. Another characteristic is the fact that the membrane stress does not drop to zero which indicates a remaining load carrying capability. This is in good agreement with the predicted punch forces which does hardly seem to be affected by the buckling formation. As regards the successfully bent pipe it is a

somewhat different picture: The stress raises faster here, and after approximately 8 msec a vibrational effect appears, however, the membrane stress is reasonable steady and shows a slightly increasing value indicating that the region starts unloading from approximately 8 msec.

It may be noticed that for the present example we have a deviation between surface stresses before the point in time where loss of instability is found with the CSP- and the Rayleigh-measure; this is different from the beam and plate buckling and the flange wrinkling which are examples where the loss of stability may be detected from postprocessing the resulting stresses.

The results obtained with the instability indicators suggest that this particular process is very sensitive to the description of hardening behaviour. In order to check how important this can be two analyses are performed. The analyses are identical apart from the initial yield strength prescribed. The hardening is assumed to follow a Hollomon-Swift curve generated with n=0.06 and K=1230 MPa, ϵ_0 is determined from an initial yield stress of 300 and 400 MPa, respectively, Figure 9.47 shows the contours of von Mises equivalent

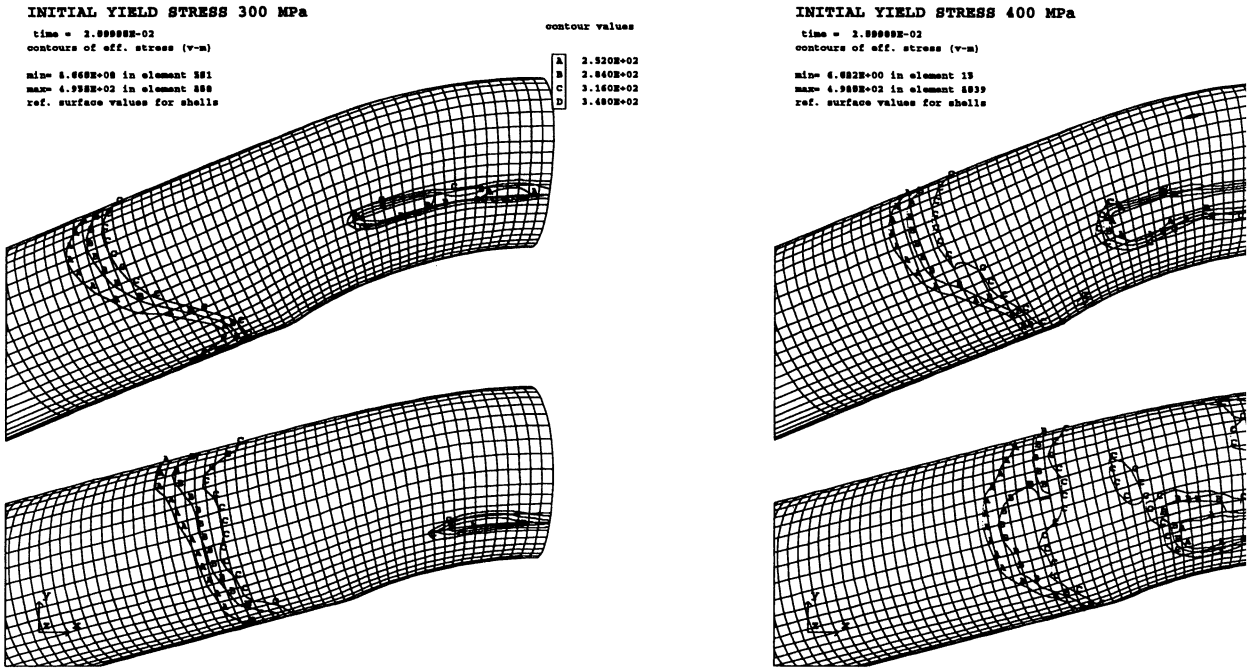

Figure 9.47: *The figures show the distribution of von Mises equivalent stress at two stages in the process. The material was modelled with n=0.06 and C=1230 MPa and a given initial yield stress. Left where the initial yield stress was 300 MPa and right 400 MPa.*

stress at two stages (relatively early) in the bending process. Left for the situation where the initial yield strength is 300 MPa and right the situation where the initial yield strength is 400 MPa. The contour lines are made so that an equivalent stress corresponding to onset of yielding is placed between contours B and C. If we first consider the three contour lines placed left on each pipe it can be seen that the zone which is experiencing plastic loading is significantly larger for the pipe modelled with $\sigma_0 = 300$ MPa. Another aspect can also be seen: The part of the pipes being close to the symmetry plane indicates that larger regions

have been unloaded for the pipe with $\sigma_0 = 400$ MPa than for the pipe with $\sigma_0 = 300$ MPa. It can thus be stated that the explanation to the fact that the two methods lead to a very scattered response indeed is due to a local unloading of the pipe.

These analyses of the bending process may not be too accurate in an absolute sense, but the qualitative results obtained are believed to be just as important and it is possible to explain the phenomena. With this understanding it becomes possible to solve the process problem more efficiently than with the traditional trial and error approach.

9.4.5 Optimization of tool geometry

Another well-known problem when bending tubes is that the cross section in the bent pipe is not circular; during bending the tubes tend to become oval rather than circular. In order to improve the shape of the cross section one can change the tool geometry. Franz [73] considers various methods for cold bending of tubes and notices that use of tools with an elliptical shape of the cross section can improve the final result.

In the following we consider a tube made of the material that is described as successful in section 9.4.3. To illustrate the possibilities of using numerical analyses already in the design/tool design phase a number of analyses are performed showing the effect of variations in tool geometry.

As an example of how to obtain an "ideal" tool geometry the following criterion is set up. As a measure of the quality of a bent tube we will use the cross section at the symmetry plane. The ideal shape is circular and the deviation from the circle is calculated as the sum of the squared distances between node position and the circle; the ideal circle is taken as the mean "circle" obtained with the current tool design.

The cost function which is to be minized is:

$$ERROR = \sum_{i=1}^{n} \left(r_i - \sum_{j=1}^{m} \frac{r_j}{m} \right)^2 \tag{9.2}$$

where r_i is the actual radius in node i. For the specific discretization the value of n and m is 48. To perform the optimization two design variables (ρ_1, ρ_2) were chosen, see figure 9.48, a change of the value away from 1 leads to an elliptical cross section of the tool. The bent tubes had to fulfil some quality demands which could be used directly in the optimization procedure as constraints.

- Buckling: Maximum 25 per cent of the wall thickness
- Ovality: Maximum 6 per cent calculated as:
  $2(d_{max} - d_{min})/(d_{max} + d_{min})$
- Bending angle: Maximum deviation:
  - +/- 2 degrees for $d > 200$ mm
  - +/- 1 degrees for $d > 200$ mm

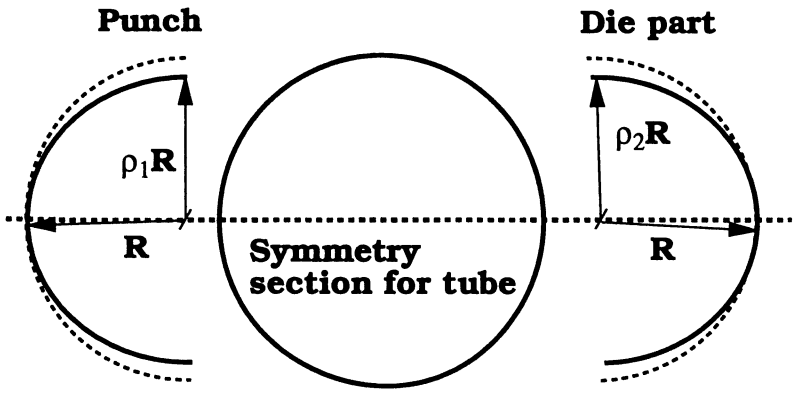

Figure 9.48: *The design variables ρ_i have the initial value 1, corresponding to circular cross sections of the tool parts. By choosing the design variables different from 1 an elliptical shaped cross sections are obtained for the tool parts.*

- Thinning: Minimum 85 per cent of nominal thickness

The demands arise from international norms and fulfilling of the norms is a must for the company. In the optimization there was no control of the bending angle, as it was considered uncritical compared to the other demands. To obtain a correct angle the main problem is to adjust the punch stroke length.

First a basic analysis with $\rho_i = 1$ (corresponding to the present geometry) is performed followed by two analyses where ρ_1 and ρ_2 are changed, respectively, in order to estimate the sensitivity to variations of the tool geometry. This sensitivity was calculated by using finite differences and the change in ρ_i for this purpose was 0.001 which turned out to be rather stable.

In order to choose the next design stage some additional constraints were given: The maximum allowable change in design variable between two stages is set to 0.02, and furthermore in the case where the ratio between the two sensitivities $(\frac{\partial ERROR}{\partial \rho_i})$ increased above a factor of 10 only the strongest sensitivity was taken into account.

Based on these rules and the design sensitivity a new basic design is chosen by using the steepest descent method. By following this procedure the improvement in shape of the cross section illustrated in figure 9.49 can be obtained. Figure 9.49 shows the obtained geometry for the cross section at each stage in the optimization. In the figures the cross section obtained for a given set of design variables is plotted with a full line. The dotted line gives the corresponding ideal shape (the mean circle). Upper left is shown the resulting geometry with ($\rho_1 = 1$, $\rho_2 = 1$). Upper right is given the first improved tool design with ($\rho_1 = 0.98$, $\rho_2 = 0.98$), the changes in design variables found with the steepest descent method were above 0.02 which activate the additional constraint. The middle left figure shows the second improved geometry; here only ρ_2 is changed due to the constraint where the lowest sensitivity is set to zero if the factor between the two sensitivities exceeds 10. Furthermore the step is limited by the maximum allowable step length. Middle right shows the situation for the third improved stage - the procedure to arive at this design stage is similar to the previous one. This geometry is very close to the mean circle, but it can be noticed that the regions which for the initial design were outside the circle now appear

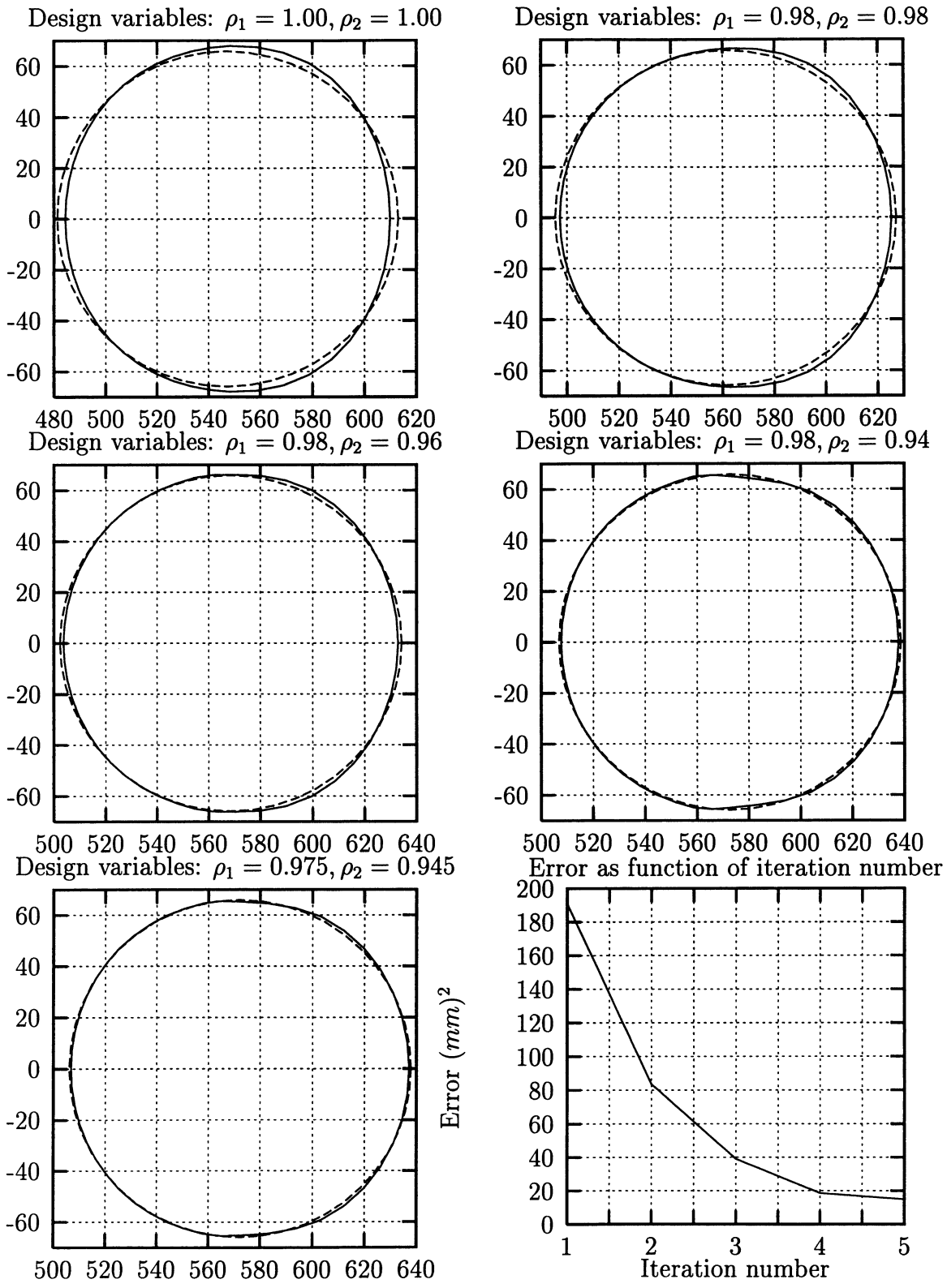

Figure 9.49: *Obtained shape for the symmetry section for current tool geometry ($\rho_1 = 1, \rho_2 = 2$) followed by four stages in the optimization procedure. (The values of the design parameters are shown above the figure). The last figure indicates the error as function of iteration (1 corresponds to initial design). Dotted lines indicate the optimal circular shape and the fully drawn line is the predicted cross section.*

on the inside the circle. The fourth and final obtained design stage (lower left part of the figure) corrects this "overshoot" - the design variables (0.975, 0.945) are now obtained without the two additional constraints being active. In the lower right part of the figure is given the value of the error function as function of design stage with 1 being the initial geometry and 5 corresponding to the fourth improved geometry. The initial deviation is as high as 190 mm^2, already after one change in geometry the error is decreased to $\approx$ 80 mm^2. After four improvements the resulting error is as low as 17 mm^2 which is believed to be close to the optimal (with the current principle of describing the tools). The curve indicates a fast improvement in the error function and the curve appears to converge towards a value around the 17 mm^2.

9.4.6 Conclusion

Based on the analysis it is concluded that the choice of hardening description can be crucial for the results. Especially when using the material option 18 in LS-Dyna3d one must be aware of the estimated initial yield strength, which typically is estimated too low. In most practical sheet forming analyses this does not have any crucial effect, but when analysing wrinkle formation this can lead to an effective modulus far too low compared with experimental results.

It can also be concluded that analyses very close to what is seen in an industrial environment can be performed and it is clearly demonstrated how effectively the FE-analysis can be used for practical purposes. FEM-simulations can be used to verify the effect of possible variations, in this particular example it was variations in material properties, and based on this new information changes can be made in the production in order to eliminate the problem. It is also clearly demonstrated how effectively the simulations can be used to perform an optimization of tool geometries. If the same information had to be obtained by experimental means (trial and error) the cost would have been substantially higher.

Although the analysis was made without any direct experimental verification apart from the visual judgement, it is concluded that the model yields reliable results.

Chapter 10

Conclusion and Future Work

Several examples have been analysed using the explicit finite element method and we can draw the conclusion that the method is indeed very stable. But on the other hand, it is realized that a considerable training is required to become acquainted with LS-Dyna3d primarily due to the complexity of the programme. In my opinion it is necessary to have an employee who works almost full time with the code and the problem class in order to be able to perform an efficient modelling and to keep up with the development of the code. One may suggest that the code is simplified and altered directly towards sheet forming problems, however, I believe that it is the huge amount of possibilities available in LS-Dyna3d, which makes the difference between LS-Dyna3d and most other available FE-programmes (which are suitable for simulating sheet forming): It is hard to imagine a sheet forming operation which cannot be modelled with LS-Dyna3d - but I do not go as far as to say that it is easy.

Several solution strategies are discussed which lead to the conclusion that, if possible, the loads should be applied following trigonometric functions in order to reduce disturbances when loading the model.

Today adaptive remeshing is of great interest, however, I believe that nothing can be gained seen in relation to sheet metal forming; as the computer resources become cheaper one may just as well employ a fine mesh from the beginning of the analyses. If it is necessary with a very fine mesh, e.g. when the sheet passes a draw bead, it is doubtful whether a shell formulation is suitable at all. It is obvious that in the area of bulk forming the situation is different due to a very high distortion of elements, however, as long as the sheet forming problems are modelled with shell elements (assuming plane stress) I do not find that adaptive remeshing is any significant improvement.

The simulation of spring back is a weak point in the explicit method, especially when the parts are relatively flexible. This point has been reduced by by combining explicit and implicit solvers. However, these first attempts do not eliminate the problem due to the nature of the explicit method where the stress situation change from one time step to the next; assuming that the stress distribution corresponds to the static load before spring back is apparently wrong.

As regards the solution methods I conclude that the level of today's codes and theories is

sufficient to perform efficient analysis - the weak point is still the constitutive models of material behaviour and friction.

If we consider a typical approach which is based on shell elements, the solution methods may be improved by taking contact pressure into account in the stress update; the contact stresses can in some deep drawing operations be relatively high and hereby influence the process results.

In the thesis three methods are proposed for the detection of instability points during the analysis. The methods seem to give a response which can be interpreted directly for the simple examples given in the thesis. The method based on Hill's uniqueness criterion does not detect the buckling phenomena for the square plate investigated; this is believed to be due to the nature of the problem. If the plate is perfect a bifurcation point is most likely not to be detected during analysis; the deformation will follow the primary (unstable after the bifurcation point) path. In the analysis a trigger force is used to force the deformation to follow the second path, however, this particular example is stiffening after the bifurcation. The methods based on the CSP-measure and Rayleigh coefficient seem to be very strong to capture most of the instability problems (for the simple examples investigated).

When it comes to more complicated situations it is much harder to decipher the direct meaning of the resulting curves. In order to be an efficient tool the methods must be refined and may thus become of practical use for an analyst.

For the wrinkling behaviour some interesting aspects have been discovered. Provided that the loading rate is sufficiently low we obain very good results when the material anisotropy is taken into account. When anisotropy is taken into account it becomes possible to predict the non-symmetric wrinkling typically seen in practise. This indicates once again the importance of a correct modelling of the material behaviour. The analyses also show that the resulting wrinkling mode results from one or more lower modes present relatively early in the process - these findings indicate that the classical approaches over-estimates the onset of wrinkling - however, this is of course dependent on the definition of wrinkling.

The implemented user material gives some additional possibilities compared to the standard material models available in LS-Dyna3d version 920. Especially the option to use coefficients in the yield criterion of an arbitray order makes it possible to model a wide range of materials including Tresca, von Mises, Hill's 48 criterion, and some criteria where an arbitrary choice of exponent can be made, but where in-plane anisotropic behaviour is not taken into account.

In connection with the determination of material parameters it is noticed that the anisotropy depends on the level of plastic straining. Some of the examples indicate that Barlat's 2D criterion in combination with a Hollomon-Swift hardening law cannot take evolution of anisotropy (especially for a high level of strain) into account.

The MK-analysis gives reasonable results and is indeed an effective tool to clarify the influence from various material parameters. With the current programme it is made possible to

utilize two different material descriptions of the homogeneous and the imperfection zone, respectively. Furthermore the material axis can be rotated relative to the prescribed loading (principal strain increments) and, what is different from most reported MK-analyses, the programme takes elasticity into account.

The examples where the analyses are performed with Barlat's 2D criterion produce results close to experimental results in most cases. It is illustrated how important the exponent is both with regard to process performance and the part geometry. These illustrations are evaluated to be important as one apparently must be aware of the influence from the yield function shape on the final product properties. For some of the examples the process signature concept is used to illustrate variations in the process; the concept gives a fast overview of the process and it works directly together with forming limit diagrams. This concept ought to be directly available when postprocessing FE-results.

One of the aspects which is not treated in detail in this thesis is the frictional behaviour. It has been shown by examples that one of the most crucial aspects with regard to obtaining reliable predition is a correct modelling of boundary conditions. For this reason it is concluded that in order to obtain further improvements in the numerical capability to predict sheet metal forming operations the friction phenomena must be understood and described in more detail for future work.

The constitutive behaviour must be described by means of better models in order to improve simulation results, especially when dealing with materials different from mild steel. To improve the constitutive modelling it will be necessary with both more general criteria of yielding and not least a better understanding and description of the change in anisotropy due to straining.

Future work in this area will be the development of a plane stress constitutive model based on the criterion proposed by Barlat and extended to take damage into account as proposed by Lemaitre. The model should be based on parameters that follow the development of straining. Suh et al. [201] indicate in their work a strong dependency between the exponent in Barlat's criterion and the plastic straining.

In the thesis it has been shown that the n-value seems to be important with regard to formability and strain distribution. Formability is strongly connected to this value when formability is estimated from the classical theories. This is also the situation for the process limitations found directly by performing FE-analysis up to the localization of deformation.

However, it is specified with norms that the parameters used in a Hollomon relation is determined from strains within the range 5-20 per cent. This is a very limited range if compared to general sheet forming problems. It can as shown for the bending process lead to problems for low strain processes as well, and it is therefore suggested that more experimental work is performed in order to obtain a hardening description which agrees as much as possible. In this connection I believe that efforts should be made to ensure that biaxial loading is correctly modelled, an improvement may be reached by employing a yield criteria similar to Hill's 92 criterion. The determination of R-values is also specified with norms, but in my opinion some of the norms should be updated, and this in a way

which is more consistent with the theories typically employed in simulations.

Many theories for determining limit strains are available and may be used to estimate formability. However, the theories are based on constitutive modelling and with the above remarks in mind we cannot expect to obtain very accurate results when determining a FLD from the classical theories. The classical methods give possible explanations of mechanisms involved in the fracturing process, and as such they are important to understand in order to solve process problems.

Seen from a practical point Jun's method seems to be able to predict FLDs with a reasonable accuracy when one or more limiting strain points are known. In connection with FE-simulations it is simple to include the FLD for linear strain pahts. However, most processes lead to nonlinear strain paths and in order to take these into account when judging the process severity and remaining formability I propose to use the method suggested by Müschenborn and Sonne (in the simple cases) or to use the FLSD concept; this primarily due to the simplicity with which these can be implemented.

For the experimental determination of FLDs it is concluded that the Marciniak Double Blank Method is the best test method, especially if we claim that a FLD for a given material does exist. It is also concluded that it is dangerous to rely to heavily on simulative tests when evaluating one material compared to another: For the Erichsen test it is shown that one may obtain a larger Erichsen Index for a sheet compared to another even though the other sheet has a FLD above the FLD of the first sheet.

One thing is to propose a lot of possible improvements, another thing is to prove their validity - and it is clear that a considerable amount of work must be carried out in order to provide the necessary background for the proposal of new constitutive models. One of the reasons why we see the limitations in constitutive modelling is due to the experimental difficulties when it is required to obtain a relation between stresses and strains for a loading situation different from uniaxial tension. The most promising approach here may be the use of inverse techniques.

Seen from an industrial point of view the FE-method is in a broad sense ready for implementation in companies. But at the same time it is, based on my own experience, necessary for a company to have sufficient manpower to obtain and not least maintain the competence in the area of FE-simulation of plastic forming operations.

Finally, but not least, I emphasize the potential of using FE-analysis in connection with sheet forming processes. Although it does not seem possible to predict accurate product tolerances if the necessary experience with the actual process and material class lacks, it is postulated that only the qualitative results give tremendous possibilities to solve process problems, investigate process and tool layout and develop new processes.

I believe it will cause so many disadvantages to companies, who do not take full advantage of analysis tools compared to companies who do utilize simulation, with the result that they may not remain competitive.

References

[1] F. Aberlenc and J. L. Babeau. Optris and ficture: industrial tools to modelize sheet metal forming. *VDI Berichte*, (894):467–477, 1991.

[2] P. Adkin and S. J. Harvey. A kinematic hardening model for cyclic plasticity. In *Consitutive Laws for Engineering Materials. Theory and Applications, Vol. I*, pages 485–494. Elsevier, New York, 1987.

[3] S. Aita, E. Di Pasquale, and D. Lefebvre. Industrial sheet metal forming simulations issues in code development, material modelling, validation and design methods. In *COMPLAS III*, 1992.

[4] K. Albrektsen. *Sheet metal testing methods and strain history analysis in sheet metal forming, Ph.D. thesis (in Danish)* . Department of Production, Aalborg University, 1994.

[5] K. Albrektsen, J. F. Andersen, K. B. Nielsen, and J. Danckert. *Eksperimentalkursus i pladeforarbejdning.* Aalborg Universitetscenter, Institut for Produktion, Aalborg, 1994.

[6] J.F. Andersen. *Hydromechanical forming of high strength sheet steels - Ph.D. thesis (in Danish)* . Department of Production, Aalborg University, 1993.

[7] H. Armen. Assumptions, models, and computational methods for plasticity. *Computers and Structures*, 10:161–174, 1979.

[8] R. Arrieux and M. Boivin. Determination of the forming limit stress curve for anisotropic sheets. In *Annals of the CIRP, Vol. 36*, pages 195–198. IDDRG, 1987.

[9] R. Arrieux, M. Brunet, P. Vacher, and T. Nguyen Nhar. A method to predict the onset of necking in numerical simulation of deep drawing operations. In *Annals of the CIRP, Vol. 45*, pages 255–258. IDDRG, 1996.

[10] R. Arrieux and T. N. Nhat. Stress analysis for off axes solicitations in drawing operations. In *IDDRG, 18th Biennal Congress 1994, Recent Developments In Sheet Metal Forming Technology*, pages 339–350. IDDRG, 1994.

[11] D. P. Atherton. *Stability of Nonlinear Systems* . Research Studies Press, USA, 1981.

[12] F. Barlat. Crystallographic texture, anisotropic yield surface and forming limits of sheet metals. *Mat. Sci. Engng.*, 91:55–72, 1987.

[13] F. Barlat, D. J. Lege, and J. C. Brem. A six-component yield function for anisotropic materials. *Int. J. Plasticity*, 7:693–712, 1991.

[14] F. Barlat and J. Lian. Plastic behaviour and stretchability of sheet metals. part 1: A yield function for orthotropic sheets under plane stress conditions. *Int. J. Plasticity*, 5:51–66, 1989.

[15] R. M. Bassette, L. A. Ianonne, M. I. Kapij, and D. W. Mathey. *Instruction Manual, Table Model Version 3.3* . Camsys, New York, 1992.

[16] P. S. Bate. *Finite element modelling of the hydraulic bulging of sheet metal.* Dept. of Metallurgy and Materials Engineering, Aston, Birmingham, newer than 1979.

[17] K. J. Bathe. *Finite Element Procedures in Engineering Analysis* . Prentice-Hall Inc., Englewood Cliffs, New Jersey, 1982.

[18] J. L. Batoz, Y. Q. Guo, and F. Mercier. Accounting for bending effects in sheet metal forming using the inverse approach. In *COMPLAS IV, April 3-6, Barcelona.* Pinerigde Press, 1995.

[19] J. L. Batoz, Y. Q. Guo, and F. Mercier. The inverse approach including bending effects for the analysis and design of sheet metal forming parts. In *Numiform'95.* Balkema, 1995.

[20] N. Bay, T. Wanheim, J. Danckert, and K. B. Nielsen. Modelling and prediction of metal forming. In *Numerical Predictions of Deformation Processes and the Behaviour of Real Materials, editors Andersen, S. I. et al*, pages 1–32. Risø National Laboratory, Denmark, 1994.

[21] Z. P. Bazant and L. Cedolin. *Stability of Structures.* Oxford University Press, New York, 1991.

[22] M. Bellet, E. Massoni, and J. L. Chenot. Numerical simulation of thin sheet forming processes by the finite element method. 7:21–31, 1990.

[23] T. Belytschko. An overview of semidiscretization and time integration procedures. In *Computational methods for transient analysis.*, pages 1–65. Elsevier Science Publishers, B.V., New York, 1983.

[24] T. Belytschko and W.E. Bachrach. Efficient implementation of quadrilaterals with high coarse-mesh accuracy. *Computer Methods in Applied Mechanics and Engineering*, (54):279–301, 1986.

[25] T. Belytschko and L.P. Bindemann. Assumed strain stabilization of the 4-node quadrilateral with 1-point quadrature for nonlinear problems. *Computer Methods in Applied Mechanics and Engineering*, (88):311–340, 1991.

[26] T. Belytschko and B. E. Engelmann. Explicit time integration with enchanced stability for structural dynamics. *Computers and Structures*, 29(4):587–590, 1988.

[27] T. Belytschko and T. J. R. Hughes. *Computationel methods for transient analysis.* Elsevier Science Publishers, Evanston, USA, 1983.

[28] J.Br. Benson. Computational methods in lagrangian and eulerian hydrocodes. *Comp. Meth. Appl. Mech. and Eng.*, (99):235–394, 1992.

[29] P. G. Bergan and T. Søreide. Solution of large displacement and instability problems using the current stiffness parameter. In *Finite Elements in Non-linear Mechanics.* Tapir Press, 1977.

[30] B. Besdo. Total lagrangean strain-space-representation of the elasto-plasticity of metals. In *Consitutive Laws for Engineering Materials. Theory and Applications, Vol. II*, pages 1357–1364. Elsevier, New York, 1987.

[31] D. Besdo. Constitutive laws for metal forming purposes in stress- and strain-space representation. *VDI Berichte*, (894):1–15, 1991.

[32] J. F. Besseling. A Theory of Elastic, Plastic, and Creep Deformations of an Initially Isotropic Material Showing Anisotropic Strain-Hardening, Creeep Recovery, and Secondary Creep. . *Journal of Applied Mechanics*, (58-APM-17):529–536, 1958.

[33] R. O. Bjaerum. *Finite element formulations and solution algorithms for buckling and collapse analysis of thin shells* . Ph. D. thesis, Norges Teknisk Høgskole, Trondheim, 1992.

[34] T. Z. Blazynski(editor). *Plasticity and Modern Metal Forming Technology* . Elsevier Science Publishers Ltd., Cambridge, 1989.

[35] H. E. Boyer. *Atlas of Stress-Strain Curves* . ASM International, Ohio, 1987.

[36] N. Brännberg. *Computational Aspects on Simulation of Sheet Metal Forming.* Institute of Technology, Dept. of Solid Mechanics, LIU-TEK-LIC-1994:08, Linköping, 1994.

[37] N. Brännberg, K. B. Nielsen, and J. F. Andersen. Deep draw anisotropic cylindrical cups. In *Sixth Nordic Seminar on Computational Mechanics, University of Linköping, Sweden*, 1993.

[38] J. D. Bressan and J. A. Williams. The use of a shear instability criterion to predict local necking in sheet metal forming. *Int. J. Mech. Sci.*, 25:155–168, 1982.

[39] J. S. Brew and D. M. Brotton. Non-linear Structural Analysis by Dynamic Relaxation. *Int. J. for Numerical Methods in Engineering*, 3:463–483, 1971.

[40] L. Cannizzaro, F. Micari, and S. Noto la Diega. Finite element analysis of the reversal drawing process. *Jour. Mat. Processing Tech.*, (24):441–450, 1990.

[41] J. Cao, R. Bakkestuen, P. Jalkh, M. C. Boyce, and E. H. Hardt. Improvement of forming height and stability of aluminum parts using active binder control. In *IDDRG, 18th Biennal Congress 1994, Recent Developments In Sheet Metal Forming Technology*, pages 555–566. IDDRG, 1994.

[42] S. Cescotto and Z. Y. Zhu. Modelling of ductile fracture initiation during bulk forming. In *Proceedings of the Fourth International Conference on Computaional Plasticity, Fundamentals and Applications, Part 1*, pages 987–998. Pineridge Press, Swansea, 1995.

[43] X. Chen and R Sowerby. The development of ideal blank shapes by the method of plane stress characteristics. *Int. J. Mech. Sci*, 34(2):159–166, 1992.

[44] E. Chu, M. F. Shi, and J. C. Gerdeen. On a new approach for finite elastoplastic deformations. In *Consitutive Laws for Engineering Materials. Theory and Applications, Vol. II*, pages 1365–1372. Elsevier, New York, 1987.

[45] K. Chung and O. Richmond. Sheet forming process design based on ideal forming theory. In *Numiform'92 - Numerical methods in industrial forming processes.* Balkema, Rotterdam, 1992.

[46] R. D. Cook, D. S. Malkus, and M. E. Plesha. *Concepts and Applications of Finite Element Analysis,3'rd Ed.* . John Wiley and Sons, Madison, Wisconsin, 1989.

[47] M. A. Crisfield. *Non-linear Finite Element Analysis of Solids and Structures* . John Wiley and Sons Ltd, England, 1991.

[48] Y. F. Dafalias. Anisotropy, reference configuration and residual stresses. In *Consitutive Laws for Engineering Materials. Theory and Applications, Vol. I*, pages 69–80. Elsevier, New York, 1987.

[49] F. F. Damborg and M. R. Jensen. *Optimization of draw die geometry with respect to wear using FEM. (Master thesis, in danish).* Dept. of Production, Aalborg University, 1995.

[50] F. F. Damborg et al. *Tube bending (student report, in danish).* Aalborg University, Dept. of Production (not published), Aalborg, 1994.

[51] J. Danckert. *Pladeforarbejdning, Kompendiemateriale.* Aalborg Universitetscenter, Institut for Produktion, Aalborg, 1989.

[52] J. Danckert. Residual stresses in deep draw cylindrical cups. In *Computational Plasticity, Fundamentals and Applications (COMPLAS IV)*, pages 1493–1503. Pineridge Press, Swansea, 1995.

[53] J. Danckert. Experimental investigation of a square cup deep drawing process. In *Numisheet'93, 2nd Int. Conf. Numerical Simulation of 3-D Sheet Metal Forming Processes*, Aug-Sep 1993.

[54] P. P. Date and K. A. Padmanabhan. On the prediciton of the forming-limit diagram of sheet metals. *Int. J. Mech. Sci.*, 34(5):363–374, 1992.

[55] R. De Borst. Integration of plasticity equations for singular yield functions. *Comp. and Struc.*, 26(5):823–829, 1987.

[56] R. De Borst and P. H. Feenstra. Studies in anisotropic plasticity with reference to the hill criterion. *Int. J. Num. Meth. Engng.*, 29:315–336, 1990.

[57] R. De Borst, H.-B. Mühlhaus, J. Pamin, and L. J. Sluys. Computational modelling of localization of deformation. In *COMPLAS III*, pages 483–508. Swansea University, 1992.

[58] E. A. De Souza Neto, D. Peric, and D. R. J. Owen. A model for elastoplastic damage at finite strains: Algorithmic issues and applications. *Engineering Computations*, 11:257–281, 1994.

[59] O. Debordes, M. E. Mouatassim, and G. Touzot. Local numerical integration of large strain elasto-plastic constitiutiv laws. In *Consitutive Laws for Engineering Materials. Theory and Applications, Vol. II*, pages 1373–1382. Elsevier, New York, 1987.

[60] J. S. DeNatale. Computer-aided calibration of constitutive models. In *Consitutive Laws for Engineering Materials. Theory and Applications, Vol. II*, pages 1181–1188. Elsevier, New York, 1987.

[61] E. Di Pasquale, F. El-Khaldi, E. Haug, and S Aita. Development and validation of a general industrial stamping simulation code based on mindlin shell formulation. In *16th Congress IDDRG: sheet metals in forming processes.* Borlaenge, 1990.

[62] B. Dodd and K. Naruse. Limitations on isotropic yield criteria. *Int. J. Mech. Sci.*, 31(7):511–519, 1989.

[63] R. H. Dodds. Numerical techniques for plasticity in finite element analysis. *Computers and Structures*, 26(5):767–779, 1987.

[64] I. St. Doltsinis. Aspects of modelling and computation in the analysis of metal forming. 7:2–20, 1990.

[65] D. C. Drucker. A more fundamental approach to elastic stress-strain relations. In *Proc. of the First U.S. Nat. Conbr. of Appl. Mechanics, ASME 1951*, 1951.

[66] J. L. Duncan and W. Johnson. Plastic deformation and failure of thin square diaphragms. *Int. J. Mech. Sci.*, 10:157–168, 1968.

[67] J. L. Duncan and W. Johnson. The ultimate strength of rectangular anisotropic diapragms. *Int. J. Mech. Sci.*, 10:143–155, 1968.

[68] J. L. Duncan and W. Johnson. The ultimate strength of rectangular anisotropic diaphragms. *Int. J. Mech. Sci.*, 27(9):595–607, 1985.

[69] M. El-Mouatassim, K.M. Detraux, J.L. Batoz, and Y.Q. Guo. Application of an inverse fe-procedure to sheet forming. In *VDI-berichte 894: FE-simulation of 3-D sheet metal forming processes in automotive industry.* VDI-verlag, Düsseldorf, 1991.

[70] S. Ellagoune and M. Boivin. Crit'ere d'apparition des plis en emboutisage. *M'emoires et Etudes Scientifiques Revue de M'etallurgie.*, pages 211–221, 1988.

[71] EN 10 130. *Cold rolled carbon steel flat products for cold forming - Technical delivery condition.* European Commitee for Standardisation, Brussels, 1991.

[72] D.P. Flanagan and T. Belytschko. A uniform strain hexahedron and quadrilateral with orthogonal hourglass control. *Int. J. Num. Meth. in Eng.*, 17:679–706, 1981.

[73] W. D. Franz. *Das kalt biegen von Rohren, Verfahren und Maschinen.* Springer-Verlag, Berlin, 1961.

[74] P. C. Galbraith, J. Finn, S. R. MacEwen, A. R. Carr, K. M. Gatneby, T. L. Lin, G. A. Clifford, J. O. Hallquist, and D. Stillman. Evaluation of an LS-DYNA3D model for deepdrawing of aluminium sheet . *VDI Berichte*, (894):441–466, 1989.

[75] P. C. Galbraith and Hallquist. Sheel element formulations in ls-dyna3d: Their use in modelling sheet metal forming. In *Numisheet'93, 2nd Int. Conf. Numerical Simulation of 3-D Sheet Metal Forming Processes*, Aug-Sep 1993.

[76] J. C. Gerdeen, S. R. Bhonsle, and V. K. Wong. Stress analysis of yoshida buckling test speciment using photoelasticity and finite element method. In *14th Congress IDDRG: Sheet metals-rquirements and solutions*, pages 474–475. München, 1986.

[77] A. Ghali and A. M. Neville. *Structural analysis, 2'nd edition.* Chapman and Hall Ltd., London, 1978.

[78] G. M. Goodwin. Application of strain analysis to sheet metal forming problems in the press shop. *SAE-paper Number 680093*, 1968.

[79] M. Gröber and K Gruber. Numerical simulation of sheet metal forming and large car body components . *VDI Berichte*, (894):587–600, 1989.

[80] J. Gronostajski. Sheet metal forming-limits for complex strain paths. *J. Mech. Work. Tech.*, 10:349–362, 19845.

[81] J. Gronostajski and A. Dolny. The influence of strain path on sheet metal forming limits. In *International Conference on Developments in the Drawing of Metals*, pages 83–86. London, 1983.

[82] M.E. Gurtin. *An introduction continuum mechanics* . Academic Press, Inc., Pittsburg, Pennsylvania, 1981.

[83] J. O. Hallquist. *LS-DYNA3D, Theoretical Manual, LSTC Report 1018.* Livermore Software Technology Corporation, Livermore, 1991.

[84] J. O. Hallquist, D. W. Stillman, and T.-L. Lin. *LS-DYNA3D, Ver. 920, Usermanual: Nonlinea Dynamic Analysis of Structures in Three Dimensions* . Livermore Software Technology Corporation, Livermore, 1992.

[85] J. O. Hallquist, D. W. Stillman, K Scweizerhof, and K. Weimar. Explicit time integration and contacts simulations for thin sheet metalforming. In *Int. Conf. FE-simulation of 3-D Sheet Metal Forming Processes in Automotive Industry*, May 1991.

[86] E. Haug, E. Di Pasquale, A. K. Pickett, and D. Ulrich. Industrial sheet metal forming simulation using explicit finite element methods. In *Int, VDI Conference with workshop FE-simulation of 3-D sheet metal forming processes in automotive industry*, May 1991.

[87] H. Hayashi. Simulation of geometrical surface defects in sheet metal forming by ybt - systematization of a diagonal tensile test of a square plate. In *14th Congress IDDRG: Sheet metals-requirements and solutions*, pages 472–473. München, 1986.

[88] H. Hayashi, K. Miyauchi, and K. Yoshida. Yoshida buckling test: Data sheets. *IDDRG, Detroit,1982*, 1982.

[89] S. S. Hecker. Simple technique for determining forming limit curves. *Sheet Metal Industries*, 11:671–676, 1975.

[90] K Heiduschke, E. Anderheggen, and J. Reissner. Constitutive equations for sheet metal forming. *VDI Berichte*, (894):17–37, 1991.

[91] R. Hill. *The mathematical theory of plasticity* . Oxford University Press, Oxford, 1950.

[92] R. Hill. A general theory of uniqueness and stability in elastic-plastic solids. *J. Mech. Phys. Solids*, 6:236–249, 1959.

[93] R. Hill. A user-friendly theory of orthotropic plasticity in sheet metals. *Int. J. Num. Mech. Sci.*, 35:19–25, 1993.

[94] Y. Hirose, H. Uto, and K Kazama. Square cup deep drawing. In *Numisheet'93, 2nd Int. Conf. Numerical Simulation of 3-D Sheet Metal Forming Processes*, Aug-Sep 1993.

[95] C. Hoff and R. L. Taylor. Higher derivative explicit one step methods for non-linear dynamic problems. part 1: Design and theory. *Int. J. Num. Meth. Eng.*, 29:275–290, 1990.

[96] C. Hoff and R. L. Taylor. Higher derivative explicit one step methods for non-linear dynamic problems. part 1: Practical calculations and comparisons with other higher other methods. *Int. J. Num. Meth. Eng.*, 29:291–301, 1990.

[97] A. Honecker and K Mattiason. Finite element procedures for 3D sheet forming simulation. In *Numiform 89*, pages 457–463, 1989.

[98] A. Honecker and K. Mattiasson. Finite element procedures for 3d sheet forming simulation. In *NUMIFORM'89 Numerical Methdos in Industrial Forming Processes.*, pages 465–479. Balkema, Rotterdam, 1989.

[99] P. Hora, T. Longchang, and J. Reissner. Prediction methods for ductile sheet metal failure using fe-simulation. In *IDDRG, 18th Biennal Congress 1994, Recent Developments In Sheet Metal Forming Technology*, pages 363–375. IDDRG, 1994.

[100] W. F. Hosford and R. M. Caddell. *Metal forming - mechanics and metallurgy.* Ann Arbor, Michigan, 1983.

[101] T. J. R. Hughes and W. K. Liu. Nonlinear finite element analysis of shells - part 2: Two dimensional shells. *Cpmp. Meth. App. Mech. Eng.*, 27:167–181, 1981.

[102] T. J. R. Hughes and W. K. Liu. Implicit-explicit finite elements in transient analysis: Implementation and numerical examples. *J. App. Mech.*, 45:371–378, June 1978.

[103] T. J. R. Hughes and W. K. Liu. Implicit-explicit finite elements in transient analysis: Stability theory. *J. App. Mech.*, 45:371–378, June 1978.

[104] T. Huo and E. Nakamachi. Evaluation of dynamic explicit/elasto viscoplastic finite element method in sheet forming simulation. In *Numisheet'93, 2nd Int. Conf. Numerical Simulation of 3-D Sheet Metal Forming Processes*, Aug-Sep 1993.

[105] K. W. Hutchinson and K.W. Neale. Sheet necking - ii. time independent behaviour. In *Mechanics of Sheet Metals Forming*, 1978.

[106] S. Imatani and T. Inoue. Material anisotropy induced by prior plastic deformation. In *Consitutive Laws for Engineering Materials. Theory and Applications, Vol. I*, pages 573–580. Elsevier, New York, 1987.

[107] H. Iseki, T. Murota, and T. Jimma. Finite element method in the analysis of the hydrostatic bulging of a sheet metal (part 2). *Bulletin of the JSME*, 20:285–291, 1977.

[108] H. Iseki, T. Murota, and T. Jimma. Finite element method in the analysis of the hydrostatic bulging of a sheet metal. *Bulletin of the JSME*, 20(141):285–291, 1977.

[109] H. Ishikawa and K Sasaki. Constitutive modelling of cyclic plasticity considering induced anisotropy. In *Consitutive Laws for Engineering Materials. Theory and Applications, Vol. I*, pages 581–596. Elsevier, New York, 1987.

[110] J. W. Ju, J. C. Simo, K. S. Pister, and R. L. Taylor. A parameter estimation algorithm for inelastic material models. In *Consitutive Laws for Engineering Materials. Theory and Applications, Vol. II*, pages 1233–1240. Elsevier, New York, 1987.

[111] G. Jun. An extension of shear instability model on localized necking. *Advanced Technology of Plasticity*, 3, 1990.

[112] B. Kaftanoglu. Deitrag zur ermittlund der falten 1. ordnung beim tiefziehen. *Blech Rohre Profile*, 32(3):143–149, 1985.

[113] A. P. Karafillis and M. C. Boyce. Tooling design in sheet metal forming using springback calculations . *Int. J. Mech. Sci.*, 34(2):113–131, 1992.

[114] M. Karima, N. Chandrasekaran, and W. Tse. Process signatures in metal stamping: Basic concepts. *J. Mater. Shaping Technol.*, 7:169–183, 1989.

[115] M. Kawka and A. Makinouchi. Shell element formulation in the static explicit fem code for simulation of sheet stamping. In *Numisheet'93, 2nd Int. Conf. Numerical Simulation of 3-D Sheet Metal Forming Processes*, Aug-Sep 1993.

[116] P. Keck, M. Wilhelm, and K. Lange. Application of the finite element method to the simulation of sheet forming processes: Comparison of calculation and experiments. *Int. J. Num. Meth. Eng.*, 30:1415–1430, 1990.

[117] S. P. Keeler. Plastic instability and fracture in sheets stretched over rigid punches. *Dept. of Metallurgy, Massachusetts Institure of Technology*, 1961.

[118] S. P. Keeler. Determination of forming limits in automotive stampings. *SAE-paper Number 650535*, 1965.

[119] S. P. Keeler and W. A. Backofen. Plastic instability and fracture in sheets stretched over rigid punches. *Transactions of the A.S.M.*, 56:25–48, 1963.

[120] T. Keum, E. Nakamachi, R. H. Wagoner, and J. K. Lee. Compatible description of tool surfaces and fem meshes for analysing sheet forming operations. *Int. J. Num. Meth. Eng.*, 30:1471–1502, 1990.

[121] S.W. Key, C.M. Stone, and R.D. Krieg. Dynamic relaxation applied to the quasi-static, large deformation, inelastic response of axisymmetric solids. In *Nonlinear finite element analysis in structural mechanics. Eds. W. Wunderlich et all.*, pages 585–620. Springer, Berlin, 1981.

[122] H. K. Khalil. *Nonlinear Systems* . Macmillan Publishing Company, New York, 1992.

[123] Y. J. Kim and D. Y. Yang. A rigid-plastic finite element formulation considering the effect of geometric change and its application to hydrostatic bulging. *Int. J. Mech. Sci.*, 27(18), 1985.

[124] H. J. Kleemola and J. O. Kumpulainen. Factors influencing the forming limit diagram: Part i - the experimental determination of the forming limits of steel sheet. *J. Mech. Work. Tech.*, 3:289–302, 1980.

[125] H. J. Kleemola and A. J. Ranta-Eskola. Hydraulic bulge device for sheet metal testing. *Acta Polytechnica Scandinavica*, (124):1–19, 1975.

[126] S. Krenk. *Non-linear analysis with finite elements.* University of Aalborg, Aalborg, 1993.

[127] A. C. W. Lau, R. Shivpuri, and P. C. Chou. An explicit time integration elastic-plastic finite element algorithm for analysis of high speed rolling. *Int. J. Mech. Sci.*, 31(7):483–497, 1989.

[128] C. H. Lee and S. Kobayashi. New solutions to Rigid-Plastic Deformation Problems using a Matrix Method . *Trans. ASME, J. Engr. Ind.*, 95:865, 1973.

[129] D. Lee and F. Jr. Zaverl. The influence of material parameters on nonuniform plastic flow in simple tension. *Acta Metallurgica*, 28:1415–1426, 1980.

[130] E. H. Lee and A. Agah-Tehrani. On elastic-plastic finite deformation with strain-induced anisotropy. In *Consitutive Laws for Engineering Materials. Theory and Applications, Vol. I*, pages 161–172. Elsevier, New York, 1987.

[131] J. K. Lee, G. L. Kinzel, and R. H. editors Wagoner. *Numisheet'96 Numerical simulation of 3-D sheet metal forming processes - Verifications of simulations with experiments.* Numisheet'96, Columbus, Ohio, 1996.

[132] S. H. Lee and S. Kobayashi. Rigid-Plastic Analysis of Bore Expanding and Flange Drawing with Anisotropic Sheet Metals by the Matrix Method . In *Proc. 15th Int. Mach. Tool Des. Res. Conf.*, page 561, 1975.

[133] D. J. Lege, F. Barlat, and J. C. Brem. Characterization and modeling of the mechanical behaviour and formability of a 2008-t4 sheet sample. *Int. J. Mech. Sci.*, 31(7):549–563, 1989.

[134] J. Lemaitre. *A Course on Damage Mechanics* . Springer-Verlag, Berlin, 1992.

[135] Z. H. Li and D. R. J. Owen. Elasto-plastic analysis of laminated anisotropic shells by a refined finite element laminated model. *Computers and Structures*, 32(5):1005–1024, 1989.

[136] J. Lian, F. Barlat, and B. Baudelet. Plastic behaviour and stretchability of sheet metals. part 2: Effect of yield surface shape on sheet forming limit. *Int. J. Plasticity*, 5:131–147, 1989.

[137] L. E. Lindgren and J Edberg. Explicit versus implicit finite element formulation in simulation of rolling. *J. Mater. Proc. Tech.*, 24:85–94, 1990.

[138] Z. H. Lu and D. Lee. Prediction of history-dependent forming limits by applying different hardening models. *Int. J. Mech. Sci.*, 29(2):123–137, 1987.

[139] A. Makinouchi, E. Nakamachi, E. Onate, and R. H. editors Wagoner. *Numisheet'93 Numerical simulation of 3-D sheet metal forming processes.* Numisheet'93, Tokyo, 1993.

[140] L. E. Malvern. *Introduction to the mechanics of a continuos medium* . Prentice-Hall, Inc., Englewood Cliffs, N.J., 1969.

[141] Z. Marciniak and J. Duncan. *Mechanics of sheet metal forming* . Edward Arnold, Great Britain, 1992.

[142] Z. Marciniak and K. Kuczynski. Limit strains in the processes of stretch-forming sheet metal. *Int. J. Mech. Sci.*, 9:609–620, 1967.

[143] M. J. M. B. Marques and R. M. S. O. Baptista. Theoretical and Experimental Analysis of Axisymmetric Deep Drawing. *J. Mat. Pro. Tech.*, 24:53–63, 1990.

[144] K. K. Mathur and P. R. Dawson. On modelling the development of crystallographic texture in bulk forming processes. *Int. J. Plasticity*, 5:67–94, 1989.

[145] K. Mattiasson, L. Bernspång, A. Honecker, E. Schedin, T. Hammam, and A. Melander. On the use of explicit time integration in finite element simulation of industrial sheet forming processes . *VDI Berichte*, (894):479–497, 1989.

[146] P. Mazilu, S. Luo, and J. Kurr. Anisotropy evolution by cold prestrained metals described by ict-theory. *Jour. Mat. Processing Tech.*, (24):303–311, 1990.

[147] M. Meier and J. Reissner. Bildung and verhinderung von falten im flansch eines tiefziehteiles. *VDI Berichte*, (450):173–179, 1982.

[148] H. Mikkelsen and J. O. Riis. *Grundbog i Projektledelse, 3'th edition* . Forlaget Promet, Copenhagen, 1989.

[149] G. G. Moore and J. F. Wallace. The effect of anisotropy on instability in sheet-metal forming. *Journal of the Institute of Metals*, 9:33–38, 1964-65.

[150] J. Mortensen. *FEM-simulation of metal forming processes (Master thesis, in danish).* Dept. of Production, Aalborg University, 1993.

[151] J. Mortensen, J. Dirks, and P. Christensen. A combined physical and numerical simulation of tool performance in convenctional deep-drawing operations. In *IDDRG, 18th Biennal Congress 1994, Recent Developments In Sheet Metal Forming Technology*, pages 233–240. IDDRG, 1994.

[152] J. Mortensen and K. B. Nielsen. Backward can extrusion of stainless steel. In *Internationale Cold Forgin Group, 28th ICFG Plenary Meeting, Denmark*, -8 1995.

[153] H. Murakami and A. Chopra. On simulating cyclic hardening of metals. In *Consitutive Laws for Engineering Materials. Theory and Applications, Vol. I*, pages 615–622. Elsevier, New York, 1987.

[154] S. Murakami. Anisotropic damage theory and its application to creep crack growth analysis. In *Consitutive Laws for Engineering Materials. Theory and Applications, Vol. I*, pages 187–194. Elsevier, New York, 1987.

[155] W. Müschenborn and H. M. Sonne. Einfluss des formänderungsweges auf die grenzformänderungen des feinbleches. *Arch. Eisenhüttenwes.*, 46:597–602, 1975.

[156] J. C. Nagtegaal and L. M. Taylor. Comparison of implicit and explicit finite elements methods for analysis of sheet forming problems . *VDI Berichte*, (894):705–725, 1991.

[157] M. O. Neal and T. Belytschko. Explicit-Explicit Subcycling with Non-Integer Time Step Ratios for Structural Dynamic Systems. *Computers and Structures*, 31(6):871–880, 1989.

[158] K. W. Neale and P. Tugcu. A numerical analysis of wrinkle formation tendencies in sheet metals . *Int. J. Num. Meth. Eng.*, 30:1595–1608, 1990.

[159] S. Nemat-Nasser and M. Obata. Micromechanis of plastic flow. In *Consitutive Laws for Engineering Materials. Theory and Applications, Vol. I*, pages 195–206. Elsevier, New York, 1987.

[160] Q. Q. Nie and D. Lee. The effect of rate sensitivity on history dependent forming limits of anisotropic sheet metals. *Jour. Mat. Shap. Tech.*, (0):0–0, 1991, copy for review.

[161] K. B. Nielsen and N. Brännberg. Simulation of the square box deepdrawing process. In *Numisheet'93, 2nd Int. Conf. Numerical Simulation of 3-D Sheet Metal Forming Processes*, Aug-Sep 1993.

[162] K. B. Nielsen, N. Brännberg, and L. Nilsson. Sheet metal forming simulation using explicit finite element methods. In *Structural Dynamics, Eurodyn'93, Volume 2, 2nd European Conf. on Structural Dynamics*, June 1993.

[163] L. Nilsson and M. Larsson. *Saab "crash" program: a route to customer safety* . The SAAB-SCANIA Griffin, LinköpinG, 1987.

[164] P. Nordlund. *Some computational procedures for cracks and wrinkles.* Royal Institute of Technology, Dept. of Solid Mechanics, Stockholm, 1995.

[165] J. T. Oden and J. A. C. Martins. A simple model for dynamic friction effects on mettallic surfaces. In *Constitutive Laws for Engineering Materials. Theory and Applications, Vol. I*, pages 207–212. Elsevier, New York, 1987.

[166] T. Ohwue and E Nakamachi. Finite element analyses of box-shaped cup-drawing and comparison with experiments . *VDI Berichte*, (894):871–880, 1989.

[167] E. Onate and C. A. de Saracibar. Finite element analysis of sheet metal forming problems using a selective viscous bending/membrane formulation. *Int. J. Num. Meth. Eng.*, 30:1557–1593, 1990.

[168] M. Ortiz and E. P. Popov. Accuracy and stability of integration algorithms for elastoplastic constitutive relations. *Int. J. Num. Met. Eng.*, 21:1561–1576, 1985.

[169] M. Ortiz and J. C. Simo. An analysis of a new class of integration algorithms for elastoplastic constitutive relations. *Int. J. Num. Met. Eng.*, 23:353–366, 1986.

[170] N. S. Ottosen. *Aspects of constitutive modelling* . Lund Institute of Technology, Lund, Sweden, 1987.

[171] M. Papadrakakis. Accelerating Vector Iteration Methods. *Journal of Applied Mechanics*, 53:291–297, 1986.

[172] M. Papadrakis. A Method for the Automatic Evaluation of the Dynamic Relaxation Parameters. *Comp. Meth. App. Mech. and Eng.*, 25:35–48, 1981.

[173] K. C. Park. Practical aspect of numerical time integration. *Computers and Structures*, 7:343–353, 1977.

[174] K. C. Park. A Family of Solution Algorithms for Nonlinear Analysis based on Relaxation Equations. *Int. J. for Numerical Methods in Engineering*, 18:1337–1347, 1982.

[175] L. Penazzi, E. Di Pasquale, S. Aita, and E. Haug. Material characterization for the cae finite element simulation of sheet metal forming. In *IDDRG, 17th Biennal Congress 1992, Advanced Sheet Metal Forming Technology*, pages 149–165. IDDRG, 1992.

[176] D. Peric, M. Dutko, and D. R. J. Owen. Universal anisotropic yield criterion based on superquadric functional representation: Computational issues with applications. In *COMPLAS III*, pages 77–102. Swansea University, 1992.

[177] D. Peric and D. R. J. Owen. Computational strategies for strain localisation problems. In *Computational Methods in Applied Science*, pages 63–78. Elsevier Science Publishers B. V., 1992.

[178] W. Prager. Recent developments in the mathematical theory of plasticity. *J. Appl. Phys.*, 20:235–241, 1949.

[179] S. N. Rasmussen. *Limit strains in sheet metal forming.* Laboratory for Mechanical Processing of Materials, Technical University of Denmark, 1981.

[180] S. N. Rasmussen. Discussion on the forming limit stress diagram for prediction of strain path effects in sheet metal forming. *IDDRG, Working Group Mettings, Helsinki, WG II*, 1983.

[181] N. Rebelo, J. C. Nagtegaal, and H. D. Hibbitt. Finite element analysis of sheet forming processes. *Int. J. Num. Meth. Eng.*, 30:1739–1758, 1990.

[182] K. Runesson and A. Samuelsson. Aspects on numerical techniques in small deformation plasticity. In *NUMETA 85, Numerical Methods in Engineering: Theory and applications, ed. J Middleton et al.*, pages 337–348. A. A. Balkema, Rotterdam, 1985.

[183] A. Samuelsson. Mathematical simulation of deep drawing and stretching (abstract). In *Sheet metal forming - Borlänge*, page 6. Swedish Society for Material Technology, Swedish Deep Drawing REsearch Group and Materials Centre HTM, 1992.

[184] I. S. Sandler and D. Rubin. The consequences of nonassociated plasticity in dynamic problems. In *Consitutive Laws for Engineering Materials. Theory and Applications, Vol. I*, pages 345–352. Elsevier, New York, 1987.

[185] M. J. Saran and A. Samuelsson. Elastic-viscoplastic implicit formulation for finite element simulation of complex sheet froming processes. *Int. J. Num. Meth. Eng.*, 30:1675–1697, 1990.

[186] K. Schweizerhof and J. O Hallquist. Explicit integration schemes and contact formulations for thin sheet metal forming. *VDI Berichte*, (894):405–439, 1991.

[187] K. Shung and K. Shah. Finite element simulation of sheet metal forming for planar anisotropic metals. *Int. J. Plasticity*, 8:453–476, 1992.

[188] J. C. Simo and T. J. R. Hughes. General return mapping algorithms for rate-independent plasticity. In *Consitutive Laws for Engineering Materials. Theory and Applications, Vol. I*, pages 221–232. Elsevier, New York, 1987.

[189] J. C. Simo and T. J. R. Hughes. *Elastoplasticity and Viscoplasticity* . No publisher, textbook used for courses, USA, 1988.

[190] J. C. Simo, J. W. Ju, R. L. Taylor, and K. S. Pister. On strain-based continuum damage models: Formulation and computational aspects. In *Consitutive Laws for Engineering Materials. Theory and Applications, Vol. I*, pages 233–246. Elsevier, New York, 1987.

[191] J. C. Simo and R. L. Taylor. Consistent tangent operators for rate-independent elastoplasticity. *Com. Met. App. Mech. Eng.*, 48:101–118, 1985.

[192] M.P. Sklad. Modelling of part shape and deformation evolution in conventional forming of large sheet metal components. In *Numisheet'93, 2nd Int. Conf. Numerical Simulation of 3-D Sheet Metal Forming Processes*, Aug-Sep 1993.

[193] P. Smolinski. An explicit multi-time step integration method for second order equations. *Comp. Meth. App. Mech. Eng.*, 94:25–34, 1992.

[194] W. Sosnowski and E. Onate. Recent developments on the finite element analysis of sheet metal forming problems using a viscoplastic formulation. In *VDI-berichte 894: FE-simulation of 3-D sheet metal forming processes in automotive industry.* VDI-verlag, Düsseldorf, 1991.

[195] R. Sowerby, J. Duncan, and E. Chu. The modelling of sheet metal stampings. *Int. J. Mech. Sci*, 28(7):415–430, 1986.

[196] A.J.M. Spencer. *Continuum mechanics* . Longmad Group Limited, London, 1988.

[197] Stahl-Eisen Prüfblatt 1126. *Ermittlung der senkrechten Anisotropie (r-Wert) von Feinblech im Zugversuch, 1. Ausgabe.* Verlag Stahleisen, Düsseldorf, BDR, 1984.

[198] P. S. Steif. Delaminating stresses at the neck of a coated metal. *Int. J. Mech. Sci.*, 31(7):533–536, 1989.

[199] E. Stein, P. Steinmann, and C. Miehe. Computational modelling of instability phenomena in plasticity. In *Computational Plasticity, Fundamentals and Applications (COMPLAS IV)*, pages 481–508. Pineridge Press, Swansea, 1995.

[200] S. Stören and J. R. Rice. Localized necking in thin sheets. *Journal of the Mechanics and Physics of Solids*, 23:421–441, 1975.

[201] Y. S. Suh, F. I. Saunders, and R. H. Wagoner. Anisotropic yield functions with plastic-strain-induced anisotropy. *Int. J. Plasticity*, 12:417–438, 1996.

[202] L. Szabo and A. Kovacs. Numerical implementation of pragers kinematic hardening model in exactly integrated form for elasto-plastic analysis. *Comp. and Struc.*, 26(5):815–822, 1987.

[203] C. Teodisi, H. L. Cao, T. Ladreyt, and J. M . Detraux. Implicit versus explicit methods in the simulation of sheet metal forming. *VDI Berichte*, (894):601–627, 1991.

[204] W.T. Thomson. *Theory of vibration - with applications, 3rd edition* . Prentice Hall, Englewood Cliffs, New Jersey, 1988.

[205] S. P. Timoschenko and J. M. Gere. *Theory of elastic stability.* McGraw-Hill, New York, 1963.

[206] J. Tirosh and P Konvalina. On the hydrodynamic deep-drawing process. *Int. J. Mech. Sci.*, 31(6):871–880, 1989.

[207] Tisza. A knowledge based expert system for process planning of deep-drawing. In *The 4th ICTP Conference, Beijing*, 1994.

[208] P. Tong. *An Adaptive Dynamic Relaxation Method for Static Problems.* Unknown, Transportation Systems Center, Cambridge, USA, newer than 1977.

[209] G.J. Turvey and M. Salehi. Dr large deflection analysis of sector plates. *Computers and Structures*, 34(1):101–112, 1990.

[210] P. Underwood. Dynamic relaxation. In *Computational methods for transient analysis. Eds. T Belytschko & T.J.R. Hughes.*, pages 245–265. Elsevier, Amsterdam, 1982.

[211] M. Usuda, Y. Ishii, T. Fujii, K. Hashimoto, and H. Hayashi. Influencing factors on elastic constant of steel sheets. *IDDRG, Working Group Mettings, Lisboa*, 1994.

[212] C. C. Veerman, L. Hartman, and P.F. Peels, J.J amd Neve. Determination of appearing and admissible strains in cold-reduced sheets. *Sheet Metal Industries*, 11:678–680 and 692–694, 1975.

[213] J. H. Vogel and D. Lee. The automated measurement of strains from three-dimensional deformed surfaces. *Journal of Metals*, (2):8–13, 1990.

[214] R. H. Wagoner, E. Nakamachi, and Y. Germain. Experience with explicit and implicit finite element programs for sheet forming analysis. In *Modelling of Metal Forming Processes, eds. J. L. Chenot and E. Onate*, pages 131–138. Kluwer Academic Publishers, 1988.

[215] R. H. Wagoner, C. T. Wang, and E. Nakamachi. Quick analysis of sheet forming using sectional fe. In *Proc. 1st Japan Int. SAMPE Symp. Exhibition*, pages 695–700. SAMPE, 1989.

[216] R. H. Wagoner and D. Zhou. Analysis of sheet forming operation - recent numerical and experimental andvances. In *Numiform'92 - - Numerical methods in industrial forming processes*, pages 123–132. Balkema, Rotterdam, 1992.

[217] N. M. Wang and B. Budiansky. Analysis of Sheet Metal Stamping by a Finite Element Method . *J. Applied Mechanics*, 45:73–82, 1978.

[218] A. J. Wathen. On relaxation of Jacobi iteration for consistent and generalized mass matrix. *Communications in Applied Numerical Methods*, 7:93–102, 1991.

[219] T. Wertheimer. Numerical simulation of metal sheet forming processes . *VDI Berichte*, (894):517–548, 1989.

[220] M. L. Wilkins. Calculation of elastic-plastic flow. In *Methods of Computational Physics, Vol. 3, Ed. B Alder et al.* Academic Press, 1964.

[221] D. M . Woo. Analysis of the cup-drawing process. *J. Mech. Eng. Sci.*, 6(2):116–131, 1964.

[222] W. L. Wood. Note on Dynamic Relaxation. *Int. J. for Numerical Methods in Engineering*, 3:145–147, 1971.

[223] D. Y. Yang and Y. J. Kim. Analysis of hydrostatic bulging of anisotropic rectangular diaphragms by the rigid-plastic finite element method. *Journal of Engineering for Industry*, 109:148–154, 1987.

[224] S. Yossifon and J. Tirosh. Rupture instability in hydroforming deep drawing process. *Int. J. Mech. Sci.*, 27(9):559–570, 1985.

[225] J. Yu, D. Peric, and D. R. J. Owen. Adaptive finite element analysis of a strain localisation problem for the elasto-plastic Cosserat continuum. In *COMPLAS III*, pages 551–566. Swansea University, 1992.

[226] L. C. Zhang, T. X. Yu, and R. Wang. Investigation of Sheet Metal Forming by Bending - Part 1. Axisymmetric Elastic-Plastic Bending of Circular Sheets Pressed by Cylindrical Punches. *Int. J. Mech. Sci.*, 31(4):285–300, 1989.

[227] L. C. Zhang, T. X. Yu, and R. Wang. Investigation of Sheet Metal Forming by Bending - Part 2. Plastic Wrinkling of Circular Sheets Pressed by Cylindrical Punches . *Int. J. Mech. Sci.*, 31(4):301–308, 1989.

[228] Z. H. Zhong and L. Nilsson. A single surface contact-impact treatment based on the hierarchy-territory and the defence node algorithms. In *Numerical Methods in Engineering 92*, pages 127–134. Elsevier Science Publishers B. V., 1992.

[229] O. C. Zienkiewicz and R. L. Taylor. *The finite element method, Volume 1 & 2* . McGraw-Hill Book Company, Berkshire, England, 1989.

Chapter 11

Appendix A

On the following pages is given the fortran code used in the material routine. The coding does not include the options regarding instability (Hill's uniqueness criterion) and the options regarding forming limits. In order to ease the reading of the code there is added a number of comments.

```
      subroutine umat43(cm,eps,sig,hisv,dt,capa,etype,time)
      implicit double precision (a-h,o-z)
      real  cm(*),eps(*),sig(*),hisv(*),dt,capa,time
c Double precision has been used in the routine due to numerical
c problems when using single precision. As Dyna3d normally (previously)
c primary operated on single precision variables the real statement
c is necessary to take variables as input to the routine.
      character*(*) etype
      ymod=cm(1)                c Young Modulus
      pr  =cm(2)                c Poisson Ratio
      d1=eps(1)                 c Strain components 1-6
      d2=eps(2)
      d3=eps(3)
      d4=eps(4)                 c Shear strain (local x-y)
      d5=eps(5)
      d6=eps(6)
      roption=cm(5)             c Control options for: strain rate dep.
      voption=cm(6)             c Load scaling incl strain rate dep.
      soption=cm(7)             c Strain or work hardening
      yoption=cm(15)            c Choice of yield criterion
      hoption=cm(16)            c Choice of hardening option
c In the following the parameters for the available yield functions are set
      if(yoption.eq.2) then
      rta=cm(12)
      endif
      if(yoption.eq.3) then
      r00=cm(9)
      r45=cm(10)
      r90=cm(11)
```

```
      endif
      if(yoption.eq.4) then
      a=cm(17)
      a=a/2.
      c=cm(18)
      c=c/2.
      b=cm(19)
      h=cm(20)
      p=cm(21)
      endif
c In the following the parameters for options
c for the hardening rules available are set.
      if(hoption.eq.1) then
        sigini=cm(25)
        eh=cm(26)
      endif
      if(hoption.eq.2) then
        qk=cm(28)
        qm=cm(29)
      endif
      if(hoption.eq.3) then
        qk=cm(31)
        av=cm(32)
        qm=cm(33)
      endif
      if(hoption.eq.4) then
        qk=cm(34)
        qm=cm(35)
      endif
      if(hoption.eq.5) then
        sigini=cm(25)
        qk=cm(34)
        qm=cm(35)
      endif
c Take into account strain rate effects.
      fara=1.0
      if(roption.eq.1) then
        eref=cm(37)
        em=cm(38)
      endif
      if(roption.eq.2) then
        eref=cm(39)
        em=1./cm(40)
      endif
c Options for taking into account non-physical load scalings.
      if(voption.eq.1) then
        scsi=cm(23)*sin(3.141593/cm(24)*time)
```

```
        if(scsi.gt.1) scsi=1
      endif
      if(voption.eq.2) then
        scsi=cm(22)
      endif
c Calculate elastic coefficients.
      itp=cm(14)
      d11=ymod/(1.-pr**2)
      d12=pr*d11
      d33=.5*ymod/(1+pr)
c Plastic transversal strain increment initializing.
      st3=0
      fail=0
      g   =1.0/(1.0+pr)*ymod
      blk =-1.0/(1.0-2.*pr)*ymod
      wq1 =pr/((1.00+pr)*(1.00-2.00*pr))*ymod
      wq2 =.50*g
      wq3 =1.00/(wq1+2.00*wq2)
      wq4 =capa*wq2
      d3=-(sig(3)+wq1*(d1+d2))*wq3
c Take into account strain rate effects.
      if(roption.gt.0.5) then
        davg=-1.00/3.00*(d1+d2+d3)
        d1d=d1+davg
        d2d=d2+davg
        d3d=d3+davg
        if(dt.eq.0.0) then
          dti=0.0
        else
          dti=1./dt
        endif
        effs=dti*sqrt(2./3.*(d1d*d1d+d2d*d2d+d3d*d3d+0.5*d4*d4))
      endif
c Take into account load scalings.
      if(voption.eq.1.or.voption.eq.2) then
        effs=effs*scsi
      endif
      if(roption.eq.1) then
        fara=(effs/eref)**em
      endif
      if(roption.eq.2) then
        fara=(1+(effs/eref)**em)
      endif
c Compute trial stresses.
 39   continue
      sb1=sig(1)+d11*d1+d12*d2
      sb2=sig(2)+d12*d1+d11*d2
```

```
      sb4=sig(4)+wq2*d4
      sb5=sig(5)+wq4*d5
      sb6=sig(6)+wq4*d6
c Compute current value of the yield function.
 39   continue
      dep=0
      ep=hisv(1)
      if(hoption.eq.1) then
      sig0=fara*(sigini+eh*ep)
      endif
      if(hoption.eq.2) then
      if(ep.lt.1e-10) ep=1e-10
      sig0=qk*ep**qm
      endif
      if(hoption.eq.3) then
      sig0=fara*qk*(1-av*2.7182818**(qm*ep))
      endif
      if(hoption.eq.4) then
      epi=(ymod/qk)**(1.00/(qm-1.00))
      sig0=fara*qk*(epi+ep)**qm
      endif
      if(hoption.eq.5) then
      epi=(sigini/qk)**(1./qm)
      sig0=fara*qk*(epi+ep)**qm
      endif
c Compute current value of equivalent stress.
      if(yoption.eq.1) then
c von Mises
      bj1=sqrt(sb1**2+sb2**2-sb1*sb2+3*sb4**2)
      endif
      if(yoption.eq.2) then
c transversal anisotropic version of Hill 48
      bj1=sqrt(sb1**2+sb2**2-2*rta/(rta+1)*sb1*sb2+
     1      +2*(2*rta+1)/(rta+1)*sb4**2)
      endif
      if(yoption.eq.3) then
c in-plane anisotropic version of Hill 48
      ha1=1
      ha2=2./(1./r00+1)
      ha3=(1./r90+1)/(1/r00+1.)
      ha4=2*(r45+0.5)*(1./r00+1/r90)/(1./r00+1)
      bj1=sqrt(ha1*sb1**2-ha2*sb1*sb2+ha3*sb2**2+ha4*sb4**2)
      endif
      if(yoption.eq.4) then
c Barlat yield criterion:
      bk1=0.5*(sb1+h*sb2)
      bk2=sqrt(0.25*(sb1-h*sb2)**2+p**2*sb4**2)
```

```
      bj1=((a*(abs(bk1+bk2))**b+a*(abs(bk1-bk2))**b+
     1     c*(2*bk2)**b))**(1/b)
      endif
c Check the yield criterion, evt. update stresses.
      ak1=bj1-sig0
      scle=.500+sign(0.50,ak1)
      if (scle.eq.0.0) then
        sig(1)=sb1
        sig(2)=sb2
        sig(3)=0.
        sig(4)=sb4
        sig(5)=sb5
        sig(6)=sb6
        eps(3)=d3
        return
      endif
      a2s3=1.15470054
c Iterate to fulfil yield criterion.
      do 300 iter=1,itp
      if(yoption.eq.1) then
c evaluate plastic strain direction von Mises
      sigvM=sqrt(sb1**2+sb2**2-sb1*sb2+3*sb4**2)
      a1=(sb1-0.5*sb2)/sigvM
      a2=(sb2-0.5*sb1)/sigvM
      a3=3*sb4/sigvM
      endif
      if(yoption.eq.2) then
c evaluate plastic strain direction transversal Hill
      sigtvH=sqrt(sb1**2+sb2**2-2*rta/(rta+1)*sb1*sb2+
     1      +2*(2*rta+1)/(rta+1)*sb4**2)
      a1=(2*sb1-2*rta/(rta+1)*sb2)/2./sigtvH
      a2=(2*sb2-2*rta/(rta+1)*sb1)/2./sigtvH
      a3=(4*(2*rta+1)/(rta+1)*sb4)/2./sigtvH
      endif
      if(yoption.eq.3) then
c evaluate plastic strain direction in-plane anisotropic Hill
      sigipH=sqrt(ha1*sb1**2-ha2*sb1*sb2+ha3*sb2**2+ha4*sb4**2)
      a1=(2*ha1*sb1-ha2*sb2)/2./sigipH
      a2=(2*ha3*sb2-ha2*sb1)/2./sigipH
      a3=(2*ha4*sb4)/2./sigipH
      endif
      if(yoption.eq.4) then
c evaluate plastic strain direction
      sa=bk1+bk2
      sb=bk1-bk2
      sc=bk2
      bdif=1/b-1
```

```
      f1=(a*abs(sa)**b+a*abs(sb)**b+c*(2*bk2)**b)**bdif
      f2=a*sa*abs(sa)**(b-2)
      f3=a*sb*abs(sb)**(b-2)
      f4=c*2**b*bk2**(b-1)
      a1=f1*(f2*(0.5+(sb1-h*sb2)/4./bk2)
     1      +f3*(0.5-(sb1-h*sb2)/4./bk2)
     2      +f4*(sb1-h*sb2)/4./bk2)
      a2=f1*(f2*(h*0.5-h*(sb1-h*sb2)/4./bk2)
     1      +f3*(h*0.5+h*(sb1-h*sb2)/4./bk2)
     2      +f4*(-h)*(sb1-h*sb2)/4./bk2)
      a3=2*f1*sb4/bk2*(f2-f3+f4)*p**2/2.
      endif
c calculate bsig
       if(soption.eq.1) then
         bsig=a2s3*sqrt(a1**2+a2**2+a1*a2+a3**2)
       endif
       if(soption.eq.2) then
         bsig=(sb1*a1+sb4*a3+sb2*a2)/bj1
       endif
c calculate actual hardening modul
      if(hoption.eq.1) then
        hdot=fara*eh
      endif
      if(hoption.eq.2) then
        if(ep.lt.1e-10) ep=1e-10
        hdot=fara*qm*qk*ep**(qm-1)
      endif
      if(hoption.eq.3) then
        hdot=-fara*qk*av*qm*2.7182818**(qm*ep)
      endif
      if(hoption.eq.4.or.hoption.eq.5) then
        hdot=fara*qm*qk*(epi+ep)**(qm-1)
      endif
       adot=bsig*hdot
c calculate C*a
       atca=ymod/(1-pr**2)*(a1*(a1+pr*a2)+a2*(a1*pr+a2)
     1      +a3*a3*0.5*(1-pr))
       dlam=ak1/(atca+adot)
c relax stresses
       dy1=dlam*ymod/(1-pr**2)
       sb1=sb1-dy1*(a1+a2*pr)
       sb2=sb2-dy1*(a1*pr+a2)
       sb4=sb4-dy1*a3*0.5*(1-pr)
       dep=dlam*bsig
c update plastic strain increment
       st3=st3-dlam*(a1+a2)
      if(yoption.eq.1) then
```

```
        bj1=sqrt(sb1**2+sb2**2-sb1*sb2+3*sb4**2)
      endif
      if(yoption.eq.2) then
        bj1=sqrt(sb1**2+sb2**2-2*rta/(rta+1)*sb1*sb2+
     1        +2*(2*rta+1)/(rta+1)*sb4**2)
      endif
      if(yoption.eq.3) then
        ha1=1
        ha2=2./(1./r00+1)
        ha3=(1./r90+1)/(1/r00+1.)
        ha4=2*(r45+0.5)*(1./r00+1/r90)/(1./r00+1)
        bj1=sqrt(ha1*sb1**2-ha2*sb1*sb2+ha3*sb2**2+ha4*sb4**2)
      endif
      if(yoption.eq.4) then
        bk1=0.5*(sb1+h*sb2)
        bk2=sqrt(0.25*(sb1-h*sb2)**2+p**2*sb4**2)
        bj1=(a*(abs(bk1+bk2))**b+a*(abs(bk1-bk2))**b+
     1       c*(2*bk2)**b)**(1./b)
      endif
      if(hoption.eq.1) then
        sig0=fara*(sigini+eh*(ep+dep))
      endif
      if(hoption.eq.2) then
        sig0=qk*(ep+dep)**qm
      endif
      if(hoption.eq.3) then
        sig0=fara*qk*(1-av*2.7182818**(qm*(ep+dep)))
      endif
      if(hoption.eq.4.or.hoption.eq.5) then
        sig0=fara*qk*(epi+ep+dep)**qm
      endif
      ak1=bj1-sig0
      ep=ep+dep
      if(abs(ak1).lt.5e-5) then
        go to 310
      endif
300   continue
      print*,'Convergency not obtained at',time,'within',iter,'iterations'
      print*,'Error',ak1
c Upate of variables
310   hisv(1)=ep
      d3=st3-pr/ymod*(sb1-sig(1)+sb2-sig(2))
      sig(1)=sb1
      sig(2)=sb2
      sig(3)=0.
      sig(4)=sb4
      sig(5)=sb5
```

```
sig(6)=sb6
eps(3)=d3
return
end
```

Options in the material routine

In order to utilize the routine a total of 3 choices must be performed, the remaining may be taken as default. The first option is the choice of the yield criterion. In the routine it corresponds to the value of "yoption":

- yoption=1 von Mises' yield criterion
- yoption=2 Hill's 48 yield criterion for in-plane isotropy
- yoption=3 Hill's 48 yield criterion for in-plane anisotropy
- yoption=4 Barlat's 2D yield criterion

The second choice is the specification of the hardening law (hoption):

- hoption=1 linear hardening
- hoption=2 Hollomon hardening (including the initial yield strength)
- hoption=3 Voce hardening (including the initial yield strength)
- hoption=4 Hollomon-Swift (the yield strength estimated from C, n and E)
- hoption=5 Hollomon-Swift with the possibility to specify the initial yield strength.

There is a possibility to choose between work and strain hardening. The option is in the routine "soption":

- soption=1 strain hardening
- soption=2 work hardening

The next (optional) option is to take strain rate effects (roption) into account:

- roption=0 no strain rate dependency (default value)

  vspace-3mm

- roption=1 Norton strain rate model

  vspace-3mm

- roption=2 Wagoner-Swift model

Finally, there is a possibility to use load scaling and at the same time take strain rate effect into account (voption).

- roption=1 inverse sine scaling (assumed constant physical loading and a sine shaped velocity profile in the simulations)

  vspace-3mm

- roption=2 constant scaling (assumed sine profile in both the physical and the modelled loading rate)

Card specifications

To specify the material a standard input deck is used (see LS-Dyna3d v930, manual). The difference compared to normal material models is that an additional card must be specified in order to identify parameters which are needed outside the material routine. Furthermore, the number of user materials must be specified in the input deck (card 1, column 70).

—-1—-	—-2—-	—-3—-	—-4—-	—-5—-	—-6—-	—-7—-	—-8—-
E[MPa]	ν	β [MPa]	G [MPa]	roption	voption	soption	
R_{00}	R_{45}	R_{90}			itp	yoption	hoption
a	c	M	h	p	scale f.	scale f.	T [msec]
σ_0 [MPa]	E_p [MPa]	σ_0 [MPa]	C	m	σ_0 [MPa]	B	A
m	C	m	n	$\dot{\epsilon}_{ref}$	n		
3	0	1	0				

Table 11.1: *The table shows the position of the constitutive parameters and control settings.*